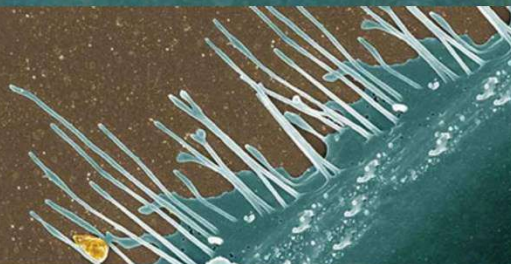


26º

**CONGRESSO
BRASILEIRO DE
MICROSCOPIA**

**4 a 7
DE JUNHO
2017
Búzios • RJ**

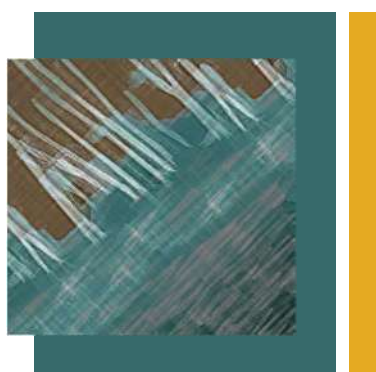


CADERNO DE ANAIS

**RESUMOS APRESENTADOS NO
26º CONGRESSO BRASILEIRO DE
MICROSCOPIA E MICROANÁLISE
DA SBMM. BÚZIOS - RJ, 2017**



CADERNO DE ANAIS



**RESUMOS APRESENTADOS NO
26º CONGRESSO BRASILEIRO DE
MICROSCOPIA E MICROANÁLISE
DA SBMM. BÚZIOS - RJ, 2017**



DIRETORIA DA SBMM (2016-2018)

Presidente

Kildare Rocha de Miranda (UFRJ)

Vice-Presidente (Ciências de Materiais)

Daniel Lorscheitter Baptista (UFRGS)

Vice-Presidente (Ciências Biológicas)

Celso Vataru Nakamura (UEM)

Tesoureiro

André Linhares Rossi (CBPF)

Secretário-Geral

Leonardo Tavares Salgado (IPJBRJ)

Coordenadora de Divulgação

Marcia Attias (UFRJ)

COMISSÃO ORGANIZADORA LOCAL

Anderson Franzen (UEZO/RJ)

André Gomes (IBQM/UFRJ)

André Linhares Rossi (CBPF/RJ)

André Luiz Pinto (CBPF/RJ)

Carlos Achete (Inmetro/RJ)

Celso B. de Sant'Anna Filho (Inmetro/RJ)

Claudia Franca Barros (JBRJ)

Eduardo José Lopes Torres (UERJ/RJ)

Fernando Pereira de Almeida (CENABIO/UFRJ)

Guillermo Solórzano (PUC/RJ)

Kildare Rocha de Miranda (IBCCF/UFRJ)

Leonardo Salgado (JBRJ/RJ)

Luiz Henrique de Almeida (COPPE/UFRJ)

Marcia Attias (UFRJ)

Marlene Benchimol (UNIGRANRIO/RJ)

Sergio Seabra (UEZO/RJ)

Suzana Corte-Real Farias (IOC/Fiocruz/RJ)

Wendell Girard-Dias (IOC/Fiocruz/RJ)

EDIÇÃO DOS ANAIS

Emerson Campos Gonçalves (UFES)

COMISSÃO CIENTÍFICA NACIONAL

BIOLOGIA

Ana Maria Martinez (ICB/UFRJ)
André Gomes (IBQM/UFRJ)
Ana Claudia G. Araújo (CENARGEN/EMBRAPA)
Carlos Lenz Cesar (Unicamp/SP)
Claudia Franca Barros (JBRJ/RJ)
Edilene Oliveira da Silva (UFPA/PA)
Flávio Costa Miguens (UENF/RJ)
Gilberto Weissmuller (IBCCF/UFRJ/RJ)
Hernandes F. Carvalho (UNICAMP/SP)
Kildare Miranda (IBCCF/UFRJ)
Leonardo Tavares Salgado (JBRJ/RJ)
Jacenir Reis dos Santos Mallet (IOC/Fiocruz/RJ)
Marcos Farina (ICB/UFRJ)
Maura da Cunha (UENF/RJ)
Maurílio José Soares (Fiocruz/PR)
Paulo M. Bisch (IBCCF/UFRJ/RJ)
Sonia N. Bao (UNB/DF)
Rodrigo Portugal (LNNANO/SP)
Rossiane Vommaro (IBCCF/UFRJ/RJ)
Ulysses Lins (IMPPG/UFRJ)

MATERIAIS

Alberto Moreira Jorge Junior (UFSCar/SP)
André Luiz Pinto (CBPF/RJ)
Ângelo Fernando Padilha (EDUSP/SP)
Bráulio Soares Archanjo (Inmetro/RJ)
Carlos Achete (INMETRO/RJ)
Daniel Ugarte (UNICAMP/SP)
Fernando Galembeck (UNICAMP/SP)
Gloria Dulce de Almeida Soares (UFRJ/RJ)
Guillermo Solórzano (PUC/RJ)
Jefferson Bettini (LNNANO/SP)
Luiz Henrique de Almeida (COPPE/UFRJ)
Maria do Carmo Gonçalves (UNICAMP/SP)
Paulo F. P. Fichtner (UFRGS/RS)
Walter Botta Junior (UFSCar/SP)

TODOS OS DIREITOS RESERVADOS.

SOCIEDADE BRASILEIRA DE MICROSCOPIA E MICROANÁLISE - SBMM

Instituto de Biofísica Carlos Chagas Filho – UFRJ. Av. Carlos Chagas Filho, 373 edifício do CCS Bloco G. CEP 21941-902 - Rio de Janeiro - RJ Brasil

Congresso Brasileiro de Microscopia e Microanálise da SBMM (26. : 2017 : Búzios, RJ)

Anais do 26º Congresso Brasileiro de Microscopia e Microanálise da SBMM, 4 a 7 de setembro de 2017 em Búzios/RJ [recurso eletrônico, PDF] – Rio de Janeiro, UFRJ, SBMM, 2017.

Edição digital

Disponível em:

ISSN –

1. Microscopia. 2. Microanálise. I. Título.

PATROCÍNIO



APOIO



SUMÁRIO

PARTE 1

COMUNICAÇÕES ORAIS - BIOLOGIA

Study of HA Nanoparticles Internalization on SaOS-2 Cell Line by Dual Beam Microscopy.....	20
<i>Longuinho MM, Tanaka M, Farina M, Rossi AL</i>	
Cytotoxic Effects Of Novalurom® Insecticide In The Midgut Of The Silkworm Bombyx mori (Lepidoptera: Bombycidae).....	22
<i>Santorum M, Reis GH, Pedroso OC, Brancalhão RMC, Scudeler EL, Santos DC</i>	
Evaluation Of Different Sample Preparation Methods For Glomerular Morphological Evaluation: Coated Or Uncoated?.....	24
<i>Santos PF, De Souza DB, Torres EJJ, Sampaio FJB, Costa WS, Gregorio BM</i>	
Plunge freezing as a cryofixation alternative which maintains the morphological characteristics of animal tissue architecture	26
<i>Dias FF, Kitten GT, Silva ER</i>	
Dyspermic fusion protocol for androgenetic induction in the <i>Astyanax altiparanae</i> (Garutti & Britski): ultrastructural analysis	28
<i>Pereira-Santos M, Yasui GS, Spandri VC, Nascimento NF, Silva RC, Senhorini JA, Nakaghi LSO</i>	
Three-dimensional Visualization of Ion Nanodomains in Subcellular Compartments.....	30
<i>Girard-Dias W, De Souza W, Miranda K</i>	
Calcium Silicate Hydrated Incorporated With Silver Ions For Biomaterials Application	32
<i>Yoshihara NMA, Castro KLS, Ribeiro AR, Archanjo BS, Achete CA</i>	
Nanotoxicological evaluation of nano-bio interface using 3D bone cell models.....	34
<i>Gemini-Piperni S, Souza W, Archanjo BS, Rossi AL, Rocha LA, Borojevic R, Granjeiro JM, Ribeiro AR</i>	
The Improvement Of Osteoblast Adhesion And Proliferation on TiO ₂ Nanotubes Coated With Lectin From <i>Oreochromis niloticus</i>	36
<i>Dos Anjos KFL, De Melo JV, De Matos AB, Machado G, Da Silva CDC, Coelho LCBB, De Figueiredo RCBQ</i>	
Influence of pH on the size of gold nanoparticles synthesized using <i>Virola oleifera</i> extract.....	38
<i>Contreras LA, Oliveira JP, Guimarães MCC</i>	
Structural Colors in <i>Chalcopteryx rutilans</i> Male Dragonfly Wings	40
<i>Valeriano WW, Andrade RR, Vasco JP, Neves BRA, Rodrigues WN, Guimarães PSS, Silva ER, Machado ABM</i>	
Biomineralization Process and Time Resolved Oxidation Study on Magnetotactic Bacteria	42
<i>Werckmann J, Cypriano J, Lefèvre CT, Dembelé K, Ersen O, Bazylnski DA, Lins U, Farina M</i>	
Cohesive Geometry of <i>Cryptococcus neoformans</i> Adhesion Contributes to Flower-Like Biofilms Formation	44
<i>Lopes W, Vainstein MH, Araújo GR, Carvajal SF, Staats CC, Almeida MC, Schrank A, Kmetzsch L, Vainstein MH</i>	

High-resolution and quantitative three-dimensional Analysis of Plasmodium chabaudi Hemozoin Crystals46

Wendt C, Gomes F, Souza W, Miranda K

Ultrastructural Identification of Flagellar Ectosomes-Like Structures in the Protists Tritrichomonas foetus and Trichomonas vaginalis48

Pereira-Neves A

Impact Of Dengue Virus Serotype 3 (DENV-3) Infection On Lung Of BALB/c Mice: A Histopathological And Ultrastructural Analysis.....50

Caldas GC, Silva MAN, Jácome FC, Rasinhas AC, Almeida ALT, Barth OM, Barreto-Vieira DF

Ultrastructural Analysis Of Alterations Caused By A Dengue Virus Secondary Infection In BALB/c Mice Hearts.....52

De Souza DDC, Jácome FC, Caldas GC, Silva MAN, Rasinhas AC, Almeida ALT, Barth OM, Barreto-Vieira DF

Multivesicular Bodies In The Protozoan Parasite Giardia intestinalis: The Peripheral Vesicle Gathers One More Function54

Midlej V, Souza W, Benchimol M

PARTE 2

COMUNICAÇÕES ORAIS – MATERIAIS

Superconductivity in Bi-Ni bilayers: a High Resolution Transmission Electron Microscopy Study..57

Xing YT, Liu LY, Merino IC, Micklitz H, Franceschini DF, Baggio-Saitovitch E, Solórzano IG

Using DFT and STEM for structural and electronic properties of LaAlO₃/Ge system 59

Arrouvel C, Campos APC, Mortada H, Dentel D, Derivaz M, Bischoff JL, Werckmann J

New Methodology Of Precipitates Characterization In 2.25Cr-1Mo Steels..... 61

Lima WF, de Almeida LH, Furtado HC

Microscopy Aided by Image Processing as a Tool for Assessing Aging and Creep Damage in HP-Modified Steel Reformer Tubes.....63

Guimarães AV, Nascimento MLC, Araujo LS, Almeida LH, Queiroz FS

Charaterization of the depostion of SmBaCuO superconducting ceramic on lean duplex stainless steel UNS S32304 65

Passos CAC, Lepich R, Miranda KC, Simões J, Passamai Jr JL, Orlando MTD

Microstructural and Fractographic Analysis of AISI 317L Steel Thermally Aged at 450°C..... 66

Farneze HN, Tavares SSM, Pardal JM, Cunha RPC, Vinhosa RA, Rangel FLC

Influence of Zirconium Concentration on Duplex Microstructure Formation in β/β' -alumina Electrolytes..... 68

Rodrigues DC, Souza DPF

718 Inconel Characterization During Oxidation Assisted Intergranular Cracking by Scanning Electron Microscopy and EDS Mapping 70

Varela A, Deus HD, Rezende MC, Almeida LH

Thermal failure analysis in multilayer ceramic capacitors..... 72

Fonseca RT, Antonelli E, Matos CP

Quantitative characterization of nanostructured materials using TKD in SEM.....	74
<i>Palasse L, Goran D</i>	
Using EBSD to Better Describe a Cr-Mo Ferritic-Bainitic Microstructure.....	76
<i>Pinto AL, Silva CL, Alves FP</i>	
Nanoscale Orientation Mapping Characterization of Nanocrystalline Phases in Metallic Alloys.....	78
<i>Afonso CRM, Amigó V, Botta WJ, Kiminami CS</i>	
Orientation and Phase Mapping In the Transmission Electron Microscope Using Diffraction Spot Recognition in Several Kinds of Materials.....	80
<i>Jorge Jr AM, Coimbra DD, Botta WJ</i>	
An SEM-EDS-assisted LA-ICP-MS Study of REE-Bearing Minerals From the Cerro La Tuna Tourmalinite, Paso Del Dragón Complex, Northeastern Uruguay.....	82
<i>Garda GM, Andrade S, Sayeg IJ, Peel-Canabal</i>	
Effect of pH on Liquid Crystalline Interface from Crude Oil Emulsion Fractions.....	84
<i>Duncke ACP, Freitas GB, Soares IF, Silva AB, Barbato CN, Nele</i>	
SEM Imaging Applied to U-Pb Geochronology in Zircon of Espera Feliz Region: Ages of Protoliths, Magmatism and Metamorphism.....	86
<i>Cardoso LMC, Geraldes MC, Bonifacio JF, Tavares AD, Alves MI, Rodrigues IR</i>	
Automatic Characterization of Iron Ore through Image Processing and Analysis.....	88
<i>Iglesias JCA, Paciornik S, Augusto KS, Gomes OFM, Domingues ALA, Casagrande C</i>	
Microestrutural Evolution of Nickel-Based Superalloy Processed By Equal Channel Angular Pressing (ECAP).....	90
<i>Dias RAF, Monteiro WA</i>	
EELS 3D Tomography of Plasmonic Nanoantennas.....	92
<i>Archanjo BS</i>	
Nanostructured Alpha-NiCe Mixed Hydroxide Electrodes for Sensitive Amperometric Prednisone Sensors.....	93
<i>Gonçalves JM, Guimarães RR, Brandão BBNS, Saravia LPH, Saravia LPH, Rossini PO, Bernades JS, Bertotti M, Agnes L, Araki K</i>	
Structural and Morphological Characterization of Ag/TiO ₂ Nanocomposites Using High Resolution Transmission Electron Microscopy.....	95
<i>Gomes GHM, Mohallem NDS</i>	
Magnetic Vortices in Nanostructures Made by Lithography.....	97
<i>Sampaio LC, Brandão J, Froes D, Ramon P, Soledade P, Pinto A, Garcia F, Sinnecker JP</i>	
Electron Beam Induced Current Characterization of Dye Sensitized Solar Cells.....	99
<i>Lima CF, Kohlrausch EC, Santos ML, Vasconcellos MA</i>	
3D X-Ray Microscopy Analysis of Nanocomposite Bamboo with Different Silver Nanofillers.....	101
<i>Pandoli O, Martins RS, Paciornik S, Mauricio MHP, Barbosa BA, Valiente H, Letichevski S, Koller SML, Ghavami K</i>	
Porosity Characterization of Iron Ore Pellets by X-Ray Microtomography.....	103
<i>Augusto KS, Paciornik S</i>	

Study of Iron Sulfide Phases Formation with Russian Doll Sulfurization Apparatus.....	105
<i>Silva MFO, Souza LP, De Oliveira S, Ferlauto AS, Rodrigues WN</i>	
Niobium Addition on Ti-Nb Alloys anodized: Effect on the Microstructure and Nanotubes Growth	107
<i>Da Luz AR, Kuroda PB, Lepienski CM, Grandini CR, Kuromoto NK</i>	
Casting, Rolling and Friction Stir Welding in Magnesium alloys with Mischmetal Addition	109
<i>Silva EP, Alfaro U, Ferrinho VP, Requena GC, Pinto HC</i>	
Influence of Processing Routes on δ Phase Precipitation, Grain Boundary Character Distribution and Grain Size of Superalloy 718.	111
<i>Medeiros MAR, Guimarães AV, Pinto AL, Araujo LS</i>	
Phase Characterization of AlFeCrNiCoBx High Entropy Alloys with Minor Boron Content	113
<i>Zepón G, Coimbrão DD, Ferrari V, Wolf W, Botta WJ</i>	
Retained Austenite Volume Fraction in 52100 Steel Determined by Electron Backscatter Diffraction	115
<i>Perez G, Archanjo BS, Kuznetsov O, Achete CA</i>	
Optically Efficient Probes for Tip-Enhanced Raman Spectroscopy.....	117
<i>Vasconcelos TL, Archanjo BS, Oliveira BS, Jorio A, Achete CA, Caçado LG</i>	

PARTE 3

COMUNICAÇÕES ORAIS – OUTROS

Raman Spectroscopy in the Study of Coralline Algae Mineralogy from the Brazilian Shelf	120
<i>Carvalho RT, Rocha GM, Bahia RG, Karez CS, Amado Filho GM, Salgado LT</i>	
Dolomite in Abrolhos reefs, Northeast Brazil	122
<i>Ayres AEA, Giannini PCF, Nash M, Sayeg IJ, Torrano-Silva BN, Campos V</i>	
Bone Biofabrication From Human Adipose Stem Cell Spheroids Seeded Into Pla/Cha 3D Printing Scaffold	124
<i>Kronemberger GS, Silva KR, Rossi AM, Granjeiro JM, Baptista LS</i>	
Ichthyophthirius multiphiliis in Carassius auratus (Goldfish) - Ultrastructure Observation of Parasite Stage and Host Cells	126
<i>Moyses CRS, Spadacci-Morena DD, Xavier JG, Alvares-Saraiva AM, Rocha PRDA, Lallo MA</i>	
Titanium Dioxide Nanoparticles Identification In Fish Cells: Subcellular Internalization	128
<i>Souza IC, Mendes VAS, Duarte ID, Matsumoto ST, Elliot M, Wunderlin DA, Monferrán MV, Fernandes MN</i>	

PARTE 4

PÔSTERES – BIOLOGIA

Morphological And Morphometrical Analysis Of The Initial Segment And Cauda Of Epididymis In Obese Wistar Rats Submitted To Duodenal-Jejunal Bypass Surgery.....	131
<i>Retameiro ACB, Scarton SRS, Beu CCL</i>	
Biological Evaluation of 2,1,3-Benzoselenodiazole Derivatives as New Lipids Probes for Cellular Imaging.....	133
<i>Barbosa ALA, Correa JR, Medeiros IR, Andrade LP, Brenno AD</i>	

The Use of Scanning Electron Microscopy to Characterize Veterinary Dental Pathologies	135
<i>Zeemann L, Zeemann A</i>	
Cerebral Palsy In Rats Alters The Ultrastructure Of Striated Skeletal Muscle.....	137
<i>Barbosa A, Buratti P, Covatti C, Maximo DS, Centenaro LA, Ribeiro LC, Torrejais MM</i>	
Analysis of Skeletal Muscle Fibers of Obese Wistar Rats Submitted to Duodenojejunal Bypass .	139
<i>Barbosa A, Oliveira MC, Buratti P, Kuhn C, Covatti C, Balbo SL, Torrejais MM</i>	
Ezrin Expression In Equine Endometritis - Preliminary Results	141
<i>Batista BPS, Silva KVGC, Leite JS, Ferreira AMR</i>	
Chronic Equine Endometritis: HER-2 Receptor Expression - Preliminary Results	143
<i>Batista BPS, Silva KVGC, Leite JS, Ferreira AMR</i>	
Histopathological Analysis of Gills as an Indicator of the Aquatic Environment Quality in South Brazilian Grasslands	145
<i>Zwetsch BZ, Souza MS, Corte RBD, Gehlen G</i>	
Effects of Type 1 Diabetes Mellitus on Developing Enamel	147
<i>Silva BLL, Medeiros DL, Soares AP, Line SRP, Pinto MGF, Soares TJ, Do Espírito Santo AR</i>	
The Effect of Type 1 Diabetes Mellitus on Mature Enamel Structure and Physicochemical Properties	149
<i>Silva BLL, Medeiros DL, Soares AP, Line SRP, Pinto MGF, Soares TJ, Do Espírito Santo AR</i>	
Differentiation of the species of the sturtevanti subgroup (saltans group, Drosophila) based on morphological characteristics analyzed by SEM.....	151
<i>Roman BE, Madi-Ravazzi</i>	
Finasteride alters female prostate initial development.....	153
<i>Sanches BDA, Maldarine JS, Zani BC, Vilamaior PSL, Taboga SR</i>	
Pre- And Post-oviposition Egg Morphology And Its Interaction with Sperm Cell In <i>Loxosceles intermedia</i> (ARANEAE: SICARIIDAE).....	155
<i>Dos Reis CA, Soares MAM, Gomes JR, Costa-Ayub CLSA</i>	
The Effects Of Chitosan and Alginate Membranes Doped With Extract Of <i>Ilex paraguariensis</i> On Cell Proliferation During The Wound Skin Healing Process	157
<i>Correa FAC, Fontes ALG, Dos Reis CA, Omar NF, Soares MAM, Pereira AV, Gomes JR</i>	
An Evaluation of an Animal Model of Cerebral Palsy: the Effects on the Ultrastructure of the Extensor Digitorum Longus Muscle	159
<i>Kuhn C, Covatti C, Buratti P, Centenaro LA, Brancalhão RMC, Torrejais MM</i>	
Morphological Study of the Extensor Digitorum Longus in the Offspring of Rats Submitted or Not to Roux-en-Y Gastric Bypass – RYGB.....	161
<i>Kuhn C, Buratti P, Covatti C, Beraldi EJ, Balbo SL, Torrejais MM</i>	
Ultrastructural Aspects of <i>Trichodina heterodentata</i> in <i>Carassius auratus</i> (Goldfish) Gills	163
<i>Moyses CRS, Spadacci-Morena DD, Xavier JG, Alvares-Saraiva AM, Lallo MA</i>	
Neem Oil Compromises The Cellular Cortex Of The Midgut Cells Of <i>Ceraeochrysa claveri</i> (Neuroptera: Chrysopidae)	165
<i>Silva CMM, Carvalho SF, Scudeler EL, Santos DC</i>	

Role of Native Microorganisms in Iron and Manganese Cycling in Doce River and Tributaries Affected by Mining Waste from Collapsed Fundão Dam	167
<i>Keim CN</i>	
Biological Activity of the Combination of Benzonidazole with Copaiba Oil (<i>Copaifera Martii</i>) and Kaurenoic Acid against <i>Trypanosoma Cruzi</i>	169
<i>Kian D, Lancheros CAC, Pavanelli W, Pinge-Filho P, Arakawa NS, Da Veiga Junior VF, Nakamura CV, Yamada-Ogatta SF, Yamauchi LM</i>	
Evaluation of Ectonucleotidase Activity and NTPDase-1 Immunolocalization in Different Strains and Clones of <i>TRYPANOSOMA CRUZI</i>	171
<i>Neves-do-Valle MAA, Oliveira CM, Santos HCP, Menezes WA, Bressan GC, Almeida MR, Fietto JLR</i>	
Notch inhibition enhances myoblast proliferation during chick myogenesis.....	173
<i>Andrade IR, Manoel Costa, Mermelstein C</i>	
Extracellular Matrix Affects Focal Adhesion Kinase (FAK) Localization in Prostatic Smooth Muscle Cells	175
<i>Rodríguez DO, Santos AM, Carvalho HF</i>	
Biological Activity of the Compound Synthetic 4-[(2e)-N'-(2,2'-bithienyl-5-methylene)hydrazinecarbonyl]-6,7-dihydro-1-phenyl-1h-pyrazolo[3,4-d]pyridazin-7-one in Promastigotes of <i>Leishmania infantum</i>	177
<i>Volpato H, Lazarin-Bidóia D, Scariot DB, Jacomini AP, Rosa FA, Ueda-Nakamura T, Rubira AF, Soares EFP, Souza MC, Borges O, Nakamura CV</i>	
In vitro Anti- <i>Leishmania</i> Activity of a Synthetic Compound Loaded in Glucan Particles Extracted from the Cell Wall of <i>Saccharomyces cerevisiae</i>	180
<i>Volpato H, Lazarin-Bidóia D, Scariot DB, Jacomini AP, Rosa FA, Ueda-Nakamura T, Rubira AF, Soares EFP, Souza MC, Borges O, Nakamura CV</i>	
Mammary Adenocarcinoma Cells Diminished Functional Activity of RAW264.7 Macrophages....	182
<i>Silvestro DM, Carvalho JR, Albuquerque T, Konno TC, Bonamin L, Lallo MA, Hurtado ECP</i>	
3D study of the evolution of the tachyzoite form of <i>Toxoplasma gondii</i> inside the host cell	184
<i>Dolzani D, Attias M</i>	
Biological evaluation of lapachones derivatives as the new mitochondrial probes for cellular imaging	186
<i>Brandão DC, Santos F, Dias GG, Freitas RP, Santos LS, Lima GF, Duarte HA, Simone CA, Rezende LMSL, Vianna MJX, Neto BAD, Silva Júnior EN, Correa JR</i>	
<i>Physalis angulata</i> promotes death of promastigotes and amastigotes of <i>Leishmania (Leishmania) infantum chagasi</i>	188
<i>Pereira SWG, da Silva BJM, Rodrigues APD, Silva EO</i>	
Epifluorescence And Laser Scanning Confocal Microscopy Applications at Universidade Federal De Lavras – UFLA	190
<i>Alves E, Moreira SI, Silva FF, Nery EM, Lopes SL, Castro EM, Ferreira AN</i>	
Preliminary studies on the localization and ultrastructural characterization of processing bodies in <i>Trypanosoma cruzi</i>	192
<i>Glejzer E, Girard-Dias W, De Souza W, Miranda K</i>	
Antifungal Activity of Lectin from <i>Alpinia purpurata</i> Inflorescence against <i>Candida</i>	194
<i>Ferreira GRS, Brito JS, Procópio TF, Lima BJRC, Bento EFL, Coelho LCBB, Paiva PMG, Soares T, Moura MC, Napoleão TH</i>	

Trypanosoma cruzi Reservosomes Change In Number And Volume Before Cell Division.....	196
<i>Gama FS, Alcântara CL, Alves AA, Cunha-e-Silva NL</i>	
Microscopy of Light and Confocal Laser Scanning of Gelidium floridanum Tetraspores Germination Treated with EGTA	198
<i>Bouvie F, Tomazi D, Kreuch M, De Bortoli N, Filipin E, Batista D, Ouriques L, Bouzon Z, Simioni C</i>	
Histopathological Analysis of livers of Danio rerio Exposed to Manganese.....	200
<i>Rodrigues GZP, Zwetsch BG, Gehlen G</i>	
Analysis of Nuclear Morphology for Evaluation of Manganese Induced Genotoxicity in Danio rerio	202
<i>Rodrigues GZP, Panizzon J, Gehlen G</i>	
HRTEM and STEM Tomography of Nano-sized Magnetic Crystal Produced by Bacteria.....	204
<i>Vargas G, Cypriano J, Vieira DGI, Leão P, Abreu F, Lins U</i>	
Histopathological Evaluation of Gills from Astyanax jacuhiensis Exposed to Water from Different Stages of a Water Treatment Process.	206
<i>Gehlen G, Rodrigues GZP, Zwetsch BG, de Souza MS</i>	
Virtual Reconstruction and Three-Dimensional Printing of Blood Cells as a Tool in Cell Biology Education	208
<i>Augusto I, Monteiro D, Girard-Dias W, Guimarães M, Miranda K</i>	
Ultramorphological Characteristics of Immature Stages of Piophilidae (Diptera: Piophilidae)..	210
<i>Barros-Cordeiro KB, Gracielle IMS, Savino AG, Lopes WR, Pujol-Luz JR, Bão SN</i>	
Anatomy and Ultrastructure of Barbacenia purpurea Hook. (Velloziaceae) Leaves.....	212
<i>Andrade IF, Santiago LJM, Louro RP</i>	
In vitro Antileishmanial Activity of a New Synthetic β -carboline Compound Against Leishmania amazonensis	214
<i>Paula J C, Stefanello TF, Lazarin-Bidóia D, Ueda-Nakamura T, Barea P, Sarragiotto MH, Nakamura CV</i>	
The Role of Sonic Hedgehog Signaling During Chick Muscle Differentiation.....	216
<i>Teixeira JD, De Andrade Rosa I, Brito Neto J, Mermelstein C</i>	
Jurona Virus Induces Encephalitis in BALB/c Adult Mouse Model by Sequential Intranasal Inoculations	218
<i>Diniz JAP, Araújo LM, Vasconcelos PF</i>	
Structural Changes And Apoptosis In The Submandibular Gland Of Rat Following Fluoxetine Treatment.....	220
<i>De Pizzol-Júnior JP, Navarro LG, Sasso-Cerri E, Cerri PS</i>	
Central Nervous System and Oncosis	222
<i>Oliveira JL, Benigno MIM, Scaff RMC, Alvarez-Silva M</i>	
Expression Of HER2 Oncogene In Feline Mammary Carcinomas.....	224
<i>Cunha SCS, Silva KVG, Silva FBF, Ferreira AMR</i>	
Relation Of HER2 And KI67 Expression To Histologic Graduation In Canine Mammary Carcinomas	226
<i>Silva FBF, Silva KVG, Leite JS, Cunha SCS, Ferreira AMR</i>	

Differential Effects Of Lemon Grass (<i>Cymbopogon citratus</i> , <i>Lippia alba</i> And <i>Melissa officinalis</i>) Ethanol Extracts On The Nucleolar Activity In Ehrlich Ascites Cells.....	228
<i>Giordano LS, Bellini MF, Orcini WA, Peruquetti RL</i>	
Method of Inclusion with Microwave of Cashmere Fiber for Characterization by Transmission Electron Microscopy.....	230
<i>Coelho LS, Gonçalves NR</i>	
Ultrastructural Characterization of EGTA Effects on Calcium Signaling During Early Development of Tetraspores of <i>Palisada flagellifera</i> (Ceramiiales, Rhodophyta)	232
<i>Ouriques LC, Barros JPK, Bouvie F, Bouzon ZL, Simioni C</i>	
The ultrastructure of <i>Malassezia furfur</i> and <i>Malassezia pachydermatis</i> and their interactions with macrophages	234
<i>Moreira RTF, Lallo MA, Spadacci-Morena DD, Xavier JG, Perez EC, Dalboni LC, Coutinho EDA</i>	
In Vitro Phagocytosis of <i>Encephalitozoon cuniculi</i> by Adherent Peritoneal Cells	236
<i>Pereira A, Dalboni LC, Spadacci-Morena DD, Alvares-Saraiva AM, Perez EC, Lallo MA</i>	
Structural Chraterization of the <i>Trichuris muris</i> egg and.....	238
<i>Lima LR, Miranda KR, Torres EJJ</i>	
Morphology Characterization of Nematodes associated of Parasitic Otitis in Bovines	240
<i>Caracciolo EM, Torres EJJ</i>	
Relationship Between Aging And Structural Alteration On Chromatoid Bodies	242
<i>Santos EG, Silva MA, Orcini WA, Peruquetti RL</i>	
Outbreak of encephalitis caused by human herpesvirus type 1 (HSV-1) in nonhuman primates. Diagnosis by transmission lectron microscopy	244
<i>Catroxo MHB, Martins AMCRPF, Queiróz FF, Oliveira Júnior GP</i>	
Morphological Evaluation of the Expression and Distribution of Collagen Type I, Fibronectin and Laminin Glycoproteins in Human Placenta at Term.....	246
<i>Gargioni R, Dutra MF, Alvarez-Silva M</i>	
Transfection of placenta-derived mesenchymal stem cells with green fluorescent protein	248
<i>Pérez RL, Dutra MF, Alvarez-Silva M</i>	
Comparison of Two Strains of <i>Toxoplasma gondii</i> by Scanning Electron Microscopy and Transmission Electron Microscopy.....	250
<i>Mota MA, Attias M, Moreira-Souza Aline CA</i>	
Cell-scale Biomaterial Topography Influences the Organization of Epithelial Monolayers	252
<i>Rougerie P, Pieuchot L, Sgambato N, Canuto T, Bigerelle M, Farina M, Anselme K</i>	
In vivo compatibility of PLGA membranes produced by electrospinning.....	254
<i>Chor A, Gonçalves R, Guerra B, Takiya C, Lopes M, Farina M, Andrade L</i>	
In vitro evaluation of Carbon C-Dot produced from coffee waste.....	256
<i>Vilioni MV, Rodrigues VS, Rodrigues MO, Neto BAS, Correa JR</i>	
Expression of proteins fibronectin and laminin by rhodium (II) citrate-coated maghemite nanoparticles in breast tumor	258
<i>Rocha M, Radicchi MA, Bão SN</i>	

Decalcification of fish scales for histological processing in biomonitoring studies	260
<i>Souza MS, Correa MZ, Gehlen G</i>	
Effects of a Model of Cerebral Palsy on the Intramuscular Collagen in Wistar Rats	262
<i>Zazula MF, Buratti P, Covatti C, Maximo DS, Centenaro LA, Torrejais MM</i>	
Cerebral Palsy Affects Nuclei/Fiber and Capillary/Fiber Relations in Striated Skeletal Muscle	264
<i>Zazula MF, Buratti P, Kuhn C, Covatti C, Maximo DS, Centenaro LA, Torrejais MM</i>	
Evaluation of the Muscular Fiber Area of the Extensor Digitorum Longus in Wistar Rats Submitted to Duodenojejunal Bypass	266
<i>Oliveira MC, Buratti P, Covatti C, Barbosa A, Jeronimo LC, Bonfleur ML, Torrejais MM</i>	
Effects of a Cerebral Palsy Model on the Skeletal Muscular Fiber in Wistar Rats	268
<i>Oliveira MC, Buratti P, Covatti C, Maximo DS, Centenaro LA, Torrejais MM</i>	
A C-type Lectin from Bothrops leucurus Venom Forms Amyloid Aggregates In Culture Medium And Are Efficiently Phagocytosed By Peritoneal Macrophages.....	270
<i>Aranda-Souza MA, Lorena VMB, Correia MTS, Pereira-Neves A, de Figueiredo RCBQ</i>	
Ontogeny and Calcification Process in Coralline Algae Lithophyllum corallinae (Corallinophycidae, Rhodophyta).....	272
<i>Carvalho RT, Willemes MJ, Rocha GM, Bahia RG, Farina M, Amado Filho GM, Salgado</i>	
Ultrastructural analysis of Rhodnius prolixus metasternal gland	274
<i>Lopes RL, Gomes SAO, Barbosa CF, Feder D, Spiegel CN</i>	
Morphological Characterization Of A Eucalyptus Soil Aspergillus Strain	276
<i>Pereira VM, Souza SC, Moreira SI, Guimarães SSC, Moreira GM, Mendes OM, Nery EM, Alves E, Souza SMC, Batista LR</i>	
Characterization and Evaluation of the Cytotoxic Effect of Solid Lipid Nanoparticles Containing Docetaxel in Ovary Carcinoma in vitro.....	278
<i>Andrade BYG, Rocha MCO, Longo JPF, Bão SN</i>	
Leishmania amazonensis infection induces migration of fibrocytes.....	280
<i>Guerra C, Macedo-Silva RM, Pereira PRP, Yazeji-Lanzelote M, Côte-Real S</i>	
In Vitro Activity of Dysidea avara Extract Against Helicobacter pylori.....	282
<i>Martins TK</i>	

PARTE 5

PÔSTERES – MATERIAIS

Self-assembly of Gold Nanoparticles for Nanoscale Devices.....	285
<i>Nunes LGL, Del Caro LFC, Prado AR, Oliveira JP, Pereira RHA, Guimarães CCM, Nogueira BV, Ribeiro MRN, Pontes MJ</i>	
MATERIALS LIFE: Publication of Images That Explain Behaviors	287
<i>Zeemann A, Zeemann G</i>	
Characterization of Hydrogen-Induced Cold Cracks in a Thick C-Mn Welded Steel Plate.....	289
<i>Nunes ARV, Zeemann A, de Almeida LH</i>	
Laves Phase Identification in Inconel 625 Produced by 3D Laser Melting.....	291
<i>Labre C, Pinto AL, Solórzano IG</i>	

Structural and electronic properties of NiO catalyst.....	293
<i>Arrouvel C, Werckmann J, Sanches SG, Eon JG</i>	
Analysis by Optical Microscopy and X-ray Diffraction of Composite Cu-Cr-Ag-Al ₂ O ₃ Synthesized Using Powder Metallurgy	294
<i>Fonseca DPM, Monteiro WA</i>	
Microstructural Analysis of Composite Cu-Cr-Ag-(CeO ₂ , Al ₂ O ₃) Processing by Powder Metallurgy	296
<i>Fonseca DPM, Monteiro WA</i>	
Microstructural Features of Intermetallic Phases of Recycled 6061 Aluminum Alloy Processed by Different Techniques.....	298
<i>Pereira LH, Otani LB, Coimbra DD, Kiminami CS, Bolfarini C, Botta WJ</i>	
Characterization of Al-Cu-Fe-Cr Quasicrystals by Means of EDX Mapping and Electron Diffraction Analysis.....	300
<i>Wolf W, Segantin E, Bolfarini C, Kiminami CS, Botta WJ</i>	
SEM-EDS Characterization of Precipitates in Eucalyptus and Sugar Cane Biochars Used in Processes to Decontaminate Water	302
<i>Tonetto EM, Borba RP</i>	
An SEM Study of a Low-Temperature Mineral Assemblage Associated With Native Copper Mineralization in the Serra Geral Formation, Nova Prata do Iguaçu, State of Paraná, Brazil	304
<i>Garda GM, Filgueira DA, Sayeg IJ</i>	
Effect of Surface Irregularity in the SEM-EDS Analysis of Ca-Mg Carbonates.....	306
<i>Matos HLS, Araújo IMCP, Brod JA, Carvalho JF</i>	
Investigation of PBAT/TPS Compatibilized Blend Morphology.....	308
<i>Loureiro HC, Silva LCE, Gonçalves MC</i>	
A new protocol for quantification of inter-particle spacing caused by thiol self-assembled monolayers using transmission electron microscopy.....	310
<i>Oliveira JP</i>	
Hydrothermal Synthesis of Magnesium Silicates	312
<i>Carvalho JF, Bosco EMR, Araújo IMCP, Marcondes SP, Maia LJQ, Brod JA</i>	
Internal Structure And Morphology Of Zircon Grains On Recent Sediments From The Amazon River Mouth: SEM (Back Scattered and Cathodoluminescence) images and Implications On LAICPMS Technique	314
<i>Bonifacio JF, Cardoso LMC, Gerales MC, Tavares AD, Alves MI</i>	
Microscopy Study of Conventional Together with Discontinuous Precipitation in a High Cr-Ni Superalloy	316
<i>Spadotto JC, Solorzano IG</i>	
Oxidation of Iron Catalyst (ZVI) for Removal of Organic Matter in Present in Surface Water	318
<i>Santos NO, Spadotto JC, Lacombe M, Solórzano IG, Teixeira LAC</i>	
Microscopy Analysis of a Biocorrosion Degradation of C-Mn Steel	320
<i>Ananias J, Cassino FSL, Magalhães PHV, Trindade VB</i>	
Interdiffusion Zone Evaluation of the System Steel/Inconel 625 Thermal Spray Coating.....	322
<i>Ananias J, Trindade VB</i>	

Quantitative EDS analysis of metallic alloys	324
<i>Balzuweit K, Rodrigues WN, Souza MCC, Ribeiro RC, Moreira BB, Flores MA, Garcia L R, Delben I, Alves P</i>	
Phase and Elemental Mapping by STEM-EELS Spectrum-Image.....	326
<i>Freitas ETF, Balzuweit K, de Souza C, Caldeira CL, Ciminelli VST</i>	
3D X-ray microscopy analysis of lignocellulosic fibers used as reinforcement in composite materials of polymer matrix	328
<i>Gontijo LOL, Mauricio MHP, Paciornik S, D'Almeida JRM</i>	
Tridimensional Characterization of Epoxy Matrix Glass-Fiber Reinforced Composites.....	330
<i>De La Hoz AL, Paciornik S, D'Almeida JRM, Mauricio MH, Lopes HÁ</i>	
Identification of Quaternary Phases With Mg of Alloy B390.0 (Al-Si-Cu) by Electrons Backscattering Coefficients (η).....	332
<i>Souza MCC, Balzuweit K</i>	
STEM Study of Cu-Ni Matrix Nanocomposites Reinforced with Al ₂ O ₃ Nanoparticles After heat Annealing at 600 for 300min.....	334
<i>Ramos MI, Brocchi EA, Solorzano G</i>	
Niobium Carbide Morphology in HP-Modified Steel Reformer Tubes as an Indicator of Temperature Surges	336
<i>Nascimento M, Campolina M, Nogueira L, de Almeida LH, Le May I</i>	
Microstructural effects of aging after a temperature surge event on Centrifugally Cast HP-Steels Used in Steam Reformer Furnaces.....	338
<i>Mendes MC, De Almeida LH, Dille J</i>	
Microstrutural characterization of the interface between cuag/cu joint brazed with SnCu0,7Ni alloy	340
<i>Bagnato OR, Pimentel PM, Ambrosio C, Capovilla MM, Silva FE</i>	
Evaluation of the shot peening effect on the resistance of SAE 9254 steel springs and analysis of failure by scanning electron microscopy	342
<i>Bagnato OR, Filho MC, Bresciani RL, Silva RS, Pimentel PM</i>	
Size And Polydispersity Trends Found In Gold Nanoparticles Synthesized By Coconut Water ...	344
<i>Valotto RS, Keijok WJ, Costa DS, Oliveira JP, Guimarães MCC</i>	
Non-destructive, microstructural and mechanical performance evaluation of metal-polymer hybrid structures.....	346
<i>Pinto RP, Paciornik S, André NM, Borba NZ, Feistauer EE, Mauricio M, dos Santos JF, Amancio-Filho ST</i>	
Characterization by X-ray Computed Tomography of Class G Oil Well Cement Paste Exposed to Elevated Temperature	348
<i>Lorenzoni R, Paciornik S, Mauricio MHDP, Silva FA</i>	
Nanostructures based in TiO ₂ on titanium.....	350
<i>Seixas RS, Silva IR, Lunz JN, Jardim PM</i>	
Characterization of Oxide Layer Formed on External Surface from Steam Reformer Furnaces Tubes	352
<i>Silveira RMS, Almeida LH, Rocha AC, Eckstein CB</i>	

Study and analysis of failures in multilayer ceramic capacitors by mechanical stress	354
<i>Fonseca RT, Antonelli E, Matos CP</i>	
Artifacts on the Characterization of Copolymer Micelles by TEM Using Phosphotungstic Acid for Negative Staining	356
<i>Oliveira IS, Bernardo RA, Santos TO, Lima ECD</i>	
Study of Physicochemical Properties of a Hybrid Coagulant Used in Potable Water Treatment ..	358
<i>Campos V, Peralta JSJ, Sayeg IJ</i>	

PARTE 6

PÔSTERES – OUTROS

Evaluation of the Cytotoxicity of Graphene Oxide Nanosheets Associated with Aluminum Chloride-Phthalocyanine as an Agent for Photodynamic and Photothermal Therapies Combined	361
<i>Silva ALG, Santos MSC, Moura LD, Paterno LG, Souza PE, Azevedo RB, Bão SN</i>	
TEM Study on Size and Morphology of TiO ₂ Nanorods Within a MgH ₂ -TiO ₂ Nanocomposite Produced Via High Energy Ball Milling.....	363
<i>Pereira AF, Jardim PM</i>	
Analytical TEM study of calcium phosphate nanoparticles in an intracellular environment.....	365
<i>Rossi AL, Longuinho MM, Tanaka M, Farina M</i>	
Quasi-spherical and monodisperse synthesis of Virola oleifera-capped gold nanoparticles	366
<i>Guimarães MCC, Oliveira JP, Corrêa AS</i>	
Sodium Niobate Nanostructure Synthesized Over Metallic Niobium by Alkali Hydrothermal Route	368
<i>Canabarro BR, Jardim PM</i>	
Phenolic Lipid 2-(3,5-Dimethoxy-2-Octanoyl Phenyl) Acetic Acid Effects in The MCF-7 Breast Adenocarcinoma Treatment	370
<i>Gomes DRF, Pessatto LR, Jorge J, de Oliveira RJ, Beatriz A, Martines MAU</i>	
Application of Calcium Phosphates: In Vivo Test in Sheep	372
<i>Dalmônico GM, Camargo NHA, Rossi AL, Dallabrida AL, Cambra-Moo O, Rodríguez MA</i>	
Micromorphology and Composition of Bioconstructions of Sessile Gastropods from the Brazilian Coast.....	374
<i>Toniolo TF, Giannini PCF, Sayeg IJ, Angulo RJ, Souza MC, Pessenda LCR</i>	
Evidences of Bioclast Pseudomorphous Replacement in the Eolianites of Fernando de Noronha Archipelago, Northeast Brazil	376
<i>Arias VE, Giannini PCF, Sayeg IJ, Cagliari R, Angulo RJ, Souza MC</i>	
Crystallographic orientation of spicules from the sponge <i>Sycettusa hastifera</i>	378
<i>Coelho LS, Longuinho MM, Farina M, Werckmann J, Rossi AL</i>	
Green synthesis of gold nanoparticles with Epigallocatechin Gallate	379
<i>Schuenck GPD, Knidel C, Guimarães MCC</i>	
Synthesis and Characterization of Alginate/Chitosan Nanoparticles Containing Lapazine with Potential Antituberculosis Activity.....	381
<i>Longuinho MM, Leitão SG, Silva RSF, Rossi AL, Silva PEA, Finotelli PV</i>	

Biosynthesis, Characterization and Evaluation of Antibacterial Effects of Silver-based Nanoparticles	383
<i>Eugenio M, Ferreira V, Müller N, Frasés S, Lemgruber L, Farina M, De Souza W, Sant'Anna C</i>	
NaX zeolite synthesis employing microwave heating source and its surface functionalization via esterification reaction.	385
<i>Povinelli APR, Zazeri G, Mendes MTS, Laurenti JB, Nery JG</i>	
Image-based high content analysis to accesses the antiproliferative effect of silver chloride and silver/silver chloride nanoparticles against glioblastoma multiforme.....	387
<i>Müller N, Eugenio M, Campanati L, Lima LMTR, Sant'Anna C</i>	
Titanium rutile nanoparticles: a glance of nanobiointerface applied to sunscreens	389
<i>Gemini-Piperni S, Laviola-Sanches P, Souza W, Rossi AL, Rocha LA, Borojevic R, Granjeiro JM, Benchimol M, Ribeiro AR</i>	
Coumarin-containing Thermoresponsive Hyaluronic Acid-based Nanogels as Delivery Systems for Anticancer Chemotherapy	391
<i>Stefanello TF, Couturaud B, Szarpak-Jankowska A, Fournier D, Louage B, Garcia FP, Nakamura CV, De Geest BG, Woisel P, van der Sanden B, Auzély-Velty R</i>	
Temperature-controlled particle size distribution of <i>Camellia sinensis</i> silver nanoparticles synthesized.....	389
<i>Keijok WJ, Oliveira JP, Guimarães MCC</i>	
Nanoparticles Characterization de Magh-Rh ₂ (H ₂ cit) ₄	395
<i>Lago WF, Sousa MH, Bão SN</i>	

APRESENTAÇÃO

Caros leitores e companheiros de pesquisa,

O mundo da microscopia é constituído por um amplo conjunto de instrumentos e metodologias de análise que evoluem de forma incessante. Estes equipamentos servem aos campos da Ciência dos Materiais, Biologia, Metalurgia, Medicina, Física, Farmácia, Geologia e Ciência Forense com inúmeras aplicações na área industrial e em empresas prestadoras de serviços.

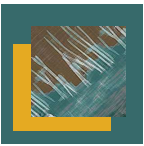
Um rápido olhar para a história da microscopia mostra que desde os patriarcas da Nova Ciência do Século XVI até os desdobramentos da Ciência Moderna do Século XX, as reuniões científicas têm tido um papel fundamental na troca de experiências entre diferentes campos do conhecimento. Esta intensa troca tem nos conduzido neste início do século XXI a um momento de convergência de diferentes tecnologias integradas em equipamentos cada vez mais sofisticados na sua capacidade ampliada de proporcionar respostas a perguntas científicas e tecnológicas mais complexas.

Nesse caminho, o 26º Congresso Brasileiro de Microscopia e Microanálise da SBMM buscou atrair os mais importantes pesquisadores nacionais e estrangeiros para criar um ambiente de intensa troca de experiências com estudantes, profissionais e técnicos da área de microscopia.

Nestes anais, estão reunidos os resumos das exposições orais e dos pôsteres apresentados no 26º CSBMM. A publicação desses trabalhos tem como objetivo compartilhar os debates científicos realizados na ocasião, fomentando o estabelecimento de vínculos colaborativos entre diferentes núcleos de pesquisa e fortalecendo o compromisso da SBMM com a consolidação de uma atmosfera de constante formação de recursos humanos de alto nível no Brasil.

Desejamos um proveitosa leitura!

Diretoria da SBMM (2016-2018)



DOI: [INSERIR ENDEREÇO DO DOI AQUI.](#)

Caderno de Resumos do 26º Congresso Brasileiro de Microscopia da SBMM – ISSN: [INSERIR AQUI](#)

PARTE 1

COMUNICAÇÕES ORAIS
- BIOLOGIA



Study of HA Nanoparticles Internalization on SaOS-2 Cell Line by Dual Beam Microscopy

Mariana Moreira Longuinho^{1*}, Marcelo Tanaka¹, Marcos Farina² and André Linhares Rossi¹

1. Condensed Material, Applied Physics and Nanoscience Coordination, Brazilian Center for Physics Research, Rio de Janeiro, Brazil.

2. Institute of Biomedical Sciences, Federal University of Rio de Janeiro, Rio de Janeiro, Brazil.

*Email: mariana.longuinho@gmail.com

Hydroxyapatite (HA) is a biomaterial widely used in bone implants due to its similarity with the mineral phase of bone and to its chemical, mechanical and toxicological characteristics [1, 2]. HA nanostructured biomaterials allow better absorption by cells for its reduced size and higher surface to volume ratios area, facilitating their transport to the cell interior and further solubilisation [3, 4]. Since its characteristics change with the particles size, the toxicological effects of HA nanoparticles in osteoblasts must be better studied, as it is not well described in literature. With FIB-SEM dual beam microscopy, it is possible to observe the analyzed material in three dimensions, by serial cuts. This technique allows for analysis of nanoparticles internalization mechanism by cells and their modifications on the cytosol. The aim of this work was the understanding of the behavior of SaOS-2 (osteosarcoma) cell line on a medium containing HA nanoparticles. SaOS-2 was cultured in McCoy's 5A Medium supplemented with 10% fetal bovine serum and maintained in a humidified atmosphere. Cells were seeded using a 6-well plate at a density of 105 cells per well. After 24 hours the cells were exposed to HA-NPs containing 50 µg/mL during 2 and 24h. The samples were rinsed in buffer and fixed in Karnovsky, post-fixed with osmium tetroxide and potassium ferrocyanide 1:1 (v/v), dehydrated in ethanol series and embedded in epoxy resin (EPON) until polymerization. Tomographic datasets were obtained through "slice and view" technique using a LYRA-3 dual beam workstation (TESCAN - Czech Republic). The 3D image was reconstructed with 150 nm slices using the focused ion beam (FIB) and images of the exposed block face were made by SEM using back-scattered detector (BSED - Oxford). Figure 1 shows the morphological difference between SaOS-2 cells on different times, indicating differentiation after 24 h. Figure 2A shows the 3D model of SaOS-2 cell incubated for 24 h with 50 µg of HA. It can be observed the different cell morphology, with irregular cell membrane and release of vesicles to the extracellular space. Figure 2B shows two different crystal agglomerates close to cell membrane. One bigger and more disperse, and another thinner and more compact. Both agglomerates show interaction with the cell membrane. Large clusters inside the cell can be observed (asterisks), confirming the internalization of the HA added to the culture medium. In addition, Figure 2B also shows organelles with a characteristic morphology of rough endoplasmic reticulum or Golgi apparatus, organelles usually overexpressed when the digestion process increases [5]. In Figure 2A, lysosomes are represented by yellow vesicles. The mean concentration of HA inside phagosomal vesicle is equal to 781 ±0,44 mg/ml, which is 100 times higher than the concentration described in literature [6]. These finds enrich the understanding on how osteoblasts interact with nanoparticles of HA and confirm that SaOS-2 have an active role in particles metabolization since two types of crystals and vesicles containing HA agglomerates are observed. Further studies are needed to confirm HA nanoparticles toxicity.

REFERENCES

- [1] J.L. Xu et al., *Biomaterials* 30 (2009) 5385.
- [2] S. V. Dorozhkin, *Materials* 2 (2009) 399.
- [3] A.J. Huh and Y.J. Kwon, *J. Control. Release* 73 (2001) 121.
- [4] S. Parveen et al., *Nanomed. Nanotech. Biol. Med.* 8 (2012) 147.
- [5] P. Kalia et al., *J. R. Soc. Interface.* 11 (2014) 20140004.
- [6] R. Bloebaum et al., *J. Biomed. Mater. Res.* 40 (1998) 104.
- [7] This research was supported by CNPq (Brazil) and FAPERJ (Brazil).

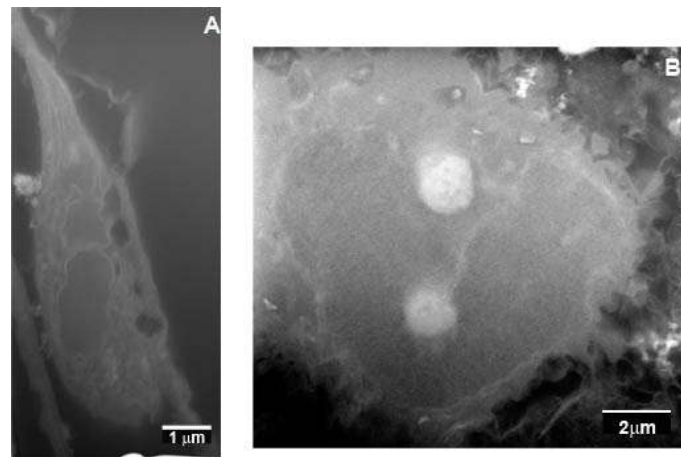
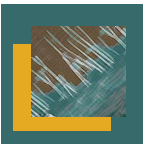


Figure 1. SEM micrograph of SaOS-2 cells A) after 2 h of incubation with HA 50 µg/mL and B) after 24 h of incubation with HA 50 µg/mL.

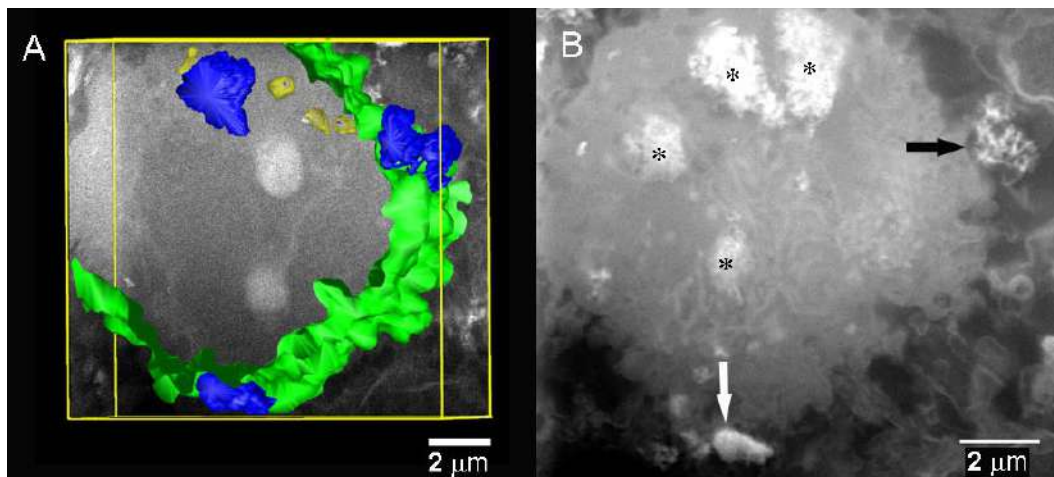
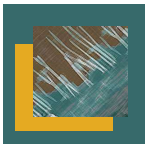


Figure 2. FIB electron tomography of SaOS-2 cells after 24h of incubation with HA 50 µg/mL. A) 3D reconstruction obtained by Slice and View method superposed to one image from the tomography series; blue: large agglomerates of HA NP; yellow: phagosomal vesicles; green: cellular membrane. B) An image corresponding to a different section plane from the tomography series shown in (A). The black arrow indicates a HA-NP agglomerate with large and disperse crystals; the white arrow indicates a HA NP agglomerate with smaller and compact crystals; the asterisks indicate internalized HA agglomerate.



Cytotoxic Effects Of Novalurom® Insecticide In The Midgut Of The Silkworm *Bombyx mori* (Lepidoptera: Bombycidae)

Marilucia Santorum^{1*}, Gustavo Henrique dos Reis², Oliver C. Pedroso³, Rose Meire Costa Brancalhão³, Elton Luiz Scudeler¹ and Daniela Carvalho dos Santos¹

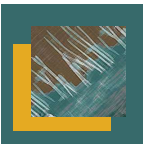
1. Laboratório de Insetos, Departamento de Morfologia, Instituto de Biociências de Botucatu, UNESP, SP, Brasil.
2. Programa de Pós-Graduação em Anatomia Patológica, Universidade Federal do Rio de Janeiro, RJ, Brasil.
3. Centro de Ciências Biológicas e da Saúde, Universidade Estadual do Oeste do Paraná, Cascavel, PR, Brasil.

*Email: mari_santorum@hotmail.com

The silkworm *Bombyx mori* (Lepidoptera: Bombycidae) is the insect of major economic importance for the production of silk in the country. It feeds on mulberry leaves and is highly sensitive to pesticides, thus the use of insecticides in crops surrounding the mulberry plantations can affect the creation of *B. mori*, causing an imbalance in its metabolic functions and compromising the production of the cocoon [1]. Among these insecticides stands out the Novalurom, inhibitor of chitin synthesis in insects and used in the control of insect pests of crops near mulberry plantations [2]. Thus, the objective of this study was to evaluate the cytotoxic effects of Novalurom in the midgut of *B. mori*. *B. mori* larvae, were randomly selected into 2 experimental groups: control group (CG) and treatment group (TG: treated with sublethal concentration of 0, 15 mL/L Novalurom). After ecdysis from the 2nd to the 3rd instar, the TG larvae were fed for 24 hours ad libitum with mulberry leaves treated with the insecticide. In parallel, a new exposition was carried out, however in larvae that carry out the ecdise from the 4th to the 5th instar. *B. mori* larvae at 3rd, 4th and 5th instar were anesthetized and midgut segments were collected and conventionally processed for light microscopy and scanning electron microscopy. In the analysis of the epithelial cells in the midgut of *B. mori* larvae of TG, we verified morphological alterations by exposure to the insecticide in the 3 instars analyzed, where extreme tissue disorganization was observed in the 3 typical cell types of this epithelium (Fig. 1). The columnar cells were elongated, with the apical region more dilated and cytoplasmic protrusions, similar to vesicles, visualized along the epithelium and in the intestinal lumen, this cell type also presented its sparse and/or absent microvilli in some regions. Thus, the apical surface of the epithelium demonstrated a more irregular aspect compared to CG (Fig. 1). The goblet cells also presented more elongated following the same pattern of columnar cells (Fig. 1B). In the regenerative cells, we observed the occurrence of hypertrophy, in addition to a reduction in its number, where the nests of regeneration were no longer visualized which are characteristic in this type of cell in Lepidoptera. In some regions, we observed a spacing between the epithelial cells and the basal lamina, and spacing between the epithelium and the muscular layer. We have identified the detachment of some cells towards the lumen (Figs. 1C and F). Our results are similar to other studies on the toxic effects of insecticides in the midgut of insects [1, 3]. We conclude that Novalurom had a cytotoxic effect on the midgut of *B. mori*, which could compromise its creation and consequently the entire silk production chain.

REFERENCES

- [1] R.E.F. Munhoz et al., OJAS, 3 (2013) 343-353.
- [2] Ministério da Agricultura, Pecuária e Abastecimento – MAPA (2015).
- [3] E.L. Scudeler; D. C. Santos. Micron, 44 (2013) 125-132.
- [4] This research was supported by FAPESP (2015/07119-9) (Brazil).



[5] Acknowledgement: Electron Microscopy Center of UNESP-Botucatu, SP, Brazil.

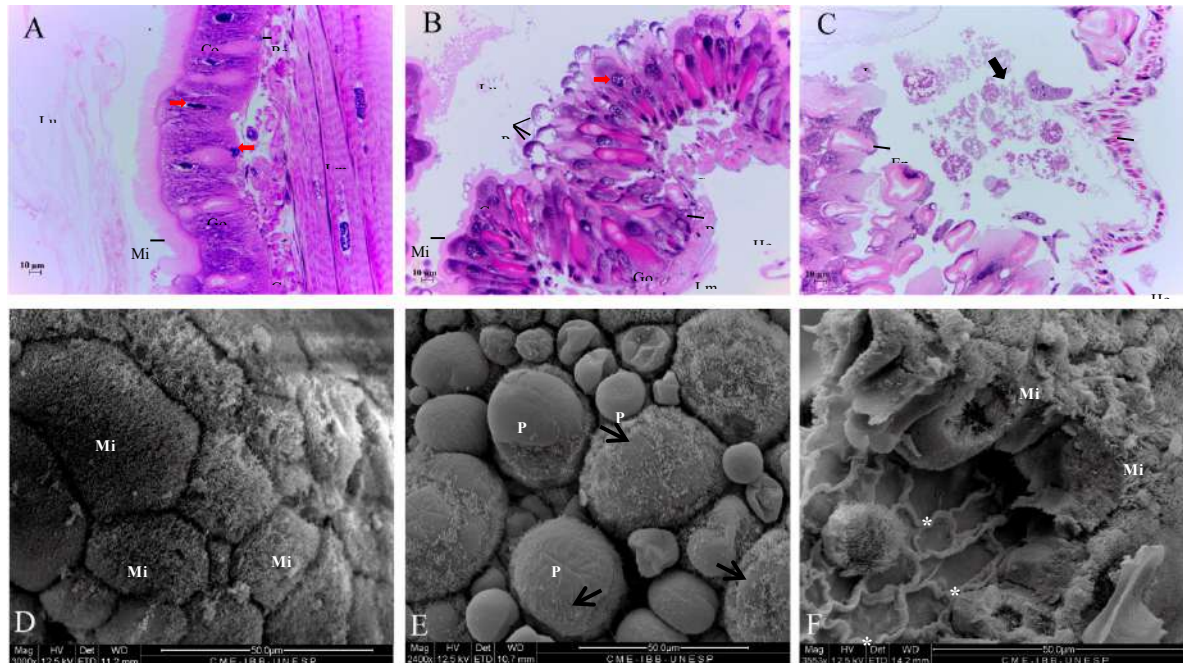
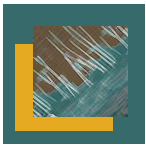


Figure 1. Photomicrography of the midgut of *B. mori* larvae. (A-C). In A, Control Group with columnar cells (Co) with microvilli (Mi) in the apical region facing the lumen of the intestine (Lu) and goblet cells (Go) and regenerative cells (Re). Nucleus (red arrow); circular muscle (Cm) and longitudinal muscle (Lm). In B-C, Treatment Group, where in B, tissue disorganization is noted, with columnar cells (Co) elongated, with the apical region more dilated and cytoplasmic protrusions (P) towards the intestinal lumen (Lu) and in C, note region of epithelial detachment (Ep) towards the lumen (black arrow). Hemocoel (He). Bars = 10 µm. Hematoxylin and eosin staining. Electromicrographs of the midgut of *B. mori* larvae (D-F). In D, Control Group with the epithelial surface of the midgut with columnar cells with regular pattern of microvilli (Mi). In E-F, Treatment Group, where in E, note alterations in the format of the columnar cells, with the apical region dilated and with large number of cytoplasmic protrusions (P) and sparse and/or absent microvilli in some regions (black arrow) and in F, note the empty spaces (asterisks) previously occupied by the columnar cells. Bars = 50 µm.



Evaluation Of Different Sample Preparation Methods For Glomerular Morphological Evaluation: Coated Or Uncoated?

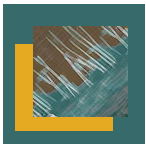
Priscila Fernandes dos Santos¹, Diogo Benchimol de Souza^{2*}, Eduardo José Lopes Torres³, Francisco José Barcellos Sampaio⁴, Waldemar Silva Costa⁵, Bianca Martins Gregório⁶.

1. Master student, Urogenital Research Unit/ Department of Anatomy, UERJ, Rio de Janeiro, Brazil,
2. Associate Professor, Urogenital Research Unit / Department of Anatomy, UERJ, Rio de Janeiro, Brazil,
3. Associate Professor, Helminthology Laboratory Romero Lascasas Porto / Department of Microbiology, Immunology and Parasitology, UERJ, Rio de Janeiro, Brazil,
4. Full Professor, Urogenital Research Unit / Department of Anatomy, UERJ, Rio de Janeiro, Brazil,
5. Visiting Professor, Urogenital Research Unit / Department of Anatomy, UERJ, Rio de Janeiro, Brazil,
6. Associate Professor, Urogenital Research Unit / Department of Anatomy, UERJ, Rio de Janeiro, Brazil.

*Email: diogobenchimol@gmail.com

The renal glomerulus is a spherical capillary tuft contained by Bowman's capsule, and responsible for performing the selective filtration of the circulating blood for the formation of the primordial urine. These capillaries are coated by fenestrated endothelial cells and externally covered by specialized epithelial cells, known as podocytes [1]. These differentiated epithelial cells consist of a body from which several prolongations, called foot processes, emerge. The interdigitation with the foot processes of the neighbor podocyte, creates what is known as the slit diaphragm [2]. It is of interest to analyze the glomerular ultrastructure (especially of the slit diaphragm), since some diseases promote changes in this normal morphology. In this sense, scanning electron microscopy becomes an important and effective tool for these studies [3]. Normally, samples destined for scanning microscopy are covered with a thin metallic layer (more commonly of gold or palladium-gold) to make the sample conductive of electric charges [4]. However, this step can be dispensed for some analyzes, reducing and accelerating the sample preparation process. The aim of the present study was to compare coated and not coated samples for evaluation of the glomerular morphology of the Wistar rat kidney. Ten fragments of approximately 1mm³ of the cortical region of the kidney of the 3-month-old male Wistar rat were used. The fragments were fixed by immersion with 2.5% glutaraldehyde in phosphate buffer (pH 7.3) and post-fixed in 1% OsO₄ for 40 minutes. Soon after, they were washed three times in phosphate buffer and dehydrated in increasing order of ethanol in the concentrations of 20%, 30%, 50%, 70%, 90% and three times of absolute, for 20 minutes each. The fragments were then dried at critical point with liquid CO₂. Of the 10 fragments, 5 were coated with palladium gold and the remaining fragments were not coated. The samples were observed in the Auriga Compact FIB - SEM scanning electron microscope of the Urogenital Research Unit - UERJ. In these samples we sought to observe the interdigitations of the glomerular foot

process and the quality of the image obtained in different increases and voltages was evaluated. In all samples (coated or uncoated), ultrastructural glomerular morphology could be observed. For the uncoated samples (Fig. 1D, 1E, 1F), when using voltages of 2 KV (or higher) a great charging was observed, impairing the use of such voltage. Thus, these samples were always observed under voltage of 0.5 KV. On the other hand, in the coated samples (Fig. 1A, 1B, 1C), the use of 2 KV was adequate. Almost as a consequence, in the coated samples, the podocyte structures were better characterized, generating better images. Inversely, in the uncoated samples, it was possible to



visualize the desired structures and to detect the morphological characteristics of these. The results showed that it is possible to use kidney samples without previous coating to evaluate the glomerular morphology at the ultrastructural level, serving as a tool in the study of pathologies. However, whenever possible, coating should be preferred as it enables higher quality images.

Keywords: SEM, low voltage.

REFERENCES

- [1] R. Lennon et al., The Importance of Podocyte Adhesion for a Healthy Glomerulus. *Front Endocrinol (Lausanne)*. 5 (2014) 160.
- [2] M. Relle et al.; New perspectives on the renal slit diaphragm protein podocin. *Mod Pathol*. 24 (2011) 1101–1110.
- [3] D. B. de Souza et al., Evaluation of the Glomerular Filtration Barrier by Electron Microscopy, *Modern Electron Microscopy in Physical and Life Sciences*, Dr. Milos Janecek (Ed.), InTech, 2016.
- [4] W. Souza, *Técnicas de microscopia eletrônica aplicadas às ciências biológicas*. Soc. Bras. Microsc, 3 (2007).

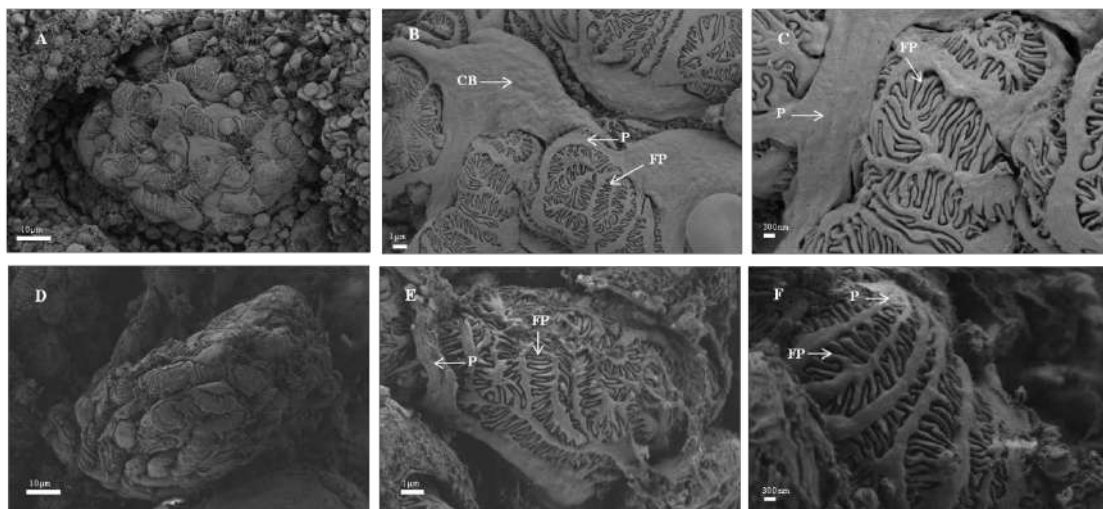
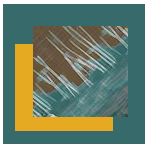


Figure 1. Glomerular ultrastructure. Coated samples showed in A, B, C and uncoated samples showed in D, E, F. (A) General morphology of the glomerulus; (B) glomerular ultrastructure: the cell body [CB] of the podocytes [P] and foot process [FP]; (C) podocytes [P] and foot process [FP]; (D) General morphology of the glomerulus, (E) and (F) shows the podocytes [P] and foot process [FP].



Plunge freezing as a cryofixation alternative which maintains the morphological characteristics of animal tissue architecture

Felipe F. Dias^{1*}, Gregory T. Kitten¹ and Elizabeth R. Silva¹

1. Microscopy Center, Federal University of Minas Gerais, Brazil

*Email: ffdias@gmail.com

Cryotechniques have become widely utilized during the last decade to improve transmission (TEM) and scanning electron microscopy (SEM) imaging of biologic samples. Cryofixation enables vitrification of the water in biological samples without forming ice crystals, which cause artifactual redistribution of cellular components. When followed by freeze substitution, in which vitrified water is removed from the sample at low temperatures, an ultrastructural morphology in a near physiological state can be achieved [1]. Although the high pressure freezing (HPF) approach is routinely used for cell suspensions and thin layers of cells, it is not commonly used to cryofix plant or animal tissues because of their volume and the limitations of the tools employed during the rapid freezing procedure [2]. In these cases, plunge freezing has become an excellent alternative in which a simple apparatus enables the cryofixation of larger samples, including biopsies or dissected fragments of living tissues [3]. With the aim of establishing EM cryotechniques in the multiuser Microscopy Center at UFMG, experiments using a simple plunge freezing system followed by freeze substitution and preparation for SEM were conducted to verify animal and plant tissue ultrastructure. Two BALB/c mice were euthanized and samples of heart, liver and kidney were collected (Fig. 1). 1-2 μm^3 fragments were quickly dissected in PBS and transferred onto small copper supports (high thermal conductivity) and then directly plunged into liquid nitrogen (LN2) cooled cryogen (isopentane – C₅H₁₂; freezing point -160°C). After 10 seconds, frozen fragments were rapidly transferred to LN2 and then transferred to 2.0 ml cryotubes containing LN2 above 1.0 ml of a frozen mixture of 1% osmium tetroxide/anhydrous acetone. Cryofixation was followed by freeze substitution, starting at -90°C and slowly warming up to 20°C over a 4-day period. During substitution, frozen water is removed from the samples by anhydrous acetone at a temperature low enough to prevent the cellular water from recrystallizing. The samples were washed two times in acetone to remove osmium residues and processed for conventional SEM. All three types of selected murine tissues were well preserved, without large ice crystal artifacts (Fig. 2). Heart muscle fiber architecture was composed of many myofibrils within the cardiac sarcolemma (Fig. 2A). Liver ultrastructure was characterized by rows of hepatocytes surrounding a lobular central vein. Some cells were fractured, allowing observation of subcellular organelles (Fig. 2B). Kidney ultrastructure showed the presence of renal convoluted tubules surrounded by red blood cells and extracellular matrix filaments (Fig. 2C). Stomata and ultrastructural details on the surface of cryofixed plant leaves were well preserved (Fig. 2D). The results shown here indicate that SEM cryotechniques can be used to study animal and plant tissues in physiological or pathological conditions and will compliment light and fluorescent microscopy methods. Further analyses of the tissues using TEM are in progress and will help to establish the technique.

This research was supported by CNPq, CAPES and FAPEMIG (Brazil). We gratefully thank Rodrigo Novaes and Marcelo de Souza for technical assistance.

REFERENCES

- [1] R.A. Fleck, *Methods in Molecular Biology*, 1257 (2014) 243.
- [2] B.M. Humbel, *Handbook of Cryo-Preparation Methods for Electron Microscopy*, (2009) 319.
- [3] M.J. Dobro et al., *Methods in Enzymology*, 481 (2010) 63.

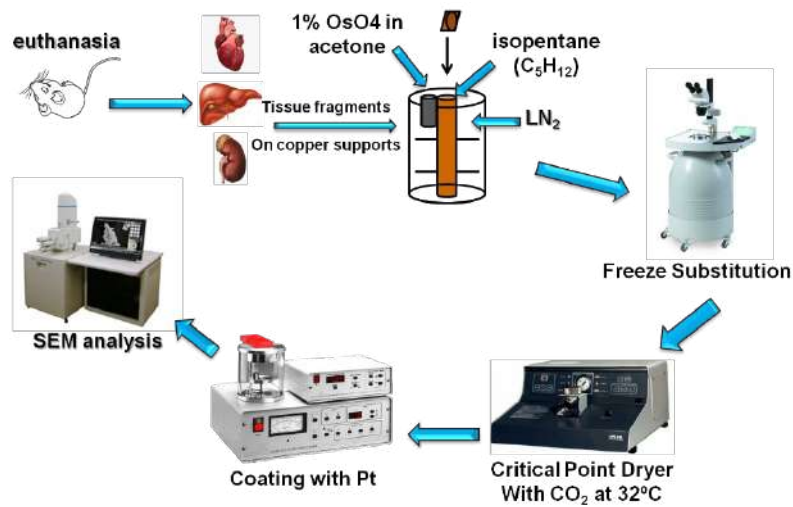
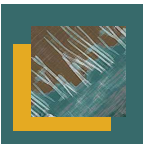


Figure 1. Plunge freezing protocol. Small tissue fragments were collected, placed onto copper supports and immediately plunged into LN₂ cooled isopentane (C₅H₁₂). After 10 seconds, the frozen samples were immersed in LN₂ and transferred to cryotubes containing a frozen mixture of 1% osmium tetroxide in anhydrous acetone. Fixation was performed in a freeze substitution device, starting at -90°C/72 hours and continued with slopes of 30°C/6 hours and pauses of 8 hours for each slope until warm up to 20°C. Samples were washed two times/10 minutes in anhydrous acetone and processed for conventional SEM.

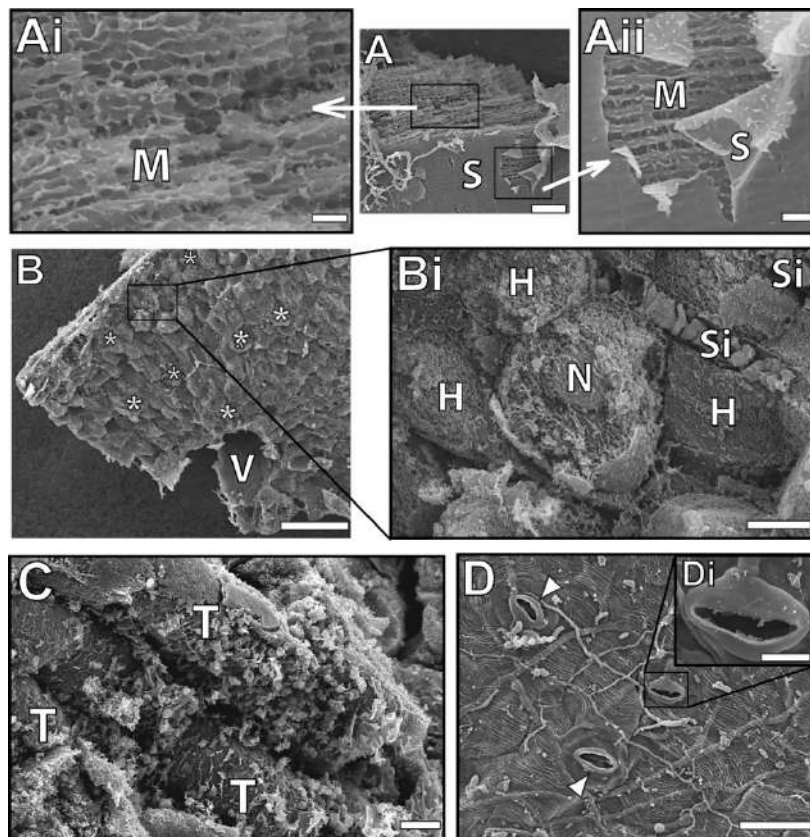
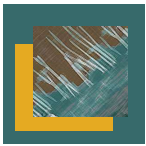


Figure 2. Scanning electron-micrographs of murine tissue and leaf fragments prepared using plunge freezing fixation and conventional SEM (A) Heart muscle fiber showing longitudinal disposed myofibrils (M) (Ai, Aii) enclosed by cardiac sarcolemma (S). (B) Longitudinal section of the liver showing rows of hepatocytes (*, H), with some of them displaying a central nucleus (N) (Bi), and a lobular central vein (V). (C) Renal convoluted tubules (T) with red blood cells and extracellular matrix filaments spread over them. (D) Stomata (arrowheads) on a leaf surface. Ai, Aii, Bi and Di represent large areas of the respective boxed areas in A, B and D. Si: sinusoids; Bars (A; Bi; Di): 10µm; (Ai, Aii): 2µm; (B): 100µm; (C): 20µm; (D): 50µm.



Dyspermic fusion protocol for androgenetic induction in the *Astyanax altiparanae* (Garutti & Britski): ultrastructural analysis

Matheus Pereira dos Santos^{1*}, George Shigueki Yasui², Victor Costa Spandri², Nivaldo Ferreira do Nascimento¹, Regiane Cristina da Silva¹, José Augusto Senhorini², Laura Satiko Okada Nakaghi¹.

1. UNESP Aquaculture Center, Department of Animal Physiology and Morphology, UNESP, Jaboticabal, Brazil.

2. National Center for Research and Conservation of Continental Fishes, Laboratory of Fish Biotechnology, Pirassununga, Brazil.

*Email: matheusps.pereira@gmail.com.

In studies with biotechnology applied to the conservation of genetic resources in fish, the diploidy of the androgenetic progeny is necessary to guarantee the survival of the embryos. Dyspermic fusion and subsequent fertilization may be an alternative in this regard. The protocol may give rise to a progeny of androgenetic diploid individuals with exclusively paternal genetic material. The aim of this work was to evaluate the ultrastructure and consequent viability of a protocol for dyspermic fusion in the *Astyanax altiparanae* species. The protocol established by Spandri [1] was used. The semen sample was activated at a dilution of 20x with distilled water. Five samples with progressive motility above 80% and concentration above 8.4×10^8 spz mL⁻¹ were selected and the samples were diluted with modified Ringer's solution so that the final concentration was 7×10^8 in 250 μ l. After dilution, 10 μ l of the semen was used and mixed with 10 μ l of 60 mM MgCl₂ solution for 10 minutes at 25°C. For scanning electron microscopy (SEM), the samples previously fixed in 2.5% glutaraldehyde + PBS solution were postfixed in 1% osmium tetroxide for two hours, washed in sodium phosphate buffer pH 7.4 and dehydrated in graded ethanol series. Then the samples were dried at the critical point in liquid CO₂ drier, mounted on stubs and coated in palladium gold ions (DENTON Vacuum Desk II) and subsequently observed and electronographed in a scanning electron microscope (Jeol-JSM 5410, Akishima, Tokyo, Japan). It was possible to show how the application of the protocol affects the cellular morphology and, consequently, the potential of fertilization. Dyspermic fusion protocol was effective for the species, with many cells showing fusion (Fig 1). Spermatozoa were aggregated from the head to the extent of the flagella (Figs 1A, B) or only by the head (Figs 1C, D). Some studies highlight the efficiency of the application of divalent cations for induction to dyspermic fusion. In *Misgurnus anguillicaudatus*, solutions of 1.25 mM of magnesium and calcium presented sperm fusion [2]. The results are similar to that observed for *Astyanax altiparanae*, where the fusion occurred in a solution of 80 mM magnesium chloride [1]. However, other studies have pointed out that the protocols for dyspermic fusion can be varied and species-specific. Satisfactory results were describe in induction to the dyspermic fusion in the *H. caudovittatus* species with 2.5% solutions of polyethylene glycol [3], results similar to that observed by [4], which report the use of 1% polyethylene glycol in the sperm fusion of the species *Puntius conchonius*. In addition to the fusion itself, other parameters should be taken into account for the establishment of a specific protocol such as motility before and after fusion, cell integrity and viability [2]. The results represent an alternative to the induction of androgens in the species.

REFERENCES

- [1] V. C. Spandri. Anhembi Morumbi University. 2014.
- [2] G. S. Yasui, *et al.* Aquaculture. 2012.
- [3] J. D. Clifton; T. J. Pandian. Current Science, 95(1), 2008.
- [4] S. Kirankumar; T. J. Pandian. Genome. 47, 2004.
- [5] Financial support from CAPES and FAPESP (2011/11664-1).

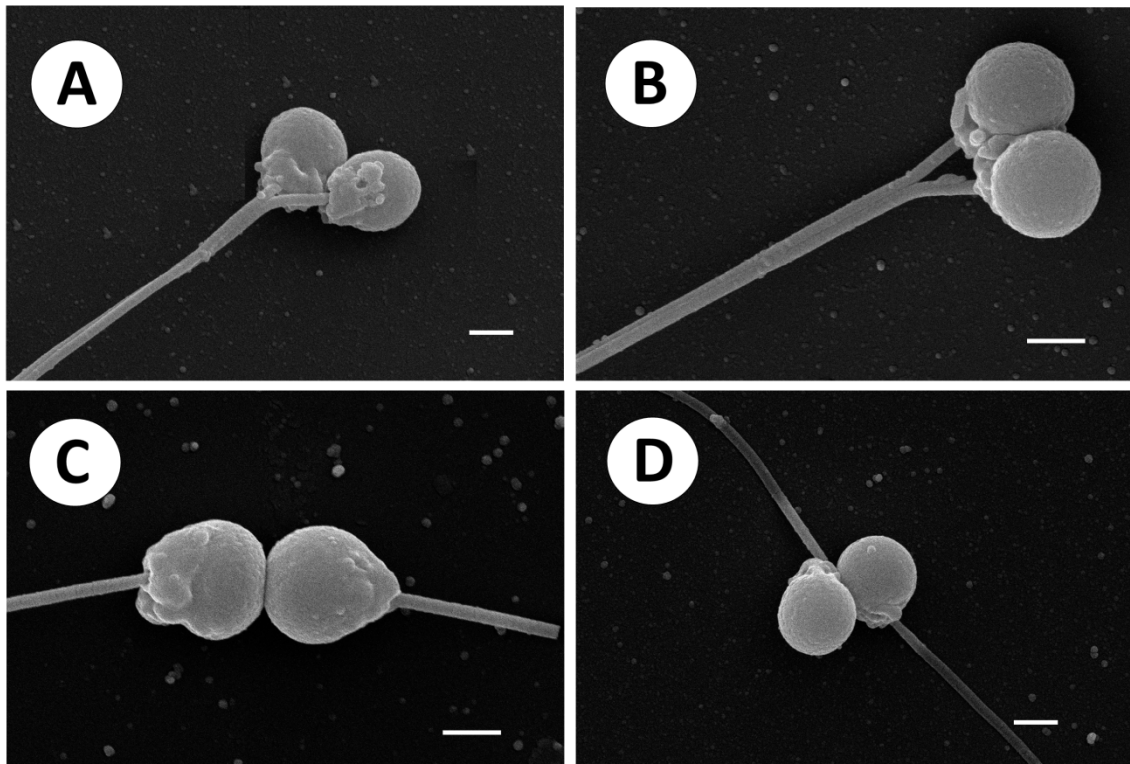
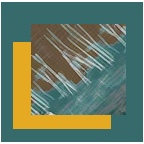


Figure 1: Scanning Electron Microscopy (SEM) of the semen of *Astyanax altiparanae* after protocol of dyspermic fusion, evidencing the adhesion sites between the gametes. Fusion from the head extending throughout the flagellum (A, B) and fusion by the head (C, D). Scale bar: 1 μm.



Three-dimensional Visualization of Ion Nanodomains in Subcellular Compartments

Wendell Girard-Dias^{1,2}, Wanderley De Souza¹ and Kildare Miranda^{1*}

1. Laboratório de Ultraestrutura Celular Hertha Meyer, Instituto de Biofísica Carlos Chagas Filho and Centro Nacional de Biologia Estrutural e Bioimagem / Universidade Federal do Rio de Janeiro, Rio de Janeiro, Brazil.

2. Plataforma de Microscopia Eletrônica Rudolf Barth, Instituto Oswaldo Cruz / Fiocruz, Rio de Janeiro, Brazil.

*Email: kmiranda@biof.ufrj.br

Understanding mechanisms involved in osmoregulation control in protozoan parasites has been a challenge for many research groups. Over the past years, a number of key players in cell signaling in trypanosomatid parasites have been identified. Among these, inorganic polyphosphate (PolyP) polymers have proven to play important roles in cell physiology, both as an energy source, stored in its constituent phosphoanhydride bonds, and as a polyanion that might activate a number of physiological processes [1]. A number of methods for PolyP localization and quantification are available, including DAPI-staining followed by microscopic visualization and quantification, P-NMR analysis, enzymatic assay using recombinant exopolyphosphatases and analytical electron microscopy (AEM). From the AEM point of view, X-ray microanalysis combined with elemental mapping as well as energy filtered TEM have been the most employed techniques carried out to explore the two-dimensional composition and distribution of (poly)ions (including polyphosphate stores) within cells [2]. In this work, we used a combination of cutting edge electron microscopy techniques to map the 3D distribution of diffusible ions within the whole volume of ion-rich organelles present in the protozoan parasite *Trypanosoma cruzi*, at high resolution, using X-rays microanalysis. Cryofixed cells were analyzed by scanning transmission electron tomography (STEM-Tomography) combined with energy dispersive X-ray microanalysis (EDS), using the latest high performance setup of multiple X-ray detectors [3] to obtain 3D elemental maps (EDS tomography) of ion-rich organelles with nanoscale dimensions. We showed a heterogeneous three-dimensional distribution of ions within the shell of polyphosphate polymers forming segregated nanochemical domains (figure 1). Pearson correlation analysis showed that phosphorus, present namely in the form of polyphosphate anions, appear homogeneously distributed along the sampling volume whereas cations such as magnesium, calcium, potassium and zinc display heterogeneous distribution with a self-excluding pattern (cations self-exclude themselves). This is the first direct evidence for the asymmetric distribution of cations bound to a polyphosphate polymer, raising questions about polyphosphate assembly mechanisms and its influence on the functional role of polyphosphate in cell physiology. In addition, these strategies were used here to explore the three-dimensional elemental distribution are novel for biological materials. We believe that the experimental pipeline shown here can be applied to a variety of models (synaptic vesicles, endoplasmic reticulum, etc) where ion mobilization plays a crucial role in the broad physiological processes.

REFERENCES:

- [1] Docampo R et al., *Nat Rev Microbiol* 3(3) (2005), p. 251-61.
- [2] Friel JJ and Lyman CE, *Microsc Microanal* 12(1) (2006), p. 2-25.
- [3] Schlossmacher P et al., *Microscopy Today* 18(4) (2010), p. 14-20.
- [4] This research was supported by CNPq, FAPERJ, CAPES and FINEP (Brazil)

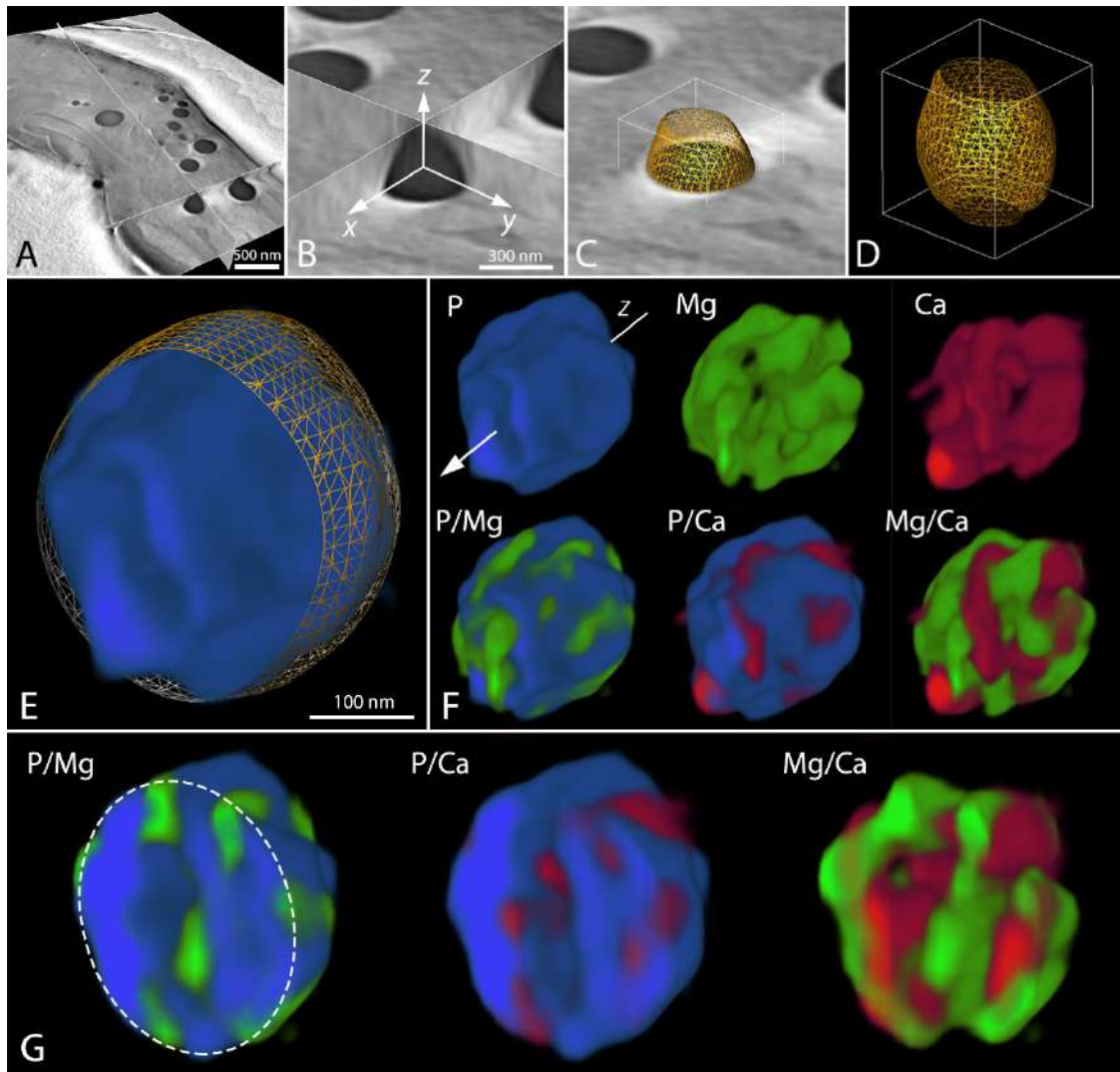
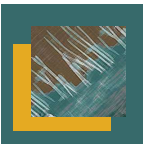


Figure 1. Distribution of ions inside acidocalcisomes. A, STEM-tomography of whole parasite. B-D, 3D model of an acidocalcisome (orange). E-G, 3D distribution of phosphorus (blue), magnesium (green) and calcium (red). The overlay between different elements shows a self-exclusion pattern mainly with magnesium and calcium. In "G" is showed the core of the virtually sliced acidocalcisome and its elemental distribution.



Calcium Silicate Hydrated Incorporated With Silver Ions For Biomaterials Application

Yoshihara, N. M. A^{1*}, Castro, K. L. S.¹, Ribeiro, A. R.²; Archanjo B. S.¹, Achete, C. A.¹.

1. Divisão de Metrologia de Materiais, Instituto Nacional de Metrologia, Qualidade e Tecnologia– INMETRO, RJ, Brasil.

2. Universidade do Grande Rio – UNIGRANRIO, RJ Brasil.

*Email: natalia.yoshihara@gmail.com

Calcium silicate (CS) ceramics has been investigated for bone substitutes in clinical applications purpose due to its high bioactivity [1]. Incorporating these materials with specific metallic ions is an approach that aims to improve bone healing, as well as bioactivity, antibacterial effect, among others deficient or absent properties in this material [2]. In this study, calcium silicates hydrated (CSH) and calcium silicate incorporated with silver a biofunctional metallic element (Ag- incorporated CSH - on different concentrations (1%, 3%, 5% and 10%) powder was prepared by chemical precipitation according to procedure proposed by Wan et al [3]. The material was characterized by scanning electron microscopy (SEM), scanning electron microscopy operated in transmission mode (TSEM), X-ray photoelectron spectroscopy (XPS), X-Ray Fluorescence (XRF) and X-ray diffraction (XRD). The in vitro bioactivity, was evaluated through incubation in simulated body fluid solution (SBF) as recommended by ISO 23317:2007 standard. The antibacterial effects will be tested on gram-positive bacterium *Staphylococcus aureus*. Partial results showed the presence of silver, as well as few significantly modification in the morphology and crystal structure in all incorporated samples. The XPS results shows the presence of metallic silver while in the XRD two phases of silver (metallic silver and silver chloride) were found. In addition, the CSH crystallinity is slightly reduced as the silver is incorporated. All samples showed bioactivity. Ag-decorated CSH pellet presented bioactivity similar to the unincorporated CSH, but the apatite aggregates have different shapes which can be related with different chemical compositions.

REFERENCES

- [1] ZHU, Y. et al. Substitutions of strontium in mesoporous calcium silicate and their physicochemical and biological properties. *Acta Biomaterialia*, v. 9, p. 6723-6731, 2013.
- [2] DU, H.; WEI, Z. Surface microstructure and cell compatibility of calcium silicate and calcium phosphate composite coatings on Mg–Zn–Mn–Ca alloys for biomedical application. *Colloids and Surfaces*, v. 83, p. 96-102, 2011.
- [3] WAN, X.; CHANG, C.; MAO, D.; JIANG, L.; LI, M. Preparation and in vitro bioactivities of calcium silicate nanophase materials. *Materials Science and Engineering*. v. 25, p. 455-461, 2005.
- [4] This research is supported by CNPq (Brazil).

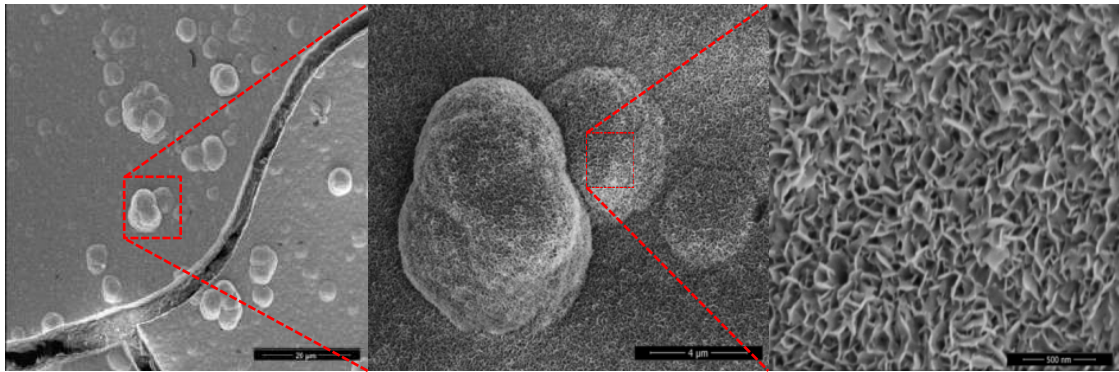
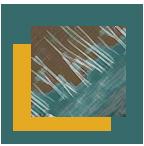


Figure 1. SEM Micrograph of pure calcium silicate after 14 days in SBF solution.

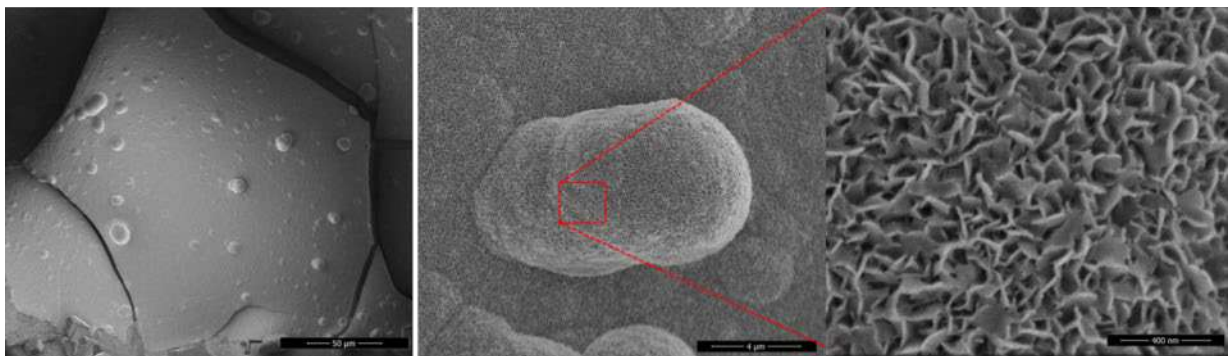


Figure 2. SEM Micrograph of calcium silicate incorporated with 10% of Ag after 14 days in SBF solution.

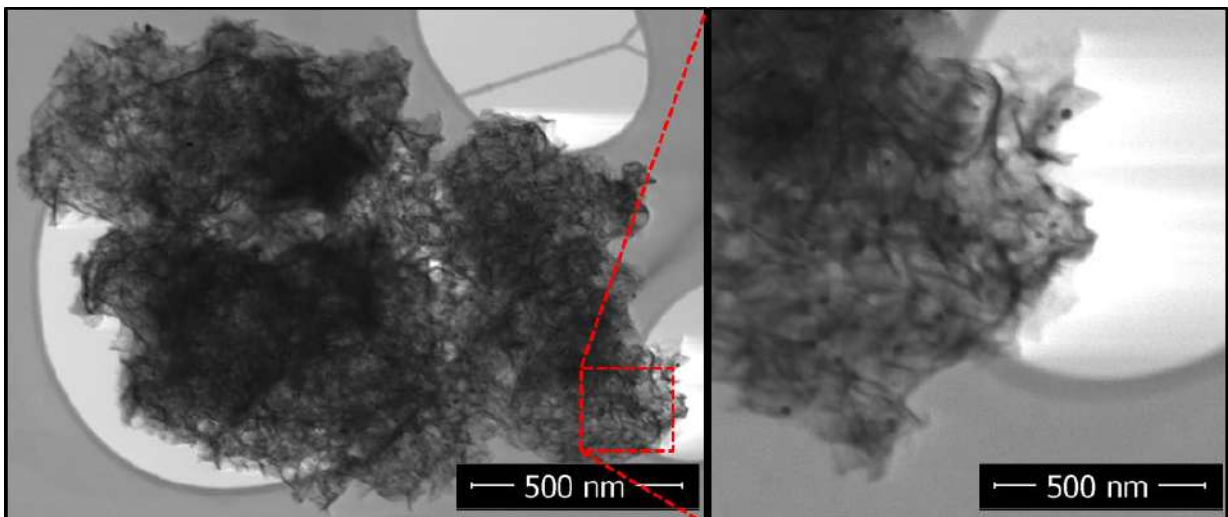


Figure 3. TSEM Micrograph of calcium silicate incorporated with 3% Ag.



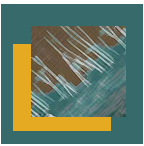
Nanotoxicological evaluation of nano-bio interface using 3D bone cell models

S. Gemini-Piperni^{1*}, W. De Souza², Bráulio Archanjo³, André Linhares Rossi¹, L.A. Rocha⁴, R. Borojevic⁵, M. Granjeiro², A. R. Ribeiro⁶

1. Applied Physics Department, Brazilian Center for Physics Research- CBPF Rio de Janeiro, Brazil
2. Directory of Life Sciences Applied Metrology, National Institute of Metrology Quality and Technology, Rio de Janeiro, Brazil
3. Materials Metrology Division, National Institute of Metrology Quality and Technology, Rio de Janeiro, Brazil
4. Physics Department, University Estadual Paulista, Bauru, Brazil
5. Center of Regenerative Medicine, Faculty of Medicine - FASE, Petrópolis, Brazil
6. Postgraduate Program in Translational Biomedicine, University of Grande Rio, Duque de Caxias, Brazil

*Email: sara.gemini@hotmail.com

Titanium (Ti) and its alloys are extensively used in dentistry due to their good biocompatibility properties that provide more comfortable and durable implants to patients [1]. However, metallic ions and debris (in micro and nanoscale) released by Ti-based implants surface degradation may lead to implant loss [2,3]. 2D cell culture monolayer commonly used in nanotoxicity studies loses the original tissue organization. To overcome these challenges, the development of 3D cell model able to maintain the protein-protein interactions, cell polarity and original tissue organization are being used in nanotoxicology [4]. This study focused on the interaction of titanium dioxide nanoparticles (NPs) with a 3D bone cells spheroidal model. We explored the events occurring at the nano-bio interface, to better understand the biological interactions with nanoscale titanium dioxide particles in a model able to mimic original tissue organization. Spheroid formed by different cell number were characterized for size, volume and viability and the model formed by 10000 cell/well showed the best characteristic to following studies with NPs. This model was exposed to dispersed anatase NPs at the concentration of 5 and 100 µg/mL during 72h. Cell viability and cell cycle analyses were performed using flow cytometry, founding no differences after NPs exposition. Cytochemical staining for alkaline phosphatase and alizarin red were performed to confirm cell differentiation and mineralization. Results show that, despite NPs exposition, SAOS2 cells in 3D culture are able to differentiate as well as mineralize. Moreover, Helium Ion Microscopy (HIM) images of sub-nanometer resolution demonstrated that the 3D structure is not compromised by NPs presence. It is important to note how this innovative technic permits to investigate sub nanometer resolution without interference generating by carbon and gold coatings. Transmission Electron Microscopy (TEM) analyses showed internalization both in low and high NPs concentration after 72 hours exposition. Moreover, anatase suspensions in culture medium supplemented with BSA were investigated by TEM analysis. Nano-Bio interface studies were performed using elemental map analyses confirming the ion shell rich in calcium and phosphorus formed around NPs. SDS-page and mass spectrometry was used to identify protein corona adsorbed to NPs. Proteins like serum albumin and glycoproteins founded adsorbed to NPs surface suggesting a very important role of those proteins in NPs internalization and transport as well as influence in the mineral phase of bone, thanks their affinity for calcium ions. Hematoxilin eosin and Masson's Trichrome staining showed a NPs accumulation in a side of the sphere, and a higher collagen spot after high dose TiO₂ exposition. Microscopy technics used in this work strongly suggest that higher TiO₂ internalization in 3D spheroidal cell model do not cause toxic effect. Moreover, cellular differentiation and mineralization are not compromised by short time NPs exposition. Finally, increased bone organic matrix production after



exposition to high concentration of NPs open the possibility of use this system in bioengineering application.

REFERENCES

- [1] U. Diebold, Sci Rep. 48 (2003) 53
- [2] D.M. Vasconcelos et al., Biomaterials (2016)
- [3] J.J. Jacobs et al., J. Arthroplasty, 19 (2004) 59
- [4] S. L. Chia et al, Small. 11 (2014) 702
- [5] This research was supported by INMETRO, CBPF, FAPERJ and CNPQ.

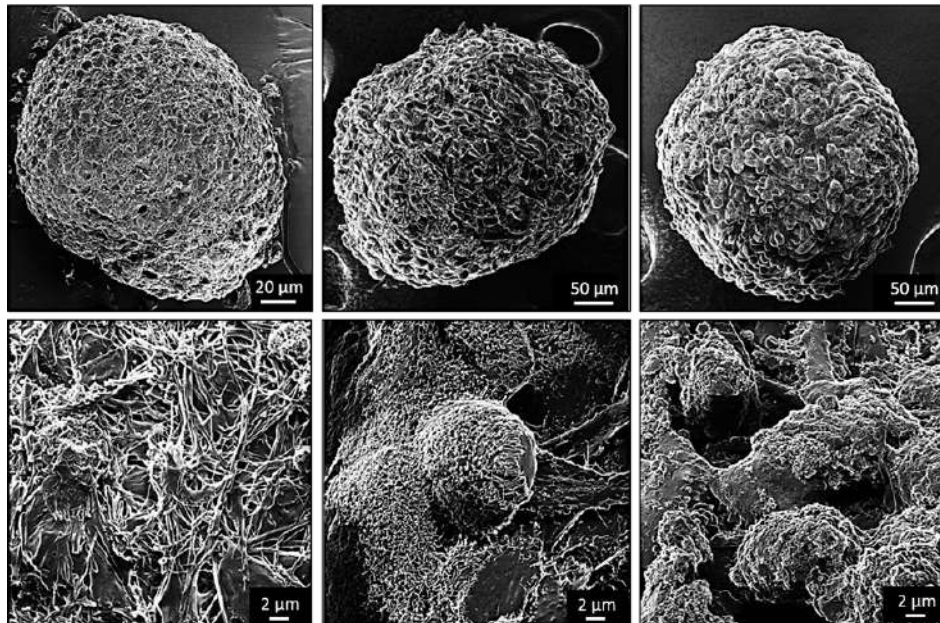


Figure 1. HIM micrograph of spheroid exposed to (a and d) 0, (b and e) 5, (c and f) 100 µg/ml NPs during 72 hours.

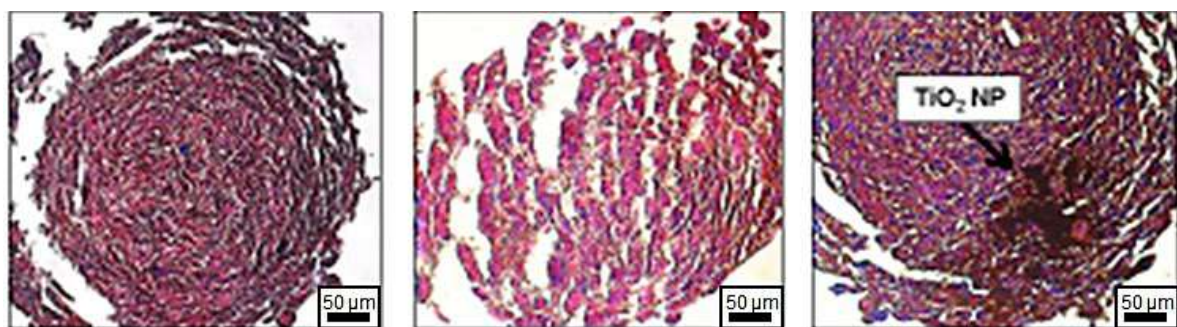


Figure 2. Masson Thricomic staining of spheroid exposed to (A) 0, (B) 5, (C) 100 µg/ml NPs during 72 hours. Black arrow indicates NPs deposition, Blue spot shows positive staining for collagen presence.



The Improvement Of Osteoblast Adhesion And Proliferation on TiO₂ Nanotubes Coated With Lectin From *Oreochromis niloticus*

Keicyanne Fernanda Lessa dos Anjos¹, Janaina Viana de Melo², Alessandra Batista de Mattos², Giovanna Machado², Cynarha Daysy Cardoso da Silva¹, Luana Cassandra Breitenbach Barroso Coelho³, Regina Célia Bressan Queiroz de Figueiredo^{1*}.

1. Instituto Aggeu Magalhães, Departamento de Microbiologia, Recife, Brasil.

2. Centro de Tecnologias Estratégicas do Nordeste, Laboratório de Microscopia e Microanálise, Recife, Brasil.

3. Universidade Federal de Pernambuco, Departamento de Bioquímica e Biofísica, Recife, Brasil.

*Email: bressan@cpqam.fiocruz.br

Titanium (Ti) and Ti-based alloys are widely used in orthopedic and dental implants, due to their excellent biocompatibility, corrosion resistance and mechanical properties. However, the bio-inert nature of Ti requires a long osseointegration period, increasing the risk of implant loosening. In this regard, many efforts have been made in attempt to optimize the osseointegration and biocompatibility of implant surface [1]. Lectins, proteins that specifically bind to carbohydrate moieties of diverse molecules [2], play important roles in a wide range of biological processes, including cell adhesion and bone remodeling [3]. In this study we aimed to explore the potential of the lectin OniL, from the serum of fish *Oreochromis niloticus*, in improve the biocompatibility of TiO₂ nanotubes. TiO₂ nanotubes (TiO₂-NT) were synthesized by anodization and their surface were negatively charged by incubation in Ethanol-NaOH solution (TiO₂-NTneg). The OniL (200 µg/mL) was adsorbed to the surface of TiO₂-NTs by spin coating. (TiO₂-NTlec). The TiO₂-NT, TiO₂-NTneg and TiO₂-NTlec were morphologically characterized by scanning electron microscopy (SEM). The lectin absorption was determined by Fourier Transform Infrared Spectroscopy (FTIR), electrochemical impedance spectroscopy (EIS) and cyclic voltammetry (CV). For adhesion assays, the osteoblasts were cultivated on different titanium surfaces for 24, 48 and 72 hours, stained with DAPI and Rhodamine-phalloidin and observed by fluorescence microscopy. The number of adhered cells was evaluated by measuring the amount of stained nucleus in 100 randomly chosen fields. The cell proliferation was assayed by alkaline phosphatase activity test. As showed in Fig 1, after anodization process the TiO₂ nanotubes exhibited organized and uniform columnar microstructure. No difference in this profile was observed in TiO₂-NTlec, suggesting that OniL forms a thin layer on the surface of NTs. The presence of lectin on the surface of NTs was confirmed by VC, EIE and FTIR. The TiO₂-NTlec enhanced the number of adhered cells, after 48 hours of cultivation (Fig.2A-B), followed by an increase in the alkaline phosphatase activity indicative of intense cell proliferation (Fig.2C). Although further studies are still necessary to better elucidate the role of OniL in osseointegration, our results demonstrated that this lectin improved the biocompatibility of TiO₂-NTs.

REFERENCES

- [1] R.L. Oréfice, Biomateriais : Fundamentos e Aplicações, 2 (2012)
- [2] S. Misquiti et al, J. Biol. Chem., (1994).
- [3] Chan et al. eLife (2016)
- [4] Supported by: CNPq, FIOCRUZ, CETENE.

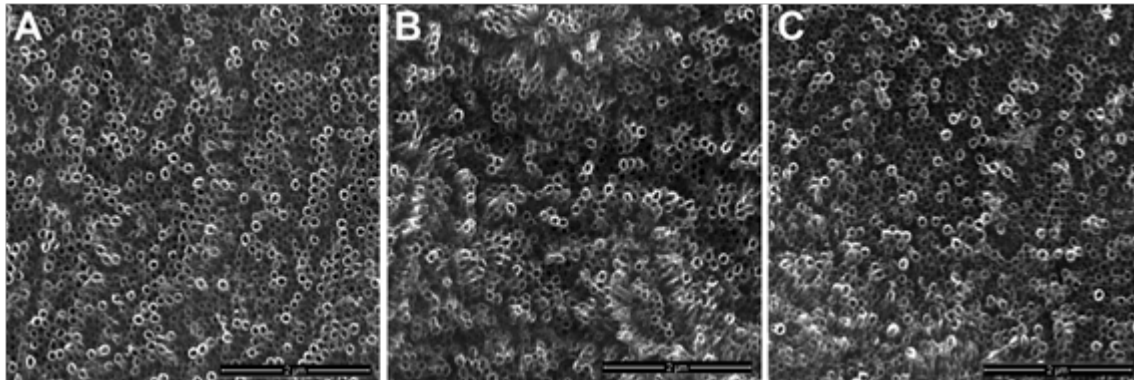
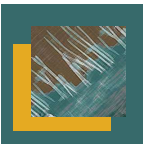


Figure 1. Scanning electron microscopy images of (A) TiO₂-NT, (B) TiO₂-NTneg, (C) TiO₂-NTlec, bars=2μm.

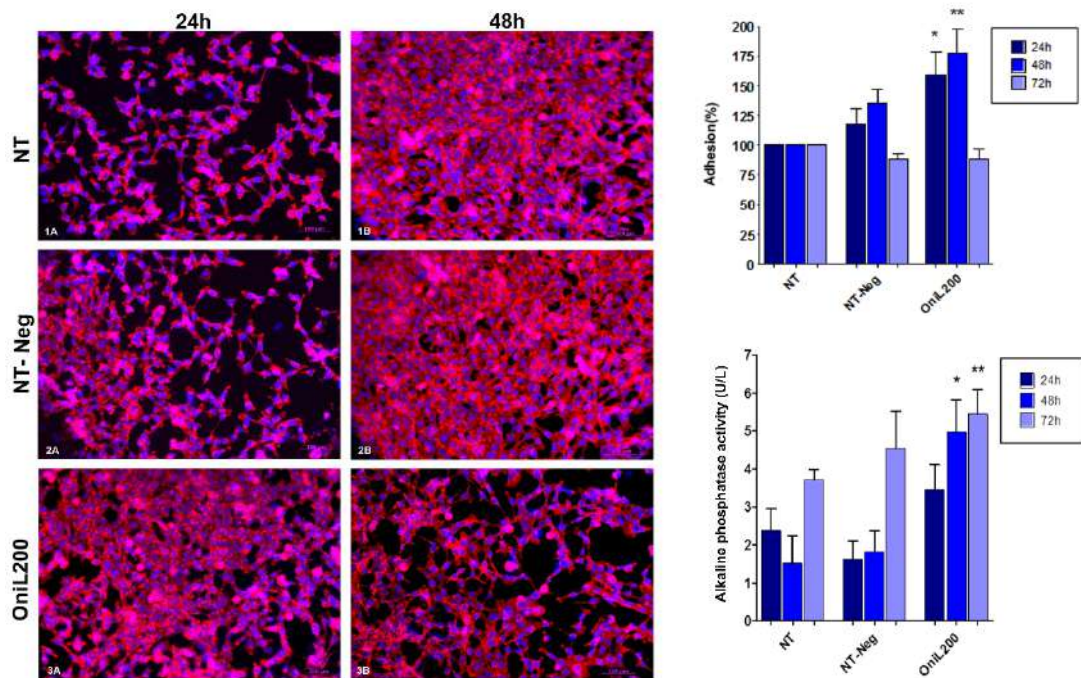


Figure 2. (A) Representative fluorescence microscopy images of cells adhered to different TiO₂ nanotube surfaces. NT= TiO₂ nanotube; NT-neg = negativated TiO₂ nanotubes; Onil200=TiO₂ covered with OniL at 200 μg/mL; Bars=100 μm. (B) Effects of OniL on cell adhesion. *p < 0.001 and **p < 0.0005 compared with NT 24 hours and 48 hours of cultivation, respectively; (C) Effect of Onil on cell proliferation. *p < 0.05 and **p < 0.02 compared with NT 48 hours and 72 hours of cultivation, respectively.



Influence of pH on the size of gold nanoparticles synthesized using *Virola oleifera* extract

Luis Alberto Contreras¹, Jairo Pinto de Oliveira¹, Marco Cesar Cunegundes Guimarães¹

1. Laboratório de Ultraestrutura Celular Carlos Alberto Redins, Universidade Federal do Espírito Santo - Av. Marechal Campos, 1468, Maruípe, Vitória, E.S. 29.042-755 – Brasil, Tel: +55 (27) 3335-7365.

*Email: marco.guimaraes@ufes.br

In this study, we investigated the pH effects on the size of gold nanoparticles (AuNPs). AuNPs synthesized from *Virola oleifera* (Schott) A. C. Smith, which has antioxidant properties, extract was characterized using UV-Vis spectroscopy and Transmission Electron Microscopy (TEM). The pH of the starting solution varied from 3 to 7. It was found that pH influenced inversely on the nanoparticles sizes. As we increase the pH, the AuNPs size becomes smaller. Moreover, we observed that the best extract concentration was 0,5 mg.ml⁻¹. Growth of gold nanoparticles was confirmed in all conditions used by UV-Vis absorption spectroscopy (Fig. 1). Peak wavelength was observed between 530 and 540 nm. We achieved size variations between 9 nm and 16 nm. The morphology was confirmed by TEM, observing at pH 5 hexagonal nanoparticles and at pH 7 mostly spherical nanoparticles. (Figures 2 and 3). Concluding that the pH variation of the *Virola oleifera* solution in the AuNPs synthesis allows obtaining nanoparticles of different sizes and shapes. [1] [2]

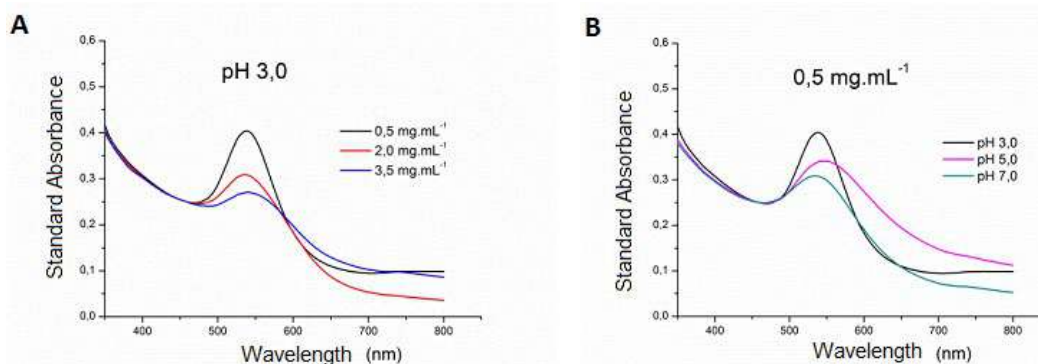
REFERENCES

[1] BÔA I.S.F; PORTO, M.L; PEREIRA, A.C.H; RAMOS, J.P.L; SCHERER, R., OLIVEIRA, J.P., et al. Resin from *V. oleifera* Protects Against Radiocontrast-Induced Nephropathy in Mice. *Journal PLoS ONE*, v.10, n.12, p.1-15, 2015.

[2] IRAVANI, S. Green synthesis of metal nanoparticles using plants. *Green Chemistry*, v. 13, n. 10, p. 2638, 2011.

ACKNOWLEDGEMENTS

This work was supported by the Laboratory of Cellular Ultrastructure Carlos Alberto Redins (LUCCAR), CAPES, FINEP and LABIOM.



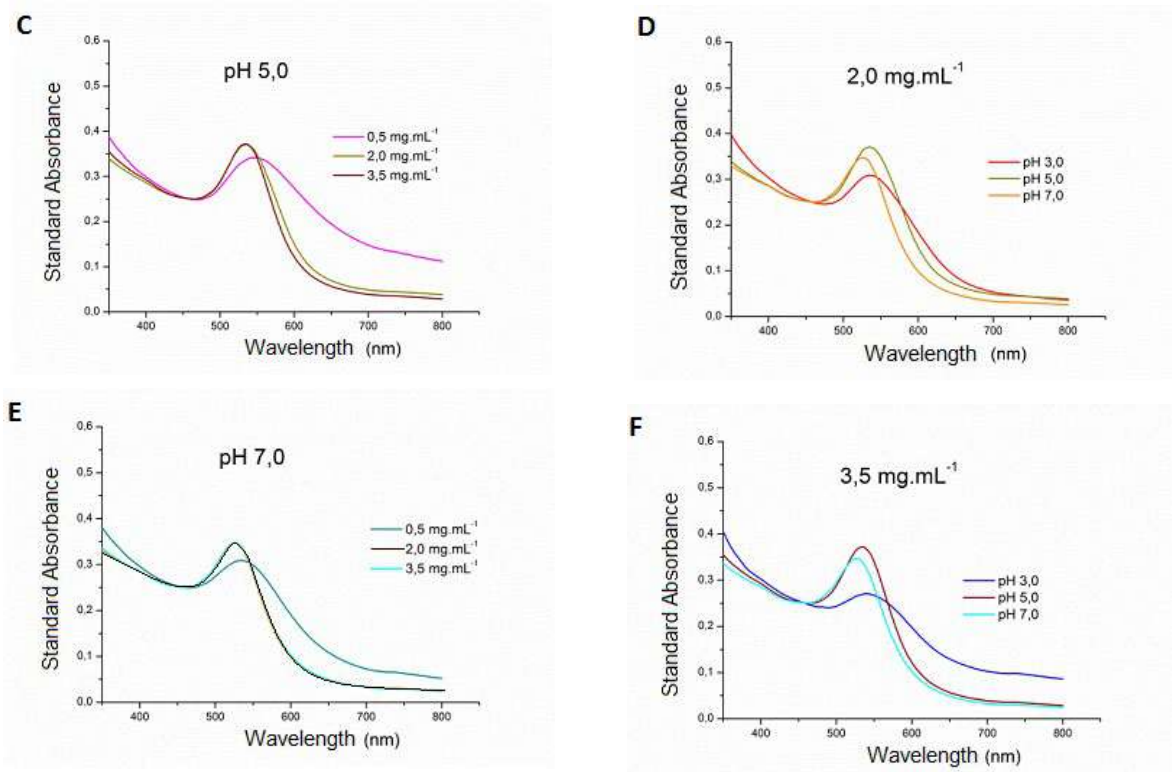
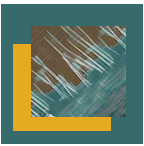


Figure 1. UV-Visible absorption spectroscopy. Comparison of different pH (A - C - E). Comparison of different concentrations of *V. oleifera* extract (B - D - F).

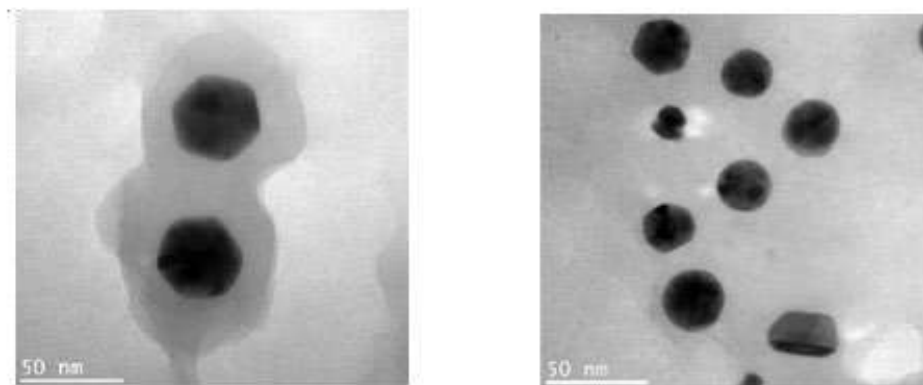
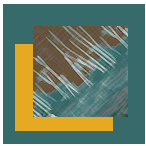


Figure 1. Transmission electron microscopy assay (pH 5 - 0.5 mg ml⁻¹ extract). **Figure 3.** Transmission electron microscopy assay (pH 7 - 0.5 mg ml⁻¹ extract).



Structural Colors in *Chalcopteryx rutilans* Male Dragonfly Wings

Wescley Walison Valeriano^{1*}, Rodrigo Ribeiro Andrade², Juan Pablo Vasco¹, Bernardo Ruegger Almeida Neves¹, Wagner Nunes Rodrigues^{1,2}, Paulo Sergio Soares Guimarães¹, Elizabeth Ribeiro da Silva^{2,3}, Ângelo Barbosa Monteiro Machado⁴

1. Departamento de Física, Instituto de Ciências Exatas, UFMG
2. Centro de Microscopia, UFMG
3. Departamento de Morfologia, Instituto de Ciências Biológicas, UFMG
4. Departamento de Zoologia, Instituto de Ciências Biológicas, UFMG

In dragonflies color has many functions the most important being sex recognition, courtship and territory behaviors. In *Chalcopteryx rutilans* - a dragonfly found in the Amazonian rain forest – those functions are performed by displaying their strongly iridescent hind wings (Figure 1), whereas the hyaline forewings are used to maintain the flight. The phenomenon of iridescence results from physical optics effects such as diffraction and interference [1]. The aim of this work is to study the structures responsible for the male wing iridescence in *Chalcopteryx*. Visible range reflectance was measured for each different colored regions of the wings. In order to determine the internal microstructure of the region that exhibits the same color, Scanning Electron Microscopy – SEM – was performed in cross-sections of the wings, after cutting in situ by Focused-Ion Beam – FIB (Figure 2). SEM and TEM images revealed that the wings have a multilayered structure alternating different electron density materials. The number and thicknesses of the layers change across the wing, correlating with the local color. The composition of the layers is considered as being of chitin with different levels of melanin pigmentation. Optical reflectance measurements were performed in two different polarizations, as shown in Figure 3, as well the theoretical modelling of the structure. The electron density profile as seen in the SEM cross section is proportional to the optical density (Figure 2). The optical reflectance resulting from a structure with such a modulated refractive index was calculated numerically, using a guided mode expansion method [2], and shown in Figure 3. Electric Force Microscopy was used to measure the local dielectric constant of the different layers, as shown in Figure 4. A good correlation of the modeled structure with the experimental data is obtained, confirming that *Chalcopteryx rutilans* male wings colors result from a multi-layer structure, i.e., these wings are natural one-dimensional photonic crystals.

ACKNOWLEDGEMENT

The authors would like to acknowledge CNPq and FAPEMIG for supporting this research. We acknowledge the Center of Microscopy of the Universidade Federal de Minas Gerais (<http://www.microscopia.ufmg.br>) for providing the equipment and technical support for the microscopy experiments.

REFERENCES

- [1] “Iridescences, The Physical Colors of Insects”, Serge Berthier, Springer, 2007.
- [2] J. P. Vasco, P.S.S. Guimarães, D. Gerace, Physical Review B 90, 155436 (2014).

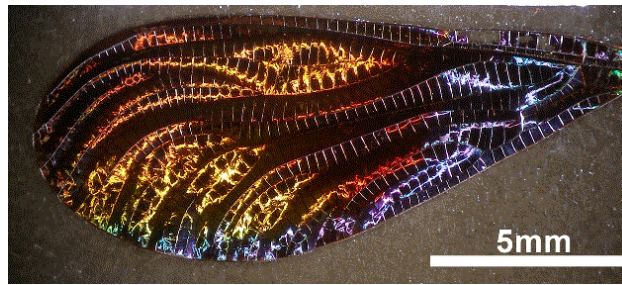
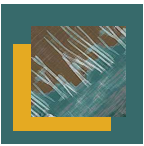


Figure 1. Top surface of a male hind wing of *Chalcopteryx rutilans*.

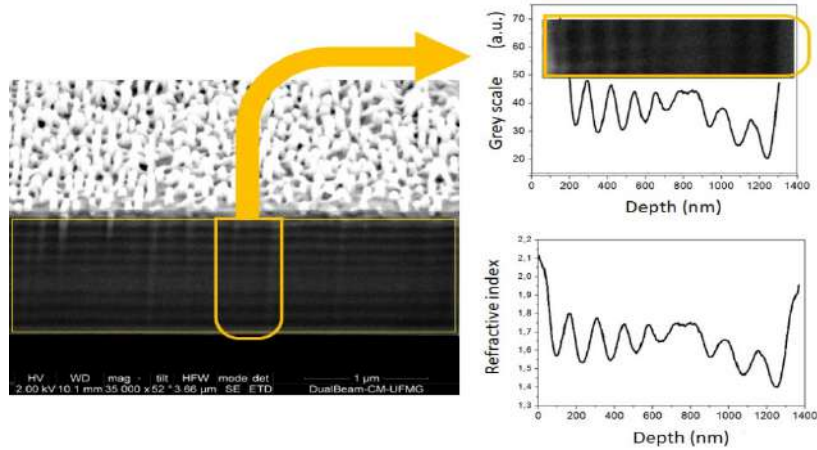


Figure 2. SEM image of the blue region with the gray scale of the selected area and the corresponding refractive index profile.

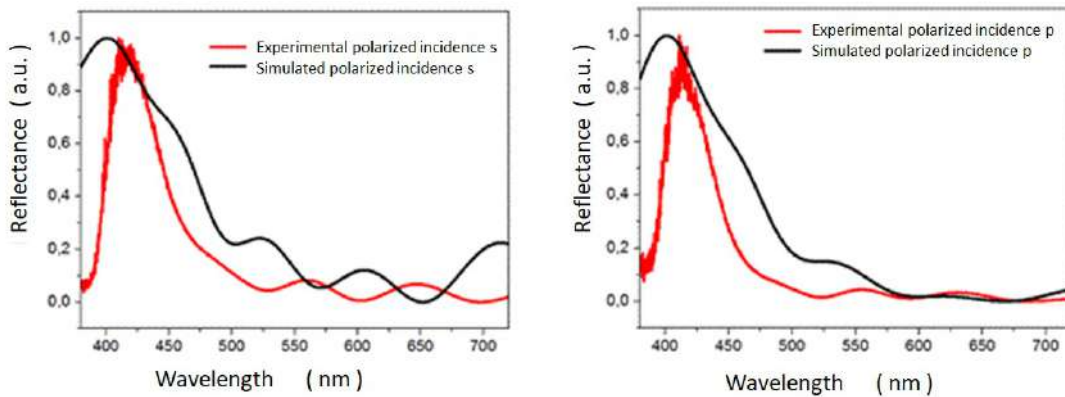


Figure 3. Comparison of simulation and experimental measurement of the reflectance with polarized incidence (s and p) of the blue region.

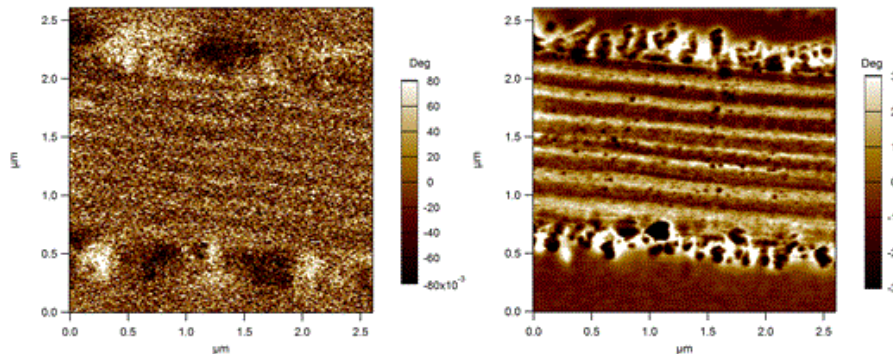


Figure 4. To the left an EFM image with applied voltage of 0 V, in the right with applied test of -10 V.



DOI: [INSERIR ENDEREÇO DO DOI AQUI.](#)

Caderno de Resumos do 26º Congresso Brasileiro de Microscopia da SBMM – ISSN: [INSERIR AQUI.](#)

Biom mineralization Process and Time Resolved Oxidation Study on Magnetotactic Bacteria

Jacques Werckmann^{1,2*}, Jefferson Cypriano³, Christopher T. Lefèvre⁴, Kassioyé Dembelé⁵, Ovidiu Ersen⁵, Dennis A. Bazylinski⁶, Ulysses Lins³ and Marcos Farina¹

1. Instituto de Ciências Biomédicas, Universidade Federal do Rio de Janeiro, 21941-902, Rio de Janeiro, Brazil

2. Centro Brasileiro de Pesquisas Físicas, Rua Dr. Xavier Sigaud, 150 - Urca - Rio de Janeiro - RJ - Brazil - CEP: 22290-180

3. Instituto de Microbiologia, Universidade Federal do Rio de Janeiro, 21941-902, Rio de Janeiro, Brazil.

4. CNRS/CEA/Aix-Marseille Université, UMR7265 Institut de biosciences et biotechnologies, Laboratoire de Bioénergétique Cellulaire, 13108, Saint Paul lez Durance, France

5. Institut de physique et chimie des matériaux de Strasbourg (IPCMS) UMR 7504 CNRS 23 rue du Lœss - BP 43 67034 Strasbourg Cedex 2, France

6. School of Life Sciences, University of Nevada at Las Vegas, Las Vegas, Nevada 89154-4004, USA.

*Email: j.werckmann@gmail.com

Magnetotactic bacteria (MTB) are the simplest organisms which produce biomineral like magnetite or greigite. They play a fundamental role in the iron cycling in the earth. So it is important to understand both the process of biomineralization as well as the evolution of magnetite sediments in the geological layers. To highlight these questions two approaches were implemented by transmission electron microscopy: the quantitative use of analytical scanning transmission electron microscopy and the in situ following of the oxidation process under temperature and oxygen. Note that the magnetite crystals under study grow inside vesicles (magnetosome membranes) produced by the invagination of the cytoplasmic membrane of the bacteria [1] i) Crystals are nucleated and grow from iron carried inside the vesicle by specific proteins. One of the unaddressed question is to know if it is possible to spatially map the iron carried inside the bacteria by electron microscopy? A partial answer was obtained in this work by studying cultivated and uncultivated bacteria. XEDS mapping showed that magnetosomes are enmeshed in a magnetosomal matrix in which iron accumulates close to the magnetosome forming a continuous layer visually appearing as a corona. EELS, obtained at high spatial resolution, confirmed that iron was present close to and inside the lipid bilayer magnetosome membrane. This study provides important clues to magnetite formation in MTB through the discovery of a mechanism where iron ions accumulate prior to magnetite biomineralization. ii) Many miniaturized chemical reactors have been developed to study reactions by using perfectly controlled experimental parameters. Some typical reactors are for instance microfluidic “lab-on-chip” devices, electron-microscope liquid [2] and solid-gas heating holder [3]. The last one is constituted by silicon carbon nitride heater with 6 micrometric holes isolated from the outside by two thin silicon nitride membranes allowing to reach a pressure of the reactive gas (oxygen in this example) up to 1 atmosphere. Before closing the cell a solution containing extracted and purified magnetosomes were deposited on the nitride heater and dried in air. The experiment was conducted with a temperature increase rate of 0.5°C/s up to 500°C by following in the same time the chosen areas by TEM mode. The results show that no modification of the structure happens before 300°C. Starting from this temperature, the Kirkendall effect is activated and creates at the core of the particles well defined cavities surrounded by nano-sized crystals.

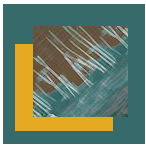


DOI: [INSERIR ENDEREÇO DO DOI AQUI.](#)

Caderno de Resumos do 26º Congresso Brasileiro de Microscopia da SBMM – ISSN: [INSERIR AQUI.](#)

REFERENCES

- [1] Arash Komeili. Molecular mechanisms of compartmentalization and biomineralization in magnetotactic bacteria. *FEMS Microbiol Rev.* 36 (2012) 232-255.
- [2] Taylor J. Woehl, Sanjay Kashyap, Emre Firlar, Teresa Perez-Gonzalez, Damien Faivre, Denis Trubitsyn, Dennis A. Bazylinski & Tanya Prozorov. Correlative Electron and Fluorescence Microscopy of Magnetotactic Bacteria in Liquid: Toward In Vivo Imaging. *SCIENTIFIC REPORTS* 2014 | 4 : 6854 |
- [3] Goergian Melinte, Ileana Florea, S Moldovan, Izabela Janowska, Walid Baaziz, Raul Arenal, Andreas Wisnet, C Scheu, Sylvie Begin-Colin, Dominique Bégin, C Pham-Huu, Ovidiu Ersen. A 3D insight on the catalytic nanostructuring of few-layer graphene. *Nature Communications* 2014 | 5:4109 |
- [4] This research was supported by: PROMETRO-INMETRO, FAPERJ; CNPq, CAPES, NSF, LIA-CNRS, French ANR



Cohesive Geometry of *Cryptococcus neoformans* Adhesion Contributes to Flower-Like Biofilms Formation

William Lopes¹, Mendeli HenningVainstein², Glauber R. De S. Araújo³, Susana Frases Carvajal³, Charley C. Staats¹, Rita Maria Cunha de Almeida², Augusto Schrank¹, Livia Kmetzsch¹ and Marilene H. Vainstein^{1*}

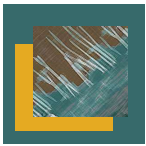
1. Centro de Biotecnologia, Universidade Federal do Rio Grande do Sul, Porto Alegre, Brazil;
2. Instituto de Física, Universidade Federal do Rio Grande do Sul, Porto Alegre, Brazil;
3. Instituto de Biofísica Carlos Chagas Filho, Universidade Federal do Rio de Janeiro, Rio de Janeiro, Brazil.

*Email: mhv@cbiot.ufrgs.br

The use of medical devices increased substantially and their utilization are all often complicated by infections with biofilm-forming microorganisms and by the improved resistance to antimicrobial agents. Microbial biofilms are recognized as highly structured, adaptive and dynamic communities in which phenotypic diversification allow microorganisms to adapt to different environments under distinct conditions. Notably, it is estimated that up to 80% of all microorganisms in the environment exist in this lifestyle [1]. The yeast *Cryptococcus neoformans* can form biofilms on medical devices, including ventriculoatrial shunt catheters, peritoneal dialysis fistula, cardiac valves and prosthetic joints [2]. The increasing use of ventriculoperitoneal shunts to manage intracranial hypertension associated with cryptococcal meningoencephalitis highlights the importance of investigating the biofilm-forming properties of this organism. Although previous studies using confocal microscopy provided initial insights into cryptococcal biofilm structure, conventional techniques of scanning electron microscopy (SEM) do not achieve preservation and resolution of mature biofilm ultrastructure. In this context, this work aims to study the details of ultrastructural organization of cryptococcal biofilms and highlight its importance in host biogeography. For biofilm formation, *C. neoformans* (B-3501 strain) cells were grown for 24 h at 30 °C in Sabouraud broth media. Cells were then collected by centrifugation, counted using a hemacytometer and suspended at 107 cells/mL in Dubelcco's modified eagle media with high glucose. After that, the suspension was added into individual wells of polystyrene 24-well plates containing sterile glass coverslips and incubated at 37 °C for 48 h. Following incubation, the biofilms were prepared for SEM by applying a modified protocol developed for visualization of *C. neoformans* planktonic cells [3]. To characterize the underlying geometrical structure of cell distribution during biofilm formation, SEM images were analyzed with the software ImageJ. The nearest neighbors were calculated by means of a Delaunay Triangulation using Fortune's algorithm. It was found that there is a correlation between biofilm formation and more orderly underlying structures (Fig. 1). Our study revealed a predominant organization of biofilms consisted of a dense layer of extracellular matrix extending to the top, over and among cells. The hallmark of this study was the detection of a well-shaped ultrastructure of *C. neoformans* biofilms resembling a flower-like pattern. Distinct levels of spatial organization were observed: adhered cells, clusters of cells, as well as the community of clusters (Fig. 2). This fact triggers the importance to investigate the complications of cryptococcal meningoencephalitis associated to spatial distribution of clusters [4].

REFERENCES

- [1] Donlan RM. *Emerg Infect Dis.* 8 (2002) 881-890.
- [2] Martinez LR, Casadevall A. *Microbiol Spectr.* 3 (2015).
- [3] de S Araújo GR, et al. *J Struct Biol.* 193 (2016) 75-82.



[4] This research was supported by CNPq (Brazil). We also thank Dr. Kildare Miranda and Rachel Rachid of CENABIO-UFRJ for their support.

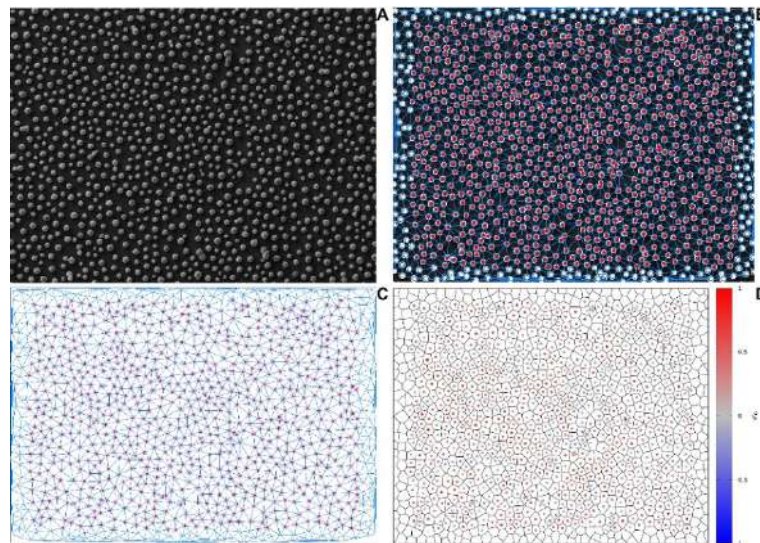


Figure 1. Geometrical distribution of *C. neoformans* B3501 cells during biofilm formation. (A) SEM, 1kx of magnification. (B-C) Dots represent the centers of the ellipses fitted to the cells with ImageJ. Blue line segments are the Delaunay triangulation. (D) It was found that there is a correlation between higher levels of biofilm formation and more orderly underlying structures. For instance, B3501, a good biofilm producer has $\psi_6=0.21$

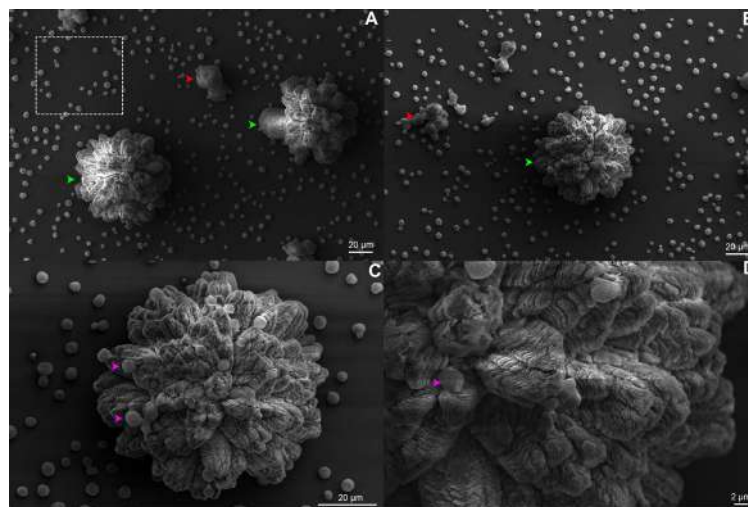
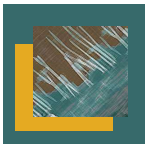


Figure 2. SEM of *C. neoformans* B3501 flower-like clusters. Biofilm showed a complex structure and spatial organization. (A) The dotted square indicates cryptococcal cells attached to the surface. (A, B) Community of clusters with unshaped and asymmetrical structure (red arrows) and mature biofilm resembling flower-like shapes (green arrows). Flower-like cluster shown in higher magnification (C, D) with cells interwoven the ECM (pink arrows).



High-resolution and quantitative three-dimensional Analysis of *Plasmodium chabaudi* Hemozoin Crystals

Wendt, C.¹, Gomes, F.¹, de Souza, W.¹ and Miranda, K.¹

1. Laboratório de Ultraestrutura Celular Hertha Meyer, Instituto de Biofísica Carlos Chagas Filho and Instituto Nacional de Ciência e Tecnologia em Biologia Estrutural e Bioimagens – Universidade Federal do Rio de Janeiro, Rio de Janeiro, Brazil.

Malaria is a disease caused by protozoan parasites from the genus *Plasmodium* with the highest impact on public health in endemic areas. Morbidity and mortality of malaria results from the asexual replication of *Plasmodium* in the erythrocyte of the mammalian host. In the course of its intraerythrocytic development, malaria parasites incorporate massive amounts of the host cell cytoplasm. Internalized hemoglobin is digested in a compartment with acidic pH named food vacuole, producing aminoacids and others by products, namely heme. Due to its toxic effects, free heme is immobilized and stored in a crystal form known as hemozoin. This mechanism is essential to parasite development and represents a physiological step used as target for many antimalarial drugs [1]. The physical and chemical properties of hemozoin crystals have been extensively investigated using its chemical analogous, β -hematin, prepared synthetically in vitro [2]. Although the structure of β -hematin has been characterized in detail, information on the structure of hemozoin crystals is restricted to a few data. In addition, the specific mechanisms that nucleate and propagate hemozoin crystallization within the food vacuole remain under debate. In this work, we studied the hemozoin crystals structure of the murine malaria parasite *Plasmodium chabaudi* using transmission electron tomography and high-resolution transmission electron microscopy. Transmission electron tomography revealed the three-dimensional (3D) dispersion of hemozoin crystals within the food vacuole. At the schizont stage (late stage of development), we noticed a large food vacuole completely filled with hemozoin crystals. Volume analysis of hemozoin crystals after segmentation and 3D reconstructed revealed that crystal size varied considerably within a single vacuole (figure 1). Isolated hemozoin crystals obtained from late developmental stages were also analysed by high-resolution transmission electron microscopy (figure 2), which revealed the crystalline planes of the hemozoin crystal measuring about 1.1 nm. Taken together, these results provide new insights on structure of hemozoin crystals in rodent malaria parasites.

REFERENCES

- [1] P. A SIGALA; D. E. GOLDBERG, Annual Review of Microbiology, 68 (2014) 259–278.
[2] S. PAGOLA et al, Nature, 404 (2000) 307–310.

This work was supported by CNPq, FAPERJ, FINEP and CAPES (Brazil)

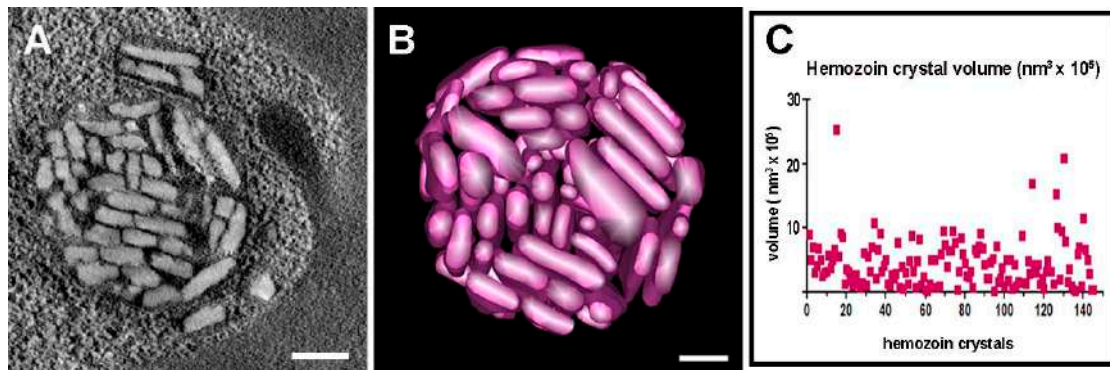
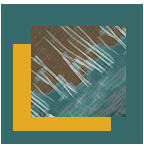


Figure 1. Spatial distribution of hemozoin crystals in a schizont stage parasite. A large food vacuole was observed in the central portion of the cell (A). Three-dimensional modeling (B) allowed a better examination of hemozoin crystals dispersion inside the food vacuole. Volume analysis (C) revealed that most crystals had a volume between 0.2×10^{-5} to $25 \times 10^{-5} \text{ nm}^3$ (D). Scale bar: 100nm.

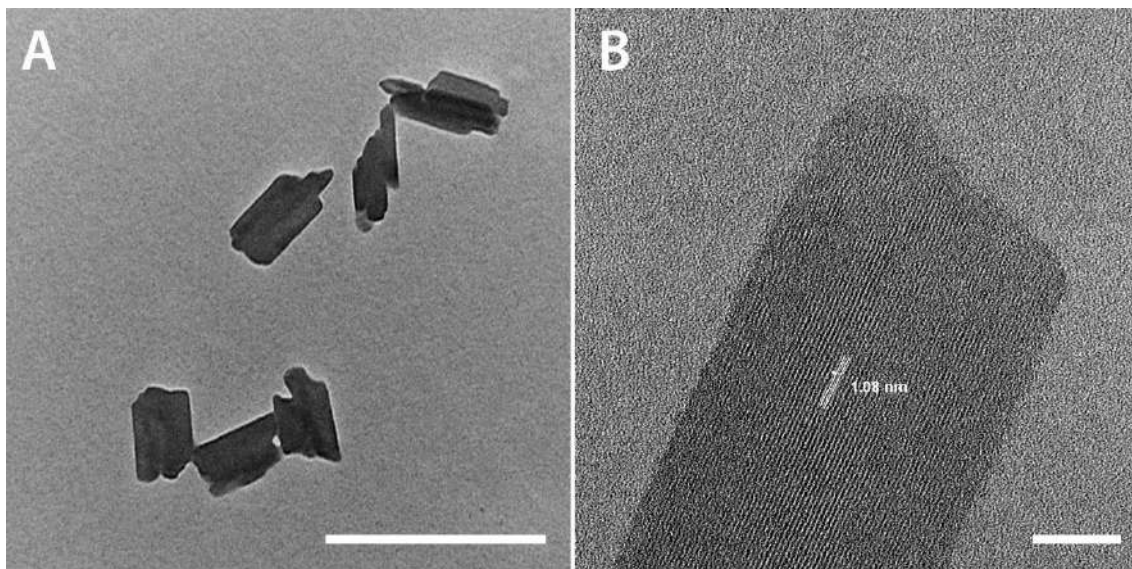
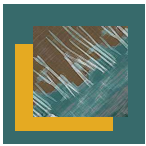


Figure 2. Hemozoin crystals isolate from *Plasmodium chabaudi* (A) were observed by high resolution electron microscopy, which revealed its crystalline morphology. Scale bar: 500 nm (A); 20nm (B).



Ultrastructural Identification of Flagellar Ectosomes-Like Structures in the Protists *Tritrichomonas foetus* and *Trichomonas vaginalis*

Antonio Pereira-Neves^{1*}

1. Fiocruz Pernambuco, Instituto Aggeu Magalhães – Departamento de Microbiologia, Recife, Brazil

*Email: antoniopnn@yahoo.com.br

Flagella/cilia are microtubule-based protrusions of the plasma membrane that were first noticed for their role in cell motility and locomotion. In recent decades, it has become clear that flagella/cilia also have important sensory roles and act as antennae, sensing the cell's environment [1]. In addition to its role as sensory receiver, the flagella/cilia also release extracellular vesicles (EVs) [2]. EV is a broad term referring to any extracellular membrane bound vesicle that includes exosomes derived from multivesicular bodies and ectosomes formed via outward budding of the plasma membrane. Exosomes and ectosomes are tiny: less than 100nm for exosomes and between 100nm–1µm for ectosomes [2]. The release of EVs is a conserved form of intercellular communication used by prokaryotes and eukaryotes. Recent works with the green alga *Chlamydomonas*, the nematode *Caenorhabditis elegans* and mice demonstrated that ectosomes can be released from the flagella/cilia and can mediate the intercellular communication [2-3]. In this context, Trichomonads (Excavata, Parabasalia) are flagellated protists found in several environments. Among the most important trichomonads are *Tritrichomonas foetus* and *Trichomonas vaginalis*, which are parasites of urogenital tract of cattle and humans, respectively [4]. *T. foetus* causes premature abortion in cattle, while *T. vaginalis* provokes vaginitis and increases the risk of HIV transmission. The flagella in trichomonads vary in number and size in each species. *T. foetus* has three anterior flagella, whereas *T. vaginalis* has four, and both have one recurrent flagellum that runs toward the posterior region of the cell, forming an undulating membrane [4]. There are few studies about EVs in trichomonads [5] and neither of them report the presence of flagellar ectosomes. Consequently, the aim of this study is to identify flagellar ectosomes-like structures in *T. foetus* and *T. vaginalis*. To this, both parasites were cultivated in a TYM (trypticase, yeast extract and maltose) medium supplemented with 10% fetal bovine serum for 30 h at 37°C, which corresponds to the logarithmic growth phase, and prepared for scanning (SEM) and transmission (TEM) electron microscopy, as previously described [6]. SEM revealed numerous EVs ranging in diameter from approximately 50 nm–200 nm closely apposed to the tip and along the flagella of *T. foetus* and *T. vaginalis* (Fig. 1). Vesicular structures that seems to be in process of budding directly from the membrane of flagella were observed using TEM (Figs. 2a-e). In addition, some EVs were also seen surrounding the flagella (Figs. 2e-f). The structures found here are morphologically similar to the flagellar/ciliary ectosomes described in *Chlamydomonas*, *C. elegans* and mammals [2-3]. Thus, the results demonstrate the presence of flagellar ectosomes-like structures in Trichomonads; however, further studies are necessary to better characterize these structures and their role in the parasites' biology. [7].

REFERENCES

- [1] P. Avasthi, W. Marshall, *Curr Biol*, 23 (2013) R471.
- [2] J. Wang, M.M. Barr, *Cell Mol Neurobiol*, 36 (2016) 449.
- [3] C.R. Wood, J.L. Rosenbaum, *Trends Cell Biol*, 25 (2015) 276.
- [4] M. Benchimol, *Microsc. Microanal*, 10 (2004) 528.
- [5] O. Two, et al., *PLoS Pathog*, 9 (2013) e1003482.
- [6] A. Pereira-Neves, et al., *PLoS One*, 10 (2015) e0129165.
- [7] This work was supported by the Program for Technological Development in Tools for Health-PDTIS/FIOCRUZ.

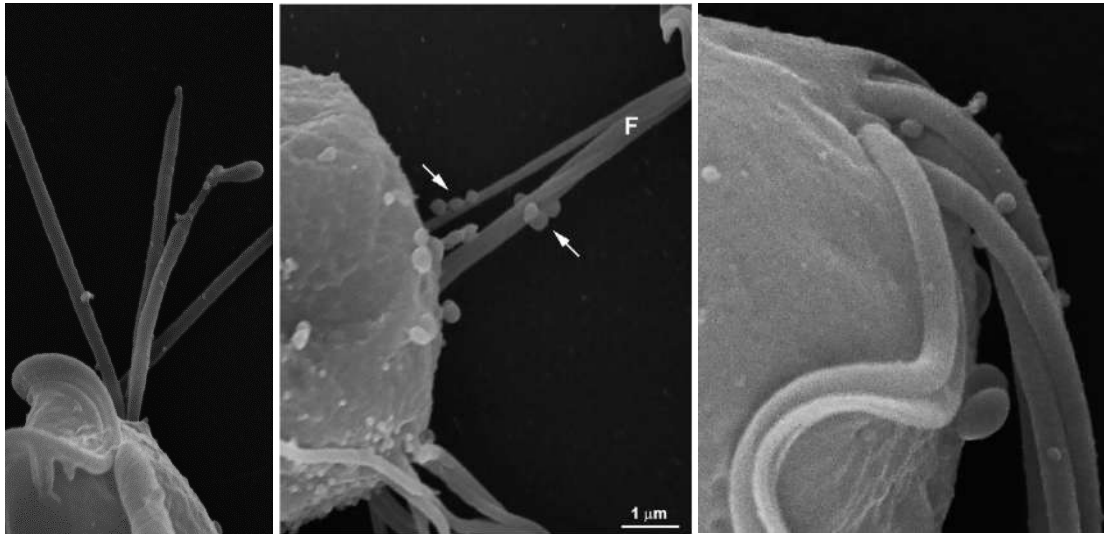
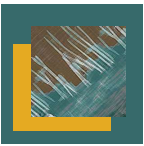


Figure 1. SEM of anterior region of *T. foetus* (a) and *T. vaginalis* (b-c) showing detailed views of flagella (F). Some EVs (arrows) can be seen closely apposed to the tip (a) and along (b-c) the flagella. Bars.: a-b, 1 µm; c, 500 nm.

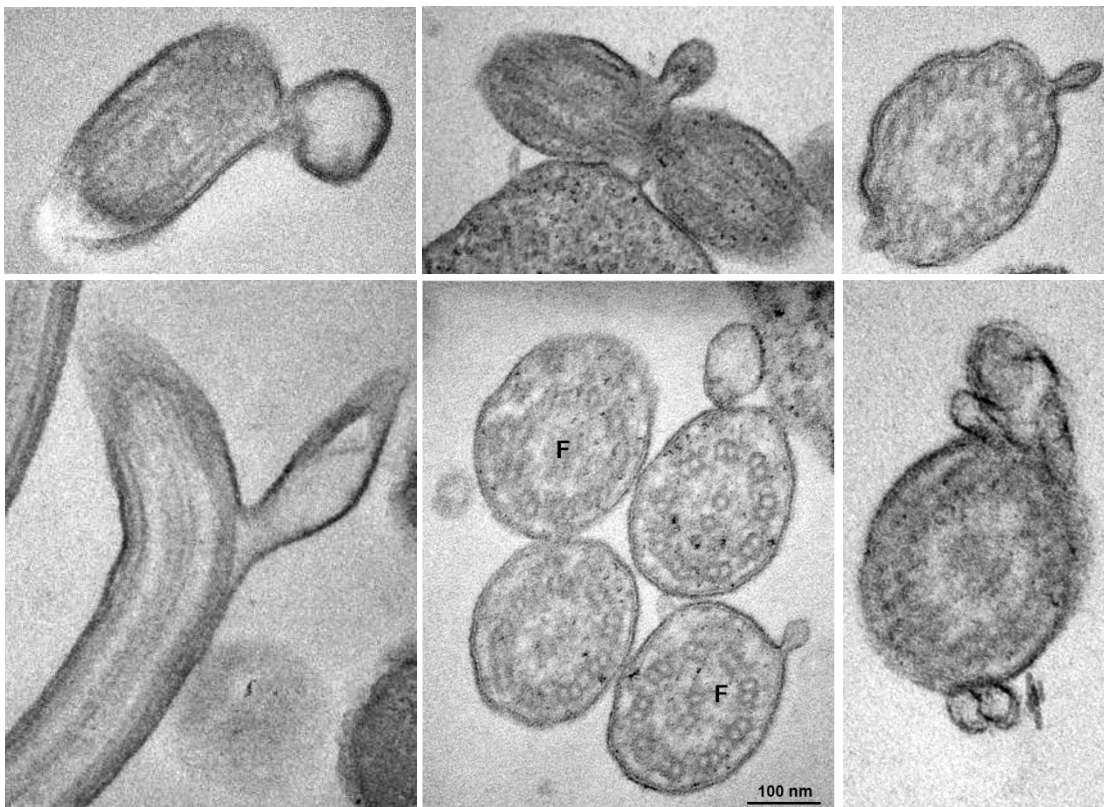
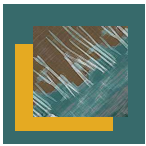


Figure 2. TEM of ultrathin sections through the flagella of *T. foetus* (a-c) and *T. vaginalis* (d-f). Ectosomes-like structures (arrows) seems to be in process of budding from the flagellar membrane. Some EVs (arrowheads) can also be seen closely apposed to the flagellar membrane. Bars.: a, c-f, 100 nm; b, 200 nm.



Impact Of Dengue Virus Serotype 3 (DENV-3) Infection On Lung Of BALB/c Mice: A Histopathological And Ultrastructural Analysis.

Caldas, G.C.*¹; Silva, M. A. N. ¹; Jácome, F.C.¹; Rasinhas, A. C. ¹; Almeida, A.L.T. ¹; Barth, O.M.¹; Barreto-Vieira, D.F¹.

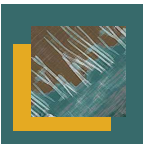
1. Laboratório de Morfologia e Morfogenese Viral/Instituto Oswaldo Cruz – Fundação Oswaldo Cruz, Rio de Janeiro, Brasil.

*Email: gabrielacardosocaldas@gmail.com

Dengue fever (DF) is an acute infectious disease caused by dengue virus (DENV), the most medically important arthropod-borne virus worldwide and a major public health challenge [1]. In Brazil, several epidemiological studies have correlated DENV-3 infection to severer signs and symptoms, such as shock, abdominal pain and exanthema, compared to other serotypes [2]. Changes in lung of DENV-infected individuals are commonly observed and include presence of mononuclear inflammatory infiltrate, interalveolar septum thickening, alveolar macrophages hyperplasia, interstitial oedema, bleeding foci, and diffuse alveolar congestion [3,4]. The development of animal models for studies of DENV infections is of great relevance for researches on pathogenesis, immunity and development and testing of drugs and vaccines. However, studies have met numerous challenges, since circulating epidemic virus does not naturally infect non-human species [5]. In this scenario, the main purpose of this study was to verify possible morphological changes in lung samples of BALB/c mice experimentally infected with epidemic and non-neuroadapted DENV-3. Adult male BALB/c mice were inoculated by intravenous route with DENV-3, anaesthetized and euthanized after 72 h p.i. Lung fragments were collected from infected and non-infected mice. For photonic microscopy analysis, samples were fixed in Millonig's fixative, dehydrated in ethanol, and paraffin-embedded. Five-µm-thick sections were stained with haematoxylin and eosin. For TEM analysis, the animals were peritoneally anaesthetized and fixed by perfusion with 4% paraformaldehyde in sodium phosphate buffer by 30 min. Subsequently the lungs were carefully collected, the fragments post-fixed by immersion in 2% glutaraldehyde in sodium cacodylate buffer, followed by 1% buffered osmium tetroxide, dehydrated in crescent concentrations of acetone, embedded in epoxy resin, and polymerized at 60°C during three days. Ultrathin sections, around 50-70 nm thick, were picked up onto copper grids and stained with uranyl acetate and lead citrate [6] and observed at a Zeiss EM-900 TEM. All procedures carried on during the study were approved by Fiocruz Ethics Committee (LW50-11). Morphological analyzes of lung from uninfected BALB/c mice (negative controls) showed fully preserved tissue areas without any change. In infected mice with DENV-3, our results demonstrated swollen interalveolar septa, vascular congestion, signs of necrosis, focus of hemorrhage, edema, infiltrate in the peribronchiolar space, presence of platelets, mononuclear and polymorphonuclear inflammatory cells inside blood vessels and interalveolar septa. Presence of phyllopod in endothelial cells, platelets and polymorphonuclear cells could be also observed. These changes resemble those observed in samples from fatal cases of DF in humans pointing, therefore, to lung involvement during DENV infection in BALB/c model as well as in human cases.

REFERENCES

- [1] M.G. Guzman & E. Harris. *Lancet*. 385. (2015) 453–65.
- [2] M.N.P. Passos et al., *Rev Soc Bras Med Trop*. 37 (2004) 293-295.
- [3] C.A. Basílio-de-Oliveira et al., *Braz J Infect Dis*. 9 (4) (2005). 341-7.
- [4] T.F. Póvoa et al., *PLoS One*. 9(4) (2014). e83386.
- [5] S. Zompi & E. Harris, *E. Viruses*. 4(1) (2012) 6282.



[6] E.S. Reynolds. *J Cell Biol.* 17. (1963). 208-12.

This research was supported by CNPq (Brazil).

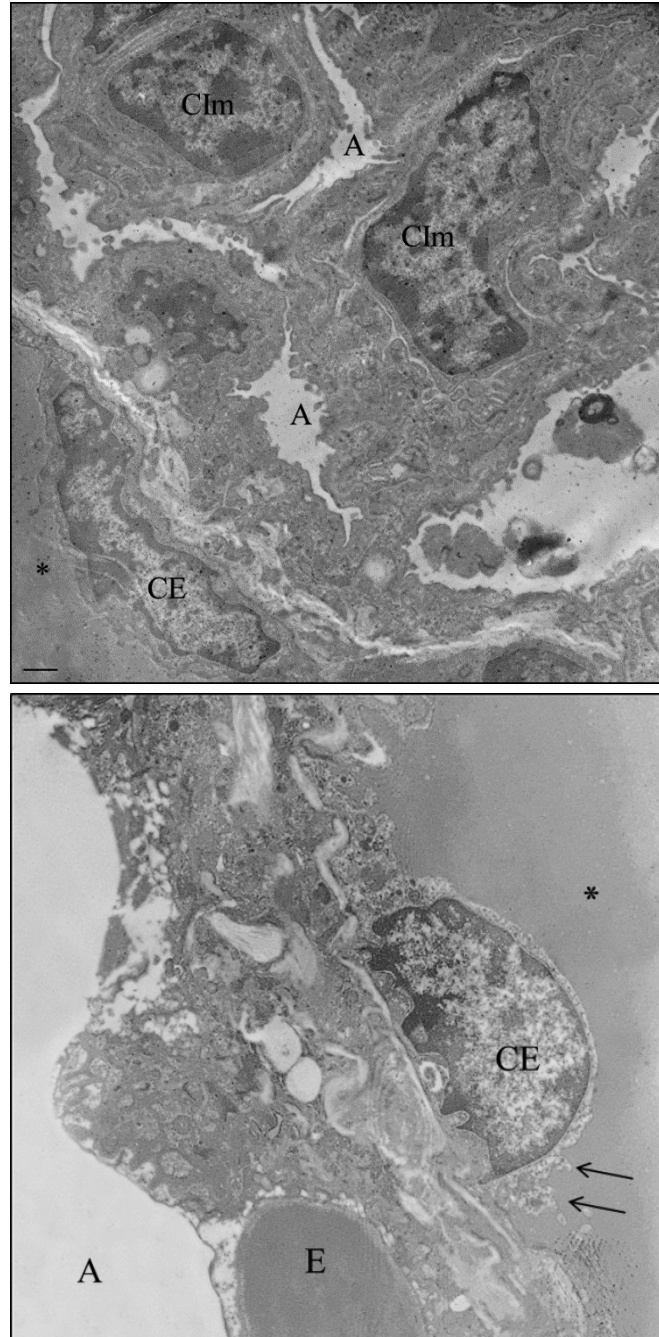
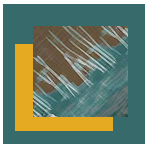


Plate 1. Ultrathin lung sections of BALB/c mice 72 h.p.i. by DENV-3. [A] Alveolar compression (A) due to thickening of the interalveolar septa. Presence of mononuclear inflammatory cells (CIm) and edema (*) in the blood capillary. Endothelial cell (CE) Bar=5 µm. [B] Presence of phyllopod (arrows) of an endothelial cell (CE) and edema (*) in the blood capillary. Alveolus (A). Erythrocyte (E). Bar=5 µm.



Ultrastructural Analysis Of Alterations Caused By A Dengue Virus Secondary Infection In BALB/c Mice Hearts

De Souza, D.D.C¹.; Jácome, F.C¹.; Caldas, G.C.¹.; Silva, M. A. N.¹.; Rasinhas, A.C.¹.; Almeida, A.L.T.¹.; Barth, O.M.¹.; Barreto-Vieira, D.F*¹.

1. Laboratório de Morfologia e Morfogenese Viral, Instituto Oswaldo Cruz, Fundação Oswaldo Cruz, Rio de Janeiro, Brazil.

*Email: barreto@ioc.fiocruz.br

Dengue, considered the most important arthropod-borne viral disease which affects humans, is transmitted by the bite of mosquitoes of the *Aedes* genus and caused by one of the four distinct serotypes of dengue virus (DENV-1, -2, -3 and 4). The virus belongs to the Flavivirus genus, presenting approximately 60 nm in diameter, and its genome is a positive-sense, single-strand RNA which encodes a precursor polyprotein containing three structural proteins: capsid (C) envelope (E) and pre membrane (PrM), and five non-structural ones: NS1, NS2, NS3, NS4 and NS5 [1,2,3]. Infection with one of the four serotypes provides lifelong homotypic immunity. However, immunity against another heterologous serotype is transient. Therefore, secondary infection may lead to severe manifestations due to cross-reactivity of antibodies and T-cells [4]. Over 500,000 people are hospitalized every year and around 2.5 million, living in endemic areas, are at risk of infection, which makes the development of a vaccine of the utmost importance. Given the background, studies aimed at establishing animal models are of great relevance for better understanding the disease, as well as testing of vaccine candidates and anti-viral drugs [3]. This study purpose is investigating ultrastructural alterations caused by DENV secondary infection in BALB/c mice hearts. To achieve our goal, six BALB/c mice were infected with DENV-1 and, four months later, they were reinfected with DENV-2. Uninfected mice were used as negative controls. 72h post-reinfection the mice were anesthetized, euthanized and fixed by perfusion with 4% paraformaldehyde in sodium phosphate buffer for 30 min. Heart fragments were collected, post-fixed by immersion in 2% glutaraldehyde in sodium cacodylate buffer and 1% buffered osmium tetroxide, dehydrated in crescent concentrations of acetone, embedded in epoxy resin, and polymerized at 60°C during 3 days. Ultrathin sections were picked up onto copper grids and stained with uranyl acetate and lead citrate [5] and observed with a Jeol JEM 1011 transmission electron microscope. All procedures carried on during the study were approved by Fiocruz Ethics Committee (LW50-11). Ultrastructural analysis of infected mice hearts showed edema, endothelium activation characterized by presence of transport vesicles, free platelets inside the interstitium, mitochondria presenting rarefied cytoplasm, and disorganization of muscle fibers. These results point not only to BALB/c mice susceptibility to DENV infection, but also to the fact that, although it is not an often reported occurrence [6], dengue can lead to heart compromise.

REFERENCES

- [1] C.M. Rice et al., *Science* 229 (4715) (1985) 726-733.
- [2] D.J. Gubler. *Trends Microbiol.* 10 (2002).100-103.
- [3] M.G. Guzman et al., *Nat. Rev. Microbiol.* 8 (2010).7-16.
- [4] M.M. Remmy. *Inflamm. Allergy Drug Targets.* 13(4) (2014) 262-274.
- [5] E.S. Reynolds. *J. Cell Biol.* 17 (1963) 208-212.
- [6] M. Arora and R.S. Patil. *Journal of the Association of Physicians of India* 64 (2016) 40-44.

This research was supported by CNPq (Brazil)

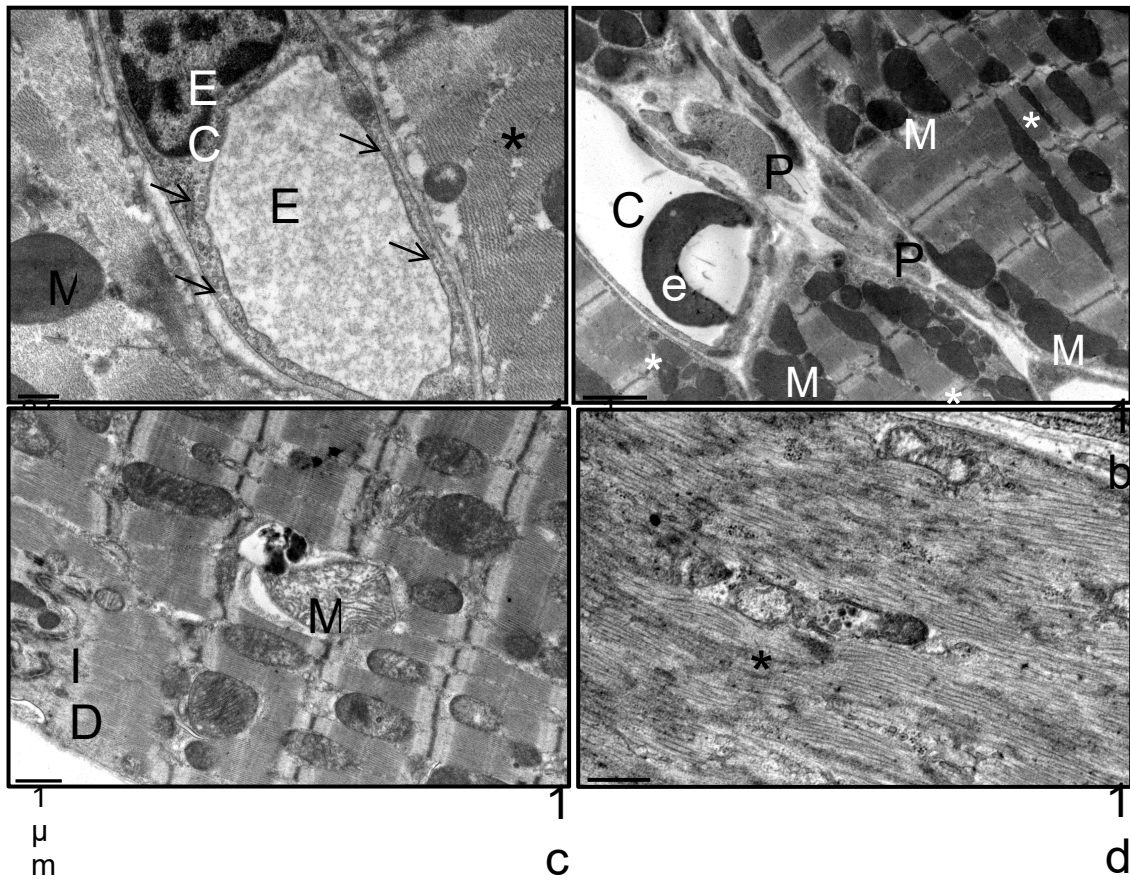
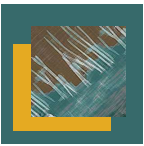
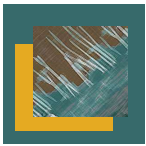


Figure 1. BALB/c mice heart (primary infection DENV-1 and secondary infection DENV-2). (1a): endothelium activation characterized by presence of transport vesicles (arrows), edema (E), endothelial cell (EC); (1b): platelets (P) inside the interstitium, capillary (C), erythrocyte (e), mitochondria (M); (1c): rarefied mitochondrial cytoplasm (M); (1d): disorganization of muscle fibers: cardiomyocyte (*).



Multivesicular Bodies In The Protozoan Parasite *Giardia intestinalis*: The Peripheral Vesicle Gathers One More Function

Victor Midlej^{1*}, Wanderley de Souza¹ and Marlene Benchimol^{1,2}

1. Instituto de Biofísica Carlos Chagas Filho, UFRJ – Brazil

2. Universidade do Grande Rio (UNIGRANRIO) - Brazil

*Email: vmidlej@hotmail.com

Giardia intestinalis is an unicellular eukaryotic parasite that commonly causes diarrheal disease all over the world. During its life cycle the protozoan presents two developmental stages: the flagellated trophozoite and the cyst. *Giardia* presents an endomembrane system consisting of the endoplasmic reticulum (ER) and peripheral vesicles (PVs). PVs gather many functions, such as endocytosis and material degradation, acting as a lysosome-like organelle [1]. Recently, it was shown *G. intestinalis* releases microvesicles [2], however where these microvesicles are originated and how they are released remains unclear. Based in advanced microscopy, our previous data suggested that PVs might present multivesicular bodies (MVB) in its interior, which enhance during encystation. In this study, we took advantage of the Structural Illumination Microscopy (SR-SIM) methodology, Electron Tomography (ET) and Dual-beam (FIB – Focused Ion Beam) microscopy to analyze the origin of MVB in the PVs and its role during encystation. The SR-SIM is a super resolution fluorescent light microscopy technique, where the image is captured by a grid pattern superimposed on the specimen, reaching an axial resolution between 150/300 nm. ET and FIB microscopy are used to obtain detailed information of sub-cellular structures: ET retrieves 3D structural information from a tilt series of 2D projections, while FIB can directly "mill" the specimen surface using the gallium ion beam, combining SEM information to acquire 3D results. To investigate the behavior of PVs in trophozoites and during the differentiation process, *G. intestinalis* were grown in conventional medium and induced to encyst in vitro. The PVs are tracked using specific fluorescent dyes: Lucifer yellow (LY) and Acridine orange (AO), and anti-clathrin heavy chain antibody. The cells labeled dyes were observed by confocal, while the anti-clathrin IFA data was analyzed using the SR-SIM. Acid phosphatase cytochemistry was used in order to analyze ultrastructural features of PVs by TEM. ET and FIB microscopy were applied to better understand the biogenesis of MVBs. Both methodologies were performed after vegetative and encysted parasites were routinely processed for TEM. The epon-embedded material was sectioned, 200 nm thicker, and analyzed with electron tomography or taken directly to FIB microscope and submitted to the gallium ion beam. In both methodologies, 3D reconstructions were acquired using Imod software. Our light microscopy data show that anti-clathrin antibody labeled PVs in vegetative and encysting cells. LY and AO showed a fluorescence decrease during the encystment process. Cytochemical localization of acid phosphatase allowed similar results. ET and Dual-beam microscopy showed MBV inside the PVs. Moreover, during the encystation process it was seen a membrane fusion of MVBs by ET, this event could characterizes an exocytosis process. In conclusion, a change of PVs behavior happens during parasite differentiation. We observed a partial acid phosphatase translocation from peripheral vesicles to the plasma membrane by TEM, and MVBs inside PVs by ET and FIB, with a probable role during parasite differentiation. The microscopy methodologies have a fundamental role to achieve these results.

REFERENCES

- [1] Lanfredi-Rangel et al., J. Struct. Biol. 123 (1998) 225.
- [2] Evans-Ossees et al., Eur. J. Cell Biol. 96 (2017) 131.
- [3] This work was supported by CNPq, FAPERJ, CENABIO and INBEB.

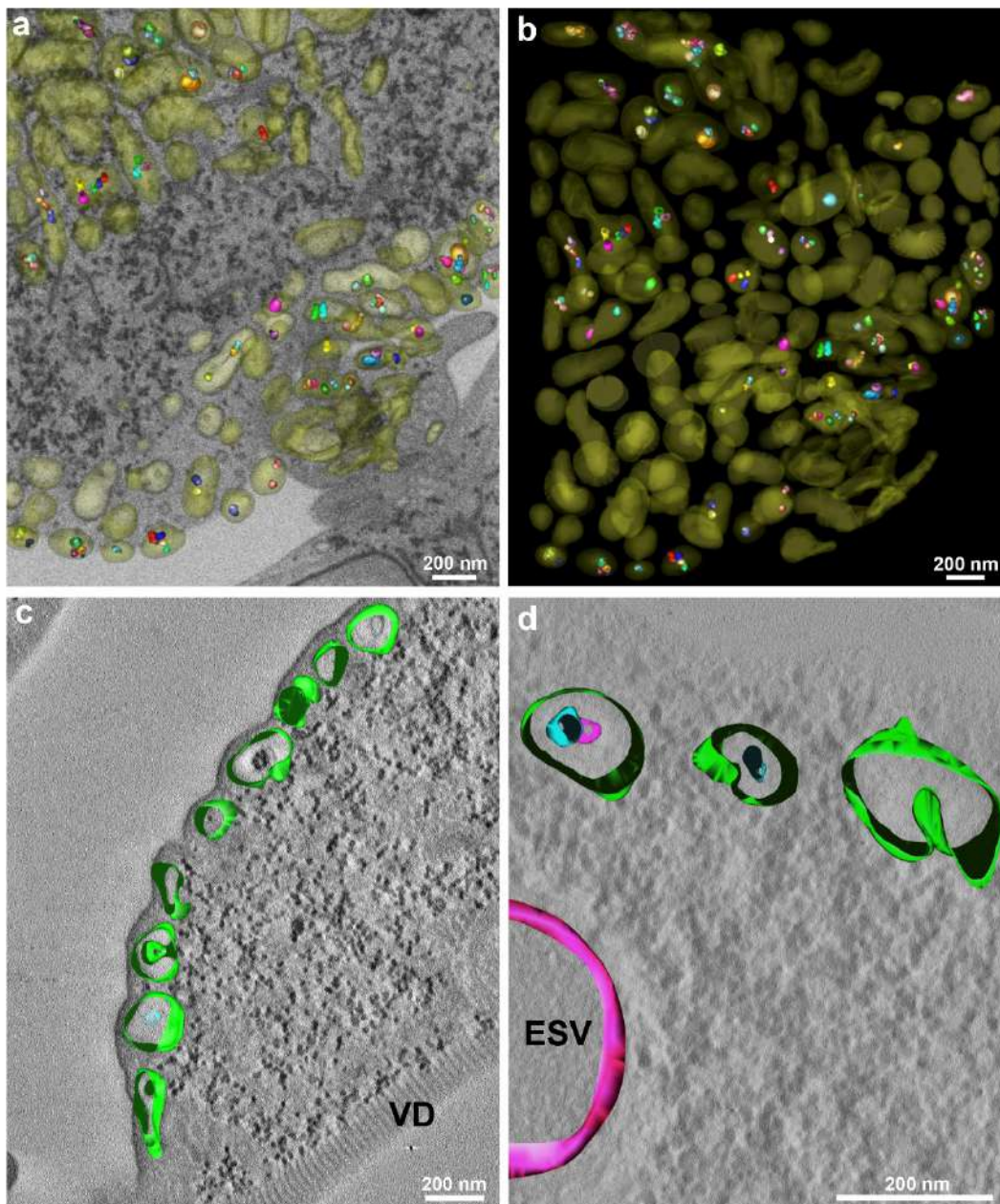
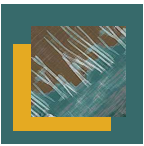
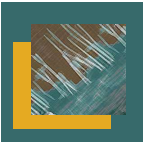


Figure 1. Multivesicular bodies in *G. intestinalis* by dual-beam microscopy (Figs. a-b) and electron tomography (Figs. c-d). Trophozoite (Figs. a-b) and 6h-21h encysted cells (Figs. c-d). Overlay of peripheral vesicles (PV) after 3D reconstruction (green). Figure b shows the 3D reconstruction. The figure d indicates an ESV (pink) after electron tomography overlay. Note that PVs in trophozoites present multivesicular bodies (MVB) inside, and they are not in contact with PVs membranes (Figs. a-b). However, in encysting cells (Figs. a-b) MVBs are in close contact with PV membrane, suggesting an exocytosis process. ESV, encystation secretory vesicles; VD, ventral disc.



DOI: [INSERIR ENDEREÇO DO DOI AQUI.](#)

Caderno de Resumos do 26º Congresso Brasileiro de Microscopia da SBMM – ISSN: [INSERIR AQUI.](#)

PARTE 2

COMUNICAÇÕES ORAIS
- MATERIAIS



Superconductivity in Bi-Ni bilayers: a High Resolution Transmission Electron Microscopy Study

Yutao Xing^{1*}, Liying Liu², Isabel Castro Merino³, H. Micklitz³, D. F. Franceschini¹, Elisa Baggio-Saitovitch³, I. G. Solórzano²

1. Instituto de Física, Universidade Federal Fluminense, Niterói 24210-346, Brazil

2. DEQM, Pontifícia Universidade Católica do Rio de Janeiro, Rio de Janeiro, Brazil

3. Centro Brasileiro de Pesquisas Físicas, Rio de Janeiro 22290-180, Brazil

*Email: xing@if.uff.br

Despite crystalline bismuth (rhombohedral structure) and nickel (Face Centered Cubic structure) being not superconducting, Bi/Ni bi-layers show a superconducting transition at ~ 4 K [1, 2] and this has been attracted attention. There are different interpretations for the superconductivity (SC) in Bi/Ni, for example: the Ni presence induces the modification of Bismuth structure to FCC [1]; Bi induced superconductivity in Ni layer and formation of a very thin amorphous Bi layer formed at the interface of Ni and Bi[4], formation of NiBi₃ during the deposition[3], etc. We have studied the superconductivity and microstructure of the Bi/Ni bilayer and nanoparticle systems by means of electric transport and magnetic measurements, and high resolution transmission electron microscopy (HRTEM). Cross section electron transparent samples required meticulous focused ion beam (FIB) preparation. A Jeol 2100F TEM/STEM instrument was used, operating at 200 kV, under diffraction contrast and phase contrast modes. Two step transitions have been observed in Bi/Ni bilayers. The observed microstructure shows that two intermetallic phases (NiBi and NiBi₃) have been formed during the sample preparation by pulsed laser deposition as shown in figure 1, constituting the origin of the superconductivity in Bi/Ni systems. One interesting phenomenon that has been observed is that the Bi-rich phase (NiBi₃) is formed near the Ni layer. However, the Ni-rich phase (NiBi) is formed after the NiBi₃ layer, which is not expected by us but interpreted as consequence of the limited supply of atoms in the inter-diffusion process. The EDS results at nanometer scale clearly show an unusual increase of Ni concentration near the interface of Bi/Substrate (as shown in figure 2), which was confirmed by the observation in the HRTEM study. Bilayers of Bi/Ni nanoparticles and Ni/Bi nanoparticles have been studied as well and the samples do not show a full superconducting transition. The result confirmed that the appearance of superconductivity in Ni-Bi system is a diffusion controlled process and this strongly support that the SC in the sample is from the formation of NiBi and NiBi₃ phases [5].

REFERENCES

- [1] J. Moodera, R. Meservey, Physical Review B, 42(1990)179.
- [2] P. Leclair, J. S. Moodera, J. Philip, D. Heiman, Phys. Rev. Lett., 94(2005)037006.
- [3] V. I. Petrosyan, et.al, V. N.Molin, O. I.Vasin, P. A. Skripkina, S. I. Stenin, E. G. Batyev, Soviet Journal of Experimental and Theoretical Physics, 39(1974)485.
- [3] V. Siva et.al, Journal of Applied Physics, 117(2015.)083902.
- [5] This research was supported by CNPq, FAPERJ e CAPES(Brazil).

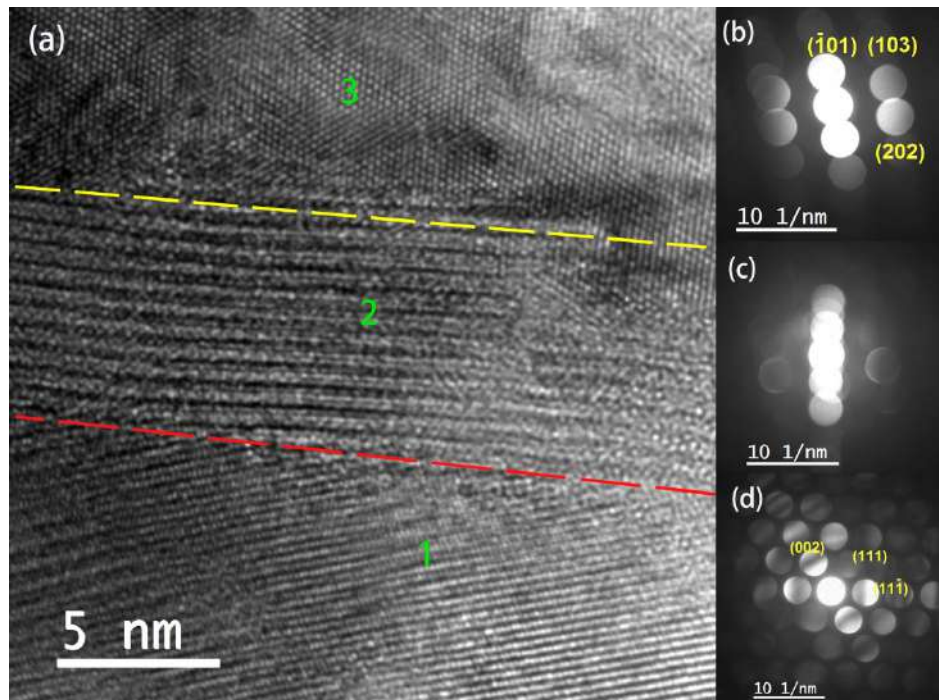
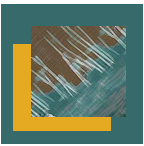


Figure 1. (a) HRTEM image of Bi(38nm)Ni(30nm) and (b), (c), (d) are the convergent beam electron diffraction patterns of the region marked as 1, 2, 3 in (a). The lower layer (marked as 1) can be indexed as pure Ni, the layer in between is most likely NiBi₃ and the upper layer (marked as 3) is indexed as NiBi. The sample preparation is as follows: first deposited pure Bi and then pure Ni. The NiBi₃ and NiBi are formed during the deposition by pulsed laser deposition.

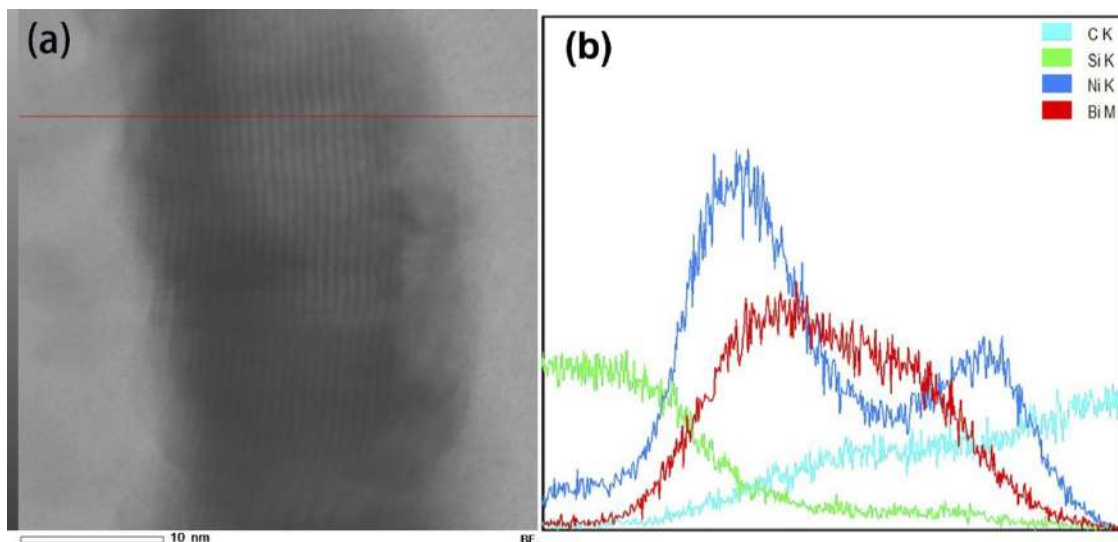


Figure 2. (a) STEM image of Bi₃₈Ni₈ sample and (b) EDXS line scan at the position marked in (a) shows the elemental distribution. An unexpected peak of Ni concentration at the interface of SiO₂ and Bi has been observed.



Using DFT and STEM for structural and electronic properties of LaAlO₃/Ge system

C. Arrouvel^{1,*}, A. P. C. Campos², H. Mortada³, D. Dentel³, M. Derivaz³, J.L. Bischoff³, J. Werckmann⁴

1. UFSCar, DFQM/CCTS, Campus Sorocaba, Sorocaba, Brazil
2. Université Aix-Marseille, CP2M, Faculté des Sciences, Campus de St Jérôme, Marseille, France
3. Université de Haute-Alsace, CNRS, Institut de Science des Matériaux de Mulhouse (UMR CNRS UHA 7361), Mulhouse, France
4. UFRJ, Centro de Ciências da Saúde, Instituto de Ciências Biomédicas, Laboratório de Biomineralização, Rio de Janeiro, Brazil.

*Email: corinne@ufscar.br

Germanium nanoparticles can be used as quantum dots (QDs) for a wide range of applications: electronics (e.g. memory storage), photonics (e.g. solar cells, optical probes in biomedicine)[1-3]. They usually grow on a substrate under three types of heteroepitaxy mechanisms and the structural differences of the Ge films-islands may affect drastically the optoelectronic properties of the material. We investigate the stability of surfaces and the adsorption of Ge on LaAlO₃ (LAO)/(001) grown by molecular deposition following the Volmer-Weber mechanism. For that purpose, we combine Density Functional Theory (DFT) methods implemented in VASP software with Scanning Transmission Electron Microscopy (STEM). We simulate five (hkl) Ge surfaces, the two types of terminations of polar (001)LAO surface and we extract their key chemico-physical properties. While it is known that the diamond Ge bulk structure is an arrangement of Ge₆ cycle, with each Ge under a tetrahedral environment (i.e. sp³ hybridization), we find that the surface relaxation can induce notable structural and electronic changes. From STEM images, the Ge(001) surface is commonly observed at the interface on LAO(001) surface. Surface energy calculations indicate that the (113) surface is however the most stable one (under vacuum, $\Gamma_{113}=0.92$ J/m² and $\Gamma_{001}=1.24$ J/m²) and dominates the shape of QDs at 76% of surface area (see figure). Interestingly, the (112) and (113) surfaces have been the most strongly stabilized with the formation of Ge₅ cycles, exposing Ge atoms with an sp² hybridization and bridging Ge with lone pairs as it has been observed with ELF (Electron Localization Function). From the reconstruction of the Ge QD surfaces and the monolayer formation at the Al-O₂ terminated LAO surface, some featuring is correlated to the improvement of the charge mobility.

REFERENCES

- [1] Dentel, D. et al., R. Acta Materialia, 60, 1929-1936 (2012).
- [2] Xia, J. S. et al., Y. Applied Physics Letters, 89, 3 (2006).
- [3] Prabakar, S. et al. Chemistry of Materials, 22, 482-486 (2009).

ACKNOWLEDGMENT: CENAPAD-SP for computing resources, FAPESP for financial support.

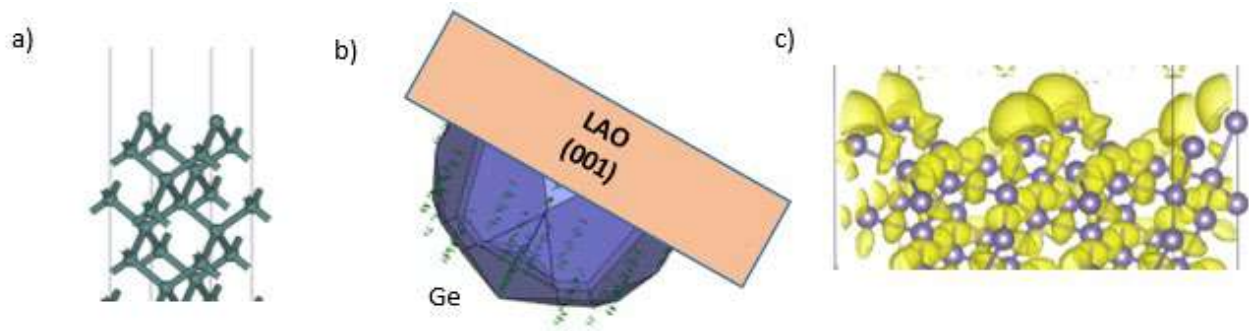
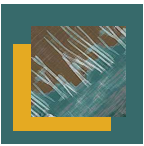
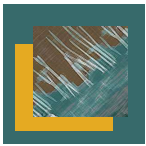


Figure: DFT calculations a) Ge(001) surface structure, b) Equilibrium morphology of Ge with (001) interface on LAO(001), c) ELF isosurface = 0.6 of (113) surface. Acknowledgment: CENAPAD-SP for computing resources, FAPESP for financial support.



New Methodology Of Precipitates Characterization In 2.25Cr-1Mo Steels

Wagner Ferreira Lima^{1*}, Luiz Henrique de Almeida² and Heloisa Cunha Furtado³

1. CEPEL, DLE, Rio de Janeiro, Brazil. wagnerfl@cepel.br

2. UFRJ, COPPE, PEMM, Rio de Janeiro, Brazil. lha@metalmat.ufrj.br

3. CEPEL, DTE, Rio de Janeiro, Brazil.

*Email: heloisac@cepel.br

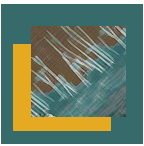
Cr-Mo steels are widely used in applications under creep conditions, notably in the petrochemical and power generation industries as pressure vessels, piping, boilers and structural parts. These steels present good resistance to creep and corrosion, high toughness and good weldability, and they have an excellent cost/benefit ratio. These factors make Cr-Mo steels very attractive to operate at high temperatures and under low stresses. The mechanical properties of 2.25Cr-1Mo steel depend on the microstructure, which, in turn, is influenced by the cooling rate from the austenitizing temperature [1]. Commercial grade 2.25Cr-1Mo steel can be processed into different microstructures as ferrite-pearlite, ferrite-bainite, fully bainite and tempered martensite, with the first two being typical morphologies for tube fabrication [2]. The studies that estimate the remaining life of a component operating under pressure and at high temperatures are based on the data of the literature for 2.25Cr-1Mo steel concerning microstructural evolution and creep behavior.

Literature on Cr-Mo steels presents well-established microstructural degradation criteria for a ferrite-pearlite microstructure, such as the Toft and Marsden methodology based on the gradual pearlite spheroidizing and carbide coarsening [3]. However, a similar criterion specific to the ferrite-bainite microstructure has not been formally published. The ferrite-bainite microstructure does not exhibit a clear change during aging, and sometimes, the hardness values remain as those observed in a new material, which makes its assessment using traditional techniques more difficult to apply [4,5]. The main feature is the coalescence of the precipitates. This phenomenon captures elements from the matrix with a consequent reduction of solid solution hardening [4], and precipitates evolution. Several works [6] indicate that M_6C phase is the most evolved phase until the rupture of samples in a creep test of this class of steels. So, this suggests that until the emergence of that phase, the component is in a safe condition.

The question is how to identify quickly M_6C carbides in a structure if the conventional precipitate characterization techniques, as the EDS spectra and diffraction patterns both using TEM, demand a lot of time to conclude their analyzes. Thus, it is necessary to elaborate a more efficient procedure in the characterization of precipitates in 2,25Cr-1Mo steels. According to the literature [6,7], carbides present in this class of steels have characteristic stoichiometry, which allow the correct identification of each type, and in the case of M_6C phase, there is a significant concentration of Mo and Si in its composition. So, if a mapping of composition using replicas samples in a TEM were realized, and those elements were presented in the same precipitate, there is a great chance to find M_6C carbides.

The methodology of this study consisted in realizing creep tests in 2.25Cr-1Mo steel, at 575°C and 100 MPa, and it were taken replicate samples, during different times of testing, to analyses in TEM, Titan/FEI model. Cr, Mo and Si were mapped in a selected area. The results showed carbides with different compositions, and the M_6C phase presented, in the same time, significant concentrations of Mo and Si. The analyses were confirmed by conventional EDS spectra.

The conclusions indicated a more efficiency technical, in which it's possible to identify M_6C carbides spending just 10 minutes in a big area of analyses.



REFERENCES

- [1] H. Kushima et al., Metallographic Atlas for 2.25Cr-1Mo Steels and Degradation due to Long-term Service at Elevated Temperatures. OMMI. 2007;4(1):1-13.
- [2] B.Q. Wang et al., Effect of microstructure on the erosion-corrosion of steels. Wear. 1991;151(2):351-364.
- [3] L.H. Toft, R.A. Marsden, Structural processes in creep: special report no. 70. London: Iron & Steel Institute; 1961. p. 238-244.
- [4] H.K.D.H. Bhadeshia, R.W.K. Honeycombe, Steels: Microstructure and Properties. 3rd ed. Oxford: Butterworths-Heinemann; 2006.
- [5] H.K.D.H. Bhadeshia, Bainite in Steels. Cambridge: Cambridge University Press; 2001.
- [6] H.C. Furtado et al., Precipitation in 9Cr–1Mo steel after creep deformation. Materials Characterization. 2007;58(1):72-77.
- [7] S. Kuimalee et al., Quantitative analysis of a complex metal carbide formed during furnace cooling of cast duplex stainless steel using EELS and EDS in the TEM. Micron. 2010;41(5):423-429.

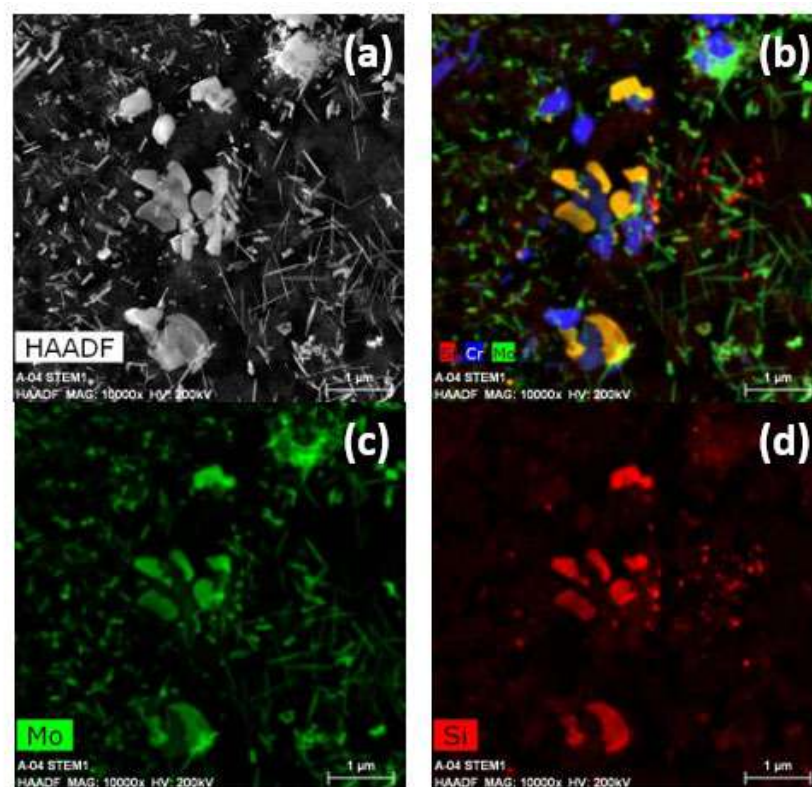


Figure 1 – Characterization of carbides by mapping elements technical: (a) image from TEM; (b) mapping of Si, Cr and Mo, where yellow carbides indicate M_6C phase; (c) mapping of Mo; (d) mapping of Si



Microscopy Aided by Image Processing as a Tool for Assessing Aging and Creep Damage in HP-Modified Steel Reformer Tubes

Alessandra Vieira Guimarães^{1*}, Mario Luiz Cruz Nascimento¹, Leonardo Sales Araújo¹, Luiz Henrique de Almeida¹ and Fabio dos Santos Queiroz¹

1. PEMM-COPPE/UFRJ, CEP 68505, Rio de Janeiro, RJ 21945-970, Brazil.

Bulk hydrogen is currently produced inside reforming furnaces at temperatures above 900°C within centrifugally cast HP grade austenitic stainless steel tubes, modified by additions of Nb (HP-Nb). Service at these temperatures causes, among other microstructural changes, secondary intradendritic precipitation of Cr carbides and transformation of primary NbC to G phase, an Ni-Nb based silicide [1], whose interface with the matrix is quoted in literature as a preferential site for creep damage nucleation [2]. This process, widely reported in literature, is known as aging and directly impacts on the material's mechanical properties [3]. Recently microalloying titanium to these steels (HP-NbTi) has shown to refine secondary precipitation and to inhibit the MC→G phase transformation [1]. Secondary intradendritic precipitation, whose distribution and size is used to evaluate aging [4], is more effortlessly observed via optical microscopy (OM). Primary Cr, Nb and NbTi carbides, G phase and creep voids are however, more easily distinguished from the matrix through scanning electron microscopy (SEM) under backscattered imaging, due to their diverse masses. This is presented in Figure 1, where the heavier NbTi carbides appear in white, G phase, Cr carbides and matrix in different shades of gray and creep voids in black. Distinction between these phases can also be seen in Figure 2, which shows the histogram for Fig.1. Quantifying these phases along the length of a tube provides important information about its operational conditions, while an analysis of the distribution of creep voids, along various of its cross sections, enables an estimation of its remaining service life [5]. This study shows that 18 bit optical and scanning electron micrographs, such as the one presented in Figure 1, can be processed through thresholding, as illustrated in Figure 3, to quantify phases and voids. Thus, the combined use of microscopy and image analysis is a relevant tool when assessing aging and creep damage in these materials.

REFERENCES

- [1] L. H de Almeida, A.F. Ribeiro, I. Le May., *Mater Charact.* 49 (n. 3) (2003) 219.
- [2] L. H de Almeida, F. C. Ferraz, I. Le May., *Microstruct Sci.* 24 (1996) 193.
- [3] C. J. Liu, Y. Chen., *Mater. Des.* 32 (n. 4) (2011) 2507.
- [4] I. U. Perez, L. N. Júnior, L. de Oliveira Bueno, L. H. de Almeida, T. L. da Silveira, *JFAP.* 13 (n. 6) (2013) 779.
- [5] I. Le May, T. L. da Silveira, C. H. Vianna., *Int J Pres Ves Pip.* 66 (1996) 233.

Support by Petrobras, who provided the materials for this study, is gratefully acknowledged.

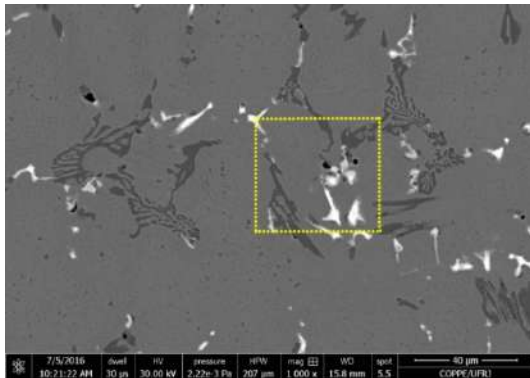
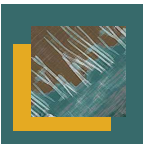


Fig.1: SEM under backscattered electron imaging mode of service aged HP-Nb. Yellow square shows region depicted in Figure 3.

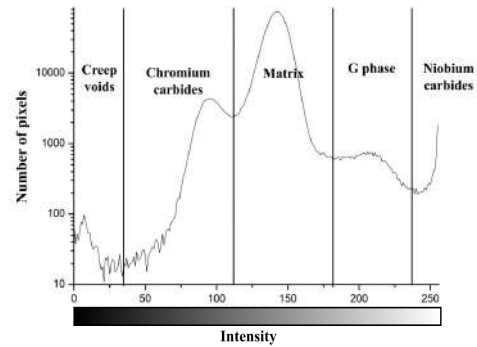
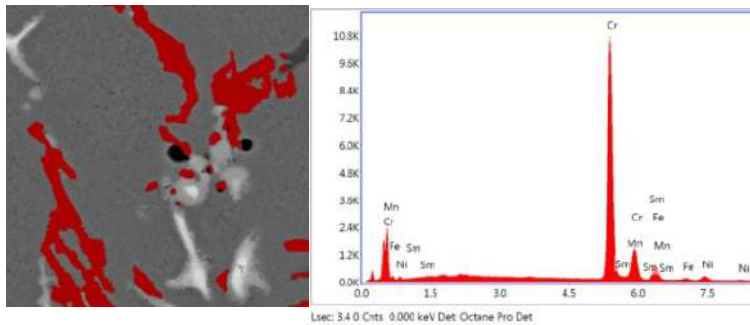
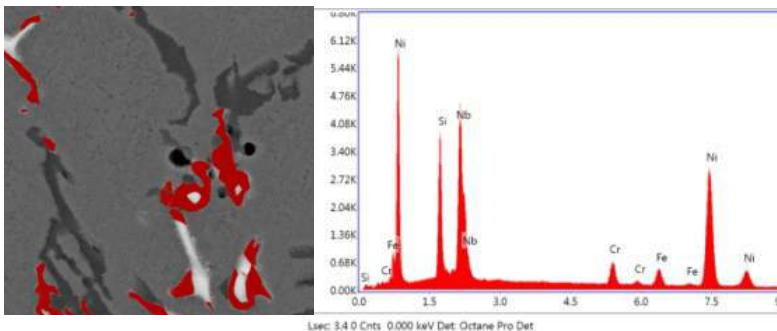


Fig.2: Histogram showing Intensity versus number of pixels for Fig.1.

(a) Chromiumcarbides



(b) G phase



(c) Nbcarbides

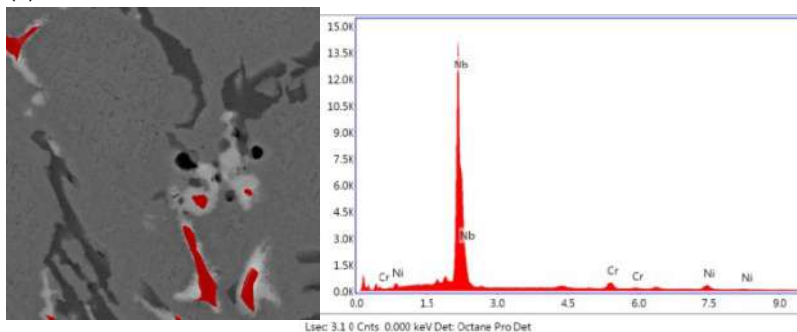
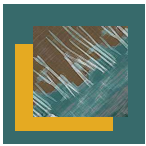


Fig.3: Area in yellow square of Figure 1 under different thresholds to highlight individual phases and corresponding EDS spectra of each phase: (a) Chromium Carbides; (b) G phase and (c) Niobium carbides.



Charaterization of the depostion of SmBaCuO superconducting ceramic on lean duplex stainless steel UNS S32304

C. A. C Passos^{1*}, R. Lepich¹, K. C. Miranda¹, J. Simões¹, J. L. Passamai Jr¹, M. T. D. Orlando¹

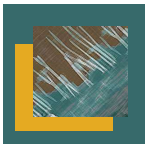
1. Programa de Pós-Graduação em Engenharia Mecânica, Universidade Federal do Espírito Santo, Vitória, BR.

Granular Superconductor-Metal composite can be regarded as the superconducting links embedded in a nonsuperconducting host material. Such composite are reported to possess novel properties, and it may completely change mechanical properties. In particular, for a specific technological application (superconducting fault current limiter) the mechanical resistance of superconducting polycrystalline ceramic must be increased. With this goal in mind, we have investigated SmBa₂Cu₃O_{7-d} lean duplex stainless steel UNS S32304 composite. Therefore, we have prepared samples of polycrystalline superconducting SmBa₂Cu₃O_{7-d} (Sm-123) solid-state reaction using commercial oxide powders of Sm₂O₃ (99.99 %), CuO (99.99 %), and BaCO₃ (99.99 %). Prior to weighing and mixing, the oxides and carbonate powders were pre-annealed at 110 °C for more than 24 h in air to release moisture. Then, the powders were weighed in a glove box, homogenized in an agate mortar for one hour, and put placed into alumina crucibles and calcined at 960 °C for 40hours in air [1-5]. The obtained precursors were again homogenized, pressed into pellets (with the a diameter of 16 mm), sintered in a horizontal tube furnace in flowing oxygen (0.2 cm³/s, 0.5 cm³/s, and 0.7 cm³/s) at about approximately 1060 °C for 0.5 h, then cooled to 520 °C and, held at this temperature for 24 h, subsequently cooled in the furnace to room temperature [6]. Next lean duplex stainless steel UNS S32304 plates were cut into rectangular pieces approximately 72 mm x 10 mm x 2mm. Then carefully, we have deposited the Sm-123 powders on stainless steel. The composites were placed again in the furnace for synthesis at 1060°C (peritectic temperature of the ceramic) for 30 min under different oxygen content: 0.2 cm³/s (sample A), 0.5 cm³/s (sample B), and 0.7 cm³/s (sample C). Then the material was cooled down to 520°C for 24 h and finally to room temperature. These composite surfaces were characterized by X-ray diffraction and Scanning Electronic Microscopy. We have observed that only the composite B presented no modification of its stoichiometry. Furthermore, the SEM results have indicated that the microstructure of all Sm-123 ceramics was completely recrystallized, and displaying a control grain-boundary size.

REFERENCES

- [1] C.A.C. Passos, M.T.D. Orlando, F.D.C. Oliveira, P.C.M. da Cruz, J.L. Passamai Jr., C.G.P. Orlando, N.A. Eloi, H.P.S. Correa, L.G. Martinez, *Supercond. Sci. Technol.* 15 (2002) 1177-1183.
- [2] A. Sin, L. Fabrega, M.T.D. Orlando, A.G. Cunha, S. Pinol, E. Bagio-Saitovich, X. Obradors, *Physica C* 328 (1999) 80-88.
- [3] C.A.C. Passos, M.T.D. Orlando, A.A.R. Fernandes, F.D.C. Oliveira, D.S.L. Simonetti, J.F. Fardin, H. Belich and, M.M. Ferreira Jr., *Physica C* 419 (2005) 25-31.
- [4] F.D.C. Oliveira, C.A.C. Passos, J.F. Fardin, D.S.L. Simonetti, J.L. Passamai Jr., H. Belich, E. F. de Medeiro, M.T.D. Orlando, M.M. Ferreira Jr., *IEEE Trans. Appl. Supercond.* 16 (2005) 15-20.
- [5] M.T.D. Orlando, C.A.C. Passos, J.L. Passamai Jr, E.F. Medeiros, C.G.P. Orlando, R.V. Sampaio, H.S.P. Correa, F.C.L. de Melo, L.G. Martinez, J.L. Rossi, *Physica C* 434 (2006) 53.
- [6] J. Maňka, A. Cigáň, J. Polovková, A. Koňakovský, A. Prnová, *Measurement Sci. Rev.* 11 (2011) 10-14.

This research was supported by FAPES foundation (#67663885/2015), Brazil.



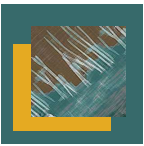
Microstructural and Fractographic Analysis of AISI 317L Steel Thermally Aged at 450°C

Humberto Nogueira Farneze^{1*}, Sérgio Souto Maior Tavares², Juan Manuel Pardal², Rachel Pereira Carneiro da Cunha³, Rafael de Abreu Vinhosa³, Francisco Luiz Correa Rangel³

1. CEFET/RJ – UnED Itaguaí - Centro Federal de Educação Tecnológica de Itaguaí. Rod. Mário Covas, Lote J2, Quadra J, CEP 23810-000, Distrito Industrial de Itaguaí, Itaguaí – RJ, Brazil.
2. UFF – Universidade Federal Fluminense, Escola de Engenharia/Departamento de Engenharia Mecânica. Rua Passo da Pátria, 156, Bl. D, Sala 302, CEP 24210-240, São Domingos, Niterói – RJ, Brazil.
3. INT – Instituto Nacional de Tecnologia, Centro de Caracterização em Nanotecnologia para Materiais e Catálise/CENANO. Av. Venezuela, 82, anexo 3/sala 101, CEP 20081-312, Praça Mauá, Rio de Janeiro – RJ, Brazil.

*Email: humbertofarneze@gmail.com

The austenitic stainless steel type AISI 317L, with high Mo content (3.0 wt% min.) in comparison with AISI 316L, was selected in the petrochemical industry for processing equipment operating at temperatures higher 400°C. However, the high Mo can induce phase transformations in high temperature services. Microstructural changes, such as precipitation of chromium carbide ($M_{23}C_6$) and intermetallic phases α' , sigma (σ) and chi (χ), can cause embrittlement [1,2]. The purpose of this work was to determine the microstructure and toughness changes caused by service at temperatures as high as 450°C. The effects of exposure at 450°C for 400 h were investigated. The chemical composition of stainless steel studied, according to the manufacturer, is (%wt): C (0.024); Mn (1.34); Si (0.47); S (0.003); P (0.031); Cr (18.13); Ni (11.41); Mo (3.03); Fe (balance). The toughness was evaluated by Charpy impact tests at 22°C. Charpy V-notch impact test samples were prepared and tested according to the ASTM A 370 standard for sub-size specimens (55 x 10 x 5 mm³). The microstructural evolution was evaluated by Field Emission Gun Scanning Electron Microscope (FEG-SEM) FEI QUANTA 450 with energy dispersive X-ray spectroscopy (EDS). Specimens were carefully polished till 1 μ m diamond paste, etched with Behara's solution (20 ml HCl, 100 ml H₂O, 0.3g potassium metabisulfite) and observed in the secondary electrons mode (SE). The fracture surface of Charpy specimens were analyzed in a Scanning Electron Microscopy (SEM) FEI INSPECT S50. Magnetic analysis with ferriscope Helmut Fisher® was used to measure the delta ferrite contents. The microstructure of un-aged sample consists of austenite (γ) and delta ferrite (δ) islands, as shown in Fig. 1(a). The ferrite volume fractions measured with ferriscope were $4.0 \pm 0.5\%$ and $1.8 \pm 0.1\%$ in un-aged and aged samples, respectively. This result indicates the transformation of ferrite into paramagnetic phases, which can be γ and intermetallic phases (IP). The decomposition of ferrite (δ) upon aging at 450°C for 400 h is observed in Fig. 1(b). At this temperature the ferrite phase undergoes spinodal decomposition into α' (Cr-rich) and α'' (Cr-depleted). Also, the grain boundary δ/γ was attacked, suggesting intergranular precipitation. EDS analysis showed a significant increase of Cr and Mo contents and Ni depletion in the ferrite phase due to aging at 450°C. These microstructural changes may cause embrittlement. For instance, the impact toughness of Charpy – V test in the un-aged specimen (108.5J) was higher than in the aged one (92.8J). Figs. 1(c-d) show the images of the fracture surfaces of un-aged and aged (450°C-400h). The fracture surface of the specimen aged shows smaller dimples, which is a signal of the decrease of toughness [3]. Considering all the results shown, it is verified that the aging at 450°C up to 400 h caused the decomposition of the ferrite (δ) phase into fine and dispersed intermetallic compounds, intergranular attack and compositional changes, which caused the decrease of toughness.



REFERENCES

- [1] R. L. Plaut et al., Materials Research. 10(4) (2007) 453.
- [2] J. Källqvist and H.O. Andrén., Materials Science and Engineering. 270(1) (1999) 27
- [3] O. A. Hilders and M. G. Santana, Metallography. 21 (1988) 151
- [4] This is research was supported by CNPq, FAPERJ and FINEP (Brazil)

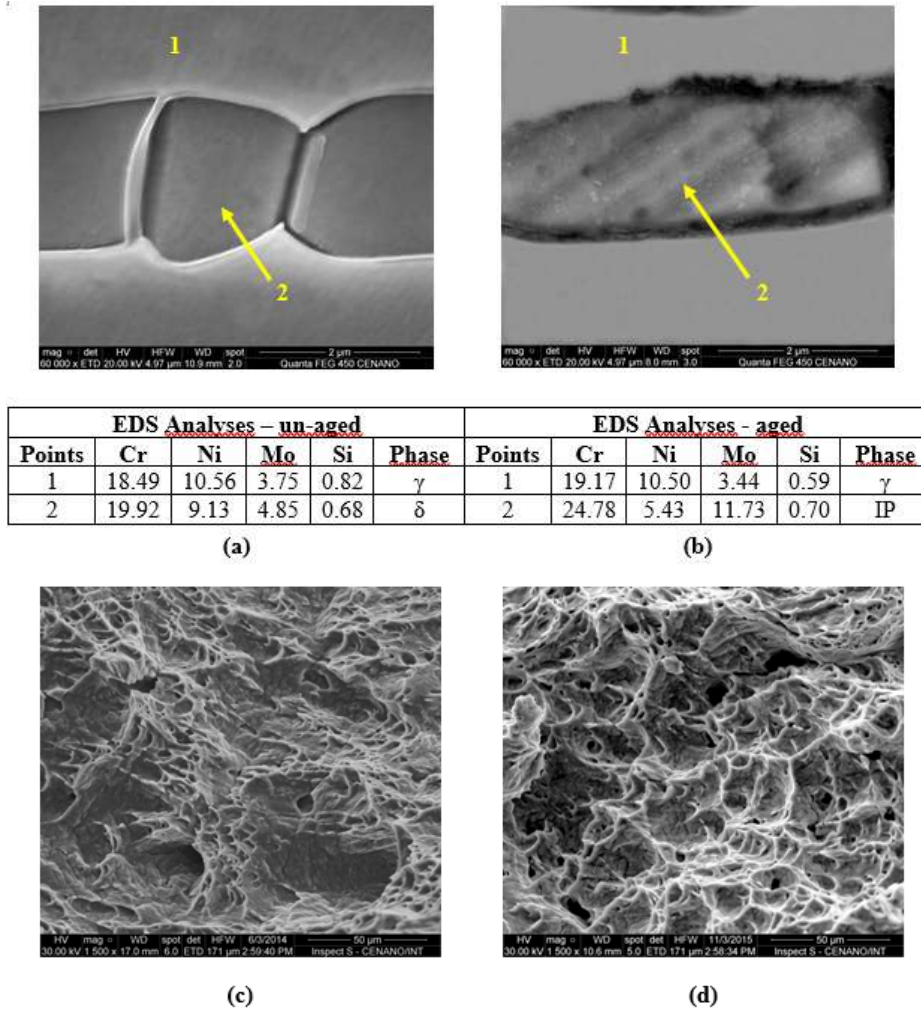


Figure 1 – FEG-SEM: (a) Un-aged sample; (b) Aged sample at 450°C for 400h; (c) Fractograph of un-aged specimen after Charpy impact test; (d) Fractograph of specimen aged 400 h at 450°C after Charpy impact test.



Influence of Zirconium Concentration on Duplex Microstructure Formation in β/β'' -alumina Electrolytes

Daisy Catharina Rodrigues^{1*}, Dulcina Pinatti Ferreira de Souza¹

1. Department of Materials Engineering, Federal University of São Carlos, P.O. Box 676, 13 565-905 S. São Carlos, SP, Brazil.

*Email: daisy.c.rodrigues@gmail.com

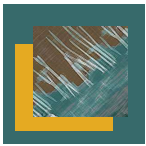
The limitations in the use of fossil fuels and the growing interest in clean and efficient transportation have stimulated the use of electrical energy storage. The ZEBRA battery is an efficient electrochemical energy storage device with high energy density and high power. It uses nickel chloride as positive electrode and sodium as negative electrode, separated by a β'' -alumina solid electrolyte [1]. This has been considered one of the key technologies for insertion into the economic market of electric vehicles and for stationary energy applications. Thus, due to its high ionic conductivity for sodium ions, are among the most promising oxide ionic conductors for the ZEBRA battery, operating at temperatures of approximately 300 °C, with high efficiency [2]. However, the greatest difficulty in using sodium- β'' -alumina is related to the instability of this phase at higher sintering temperatures, in excess of 1300 °C, moreover, the ceramic processing influences the final mechanical and electrical properties of the material [3]. Sodium- β'' -alumina electrolytes of composition 8.85% Na₂O·0.75% Li₂O·90.4% Al₂O₃ (wt%) were obtained by mechanical mixing, and subsequently co-doped with ZrO(NO₃)₂ (1 and 10 wt%) or prepared with TZ-3Y (5 and 10 wt%) addition after the calcination stage; in order to investigate the influence of zirconium on duplex microstructure formation in

β/β'' -alumina electrolytes. Samples were sintered in air at 1600 °C / 10 min, following a heat treatment at 1475 °C / 120 min. Density and β'' -alumina phase percentage analysis and scanning electron microscopy (SEM) were performed. All samples presented density higher than 98% of theoretical density (Table 1), showing that the zirconium addition does not cause great change in density values. TZ-3Y acted as pinning, reducing grain size (Figure 1b and 1c), leading to low β'' -alumina phase conversion (30.8 and 34.8%, for 5 and 10 wt% TZ-3Y, respectively) (Table 1), which will result in low electrical conductivity. ZrO(NO₃)₂ entered in solid solution with the β'' -alumina, causing an overgrowth of grains (Figure 1d and 1e) and increasing significantly the β'' -alumina percentage (Table 1), reaching 92.5% for 10 wt% sample. However, this growth causes fractures due to the effect of anisotropy on the β'' -alumina thermal expansion coefficient, that will result in decreasing of values in the mechanical and electrical properties.

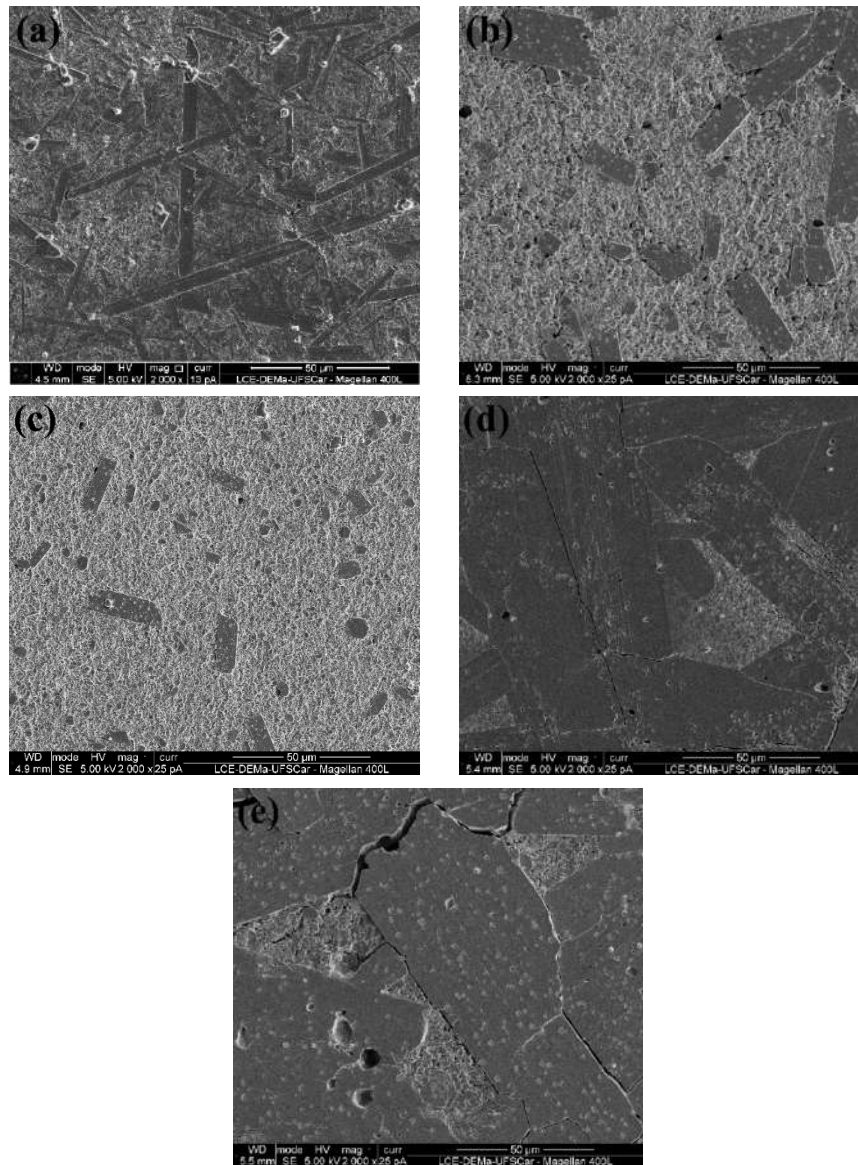
REFERENCES

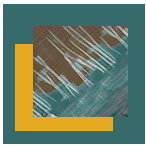
- [1] X. Lu et al., J. Power Sources, 195 (2010) 2431.
- [2] H. Pan et al., Energy Environ. Sci., 6 (2013) 2338.
- [3] J.L. Sudworth et al., The Sodium Sulfur Battery, Kluwer, 1985.

Acknowledgements: The authors are thankful for the financial support of CAPES and CNPq / Brazil and LCE – Structural Characterization Laboratory – DEMa / UFSCar.

**Table 1.** Density and β'' -alumina percentage of samples sintered at 1600 °C / 10 min.

Sample	Density (g.cm ⁻³)	β'' -alumina phase (%)
0 wt%	99.8±0.1	78.8±0.1
5 wt% TZ-3Y	98.8±0.1	30.8±0.1
10 wt% TZ-3Y	98.3±0.3	34.8±0.1
1 wt% ZrO(NO ₃) ₂	99.6±0.1	89.5±0.1
10 wt% ZrO(NO ₃) ₂	99.8±0.1	92.5±0.1

**Figure 1.** Samples sintered at 1600 °C / 10 min with (a) 0 wt%, (b) 5 wt% TZ-3Y, (c) 10 wt% TZ-3Y, (d) 1 wt% ZrO(NO₃)₂ and (e) 10 wt% ZrO(NO₃)₂.



718 Inconel Characterization During Oxidation Assisted Intergranular Cracking by Scanning Electron Microscopy and EDS Mapping

Amanda Varela^{1*}, Henrique Dias², Monica Rezende³ e Luiz Henrique de Almeida⁴

1,2,4. Departamento de Eng. Materiais e Metalurgia, UFRJ/COPPE, Rio de Janeiro, Brazil.

3. Programa de Pós-Graduação em Engenharia Metalúrgica, UFF, Rio de Janeiro, Brazil.

*Email: amandavarela@poli.ufrj.br

Nickel-based superalloys are widely applied on aerospace, nuclear and petrochemical industries, since they were developed to operate in extreme environments such as high temperatures, high pressure and corrosive conditions. 718 Inconel is the most manufactured and used nickel superalloy nowadays due to its excellent mechanical properties, oxidation resistance and structural stability up to 650°C [1,2]. Owing to the severe operational conditions, this material is strongly dependable on service integrity, since it is susceptible to thermally activated phenomenon. Literature reports that oxygen availability is associated to loss of ductility and intergranular fracture at around 650°C, both associated to the embrittlement named as OAIC (oxidation assisted intergranular cracking) [3]. This phenomena overcomes the protective effect from the chromium and aluminum oxides, as the oxygen diffuses rapidly and preferentially throughout the grain boundaries, leading to a premature fracture. Niobium, which constitutes around 5% of the 718 Inconel, is a MC-type carbide former and it is known for its oxygen affinity. Therefore, several studies have pointed out the NbC essential role on OAIC manifestation on specific temperatures [2]. The carbide would react with oxygen and produce a brittle oxide Nb₂O₅. The object of this work is, then, to characterize a forged 718 Inconel in its solubilized state, by image analysis of tensile specimens fractured between 650 and 900°C using scanning electron microscopy (VERSA 3D Dual Beam). Two types of surface were studied, one was the direct fracture surface resulting from the mechanical testing. The second was the longitudinal section of the tensile cylindrical specimens. The elements present on the fractures and their distribution were identified by chemical composition mapping on EDS (model EDAX EDS3). The results showed the effect of temperature on the fracture mode, precisely a transition at 650°C and intergranular fracture growing from the borders towards the interior, until reaching 100% at 850°C (Figure 1). The images displayed aligned niobium carbides in the fracture borders crossing grains and, more discretely, niobium segregation inside the grains (Figure 2). The microscopy analyses corroborate niobium's influence on the embrittlement of this alloy, once NbC paths were identified all over the fractures. This adds to the mechanical results and transmission microscopy on a detailed investigation.

REFERENCES

- [1] R.F. Decker, The Evolution of Wrought Age-Hardenable Superalloys - Nickel: a Century of Innovation - Overview, *Miner. Met. Mater. Soc.* (2006) 32–36.
- [2] M.C. Rezende, Estudo sobre o efeito de diferentes tratamentos térmicos na ocorrência de envelhecimento dinâmico no Inconel 718, 2015.
- [3] L. Fournier, D. Delafosse, T. Magnin, Oxidation induced intergranular cracking and Portevin-Le Chatelier effect in nickel base superalloy 718, *Mater. Sci. Eng. A.* 316 (2001) 166–173.

This research was supported by FAPERJ (Brazil).

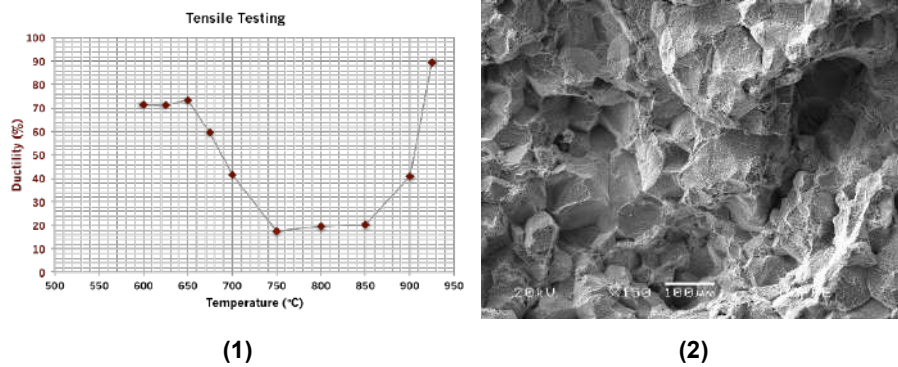
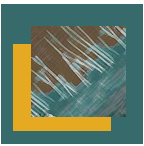


Figure 1 – The curve in (1) shows unusual drop in ductility starting at 650°C, while (2) presents 100% of intergranular fracture at 850°C.

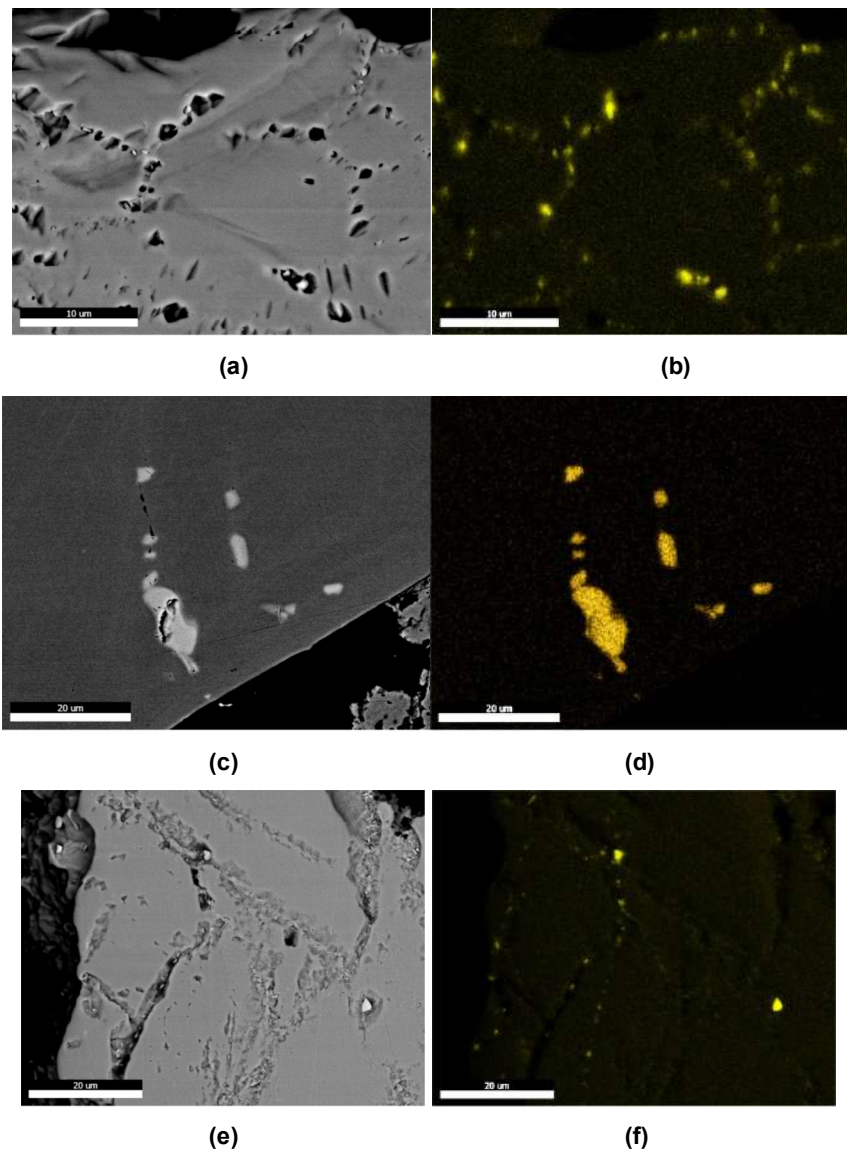
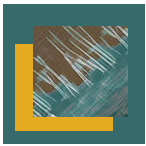


Figure 2 – 718 Inconel fractures from longitudinal section after mechanical testing at (a) 650°C, (b) 850°C and (c) 900°C. EDS mapping showing Nb in yellow at respective temperatures (d,e,f).



Thermal failure analysis in multilayer ceramic capacitors

Fonseca R. T.^{1,2*}, Antonelli E, Matos C. P.^{1,1}

1. Integration and Testing Laboratory – LIT/National Institute for Space Research – INPE, São José dos Campos – SP, Brazil.

2. Federal University of São Paulo – UNIFESP; São José dos Campos – SP, Brazil

*Email: tatiana.hazine@gmail.com, antonelli.eduardo@gmail.com

With the increase of the application of multilayer ceramic chip capacitors (MLCC) in surface mount technology (SMT), the importance of studying thermal shock properties in these devices also increased. Temperature variation in the welding stage of the SMT assembly leads to critical failures because of thermal stress in the materials [1]. Technological advances allowed the miniaturization of electronic components. Thus, the main function of a capacitor is to store energy, ideally in the smallest possible area. A capacitor is constructed as a monolithic chip in thin multilayer structure of metal (electrode) and ceramic (dielectric), Figure 1a. The exposed ends are electrically interconnected with a common conductor by means of a metallized coating, Figure 1b [2]. Often, due to thermal stress, components exhibit cracks on the surface or between layers. The presence of cracks in capacitors leads to a loss or variation of the capacitance [3]. Cracks can be found in capacitors after soldering in printed circuit boards. The study of the thermal failure crack is done by microscopy of the sectioned sample in order to evaluate the layers. The objective of this work is to analyze cracks originated from thermal shock in ceramic capacitors using impedance spectroscopy technique, optical microscopy, scanning electron microscopy and X-rays. The ceramic capacitors chosen for this study are of type X7R, which has barium titanate composition as the majority. The capacitors were subjected to temperature tests close to the manual welding limit, approximately 280 °C, in 100 cycles. Capacitance measurements were performed after 10, 30 and 100 cycles. X-ray images and microscopy were made after 100 cycles. The comparison between the impedance properties of non-stressed capacitors with the capacitors subjected to the temperature cycles shows that the impedance decreases. X-ray image analysis showed internal defects, Figure 2a. Optical and electronic microscopy made it possible to investigate the failure of these devices and confirm the results obtained by impedance, Figure 2b.

Keywords: thermal failure, scanning electronic microscope and impedance spectroscopy

REFERENCES

- [1] Maxwell J. Cracks: The Hidden Defect AVX - Technical Information. AVX Corporation
- [2] Prevallet M, Bagdy S, Prymak J, Randall M. High voltage considerations with MLCS [abstract]. 2004 [Presented at Power Modulator Symposium, 2004 and 2004 High-Voltage Workshop. Conference Record of the Twenty-Sixth International, 2004 May; 42-45; San Francisco-CA
- [3] Martin P. Electronic Failure Analysis Handbook. McGraw-Hill; 2004

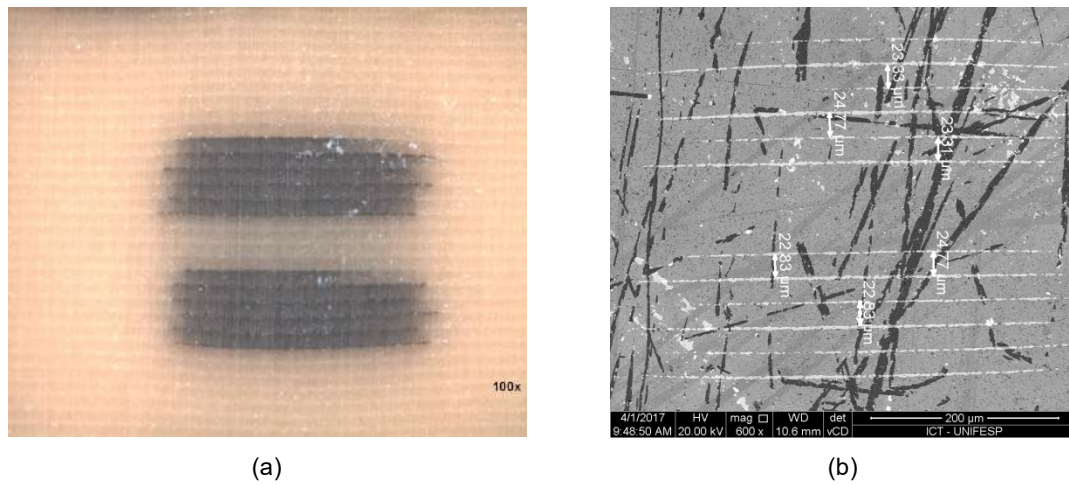
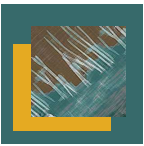


Figure 1 – Construction of the ceramic capacitor: a) microsecond capacitor and b) thickness measurements of the dielectric layers

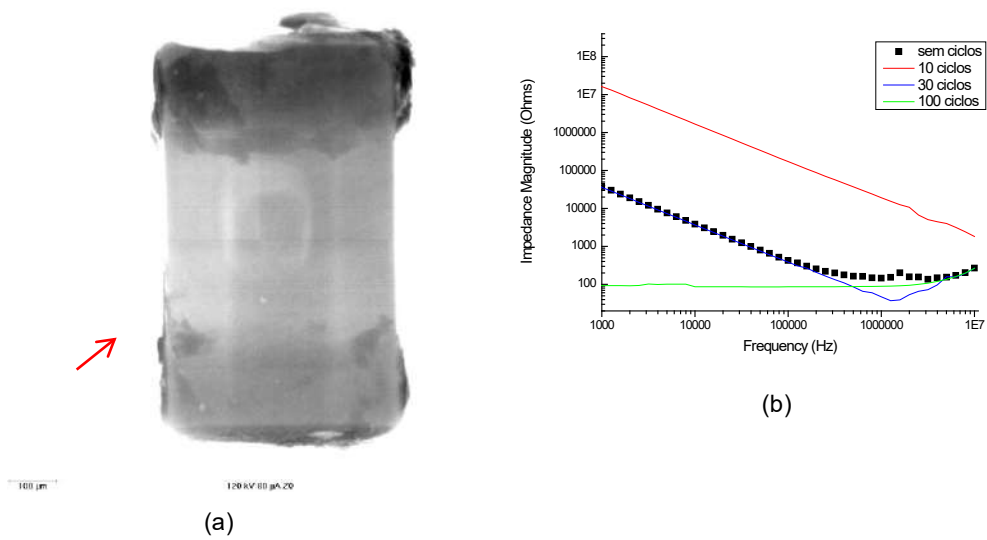


Figure 2 – Ceramic capacitor images after thermal shock: a) x-rays and b) decrease of impedance during cycles



Quantitative characterization of nanostructured materials using TKD in SEM

Laurie Palasse^{1*}, D. Goran

1. Bruker Nano GmbH, Am Studio 2D, 12489 Berlin, Germany

*Email: laurie.palasse@bruker.com

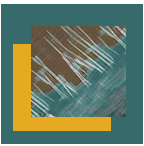
Quantitative characterization of nanostructured materials requires high spatial resolution orientation mapping at large-scale. In this aim, Transmission Kikuchi Diffraction (TKD) in SEM was developed as a technique capable of delivering similar results as EBSD but with a spatial resolution improved by up to one order of magnitude and a much larger field of view than with TEM [1,2]. TKD analysis is conducted on an electron transparent sample (FIB lamella, nanoparticles, TEM foil) using the same hardware and software as for EBSD system. If the conventional EBSD geometry is used, i.e. off-axis geometry, the transmitted Kikuchi patterns (TKP) are captured by a vertical phosphor screen. Most of the transmitted signal does not reach the phosphor screen, this is equivalent to a considerable loss of signal and the Kikuchi patterns are affected by strong distortions induced by gnomonic projection. As a result, lower quality patterns can have negative effect in the measurement quality.

In this presentation, we will present the advantages of using the on-axis TKD detection system as compared to the off-axis, i.e. standard EBSD geometry. With a horizontal phosphor screen placed underneath the sample, the transmitted signal is captured where it is the strongest and TKPs will have minimal distortions. When coupled with a fast and sensitive EBSD detector, low probe currents can be used, increasing further the spatial resolution and reducing the beam-induced specimen drift [3]. The resulting improved stability and high spatial resolution allow the user to acquire quantitative data by conducting large-area TKD orientation mapping at high speed.

Using different application examples, we will demonstrate that statistical data can be achieved for quantitative characterisation of nanostructured materials in the SEM (Fig. 1).

REFERENCES

- [1] Keller R R and Geiss R H 2012 J. Microsc. 245 245-251
- [2] Trimby P W 2012 Ultramicroscopy 120 16-24
- [3] Abbasi M, et al. 2015 ACS Nano 9 10991-1002



DOI: [INSERIR ENDEREÇO DO DOI AQUI.](#)

Caderno de Resumos do 26º Congresso Brasileiro de Microscopia da SBMM – ISSN: [INSERIR AQUI.](#)

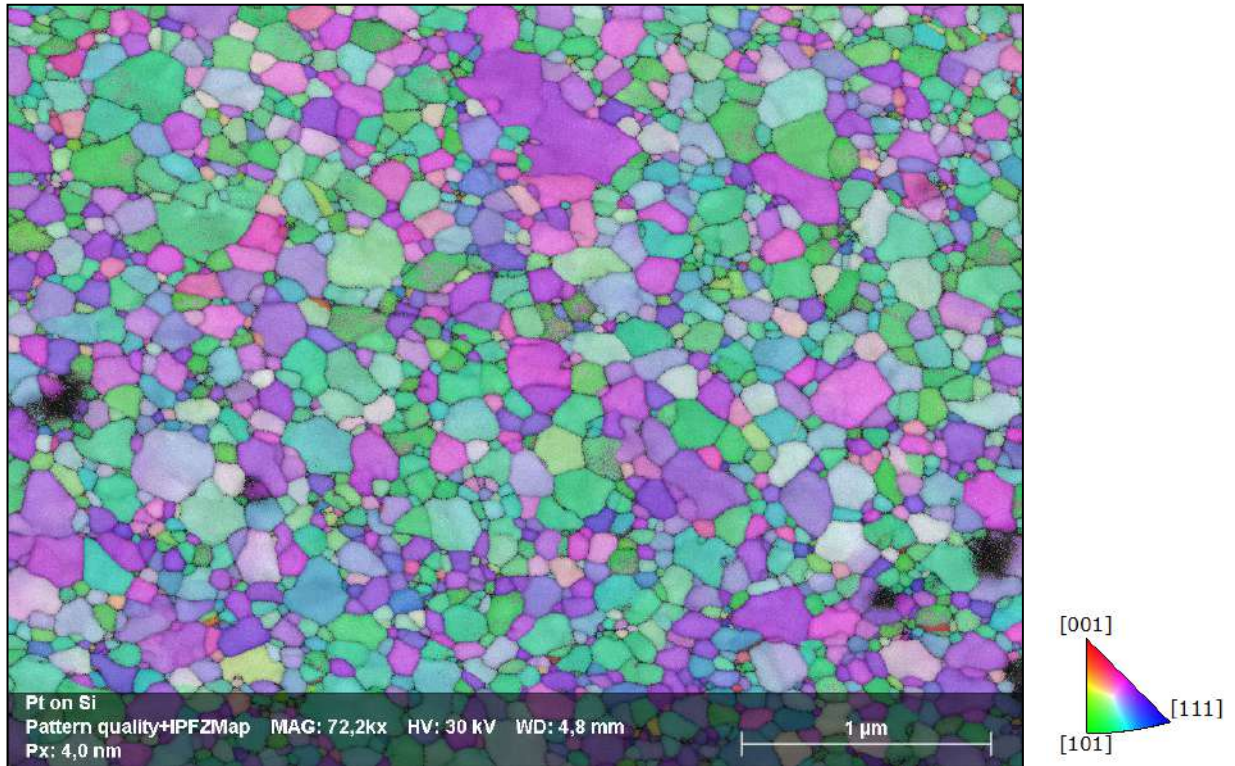
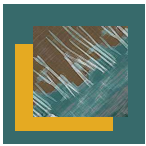


Figure 1: unprocessed orientation Transmission Kikuchi Diffraction map (Inverse Pole Figure along z axis) of Pt film on Si acquired at 328 fps using the on-axis detector configuration.



Using EBSD to Better Describe a Cr-Mo Ferritic-Bainitic Microstructure

Pinto, A. L.¹, Silva, C. L.¹, Alves, F.²

1. Centro Brasileiro de Pesquisas Físicas (CBPF)
2. TechnipFMC

Chromium-Molybdenum steels are usually employed at the gas and oil industry for high temperatures applications. Nevertheless, these materials have also been used for subsea application which must meet different requirements related to mechanical strength and toughness at low temperature. So, ASTM A182 F22 grade steels have been modified with respect to chemical composition and thermomechanical treatments for coping with such requirements. In order to properly understand the effect of such modifications it is necessary to correct interpret the microstructure thus obtained. In this work, we make use of EBSD for segmenting different phases inspired by previous attempts to do so in other alloys¹. Samples were grinded until 1500 Mesh SiC paper, followed by 3 μm diamond polishing and electrolytic polishing (133 ml acetic acid, 25 g CrO₃ and 7 ml H₂O) using graphite as cathode at 150C with 0.23-0.29 A/cm² current density. EBSD analyses were made using a Jeol 7100 FT equipped with an Oxford EBSD system (Nordlys-Max CCD camera). EBSD maps were collected at 30 kV acceleration voltage with 1 μm step size for austenite packet size observation and 0.3 μm for phase detection. Orientation maps were mounted as a mosaic as presented in Fig. 1 to allow a visual estimation of its size. Regions with size around 200 μm among finer regions with 50 μm . Fig. 2 show the Kikuchi band contrast (BC) map from a region where it is possible to have a picture from the microstructure similar to that obtained through optical microscopy. In order to distinguish between ferrite and austenite, local misorientation maps (KAM – kernel average misorientation) were constructed using a 5x5 kernel filter. Fig. 3a show this map together with the misorientation distribution which clearly show a bimodal distribution. Threshold between ferrite and bainite was initially set at 0.50 right at the sell point. Grain reference orientation distribution (GROD) angle map (Fig. 3b) revealed that bainite has regions with different angular deviation from the bainite sheaf mean orientation; it is clear that there is lath bainite and granular bainite. Closer inspection shows regions classified as ferrite at KAM maps that seems to be in reality ferrite from granular bainite. So, KAM maps allow us to separate ferrite from bainite, while GROD makes it possible to separate pro-bainitic ferrite from bainitic ferrite inside bainite packets. These results give support to the qualitative classification that has been used in optical microscopy² and opens the field for more reliable quantification. Next step in this project will be to compare the quantification of these different microconstituents with mechanical behavior obtained in samples submitted to different thermal process.

REFERENCES

- [1] Zaefferer, S. et al. Journal of Microscopy V. 230 (2008) p. 499-508.
- [2] ZAJAC et al. Technical Steel Research, Report EUR 21245EN, Luxembourg (2005), p.10.
- [3] This work was supported by CNPq and FAPERJ.

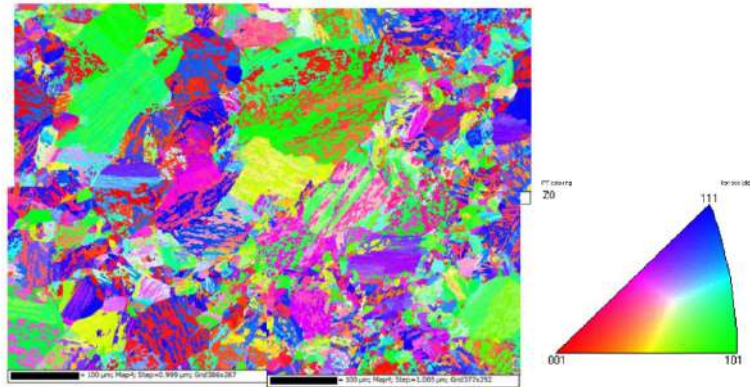
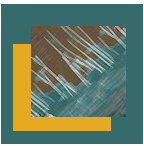


Fig. 1 – EBSD Orientation map from a F22 steel and IPF color reference triangle.

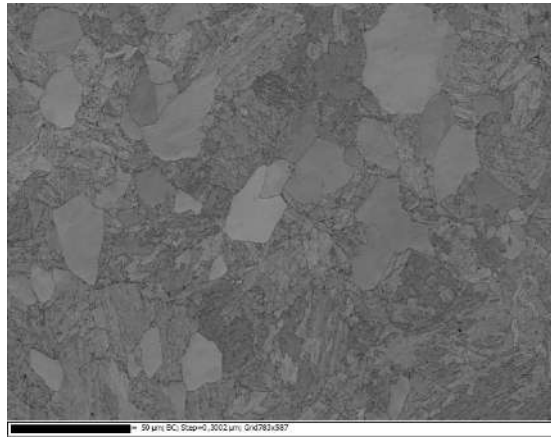


Fig. 2 – Kikuchi band contrast map from a F22 steel.

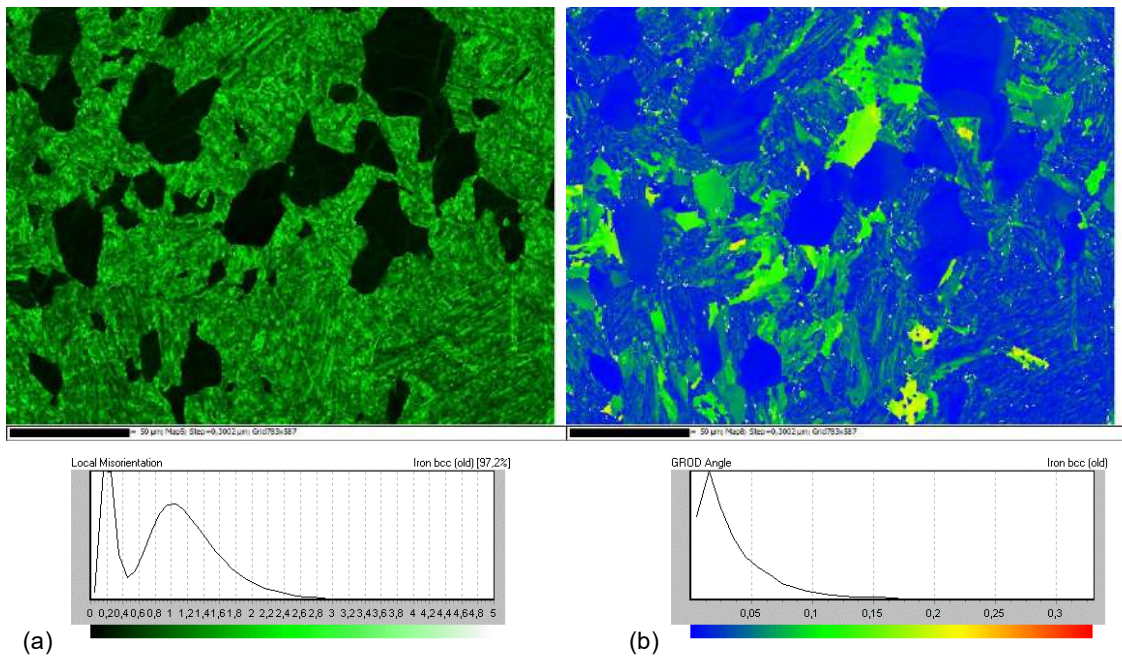
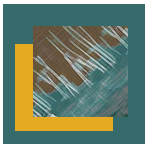


Fig. 3 – (a) Local misorientation map and (b) GROD map from a F22 steel and color reference.



Nanoscale Orientation Mapping Characterization of Nanocrystalline Phases in Metallic Alloys

C.R.M. Afonso¹, V. Amigo², W.J. Botta¹, C.S. Kiminami¹

1. Department of Materials Engineering (DEMa), Universidade Federal de São Carlos (UFSCar), Rod. Washington Luís, km 235, 13565-905, São Carlos – SP, Brazil
2. Universidad Politecnica de Valencia (UPV), Instituto de Tecnología de Materiales (ITM), Camino de Vera s/n, 46022 Valencia, Spain.

Nanocrystalline materials are constantly been developed and the need for its characterization is always advancing in order to fulfill the requirements of the resulting nanostructured phases and complex precipitates in sub-micron scale interfaces with variation of composition. Characterization of nanocrystalline materials in this work was realized using X-ray diffraction (XRD), scanning electron microscopy with field emission gun (SEM-FEG) coupled with energy dispersive spectroscopy (EDS) and electron backscattered diffraction (EBSD). In order to improve resolution for the characterization of nanoscale phases it was used TEM analysis together with associated techniques: STEM-EDS, HRTEM. The distribution of phases and grain orientation maps were determined with an Automatic Crystal Orientation Mapping (ACOM) system installed in a JEOL JEM 2100F (TEM/STEM) 200kV with field emission gun (FEG). A ASTARTM NanoMegas system was used for ACOM diffraction data acquisition [1,2]. Usually the step sizes (resolution) adopted in ASTAR mapping starts in 1 nm to 10 nm, and cover areas through the sample from 100 x 100 pixels (nm²) up to 700 x 700 pixels (µm²). Crystallographic mapping through ASTAR technique was able to characterize and identify submicron down to nanometric □ phase precipitates in PM samples as well as characterize nanograins of β-Ti, nanostructured □ and □ phase precipitates in HPT samples, becoming a very useful tool for characterization of β-Ti alloys. Other metallic materials cases were analyzed, such as interfaces in welding explosion of high strength steel with super duplex steel and Inconel 625 Ni alloy, nanocrystalline Ti-Nb thin films, automated GMAW-P welding of Al 5083 alloy, laser clad Ni- and Fe-based BMG coatings, in its interfaces, nanostructured grains and intermetallic phases.

Keywords: Nanocrystalline alloys; advanced characterization; crystallographic orientation mapping; intermetallic phases.

REFERENCES

- [1] P. Moeck, S. Rouvimov, E. F. Rauch, M. Véron, H. Kirmse, I. Häusler, W. Neumann, D. Bultreys, Y. Maniette, and S. Nicolopoulos, *Cryst. Res. Technol.* 46, 589 (2011).
- [2] F. Sun, J.Y. Zhang, M. Marteleur, C. Brozek, E.F. Rauch, M. Veron, P. Vermaut, P.J. Jacques and F. Prima, *Scripta Mater* 94, 17 (2015).

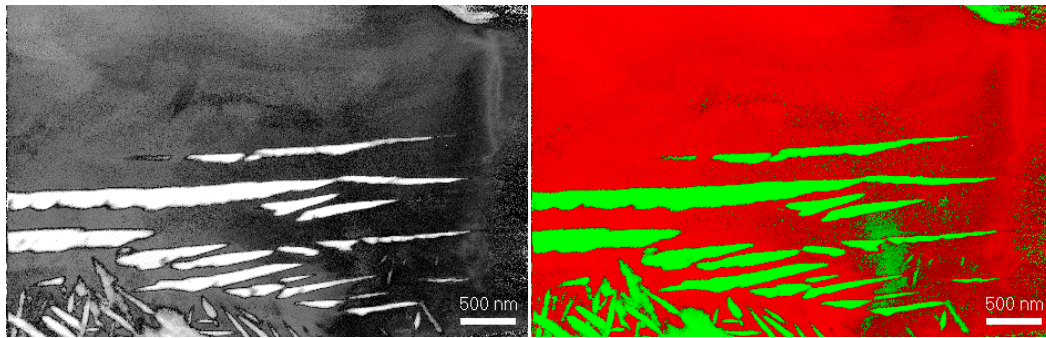
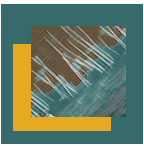


Fig. 1. TEM micrograph in a) virtual bright field (VBF) obtained by Automatic Crystal Orientation Mapping (ASTAR) of Ti35Nb10Ta alloy sintered at 1250°C with $\alpha+\beta$ region and b) PhaseMap combined with Virtual-BF image of nanoscale α phase (green) dispersed through β -Ti (red) matrix.

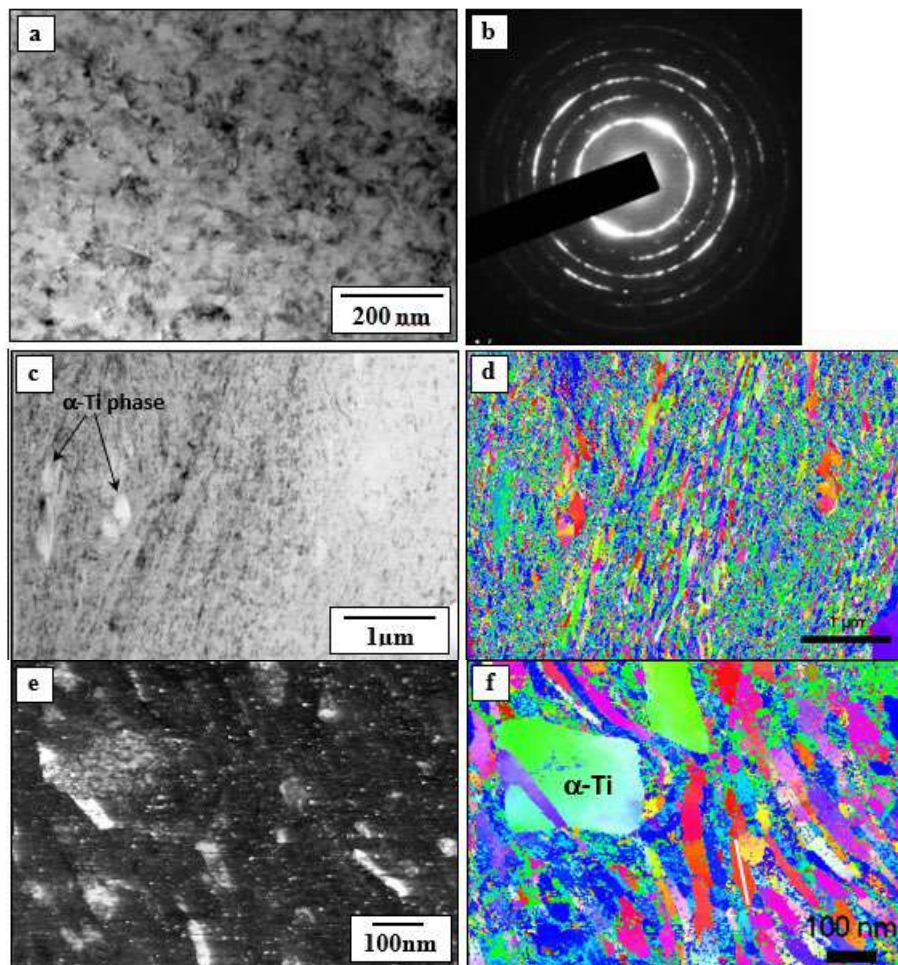


Fig. 2 – TEM micrograph in a) bright field (BF) mode of nanocrystalline β Ti35Nb10Ta alloy after HPT processing and respective b) SAD ring pattern. ACOM of HPT sample with c) virtual bright field (VBF) of nanocrystalline $\alpha+\beta$ region and d) IPF-Z showing view of nanostructure. In detail e) virtual dark field (VDF) of \square precipitates dispersed in β -Ti matrix and f) IPF-Z orientation image showing smaller soft β nanograins and α precipitates as well.



Orientation and Phase Mapping In the Transmission Electron Microscope Using Diffraction Spot Recognition in Several Kinds of Materials.

Alberto Moreira Jorge Junior^{1*}, Diego Davi Coimbra¹, Walter José Botta¹

1. Federal University of São Carlos, LCE-DEMa, 13565-905, São Carlos, SP, Brazil

*Email: moreira@ufscar.br

The recently developed technique based on transmission electron microscopy, called ASTAR, makes use of electron-beam (in precession mode or not) together with spot diffraction pattern recognition, offering the opportunity to perform automated crystal orientation mapping (ACOM) in micro- or nanoprobe mode. ACOM-TEM opens the opportunity of acquiring reliable orientation/phase maps with a spatial resolution that can go down to the nm range. In fact, ACOM-TEM closes the gap between EBSD and BF/DFTEM by providing full orientation maps with nanometer resolution. Even materials severely plastic deformed (SPD), e.g., by ECAP or HPT, can be analyzed. When SPD is performed, problems can arise when observations by EBSD are carried out, because the Kikuchi lines used by any EBSD system or in the TEM are very sensitive to the crystal orientation and they rapidly disappear if the diffracting volume suffers distortions induced by high dislocation densities. In short, the ACOM-TEM consists in scanning the electron beam (in precession or not) in the nanoprobe mode on a specimen area, thus collecting thousands of electron diffraction spot patterns to be subsequently indexed automatically through a template matching. Sample preparation for this fairly new technique is exactly the same as for standard TEM observations. However, the ACOM technique will not distinguish with certainty superimposed spot diffraction patterns arising from piled-up crystals along beam direction in thick regions of the sample. Thus, when trying to search for the best possible spatial resolution for orientation maps that can be obtained from thin foils, it is desirable to find the best agreement between expected grain size and sample thickness along the beam direction crossing the sample. Here, we briefly describe the fundamentals of the technique and present a variety of application examples relative to the characterization of microstructure/microtexture of submicron and nanocrystalline metals such as in nanocrystals embedded in amorphous matrix (Fig. 1), and severely plastic deformed materials (Fig. 2), etc, which are being routinely obtained at the Structural Characterization Laboratory at UFSCar (LCE-DEMa-UFSCar). The potentialities and limitations of the technique will be also discussed after presenting those several examples.

REFERENCES

- [1] Peter Moeck et al. in: 11th IEEE International Conference on Nanotechnology Portland Marriott. August 15-18, 2011, Portland, Oregon, USA. (2011) 754
- [2] E. Rauch et al. *Microscopy and Analysis*, 93 (2008) S5
- [3] Y. Guo et al. *Mater. Design* 111 (2016) 608
- [4] This research was supported by CNPq, CAPES and FAPESP (Brazil).

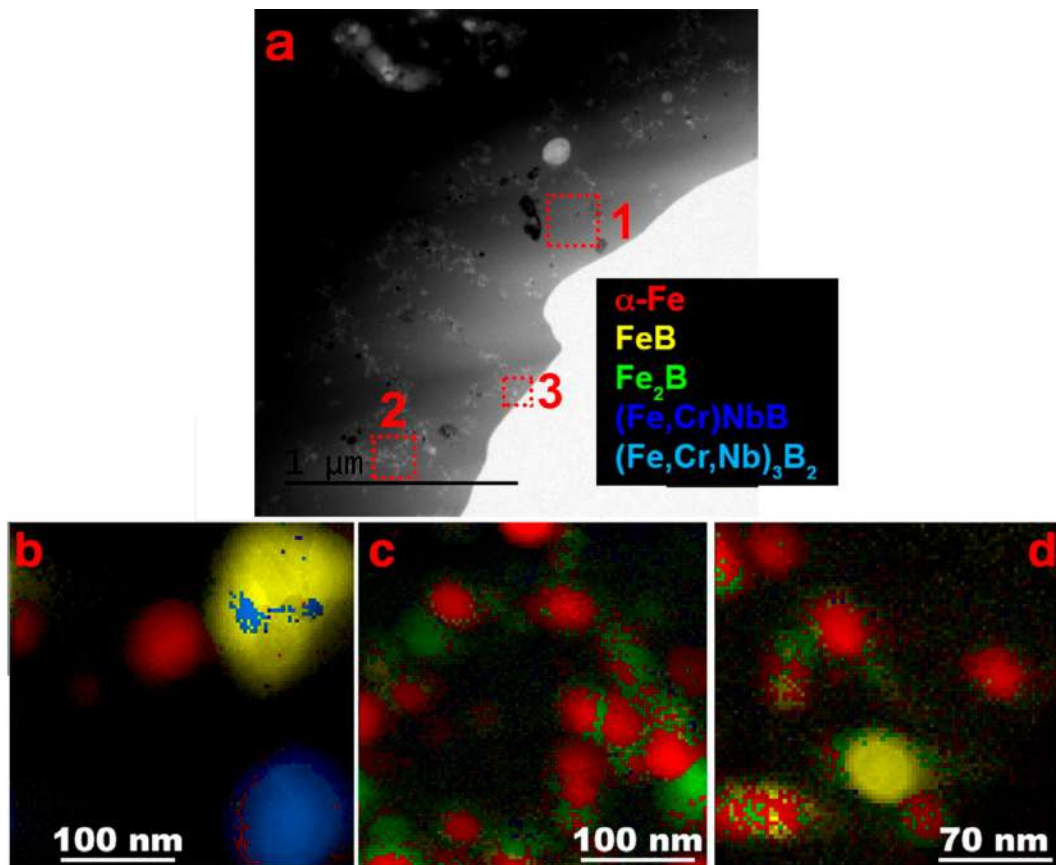
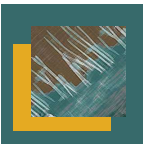


Fig. 1. (a) Conventional BF-TEM image of a High Velocity Oxygen Fuel (HVOF) coating. Phase mappings of the selected areas, 1, 2 and 3 are shown in (b), (c) and (d), respectively. Region 1 and 2 are of the size of 300 nm × 300 nm and region 3 is 210 nm × 210 nm. Color codes are presented in the inset of Fig. 1a. Black is the amorphous matrix. [3]

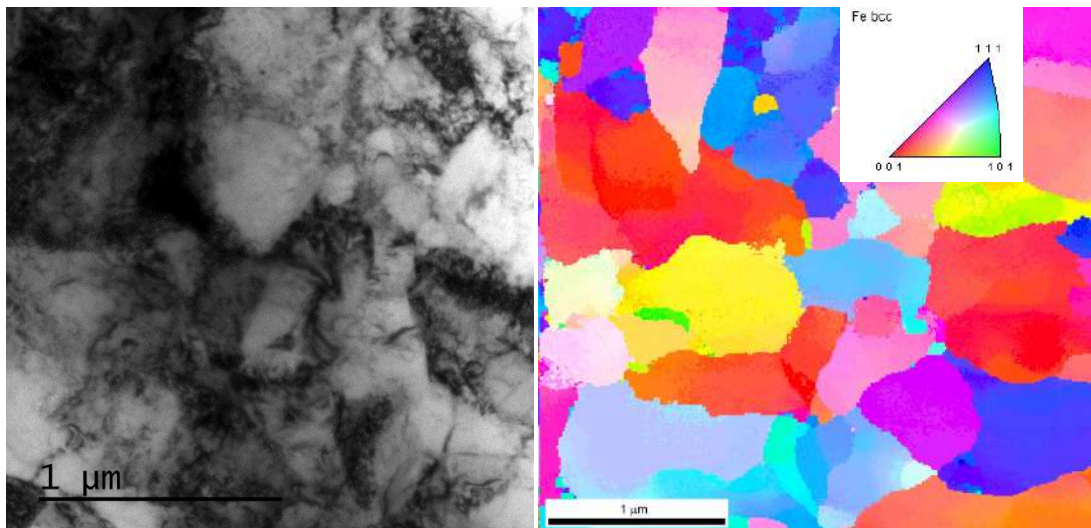


Fig. 2. Severely plastic deformed Iron ARMCO after 8 passes of Equal Channel Angular Pressing (ECAP). (a) conventional BF-TEM image and (b) orientation image mapping



An SEM-EDS-assisted LA-ICP-MS Study of REE-Bearing Minerals From the Cerro La Tuna Tourmalinite, Paso Del Dragón Complex, Northeastern Uruguay

Gianna Maria Garda^{1,*}, Sandra Andrade¹, Isaac Jamil Sayeg², Elena Peel-Canabal³

1. Dept. Mineralogy and Geotectonics/Geosciences Institute, São Paulo University, São Paulo, Brazil. giagarda@usp.br.
2. Dept. Sedimentary and Environmental Geology/Geosciences Institute, São Paulo University, São Paulo, Brazil.
3. Dept. Internal Geodynamics/Geosciences Institute, University of the Republic, Montevideo, Uruguay.

The Neoproterozoic Paso del Dragón Complex occurs east of the Siena Ballena shear zone in northeastern Uruguay. The Cerro La Tuna serpentinites, which correspond to less than 20% of the Paso del Dragón Complex, encompass deformed and metamorphosed mafic-ultramafic rocks, including magnesian and amphibolitic schists. They are usually rimmed by zones of mono- or bi-mineralic rocks of metasomatic origin. Abundant aqueous fluids leached Na, K, Al, and Ca from the ultramafic rocks and the interaction of these fluids with the host rocks produced chlorite schists, tremolite schists, talc schists, epidotes, and tourmalinites by metasomatism [1]. According to [2], rare earth elements (REE) are readily concentrated by hydrothermal processes. Light REE are more mobile hydrothermally than the heavy REE and form stable complexes with fluoride and chloride (and likely sulfate, carbonate and phosphate) at high temperatures. The Cerro La Tuna tourmalinite yields the highest total REE contents (579.5 ppm, [1]), when compared to the other rocks of the Paso del Dragón Complex produced by metasomatism. A previous LA-ICP-MS study of the Cerro La Tuna tourmalinite (analytical procedures described in [3]) showed that REE contents are very low in tourmaline, ca. 10 times lower than those obtained for the associated chlorite. In order to investigate the cause of the relatively high total REE contents in the tourmalinite, the LA-ICP-MS data from [3] were re-treated with the aid of back-scattered electron (BSE) images (Fig. 1) and semi-quantitative EDS analyses (obtained using a scanning electron microscope LEO 440I coupled with an Oxford Inca EDS system). Re-treatment of LA-ICP-MS data was possible because, once the LA-ICP-MS session is saved, a selection of the best intervals for background and signal measurement can be done off-line by means of the Glitter 4.4.2 software package. Figure 2 presents chondrite-normalized REE patterns for: 1- zircon and phosphate inclusions in tourmaline; 2- phosphate inclusions in chlorite; 3- zircon (and phosphate) inclusions in chlorite; 4 and 5- chlorite, and 6- tourmaline. Patterns 1, 2 and 3 show that zircon and phosphate inclusions in tourmaline and chlorite, detected by means of Zr, Hf and P signals, are ca. 100 times more enriched in REE, when compared to host chlorite (patterns 4 and 5) and tourmaline (pattern 6). Figure 3 presents the EDS spectra obtained for tourmaline, Ti-Mn(-Ce) oxide, zircon, and Y and REE phosphates (possibly xenotime and monazite), respectively labeled 1, 2, 3 and 4 (as in Fig. 1). These mineral phases are relatively abundant and can explain the total REE content of 579.5 ppm yielded by the Cerro La Tuna tourmalinite. The contribution from metasomatic carbonates is not ruled out, once relatively intense Ca peaks were observed in tourmaline EDS spectra. Because the tourmalinite sample was carbon-coated, no additional check for the presence of, e.g., calcite (CaCO₃), could be made.

REFERENCES

- [1] E Peel-Canabal, Ph.D. Thesis, Geosciences Institute, São Paulo University, São Paulo (2012), 198p.
- [2] AE Williams-Jones, AA Migdisov and IM Samson, *Elements* **8** (2012), p. 355-360.
- [3] GM Garda, S Andrade and E Peel-Canabal, *Microsc. Microanal.* **22**, Suppl. **3** (2016), p. 446-448.



Effect of pH on Liquid Crystalline Interface from Crude Oil Emulsion Fractions

Angela Camila Duncke^{1*}, Gizele Batalha de Freitas¹, Isabela Fernandes Soares¹, Angel Bassini da Silva², Carla Napoli Barbato³, Márcio Nele¹

1. Federal University of Rio de Janeiro

2. Veiga de Almeida University

3. Federal Institute of Education, Science and Technology of Rio de Janeiro

*Email: angeladuncke@eq.ufrj.br

Water content is an important variable for offshore crude oil production. When the crude oil and the water are mixed, emulsions are formed. However, these emulsions are unwanted and the separation of aqueous and oil phase are crucial. Thereat, the presence of very stable emulsions can lead to operational and environmental problems. It is known that the presence of lamellar liquid crystals (LC) surrounding the emulsion droplets increase the emulsion stability for cosmetics systems [1]. However, the presence of LCs in crude oil emulsions has not yet firmly assessed. Duke et al. [2] observed LC structures through polarized light microscopy in emulsion fractions of Brazilian crude oils, for the first time. Therefore, the aim of this study is to investigate the influence of pH on the LC characteristics through polarized light microscopy and, on interfacial elastic modulus of the LC bilayer by interfacial rheology. For this, emulsions were prepared employing two different crude oils (A and B) and deionized water (DW) or NaOH solution (pH 10 and 12). For all emulsion an 80 wt. % of aqueous fraction was adopted. The oil/water system was mixed in a Polytron 3100 for 3 minutes at 6,000 rpm. Liquid crystals can display optical anisotropy, thus the emulsion bottom fractions were visualized by polarized light microscopy in an Axiovert 40 MAT (Carl Zeiss). Interfacial rheology experiments were carried out using a tensiometer Tracker-H (Teclis). Volume Profile Type was selected for the oscillating tests. The total elastic modulus was determined by the interfacial tension response to sinusoidal variations of the interfacial area. The oscillation amplitude applied was 6% of the total droplet volume. Only the systems using DW and NaOH solution (pH 10) were analyzed by interfacial rheology. The crude oil A is characterized by total acid number of 2.8 mgKOH/g and density 0.939 g/cm³. The oil B presents 1.2 mgKOH/g for total acid number and density 0.918 g/cm³. The Figure 1 shows the polarized light microscopy images of all emulsions bottom fraction prepared. The LC structures (with a thickness about 1.5 μm) had a similar Maltese cross pattern for all samples assessed. For deionized water emulsions, fewer LC structures were observed compared to emulsions prepared with NaOH solutions. Comparing the emulsion made with pH 10 and pH 12, it is possible to note that, the number of LC structures increase with the increasing pH. Apparently, the emulsion fractions with NaOH solutions of oil A presents a larger number of LC structures compared to the fraction of the emulsions of oil B. This possibly can be attributed to the higher acidity of oil A. The elastic modulus values for system with neutral pH for oil A and oil B (14.8 and 11.4 mN/m) are lower than with pH 10 (19.5 and 11.6 mN/m), indicating that the increase in pH increases the interfacial elastic modulus. However, this effect was less pronounced in oil B than in oil A. According to this results, it is suggested that the acid number, which is related to the naphthenic acid content, is an important factor for LC formation and, in higher pHs conditions, the crude oils systems present a more rigid film.

REFERENCES

- [1] K. Klein, Liquid Crystals and Emulsions: a wonderful marriage. In: Skin Barrier: Chem. of Delivery Syst., (2008) 265.
- [2] A.C.P. Duncke et al., Energy Fuels, 30 (5) (2016), 3815.
- [3] The authors would like to acknowledge the financial support provided by Capes, CNPq and Petrobras, all from Brazil.

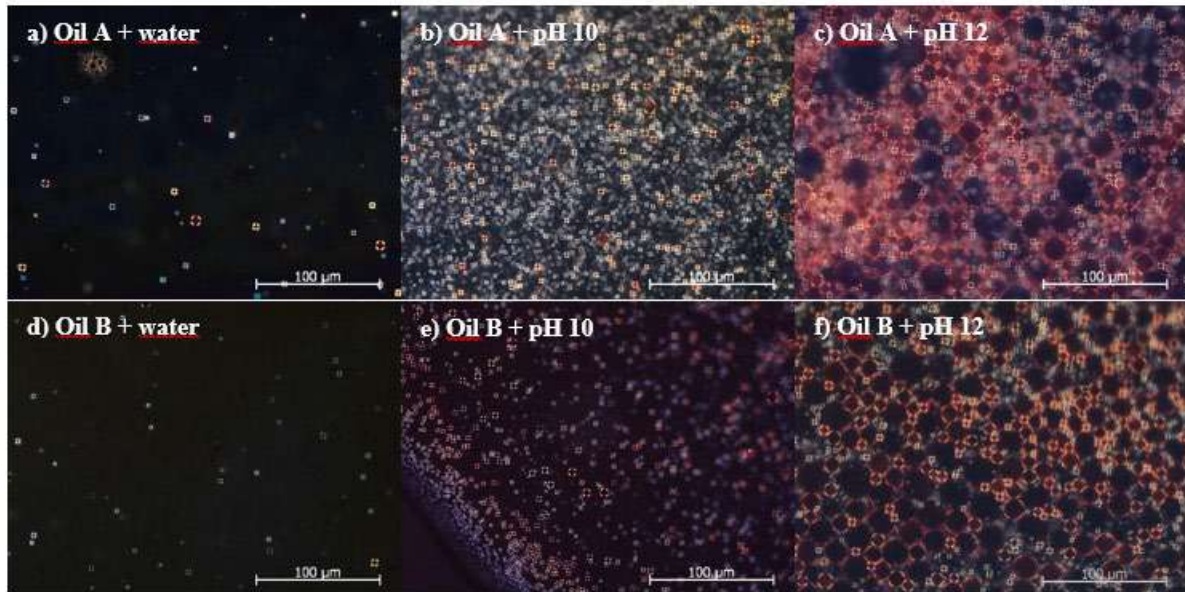
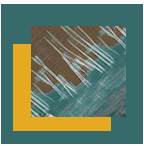
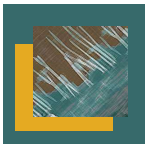


Figure 1 – Polarized light microscopy images of emulsions bottom fraction composed for: crude oil A with water (a), pH 10 (b) and pH 12 (c); crude oil B with water (d), pH 10 (e) and pH 12 (f).



DOI: [INSERIR ENDEREÇO DO DOI AQUI.](#)

Caderno de Resumos do 26º Congresso Brasileiro de Macroscopia da SBMM – ISSN: [INSERIR AQUI.](#)

SEM Imaging Applied to U-Pb Geochronology in Zircon of Espera Feliz Region: Ages of Protoliths, Magmatism and Metamorphism

Letícia Muniz da Costa Cardoso^{1*}, Juliana Fernandes Bonifácio¹, Isabella Robert Rodrigues¹, Márcio Inácio Alves¹, Armando Dias Tavares¹, Mauro César Geraldés¹

1. Universidade do Estado do Rio de Janeiro, Faculdade de Geologia, Rio de Janeiro, Brazil.

*Email: leticiamuniz_@hotmail.com

The Araçuaí belt located east of San Francisco Craton is result of a collisional event occurred at Neoproterozoic times. This range was developed during the Brazilian Cycle during diachronous events reworking the passive margin rocks deposited on San Francisco craton ended with the formation of the Gondwana supercontinent [1]. For this work nine samples were collected in Espera Feliz area, located in Espírito Santo state in order to contribute to the knowledge of the geological evolution of Araçuaí Orogen and its relation to the Ribeira Orogen. The samples was carried out in the Geological Sample Processing Laboratory (LGPA) at the State University of Rio de Janeiro (UERJ) where they were washed, crushed and pulverized, followed by mineral concentration through panning and sieving. After that procedure heavy liquids were used to separate light grains, hand magnet to separate high magnetized grains and later was used Frantz electromagnetic separator to separate grains due its magnetic susceptibility. All this procedures were made so we could separate zircon grains, they are usually belong to the last batch of separation in Frantz electromagnetic separator. This mineral is used for geochronological purposes. The zircon grains were taken to the Laboratory (MULTILAB) at UERJ, collected under a binocular loupe and mounted on epoxy used in the Scanning Electron Microscope (SEM). In this way, it was possible to visualize zircons grains' internal structure, such as morphology, growth zones and other features. SEM images as cathodoluminescence images are used to select which part of the grain will be abraded by laser beam. With the SEM images it was possible to observe that the zircon grains from Espera Feliz are elongated, rounded and hexagonal form. Also, some of the grains have inherited core, which indicate that the rock was reworked by melting, keeping the age of the rock crystallization (formation) in the zircon core and the age of its rim in growth zones. In Espera Feliz samples, we were able to get three different range of ages, each one from a different geological process and geological period. U-Pb geochronological analysis made with LA-ICP-MS show protolithic ages ranging from 2201 Ma and 1996 Ma, magma crystallization ages of 626 Ma to 622 Ma and metamorphic ages of 602 Ma to 582 Ma. These results combined with information from the literature allow us to suggest a geological evolution with the formation of the Paleoproterozoic basement rocks originated in magmatic arc environment (2201-1996 Ma) possibly related to Mineiro Belt. These rocks have been intruded by a Neoproterozoic magmatism (626-622 Ma) during the subduction process of the oceanic floor with the approximation of paleocontinentes Congo and Sao Francisco. The third event identified is the metamorphism and anatexis (602-582 Ma) during the collision and formation of Gondwana.

REFERENCE

[1] Noce C.M., Pedrosa-Soares A.C., Silva L.C., Alkmim F.F. O Embasamento Arqueano e Paeloproterozóico do Orógeno Araçuaí; *Geonomos*, 15(1), p. 17 - 23, 2007;

This research was supported by CNPq (Brazil).

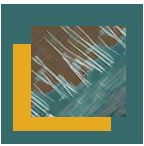


Figure 2 – Equipment used for imaging in SEM and geochemical analyses at MULTILAB-UERJ. Picture 1: binocular loupe. Picture 2: mounted epoxy with zircon grains. Picture 3: Scanning Electron Microscope (SEM). Picture 4: Laser Ablation-Inductively Coupled Plasma Mass Spectrometer (LA-ICP-MS).

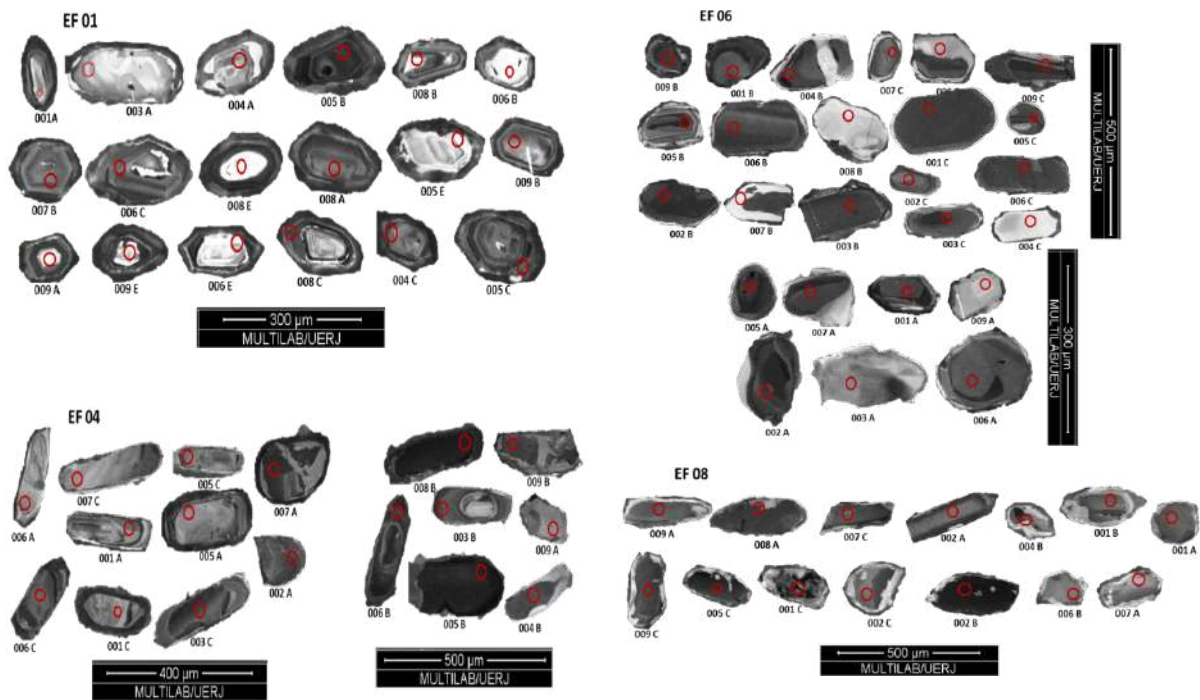


Figure 3 – Cathodoluminescence imaging on zircon grains using SEM showing morphology of the grains (elongated, hexagonal and rounded) and internal structure (growth zones and inherited cores). The red circles show which part of the grain was analysed in order to obtain an age.



Automatic Characterization of Iron Ore through Image Processing and Analysis

Iglesias, J.C.A.^{1*}; Gomes, O.F.M.²; Augusto, K.S.¹; Domingues, A.L.A.³; Casagrande, C.⁴; and Paciornik, S.¹

1. DEQM/PUC-Rio, Rua Marquês de São Vicente, 225, Gávea, Rio de Janeiro, Brazil
2. CETEM, Av. Pedro Calmon, 900, Ilha da Cidade Universitária, Rio de Janeiro, Brazil
3. CTF/VALE, Nova Lima, Minas Gerais, Brazil
4. DIPE/VALE, Av. Dante Michelina, 5500, Jardim Camburi, Vitória, Espírito Santo, Brazil

*Email: julioc.alvarez@gmail.com

In recent years, the DEQM/PUC-Rio digital microscopy research group has been working on the development of different techniques for the characterization of iron ore and its agglomerates, as part of a cooperation project with Vale [1-4]. Thus, the idea of encompassing the previously developed iron ore characterization techniques arose, with the intention of unifying them in a complete analysis of this material. For this, two fully automatic routines were created, one for image acquisition and another for image processing and analysis, as described below. The images were acquired on a motorized Zeiss AxioImager.M2m optical microscope. This allowed full software control of the microscope (Axiovision 4.9.1). Axiovision allows simpler programming based on the scripting language and a more complex macro language using Visual Basic 6.0 (VB6). Using these features an automatic image acquisition routine was created, in charge of centering the sample in the capture frame, loading the microscope and camera settings (illumination type, light intensity, filters, use of polarization, exposure time, white balance, camera frame size, etc.), acquiring and saving the images. This routine saves two images of the same region, one obtained in bright field and the other with circular polarization (Figures 1a e 1b), that serve as input to the processing/analysis routine. The processing routine is a complex, cross-platform solution, and involves software and languages such as Axiovision, ImageJ, Octave, Clojure, Scheme and VB6. It is divided into two steps. In the first one, the routine uses the image in bright field to identify by its colors hematite, magnetite, goethite and pores and to measure the area fractions of the last three phases (Table 1). The hematite binary image (Figure 1c) is used as a mask to isolate this phase in the polarized image. Since hematite is a strongly anisotropic mineral, this causes the brightness in the image to change with different orientations of the crystals when using polarized light. Thus, based on the texture, we can classify the polarized hematite in porous and compact hematite (Figures 1d e 1e). Compact hematite can be discriminated by texture into mono and poly crystalline (Figures 1f and 1g). A further shape classification leads to the separation in 3 subclasses – granular, lamellar and lobular (Figure 1h). The respective area fractions can also be obtained (Table 2).

REFERENCES

- [1] K.S. Augusto et al. 14th ICSIA, Liège (Belgium) (2015).
- [2] O.D.M. Gomes et al., Minerals Engineering, 52 (2013) 191.
- [3] J.C.A. Iglesias et al., Minerals Engineering, 24 (2011) 1264
- [4] J.C.A. Iglesias et al., Tecnologia em Metalurgia Materiais e Mineração, 7 (2010) 12.
- [4] This research was supported by CNPq, CAPES, FAPERJ and Vale.

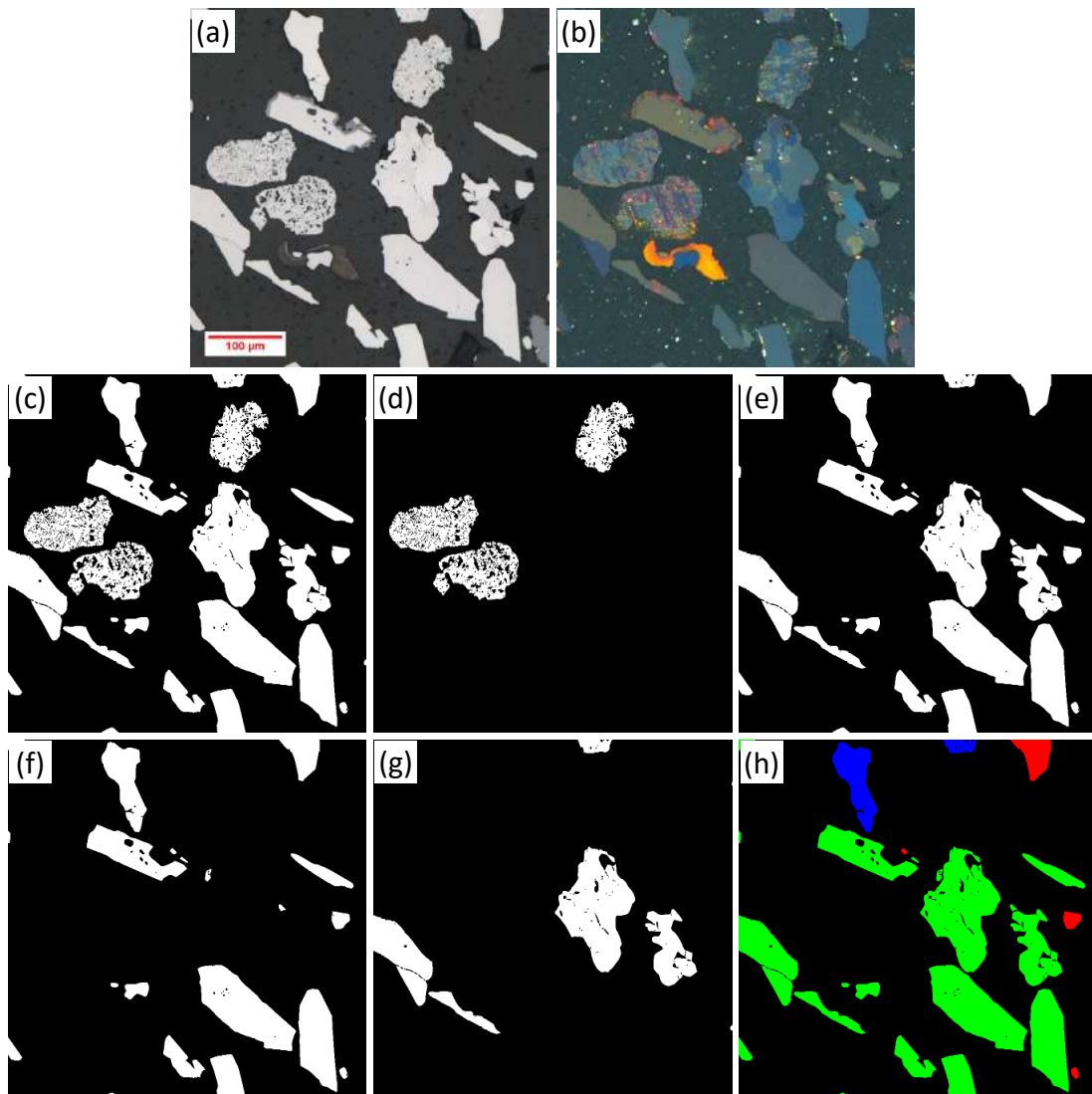
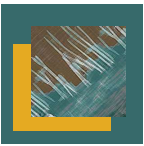


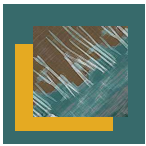
Figure 1. Iron ore images obtained during automatic acquisition and image processing.

Table 1. Area fraction of detected phases

Phase	Hematites	Martite	Magnetite	Goethite	Pores
% Area	83.43	10.24	0.99	5.34	2.33

Table 2. Area fraction of compact hematite subtypes

Subtype	Monocrystalline	Polycrystalline	Granular	Lamellar	Lobular
% Area	68.33	31.67	12.81	66.46	4.16



Microestrutural Evolution of Nickel-Based Superalloy Processed By Equal Channel Angular Pressing (ECAP)

Renan Augusto Francisco Dias^{1*}, Waldemar Alfredo Monteiro¹

1. Instituto de Pesquisas Energéticas e Nucleares – IPEN, CCTM, SP, Brazil

*Email: rafd_rafd@hotmail.com

The present work shows the microstructural (under optical microscopy) and Vickers hardness evolution of a nickel-based superalloy Inconel 600 (alloy 600) before and after deformed by Equal Channel Angular Pressing (ECAP) that significantly modified the alloy microstructure and, consequently, its strength. Alloy 600 is an austenitic nickel-based superalloy with 72% nickel, 14-17% chromium and 6-10% iron and it is commonly used in structures and components that work in aggressive environments. The grain size plays a significant role in the mechanical properties in this alloy; so, it is important to understand how processing techniques modify the microstructure of the material. In fact, ECAP is a processing technique involving the application of severe plastic deformation (SPD) used in the manufacture of metals and alloys with ultra-fine grains (UFG) and therefore with extraordinary combinations of both high strength and high ductility [1]. For the research, alloy 600 rods, supplied by Multialloy, with 8 mm diameter, were heat treated at 1200 °C for 6 h (solution), as shown in Figs. 1a and 1b, to achieve a larger grain size. The generated products were machined to the final dimensions of the specimen (6 X 6 X 25 mm) shown in Fig. 1c and then processed by ECAP, at room temperature using route A, in a D2 tool steel die, whose angles Φ and Ψ are 120° and 0° (Fig. 1d). Samples were pressed repetitively through a total of three passes, the microstructural aspect of the samples after each pass are shown in Figs. 2 and 3 with different magnifications. Metallographic preparations were made in the transverse, longitudinal and normal directions, TD, LD and ND of each sample. Sanding step with grit 320, 600 and 1200 were used. Polishing steps included 3 μ m- and 1 μ m-diamond paste and 0.05 μ m-alumina suspension and finally they were etched for optical examination using Marble's etchant (10 g CuSO₄, 50 ml HCl and 50 ml H₂O). The micrographs were taken with OLYMPUS optical microscope model BX51M, with magnifications of 100x and 200x. The hardness tests were conducted in a Buehler Micromet 2103 microdurometer in the LD of the samples. For each measurement, a load of 500 g was applied for 15 s. Five separate measurements were taken on each sample at randomly selected points and then averaged. In Figs. 1a and 1b, it is possible to see only 1 phase, a solid solution of Ni-Cr-Fe, a coarsened grain structure and annealing twins. There are slight changes in the microstructure after the first pass, some strain marks are seen. After the second and third passes the microstructure shows highly deformed grains, deformation and transition bands. The values of hardness (Tab. 1) show an increase after each pass. In summary, (1) the micrographs analysis shows all the transformations from an annealed state to a highly-deformed state; (2) the grains are yet elongated after 3 passes and possibly do not show an expected UFG structure; (3) deformation twinning is revealed and is possible to see strain marks, deformation and transition bands; (4) the hardness values increased due to the high strain imposed to the alloy.

REFERENCE

[1] ZHILYAEV, A.P. et al., The microstructural characteristics of ultrafine-grained nickel, *Mat. Sci. and Eng. A* 391 (2005) 377–389. 2004.

This research was supported by Universidade Presbiteriana Mackenzie, Instituto de Pesquisas Tecnológicas (IPT) and Instituto de Pesquisas Energéticas e Nucleares (IPEN).

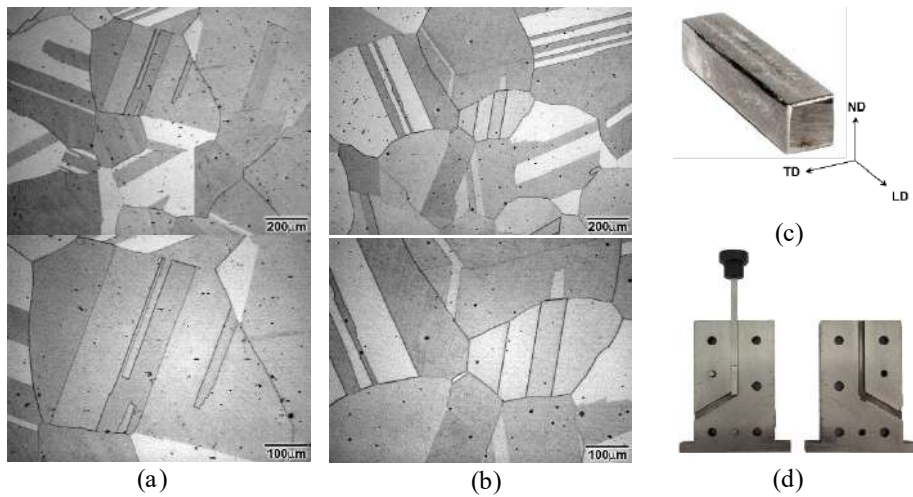
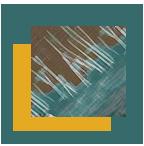


Fig. 1. (a) Microstructure of alloy 600, solution annealed, LD. (b) Microstructure of alloy 600, solution annealed, TD. (c) ECAP Sample before pressing. (d) ECAP die.

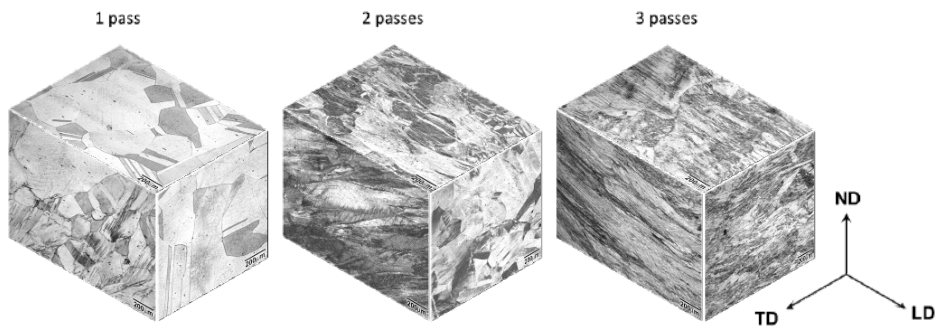


Fig. 2. Microstructure of alloy 600 after each pass. (bar = 200 μm).

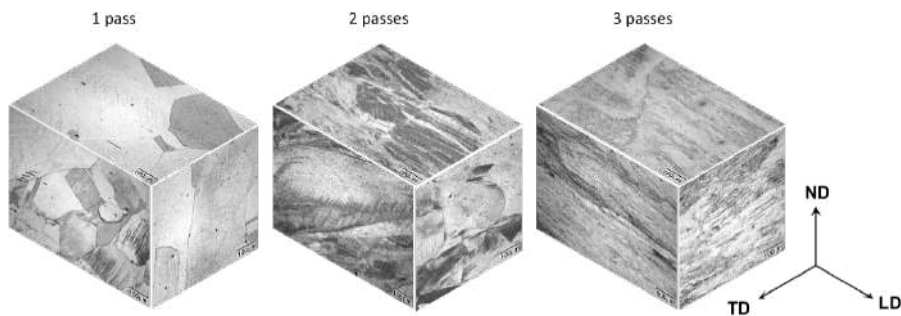
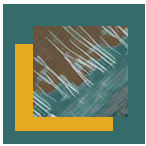


Fig. 3. Microstructure of alloy 600 after each pass. (bar = 100 μm).

Tab. 1 Table of hardness values for the samples

Sample	Hardness Vickers (HV0,5)
As-Received	302 ± 5
Solution	150 ± 7
1 pass	332 ± 14
2 passes	409 ± 15
3 passes	450 ± 18



EELS 3D Tomography of Plasmonic Nanoantennas

B. S. Archanjo^{1,2*}, T. L. Vasconcelos¹, B. S. Oliveira¹, C. Song², F. Allen^{2,3}, C. A. Achete¹, P. Ercius²

1. Divisão de Metrologia de Materiais, Instituto Nacional de Metrologia, Qualidade e Tecnologia (INMETRO), Duque de Caxias, RJ 25250-020, Brazil

2. National Center for Electron Microscopy, Molecular Foundry, Lawrence Berkeley National Laboratory, 1 Cyclotron Rd., Berkeley, California 94720, United States

3. Department of Materials Science and Engineering, University of California, Berkeley, 210 Hearst Ave., Berkeley, California 94720, United States

*Email: bsarchanjo@inmetro.gov.br

Localized surface plasmons are a collective oscillation of conduction electrons occurring on the surface of metal nanostructures. A remarkable characteristic of the localized surface plasmon resonance (LSPR) phenomena is that the resonance energy can be tuned by changing the size, shape and material of the host nanostructure. In this work, we use scanning transmission electron microscopy (STEM) and electron energy loss spectroscopy (EELS) to study the effect of 3D morphology on plasmonic properties of plasmonic nanoantennas created via helium ion microscopy (HIM). For the EELS spectral processing we first used Richardson-Lucy deconvolution to increase zero loss peak (ZLP) energy resolution. The LSPR 3D reconstructions were performed using compressed sensing (CS) electron tomography with a conjugate gradient descent algorithm implemented in Matlab. The 3D reconstructions were compared to conventional methods including filtered back projections (FBP) and simultaneous iterative reconstruction technique (SIRT) using an open-source Python package for tomographic data processing and image reconstruction Tomopy. The 3D visualization (figures and movies) were accomplished in Tomviz, also an open-source software. A metal nanoparticle boundary element method (MNPBEM) was used to simulate the nanopillar taper LSPR modes, therefore assisting the nanoantenna designing. The goal of the project is to develop new nanoscale tappers for apertureless scanning near-field optical microscopy (apertureless-SNOM), which allows optical chemical and structural characterization at the nanoscale, with spatial resolution higher than the diffraction limit of the light.

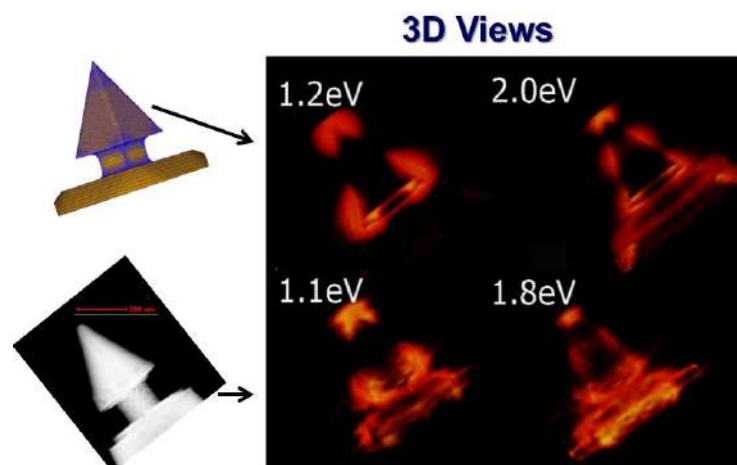


Figure showing the surface mesh of the MNPBEM simulated nanoantenna (top left) and a STEM image of the HIM fabricated nanoantenna (bottom left). In the right are shown the 3D reconstructed images of the LSPR modes from simulated and fabricated nanoantennas.



Nanostructured Alpha-NiCe Mixed Hydroxide Electrodes for Sensitive Amperometric Prednisone Sensors

Josué M. Gonçalves^{1*}, Robson R. Guimarães¹, Bruno B. N. S. Brandão¹, Lucas P. H. Saravia¹, Pamela O. Rossini¹, Juliana S. Bernades², Mauro Bertotti¹, Lucio Agnes¹, Koiti Araki¹

1. Department of Fundamental Chemistry, Institute of Chemistry, University of Sao Paulo, Sao Paulo, Brazil.

2. National Nanotechnology Laboratory (LNNano), National Center for Energy and Materials (CNPEM), Campinas, Brazil.

The nickel hydroxide ($\text{Ni}(\text{OH})_2$) have been widely studied as electroactive materials for amperometric sensor[1]. Many efforts have been made to improve the conductivity, electrochemical reversibility and stability of that material. The $\text{Ni}(\text{OH})_2$ can present polymorphs α and β , where the former has higher load capacity and superior electrochemical properties[2]. However, the α - $\text{Ni}(\text{OH})_2$ is not stable and is easily converted to the β form [1-2]. Recently was demonstrate that the combination of the two strategies, more specifically, cobalt additivation and nanostructuration, can further enhance the stability of alpha nickel hydroxide, resulting in more robust materials for application in sensors and other devices [1]. Thus, herein described is a nanostructured material exhibiting enhanced stability and electrocatalytic activity for oxidation reactions, thanks to the incorporation of Ce(III) ions into the nickel hydroxide matrix, as demonstrated by the high sensitivity and wide dynamic range for amperometric quantification of prednisone (a drug). Mixed α -NiCe hydroxide nanoparticles (α - $\text{Ni}_{0.8}\text{Ce}_{0.2}(\text{OH})_{2x+3y}$) were prepared, characterized by cyclic voltammetry (CV), electrochemical impedance spectroscopic (EIS), X-Ray diffraction (XRD), high resolution transmission electron microscopy (HRTEM) and scanning transmission electron microscopy (STEM) and its potential as sensor material for amperometric determination of prednisone was evaluated. The incorporation of cerium (III) shifted the 003 reflection to lower angles, from $2\theta = 9.21$ to 7.66° (11.56 \AA), consistent with a larger basal plane distance. In addition, the presence of cerium in the mixed nanoparticles decreased the degree of crystallinity of nickel hydroxide as confirmed by the disappearance of the 006, 101 and 110 reflection planes, probably because Ce(III) ions, with twice as large radius, impart significant stress and disorder in the alpha nickel hydroxide turbostratic structure. In fact, a larger structural disorder was observed in the HRTEM images for α -NiCe nanoparticles (Fig. 1B) when compared to α - $\text{Ni}(\text{OH})_2$ (Fig. 1A). The formation of mixed hydroxide nanoparticles was confirmed by STEM, since the bright field image (Fig. 1C, transmitted electrons, BF) and dark field (Fig. 1D, scattered in high-angle annular dark field, HAADF) exhibited similar contrast and no clear indication of segregation in $\text{Ni}(\text{OH})_2$ and $\text{Ce}(\text{OH})_3$ phases. The better electrocatalytic property for α -NiCe was revealed by EIS and reflected in the high sensitivity of the modified electrodes as prednisone sensors, as determined from the current as a function of concentration plots (Fig. 2). In fact, about an order of magnitude higher sensitivity was measured for α -NiCe as compared with pure α - $\text{Ni}(\text{OH})_2$ NPs. In short, the incorporation of 20 mol% of Ce(III) ions into $\text{Ni}(\text{OH})_2$ NPs enhanced enormously its stability in the alpha phase while conferring enhanced electrocatalytic properties responsible for the fast oxidation of prednisone on the α -NiCe NPs modified FTO electrodes, allowing the realization of amperometric sensors with sensitivity as high as $3.8 \times 10^{-2} \text{ A mol}^{-1} \text{ L}$ and LOD as low as $4.8 \times 10^{-8} \text{ mol L}^{-1}$, in a wide dynamic range from 0.0 up to 76.9 \mu M , working at $+0.5 \text{ V vs Ag/AgCl}$ ($3.0 \text{ mol L}^{-1} \text{ KCl}$).

REFERENCES

[1] Martins, P.R., et al. Rsc Advances, 2013. 3: p. 20261-20266.

[2] Rocha, M.A., et al. Journal of Nanoscience and Nanotechnology, 2011. 11: p. 3985-3996.

Acknowledgments: This work was supported by FAPESP, CNPq, SisNANO, LNNano@CNPEM.

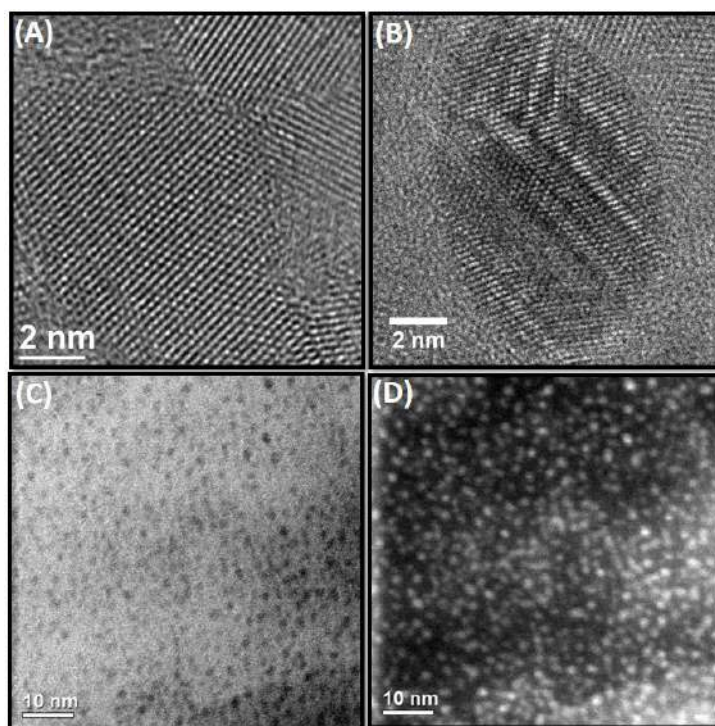


Figure 1. HRTEM images of α -Ni(OH)₂ (A) and α -NiCe (B) deposited on graphene oxide sheets. STEM images of α -NiCe nanoparticles on graphene oxide (GO) sheets: C) bright field image showing α -NiCe NPs homogeneously dispersed on GO sheets, and D) same image in E) in HAADF dark field mode where the NPs appear as bright spots.

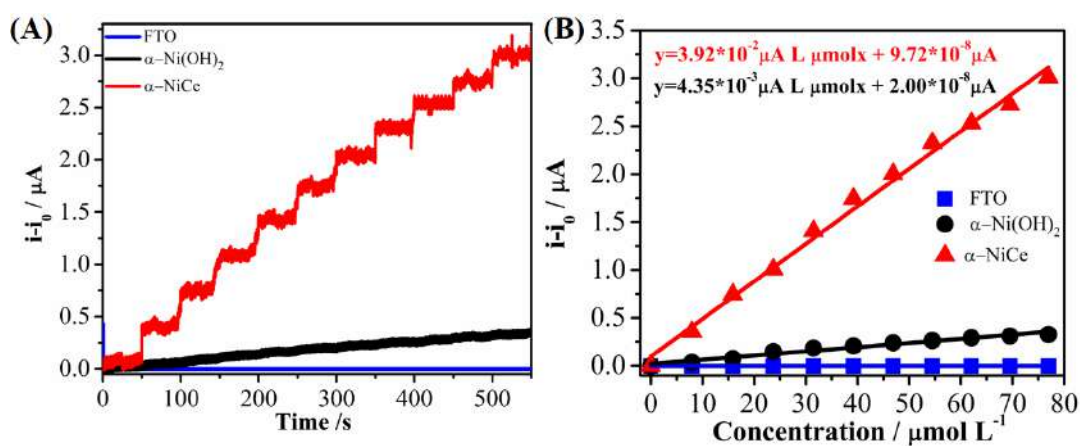


Figure 2. A) Amperometric responses recorded at 0.5 V with bare (blue line), and α -Ni(OH)₂ (black line) and α -NiCe (red line) FTO modified electrodes while successively injecting 20 μ L of prednisone in 5.0 mL of 1.0 M KOH, increasing stepwise its concentration from 0.00 to 76.9 μ M. B) Plots of current as a function of prednisone concentration.



Structural and Morphological Characterization of Ag/TiO₂ Nanocomposites Using High Resolution Transmission Electron Microscopy

Gustavo H. M. Gomes¹ and Nelcy D. S. Mohallem^{1*}

1. Laboratory of Nanostructured Materials, Chemistry Department, ICEX, UFMG, Belo Horizonte, Brazil

*Email: nelcy@ufmg.br

Titania and metallic silver nanoparticles have been applied in many technological products due to their interesting properties such as photocatalytic, bactericide and fungicide properties used for disinfection of products, films for energy cells, smart fabrics, among others [1]. Moreover, Ag/TiO₂ nanocomposites have been widely studied due to their unique properties that enhance the existing ones [2,3].

In this work, Ag/TiO₂ nanocomposites were characterized aiming to understand their role of formation. A solution including titanium (IV) isopropoxide (97% - Sigma Aldrich), isopropyl alcohol (Sigma Aldrich) and an aqueous solution of nitric acid was prepared at room temperature (25 °C) and low relative humidity of the air (40%). The solution was stirred for 48 hours to evaporate the isopropanol and then silver nitrate was added therein at 5% molar ratio Ag/Ti [1]. The mixture was kept stirring for 2 hours in a UV-C (254 nm) chamber at 160 °C to reduce the Ag⁺ to Ag⁰ [2-4]. The solution was dried under UV-vis light for 2 h to obtain the powder. UV-visible spectrophotometer (Carry, Varian 100) was used to measure the absorption (300 – 800 nm) of the powders dispersed in water to find the band-gap (eV) of their indirect transition. X-ray diffraction was carried on a Shimadzu, model XRD-7000 X. High-resolution transmission electron microscopy (HRTEM) and electron diffraction (ED) were carried on a FEI TECNAI G2-20 with acceleration tension of 200 kV to evaluate the texture, shape, phase and size of the samples. Energy dispersive spectroscopy (EDS) linked to the HRTEM microscope was used to confirm the composition of the nanoparticles.

The preparation of Ag/TiO₂ nanocomposites resulted in Ag⁰ cubic phase dispersed in anatase TiO₂ phase with particle size of 4-6 nm for TiO₂ and 7-11 nm for Ag⁰, according XRD and ED analyses (Figures 1 and 2). The introduction of Ag in the titania matrix prevented the growth of the TiO₂ nanoparticles and increased the excitation wavelength of 370 nm (TiO₂) to 439 nm (Ag/TiO₂). The Ag nanoparticles grow continuously under the action of heat and UV light, migrating to the surface of the matrix, as shown in Figure 2.

REFERENCES

- [1] M.M. Viana, et al., *Ceramics Internat*, 36 (2010) 2047.
- [2] J.Y. Wang, et al., *Catalysis Communications*, 10 (2009) 1052
- [2] M.M. Viana, et al., *Applied Surface Science*, 265 (2013) 130
- [3] M. M. Viana, et al., *J. Sol-Gel Sci and Technol.* 59 (2011) 19

The authors would like to thank FAPEMIG, CNPq and CAPES for financial support and Microscopy Center/UFMG for technical support.

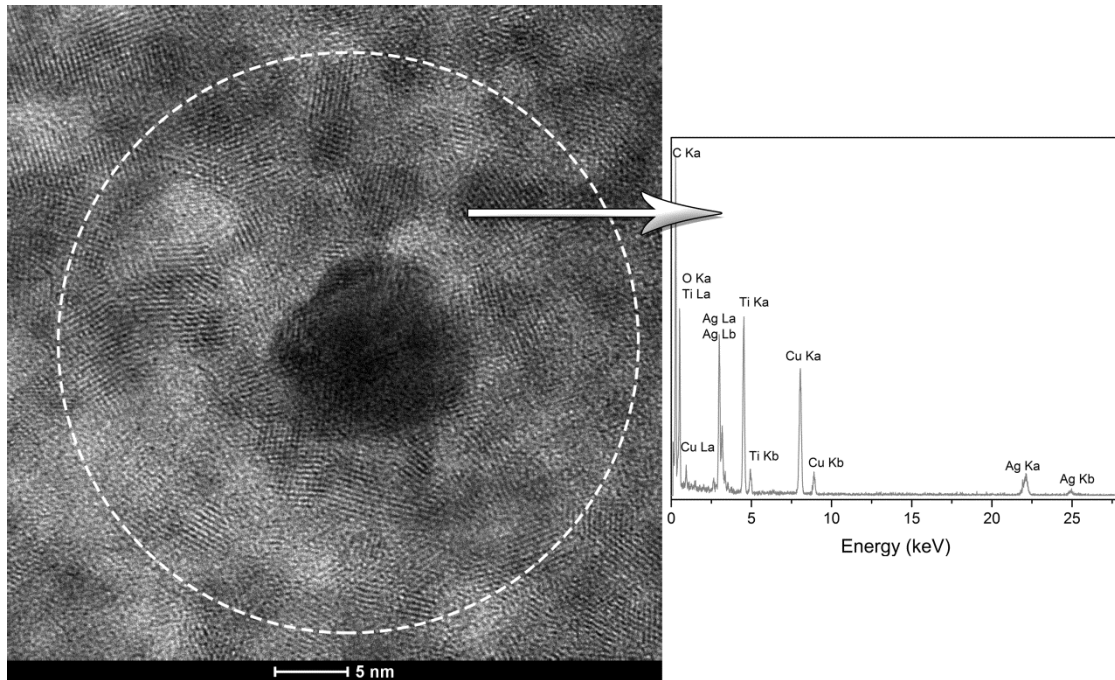
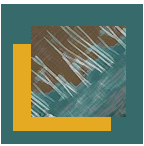


Figure 1 – HRTEM image of an Ag metallic nanoparticle dispersed in anatase TiO₂ matrix with the respective EDS spectrum of the marked region.

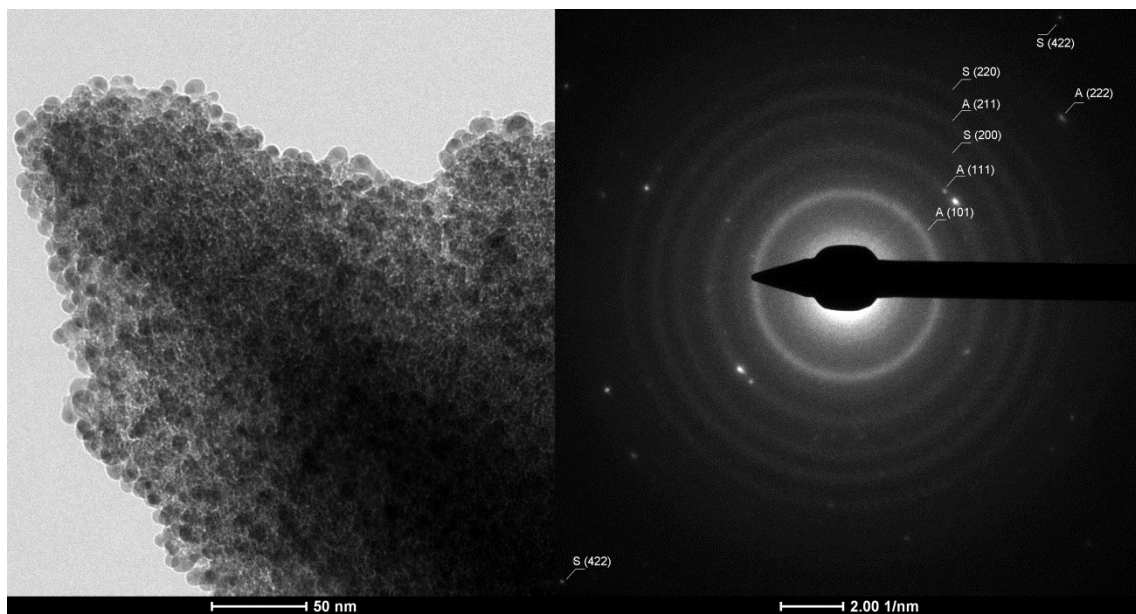
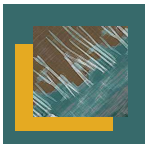


Figure 2 – TEM image of the TiO₂ matrix covered with Ag nanoparticles with the respective electron diffraction, where A – anatase and S – silver.



Magnetic Vortices in Nanostructures Made by Lithography

Luiz C. Sampaio^{1*}, Jeovani Brandão², Paulo Soledade¹, Danilo Froes¹, Pablo Ramon Batista¹, André Luiz Pinto¹, Alexandre Martins de Souza¹, Flávio Garcia¹, Alberto Passos Guimarães¹ and João Paulo Sinnecker¹

1. Centro Brasileiro de Pesquisas Físicas, Rio de Janeiro, Brazil.

2. LNILS – CNPEM, Campinas Brazil.

*Email: sampaio@cbpf.br

The manipulation and control of magnetization in small scales under presence of magnetic field, spin-polarized current, temperature gradient, and electric field have been a subject of growing interest in the last decade, with important consequences to technological applications. Magnetic materials exhibit in small scales, from few micrometers to the atomic scale, a large range of properties that can be size and shape dependent, and influenced by the interfaces of different materials present in the structure. Such dependences are also important for the existence of domain walls that can be present in confined structures like disks, triangles, squares and wires (or stripes), mainly in the magnetization reversal process. We are interested in vortex domain walls. The magnetic vortex is characterized by an in-plane magnetization that circulates clockwise (CW) or counterclockwise (CCW) (chiralities) and by the out-of-plane magnetization, at its core, that is polarized up or down, leading to four independent combinations of chirality and polarity. We have investigated the dynamical properties of vortex domain walls in nanowires and disks made by Ni₈₀Fe₂₀. Initially, we will present results of the vortex domain wall propagation in nanowires with asymmetric defects like notches and “Y” bifurcations [1]. Through focused magneto-optical Kerr effect and micromagnetic simulations we will show that depending on the degree of asymmetry of the defect the vortex chirality, and also the polarity, can be reversed, properties useful for the magnetic recording. We have measured the probability of all the magnetization reversal processes involved. For disks, we will show images of vortices moving under action of an applied magnetic field obtained by Lorentz microscopy in a transmission electron microscope. Besides that, ferromagnetic resonance experiments, for the determination of spin-wave excitations eigenmodes has been carried out via both waveguides and through the use of lithographed planar microresonators [2]. To conclude, we will summarize the processes used in the fabrication of the nanostructures (wires and disks) using the optical and electron-beam lithography. All the structures were fabricated at the LABNANO/CBPF facility. This research was supported by FAPERJ and CNPq (Brazil).

REFERENCES

- [1] J. Brandão, R. L. Novak, H. Lozano, P. R. Soledade, A. Mello, F. Garcia, and L. C. Sampaio, *Journal of Applied Physics* 116, 193902 (2014) ; P. R. Soledade, J. Brandão, A. Mello, and L. C. Sampaio, *Mater. Res. Express* 4 (2017) 025034 ; J. Brandão, A. Mello, F. Garcia, and L. C. Sampaio, *Journal of Applied Physics* 121, 093905 (2017).
- [2] R. Narkowicz, D. Suter and R. Stonies, *Journal of Magnetic Resonance* 175, 275 (2005)

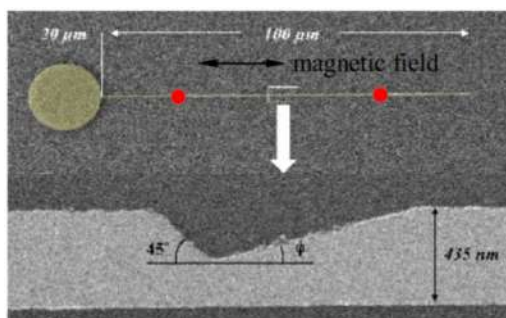


Figure 1 – Nanowire made by FeNi 100 μm long and 435 nm wide. The domain wall is nucleated on the left of the structure, in the circular pad. Under action of an applied magnetic field, the vortex domain wall moves to the right, reaching the notch (see zoom in the bottom). The red points show the position where one measures hysteresis cycles with a focused light (magneto-optical Kerr effect). According to the number of steps in the demagnetization, one can identify the vortex chirality and its probability.

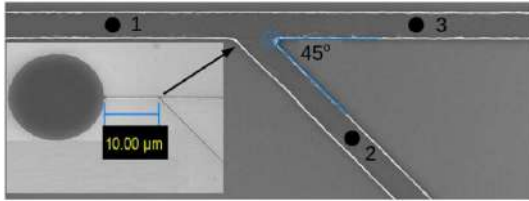
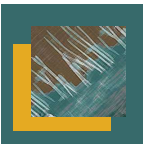


Figure 2 – Similar to Figure 1 but a different defect is introduced, an asymmetric “Y”. The width of the wire is 435 nm.

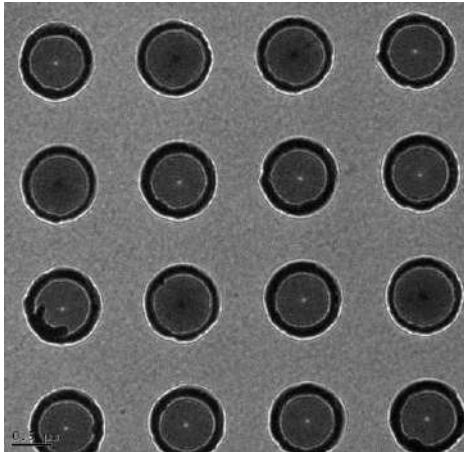


Figure 3 – Images of vortices in FeNi disks obtained by Lorentz microscopy in a transmission electron microscope. Black and white points means opposite chiralities, CW and CCW. The disks are 300 nm large.

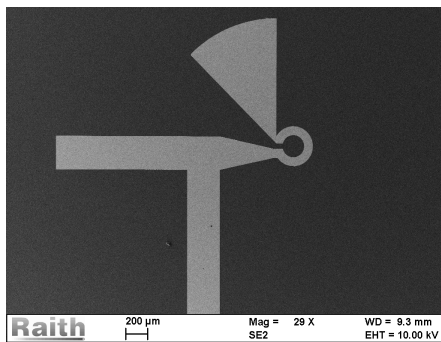


Figure 4 – Microresonator used in ferromagnetic resonance measurements. The sample is fabricated by lithography in the center of the loop (200 μm large).



Electron Beam Induced Current Characterization of Dye Sensitized Solar Cells

Lima, C. F.^{1*}, Kohlrausch, E. C.² Santos, M. J. L.², and Vasconcellos, M. A.¹

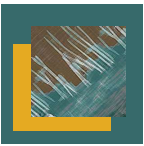
1. UFRGS, Instituto de Física, Porto Alegre, Brazil. faccini.lima@ufrgs.br

2. UFRGS, Instituto de Química, Porto Alegre, Brazil.

The Electron Beam induced Current (EBIC) mode of the scanning electron microscope is a powerful technique for monitoring of electrical properties of semiconductors such as the diffusion lengths minority carriers, defect location and depletion zone characterization. EBIC contrast depends on the current collection efficiency in the sample, thus allowing a direct visualization of electronically active features [1]. When the electron beam interacts with the sample, electron-hole pairs are generated, and in the presence of an electrical field, creates an induced current. With the appropriate detection system, the induced current is measured in synchrony with the position of the electron beam, allowing for spatial mapping of the current generation within the sample. Although EBIC imaging is commonly used for monitoring defects in solar cells [2,3], very few works have applied the technique to the electrical characterization of third-generation solar cells. The direct measurement of EBIC profiles of cross-sections of solar cells has proven to be a promising method for device characterization, allowing a charge carrier-oriented analysis and working mechanism evaluation of these devices [4]. In this work, we use an Omniprobe AutoProbe 200 nanoprobe attached to a Jeol JIB4500 Dual-Beam equipment to perform EBIC characterization of dye sensitized solar cells (DSSCs). The Dual Beam system is equipped with a conventional Scanning Electron Microscope (SEM) and a Focused Ion Beam (FIB) - which accelerates Ga ions for conformation and processing of nanostructures in samples. DSSCs are based on a photoelectrochemical process that differs from other solar cell devices in their basic construction and the physical processes [5]. The basic structure of the DSSCs used in this work is based on the work developed by Grätzel [5]: over a sheet of glass, a thin layer of fluorine-doped tin oxide FTO, which acts as the electron transporting material (ETM), is deposited. It is then covered by a semiconductor oxide layer, made by TiO₂ nanoparticles sensitized by either Ru or CdSe dye. Samples have been analysed with and without a spirobifluorene layer as the hole transporting material (HTM). Direct measurement of EBIC profiles of cross-sections of the solar cells were performed repeatedly over a period of 2 hours, yielding similar results for the cells with the Ru dye group, thus indicating the stability of the EBIC signal and the device over the relevant period of measurement. CdSe dye cells showed signs of electrical degradation after about 45 minutes. However, considering an average measurement of 5 minutes, these devices may also be considered stable. Furthermore, for all of the samples, a sharp decrease in the EBIC signal is observed in the FTO-TiO₂ interface, possibly due to poor adhesion of the TiO₂ nanoparticles on the Glass-FTO substrate. Different nanoparticle deposition methods were tested, with significant improvement of adhesion as shown by the EBIC signal.

REFERENCES

- [1] LAUSCH, D. W., M. et al. *Journal of Applied Physics* (211). 109.
- [2] MENG, L. S., A.G. et al. *Solar Energy Materials & Solar Cells* (2015). 133: 143-147.
- [3] SEKIGUCHI, T. et al. *Materials Science and Engineering* (1996). B42: 235-239
- [4] EDRI E. et al. *Nat. Comun.*(2014) 5:3461
- [5] BARBÉ, J.C., et al. *Journal of the American Ceramic Society* (1997). 80:3157-3171
- [6] This research was supported by CNPq (Brazil).



DOI: [INSERIR ENDEREÇO DO DOI AQUI.](#)

Caderno de Resumos do 26º Congresso Brasileiro de Macroscopia da SBMM – ISSN: [INSERIR AQUI.](#)

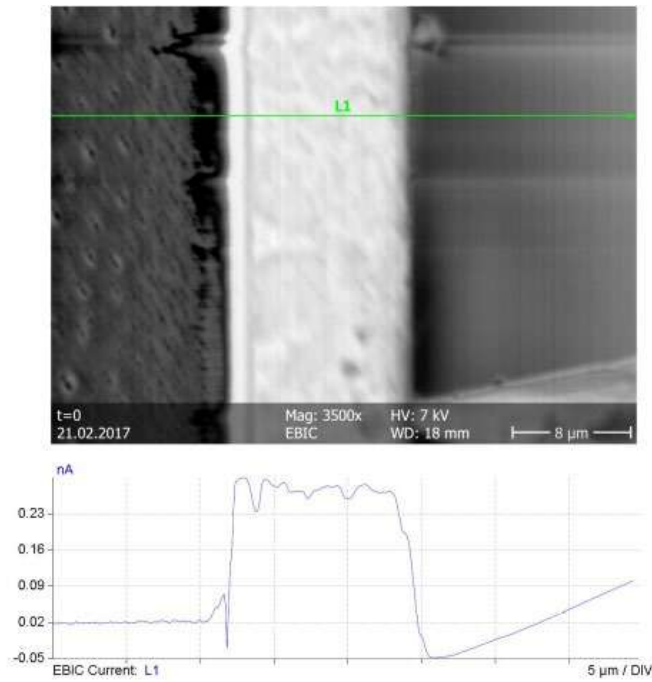


Image 1: EBIC image and EBIC profiles of cross-sections of Ru dye sensitized solar cell.

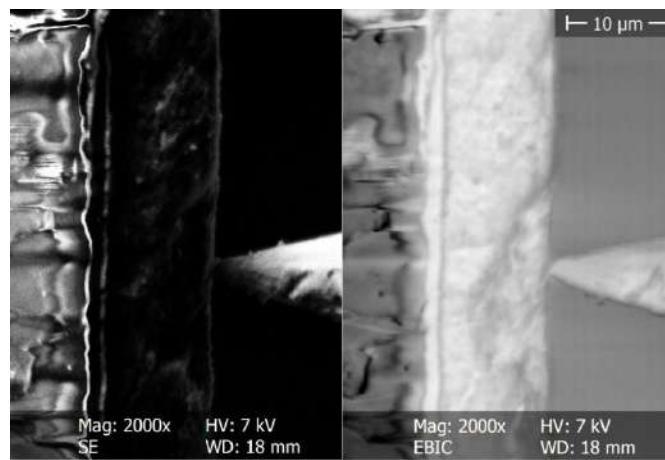


Image 2: SE image (left) and EBIC image of CdSe dye sensitized solar cell.



3DX-Ray Microscopy Analysis of Nanocomposite Bamboo with Different Silver Nanofillers

O. Pandoli^{1*}, R.S. Martins¹, S. Paciornik², M.H.P. Maurício², B.A. Barbosa¹,
H. Valiente³, S. Letichevsky², S.M. L. Koller¹ and K. Ghavami³

1. Chemistry Department, PUC-Rio, Rio de Janeiro - RJ, Brazil.

2. Chemical and Materials Eng. Department, PUC-Rio, Rio de Janeiro - RJ, Brazil.

3. Civil Engineering Department, PUC-Rio, Rio de Janeiro - RJ, Brazil.

*Email: omarpandoli@puc-rio.br

A Nanocomposite is defined as a multiphase material in which a nano object, with at least a dimension in the nanometric range, is incorporated in a polymeric matrix [1]. Silver nanoparticles are a promising nanofiller (Ag-NFs) for reinforcement and anti-bacterial effect in polymers and composites [2]. In this investigation bamboo samples, *Dendrocalamus Giganteus*, were impregnated with colloidal solutions of Ag-NFs with the goal of improving the resistance to fungi attack. X-ray Microtomography (microCT) and DRX were performed to identify and quantify the dispersion of the micro- and nanoclusters in the biological matrix. Ag-NFs stabilized with negative (sodium citrate) and positive (chitosan) charged organic ligands were synthesized with a microfluidic system in continuous flow. The metal nanostructured materials filled the internal microenvironment of bamboo creating a hybrid metal-biocomposite driven by the electric charge and size-diameter of Ag-NFs. Bamboo is a composite material composed of cellulose (55%), lignin (25%) and hemicellulose (20%). Amorphous and crystalline cellulose fibers mixed with lignin and hemicellulose, anatomically named sclerenchyma, are distributed anisotropically in a radial direction from the inner to outer section of the culm. This composite structure is responsible for the intrinsic mechanical strength and supports the vascular bundles system. The vascular bundles are straight microchannels with varied internal diameter from 50 to 200 μm , while the parenchymatic living cells are square and rectangular-shaped with variable volume of 1000-2000 μm^3 . The bamboo specimens (5x12x18mm) were submitted to 20 impregnation cycles through a vacuum system. After each cycle, a fresh Ag-NFs solution was used. The microCT revealed a gradient deposition of citrate-capped Ag-NFs in the parenchyma tissue (0,26% of the sample) with higher concentration at the outer bamboo region (Figure 1A and 2). Chitosan-capped AgNFs were deposited both in the parenchyma and in vessel bundles (1,18% of the sample) (Figure 1B and 3). The self-sorting filling of hybrid metal biocomposite bamboo was driven by the electric charge and particle dimension of organic ligands-capped Ag-NFs. DRX pattern of bamboo with AgNFs presented characteristic peaks at 16° and 22° assigned for the crystalline region of cellulose, and 37°, corresponding to (111) planes of nanostructured silver crystal. Both engineered biocomposite bamboo and untreated specimens were exposed to air and humidity (60-80%). After 14 months the treated samples were free of fungal colonies, while colonization by the fungal hyphae was present on untreated bamboo specimens.

REFERENCES

[1] N. Saba, P.M. Tahir, M. Jawaid, *Polymers* 6, (2014) 2247–2273.

[2] O. Pandoli S. Paciornik, K. Ghavami et al. Colloidal silver nanoparticles: an effective nanofiller material to prevent fungal proliferation in bamboo. *RSC Advances*, 6, (2016), 98325-98333.

[3] This research was supported by FINEP, CNPq and FAPERJ (Brazil).

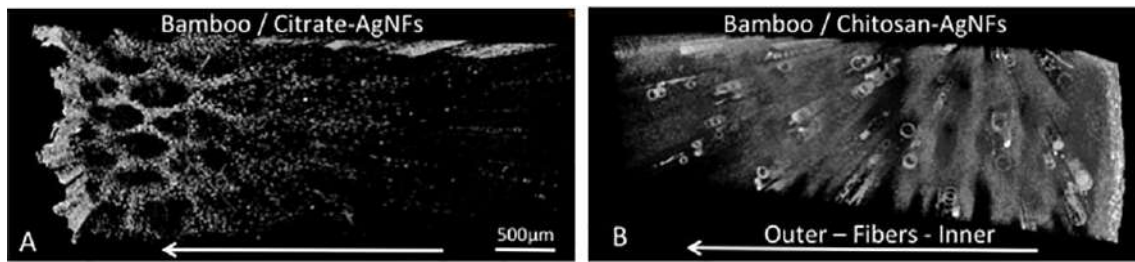
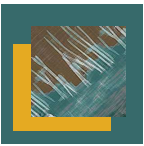


Figure 1. 3D μ CT images of bamboo after 20 impregnation cycles with citrate-capped AgNFs (A) and chitosan-capped Ag-NFs (B). The grey color represents silver aggregates with the bamboo matrix removed for easier interpretation of images.

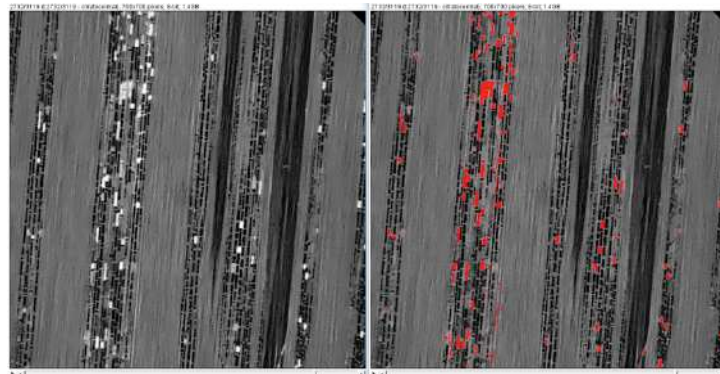


Figure 2. 2D μ CT images of citrate-capped Ag-NFs depositions in the parenchyma tissue of bamboo.

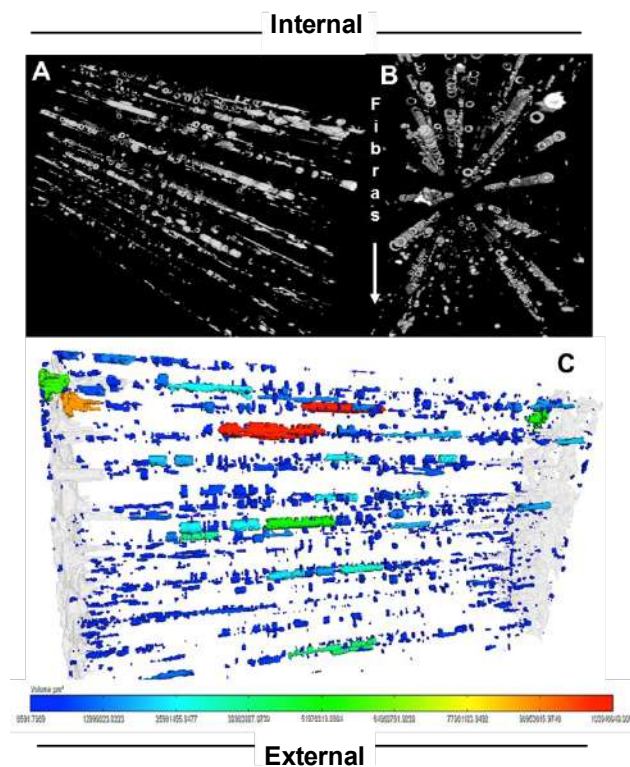
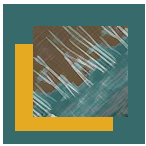


Figure 3. 3D μ CT images of chitosan-capped Ag-NFs aggregates in the vessel bundles.



Porosity Characterization of Iron Ore Pellets by X-Ray Microtomography

Augusto, K.S.^{1*} and Paciornik, S.¹

1. DEQM/PUC-Rio, Rua Marquês de São Vicente, 225, Gávea, Rio de Janeiro, Brazil

*Email: karenaugusto@yahoo.com.br

Iron ore pellets are the main raw materials for steelmaking processes. The process of pellet production, called pelletizing, consists in agglomerating iron ore fines for the formation of the green pellet and in the hardening of this pellet provided by a heat treatment. The final pelletizing product must be a porous material to allow heat transfer in the reduction furnaces, but it must have adequate mechanical strength to proceed in the process. As the reducibility and the physical resistance of the material are related to its porosity, microstructural characterization is an important step in pellet quality control. Traditionally, pellets porosity characterization is performed by optical microscopy (OM) and mercury intrusion porosimetry (MIP). In OM, the common phases are easily discriminated by their reflectance, allowing to obtain, by image analysis, the fraction, the distribution and the morphology of the pores. However, this technique is limited to the 2D space, providing information only for sections or surfaces, and it requires sample preparation steps (mounting, polishing etc.), which can compromise the quality of the material, are time consuming and prevent future analysis with other techniques. In the case of MIP, it is possible to evaluate open pores only, in other words, pores that are connected to the surface. Closed pores, which have greater impact on the physical strength of the material, cannot be evaluated by this characterization method. In addition, it is a destructive technique, as OM, and it uses mercury – a volatile and toxic metal. MicroCT is a promising 3D technique, which provides both external and internal information of the solid material structure, allowing for true 3D measurements. In addition, it requires very little or no sample preparation. The present work proposes a methodology for the characterization of porosity of iron ore pellets by microCT, which includes preparation and digital image processing steps, requiring the use of various software (FIJI, CTAn and ORS Visual). In order to validate the results, the samples were also analyzed by both the MIP and OM techniques. The MicroCT porosity values were much lower than the MIP and OM values, due to the lower spatial resolution. However, the microCT technique proved to be feasible for the characterization of porosity in iron ore pellets, allowing the study of open and closed porosity separately, and the description of the pores spatial distribution.

REFERENCES

- [1] E.N. Landis, D.T. Keane. X-ray microtomography. 2010.
- [2] I.U. Bhuiyan et al. Consideration of X-ray microtomography to quantitatively determine the size distribution of bubble cavities in iron ore pellets. Powder Technology. 2013.
- [3] This research was supported by CNPq, CAPES, FAPERJ and Alei Domingues (Vale).

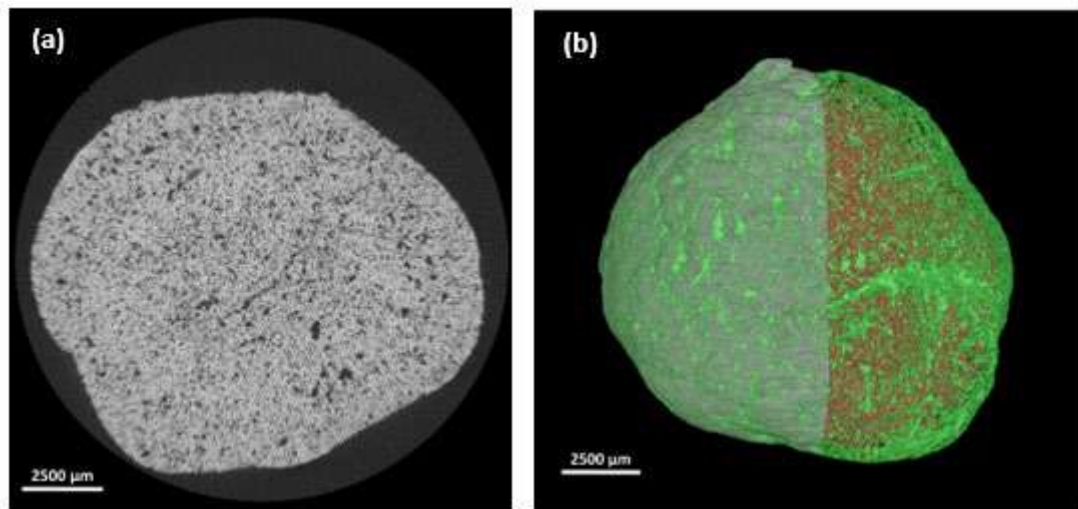
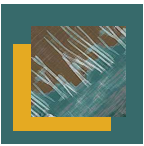


Figure 1 – (a) 2D MicroCT slice; (b) 3D Volume with the spacial distribution of open pores (green) and closed pores (red)

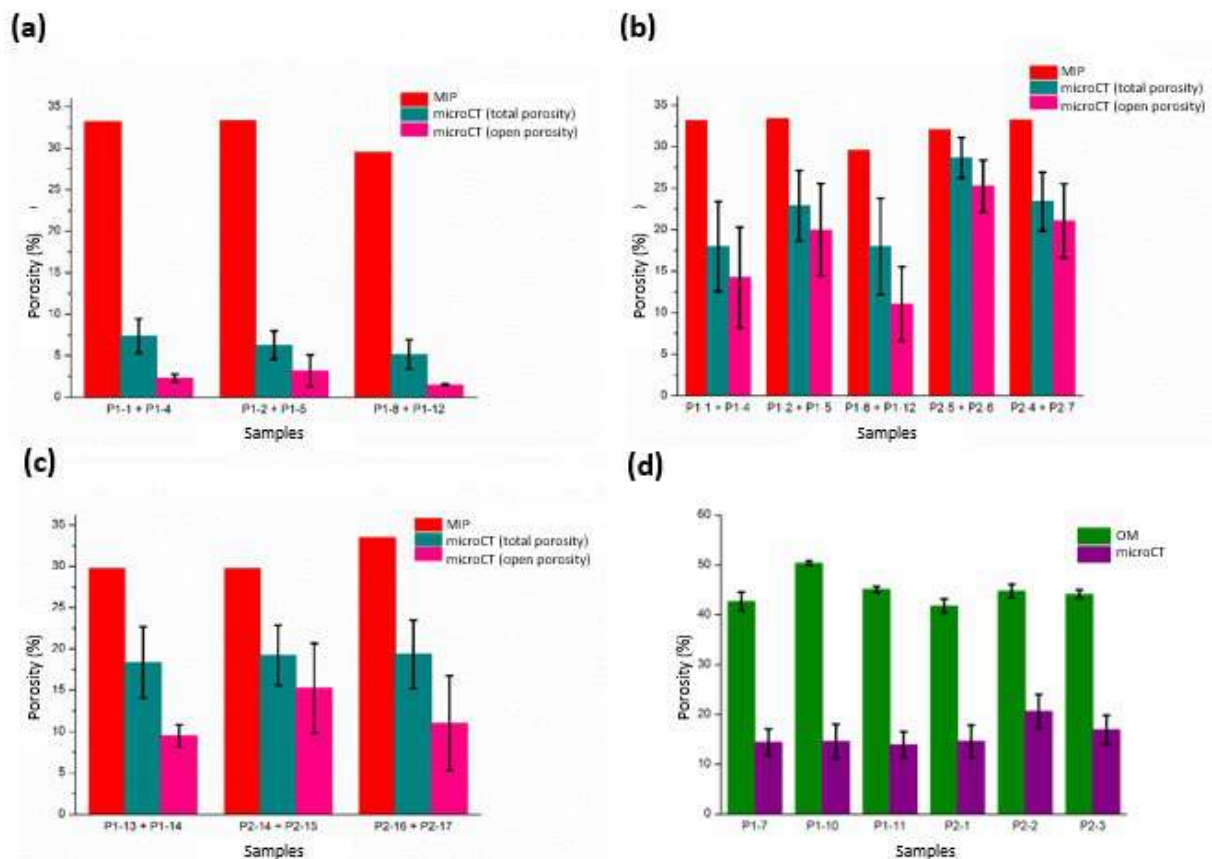


Figure 2 – Comparison of porosity: (a) MIP x MicroCT (0.4X lens, 8 µm resolution); (b) MIP x MicroCT (4X lens, 4 µm resolution); (c) MIP x MicroCT (0.4X lens, 4 µm resolution); (d) OM x MicroCT (0.4X lens, 8 µm resolution).



Study of Iron Sulfide Phases Formation with Russian Doll Sulfurization Apparatus

M.F.O. Silva^{*1}, L.P. Souza¹, S. de Oliveira¹, A.S. Ferlauto¹, W.N. Rodrigues^{1,2}

1. Universidade Federal de Minas Gerais, Departamento de Física, ICEX, Belo Horizonte, Brazil

2. Universidade Federal de Minas Gerais, Centro de Microscopia, Belo Horizonte, Brazil

*Email: mangos@ufmg.br

Metal sulfides have often played an important role in materials science, due to their vast range of applications [1]. Within this class of materials, the iron sulfide system is of particular interest due to the potential application of the pyrite (cubic FeS₂) phase in abundant, environmental friendly solar cells [2]. Even though several authors have reported synthesis of pure pyrite materials, to reduce or eliminate the secondary iron sulfide phases remains a milestone in order to build devices with reasonable efficiencies [3,4]. This work focuses on the use of a homemade apparatus, we called Russian Doll, to sulfurize spin-coated iron oxide thin films, and study the phase composition according to the synthesis parameters. We analyzed the resulting phase composition with X-ray diffraction (XRD) patterns and Scanning Electron Microscopy (SEM). Firstly, we varied the sulfurization time and temperature. We observed that the sulfurization process favored the iron disulfide phase, as intended, and it was fully completed even for the shortest time – 30 minutes. However, short sulfurization times resulted in a mix phase of the cubic (pyrite) and orthorhombic (marcasite) FeS₂ polymorphs. Moreover, as we increased the sulfurization time, SEM images unveiled a progressive decrease in the marcasite phase. Finally, higher sulfurization temperatures boosted the marcasite to pyrite transformation. Both findings are in accordance with the literature [5,6]. For temperatures higher than 550 °C, we observed the presence of pyrrhotite, which must have been occasioned by partial pyrite decomposition. The partial decomposition assumption was based in the evolution of the microstructure of the films, and the fact that the pyrite to pyrrhotite reaction follows the unreacted core model [7]. We also observed partial decomposition and complete decomposition by increasing the sulfurization time to 8 and 16 hours, respectively. Such results stem from low S₂ vapor pressure inside the Russian Doll apparatus, due to a continuous outward sulfur flow. Thus, we established a limiting enclosing time for the S₂ vapor inside our apparatus. We also varied the oxidation temperature of the precursor oxide film, and discovered that the particle size of the precursor films influenced both the particle size of the sulfurized films, as well as the pyrite to pyrrhotite decomposition reaction. The Figure 1 summarizes the above-mentioned processing conditions and findings.

ACKNOWLEDGMENTS

This work was supported by CNPq and Capes. The authors would like to thank the LabCri at the Physics Department and Microscopy Center of UFMG for the XRD measurements and SEM study, respectively.

REFERENCES

- [1] C.I. Pearce, R.A.D. Patrick, D.J. Vaughan, *Rev. Mineral Geoch*, 61 (2006) 127.
- [2] C.Wadia, A.P. Allivisatos, D.M. Kammen, *Environ. Sci. Technol.* 43 (2009) 2072.
- [3] X. Zhang, M. Manno, A. Baruth, M. Johnson, E.S. Aydil, C. Leighton, *ACS Nano* 7 (2013) 2781.
- [4] M. Limpinsel, N. Farhi, N. Berry, J. Lindemuth, C.L. Perkins, Q. Linf, M. Law, *Energy Environ. Sci.* 7 (2014) 1974
- [5] M.E. Fleet, *Can. Mineral.* 10 (1970) 225
- [6] A.R. Lennie, D.J. Vaughan, *Americ. Miner.* 77 (1992) 1166
- [7] G. Hu, K. Dam-Johansen, S. Wedel, J.P. Hansen, *Progr. En. Combust.*, 32 (2006) 295

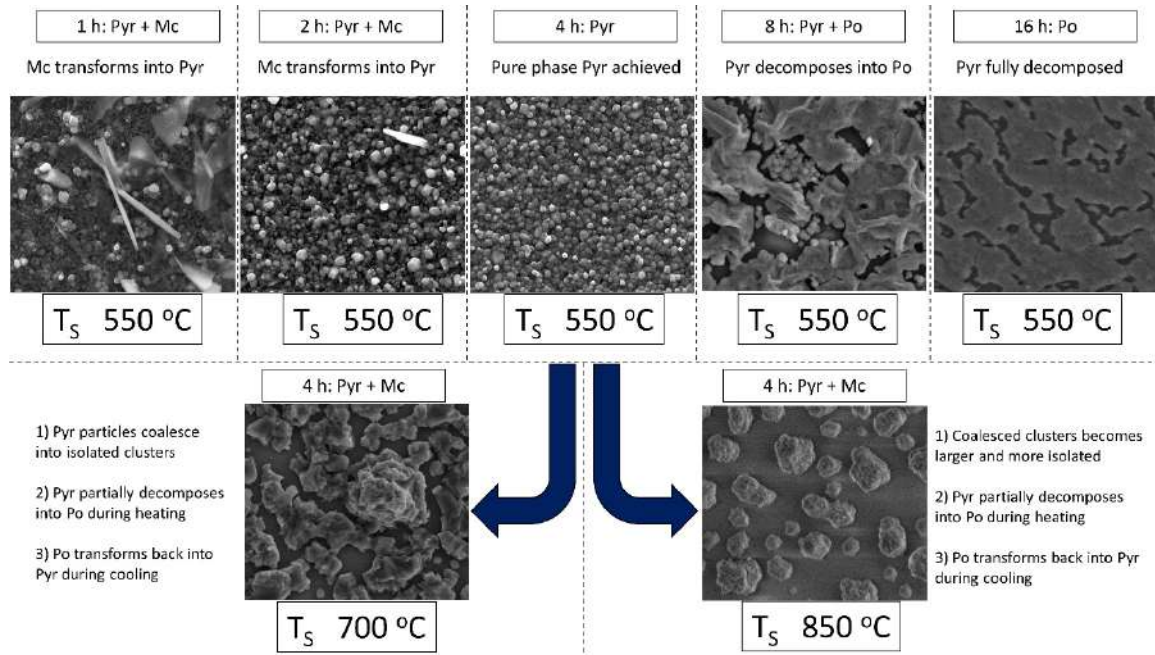
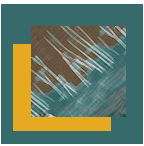
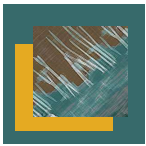


Figure 1: The different conditions of the experiments and findings are schematically presented. The codes used are: Pyr = pyrite, Mc = marcasite, and Po = pyrrhotite.



Niobium Addition on Ti-Nb Alloys anodized: Effect on the Microstructure and Nanotubes Growth

A. R. Luz^{1*}, P. B. Kuroda², C. M. Lepienski¹, C. R. Grandini², N. K. Kuromoto^{1,3}

1. Universidade Federal do Paraná, Programa de Pós-Graduação em Engenharia e Ciência dos Materiais – PIPE, Curitiba, Brazil

2. Universidade Estadual Paulista, Laboratório de Anelasticidade e Biomateriais, Departamento de Física, Unesp, Bauru, Brazil

3. Universidade Federal do Paraná, Departamento de Física, Curitiba, Brazil

*Email: arossettoluz@gmail.com

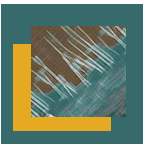
Ti-6Al-4V alloy are widely used for biomedical applications due to suitable mechanical properties, resistance corrosion and biocompatibility. However, researchers have been indicating toxic effects due to the release of Al and V ions in the body. In this way, β -type Ti alloys have been studying, which have non-toxic elements, such as Nb, Mo, Zr, Sn or Ta. These alloys are biocompatible, corrosion resistance and have better mechanical properties than conventional materials [1]. Nanotube arrays have been extensively studied to improve the surfaces of Ti and its alloys for biomedical applications [2]. However, a few works reported the effects of the microstructure of alloys on the growth of nanotubes. The aim of this work was to obtain nanotube arrays by anodic oxidation on Ti-25%Nb and Ti-35%Nb (wt.%) alloys, and analyze the effect of the substrate on the growth of nanotubes. For the microstructural analysis, the samples were prepared following standard metallographic techniques used for Ti and its alloys and etched with a Kroll's reagent. The microstructures were examined by optical microscopy. The anodic oxidation was carried out with a conventional two-electrode configuration with platinum as a counter electrode and the Ti-xNb alloy as the working electrode. The nanotubes were obtained using 0.5 M Na₂SO₄ + 0.1 %wt HF electrolyte. The applied potential was 20V under potentiostatic mode, at room temperature. The anodization time was 1 h 40 min for Ti-25Nb and 2 h 40 min for Ti-35Nb. The morphology and cross-sectional view of nanotube arrays were analyzed by Scanning Electron Microscope. The cross-sectional thickness measurements were carried out directly on the mechanically cracked sample. Fig. 1 shows the microstructures of alloys. The Ti-25Nb alloy (Fig. 1a) had needles of α -phase (light regions) in the basket-weave array, which is correspondent to Widmanstätten structures. The Ti-35Nb alloy (Fig. 1b) showed typical microstructure of the β -phase, with α -phase precipitates. These microstructures are characteristic by using a slow cooling rate from β -phase to ($\alpha + \beta$) phase [3]. Figure 2 shows the morphology and cross-sectional view of nanostructure film grown on alloys. Ti-25Nb alloy (Fig. 2a) showed a non-uniform morphology and random thickness, which were influenced by microstructure of alloy. For binary alloys, during the anodizing process occurs a selective dissolution of less stable elements and different reaction rates on different phases of an alloy [2]. Self-organized nanotubes grew on the Ti-35Nb alloy (Fig. 2b) with tube shape, which had approximately 1.1 μ m of length. The microstructure did not affect the growth of nanotubes. When the amount of Nb is 36% wt. the β -phase is completely stabilized [3]. Therefore, the β -phase in the Ti-35Nb was almost stabilized completely. The results showed that the Ti-25Nb and Ti-35Nb were composed by ($\alpha + \beta$). Thus, the amount of element beta stabilizer was not enough to stabilize completely the β -phase in the Ti-xNb alloys.

ACKNOWLEDGEMENTS

We would like to thank the Center of Electron Microscopy UFPR, the CAPES and CNPQ for the financial support.

REFERENCES

[1] Q. Chen, G., A. Thouas, Mat. Sci. Eng. R 87 (2015) 1–57.



[2] D. Khudhair, A. Bhatti et al., Mat. Sci. Eng. C 59 (2016) 1125–1142.

[3] ASM International, Titanium - Physical Metallurgy, Processing, and Applications, First, Ohio, 2015.

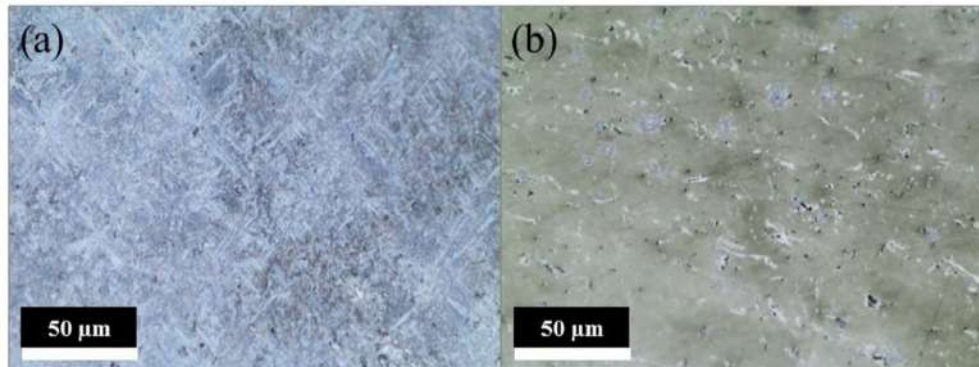


Figure 1 - Optical micrographs of homogenized alloys: (a) Ti-25Nb and (b) Ti-35Nb.

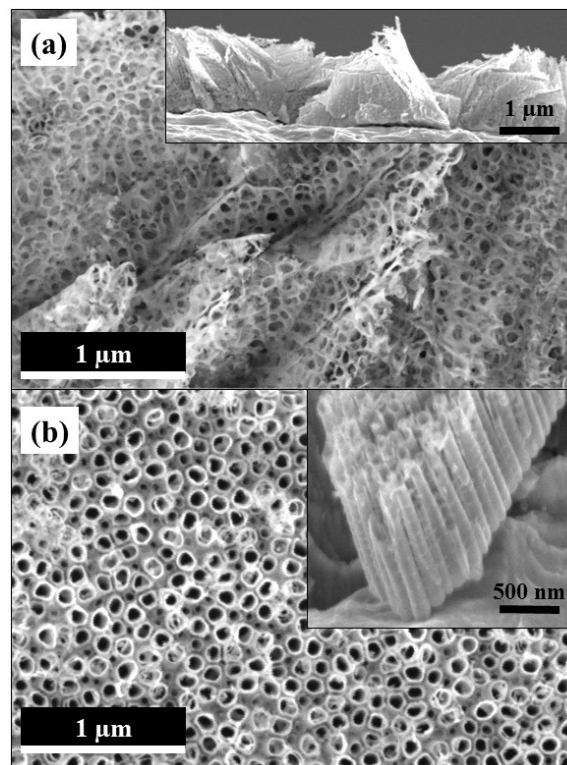
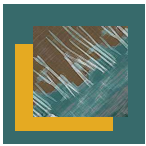


Figure 2 - Surfaces morphology of Ti-xNb oxidized. The inserts show cross-sections views indicating the nanotubes thickness: (a) Ti-25Nb and (b) Ti-35Nb.



Casting, Rolling and Friction Stir Welding in Magnesium alloys with Mischmetal Addition

*E.P. Silva^{1,a}, U. Alfaro^{3,a}, V.P. Ferrinho^{3,a}, G.C. Requena^{3,b}, H.C. Pinto^{1,b}

1. Engineering School of São Carlos, University of São Paulo, Department of Materials Engineering, São Carlos-SP, Brazil.

2. Brazilian Nanotechnology National Laboratory, Campinas-SP, Brazil.

3. German Aerospace Center (DLR) Institute of Materials Research Linder Höhe | 51147 Cologne-Germany.

*Email: erenilton.silva@sc.usp.br

The growing scarcity of renewable energy resources, as well as the continued rise in costs has required in recent decades a dramatic reduction in energy used for transportation freight and passenger, which is increasing daily all over the world. An alternative is to weight reduction with the use of light alloys, this concept the use of magnesium alloys is justified by their low density, about 1/3 lower than that of aluminum[1-5]. This work shows the studies the addition of 1.5% wt. of mischmetal (Mm) in the ZK60 alloy and effects of the casting process with mechanical mixing in the semi-solid state. Were produced the alloys: ZK60, ZK60-1.5RE with conventional casting and ZK60-1.5RE Tixo with mechanical mixing in the semi-solid state, all were hot-rolled in a symmetrical laminator and welded with friction stir welding (FSW) process. The methods of casting and cooling gave resulted in materials free of defects and chemical homogeneity, and the mechanical mixing provides homogeneous microstructure with globular grains(Fig.1). As for mechanical strength was higher for ZK60 alloy, due smaller amount and intermittent network of the intermetallic. The alloys with Mm addition had better thermal stability during welding and showed better surface quality, being possible to do a welding with rotation of 1200 rpm and advancing speed of 400 mm/min while the ZK60 alloy only was possible the welding with advancing speed of 200 mm/min. The analyzes of residual stresses had similar values and profiles and follow the flow of material as well as the texture of the weld beads. The micro hardness maps in the cross section of the weld bead showed a higher hardness in the mixing zones, and higher and more homogeneous values for ZK60 alloy, and can thus affirm that the intermetallic MgZn type has higher hardness than the MgZnRE type.

REFERENCES:

- [1] Watarai, H., Trend of research and development for magnesium alloys – Reducing weight of structural materials in motor vehicles -, (2006) Science & Technology Trends, 18, pp. 84-97.
- [2] Zhou, H.T., Zhang, Z.D., Liu, C.M., Wang, Q.W., Effect of Nd and Y on the microstructure and mechanical properties of ZK60 alloy, (2007) Materials Science and Engineering A, 445-446, p. 1-6.
- [3] E. P. Silva, L. F. Batista, B. Callegari, I. Feierabend, R. H. Buzolin, R. S. Coelho, F. Warchomicka, G. C. Requena, H. Pinto, Casting in the Semi-Solid State of ZK60 Magnesium Alloy Modified with Rare Earth Addition, (2014) Adv. Mater. Res., 922, 694–699.
- [4] Ma, Y., Zuo, R., Tang, A., Wang, W., Zhang, J., Pan, F., Effect of yttrium on morphologies of precipitation phases along grain boundaries of as-cast ZK60 magnesium alloy, (2005) Materials Science Forum, 488-489, pp. 245-248.
- [5] Wu, A., Xia, C., Wang, J., Distribution, evolution and the effects of rare earths Ce and Y on the mechanical properties of ZK60 alloys, (2006) Journal of University of Science and Technology Beijing: Mineral Metallurgy Materials (Eng Ed), 13 (5), pp. 424-428.

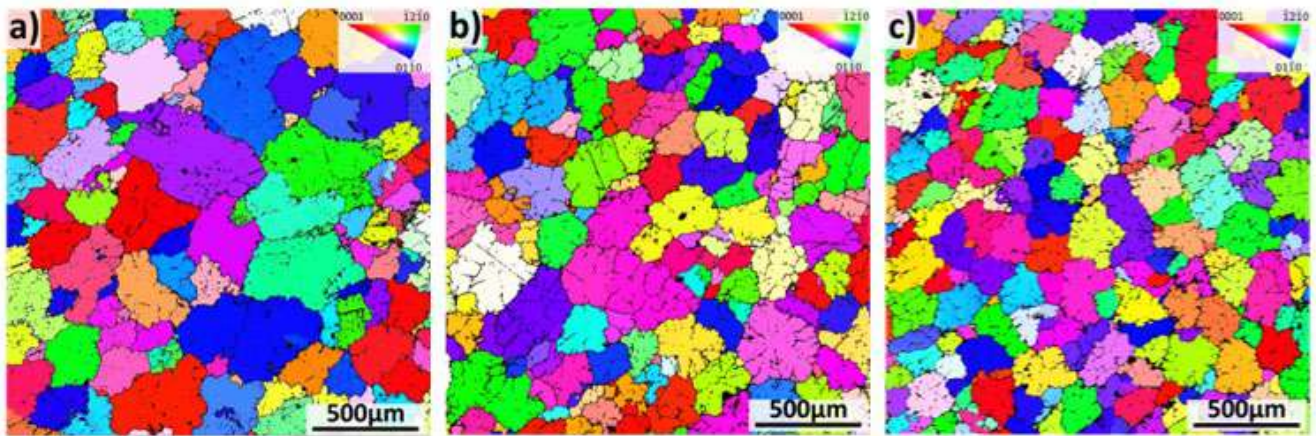
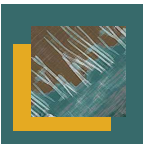
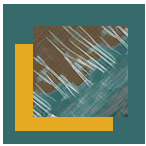


Figure 4- IPFs Mapping by Scanning Electron Microscopy (SEM) in Backscattered Electron Diffraction (EBSD) mode in alloys as cast. A) ZK60, b) ZK60-1.5RE and c) ZK60-1.5RE Tixo.



Influence of Processing Routes on δ Phase Precipitation, Grain Boundary Character Distribution and Grain Size of Superalloy 718.

Melânea Almeida Ramalho Medeiros^{1*}, Alessandra Vieira Guimarães¹, André Luiz Pinto²,
Leonardo Sales Araújo¹

1. Universidade Federal do Rio de Janeiro, Rio de Janeiro, RJ, Brazil.

2. Centro Brasileiro de Pesquisas Físicas, Rio de Janeiro, RJ, Brazil.

*Email: melanea_al@yahoo.com.br

The grain boundary character distribution (GBCD) has been largely studied in low stacking-fault energy (SFE) alloys, due to the possibility of multiplication of coherent and incoherent annealing twins via combination of cold deformation and annealing heat treatments, thereby inducing the formation of special boundaries $\Sigma 3^n$ ($\Sigma 3$, $\Sigma 9$ and $\Sigma 27$), as well as the break of the connectivity of high-energy, random boundaries [1]. For the evolution of special boundaries during processing, grain boundary mobility is needed, which can result in grain growth. This poses a problem for applications where a refined microstructure is a requisite. The alloy 718 presents high strength, that comes from γ'' (Ni_3Nb -bct) and γ' ($\text{Ni}_3(\text{Al,Ti})$ -fcc) phases. The δ phase (Ni_3Nb -orthorhombic) can be induced for grain refining in temperatures below 1010°C , aiding the $(\text{Nb,Ti})\text{C}$ carbides to pin grain boundaries. Therefore, the objective of this work is to investigate the effect of the δ phase precipitation during iterative processing for an improved GBCD and its influence on grain size. Four processing routes were used, combining cold rolling with sub- \square -solution annealing. Table 1 shows the fraction of special boundaries and the grain size achieved for each route. Figure 2 shows the SEM backscattered image of the samples after deep etching, where $(\text{Nb,Ti})\text{C}$ and \square phases are evidenced. The amount of \square phase was markedly different for the different conditions, being more evident in sample AS04, which corresponds to the condition with the smaller grain size. This route is based on about 60% cold deformation followed by sub- \square -solution annealing. This phase was present both inside the grains as well as along the grain boundaries. For the other processing conditions (BS04, CS04 and DS04), the \square phase was still present, but less evident, corroborated by the bigger grain size values measured. Electron backscatter diffraction (EBSD) analysis was performed to observe the mesotexture of all samples, as presented (Table 1). Despite the smaller grain size of sample AS04, only 45% of the boundaries were $\Sigma 3^n$, slightly different from the initial condition 47%. Route B showed also a fine grain size, but the proportion of $\Sigma 3^n$ did not improved significantly. Compared to A and B routes, C and D showed bigger grain sizes, but with a much higher fraction of special boundaries. Through routes CS04 and DS04, despite the smaller amount of \square , it was possible to achieve a relatively low grain size without impairing twinning and grain boundary migration mechanisms, and consequently increasing the formation of boundaries $\Sigma 3$, $\Sigma 9$ and $\Sigma 27$ by 64.9% and 61.3%, respectively. After aging, no significant variation from the results obtained previously on solution annealed samples was observed. Figure 3 compare the results of the present work with the of other authors.

REFERENCES

- [1] V. Randle and G. Owen, *Acta Mater.*, 54 (2006) 1777–1783.
- [2] Q. Li, B. Guyot, N. Richards, *Mater. Sci. Eng. A*, 458 (2007) 58.
- [3] C. Boehlert, D. Dickmann, and N. Eisinger, *Metall. Mater. Trans. A*, 37A (2006) 27.
- [4] L.S. Araujo, D.S. Santos, S. Godet, J. Dille, A.L. Pinto, L.H. Almeida, *Journal of Mat. Engng. and Performance*, 23(11) (2014) 4130.
- [5] This research was supported by Capes and Coppetec (Brazil).

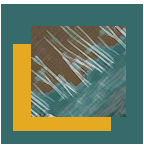


Table 1- Evolution of the fraction boundaries and grain size after annealing and aging.

Routes	$\Sigma 3 + \Sigma 9 + \Sigma 27$	Grain Size (μm)	Routes	$\Sigma 3 + \Sigma 9 + \Sigma 27$	Grain Size (μm)
Annealing Samples			Aging Samples		
AS04	43,7 \pm 2,3	4,46 \pm 0,14	AE04	45,27 \pm 0,55	4,74 \pm 0,06
BS04	45,28 \pm 5,3	16,9 \pm 2,04	BE04	49,42 \pm 1,3	17,86 \pm 0,39
CS04	64,9 \pm 3,45	26,84 \pm 1,43	CE04	63,14 \pm 2,98	19,89 \pm 4,89
DS04	61,32 \pm 1,89	14,85 \pm 1,29	DE04	59,63 \pm 2,98	16,87 \pm 2,27

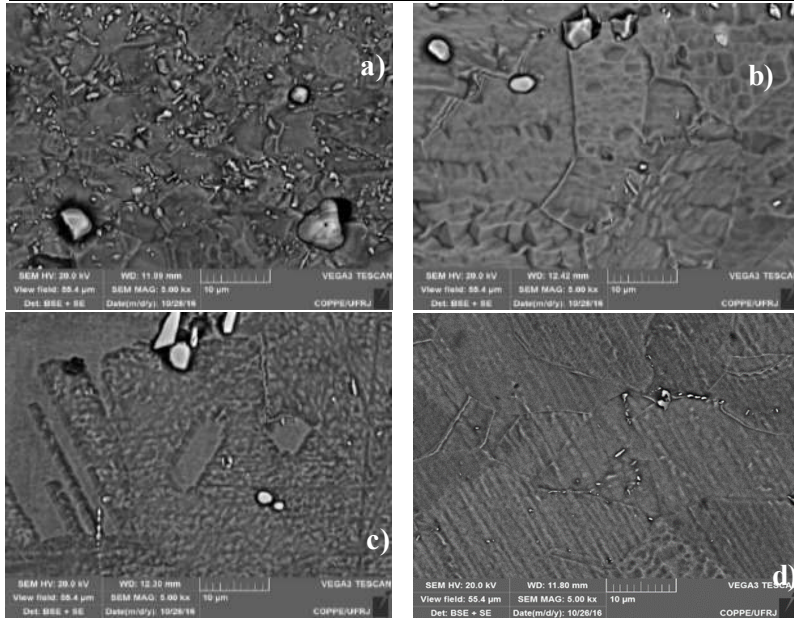


Figure 1. Microstructure observed by SEM in secondary electron of the solution annealing samples etched in glyceric reagent (a) AS04 (b)BS04 (c)CS04 e (d)DS04.

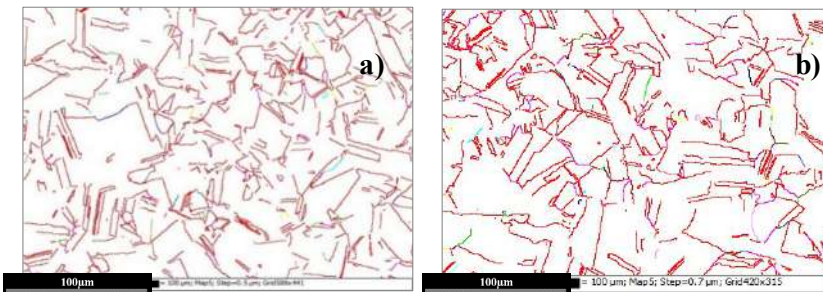


Figure 2-EBSD results for CE04 and DE04 sample after cold rolling, annealing, and aging heat treatment. (a) and (b) CSL boundaries map. Red lines: $\Sigma 3$; blue lines: $\Sigma 9$, and green lines $\Sigma 27$.

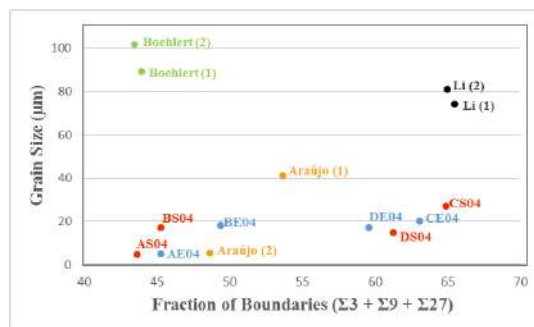
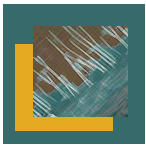


Figure 3- Comparison between grain size versus fraction of boundaries, obtained from the present work and literature. (Li(1) and Li(2) [2]; Boehlert(1) and Boehlert(2) [3] Araujo(1) and Araujo(2) [4]).



Phase Characterization of AlFeCrNiCoB_x High Entropy Alloys with Minor Boron Content

Guilherme Zepon^{1*}, Diego D. Coimbra², Vitor Ferrari¹, Witor Wolf², Walter J. Botta¹.

1. Department of Materials Engineering, Federal University of São Carlos, São Carlos-SP, Brazil.

2. Graduate Program of Materials Science and Engineering, Federal University of São Carlos, São Carlos-SP, Brazil.

*Email: zepon@ufscar.br

Traditional metallic materials are generally constituted up to two principal elements with minor alloying addition of various metallic and non-metallic elements. Recently the so called high entropy alloys (HEA) were discovered. As a general rule, these alloys are constituted by five or more elements with atomic percentage varying from 5 to 35%. Despite the great number of different “principal-elements”, in many cases, formation of a single cubic solid solution is observed. These solid solutions are formed by many different atoms within the structure and it results in great distortion of the lattice. As a consequence, these alloys present excellent mechanical properties such as high hardness and high yield strength. In the present work, the effect of minor additions of boron on the microstructure of AlCoCrFeNi high entropy alloys was analyzed. Alloys of atomic composition AlCoCrFeNiB_x, with $x = 0.05$ and 0.1 were studied. Samples were fabricated by arc-furnace and submitted to a homogenizing heat treatment in order to study the equilibrium microstructure of the different alloy compositions. Microstructural characterization was performed by X ray diffraction (XRD) scanning and transmission electron microscopy (SEM and TEM). STEM-EDX mapping and TEM phase mapping using new ASTAR technique were also carried out. The XRD patterns shown in Figure 1 (a) shows that both alloys (AlCoCrFeNiB_{0.05} and AlCoCrFeNiB_{0.1}) in the as-cast condition presents BCC ($a = 0.2873$ nm) and FCC ($a = 0.3610$ nm) phases. Addition of boron in these alloys led to the formation of borides at the interdendritic spaces as result of an eutectic reaction. Such borides can be clearly seen in the SEM image (BSE) shown in Figure 1 (b). Figure 2 (a) shows the phase mapping results carried out by ASTAR of the AlCoCrFeNiB_{0.01} alloy. Four phases could be precisely mapped, the orthorhombic (Fddd) M₂B-type boride (green), the FCC (blue), the BCC (blue) and the B2 ordered phase (red). The orthorhombic M₂B-type boride is usually a Cr-rich phase, which can drastically change the proportion of BCC/FCC solid solutions. It has been reported that the B2 phase can precipitate from the BCC in Al-containing HEA [1]. The orientation map displayed in Figure 2 (b) shows that all the FCC island are in the same orientation, indicating that the BCC phase was probably formed by decomposition of the previous existing FCC grain. Figure 3 shows a STEM-EDX mapping of the region containing BCC and B2 phases of the AlCoCrFeNiB_{0.01}. Whereas the BCC phase is rich in Al and Ni, the B2 phase is rich in Fe and Cr, suggesting that the precipitation of the B2 is accompanied by a composition separation. The use of different advanced microscopy techniques was useful to better understand the phase formation of the new HEAs.

REFERENCES

[1] T. Yang, et. al., Mater. Sci. Eng. A 648, 15 (2015).

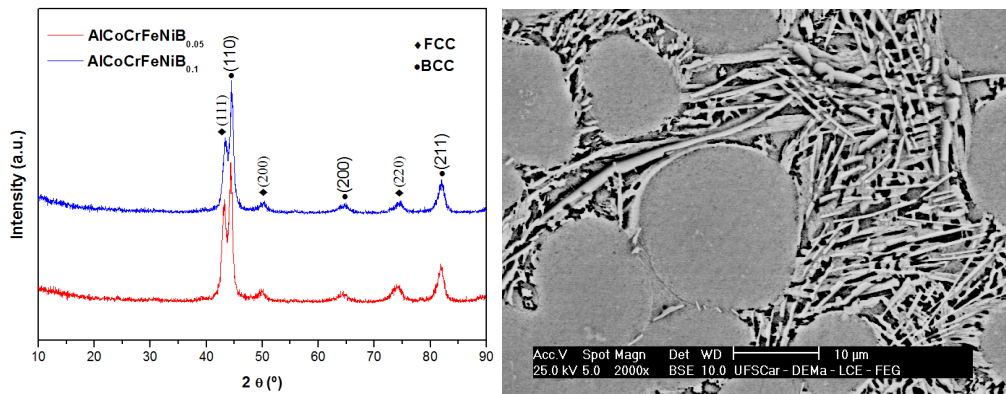
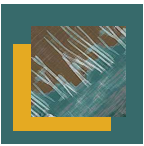


Figure 1: (a) XRD of AlCoCrFeNiB_{0.05} and AlCoCrFeNiB_{0.1} in the as-cast condition. (b) SEM image of AlCoCrFeNiB_{0.1} in the as-cast condition.

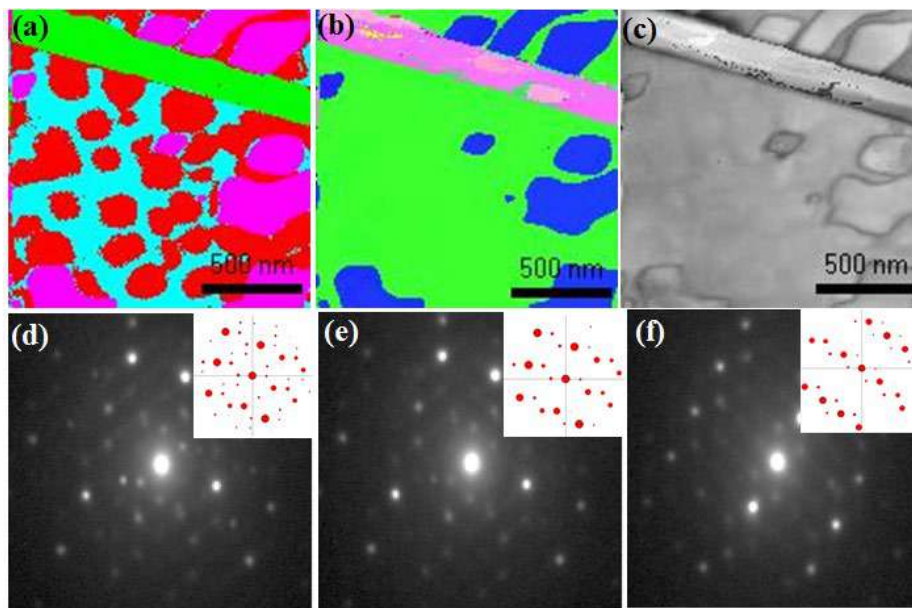


Figure 2: ASTAR phase mapping of AlCoCrFeNiB_{0.1}. (a) Phase map, M₂B-green, FCC-pink, BCC-blue, B2-red; (b) Orientation map; (c) Index map; (d) EDP of B2 (zone axis 638); (e) EDP of BCC (zone axis 638); (f) EDP of FCC (zone axis 838).

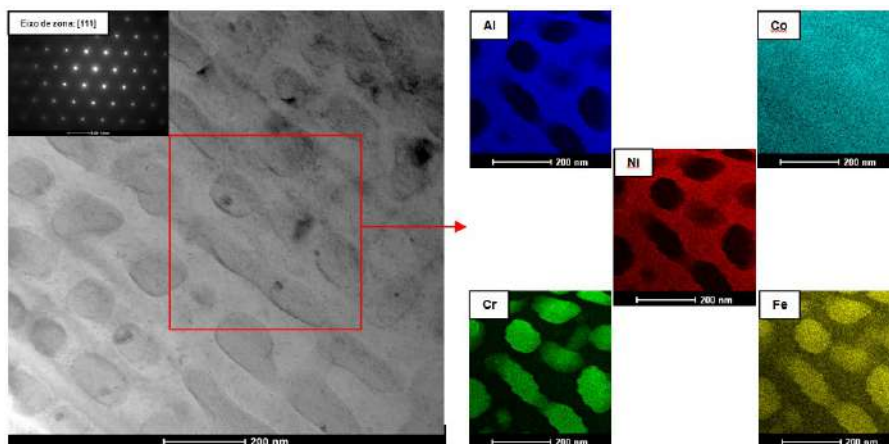
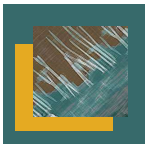


Figure 3: STEM-EDX mapping of the BCC/B2 region of the AlCoCrFeNiB_{0.1}.



Retained Austenite Volume Fraction in 52100 Steel Determined by Electron Backscatter Diffraction

Geronimo Perez¹, Bráulio Soares Archanjo¹, Alexei Kuznetsov¹, Carlos Alberto Achete¹

1. Divisão de Metrologia de Materiais, Instituto Nacional de Metrologia, Qualidade e Tecnologia (INMETRO), Duque de Caxias-RJ, 25250-020, Brazil;

The retained austenite is a well-known microstructural component of quenched steels that may cause adverse effects, positive or negative, in the properties and performance depending on the steel type. The correct determination of retained austenite fraction is one of the most sought metrological tasks in the metalworking industry manufacturers and consumers of carbon steel. In this work we determined retained austenite fractions and other secondary phases by combining electron backscatter diffraction (EBSD), dispersive X-ray spectroscopy (EDS), transmission electron microscopy (TEM) and x-ray diffraction (XRD) on samples of AISI 52100 steel with different volume fractions of retained austenite. AISI 52100 steel were quenched from different temperatures, 760 °C up to 920 °C in oil at 60 °C. EBSD combined to EDS revealed to be extremely sensitive to identify different phases (Figure 1). Transmission electron microscope (TEM) revealed details of the microstructure. Finally, systematic variation of the retained austenite fractions by XRD using three K_{α} characteristic X radiations (Cu, Cr, Mo) were discussed [1, 2]. The results obtained by EBSD match very well with the results of X-rays diffraction. Due to the high spatial resolution of the EDS, defined by thin sample (~ 100 nm), it is possible to obtain values closer to the actual amount of chromium in the grain retained austenite.

Keywords: Retained austenite; EBSD, TEM, SEM

REFERENCES

- [1] Danon, A., et al. Heterogeneous austenite grain growth in 9Cr martensitic steels: influence of the heating rate and the austenitization temperature. *Materials Science and Engineering A*, 2003, v. 348, p. 122-132.
- [2] Krauss, G. Martensite in steel: strength and structure, *Mater. Sci. Eng. A273–275*, p. 40-57, 1999.
- [3] This research was supported by CNPq (Brazil).

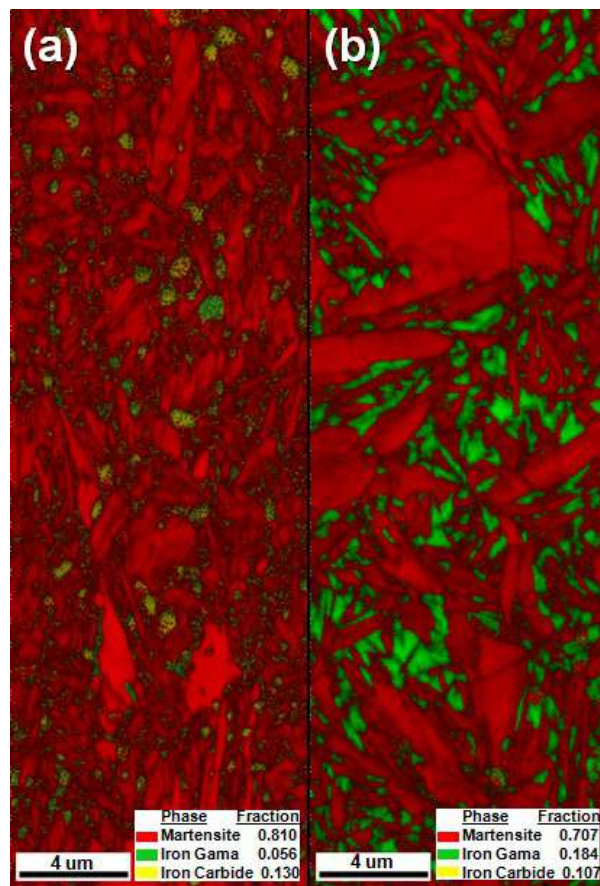
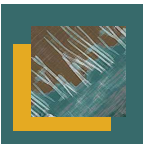


Figure 1 - Phase maps of AISI 52100 steel samples: (a) quenched from 760 °C, (b) quenched from 920 °C.

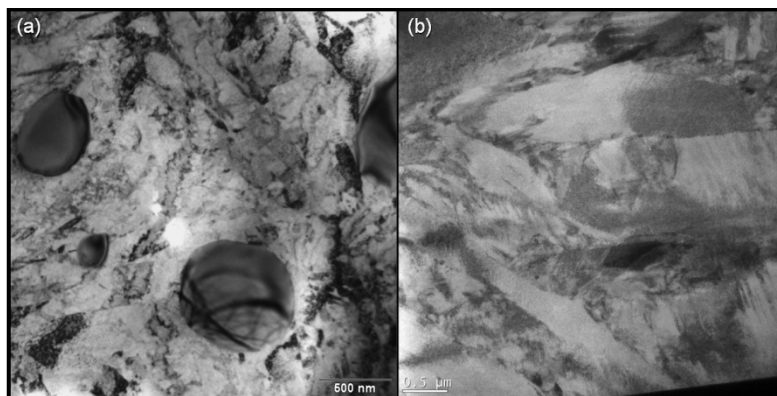


Figure 2 - TEM images of AISI 52100 steel samples: (a) quenched from 760 °C, (b) quenched from 920 °C.



DOI: [INSERIR ENDEREÇO DO DOI AQUI.](#)

Caderno de Resumos do 26º Congresso Brasileiro de Microscopia da SBMM – ISSN: [INSERIR AQUI.](#)

Optically Efficient Probes for Tip-Enhanced Raman Spectroscopy

Thiago L. Vasconcelos^{1*}, Bráulio S. Archanjo¹, Benjamin Fragneaud², Bruno S. Oliveira¹, Douglas S. Ribeiro³, Cassiano Rabelo⁴, Wagner N. Rodrigues³, Ado Jorio³, Carlos A. Achete¹, Luiz G. Cançado³.

1. Instituto Nacional de Metrologia, Qualidade e Tecnologia (INMETRO), Divisão de Metrologia de Materiais (Dimat), RJ-Brazil.
2. Departamento de Física, Universidade Federal de Juiz de Fora, MG-Brazil.
3. Departamento de Física, Universidade Federal de Minas Gerais (UFMG), MG-Brazil.
4. Programa de Pós-Graduação em Engenharia Elétrica, Universidade Federal de Minas Gerais (UFMG), MG-Brazil.

*Email: tlvasconcelos@inmetro.gov.br

Tip-Enhanced Raman Spectroscopy (TERS) has become one of the most promising tools for characterizing nanomaterials under ambient conditions since it generates optical images and spectroscopy with spatial resolution beyond the diffraction limit. However, the fabrication of optically efficient TERS probes with high reproducibility is yet challenging. As a way to solve this issue, the usage of nanostructures attached to probes apex has been reported in the literature [1,2]. The reason for this is based on the spatial confined field enhancement of localized surface plasmon resonance (LSPR) that appears only on subwavelength nanostructures. Moreover, the spectral tunability of LSPR energy by changing the nanostructure size and shape makes it suitable for several technological applications [3]. In the other hand, the fabrication processes for those probes are cumbersome and did not prove reproducible control of LSPR energy in the visible range. The challenge resides at the intrinsic difficulties to perform particle shaping at nanoscale. Here, we introduce a simple and reproducible route for generation and tuning LSPR in TERS probes [4]. The method is based on the use of a focused-ion-beam (FIB) made single groove in the vicinity of the apex of electrochemical etched gold tips (Figure 1a). The superficial line groove limits a region at the end of the tip, leading to a localized surface plasmon (LSP). Electron energy-loss spectroscopy (EELS), combined with scanning transmission electron microscopy (STEM) are employed to map the plasmon absorption energies with high spatial and energy resolution, revealing spectral tunability of its absorption energy by changing the distance between the groove and the probe apex (Figure 1b). Based on the experimental EELS data, complemented by discrete dipole approximation simulations, and taking into account the effective wavelength of the plasmon oscillation, we obtained a simple relation to guide the LSPR tuning in FIB-grooved TERS probes (Figure 1c). The protocol was used for production of test probes applied to TERS experiments which evidenced the improvement of the optical efficiency when operating on the visible-near IR range.

REFERENCES

- [1] L. Novotny and N. Van Hulst, *Nature Photonics*, 5 (2011) 83.
- [2] F. Huth et al., *Nano Letters*, 13 (2013) 1065.
- [3] K. L. Kelly et al., *J. Phys. Chem. B*, 107 (2003) 668.
- [4] T. L. Vasconcelos et al., *ACS Nano*, 9 (2015) 2015.

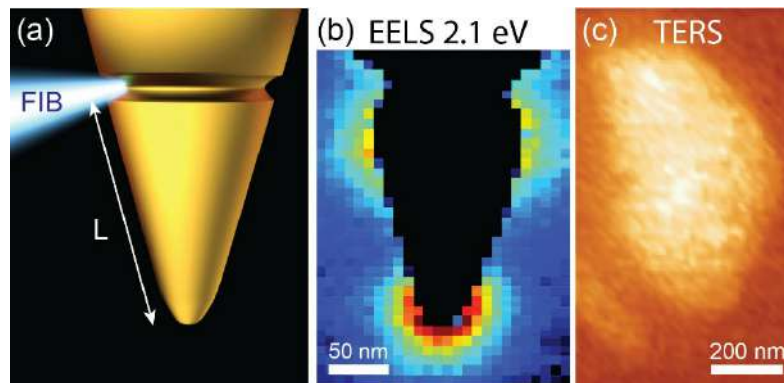
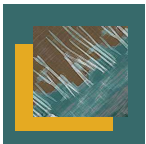
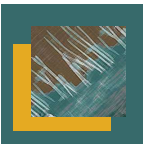


Figure 1 (a) Representative image of a gold TERS tip with a FIB-milled groove. (b) EELS intensity map plotted at 2.1 eV, where the first mode of LSPR is observed. (c) TERS hyperspectral image of a twisted bilayer graphene (tBLG) piece obtained applying a tip with groove at 240 nm from apex, suitable to promote the match between its first LSPR mode wavelength and the laser wavelength used (632.8 nm). Images adapted from [4].

ACKNOWLEDGMENTS

This work was supported by INMETRO, FAPERJ, FINEP, CNPq and FAPEMIG.



DOI: [INSERIR ENDEREÇO DO DOI AQUI.](#)

Caderno de Resumos do 26º Congresso Brasileiro de Microscopia da SBMM – ISSN: [INSERIR AQUI.](#)

PARTE 3

COMUNICAÇÕES ORAIS
- OUTROS



Raman Spectroscopy in the Study of Coralline Algae Mineralogy from the Brazilian Shelf

Rodrigo Tomazetto de Carvalho¹, Gustavo Miranda Rocha², Ricardo da Gama Bahia¹, Cláudia Santiago Karez¹, Gilberto Menezes Amado-Filho¹, Leonardo Tavares Salgado¹

1. Laboratório de Algas. Instituto de Pesquisas Jardim Botânico do Rio de Janeiro. Rua Pacheco Leão, 915/121, Jardim Botânico. Rio de Janeiro, Brazil.

2. Laboratório de Física Biológica. Instituto de Biofísica Carlos Chagas Filho. Universidade Federal do Rio de Janeiro. Ilha do Fundão. Rio de Janeiro, Brazil.

In the past decades there was an extensive study over coralline algae structure and mineralogy, especially due to possible threats posed by ocean acidification over their calcium carbonate skeleton, which is formed mainly by high Mg calcite, and it is the most soluble CaCO_3 polymorph in case of seawater pH decreasing [1]. Past studies showed that coralline algae present also other types of CaCO_3 crystals (aragonite, dolomite, etc) in their structure and this raised the question whether this algae are really responsible for the precipitation of mixed CaCO_3 polymorphs [2]. Additionally, even though Brazil presents a wide latitudinal occurrence of coralline algae [3], there is no information regarding the mineralogy of these algae. Here we described the mineralogy of 16 species of coralline algae that occurs along the Brazilian shelf, unrevealing their skeletal mineralogy, assessing the mixed CaCO_3 polymorphs precipitated by coralline algae using X-Ray Diffraction (XRD) and Raman Spectroscopy. The coralline algae species presented a skeleton formed mainly by high Mg calcite (range: 69-99 wt% high Mg calcite; mean: 91.8 wt% high Mg calcite), with almost all samples presenting considerable amounts of aragonite (up to 30 wt%) and few species presented small amounts of dolomite (up to 5 wt%). Raman mapping indicated the presence of aragonite in the walls of live cells present in the photosynthetic layer, indicating that living algae cells naturally forms the aragonite presence into the skeleton. Mg substitution at calcite lattice ranged from 13.8 to 32.5% wt%, with a mean of 21.71 wt%. This amount of Mg substitution is higher than other algae analyzed around the world. This fact could indicate that, in a near future, coralline algae formations in the Brazilian shelf will be more susceptible to climate world changes once biomineralization process can be compromised. Also, these changes can culminate in modifications in species resilience and distribution, influencing the balance of CaCO_3 net production in Southern Atlantic Ocean.

REFERENCES

[1] S.J. McCoy & N.A. Kamenos, J. Phycol. DOI: 10.1111/jpy12262 (2015).

[2] M.C. Nash, et al., Nat. Clim. Chan. DOI: 10.1038/NCLIMATE1760 (2012)

[3] G.M. Amado Filho, et al., Rhodolith/maerl beds: A Global Perspective. Springer International Publishing. <http://dx.doi.org/10.1007/978-3-319-29315-8>.

ACKNOWLEDGEMENTS

We thank Dr. Fabio Godoy from Renishaw for all the support with Raman Spectroscopy technique. We also thank Centro Brasileiro de Pesquisas Físicas for the XRD facilities. Authors thank FAPERJ, CNPq, CAPES and BRASOIL for financial support. G.M.A.F. and L.T.S. would like to thank CNPq and FAPERJ for research fellowships.

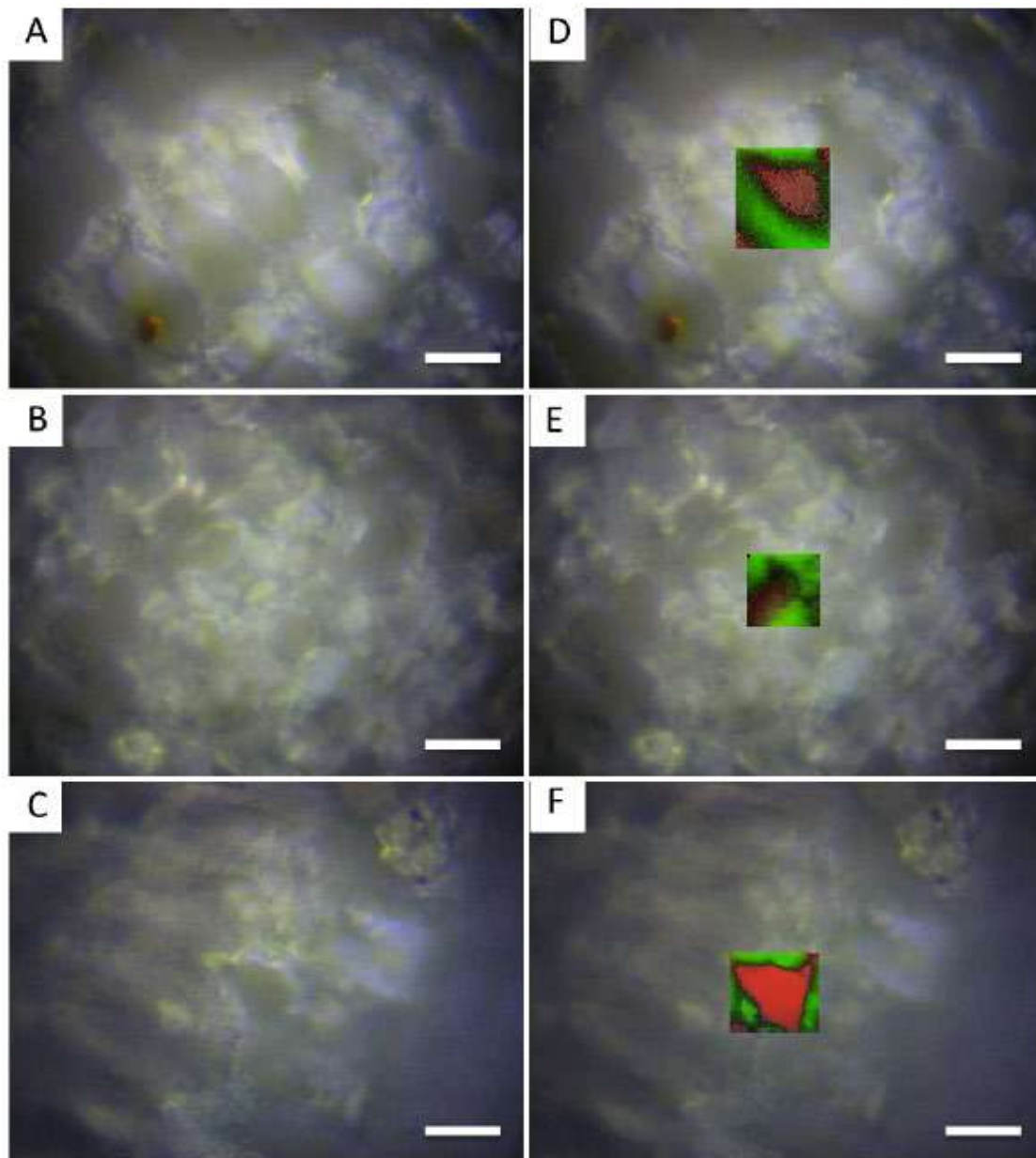
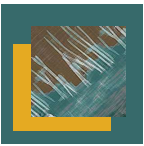


Figure 1: Bright field Optical microscopy of the three samples from the three different families of the order Corallinales (Corallinaceae, 1A; Hapalidiaceae, 1B and Sporolithaceae, 1C). Raman mapping overlaying bright field image indicates the same pattern from the three samples, with High Mg calcite in the internal cell walls and aragonite as a "shell" close to the cell membrane (green = High Mg Calcite; red = Aragonite). Scale bars = 20 μm .



Dolomite in Abrolhos reefs, Northeast Brazil

Ana Elisa Almeida Ayres^{1*}, Paulo César Fonseca Giannini², Merinda Nash^{3,4}, Isaac Jamil Sayeg²,
Beatriz Nogueira Torrano-Silva⁵, Valquíria Campos⁶

1. Institute of Oceanography of University of São Paulo (IO-USP), 2. Institute of Geoscience (IGc-USP), 3. Australian National University (ANU), 4. Smithsonian Institution, 5. Institute of Biology (IB-USP), 6. Institute of Science and Technology of São Paulo State University (ICT-UNESP).

*Email: anaelisaayres@gmail.com

The stability of modern reef structures depends on the *post-mortem* preservation of coralline algae skeletons, since coralline algae bind the reef surfaces together. There are concerns about preservation of crustose coralline algae (CCA) due their skeleton rich in high magnesium calcite, a carbonate mineral very susceptible to dissolution. Nonetheless, the recent discovery of dolomite in *Porolithon onkodes* from Australia and subsequent experiments suggested dolomite-rich CCA resist dissolution in acidified and greenhouse conditions [1][2], which brings bright perspectives to coral reefs stability. One of the unique features of Brazilian reefs is the main role of CCA as framework for the bioconstruction [3]. Despite being conspicuous and dominant in the Brazilian coast, CCA have been poorly studied in respect to their carbonate mineralogy. This research provides insights of dolomite presence in *Lithophyllum kaiseri* CCA from Abrolhos, the largest and richest coral reefs of Brazil, where CCA cover 30 up to 50% of the surface [4]. Scanning Electron Microscopy–Energy Dispersive Spectroscopy (SEM-EDS) showed dolomite (41.3-61.8 mol% MgCO₃) mainly rimming reproductive conceptacles of CCA (Figure 1), a pattern that has been reported before in dolomite-rich CCA [5][6]. Inductively Coupled Plasma Optical Emission Spectrometry (ICP-OES) and X-ray Diffraction (XRD) detected about 21.6 mol% MgCO₃. Using the method of area under the curve [2], we estimated that our CCA contained only 0.9% of aragonite. The Mg-content of this Brazilian CCA was higher than the values found for tropical *Porolithon onkodes* corallines (16.8-17.5 mol%) in [1], probably because it is a different species. XRD scans revealed a strong asymmetry in the main calcite peak towards higher 2-theta (right side) (Figure 2), which is an indicator of dolomite content [6]. With the revealed presence of dolomite in Australian CCA and the new XRD asymmetry method developed by [6], a re-assessment of CCA mineralogy was performed in published studies to determine whether those may have had dolomite. Setting as criteria that CCA with bulk MgCO₃ higher than ~18 mol % or with XRD asymmetry would contain dolomite, these authors demonstrated that dolomite could be present in CCA *Goniolithon* sp and *Porolithon* sp from tropical Indian, North Atlantic and South Pacific Oceans. Dolomite XRD peak asymmetry was found for *Lithophyllum kotschuanum* from Japan Ryukyu Islands [5]. However, dolomite was never identified before in recent *Lithophyllum kaiseri* neither in any CCA from Abrolhos, which was the main contribution of this research.

REFERENCES

- [1] M.C Nash et al. *Biogeosciences*, 8 (2011) 3331.
- [2] G. Diaz-Pulido et al. *Nature Communications*, 5 (2014) 3310.
- [3] J. Cortés., *Latin American Coral Reefs*, Amsterdam, 2003.
- [4] M.A.O Figueiredo et al. *J. Phycol*, 36 (2000) 17.
- [5] M.C. Nash et al. *Nature Climate Change*, 3 (2012) 268.
- [6] M.C. Nash et al. *Journal of Sedimentary Research*, 83 (2013) 1085.
- [7] This research was supported by CNPq (National Council for Scientific and Technological Development) (307055/2013-2) and São Paulo Research Foundation (FAPESP) (22889/2014-2)

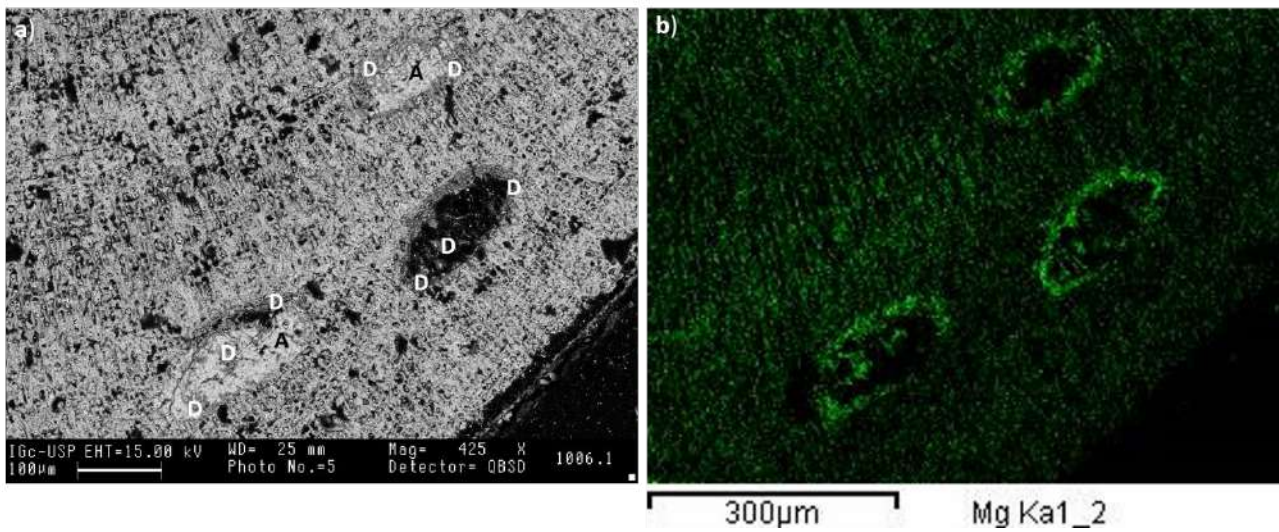
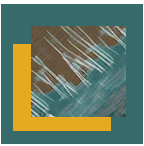


Figure 5. SEM-EDS/BSE/SE1 images of the reproductive conceptacles in coralline algae. a) Original SEM-BSE image. Dolomite (D) (41.3-61.8 mol% $MgCO_3$) occurs rimming conceptacles and as few patches inside them, while fill of the conceptacles is mainly aragonite (A) (~ 1.0 mol % $MgCO_3$; ~ 1.0 % mol Sr). (b) Chemical mapping given by SEM-EDS/BSE analyses. Mg is represented by the green color.

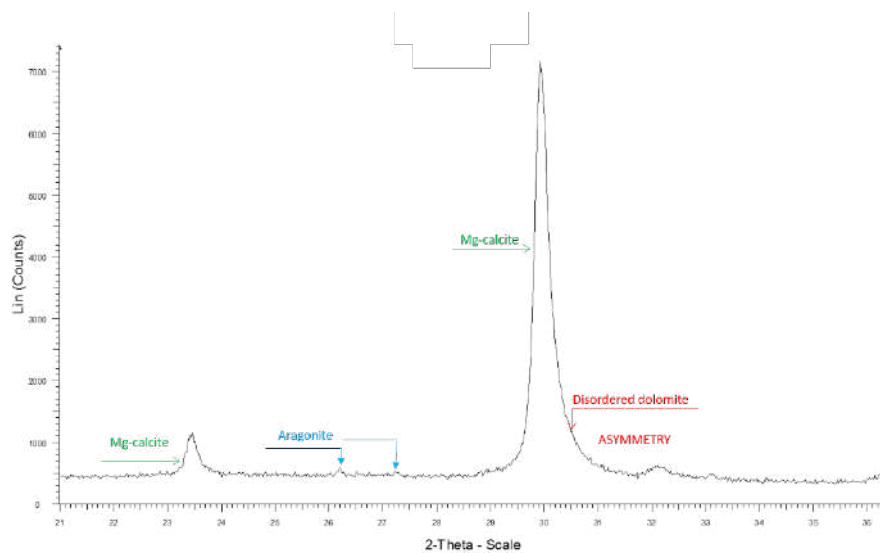
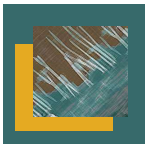


Figure 6. XRD scan covering the main carbonates peaks from *Lithophyllum kaiseri* CCA and the identification of the minerals. Notice the high asymmetry over the disordered dolomite position.



Bone Biofabrication From Human Adipose Stem Cell Spheroids Seeded Into Pla/Cha 3D Printing Scaffold

Gabriela Soares Kronemberger¹, Karina Ribeiro Silva², Alexandre Malta Rossi⁴, José Mauro Granjeiro² and Leandra Santos Baptista^{2,3*}

1. Postgraduate Program in Translational Biomedicine, UNIGRANRIO, Duque de Caxias, RJ, Brazil;
 2. Tissue Bioengineering Research Group (GBET), Metrology Board Applied to Life Sciences (DIMAV), National Institute of Metrology, Quality and Technology (INMETRO), Duque de Caxias, RJ, Brazil;
 3. Nucleus of Multidisciplinary Research in Biology (NUMPEX-Bio), Federal University of Rio de Janeiro (UFRJ)/Xerém, Duque de Caxias, RJ, Brazil;
 4. Brazilian Center of Physical Research (CBPF), RJ, Brazil;
- *Email: leandrabaptista@xerem.ufrj.br

New bone formation may be desirable in a variety of clinical settings, such as osteoporosis, skeletal deformities, and in nonunion bone fractures. Adult stem cells derived from adipose tissue (Adipose Stem Cells - ASCs) can be considered as a promising cell source because of its easy accessibility and abundance. In this context, a novel approach known as modular tissue engineering focuses on fabricating tissue using spheroids as building blocks with specific microarchitectural features. The aim of the study is to induce osteogenesis in ASCs spheroids formed by a micro-molded non adhesive hydrogel three-dimensional culture, and next seed these induced spheroids (building blocks) in a composite scaffold made of polylactic acid (PLA) and nanostructured apatite carbonate (CHA). The human lipoaspirate samples were obtained according to local research ethics committee and ASCs were isolated by a mechanical dissociation method. Cells were seeded in the micromolded resections of agarose hydrogel, at where each spheroid was formed per resection. The spheroids were maintained in vitro for three weeks in an osteogenic induction medium containing: 10 mM of β -glycerophosphate, 10^{-8} mM of dexamethasone, 50 μ M of ascorbic acid and a defined concentration of human recombinant BMP-7. Initially, morpho-quantitative analysis of the induced spheroids has been done which includes measure of diameter and structural analysis. The surface morphology of the induced spheroids was evaluated using scanning electron microscope (SEM) as well the interaction of spheroids with the scaffold after seeding. We could observe that the induced spheroids interacted with biomaterial surface, treated or not with poly-D-lysine/laminin (Fig. 1). Furthermore, all spheroids fused after 48h seeded in all biomaterial surfaces. Histological analyses have been done using alizarin red O staining for extracellular mineralization and immunohistochemistry analyzes for bone extracellular matrix components. We expected to produce an engineered constructed from induced human ASCs spheroids with PLA/CHA scaffold for bone tissue engineering.

ACKNOWLEDGEMENTS.

The authors like to thank the Conselho Nacional de Desenvolvimento Científico e Tecnológico (CNPq) for the financial support.

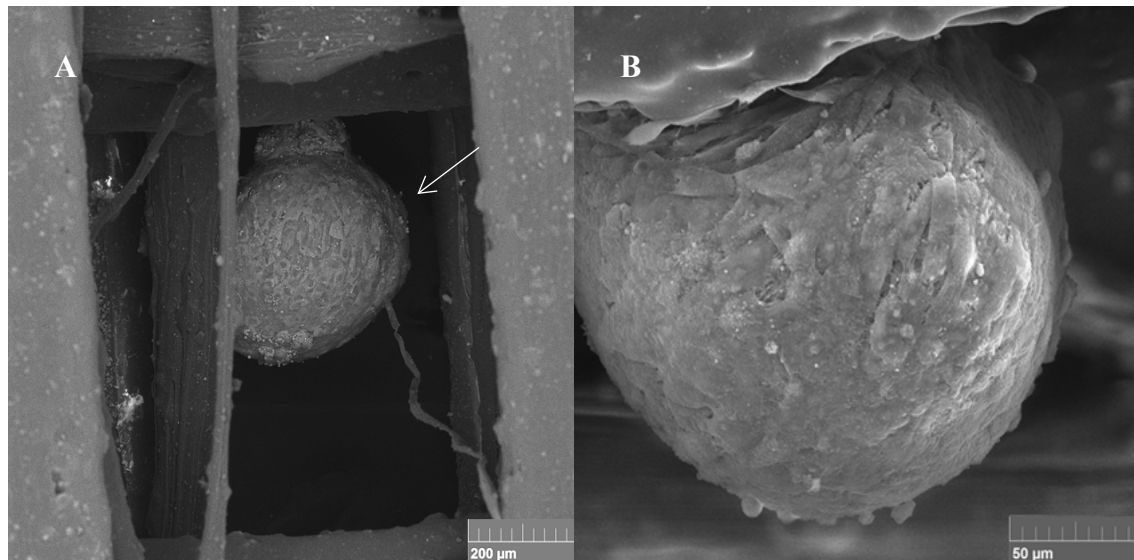
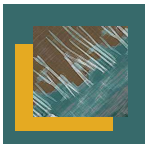
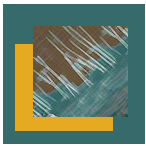


Figure 1: Scanning electron microscopy of spheroids in PLA/CHA scaffolds. (A) Fused spheroids in control medium (arrow). (B) Fused spheroids in osteogenic medium (*).



Ichthyophthirius multiphiliis in *Carassius auratus* (Goldfish) - Ultrastructure Observation of Parasite Stage and Host Cells

Carla Renata Serantoni Moyses¹, Diva Denelle Spadacci-Morena², José Guilherme Xavier¹, Anuska Marcelino Alvares-Saraiva¹, Paulo Ricardo Dell'Armeline Rocha¹, Maria Anete Lallo¹

1. Pós-Graduação em Patologia Ambiental e Experimental, Universidade Paulista, São Paulo, Brazil
2. Instituto Butantã, Laboratório de Fisiopatologia, São Paulo, Brazil

The ciliate, *Ichthyophthirius multiphiliis*, is the main parasitic threat to freshwater fish in large parts of the world and is the causative agent of white-spot in fresh-water fish, such as *Carassius auratus* (goldfish) [1]. The ciliate life cycle, which consists of three stages: an infective theront, a parasitic trophont and a reproductive tomont, is well documented [2,3]. Free-swimming theronts enter into the epidermis of fish to feed on mucus and tissue and rapidly differentiate into trophonts, and following a period of growth and development, the trophonts leave the host actively and transform to encysted tomonts [3,4]. The tomonts undergo mitosis in the cyst and release theronts, the stage infective to the fish host. Although much is known about the life cycle and the consequences of its presence in hosts, the morphological aspects related to the protist have not yet been clarified, as there are few reports of the ultrastructural aspects and lesions associated with its presence, which were objects of this study. Goldfish *C. auratus* (n= 30) with white or ulcerative skin lesions were collected and transported to the laboratory according to standard procedures. Fish were anaesthetized by immersion in solution of tricaine methane sulfonate. For transmission electron microscopy (TEM) and scanning electron microscope (SEM), small pieces of skin and gill lesions were fixed in 2% glutaraldehyde in 0.2 M cacodylate buffer (pH 7.2) at 4°C for 10 h, and post-fixed in 1% OsO₄ buffered for 2 h and routinely processed. Different types of cells were identified in inflammation area such as macrophages, lymphocytes and granulocytes (mast cells) associated with tissue breakdown in the skin and muscle (Fig.1A,B). Around the parasites, we found reactive stromal cells and erythrocytes (Fig 1A). In the host two stages were observed - tononts and trophonts. The aspect of the tononts is rounded without the presence of cilia (Fig.1C). *I. multiphiliis* trophonts are slightly flattened at the mid region, and tapers towards the apical end, resulting in a spheroidal to pyriform shape with a somewhat pointed anterior tip. The cell membrane was thick with chitin (Fig.1D). Food vacuoles with host cells or cell debris were presents increase in mature trophont. Mitochondria are uniformly spheroid and predominantly underlie the plasmalemma (Fig.1D). The surface of the parasite presents an undulating appearance and reveals the presence of numerous cilia (Fig.1E). We conclude that the presence of the parasite mobilizes inflammatory response with the presence of mast cells, macrophages, lymphocytes and polymorphonuclear cells. The presence of chitin in the protozoan cell membrane may explain its ability to resist in the environment and the different treatments used.

Keywords: MET, MEV

REFERENCES

- [1] P.T.K. Woo, D.W. Bruno, Fish diseases and disorders viral, bacterial and fungal infections, Wallingford, CABI, 2012.
- [2] A.G. Swennes et al., Dis. Aquat. Org. 69 (2006) 227–232.
- [3] H.E. Roberts et al., Vet. Clin. Exot. Anim. 12 (2009) 609–638.
- [4] J.Z. Wei et al., Lett. Appl. Microbiol. 57 (2013) 91-101.

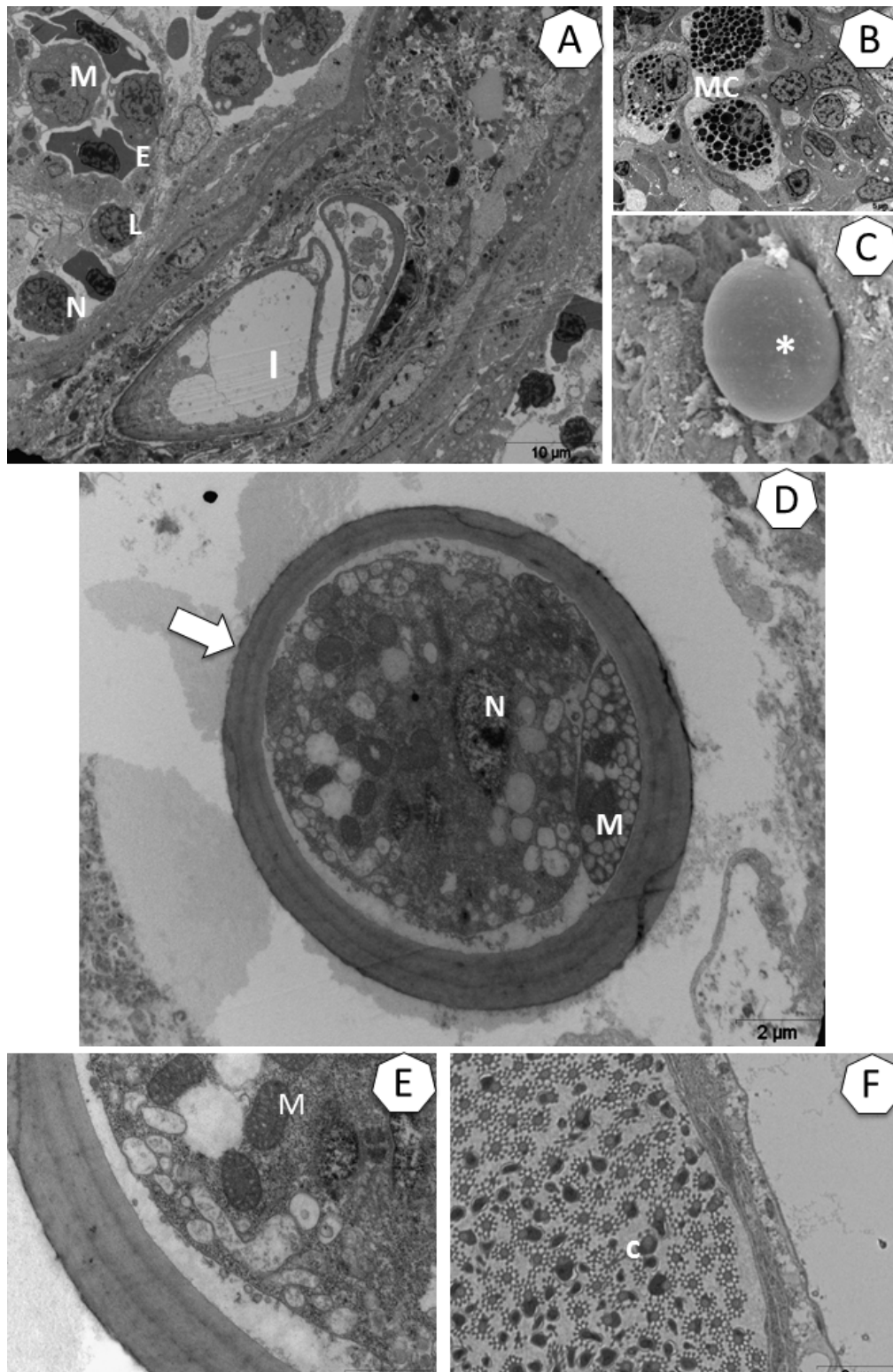
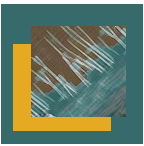


Figure 1. TEM and SEM of *Ichthyophthirius multifiliis* (I) in skin and gill. A. Macrophages (M), neutrophil (N), lymphocytes (L), erythrocytes (E) and reactive stromal cells (*) surrounding the parasites. B. Mast cells (MC). C. tononts in gill (*). D) Thick cell membrane with chitin of trophont and food vacuoles, mitochondria and the nucleus in the somatic cortex. E) Detail of cell membrane. F) Numerous cilia (c).



Titanium Dioxide Nanoparticles Identification In Fish Cells: Subcellular Internalization

Iara C. Souza¹, Vitor A. S. Mendes², Ian D. Duarte³, Livia D. Rocha³, Silvia T. Matsumoto³, Mike Elliot⁴, Daniel A. Wunderlin⁵, Magdalena V. Monferrán⁵, Marisa N. Fernandes^{1*}

1. Departamento de Ciências Fisiológicas, Universidade Federal de São Carlos (DCF/UFSCar), Ave. Washington Luiz, Km 235, 13565-905, São Carlos, São Paulo, Brazil.

2. Departamento de Engenharia de Materiais, Universidade Federal de São Carlos (DEMa/UFSCar), São Carlos, SP, Brazil Ave. Washington Luiz, Km 235, 13565-905, São Carlos, São Paulo, Brazil.

3. Departamento de Ciências Biológicas, Universidade Federal do Espírito Santo (DBV/UFES), Ave. Fernando Ferrari, 514, 29075-910, Vitória, Espírito Santo, Brazil.

4. Institute of Estuarine & Coastal Studies (IECS), University of Hull, Hull HU6 7RX, UK.

5. ICYTAC: Institute of Science and Food Technology Córdoba, CONICET and Department of Organic Chemistry, Chemistry Faculty, National University of Cordoba, University City, 5000, Córdoba, Argentina.

*Email: dmnf@ufscar.br

Among the varieties of NP produced, metal oxides have been increasingly applied due to their photocatalytic nature, particularly, the titanium dioxide NP (TiO₂-NP). Considering the presence of TiO₂-NP in the environment due industrial and sewage releasing, especially in aquatic ecosystems, *in-situ* studies are required to evaluate the behaviour of these NP in the environmental compartments and biota. Therefore, the purpose of this study was to identify the nanocrystallographic structure of TiO₂-NP in abiotic matrixes as well in fish cells. Scanning electron microscope coupled with electron backscatter detector (BSE) were used to identify chemical contrast, secondary electrons (SE) were used to identify morphology and X-ray Dispersive Energy Spectroscopy (EDS) were used to identify chemical elements. Nanodiffraction was used for particles size close to 100 nm and lower to identify the crystallographic structure. Electron nanodiffraction was performed to find axes of high symmetry zone in nanoparticles containing Ti and O using the holder TEM double tilt. Nanodiffraction pattern were indexed using Jems software (Electron Microscopy Software, P.Stade Imann, Switzerland) and theoretical crystallography of the ICSD FIZ Karlsruhe, Germany. At least 2 high symmetry zone axes of the same nanoparticle were indexed. Nanocrystallographic analyses showed that TiO₂-NP was in rutile phase in samples from atmospheric particulate matter and fish organs suggesting that atmospheric particulate matter may be the source of TiO₂-NP in these ecosystems.

Keywords: nanocrystallographic, oxidation state, atmospheric particulate matter, rutile

This research was supported by FAPES (Brazil).

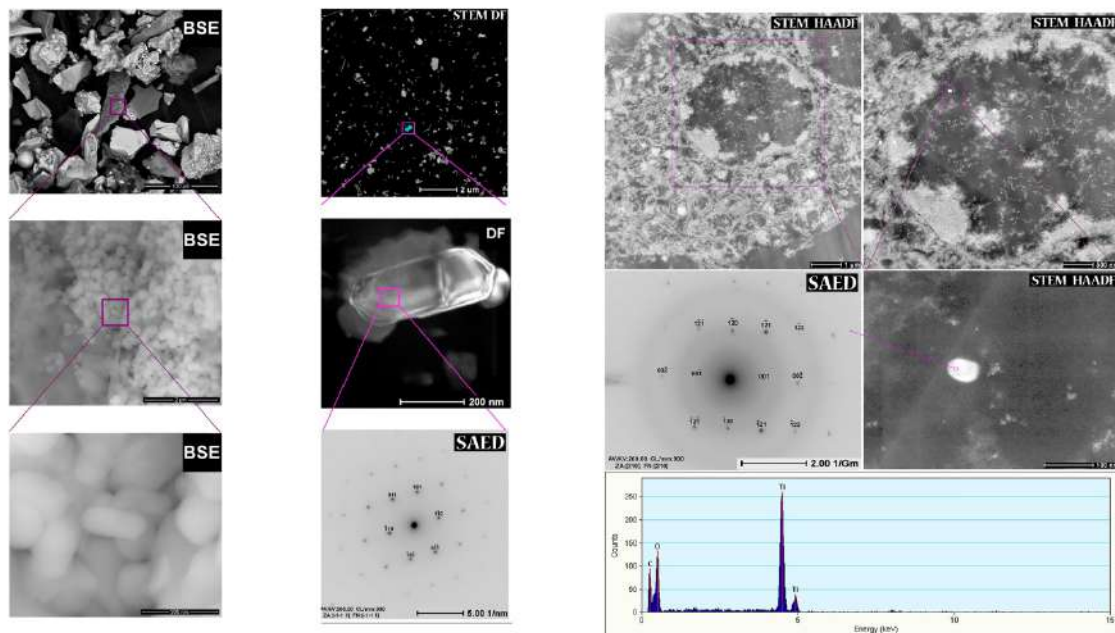
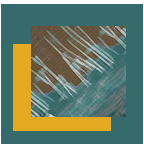
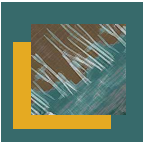


Figure 1. SEM and TEM analysis of atmospheric particulate matter from Tubarão Complex.

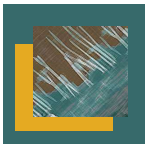


DOI: [INSERIR ENDEREÇO DO DOI AQUI.](#)

Caderno de Resumos do 26º Congresso Brasileiro de Microscopia da SBMM – ISSN: [INSERIR AQUI.](#)

PARTE 4

PÔSTERES
- BIOLOGIA



Morphological And Morphometrical Analysis Of The Initial Segment And Cauda Of Epididymis In Obese *Wistar* Rats Submitted To Duodenal-Jejunal Bypass Surgery

Ana Caroline Barbosa Retameiro*¹, Suellen Ribeiro da Silva Scarton¹ and Célia Cristina Leme Beu¹

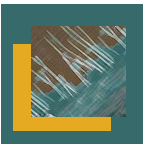
1. Universidade Estadual do Oeste do Paraná - UNIOESTE, Cascavel - Paraná, Brazil.

*Email: anaretameiro@gmail.com

Duodenal-jejunal Bypass (DJB) is a type of bariatric surgery that was used, initially, in type 2 diabetes mellitus and was posteriorly tested in treatment of obesity [1], a chronic disease that affects various parts of the body, and inclusively organs of male genital system, such as the epididymis [2]. The aim of this study was to analyze the effects of DJB in the epididymis initial segment and cauda of obese adult *Wistar* rats. All the procedures that involved animal's use were approved by the Etic Committee in the Animal Experimentation and Pratic Classes from Unioeste (44/09). Epididymis samples were collected from 24 *Wistar* rats, which ones stayed in controlled temperature ($26^{\circ} \pm 1^{\circ}$ C), received standard diet and *ad libitum* water during 8 weeks. After this period, they were randomly separated into four groups: 1) control (CON, n=6) that received standard diet and water throughout the experiment; 2) Western Diet (WD, n=6), Sham (SHAM, n=6) and 4) duodenal-jejunal Bypass (DJB, n=6). The groups WD, SHAM and DJB received cafeteria diet during 34 weeks. The animals were weighted and SHAM animals were manipulated to simulate surgical stress, while in DJB occurred a bariatric surgical procedure characterized by the complete bybass of the duodenum forming a duodenal stump, and deviation of the proximal portion of the ileum, in a way that the distal ileum was anastomosed to the stomach [3]. Epididymal initial segment and cauda samples were submitted to histological routine, to obtain sections (7 μ m), stained with hematoxylin/eosin and photodocumented in a 10X and 20 X objective to general and detailed analysis of the epithelium, respectively. Measurements body mass showed that the cafeteria diet was efficient in inducing obesity, since the CON's group weight mean differed significantly from WD, SHAM and DJB groups, with an increase of 18,5%, 19,5% and 18,92%, respectively ($p=0,0009$). The morphometric analyzes in initial segment didn't showed significant differences between groups in the epithelium's height means ($p=0,1616$), and also in lumen's diameter means ($p=0,1630$). The morphological analyzes of epididymis cauda (Figure 1A-D) were confirmed by the morphometric analyzes that showed a significant increase in mean of the epithelium height ($p=0,0001$), associated to a decrease in the lumen diameter mean ($p=0,0001$) and greater clear cells number ($p=0,0001$) in WD and SHAM groups (Figure 1 E-G). As clear cells has endocytic activity [4], remove from lumen the contents of the cytoplasmic drops released by spermatozoa [5] and mediate the acidification of the luminal contents [6], is possible that the increase of this cell type quantity is associated to its greater activity, influenced by the decrease of sperm quality and quantity in obesity[2] what leads us to infer a possible connection between this alteration and the phagocytosis of abnormal sperm degradation products [7] and spermiphagia [8]. In summary, is possible to conclude that, in the analyzed aspects, obesity had negative effects under the epididymis's cauda and the DJB procedure was efficient to reversing them.

REFERENCES

- [1] J.Greve et al. Br. J. Surg. 11 (2008) 1313.
- [2] R.M. Viguera-Villaseñor et al. Acta Histochem. 113 (2010) 214.
- [3] F. Rubino et al. Ann. Surg. 5 (2006) 741.
- [4] B. Robaire et al., Efferent ducts, epididymis and vas deferens: structure, functions and their regulation, Raven Press, New York, 1988.
- [5] L. Hermo et al. Am. J. Anat. 183 (1988) 107.
- [6] C. Isnard-Bagnis et al. Am. J. Physiol. Cell Physiol. 284 (2003) 220.
- [7] J.M. Trasler et al. Biol. Reprod. 38 (1988) 463.
- [8] H.D. Moore et al. Anat. Rec. 193 (1979) 293.



[9] This research was supported by CAPES (Brazil).

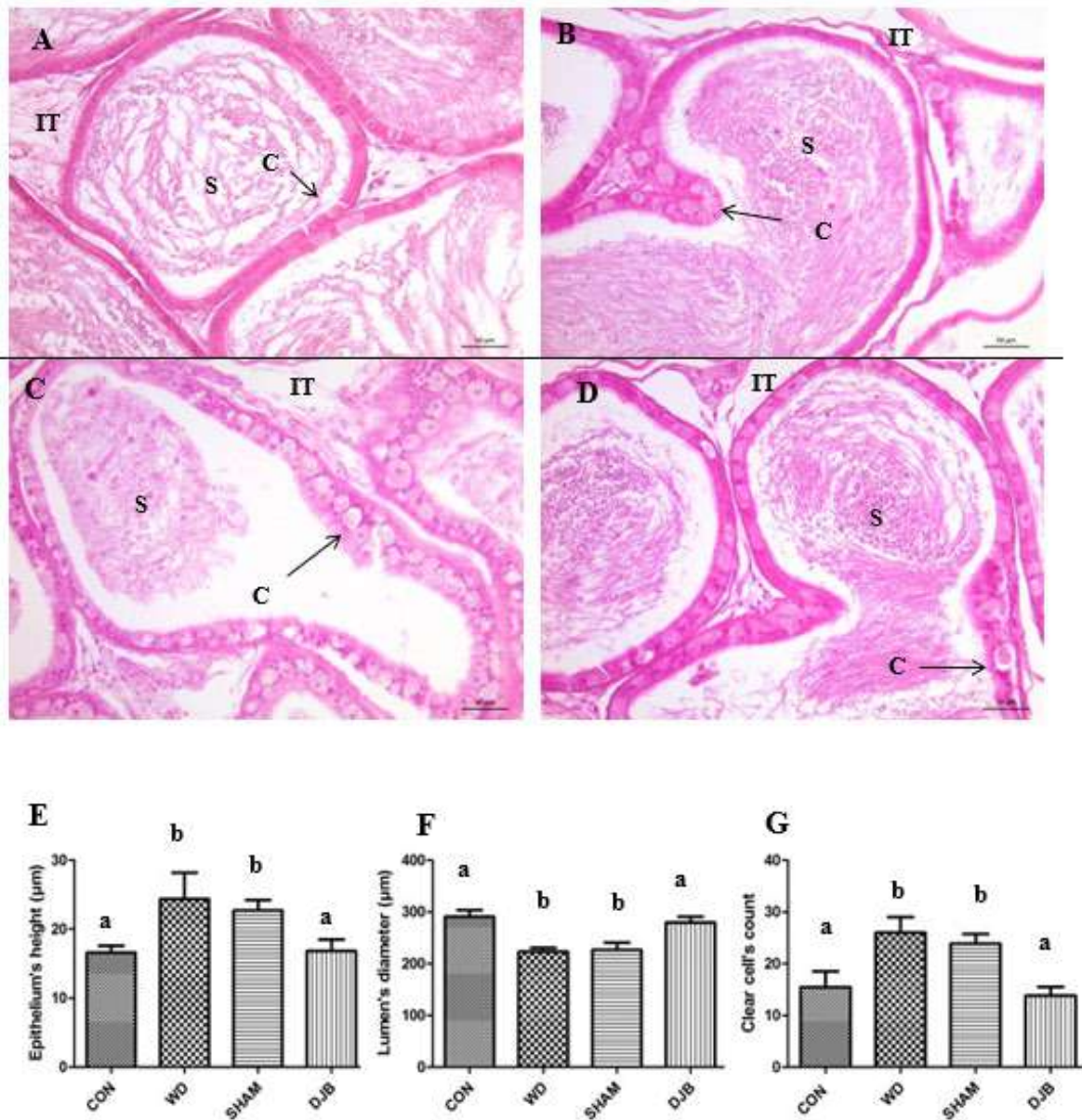


Figure 1: A-D: Photomicrographs of Wistar rats epididymis cauda from CON (A), DJB (B), WD (C) and SHAM (D) groups; E-F: graphics of the epithelium's height (E), diameter of lumen (F) and number of clear cells (G). Are indicated: clear cells (C), spermatozooids (S) and interstium (IT). H/E. Bar scale: 50 µm. 20X objective in A-D. In E-F values expressed as mean ± standard deviation. One way ANOVA, post test Tukey. Different letters represent significant statistical differences $p < 0,05$.



Biological Evaluation of 2,1,3-Benzoselenodiazole Derivatives as New Lipids Probes for Cellular Imaging

Ana L. A. Barbosa^{1*}, Ingrid R. Medeiros², Lorena P. Andrade¹, Brenno A. D. Neto², and José R. Correa¹

1. Institute of Biological Sciences, University of Brasilia, Brasília, DF, Brazil.

2. Institute of Chemistry, University of Brasilia, Brasilia, DF, Brazil

*Email: analu-ab@hotmail.com

In the 1970s, a methodology of synthesis capable to produce new selenium-based compounds was developed. This methodology produced several selenium organic derivatives, which were much less toxic than inorganic selenium, a property that attracted great attention to them [1]. In this work, we have demonstrated the in vitro application of four benzoselenodiazole derivatives (BSD) using Caco-2, MCF-7, MDA-MB-231, DU145 tumor cells and also HUVEC (normal cells). Two types of samples (live and pre-fixed cells) were used. All samples were incubated with each derivative solution at 100 nM for 30 minutes, washed three times in PBS and mounted over glass slides with antifade agent. These samples were analyzed at confocal laser scanning microscope (Leica, TCS SP5) using 405 nm excitation wavelength. To address the issue related to cellular cytotoxic effect for all tested compounds, MTT assays (tetrazolium salt) were performed. *Caenorhabditis elegans* (*C. elegans*) was chosen as a model in order to verify the applicability of these new type of fluorescent dyes in a more complex tissue. Our results demonstrated that all tested compounds were able to emit high fluorescent signal (Red, 620-680nm) without any photo-bleaching detection under standard operational conditions of the equipment. Furthermore, these compounds showed high affinity to small spherical cytoplasmic organelles in all tested samples (figure 1). Due to the fact that these organelles resembled lipid bodies, we performed a Bodipy® staining assay (Bodipy is a widely used commercial lipid marker). The results from Bodipy® assay clearly demonstrated that our compounds in fact stain lipid bodies (figure 2). The MTT assay showed that all tested compounds have no cytotoxic effect even when they were used 1000 X more concentrated than the concentration used in the fluorescent staining procedures (figure 3). The BSD derivatives were also able to stain lipids bodies in a variety of *C. elegans* tissues with high specificity (figure 4). In this work, the biological application of four BSD compounds was described, with no detected cytotoxicity and high specificity to lipids bodies. These fluorescent compounds can be applied in adherent models of mammalian cells and metazoan tissues from *C. elegans* species. Finally, these compounds also have a very wide Stoke's shift and a bright and stable fluorescence emission; besides, the photo-physics properties inherent to these compounds are essential features to all outstanding commercial fluorescent dyes.

[1] R. Caputo et al, Tetrahedron Letters. 2007. 48: 1425-1427.

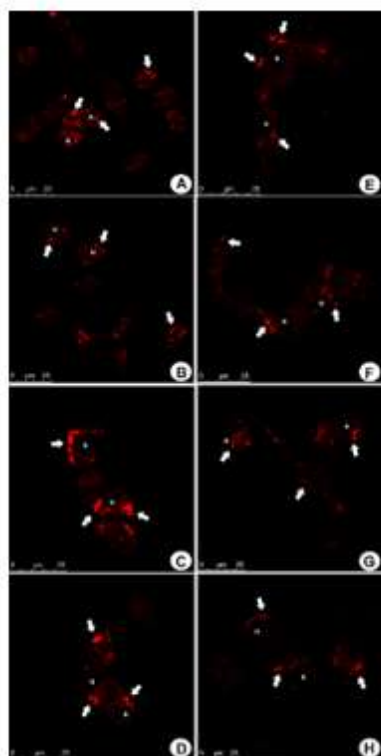
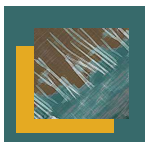


Figure 1. Fluorescent profile of CACO-2 cells, incubated with BSD 01 (A,E), BSD 2 (B,F), BSD 03 (C,G) and BSD 04 (D,H) compounds. (A-D) Live cells and (E-H) pre-fixed cells. The arrowheads (white) show the fluorescence distribution in cytoplasm of cells. It is possible to note the accumulation of fluorescent lipid bodies in both experimental conditions. (N) Nucleus.

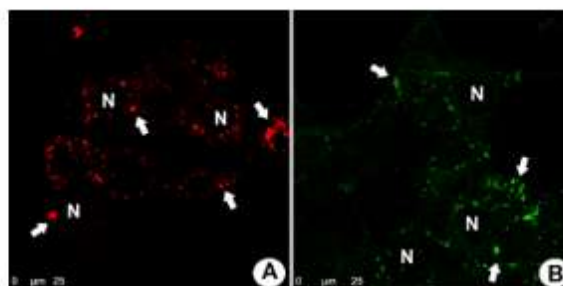


Figure2. Fluorescent profile of CACO-2 cells incubated with BSD 01 (A) and Bodipy® (B). The results from Bodipy® assay showed that our compounds stain lipid bodies (compared to BSD 01). The arrowheads (white) show the fluorescence distribution in cytoplasm of cells. (N) Nucleus.

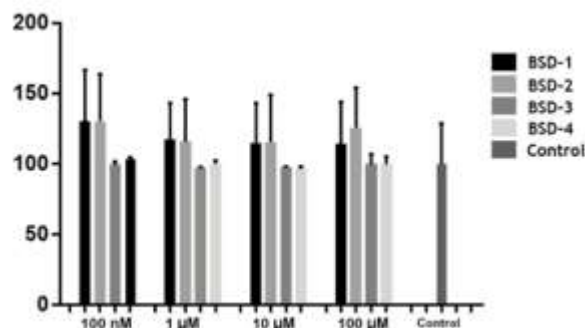


Figure 3: Cell viability assay after 24 hours incubation of samples with BSD 01, BSD 02, BSD 03 and BSD 04 compounds shows that the compounds have no cytotoxicity effect even when used 1000 times more concentrated than the concentration applied in the staining procedures (100 nM). CACO-2 cells were used in this assay. Control was incubated with the diluent only (DMSO in culture medium).

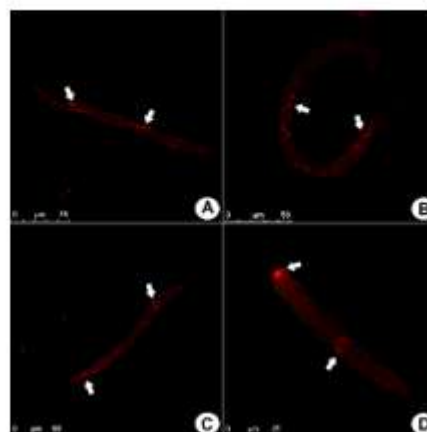
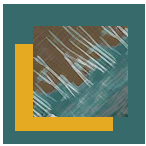


Figure 4: Fluorescent profile of *C. elegans* incubated for 1 hour with BSD 01 (A), BSD 02 (B), BSD 03 (C), BSD 04 (D). This assay shows that our compounds have affinity for lipid bodies even in this multicellular model similar to the results obtained using different cells lines. The arrowheads (white) show the fluorescence distribution in the cytoplasm of the cell.



The Use of Scanning Electron Microscopy to Characterize Veterinary Dental Pathologies

Leonardo Zeemann 1*, Annelise Zeemann 2

1. Veterinary Dentistry LZ ODONTOVETERINÁRIA

2. Microscopist at Materials Life

*Email: leozeemann@gmail.com

The diagnostic of a dental anomaly in veterinary dentistry is based on visual examination and dental X ray images, that lead to a specific treatment based on the effects of the anomalies in the animal. There are problems from genetic pathologies and some acquired during the animal life, and the characterization of the morphologies may help in the study of veterinary dentistry, as well as the histopathologic analysis. This paper presents the use of scanning electron microscopy (SEM) to characterize a genetic dental anomaly known as “dens invaginatus”, which corresponds to a flow of the dentin and enamel inside the pulp chamber during the mature of the new tooth, after the dog was born. The bad formation of the tooth creates conditions for microorganisms to enter under the gum and initiate an earlier periodontal disease, leading to bone loss, as well as the contamination inside the channel initiates an endodontic disease. Figure 1 presents the X ray image of a Yorkshire Terrier jaw with the anomaly that generated the dental disease, evidencing the effects mentioned above. The tooth was extracted, figure 2, and prepared to be characterized by SEM. The tooth preparation included cleaning with alcohol in an ultrasonic device. In this case the tooth was cut in a longitudinal section, polished using diamond paste as abrasive and it was metallized with gold, figure 3, to be analyzed by SEM adopting microscope parameters that are like the adopted for metallic materials. Figure 4 presents the SEM image of the tooth with the “dens invaginatus” anomaly. It can be observed that there is dentin and enamel inside the pulp chamber. EDS analysis were taken at different locations of the tooth and the results indicated that the substance inside the chamber presents similar composition of the tooth original dentin, but the SEM image clearly evidenced the different morphology.

ACKNOWLEDGMENT:

The authors thank the UFRJ Materials Department Microscopy Laboratory.



The yellow arrow indicates a root channel larger than it should be, the green arrow indicates bone loss due to the periodontal disease and the red arrow shows periapical radiolucencies indicative of abscess.

FIGURE 1 – X-ray image of the dog jaw, with the anomalous tooth.



FIGURE 2 – Extracted tooth.



FIGURE 3- Sectioned, polished and metallized tooth.

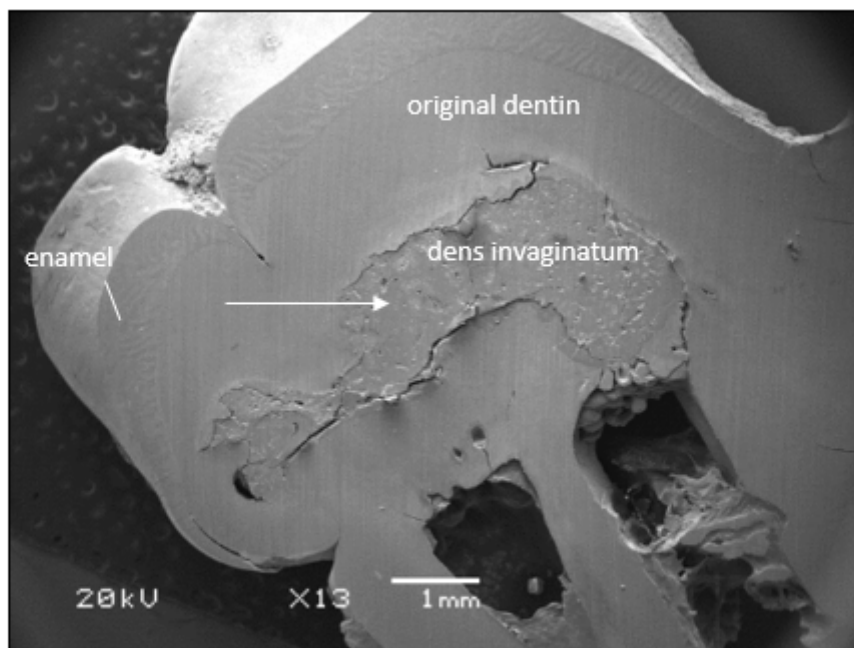
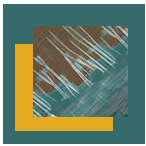


FIGURE 4 – SEM detail of a longitudinal section of the anomalous tooth showing that the dentin and enamel inside the pulp chamber (white arrow).



Cerebral Palsy In Rats Alters The Ultrastructure Of Striated Skeletal Muscle

Ariadne Barbosa¹, Pâmela Buratti*¹, Caroline Covatti¹, Dafne Strozake Maximo¹, Lúgia Aline Centenaro¹, Lucinéia Chasko Ribeiro¹, Marcia Miranda Torrejais¹

1. Universidade Estadual do Oeste do Paraná - UNIOESTE, Cascavel, Brazil.

*E-mail: pamela_buratti@hotmail.com

Studies evaluating ultrastructural changes in animal models of cerebral palsy (CP) are scarce. CP is the most common form of motor incapacity resulting from pre, peri or postnatal risk factors and causes impairment of muscle tone, movement and posture [1]. Knowing the changes that occur in the musculature is essential for understanding the impairment of the functional capacity of patients with CP [2]. The aim of this research was to evaluate the implications of an experimental model of CP on the ultrastructure of muscle fibers in the plantaris muscle of *Wistar* rats. All the procedures adopted were submitted and approved by the Ethics Committee in the Use of Animals (CEUA) of Unioeste, number 24/16. Insulates of prenatal infection by lipopolysaccharide (LPS), perinatal anoxia and sensorimotor restriction were used for CP induction. For this, adult pregnant rats were used. Part of the females were subjected to intraperitoneal injections of LPS (200 µg/kg of LPS in 100 µL of sterile saline) or vehicle (100 µL of sterile saline). These injections were performed every 12 hours, from the 17th gestational day until the end of gestation (21st gestational day). The offspring formed the following experimental groups: control group (CG, n = 5) - offspring of rats injected with vehicle during gestation; and CP group (CPG, n = 5) – offspring of rats injected with LPS during gestation. For the induction of perinatal anoxia, it was performed on the day of birth (postnatal day 0), the CPG animals were placed in a closed chamber, partially immersed in water at 37 °C ± 1, with a flow of 9 L/min of nitrogen (100%) for 20 minutes. From the first postnatal day (P1) to the 30th day postnatal (P30), the CPG animals were submitted to sensorimotor restriction 16 hours/day, with immobilization of the pelvic limbs through the use of epoxy molds and microporous adhesive tape. At 48 days of age, the plantaris muscle was collected and the left muscle antimere fixed in Karnovsky. Subsequently, the muscle was reduced to approximately 1 mm wide longitudinal fragments, which were processed for electron microscopy and evaluated in the transmission electron microscope (CM100, Philips, The Netherlands). Muscle fibers were organized in sarcomeres, containing light and dark bands (band I and band A, respectively) in GC and GPC (Figures 1A and 1B). It was evident disorganization of Z line (333,3 %; p = 0,034; Figures 1B and 1C), myofibrillar disorganization (142,8 %; p = 0,0026; Figures 1B and 1D) and Z line dissolution (184,2 %; p = 0,0011; Figures 1B and 1E), with CPG predominance when compared to CG. It was concluded that the animal model of CP that associates prenatal infection with LPS, perinatal anoxia and sensorimotor restriction affects the ultrastructural characteristics of skeletal muscle fibers, compromising the excitation-contraction mechanism due to the importance of structural integrity for the triggering of muscle contraction.

REFERENCES

- [1] M. Bax et al., *Dev. Med. Child Neurol.* 47 (2005).
- [2] C.P. Dias et al., *Sci. Med.* 23 (2013).
- [3] This research was supported by CAPES (Brazil).

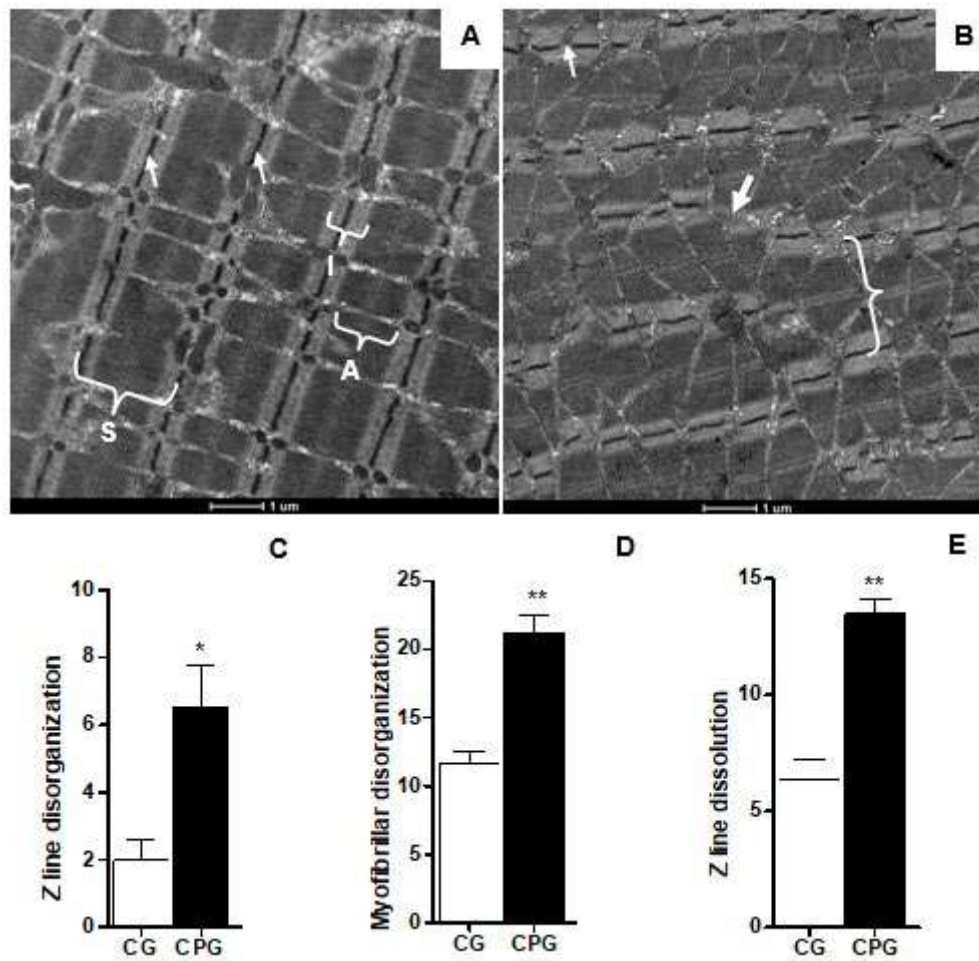
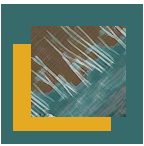
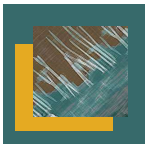


Figure 1 - Electromyographs of the plantaris muscle of *Wistar* rats at 48 days of age. Longitudinal section. **A**: Preserved muscle fiber, with structure of sarcomere (S), band A (A), band I (I) and organized Z line. Control group (CG). **B**: Muscle fiber with Z line disorganization (thin arrow), myofibrillar disorganization (key) and Z line dissolution (thick arrow). CP group (CPG). **C**, **D** and **E**: Z line disorganization, myofibrillar disorganization, and Z line dissolution in CG and CPG. Values expressed as mean \pm standard deviation. Student's *t*-test. * Represents $p < 0.05$. ** Represents $p < 0.01$.



Analysis of Skeletal Muscle Fibers of Obese Wistar Rats Submitted to Duodenojejunal Bypass

Ariadne Barbosa^{1*}, Mylena de Campos Oliveira¹, Pâmela Buratti¹, Camila Kuhn¹, Caroline Covatti¹, Sandra Lucinei Balbo¹, Marcia Miranda Torrejais¹

1. Universidade Estadual do Oeste do Paraná (Unioeste) – Cascavel, PR, Brazil.

*Email: ariadne_barbosa@hotmail.com

Obesity has become a major public health problem due to its increasing incidence [1] and is characterized by excessive accumulation of body fat, which can compromise the health of individuals [2]. Weight loss as a form of obesity treatment can be induced through diet or surgical treatment [3], and the duodenojejunal bypass (DJB) is being studied as a strategy for obesity treatment and related comorbidities [4]. As the implications of this procedure on skeletal striated muscles have not been elucidated yet, this study aimed to analyze the effects of DJB on the muscle fibers of the extensor digitorum longus muscle (EDL) of obese rats. All procedures involving the use of animals were approved by the Ethics Committee in the Use of Animals (CEUA) of UNIOESTE. Newborn Wistar rats were randomly distributed into two groups: control group (CTL; n = 5), which received saline solution (1.25mg/g body weight/day); and monosodium glutamate group (MSG; n = 10), which received MSG injections in the cervical region (4mg/g body weight/day) during the first five postnatal days to induce obesity. The rats were weaned at 21 days of age and kept on standard diet and water ad libitum. At 90 days of age, obese rats from group MSG were randomly distributed into two subgroups: group submitted to false operation (MSG FO; n= 5) and group submitted to DJB surgery (MSG DJB; n=5). Six months after surgery, the animals were killed and the EDL muscle was collected and frozen in liquid nitrogen. The right antimere muscle was sectioned (seven μ m thick) in a cryostat and submitted to the NADH-TR reaction. The samples from this technique were photo documented and used to measure the cross-sectional area of muscle fibers in four microscopic fields (20x objective). Muscle fibers were classified according to the proposal of Brooke and Kaiser [5]. The NADH-TR reaction showed muscle fibers from types I (small diameter and intense oxidative activity), IIA (intermediate diameter and moderate oxidative activity) and IIB (large diameter and low oxidative activity) in the three studied groups (Figures 1A, 1B and 1C). The average area of types I and IIB muscle fibers was reduced by 41 % in the group MSG FO in relation to CTL, whereas the type IIA fibers did not change between these two groups. When comparing the three types of fibers, the groups MSG FO and MSG DJB did not present significant differences. Thus, MSG-induced obesity was the determining factor in the alteration of the area of muscular fibers, since it resulted in the atrophy of muscular fibers that can lead to the loss of muscle function.

REFERENCES

- [1] V. M. de Oliveira & R.C. Linardi, Rev. Psiqu. Clin. 31 (2004).
- [2] A. R. O. Pinheiro et al. Rev. Nutr. 17 (2004).
- [3] G. Sergi et al. Ann. Nutr. Metab. 47 (2003).
- [4] B. Geloneze et al. Annals of Surgery. 256 (2012).
- [5] M.H. Brooke & K.K. Kaiser, J. Histochem. Cytochem. 18 (1970).
- [6] This research was supported by the Program PIBIC/UNIOESTE (Brazil).

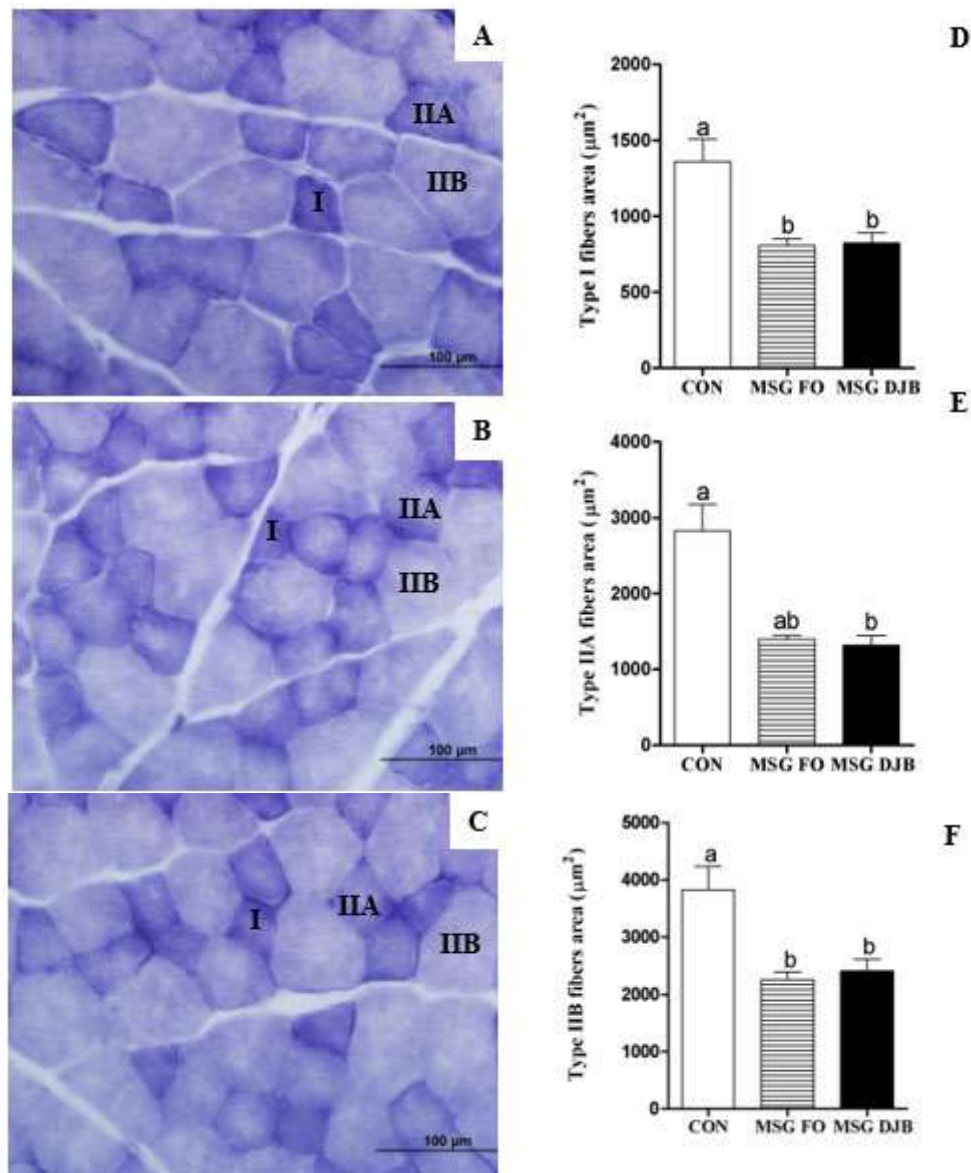
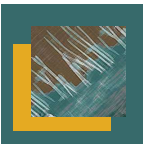
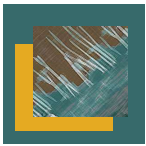


Figure 1 - Photomicrographs of the extensor digitorum longus muscle (EDL) of Wistar rats. Cross section, NADH-TR reaction. **A, B and C**: Type I, IIA and IIB muscle fibers in the control groups (CTL), MSG submitted to false operation (MSG FO) and MSG submitted to duodenojejunal bypass (MSG DJB), respectively. **D, E and F**: Average area of the different types of muscle fibers in the rats of groups CTL, MSG FO and MSG DJB. Values expressed as mean \pm standard deviation (n = 5). Different letters indicate significant differences. ANOVA: Area of fibers types I and IIB. Kruskal-Wallis: Area of fibers type IIA. ($p < 0.05$).



Ezrin Expression In Equine Endometritis – Preliminary Results

Barbara Paula dos Santos Batista^{1*}, Kássia Valéria Gomes Coelho da Silva¹, Juliana da Silva Leite², Ana Maria Reis Ferreira^{1,2}.

1. Programa de Pós-Graduação em Clínica e Reprodução Animal. Faculdade de Medicina Veterinária. Universidade Federal Fluminense, Niterói-RJ, Brazil.

2. Departamento de Patologia e Clínica Veterinária. Laboratório de Anatomia Patológica Veterinária. Universidade Federal Fluminense, Niterói-RJ, Brazil.

*Email: vetbarbara2002@yahoo.com.br

Endometritis is the major cause of infertility in mares [1], being a limiting factor in equine breeding, and may generate large economic losses [2]. The Ezrin protein is part of the ERM complex (Ezrin, radixin, moesin), a set of cytoplasmic membrane and cytoskeletal proteins, very conserved among species [3,4,5]. In cattle during the embryonic implantation phase, the relationship between endometrial glandular epithelial cells and increased expression of Ezrin was confirmed [6,7,8]. The analysis of anti-Ezrin antibody expression and its relationship with endometrial changes is unprecedented in veterinary medicine. Thus, the objective of this study was to evaluate the immunohistochemical expression of the Ezrin protein in endometritis of mares. This study was approved by the Ethics Committee on Animal Use (protocol 797/2016) of the Institution. Ten paraffin-embedded (FFPE) equine endometrial samples from mares in diestrus, ranging from four to nine years old, were selected from the archives of the Veterinary Anatomical Pathology Laboratory. Based on the histopathological classification of endometritis, samples graduated as IIb were selected [9]. Immunohistochemical evaluation (IHC) was performed using the streptavidin-biotin-peroxidase method (LSAB™ / HRP kit, Dako) for the detection of the primary anti-Ezrin antibody (polyclonal, 1:500, Santa Cruz Biotechnology). For the reading and evaluation of anti-Ezrin antibody immunostaining, a semi-quantitative scale was adopted [10], data were analyzed for high or low expression [11] and a descriptive histomorphological analysis was performed. All the samples evaluated showed high expression for Ezrin in the glandular cytoplasm, and with lower intensity it was observed immunostaining on the top and side of the endometrial gland. High expression of Ezrin in the microvilli of the endometrial glands was observed (Figure 1A). Increased expression of Ezrin occurred in glandular dilatations with fibrotic nests (Figure 1B). Inflammatory cells were extensively labelled, mainly lymphocytes (Figure 1A/B). Ezrin showed to be an important immunomarker to define the endometrial alterations of chronic and degenerative inflammatory character, thus affirming its value as a tool in the diagnosis and prognosis of equine endometritis.

REFERENCES

- [1] S.P. Brinsko et al., Manual of Equine Reproduction, 3^oed. Elsevier, 2011.
- [2] J.C.F. Jacob et al., Theriogenology, 77(6), (2012), 1159.
- [3] N. Sato et al., J. Cell Sci v. 103 (Pt 1) (1992) p.131. sep.
- [4] S. Tsukita et al., J. Cell Biol v.126 n.2 (1994) p.391. jul.
- [5] B. Fievet, D. Louvard, M. Arpin. Biochim Biophys Acta, v.1773 n.5 (2007) p.653.may.
- [6] K. Koshi et al., Placenta 32(7) (2011) 493.
- [7] H. Nakano et al., Cell Tissue Res 307(2) (2002) 225.
- [8] N. Hambruch et al., Placenta 31(1) (2010) 67.
- [9] R.M. Kenney, P.A. Doig. Equine endometrial biopsy. Philadelphia: W. B. Saunders Company. v.2. 1986.
- [10] S. Ferrari. Pediatr Blood Cancer. 50 (2008) 752
- [11] M.S. kim et al., J. Surg. Oncol. 97(2008) 456.
- [12] This research was supported by CNPq-CAPES (Brazil).

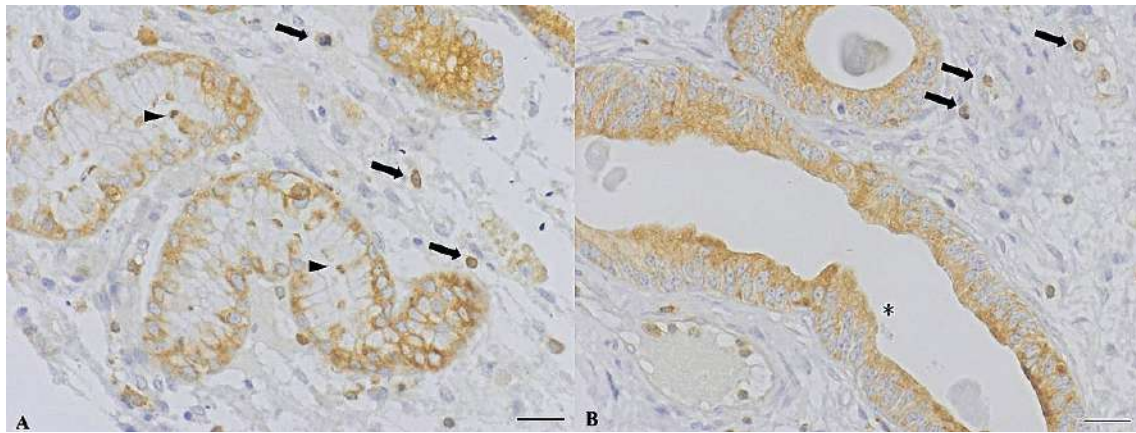
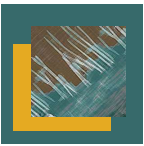
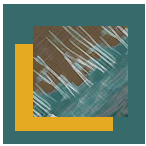


Figure 01 - Photomicrograph of equine endometritis. Immunohistochemical labelling for Ezrin. A/B. High immunoreactivity of Ezrin protein is observed in inflammatory cells (arrows). A. High immunoreactivity of Ezrin protein in the microvilli of endometrial glands (head arrow). B. High immunoreactivity of Ezrin protein in the glands with dilation and with fibrotic nests (asterisk). Bar = 20µm.



Chronic Equine Endometritis: HER-2 Receptor Expression – Preliminary Results

Barbara Paula dos Santos Batista^{1*}, Kássia Valéria Gomes Coelho da Silva¹, Juliana da Silva Leite², Ana Maria Reis Ferreira^{1,2}.

1. Programa de Pós-Graduação em Clínica e Reprodução Animal. Faculdade de Medicina Veterinária. Universidade Federal Fluminense, Niterói-RJ, Brazil.

2. Departamento de Patologia e Clínica Veterinária. Laboratório de Anatomia Patológica Veterinária. Universidade Federal Fluminense, Niterói-RJ, Brazil.

*Email: vetbarbara2002@yahoo.com.br

The endometrium, like all mucous membranes, presents cell populations that undergo constant physiological renewal, thus involving tissue growth and regression [1,2,3]. The concept of inflammation fits the theory of fibrosis development, based on altered responses to harmful stimuli, possibly due to tissue damage in the myometrium or hypoxia, leading to altered tissue repair and fibrosis [4,5]. HER-2 receptor is a transmembrane glycoprotein present in the plasma membrane of epithelial cells that transmits signals that regulate cell growth and multiplication from the outer of the cell to the nucleus [6]. The aim of this study was to evaluate the immunohistochemical expression of the HER-2 protein in chronic equine endometritis and its relation to endometrial fibrosis. This study was approved by the Ethics Committee on Animal Use (protocol 797/2016) of the Institution. Ten paraffin-embedded (FFPE) equine endometrial samples from mares in diestrus, ranging from 10 to 16 years old, were selected from the archives of the Veterinary Anatomical Pathology Laboratory. Based on the histopathological classification of endometritis, samples graduated as IIb were selected [7]. Immunohistochemical evaluation (IHC) was performed using the polymer method (Advance™ / HRP, Dako) for the detection of the anti-HER2 primary antibody (polyclonal, 1:200, Dako). HER-2 immunostaining intensity was classified according to the scoring system HerceptTest (Dako – Glostrup, Denmark). The established score was 0 to 3+ according to the staining intensity and quantity, where tumour cells were considered HER-2 positive when with scores 2+ or 3+. A descriptive statistical analysis was performed. The results obtained in the HerceptTest classification showed that 80% (n = 8/10) of the evaluated samples presented a score 2+. This classification was associated with increased HER-2 immunostaining in inflammatory and fibrotic foci, with presence of glandular dilatation (Figure 1). HER-2 immunostaining was also observed in endometrial glands in tissue growth process. High expression of HER-2 was observed on the lateral membrane of the endometrial gland, and it was even more pronounced in inflammatory and fibrotic processes (Figure 1B). HER-2 showed to be an important tool in the histomorphological evaluation of chronic equine endometritis, attesting its relationship with fibrotic and inflammatory endometrial process, and helping to diagnose it.

REFERENCES

- [1] C.P. Leblond. *Am. J. Anat.* v.160 (1981) p.114.
- [2] R.D. Medh, E.B. Thompson. *Cell Tissue Res.* v.301 (2000) p.101.
- [3] H.A. Schoon et al., *J. Reprod. Fertil. Suppl.* v.56 (2000) p.381.
- [4] G. Wegienka. *Med. Hypotheses* 79 (2012) 226.
- [5] P. Leppert, M. Fouany, J. H. Segars. *Understanding Uterine Fibroids.* J. H. Segars, (Ed.), John Wiley & Sons, Ltd, Oxford, 2013.
- [6] Roche. <http://www.roche.pt/sites-tematicos/her2/> Roche Farmacêutica Química, Ltda. (2016).
- [7] R.M. Kenney, P.A. Doig. *Equine endometrial biopsy.* Philadelphia: W. B. Saunders Company v.2. 1986.
- [8] This research was supported by CNPq-CAPES (Brazil).

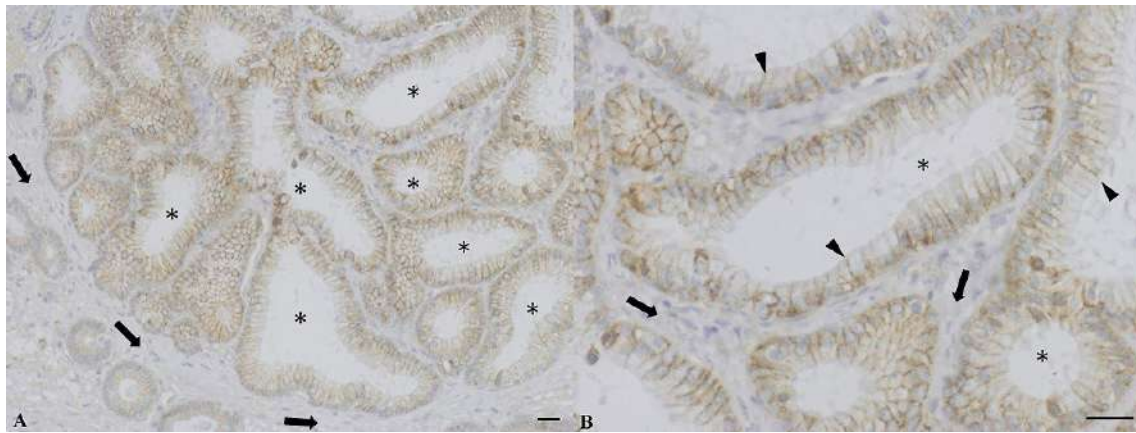
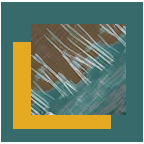
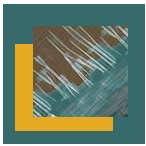


Figure 01 - Photomicrograph of equine endometritis. Immunohistochemical labelling for HER2 2+, using Herceptest scoring system. A/B. Periglandular fibrosis (arrows), with increased expression of HER-2 in the glands with dilation and fibrotic nests (asterisks). B. Increased HER-2 immunostaining in the lateral membrane of glands with dilatation and fibrotic nests (head arrow) Bar = 20µm.



Histopathological Analysis of Gills as an Indicator of the Aquatic Environment Quality in South Brazilian Grasslands

Bruna Graziela Zwetsch^{1*}, Mateus Santos de Souza¹, Renato Bolson Dala Corte² and Günther Gehlen¹

1. Laboratory of Comparative Histology, Feevale University, Novo Hamburgo, Brazil

2. Laboratory of Landscape Ecology, UFRGS, Porto Alegre, Brazil

*Email: bruna.zwetsch23@gmail.com

Water is a natural element essential to sustaining life, also supporting economic activities for social development (1). The loss of biodiversity and damage to aquatic ecosystems caused by anthropic actions have been growing at alarming rates in recent years, demonstrating the need to take measures and plan goals for the preservation and recovery of these ecosystems (2). Histological analysis has already been used as an important tool for environmental monitoring, where the analysis in gills, structures responsible for gas exchange / excretion, has been the main focus of the studies (3). The secondary lamellae are richly vascularized, covered by a simple squamous epithelium supported by pillar cells, which form gaps where the blood capillaries are inserted (4). In this context, and evidencing the importance of the Southern Fields as native natural environments in South Brazilian Grasslands (Pampa biome), the objective of this work is to evaluate changes in the aquatic environment through the histopathological analysis of the gills of *Bryconamericus iheringii* fish. The animals were collected (n = 5) in four streams in the region of São Pedro do Sul (Lajeado Monjolo, Capivari, Lajeado Quebra Dentes and Sanga das Tunas) in March 2014, and immediately sacrificed to obtain the gills. The samples were fixed in formaldehyde, embedded in paraffin, sectioned in rotating microtome in a thickness of 5µm and subsequently stained with hematoxylin and eosin. Eight fields containing four pairs of secondary lamellae per fish were analyzed, and the frequency of normal and altered lamellae was recorded, as well as the types of alterations (5). Statistical analysis of the data was performed using the Kruskal-Wallis test and differences were considered significant when $p < 0.05$. Among the alterations found, epithelial detachment was the most frequent damage, hyperplasia and hypertrophy were also observed. When evaluating the frequencies of tissue changes, we observed higher values of lamellae with damage to the animals of the Lajeado Monjolo stream, followed by the Capivari, Lajeado Quebra Dentes and Sanga das Tunas streams. The presence of histological alterations corroborates with data in the literature that suggest a relation with environmental contamination (3). However, more animals and collection points should be evaluated for a better characterization of the relationships between the data in focus.

REFERENCES

- [1] L.C. Figueiredo et al., *Geografia do Rio Grande do Sul: temas em debate*, UFSM, Santa Maria, (2010).
[2] S.H.M. Butchart et al., *Science.*, 328 (5982) (2010) p.1164. [3] J.A.P.N. Lins et al., *Revista Acadêmica: Ciências Agrárias e Ambientais.*, 8 (4) (2010) p.469. [4] T. Hibiya, *International Review of Hidrobiology.*, (1982) p. 147. [5] T. Dalzochio et al., *Biotemas.*, 29 (1) (2016) p. 75.

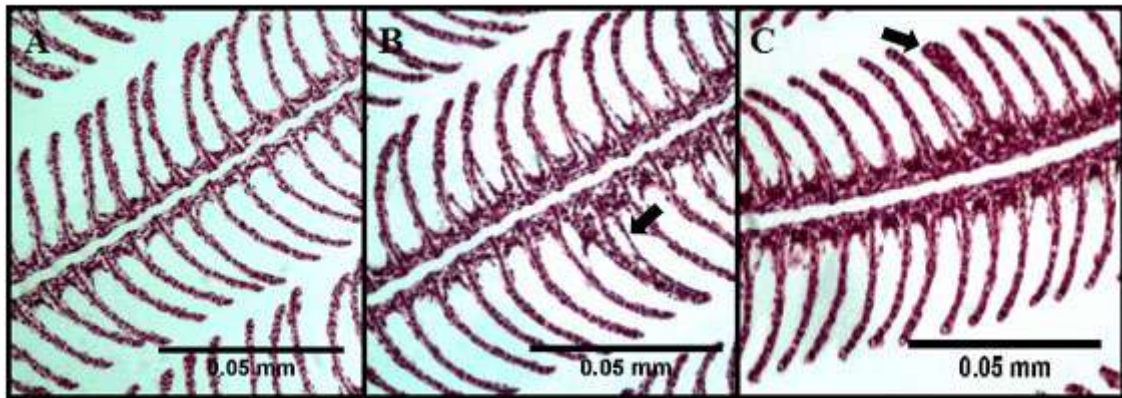
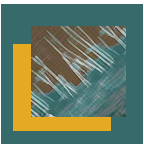
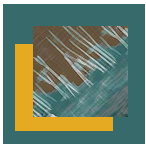


Figure 1: Representative images of histopathological changes found in *Bryconamericus iheringii* collected in four streams of the São Pedro do Sul region. (A) Normal lamella; (B) Epithelial detachment (arrow); (C) Hyperplasia and hypertrophy.



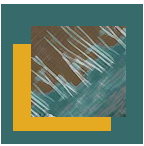
Effects of Type 1 Diabetes Mellitus on Developing Enamel

Bruna Larissa Lago Silva¹, Danila Lima Medeiros², Ana Prates Soares¹, Sérgio Roberto Peres Line³, Maria das Graças Farias Pinto⁴, Telma de Jesus Soares¹ and Alexandre Ribeiro do Espírito Santo^{5*}

1. Multidisciplinary Institute of Health, Federal University of Bahia – UFBA, Vitória da Conquista, Bahia, Brazil
2. School of Nutrition, Federal University of Bahia – UFBA, Salvador, Bahia, Brazil
3. Piracicaba Dental School, University of Campinas – UNICAMP, Piracicaba, São Paulo, Brazil
4. School of Veterinary Medicine and Zootechny, Federal University of Bahia – UFBA, Salvador, Bahia, Brazil
5. Institute of Health Sciences, Federal University of Bahia – UFBA, Salvador, Bahia, Brazil

*Email: arespirtosanto@ufba.br

Type 1 diabetes mellitus is characterised by chronic hyperglycaemia and oxidative stress caused by decrease or absence of insulin secretion by pancreatic β -cells [1,2]. These complications are responsible for structural and functional anomalies of tissues, probably including enamel defects [2,3,4], which are associated with higher susceptibility to caries [5]. Enamel formation is initiated by the secretion, processing and self-assembly of a complex mixture of proteins [6]. The establishment of an ordered enamel organic extracellular matrix (EOECM) seems to be a crucial step for the proper formation of the mineral phase. Polarizing microscopy has demonstrated that during the secretory stage, EOECM is strongly birefringent [7] and that this anisotropic property may be associated with the intact formation of enamel fluoride containing carbonated apatite crystals [8]. The aim of this study was to measure the birefringence of secretory stage EOECM of maxillary incisor teeth from rats that had been submitted to experimental type 1 diabetes mellitus. Twenty-three Wistar rats were divided into two groups: Diabetes group was submitted to a single intraperitoneal injection of streptozotocin (60 mg/kg; Alfa Aesar, Ward Hill, MA, USA) in 0.1 M citrate buffer solution, pH 4.5; and Control group was injected with equivalent volumes of 0.1 M citrate buffer solution alone, pH 4.5. Seventy-two hours after the injections and every 13 days, animals of both groups were subjected to glycaemia measurement (Accu-Chek® glucose meter, Roche, Mannheim, Germany). The rats that exhibited glycaemia dosage above 320 mg/dL were considered diabetics. Using this exclusion criterion, Diabetes group showed $n=8$ and a mean glycaemia of 568.85 ± 12.78 , and Control group exhibited $n=8$ and mean glycaemia of 113.4 ± 7.12 ($p < 0.01$; t test). Fifty-six days after the injections, animals from both groups were anesthetized with xylazine/ketamine (1/1, 0.2 mL/100g) and perfused with 2% formaldehyde, 0.5% glutaraldehyde in 0.2 M phosphate-buffered saline solution (PBS), pH 7.2. Hemimaxillae were then removed and immersed in fixative solution for 72 h. Decalcification was performed by 5% nitric acid, 4% formaldehyde for 12 h. After dehydration, decalcified samples were embedded in paraffin, and 5- μ m-thick longitudinal sections were obtained. The sections were treated with xylene for removal of the paraffin, and hydrated. Unstained sections of the hemimaxillae from each animal were analyzed in order to determine optical retardation (nm) of the area that showed the highest birefringence brightness in the secretory stage EOECM. Sections were immersed in 80% glycerin for 30 min before measurement. A Leica DM LP microscope (Leica Microsystems) equipped with polarizing filters, Brace-Köhler compensator (Wild Leitz, Wetzlar, Germany), and polychromatic light, was used [8]. Diabetic rats did not show statistically significant reduction in optical retardation values when compared with control rats ($p > 0.05$; Mann-Whitney). The results presented here suggest that the previously reported mature enamel defects caused by type 1 diabetes mellitus may not be associated with disturbance of the supramolecular organization of the secretory stage EOECM.



REFERENCES

- [1] World Health Organization (1999) Definition, diagnosis and classification of diabetes mellitus and its complications. Report of WHO consultation. Part 1. Diagnosis and classification of diabetes mellitus. WHO, Geneva.
- [2] R. Chalas et al., *Folia Morphol. (Warsz)*. 75 (2016) 275-80.
- [3] M. Atar et al., *Int. J. Paed. Dent.* 14 (2004) 301–7.
- [4] Y. T. Silva-Sousa, L. C. Peres and M. C. Foss, *Braz. Dent. J.* 14 (2003) 87–93.
- [5] R.P. Ellwood and D. O’Mullane, *J. Public Health Dent.* 56 (1996) 76-80.
- [6] M. L. Paine and M. L. Snead, *J. Bone Mineral. Res.* 12 (1997) 221-7.
- [7] A. R. do Espírito Santo et al., *Eur. J. Oral Sci.* 114 (Suppl. 1) (2006) 333-7.
- [8] A. R. do Espírito Santo et al., *Connect. Tissue Res.* 48 (2007) 39-45.
- [9] This research was supported by FAPESB (Brazil).
- [10] Bruna Larissa Lago Silva was supported by CAPES (Brazil).
- [11] Danila Lima Medeiros was supported by FAPESB (Brazil).

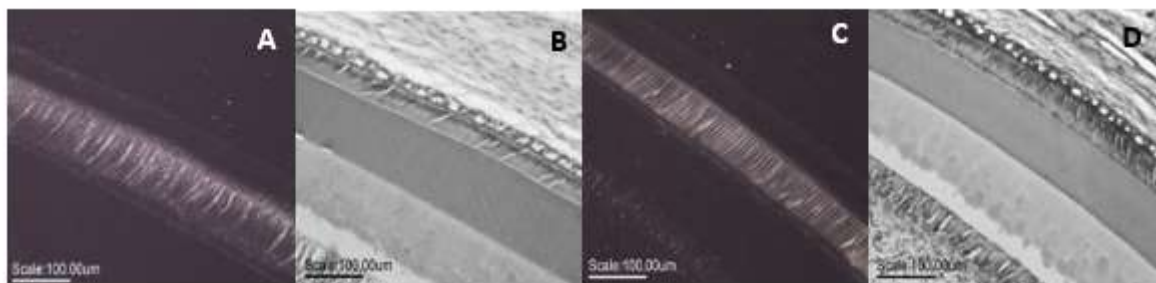


Figure 1. Light and polarizing microcopies of the enamel organic ECM from diabetic and control rats. In the polarizing microcopies, the analyzer is at 90° with the polarizer and the specimen exhibits position of maximum birefringence. Bar on the left inferior side represents 100µm. **A.** Birefringence of an unstained 5-µm-section of the enamel organic ECM from a control rat upper incisor. **B.** Bright field of section A, after staining with HE. **C.** Birefringence of an unstained 5-µm-section of the enamel organic ECM from a diabetic rat upper incisor. **D.** Bright field of section C, after staining with HE.

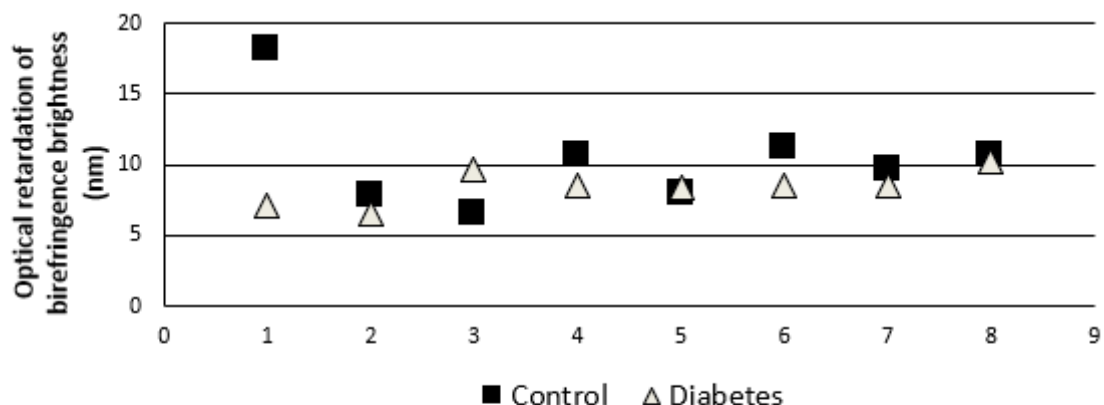
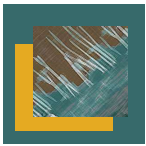


Figure 2. Optical retardations of birefringence brightness (nm) of unstained 5 µm thick sections of the secretory stage enamel organic ECM from diabetic and control rats. Experimental type 1 diabetes mellitus did not induce statistically significant decrease in optical retardation of birefringence brightness ($p > 0.05$; Mann-Whitney).



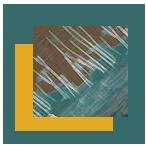
The Effect of Type 1 Diabetes Mellitus on Mature Enamel Structure and Physicochemical Properties

Bruna Larissa Lago Silva¹, Danila Lima Medeiros², Ana Prates Soares¹, Sérgio Roberto Peres Line³, Maria das Graças Farias Pinto⁴, Telma de Jesus Soares¹ and Alexandre Ribeiro do Espírito Santo^{5*}

1. Multidisciplinary Institute of Health, Federal University of Bahia – UFBA, Vitória da Conquista, Bahia, Brazil
2. School of Nutrition, Federal University of Bahia – UFBA, Salvador, Bahia, Brazil
3. Piracicaba Dental School, University of Campinas – UNICAMP, Piracicaba, São Paulo, Brazil
4. School of Veterinary Medicine and Zootechny, Federal University of Bahia – UFBA, Salvador, Bahia, Brazil
5. Institute of Health Sciences, Federal University of Bahia – UFBA, Salvador, Bahia, Brazil

*Email: arespirtosanto@ufba.br

Type 1 diabetes mellitus is characterised by chronic hyperglycaemia and oxidative stress caused by decrease or absence of insulin secretion by the pancreatic β -cells [1,2]. These complications are responsible for structural and functional anomalies of tissues, probably including enamel defects [2,3,4], which are associated with higher susceptibility to caries [5]. The aim of this study was to investigate if type 1 diabetes mellitus alters mature enamel structure and its physicochemical properties, using scanning electron microscopy (SEM), energy-dispersive x-ray (EDX) and cross-sectional microhardness assessment. Twenty-three Wistar rats were divided into two groups: Diabetes group was submitted to a single intraperitoneal injection of streptozotocin (60 mg/kg; Alfa Aesar, Ward Hill, MA, USA) in 0.1 M citrate buffer solution, pH 4.5; and Control group was injected with equivalent volumes of 0.1 M citrate buffer solution alone, pH 4.5. Seventy-two hours after the injections and every 13 days, animals of both groups were subjected to glycaemia measurement (Accu-Chek® glucose meter, Roche, Mannheim, Germany). Rats with glycaemia dosage above 320 mg/dL were considered diabetics. Using this exclusion criterion, Diabetes group showed n=8 and a mean glycaemia of 568.85 ± 12.78 , and Control group exhibited n=8 and mean glycaemia of 113.4 ± 7.12 ($p < 0.01$; t test). Fifty-six days after the injections, animals from both groups were anesthetized with xylazine/ketamine (1/1, 0.2 mL/100g) and perfused with 2% paraformaldehyde, 0.5% glutaraldehyde in 0.2 M phosphate-buffered saline (PBS), pH 7.2. Maxillary right incisors were collected, cleaned with an ultrasound, dehydrated and mounted on acrylic stubs. First they were sputter coated with carbon and submitted to EDX analysis. They were then sputter coated with gold for SEM (Jeol JSM-5600 V). Their left incisors were also collected, sectioned transversally and embedded in chemically activated polyester resin (Pre30Mi Arotec®). The specimens were then ground with 400-, 600- and 1,200-grit in a water-cooled polishing machine and cleaned with ultrasound. Soon after, Knoop microhardness tester was used to measure the enamel microhardness of specimens, with a load of 25 g for 5 s [6]. Indentations were made in the buccal enamel at 40 and 80 μ m from enamel-dentin junction. Afterwards, the specimens were polished, cleaned and sputter coated with gold for analysis of enamel rods' organization by means of SEM. Calcium/phosphorus ratios assessed by EDX were similar in Diabetes and Control groups ($p > 0.05$; Mann-Whitney). SEM revealed important ultrastructural alterations of enamel rods' organization and of enamel buccal surface. Diabetic group exhibited a significant decrease of Knoop microhardness numbers when compared to Control group ($p < 0.01$; t test). The present results indicate that type 1



diabetes mellitus may induce disturbances in structure and physical properties of mature enamel, which corroborate previous works.

REFERENCES

[1] World Health Organization (1999) Definition, diagnosis and classification of diabetes mellitus and its complications. Report of WHO consultation. Part 1. Diagnosis and classification of diabetes mellitus. WHO, Geneva.

[2] R. Chalas et al., *Folia Morphol. (Warsz)*. 75 (2016) 275-80.

[3] M. Atar et al., *Int. J. Paed. Dent.* 14 (2004) 301–7.

[4] Y. T. Silva-Sousa, L. C. Peres and M. C. Foss, *Braz. Dent. J.* 14 (2003) 87–93.

[5] R.P. Ellwood and D. O’Mullane, *J. Public Health Dent.* 56 (1996) 76-80.

[6] R.F. Gerlach et al., *Toxicology.* 175 (2002) 27.

[7] This research was supported by FAPESB (Brazil).

[8] Bruna Larissa Lago Silva was supported by CAPES (Brazil).

[9] Danila Lima Medeiros was supported by FAPESB (Brazil).

[10] We thank Professor J.A. Cury from the Department of Physiological Sciences, Piracicaba Dental School, University of Campinas – UNICAMP, for the use of Knoop microhardness tester.

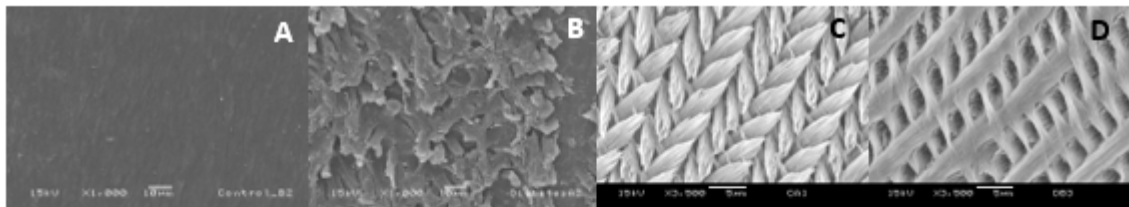
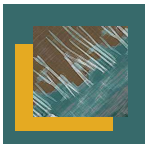


Figure 1. Scanning electron micrographs of enamel from maxillary incisor teeth of control (A and C) and diabetic (B and D) rats. Note important ultrastructural alterations in the specimens of diabetic animals.

Groups	n	Knoop microhardness number of cross-sectioned buccal mature enamel			
		At 40 µm from DEJ		At 80 µm from DEJ	
		Mean	SD	Mean	SD
Control	8	279.37	25.80	446.00	48.24
Diabetes	8	281.50	20.47	385.12	26.25
		p = 0.8578; t test		p = 0.0072; t test	

Table 1. Mature enamel cross-sectional microhardness values of diabetic and control groups. Significant difference was observed at 80 µm from enamel-dentin junction (DEJ). SD = Standard Deviation.



Differentiation of the species of the sturtevanti subgroup (saltans group, *Drosophila*) based on morphological characteristics analyzed by SEM.

Bruna Emilia Roman^{1*}, Lilian Madi-Ravazzi¹

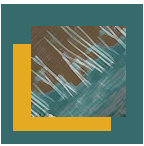
1. Departamento de Biologia, Laboratório de Genética, Ecologia e Evolução, Universidade Estadual Paulista Júlio de Mesquita Filho - UNESP/SP, Brazil.

*Email: brunaemiliar@gmail.com

The sturtevanti subgroup belongs to the saltans group of *Drosophila*, which is one of the four largest groups of the genus *Sophophora*. It is a subgroup of cryptic species identifiable by analysis of male terminalia, mainly by aedeagus. Using the scanning electron microscopy (SEM) (LEO 434VPi, Zeiss) we analyzed 10 morphological markers of the aedeagus and female's spermathecae. This study intended to study more detail possible differences among the species that could help their correct identification. The species evaluated were *D. sturtevanti*, *D. dacunhai*, *D. milleri* and a new specie *D. ehrmanii* [1]. We performed Kaneshiro's technique with some modifications to prepare the terminalia and aedeagi for SEM analysis. These structures were directly mounted to the SEM stub and sputter coated without critical-point drying. The spermathecae were placed in modified Karnovsky fixative for three days after immersed in a 1% osmium tetroxide solution in 0.05 M cacodylate buffer at pH 7.2 for 1 h at room temperature. These samples were washed with distilled water and then treated with increasing concentrations of acetone (30, 50, 70, 90 and 100%) for approximately 10 minutes in each solution. Then the spermathecae were passed through the critical point dried (K550, EMITECH) and mounted on a SEM stub with copper tape and sputter coated with gold/palladium. Images captured and analyzed using a scanning electron microscope showed the sturtevanti subgroup terminalia is characterized by an epandrium within parameres not fused and anal plates forming an U-shaped contour; the surstyli are large and concave and are joined by a small decasternum; primary and secondary teeth are present. No difference in the morphology of the terminalia was observed among the analyzed species (figure 1A-D). However, the aedeagi presented differences only observed through SEM analysis. Some characteristics of aedeagi are common to the analyzed species such as the medium ventral process and the apex of the aedeagus that form a structure similar to a duck's beak, the absent of the cape of the aedeagus, and the apodeme is short and sinuous, besides the presence of scales in the upper ventral region (figure 2 A-D). The aedeagi of these species differed mainly in relation to the size and shape of the apex of the aedeagus and in the presence or distribution of the scales in the medium ventral process (figure 2A-D). Besides, the angle formed by medium ventral process and the apical region of aedeagus is more open in *D. sturtevanti*, presenting a V shape, while *D. dacunhai* aedeagus it is wider and more curved than in *D. sturtevanti*, showing a C shape (figure 2A-D). A matrix of presence and absence of the characteristics of the aedeagus analyzed by SEM could be used to perform phylogenetic studies of the group [2][3]. The spermathecae of the analyzed species are not chitinized, contradicting the information in the literature [4]. However, the number of collars (structure observed in spermathecae) is as described in the literature data [4]. *D. sturtevanti* presents a single collar (figure 3A) while *D. dacunhai* and *D. ehrmanii* presents two collars (figures 3B, 3C). Some authors argue that the morphological characteristics no longer plays an important role in phylogenetic analyzes even associated with molecular studies [5]; however, molecular phylogeny still has limitations. Thus, we understand that the union of molecular data and morphological data is important for a more robust and reliable analysis of the complex process of speciation.

REFERENCES

- [1] L.Madi-Ravazzi et al, in preparation, (2017)
- [2] A.J. Souza et al., Plos One, 9(6) (2014) e97156
- [3] A.Yassin, Zoological Research, 30 (2009) 225
- [4] C.A. Mourão; H.E.M.C. Bicudo, Papéis Avulsos Zool. S. Paulo, 20(12) (1967) 123



[5] A.H. Wortley; R.W.Scotland, Systematic Biology 55 (2006) 677

Acknowledgments: We thanks Dr. Wolfgang Miller for providing the *D. ehmanii* strain and the FAPESP for financial support (process number 2014/059-0).

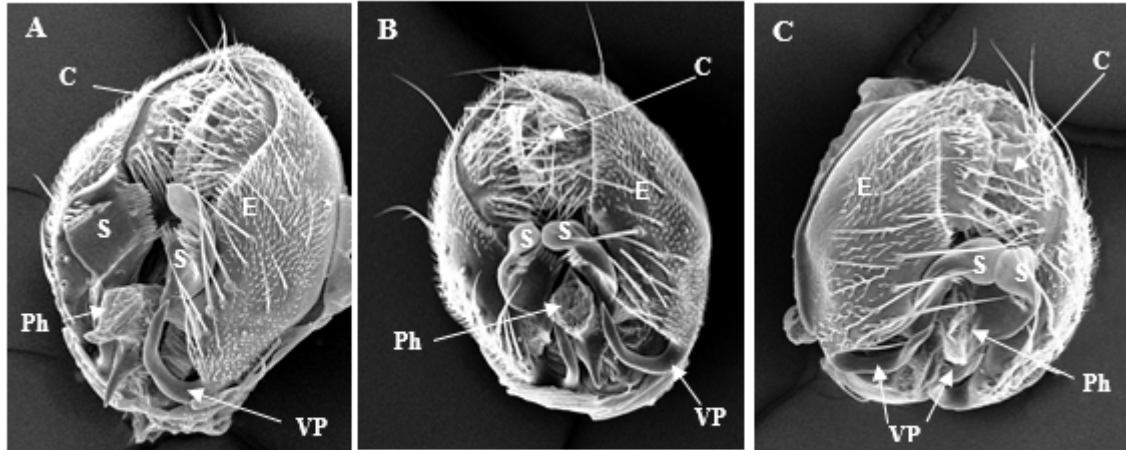


Figure 1A-C. Scanning electron microscopy of the terminalia of *sturtevantii* subgroup species. A. *D. sturtevantii*, 498 x magnification. B. *D. ehmanii*, 526 x magnification. C. *D. dacunhai*, 553 x magnification. C = cercus; E = epandrium; Ph = phallotreme; S = surstylus; VP = ventral paramere.

Figure 2A-D. Scanning electron microscopy of the aedeagus of *sturtevantii* subgroup species. A. *D. sturtevantii*, 1.490 x magnification. B. *D. ehmanii*, 1.020 x magnification. C. *D. milleri*, 1.250 x magnification. D. *D. dacunhai*, 1.680 x magnification. Note in *D. sturtevantii* and *D. ehmanii* (A and B) absence of the scales (Sc) in the middle ventral process (MVP_r) and in *D. milleri* and *D. dacunhai* (C and D) the presence of the much scales in this structure. In *D. dacunhai* (D) the double arrow head indicate a more slender shape at the end forming a groove observed too in *D. milleri* (see Souza et al 2014, figure 7C). AA = apex of aedeagus; A = apodeme; VPA = ventral paramere of the aedeagus.

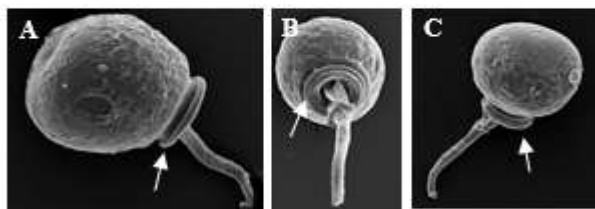
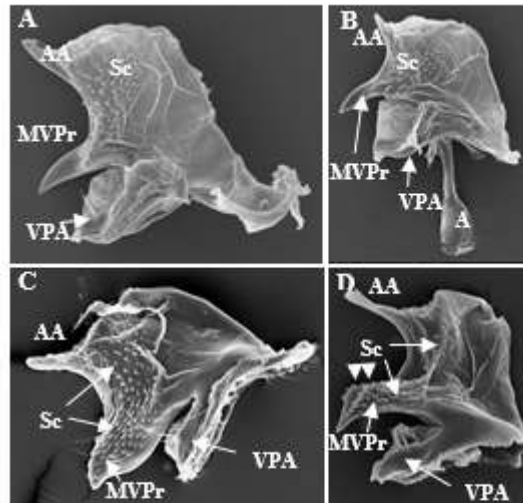
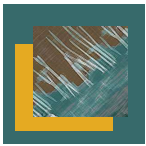


Figure 3A-C. Scanning electron microscopy of the spermathecae of *sturtevantii* subgroup species. A. *D. sturtevantii* 727x. B. *D. dacunhai* 635x. C. *D. ehmanii* 422 x The setae indicate the structure denominated collar only one in A and in B and C two collars.



Finasteride alters female prostate initial development

Bruno Domingos Azevedo Sanches^{1*}, Bruno Casagrande Zani², Juliana dos Santos Maldarine¹,
Patrícia Simone Leite Villamaior², Sebastião Roberto Taboga².

1. Institute of Biology – State University of Campinas - UNICAMP, Brazil. 2) Department of Biology - São Paulo State University – UNESP/IBILCE, Brazil.

*Email: sanchesbda@hotmail.com.

The prostate is an accessory reproductive gland that does not exist exclusively in males, in some species functional prostates are also found in females. However, the reason for the presence of functional prostate in about 90% of Mongolian gerbil females remains unclear [1,2], even in women, the occurrence of functional prostates varies from one-third to one-half of the female population and does not yet exist studies justifying such variation of occurrence [3]. In the case of the gerbil, there are also intrinsic variations in prostate development in females that may be incomplete in some individuals, so that the single lobe of the prostate does not acquire its bilateral conformation and the origins of such variations are also not elucidated. The use of finasteride, a 5 α -reductase inhibitor which leads to a reduced production of the most active form of testosterone and a decrease of androgen activity [4], in the prenatal period in gerbils could test the hypothesis that higher hormone levels of testosterone would be able to stimulate prostate development in females and justify the almost ubiquitous occurrence of prostate in female [5,6]. The aim of the present study was to evaluate the effects of a high dosage of finasteride (100 μ g BW/d) on prostatic development in gerbil females. For such purpose, pregnant females received such dose of finasteride by gavage from the 16th day of gestation until the day before birth, period in which the prostate begins its development. The pups were analyzed on the 7th day of postnatal life and the prostatic complex of the females were removed and included in PFA 4%, later histological sections were submitted to histochemical, immunofluorescence and three-dimensional reconstructions techniques. Our preliminary data demonstrated that such dosage is not yet able to inhibit the formation of the prostate in contradiction to what was previously hypothesized. Conversely, an earlier development of the gland was observed, it was evidenced by an increase in the number of prostatic branches and a greater thickening of the smooth periductal muscles. Together, the set of data points to the possibility that the reduction of androgenic activity could be associated with an increase in estrogenic action on prostate and that this would be of greater relevance for the development of the prostate in females, as previously defended for adult animals [2].

REFERENCES

- [1] R. A. FOCHI et al. *Biol. Reprod.*, 79(2008) 1084-1091.
- [2] L. S. CORRADI, *Int J Exp Pathol.*, 90(2009) 79-94.
- [3] W. DIETRICH *J Sex Med.*, 8(2011) 2816-2821.
- [4] S. AGGARWAL et al. *Steroids* 75 (2010) 109–53.
- [5] A. A. THOMSON et al. *Development* 129 (2002) 1905–1912.
- [6] B. G. TIMMS e L. E. HOFKAMP *Differentiation*, 82(2011) 173–183.

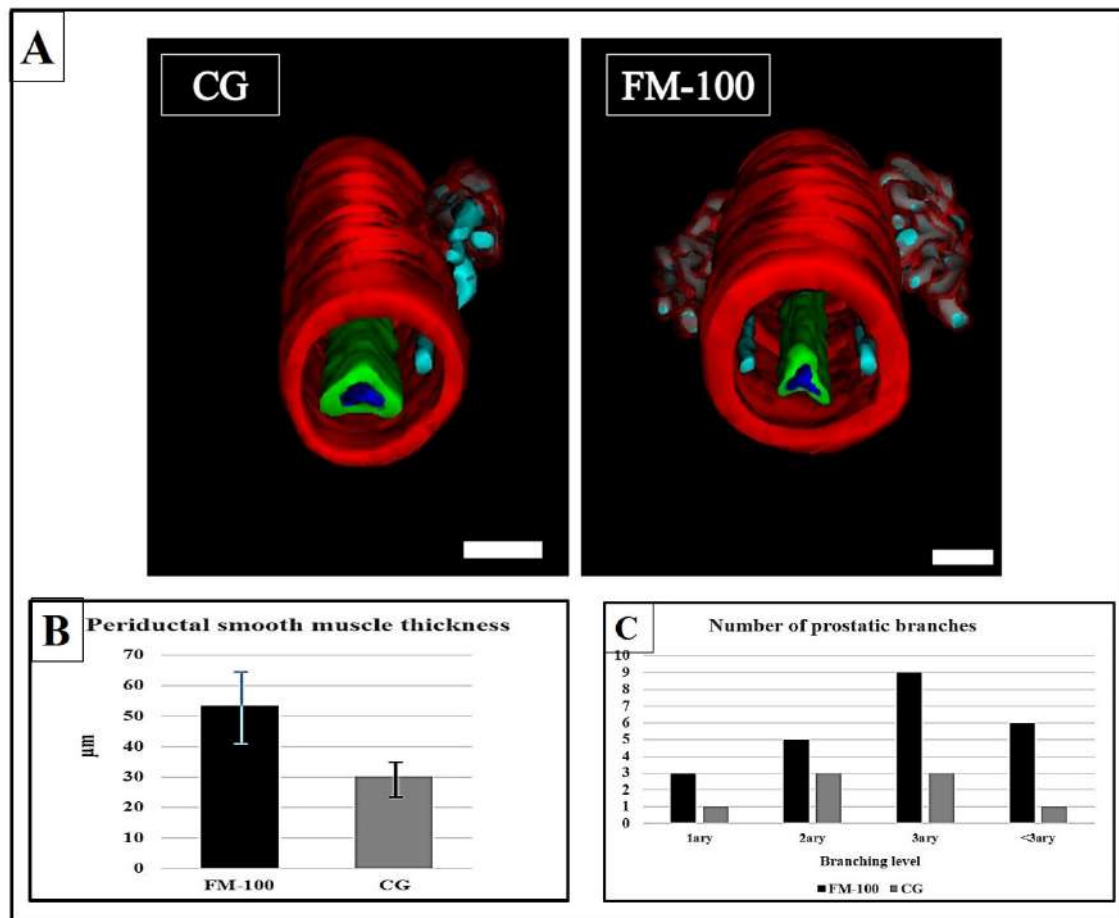
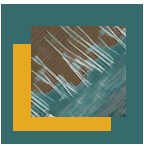
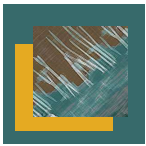


Fig. 1. (A) 3D reconstruction of the prostatic complex in females of the control group (CG) and the group treated with finasteride (FM-100) of puppies on the 7th day on postnatal life. (B) Graph in which is visualized an increase in the thickness of the periductal smooth muscle in the group treated with finasteride. (C) Graph showing an increase in the number of prostatic branches in the group treated with finasteride compared to the control group. Red (smooth muscle), cyan (prostatic branches), green (urethra), dark blue (lumen of the urethra), Bar (200µm).



Pre- And Post-oviposition Egg Morphology And Its Interaction with Sperm Cell In *Loxosceles intermedia* (ARANEAE: SICARIIDAE)

Camila Audrey dos Reis^{1*}, Maria Albertina de Miranda Soares², José Rosa Gomes², Cristina Lúcia Sant'Ana Costa-Ayub²

1. Master student of the Biomedical Science Postgraduate Program at the State University of Ponta Grossa (UEPG), Ponta Grossa, Paraná, South Brazil.

2. Structural, Molecular and Genetics Department (DEBIOGEM), Biological and Health Sciences Sector (SEBISA), State University of Ponta Grossa (UEPG), Ponta Grossa, Paraná, South Brazil.

*Email: camilaaudreyreis@gmail.com

The brown spider *Loxosceles intermedia* is a venous species largely distributed and especially abundant in the Paraná State, South of Brazil. In 2015, 2,629 accidents were registered involving this species of spider [1]. Its reproductive success, linked to the severity of the accidents, besides its great geographic distribution, characterizes this species as a public health problem [6]. In this sense, it is relevant to understand the mechanisms involved in its reproduction, thus enabling the development of strategies for its population control in urban areas. The gametogenesis [4] [8], and the initial embryonic developmental stages [5] have already been described for this species. It is also known that uncoiled sperm cells are found inside the oviduct, uterus internus and uterus externus of females at oviposition [3]. Now we have investigated some other aspects as the interaction oocyte-sperm cell during the transit inside the female reproductive ducts. For this, abdomens of *L. intermedia* adult females captured at oviposition, and newly deposited eggs were prepared for light microscopy (HE staining and Feulgen reaction). The results (Figure 1, A-H) show that: 1) during transit of oocytes through the oviducts, uncoiled sperm interact with the chorion (plates A-B); 2) a sperm cell is seen at the perivitelline region, when the oocyte passes through the uterus internus (plates C-E); 3), and in the egg, just after reaching the genital opening, chromosomes in a metaphasic plate were seen inside the cortical cytoplasm (plates F-G); 4) the same condition was observed for newly deposited eggs (plate H). Our results suggest that *L. intermedia* fertilization starts during the passage of the oocyte through uterus internus, reaching the uterus externus already as a zygote, which is partially in accord with the Suzuki and Kondo's descriptions for spiders [7]. The observation of metaphasic plate in the cortical cytoplasm of eggs passing through the genital opening and in newly deposited eggs suggest that probably the egg (still passing through its first meiotic division) is finishing its meiosis at this moment, in accord to the descriptions for *Drosophila* [2]. In our preparations, the male pronucleus and the endpoint of fertilization process was not observed. These aspects will be achieved in future investigations on the development of the zygote in the first hours after oviposition.

REFERENCES

- [1] Brazil. Ministério da Saúde/SVS - Sinan Net. 2015.
- [2] B. Loopin, et al.. *Open Biol.*, 5 (150076), 2015.
- [3] C. A. dos Reis, et al. XVIII Congresso da Soc. Bras. Biol. Cel., Anais, 2016.
- [4] C. L. S. Costa-Ayub, C.D. Faraco. *Arthr. Struct. Dev.*, 36, 2007.
- [5] M. A. Okada., Dissert. Mestrado, UFPR, 2010.
- [6] M. L. Fischer; J. Vasconcellos-Neto. *Braz. Jor. of Med. Entomol.* 43:756-65, 2005.
- [7] R. F. Foelix. *Biology of Spiders*, Oxford University Press, Oxford, 2011.
- [8] R. Morishita, et al.. *Anat. Rec. A Discov. Mol. Cell Evol. Biol.*, 273 (suppl 1) 2003.

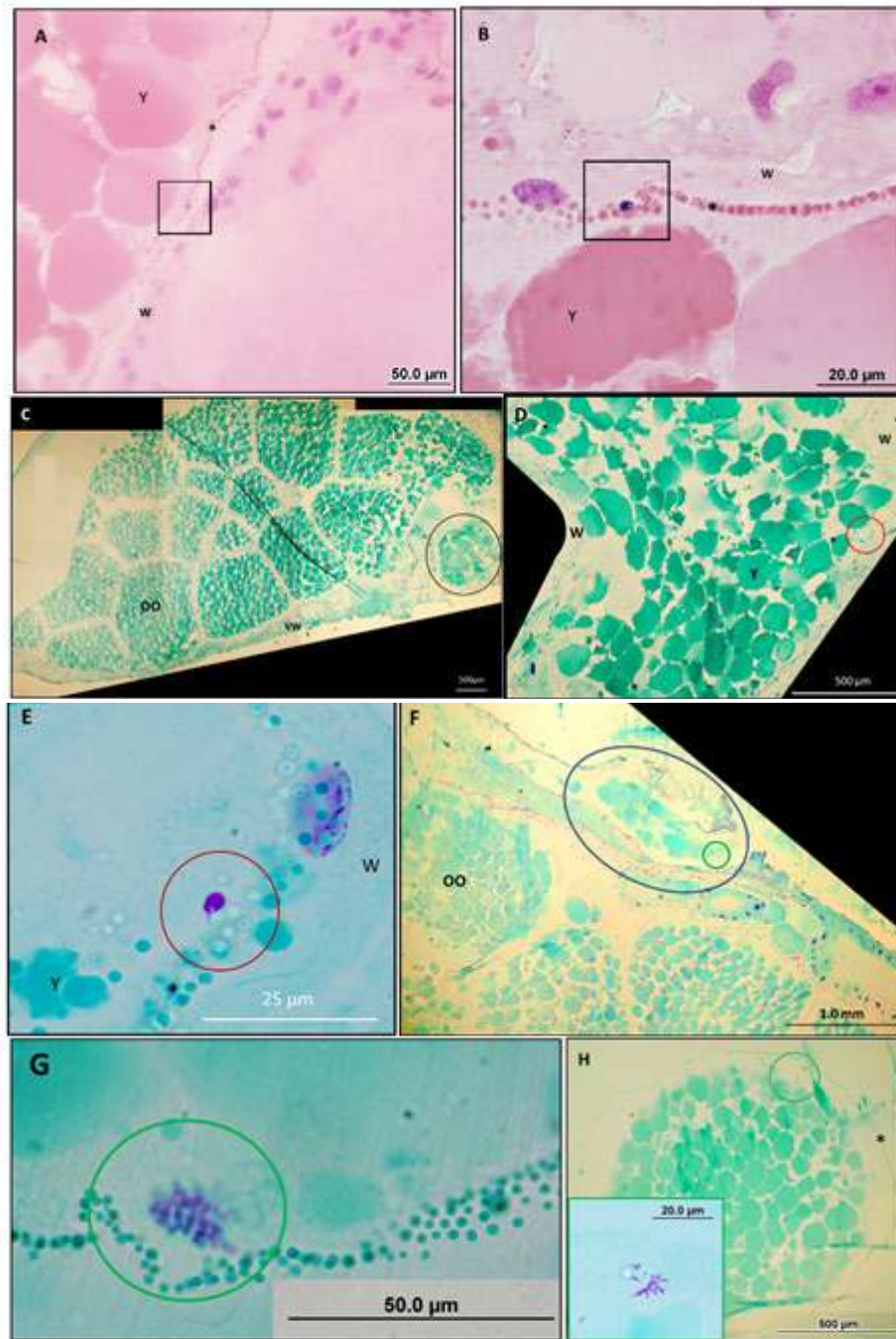
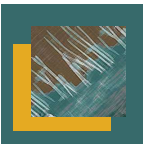


Figure 1. Plates A-E. Oocytes inside female body are passing through the female oviduct (A-B) and *uterus internus* (C-E). Sperm cell interacting with chorionic membrane (black square). F. One egg passing through the female *uterus externus*, and reaching the genital opening (blue ellipse). F-G. Chromosomes in metaphasic plate (green circle). H. Chromosomes in a metaphasic plate, at the cortical cytoplasm of a newly deposited egg (green circle). O - Oocyte, VW - Ventral wall, W - duct wall, Y - yolk grain, * - chorion. A-B. HE staining, C-H. Feulgen reaction.



The Effects Of Chitosan and Alginate Membranes Doped With Extract Of *Ilex paraguariensis* On Cell Proliferation During The Wound Skin Healing Process

Fellipe Antonio Canhetti Correa¹, Ana Luiza Glauser Fontes¹, Camila Audrey dos Reis¹, Nádia Favez Omar¹, Maria Albertina de Miranda Soares¹, Airton Vicente Pereira¹, José Rosa Gomes*¹

1. Laboratory of Cellular, Tissue and Developmental Biology - Ponta Grossa State University - Ponta Grossa – PR, Brazil

*Email: 1967jrgomes@gmail.com

The skin organ act as a protection barrier against to the external agents, being essential for the homeostasis control. Thus, treatments that could to accelerate the skin regeneration are important for the health care. Therefore, in this study we aimed to evaluate the effects of chitosan and alginate membranes doped with extract of *Ilex paraguariensis* (yerba mate) [2] on the skin cell proliferation during the wound healing process. In all, three rats were distributed in each group according to the treatments denominated as: chitosan, alginate *Ilex*, chitosan plus alginate and chitosan plus alginate plus *Ilex*. Under anesthesia with ketamine (50mg/100g) and Xilazina (2%/100g) a lesion of 1 cm² was produced on dorsal skin for each rat. Afterwards all rats received a dipyrone dose (100mg/mL diluted in water) during two days [3]. The membranes produced in the laboratory of Dr Pereira [1], were placed on the skin lesion. After 12 days, 1hour before the died under anesthesia, all rats received a i.p. injection of BrdU replication marker (1ml/kg). Skin fragments were immersed in 2% formaldehyde, dehydrated in alcoholic solution, included in paraffin and sections of 5µm were submitted to Masson's staining. Estimative of the length of lesion were taken in sections images. The sections were also submitted to the imunohistochemistry using an antibody anti-BrdU (Millipore) at 1:500µl/ml. The proliferative index was measured in epithelium, hair follicle and lesion and expressed by number of cells/sections. From the analysis of variance (ANOVA) showed that the chitosan alone reduced the length of lesion and increase the cell proliferation in the hair follicle and in the lesion region, but in the epithelium the chitosan plus alginate membrane increased the cell proliferation. Finally, it was possible to conclude that the chitosan membrane had the best effect on the cell proliferation during the wound skin healing process.

REFERENCES

- [1] M.G.N.Campus, Tese. Universidade Estadual de Campinas 2007.
- [2] C.I.Heck et al., J.Food Science, 72 (9) 2007.
- [3] Animal Ethic Committe CEUA. 05/2012.

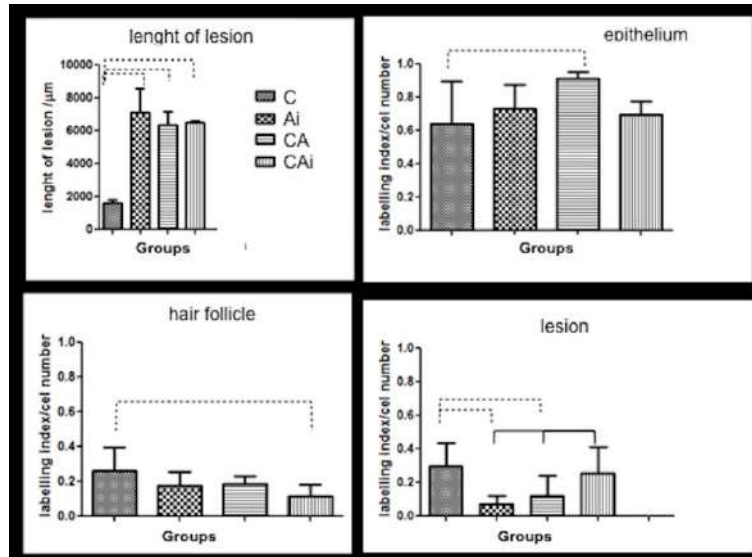
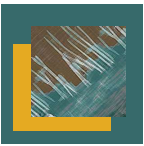


Figure 1. Mean \pm standard deviation for the lesion length and proliferative indexes for the epithelium, hair follicle and lesion. Brackets indicates $P < 0.05$.

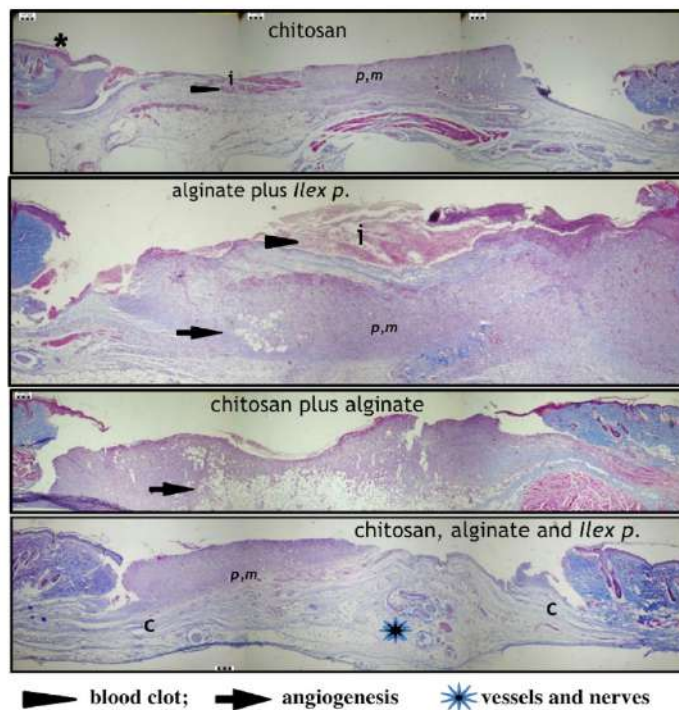
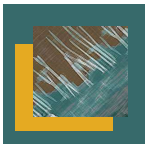


Figure 2. Representative photomicrography of the evolution of the wound repair phases: (i) inflammatory; (p,m) proliferation and migration and (c) contraction of the lesion.



An Evaluation of an Animal Model of Cerebral Palsy: the Effects on the Ultrastructure of the Extensor Digitorum Longus Muscle

Camila Kuhn¹, Caroline Covatti*¹, Pâmela Buratti¹, Lígia Aline Centenaro¹, Rose Meire Costa Brancalhão¹, Marcia Miranda Torrejais¹

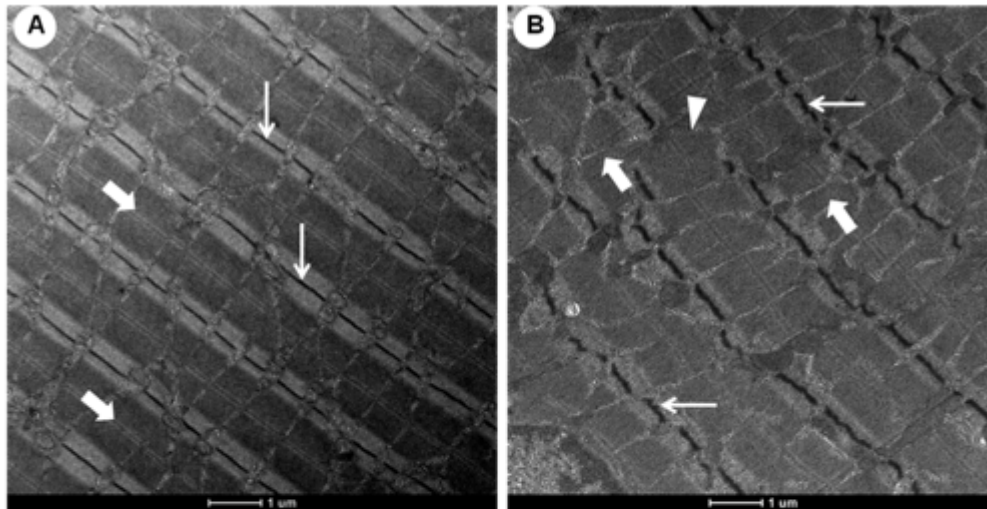
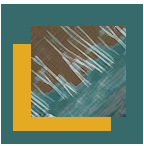
1. University of Western Paraná - UNIOESTE, Cascavel, Brazil.

*Email: carolcovatti@hotmail.com

Cerebral palsy (CP) refers to a chronic childhood encephalopathy that causes movement disorders [1], which is the main cause of physical disability [2]. The present study aimed to investigate the implications of an animal model of CP on the ultrastructure of muscle fibers in the extensor digitorum longus muscle (EDL) of Wistar rats. This research was approved by the Ethics in the Use of Animals Committee (CEUA - nº 24/16) of UNIOESTE. To obtain the litters, pregnant Wistar rats were injected intraperitoneally with vehicle (100 µl of sterile saline); and the others with LPS (200 µg/kg LPS in 100 µl of sterile saline). Both injections were performed every 12 hours, as from the 17th gestational day (G17) until the end of gestation (G21). The day of birth of the males offspring were separated into two groups: 1) the Control group - pups of rats injected with saline during pregnancy (CTL) and 2) the CP group - pups of rats injected with LPS during pregnancy, submitted to perinatal anoxia and sensorimotor restriction (CP). For perinatal anoxia the pups were placed in a closed chamber, partially immersed in water at 37° C, with a flow of 9 L/min of nitrogen (100%) for 20 minutes on day of birth (P0). The pups from the CP group underwent sensorimotor performed from P1 to P30, by immobilizing the hind limbs of the animals for 16 h / day. At 48 days of age, the right antimer was removed and reduced to longitudinal fragments, later they were submitted to routine transmission electron microscopy. The material was examined and photographed in a transmission electron microscope (CM100, Philips, The Netherlands). The morphology of the EDL muscle from the CTL group exhibited sarcoplasm with the presence of well-defined myofibrils and an organized Z-line (Figure 1A). In the animals from the CP group, there was dissolution and disorganization of the Z-line in several regions ($p < 0.05$) and rarefied or loosely arranged myofibrils ($p < 0.001$, Figures 1B and 1C) were observed. This experimental model reproduced focal ultrastructural changes similar to those found in patients with CP. Given this, could be an important tool to check the efficacy of early-start rehabilitation programs.

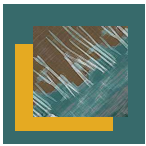
REFERENCES

- [1] N.T. Rotta. J. Pediatr. 78 (2002).
- [2] M.C. Mancini et al. Arq. Neuropsiquiatr. 60 (2002).
- [3] This research was supported by CAPES (Brazil).



C	Observations	CTL Group	CP Group
	Z Line disorganization (%)	18,3 ± 10,4	67,25 ± 8,3***
	Z line dissolution (%)	5,0 ± 5,0	23,8 ± 14,7*
	Myofibrillar disruption (%)	9,0 ± 9,6	25,8 ± 8,5*

Figure 1 - Transmission electron micrographs of 48-day-old rat EDL muscle in longitudinal section. **A:** CTL Group - Organized myofibrils (short arrow) and alignment of the Z line (long arrow). **B:** CP Group - Myofibrils, sparse or loosely arranged (short arrow), disorganization (long arrow) and dissolution of the Z line (arrowhead). Bar = 1µm. **C:** Values expressed as mean ± standard deviation. Z-line dissolution: Mann Whitney test. Other parameters: Student's t-test.



Morphological Study of the Extensor Digitorum Longus in the Offspring of Rats Submitted or Not to Roux-en-Y Gastric Bypass – RYGB

Camila Kuhn*¹, Pâmela Buratti¹, Caroline Covatti¹, Evandro José Beraldi¹, Sandra Lucinei Balbo¹, Marcia Miranda Torrejais¹

1. Western Paraná State University (UNIOESTE) – Cascavel, PR, Brazil.

*Email: camilaquiro@yahoo.com.br

Obesity is a chronic disease that grows rapidly every decade, characterized by the excess of adipose tissue. This leads to the emergence of associated diseases, including musculoskeletal disorders [1]. Maternal obesity can also affect fetal metabolism, inducing the development of diseases in adult life [2]. Bariatric operation emerge as an option for coping with obesity and its comorbidities, and the Roux-en-Y gastric bypass (RYGB) is one of the most performed bariatric surgeries [3]. As the morphological and functional integrity of muscle tissue is directly related to health [4], the aim of this study was to quantify fibers, nuclei and nuclei/fiber ratio of the extensor digitorum longus (EDL) in the offspring of rats submitted or not to RYGB operation. All procedures involving the use of animals were approved by the Ethics Committee in the Use of Animals (CEUA) of UNIOESTE. To obtain the offspring, 45 Wistar rats were distributed into two groups: control group (CTL), which received standard diet; and cafeteria group (CAF), which received cafeteria diet and soda for 15 weeks. After this period, the CAF group was divided into two groups: false operated group (CAF FO), submitted to false operation; and cafeteria RYGB (CAF RYGB), submitted to RYGB operation. After the operation, both groups continued to receive cafeteria diet until the end of the experiment. The breeding period of the three experimental groups began at 23 weeks of age. The offspring of the first generation obtained were denominated according to the treatment of the mothers (CTL-F1, CAF FO-F1, CAF DGYR-F1) and received standard diet from weaning until 120 days of age. After the animals were killed, the right EDL muscle antimere was frozen in liquid nitrogen. The samples were cryosectioned (seven μm thicknesses) and stained with Hematoxylin-Eosin (HE). The quantification of muscular fibers, nuclei and nuclei/fiber ratio was performed by the analysis of 10 photodocumented microscopic fields (40x objective). The muscle fibers of the three studied groups showed regular morphology, with polygonal, multinucleate fibers and peripheral nuclei (Figure 1A, B e C). Group CAF DGYR-F1 showed an increase of 27 % in the number of fibers, compared to group CAF FO-F1 ($p = 0,010$; Figure 1D). No difference was observed in the number of nuclei between the three studied groups ($p = 0,386$; Figure 1E). The nuclei/fiber ratio analysis showed a reduction of 17 % in the CAF DGYR-F1 group, compared to the CTL-F1 group ($p = 0,011$; Figure 1F). These results show that the RYGB operation in obese rats affected the muscular fibers in the offspring, which may compromise muscle integrity.

REFERENCES

- [1] D. Aune, et al., *Brazilian Journal of Microbiology*.353 (2016).
- [2] S. J. Dijk, et al., *International Journal of Obesity*.39 (2015).
- [3] K. Spaniolas, W. J. Pories. *Surgery for Obesity and Related Diseases*. (2016).
- [4] M. J. Benton, et al., *American Journal of Nursing*.2 (2014).
- [5] This research was supported by CAPES.

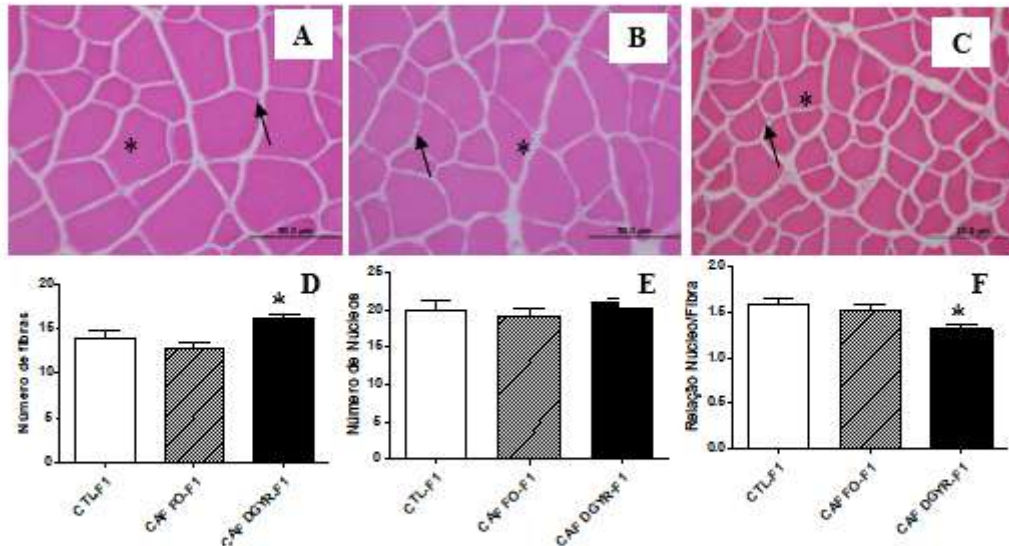
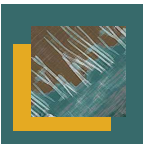
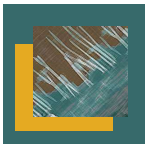


Figure 1 - Photomicrographs of the EDL muscle of Wistar rats. Cross section, HE staining. A, B and C: Muscular fibers (asterisks) and peripheral nuclei (arrow) of the control (CTL-F1), false operated (CAF FO-F1) and cafeteria groups (CAF DGYR-F1), respectively. D, E and F: Values referring to the number of muscle fibers, number of nuclei and nuclei/fiber ratio. Values expressed as mean \pm standard deviation. One-way ANOVA. * $p < 0.01$.



Ultrastructural Aspects of *Trichodina heterodontata* in *Carassius auratus* (Goldfish) Gills

Carla Renata Serantoni Moyses¹, Diva Denelle Spadacci-Morena², José Guilherme Xavier¹,
Anuska Marcelino Alvares-Saraiva¹, Maria Anete Lallo¹

1. Pós-Graduação em Patologia Ambiental e Experimental, Universidade Paulista, São Paulo, Brazil.
2. Instituto Butantã, Laboratório de Fisiopatologia, São Paulo, Brazil

The trichodinids group of peritrichs, which includes *Trichodina*, are important ectoparasites of freshwater and marine fish worldwide [1]. Infected fish often have a greyish sheen due to excess mucus production and fins may become frayed. Erosion of the epithelium can occur [2]. *Trichodina* often occur in conjuncture with other ectoparasites and their presence in large numbers is indicative of poor water quality and/or excess stocking [3]. There are few studies of the relationship between the host and parasite in trichodinid-diseased fish. Here, gills of *Carassius auratus* were analyzed by light and transmission electronics microscopy (TEM) for ultrastructural study of the parasite *Trichodina heterodontata* and the histological lesions caused by its presence. Goldfish *C. auratus* were obtained from ornamental fish farm where several fish species were growing together and separated only by age. Fish (n= 30) were collected and transported to the laboratory according to standard procedures. Fish were anaesthetized by immersion in solution of tricaine methane sulfonate until paralysis of the operculum. For TEM, small pieces of gill were fixed in 2% glutaraldehyde in 0.2 M cacodylate buffer (pH 7.2) at 4°C for 10 h, post-fixed in 1% OsO₄ buffered for 2 ` 1 h and routinely processed. Major histological changes were characterized by sub-epithelial edema with epithelial displacement of the gill filaments. There was also epithelial hyperplasia with focal areas of lamellar fusion and a slight mononuclear inflammatory infiltrate. The ectoparasitic ciliate *Trichodina heterodontata* are loosely placed between two gill filaments (Fig.1A). The general shape of trichodinid was dome-shaped or hemispherical when free, but disc-like when attached and sucking the host (Fig.1A,B), with which it remains adhered by cilia. The locomotor fringe is a complex structure. The main component is a wreath of cilia (lc), which encircles the organism near its basal end. The kinetosomes of the basal row of cilia are associated with elements of the adhesive disc (ad) (Fig.1A,B,C). The oral apparatus consists of an adoral ciliary (ad), a buccal cavity (bc), and the cytostomal area (arrow) (Fig.1C). The cytoplasm contains many food vacuoles (fv), bacteria (b) and mitochondria (m). The most prominent organelle seen in a longitudinal section of *Trichodina* (Fig. 1D) is the macronucleus (mn). The ultrastructural analysis allowed to observe the cilia structure involved in the locomotion and feeding of the parasite. The fixation to the gills by the basal cilia is a factor of aggression preponderant for the development of the inflammation observed in many cases of *Trichodina* infestation.

Keywords: MET

REFERENCES

- [1] H.E. Roberts et al., *Vet. Clin. Exot. Anim.* 12 (2009) 609–638.
- [2] P.T.K. Woo, D.W. Bruno, *Fish diseases and disorders viral, bacterial and fungal infections*, Wallingford, CABI, 2012.
- [3] A.G. Swennes et al., *Dis. Aquat. Org.* 69 (2006) 227–232.

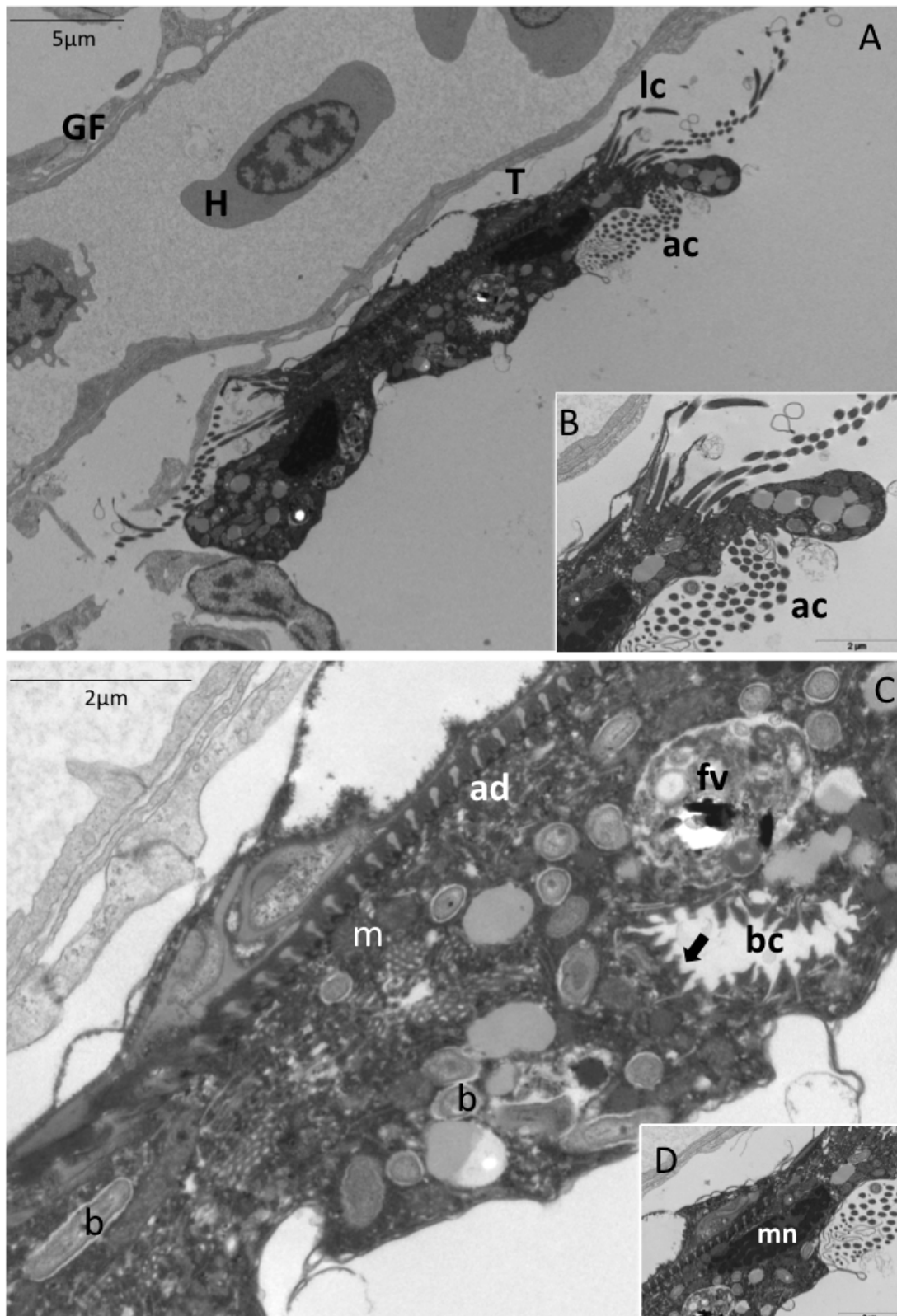
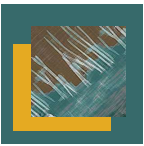


Figure 1. Transmission electron micrographs of gill epithelium infested by *Trichodina heterodentata* from goldfish. A) *Trichodina* (T) adhered to the gill filaments (GF), hemocytes (H). B) Detail of adoral ciliary (ac) and locomotor cilia (lc). C) In the cytoplasm some food vacuoles (fv), buccal cavity (bc), cytostome (arrow), bacteria (b), mitochondria (m) and adhesive disc (ad). D) Detail of macronucleus (mn).



Neem Oil Compromises The Cellular Cortex Of The Midgut Cells Of *Ceraeochrysa claveri* (Neuroptera: Chrysopidae)

Carolina Massucci Marciano da Silva^{1*}, Shelly Favorito de Carvalho¹, Elton Luiz Scudeler², Daniela Carvalho dos Santos^{1,2}

1. Electron Microscopy Center, Institute of Biosciences of Botucatu, UNESP - São Paulo State University, Botucatu, SP, Brazil.

2. Laboratory of Insects, Department of Morphology, Institute of Biosciences of Botucatu, UNESP - São Paulo State University, Botucatu, SP, Brazil.

*Email: cmassucci@ibb.unesp.br

Neem oil (*Azadirachta indica* A. Juss) (Meliaceae) is among biopesticides most widely used worldwide, highlighting the azadirachtin as main active component, responsible for the main sublethal effects on insect [1]. Many studies have shown the direct and indirect effects of exposure of natural enemies to neem products, questioning the safety and compatibility in trying to integrate biological control agents with the neem-based biopesticides. Previous works with the green lacewing *Ceraeochrysa claveri* (Navás, 1911) showed that intake of contaminated prey with neem oil during the larval stage affected the morphology of midgut epithelial cells [2]. The cellular cortex, composed of actin filament is important to maintain the integrity of the plasmatic membrane and sustain the microvilli. Therefore the cellular cortex is essential to preserve the physiological functions of the columnar cells, such as secretion and absorption processes in the midgut. To verify the action of neem oil on the cellular cortex, larvae of *C. claveri* were fed on eggs of *Diatraea saccharalis* treated with neem oil at a concentration of 0% (control group), 0.5%, 1% and 2% throughout the larval stage. The midgut obtained from larvae (third instar), pupae (fifth day) and adults (newly emerged) were processed for confocal microscopy [3]. Tissue sections (7 µm) were incubated with Phalloidin-TRITC (500 µg/1 ml methanol, diluted 1:900 in PBS) and mounting medium containing DAPI used on the sections. The samples were examined with a Leica TCS SP5 confocal microscope. We observed positivity for the striated border in larvae, pupae and adults, and especially for the cellular cortex in the apical region of columnar cells in adults of the control group (Figs. 1A-C). For all groups submitted to neem oil, we observed regions of the striated border and the cellular cortex of columnar cells with no positive reaction to F actin, indicating alterations in the cytoskeletal organization of these cells (Figs 1D-L). All evaluated concentrations induced morphological changes which were not concentration dependent. By the labelling of actin filaments by phalloidin, we note the occurrence of regions on the cell cortex with absence of positive staining for actin, which corroborates with previous observations [3, 4]. The dysfunction of the cell cytoskeletal meshwork in these regions results in the loss of the apical membrane tension, which further leads to the formation of protrusions and cell lysis [5, 6]. The loss of cytoskeleton integrity caused by neem oil intake, especially in the cell cortex, cooperates with alteration of midgut cells' morphology.

REFERENCES

- [1] E.D. Morgan. *Bioorg. Med. Chem.* 17 (2009) 4096-4105.
- [2] E. L. Scudeler; D.C. Santos. *Micron* 44 (2013) 125-132.
- [3] E. L. Scudeler et al., *Micron* 80 (2016) 96-111.
- [4] A. Anuradha et al., *Insect Biochem. Mol. Biol.* 37 (2007) 627-634.
- [5] L.F. Barros et al., *Cell Death Differ.* 10 (2003) 687-697.
- [6] G. Charras; E. Paluch. *Nature Rev. Mol. Cell Biol.* 9 (2008) 730-736.
- [7] This research was supported by FAPESP (2014/15016-2) (Brazil).

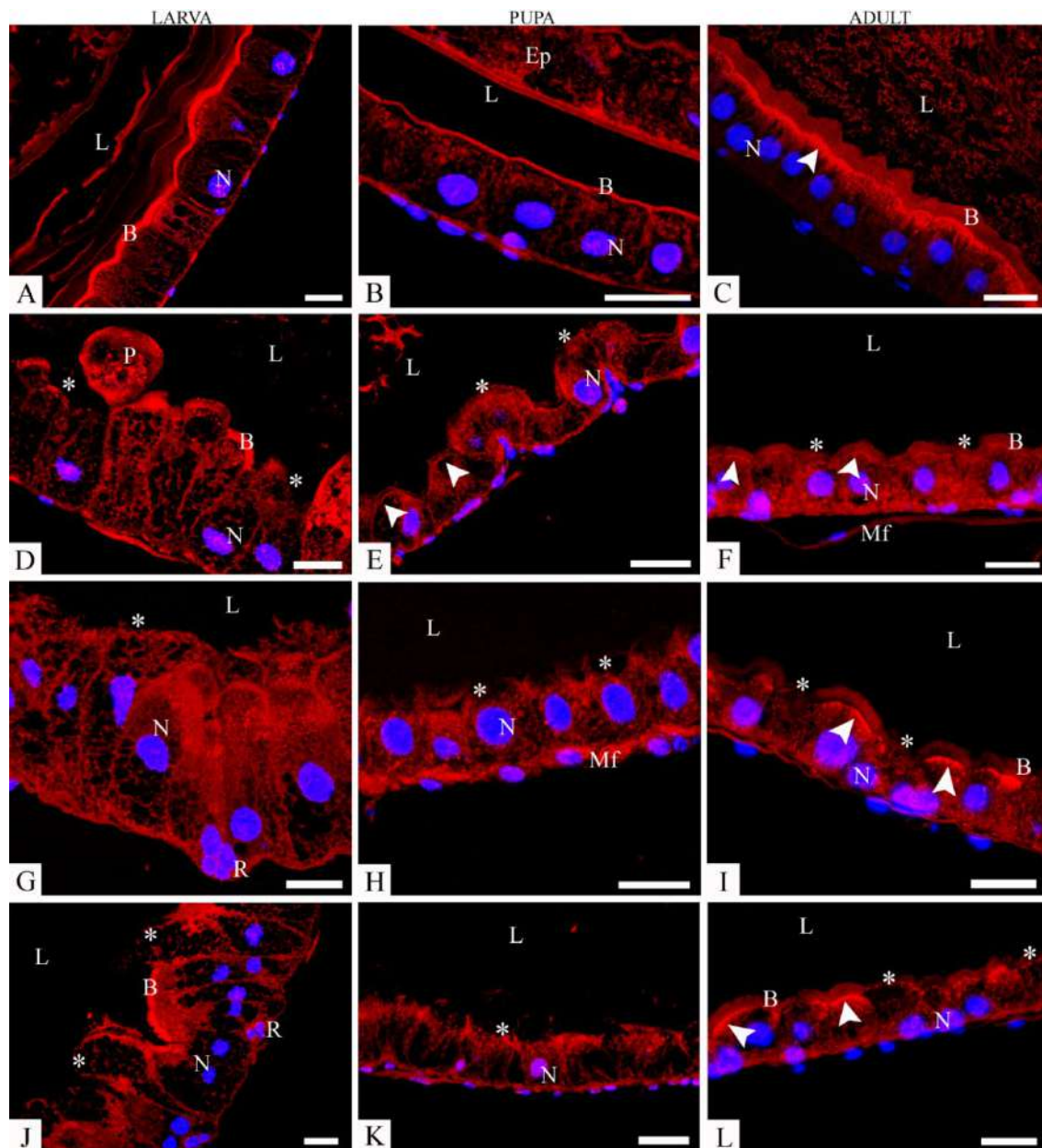
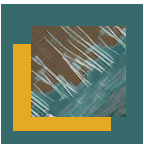


Fig. 1. Photomicrograph of the midgut epithelium of larva, pupa and newly emerged adult of *Ceratohyrcha claveri* originating of larvae subjected to the control group and treatments with neem oil. **(A-C)** Control group of larva, pupa and adult respectively. Positive reaction to F actin in the cellular cortex (▶) and striated border (B) composed by microvilli. Nuclei of columnar cells (N) and regenerative cells (R) were labeled by DAPI. **(D-F)** Neem oil 0.5%. **(G-I)** Neem oil 1%. **(J-L)** Neem oil 2, respectively. Note the regions of the cellular cortex and striated border with absence of F-actin (asterisk). Old larval midgut epithelium (Ep); Cytoplasmic protrusion (P); Muscle fibers (Mf); Lumen (L). Bars = 20 µm.



Role of Native Microorganisms in Iron and Manganese Cycling in Doce River and Tributaries Affected by Mining Waste from Collapsed Fundão Dam

Carolina N. Keim^{1*}

1. Instituto de Microbiologia Paulo de Góes, Universidade Federal do Rio de Janeiro, Rio de Janeiro, RJ, Brazil.

*Email: cnkeim@micro.ufrj.br

Doce River basin drains a main mining district in Brazil. Current and past mining of Fe, Au, Mn, and Al lead to grinding and leaching of ore rocks, generating fine particles and soluble metals, which reach Doce River and tributaries. In addition, land erosion due to conversion of forests into pastures and discharge of untreated domestic sewage led to increase in water turbidity and eutrofication. Over this scenario, on November 5th 2015, the burst of a large iron mine-tailing dam from Samarco Mining Company added estimated 34 million m³ of mine waste to Gualaxo do Norte River, Carmo River, and then Doce River mainstream. After the accident, water quality parameters such as dissolved Fe and total As, Cd, Cr, Hg, Mn, Ni, and Pb largely exceeded the current Brazilian standards [1]. Dissolved metals in natural waters depend on several factors, including pH, dissolved oxygen and Eh, organic matter, and microbial activities. In this work, we used complementary approaches to access the role of microorganisms in dissolution and precipitation of iron and manganese minerals in Doce River and its tributary Gualaxo do Norte. For observation of the ability of native microorganisms for reductive dissolution of Fe and Mn minerals, we used anaerobic enrichment cultures coupled to periodic measurements of reduced Fe(II) and Mn(II, III) species in the liquid phase. To access mineral precipitation associated to microorganisms in native biofilms, we maintained glass slides and coverslips immersed in the river to enable the growth of biofilms. Light and scanning electron microscopy of biofilms showed a thin, heterogeneous organic film containing sparse microbial cells associated to both primary and secondary mineral particles (Fig. 1a-b). EDS showed that most microbial cells contained Fe (Fig. 1c). Some cells and secondary minerals contained also Mn in addition to Fe. The presence of Fe and Mn in microorganisms and associated secondary minerals evidence the role of native microorganisms in metal concentration and/or precipitation. EDS analysis of primary mineral particles attached to the biofilm showed that most of them are composed by iron oxides or silicates (Fig. 1e), which agree with the composition of Samarco's mine waste [2] and indicate a role for biofilms in stabilization of fine-grained particulate. Reductive dissolution experiments showed that Fe-reducing microorganisms are present and active in river sediments, and that they are able to reductively dissolve Fe from synthetic iron oxy(hydro)xide. Thus, native microorganisms participate actively in the biogeochemical cycle of Fe, and also in the precipitation of Mn minerals in Doce River and tributaries. In addition, biofilms show a role in the stabilization of fine particles of mining waste [3].

REFERENCES

[1] http://portal1.snirh.gov.br/arquivos/Doce/ANA/relatorios/EncarteRioDoce_22_03_2016v2.pdf

[2] J.M.M. Pires et al., *Revista Árvore*, 27 (2003) 393-397.

[3] We thank LabNano for electron microscopy facilities. This work was supported by FAPERJ and CNPq Brazilian agencies.

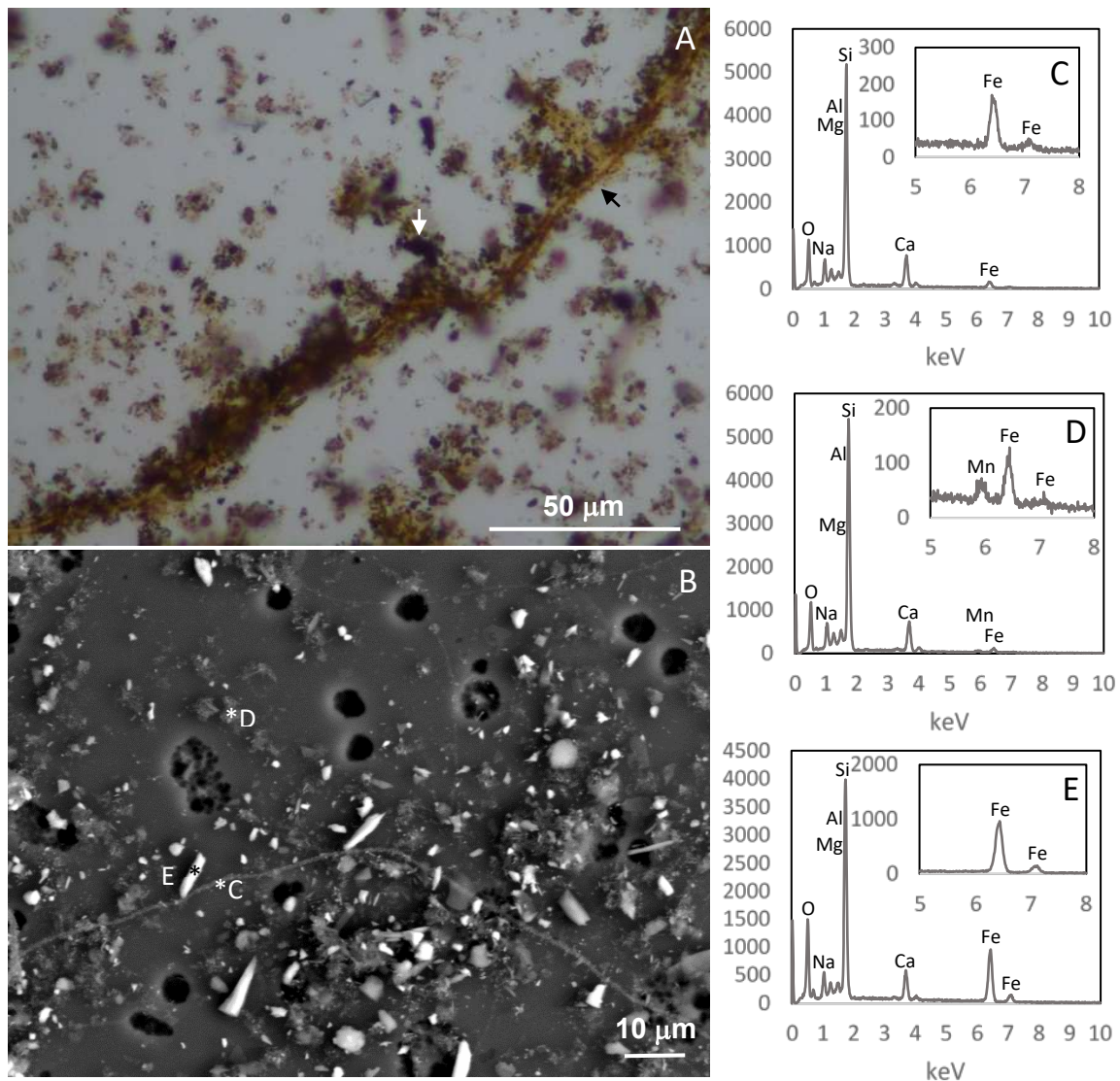
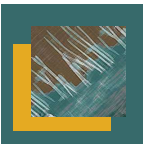


Figure 1: Microscopy and analysis of biofilms from Doce River showing filamentous microorganisms associated to both primary and secondary minerals. (A) Bright field light micrograph showing a filamentous microorganism sheath impregnated by secondary minerals (black arrow) and coated by primary mineral particles (white arrow). Note the abundance of mineral particles scattered through the field of view. (B) Scanning electron micrograph showing several filamentous microorganisms (e.g. C), as well as secondary (D) and primary (E) minerals. Asterisks mark the sites where EDS spectra were obtained. Backscattered electrons, 25kV. (C, D and E) EDS spectra of a filamentous microorganism (C), a secondary (D) and a primary (E) mineral. Observe that the filament contains Fe, the secondary mineral contains both Fe and Mn, and the primary mineral particle is rich in iron. Peaks of Na, Mg, Al, Si and Ca came from the glass coverslip used as a support.



Biological Activity of the Combination of Benzonidazole with Copaiba Oil (*Copaifera Martii*) and Kaurenoic Acid against *Trypanosoma Cruzi*

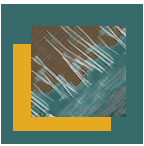
Danielle Kian^{1*} César Armando Contreras Lancheros², Wander Pavanelli³, Phileno Pinge-Filho³, Nilton Syogo Arakawa⁴, Valdir Florêncio da Veiga Junior⁵, Celso Vataru Nakamura², Sueli Fumie Yamada Ogatta¹ and Lucy Megumi Yamauchi Lioni¹

1. Department of Microbiology, State University of Londrina, Londrina, Brazil.
 2. Postgraduate in Pharmaceutical Sciences, Department of Basic Health Sciences, State University of Maringá, Maringá, Brazil.
 3. Department of Pathological Sciences, 4. Department of Pharmaceutical Sciences, State University of Londrina, Londrina, Brazil.
 5. Department of Chemistry, Federal University of Amazonas, Manaus, Brazil.
- *Email: danykian@gmail.com

Introduction: Chagas disease is a neglected disease affects about 6-7 million of people in Latin America [1]. The treatment this disease is based on two drugs nifurtimox (Lampit™) and benznidazole (Rochagan™). However, these drugs have limited efficacy in the chronic phase and different strains of the parasite may present varied responses to the drugs. The search for new therapies has been studied using natural products, molecular modification of existing compounds, synthesis of new molecules and association of drugs. In this latter approach, new compounds are generally associate with benznidazole in order to decrease its side effects and increase activity. On the other hand, natural compounds such as copaiba oil and one of its main constituents, kaurenoic acid, have shown biological activity against *T. cruzi* [2]. The objective of the present study was to evaluate the effect of copaiba oil and kaurenoic acid in association with benzonidazole against *T. cruzi*. **Material and methods:** The drug combination assay consisted of benznidazole with copaiba oil or kareunoic acid following the method proposed by Chou and Talalay [3]. Epimastigote forms (1x10⁶ cells/mL) were treated with different combinations of the compounds for 72 h at 28oC. For electron microscopy epimastigotes were treated with IC50 and IC90 and fixed with 2.5% glutaraldehyde. For scanning electron microscopy (SEM), drops of the sample were placed on coverslips, dehydrated in different concentrations of graded ethanol, critical-point dried in CO₂, coated with gold and observed in a FEI Quanta 250 scanning electron microscope. Transmission electron microscopy (TEM) was carried out with parasites post-fixed in 1% osmium tetroxide, 0.8% potassium ferrocyanide and 5 mM CaCl₂. The parasites were dehydrated in acetone series and embedded in Epon resin. Ultrathin sections were obtained and grids containing the sections were stained with 5% uranyl acetate and lead citrate for further observation in Jeol JEM 1400 transmission electron microscope. **Results:** The in vitro drug combination of benznidazole with copaiba oil or kareunoic acid showed a synergic profile with a FICI value of 0.377 and 0.926 respectively. Alterations in cell surface caused by the substance alone or in combination were observed by SEM. Kaurenoic acid leads to loss of cellular membrane integrity, alone (Figure 1B) or in combination with benznidazole (Figure 1E). The treatment with benznidazole plus copaiba oil causes loss of cellular content (Figure 1F). Alterations in the cellular ultrastructure were observed by TEM. Kareunoic acid induced the formation of myelin figures (Figure 2B) and copaiba oil treatment led to lipid bodies formation (Figure 2C), while the benznidazole cause extensive cytoplasmic vacuolization (Figure 2D). All the structural changes were observed when parasites were treated with the combinations (Figure 2E, 2F).

REFERENCES

- [1] WHO. Available in < <http://www.who.int/chagas/en/> > (2017).



[2] E. Izumi et al., *Planta Medica*; 79 (2013).

[3] T. Chou and P. Talalay. *Advances in Enzyme Regulation*; 2 (1984).

This research was supported by CNPq (Brazil).

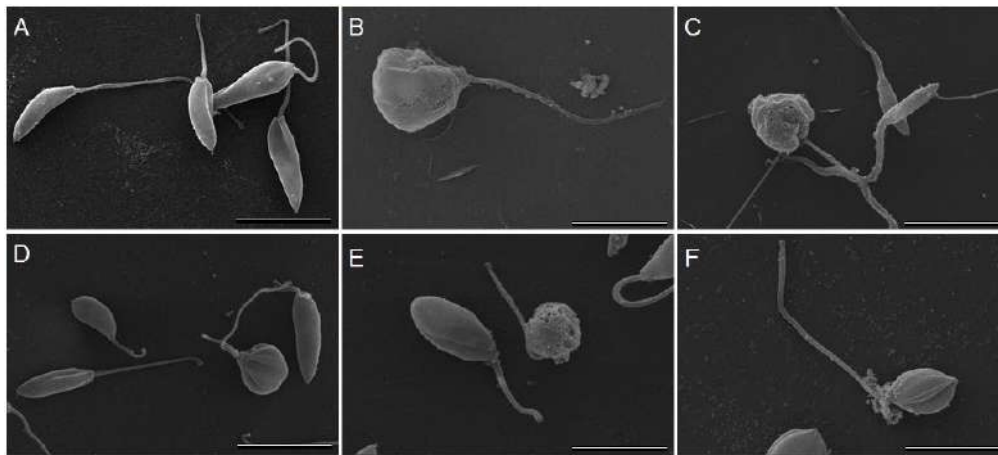


Figure 1. Scanning electron microscopy of epimastigote form of *T. cruzi* after 72 h of treatment with benznidazole plus kareunoic acid or copaiba oil. (A) Untreated control, (B) kareunoic acid, (C) copaiba oil, (D) benznidazole, (E) kareunoic acid + benznidazole, (F) copaiba oil + benznidazole. Bars = 5 μ m.

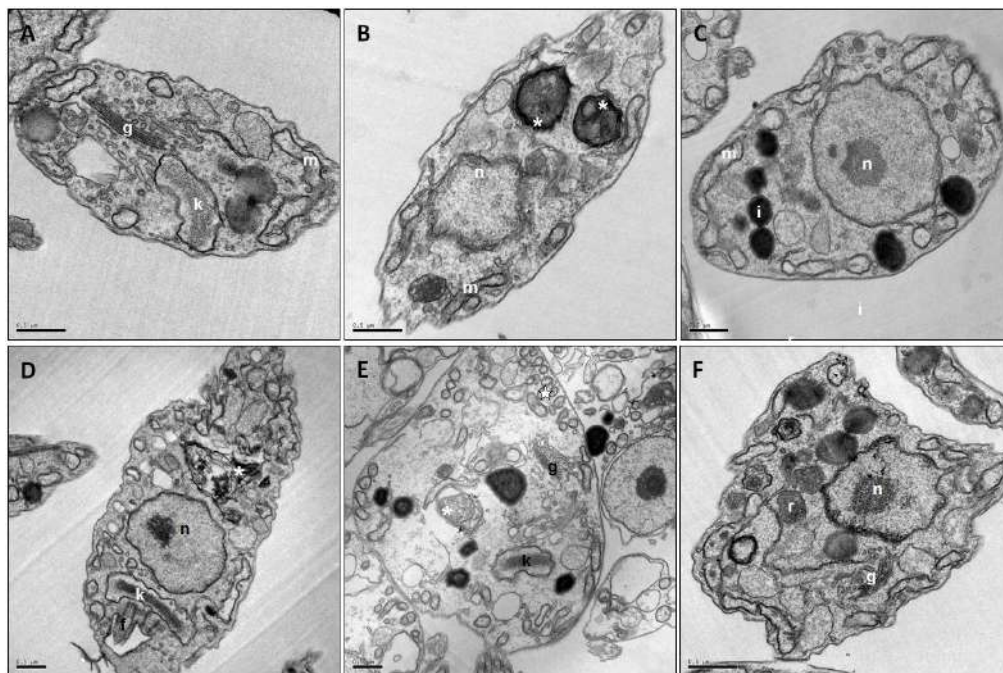
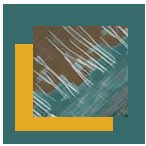


Figure 2. Transmission electron microscopy of epimastigote form of *T. cruzi* after 72 h of treatment with benznidazole plus kareunoic acid or copaiba oil. (A) Untreated control, mitochondria (m), kinetoplast (k) Golgi apparatus (g) (B) kareunoic acid, myelin figures (asterisks), (C) copaiba oil, lipid inclusions, (D) benznidazole, (E) kareunoic acid + benznidazole, (F) copaiba oil + benznidazole. Bars = 0.5 μ m.

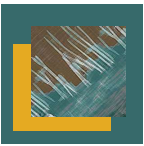


Evaluation of Ectonucleotidase Activity and NTPDase-1 Immunolocalization in Different Strains and Clones of *TRYPANOSOMA CRUZI*

Neves-do-Valle, M.A.A.^{1e2}, Oliveira, C.M.^{1e3}, Santos, H.C.P.⁴, Menezes W.A.¹, Bressan, G.C.¹, Almeida, M.R.¹, Fietto, J.L.R.^{1*}.

1. Departamento de Bioquímica e Biologia Molecular, Universidade Federal de Viçosa, MG, Brazil.
2. Instituto Federal de Educação, Ciência e Tecnologia de Minas Gerais - IFMG - campus Ipatinga, Minas Gerais, Brazil. *Email: myrianavalle@hotmail.com
3. Instituto Federal de Educação, Ciência e Tecnologia de Alagoas - IFAL, campus Santana do Ipanema, Alagoas, Brazil.
4. Instituto Federal de Educação, Ciência e Tecnologia de Minas Gerais - IFMG - campus São João Evangelista, Minas Gerais, Brazil.

Trypanosoma cruzi (Kinetoplastida: Trypanosomatidae) is a flagellate protozoan the etiological agent of Chagas disease. *T. cruzi* comprises a variety of strains and clones. Currently, the scientific community classifies this parasite into six distinct Discrete Typing Units (DTUs), *T. cruzi* I to VI. The DTUs are described as "sets of cells genetically stocks more closely related to each other than in relation to other stocks and are identified by having similar genetic, molecular or immunological markers". The genetic diversity of *T. cruzi*, therefore, may influence drug susceptibility and resistance. To validate novel chemotherapeutic potentials it is important to ensure the effectiveness of the compound used in several DTUs of the parasite [1]. The strain Y from DTU II of *T. cruzi* has ectonucleotidase activity on its surface, and a NTPDase gene was identified and cloned (TcNTPDase-1); the recombinant protein was subsequently expressed in bacterial system [2]. The TcNTPDase-1 from strain Y was previously shown as a facilitator of infection and a virulence factor highlighted it as a good target to rational drug design [3]. Thus, the aim of this work was to evaluate the ectonucleotidase activity and the TcNTPDase-1 cellular localization in the *T. cruzi* strains Berenice-62 (DTU II), Colombiana (DTU I) and in the clones CL-14 (DTU VI) and CL-Brener (DTU VI). In order to evaluate the ectonucleotidase activity, we used the Malachite Green colorimetric method for determination of free inorganic phosphate generated by the hydrolysis of nucleotides [4]. To analyze the subcellular localization of TcNTPDase-1 in the stationary phase, the epimastigotes were processed for transmission electron microscopy by the post-inclusion immunogold technique using anti-recombinant TcNTPdase-1 antibodies. To verify the ecto-nucleotidase activity of strains/clones we analyzed their capabilities to hydrolyze ATP, ADP and AMP "in vivo" using live epimastigote forms from logarithmic and stationary phases of grown. In general, we expect that the stationary phase presented increased hydrolysis of the different nucleotides, because the nutrient limitation of the medium could increase ectonucleotidase activity, as previously observed for Y strain [5]. However, the strains studied here differed significantly in the ectonucleotidase activity profile concerning the grown phase. We observed that in general the activities in the logarithmic phase were higher than in the stationary phase. These data suggest that the action of TcNTPDase-1 and/or of other ectonucleotidasas as factors of virulence and infectivity could vary in *T. cruzi*. In addition, this study showed higher activity during the high proliferative phase of grown (logarithmic phase) suggesting important role of ectonucleotidasas in the parasite nutrition and proliferation. In general, the ultrastructural analysis specific to NTPDase-1 localization shown it is expressed in the nucleus (N), kinetoplast (K), flagellum (F), reservosomes (R), cytoplasm (dotted circle) and cell surface (black dotted arrow) (Figs. 1, 2, 3 and 4). In the strain Colombiana no labeling was observed on the cell surface, which may corroborate to the absence of ectonucleotidase activity in the stationary phase. The clone CL-14 did not present immunolabeling in any cellular structure. It may be because this clone is not infective and, therefore, did not present ectonucleotidase activity in the stationary phase. The present results reinforce that NTPDase-1 may be involved in the acquisition of nutrients by epimastigotes, and its importance to the parasite, since this replicative form has high metabolic level



and requires purine and its derivatives for DNA replication and RNA transcription. In addition, the ubiquitous localization in different cell compartments indicates its possible participation in several biological processes in the parasites as suggested in studies with in strain Y of the *T. cruzi* [5]. The only exception to this rule is the non-infective clone CL14.

REFERENCES

- [1] M. Moreno, et al., Memórias do Instituto Oswaldo Cruz (2010).
- [2] J.L.R. Fietto, et al., Biochem Biophys Res Commun (2004).
- [3] R.F. Santos et al., PLoS Negl Trop Dis. 3 (2009).
- [4] P. Erman & O. Jager, Anal Biochem. 214 (1993).
- [5] C. Mariotini-Moura et al., Acta Trop. 130 (2014).
- [6] This research was supported by CAPES (Brazil).

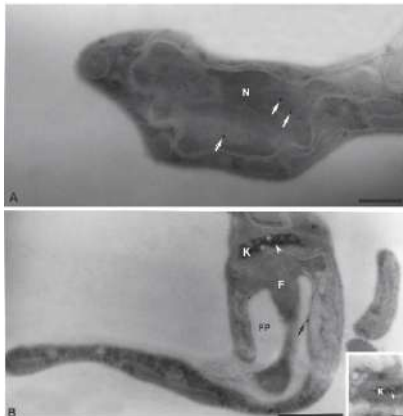


FIG. 1: Transmission electron photomicrographs show subcellular localization of TcNTPDase-1 in *T. cruzi* (Berenice-62 strain) epimastigotes using anti-TcNTPDase-1 polyclonal antibodies and colloidal gold-conjugated secondary antibody (A and B). Epimastigotes forms showed gold particles in the Nucleus (N), Kinetoplast (K) and Flagellar Pocket (FP). No labeling was visualized in the control (data not shown). Bars: A = 0,2 μ m and B = 0,5 μ m.

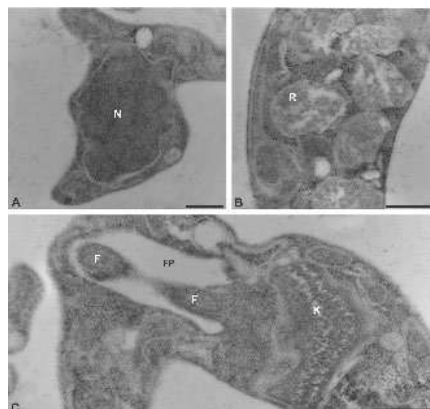


FIG. 3: Transmission electron photomicrographs of *T. cruzi* (CL-14 clone). Epimastigotes forms incubated with anti-TcNTPDase-1 polyclonal antibody and a colloidal gold-conjugated secondary antibody showed no gold particle labeling. (Nucleus (N), Kinetoplast (K), Flagellum (F), Flagellar Pocket (FP), Reservosome (R)). Bars: A-C = 0,5 μ m.

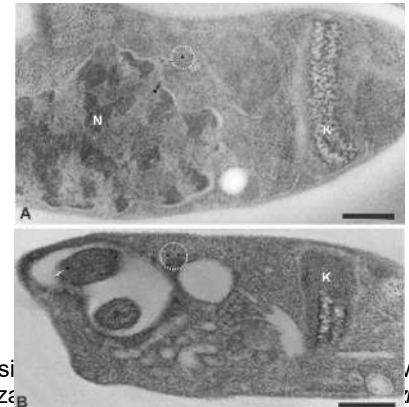


FIG. 2: Transmission electron photomicrographs show the subcellular localization of TcNTPDase-1 in *T. cruzi* (Colombiana strain) epimastigotes using anti-TcNTPDase-1 polyclonal antibodies and colloidal gold-conjugated secondary antibody (A and B). Epimastigotes forms showed gold particles in the Nucleus (N) (black arrow), Flagellum (F) (white arrow) and cytoplasm (dotted circle). No labeling was visualized in the control (data not shown). Bars: A-B = 0,3 μ m.

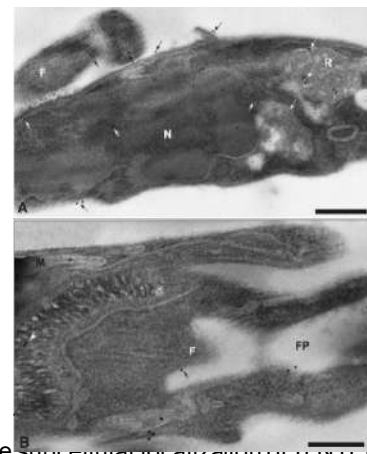
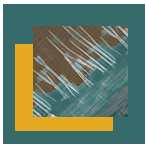


FIG. 4: Transmission electron photomicrographs show the subcellular localization of TcNTPDase-1 in *T. cruzi* (CL-Brener clone) epimastigotes using anti-TcNTPDase-1 polyclonal antibody and a colloidal gold-conjugated secondary antibody (A and B). Epimastigotes forms showed gold particles in the Núcleo (N) (white arrow), Kinetoplast (K) (white arrow head), flagellum (F) (black arrow), reservosome (R) (white dotted arrow), cell surface, Cytoplasm (circle). No staining was visualized in the control (data not shown). Bars: A = 0,3 μ m, B = 0,2 μ m.



Notch inhibition enhances myoblast proliferation during chick myogenesis

Ivone Rosa de Andrade*, Manoel Luis Costa, Claudia Mermelstein

Laboratório de Diferenciação Muscular e Citoesqueleto, Instituto de Ciências Biomédicas, Universidade Federal do Rio de Janeiro, Rio de Janeiro, Brazil

*Email: ivone.ivy@gmail.com

Notch pathway is an evolutionarily conserved pathway that plays crucial functions in organ development, tissue homeostasis, stem cell fate choice, metabolism and cancers. Notch pathway transduction is initiated upon binding of a Notch receptor (Notch1-4) with a ligand (Dll1, Dll4, Jag1, Jag2) located on a neighbor cell. Subsequently, Notch receptors are cleaved by several enzymes including α -secretase, which releases the Notch intracellular domain (NICD). NICD then translocate to the nucleus, where it binds with Rbpj and other cofactors to activate the transcription of canonical Notch targets, including Hes and Hey family genes [1]. The Notch pathway has been shown to have multiple roles in myogenesis, such as to define the anterior boundary of somites and progenitor cell fate within the somites during embryonic muscle development, to inhibit muscle differentiation in chick limb myogenesis [2], to delay the expression of the myogenic differentiation markers MyoD and myogenin in mouse C2C12 myoblast cell line [3], however, the role of the Notch pathway during embryonic chick muscle differentiation is unclear. Thus, we used the DAPT to inhibit the notch pathway in primary cultures of chick myogenic cells and analyzed its effect in muscle differentiation. Myoblasts were obtained from pectoral muscle from 11 day-old chick embryos (Granja Tolomei, RJ). Cells were plated at an initial density of 7.5×10^5 cells/ml on 35 mm culture dishes previously coated with collagen. Cells were treated with 100 μ M, 200 μ M or 400 μ M of DAPT, an inhibitor of the α -secretase and notch pathway for 48 hs. Treated cells were fixed and analyzed by immunofluorescence microscopy using anti- α -actinin (muscle cell marker) or Pax-7 (satellite cell marker). We quantified the (i) total number of nuclei, (ii) number of nuclei in myotubes (α -actinin positive cells), (iii) number of fibroblasts, (iv) number of myoblast, (v) percentage of the area occupied by muscle cells and (vi) number of Pax-7 positive cells. Cells treated with 200 μ M of DAPT presented a higher number of the myotubes and increased size. To investigate the involvement the Notch pathway in muscle satellite cells, we labeled cells with Pax-7 antibodies. In DAPT treated-cells we observed a higher number of the Pax-7 positive cells. In addition, a reduction in the number of myoblast and fibroblasts was also observed. These results suggest that inhibition of the Notch pathway activates the proliferation of satellite cells, leading to the fusion of myoblasts and to the formation of larger myotubes. This study was approved by CEUA-DAHEICB092-05/16. Support: CNPq and FAPERJ.

REFERENCES

- [1] Y. Wen, et al., Mol. Cell Biol. 32 (2012) 2300.
- [2] M.C. Delfini, et al., Development. 127 (2000) 5213.
- [3] D. Nofziger, et al., Development. 126 (1999) 1689.

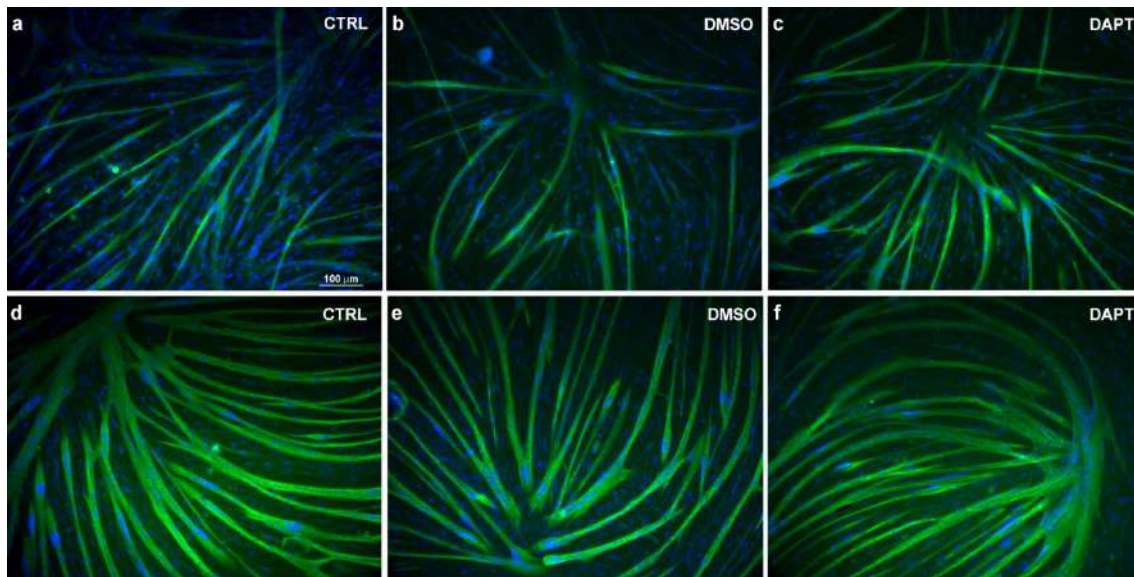
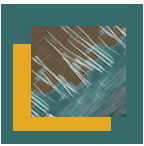
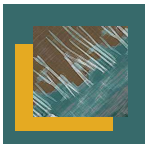


Fig. 1. Notch inhibition leads to an increase in myotube size. Immunofluorescence microscopy of chick skeletal muscle cells treated with 200µM of DAPT, an Notch inhibitor, and labelled with an anti- α -actinin antibody and with the nuclear dye DAPI. (a-c) After 24 hours of DAPT treatment no significant differences were observed between conditions. (d-f) After 48 hours of DAPT treatment it is possible to observe an increase in myotube size.



Extracellular Matrix Affects Focal Adhesion Kinase (FAK) Localization in Prostatic Smooth Muscle Cells

Daniel Andrés Osorio Rodríguez^{1*}, Aline Mara dos Santos² and Hernandes Faustino de Carvalho³

1,2,3. Department of Structural and Functional Biology, Institute of Biology, State University of Campinas (UNICAMP), Campinas SP, Brazil;

*Email: bio.andres.osorio@hotmail.com.

Smooth muscle cells (SMCs) can shift from the contractile to a synthetic phenotype in response to different environmental cues [1]. The extracellular matrix (ECM) triggers specific signaling pathways during development, homeostasis in adults and in disease. The external stimuli produced by ECM are translated through transmembrane receptors, the integrins, which bind specific ECM proteins [2]. This allows the cell to respond according to their surrounding environment. The integrin cytoplasmic domain interacts with several proteins in a complex called focal adhesion. One of these proteins is FAK, which is a 125-KDa protein-tyrosine kinase and acts as an integrator protein between the cytoskeleton and MEC [3]. Our aim is to identify how collagen, matrigel and fibrin substrates regulates SMC phenotype. In this work, we have mapped how these ECM substrates affects FAK subcellular distribution in prostatic SMC. SMCs were obtained from explants of the ventral prostate of male Wistar rats, maintained in DMEM medium supplemented with 10% fetal bovine serum, 1% penicillin/streptomycin, 10 nM dihydrotestosterone, and 5 µg/mL insulin. Subsequently, the SMCs in the fourth-to-seventh passages were seeded on plastic, type I collagen, matrigel and fibrin substrates. After 48 hours in culture, the SMCs were fixed and then incubated with antibodies against smooth muscle alpha-actin (α -SMA) and FAK A17. Images were acquired using a confocal LSM780 microscope (Carl Zeiss). ECM substrate did not affect α -SMA expression (Figure b, f, j, n) though cell morphology differed markedly. The SMCs seeded on plastic and type I collagen were widely spread, and FAK was mainly located at the focal adhesion and in the cell nucleus (Figure c, g). When cells were seeded on fibrin and matrigel, they were elongated, showing numerous cell processes and FAK was predominantly found in discrete cytoplasmic dots (Figure k, o). In contrast to the cells on plastic and collagen, some cells on fibrin and matrigel lacked nuclear staining for FAK. These observations suggest that ECM components regulate SMC behavior and that FAK might be involved in the maintenance of the SMC phenotype in the prostate, irrespective of the expression of α -SMA.

REFERENCES

[1] J.A. Beamish et al., *Tissue Eng Part B Rev* 16(5) (2010) 467-91.

[2] C. Frantz et al., *J Cell Sci* 123(24) (2010) 4195-200.

[3] S.K. Mitra et al., *Nat Rev Mol Cell Biol* 6(1) (2005) 56-68.

This research was supported by FAPESP (Brazil), (Grant No. 2009/16150-6 and 2015/03235-4).

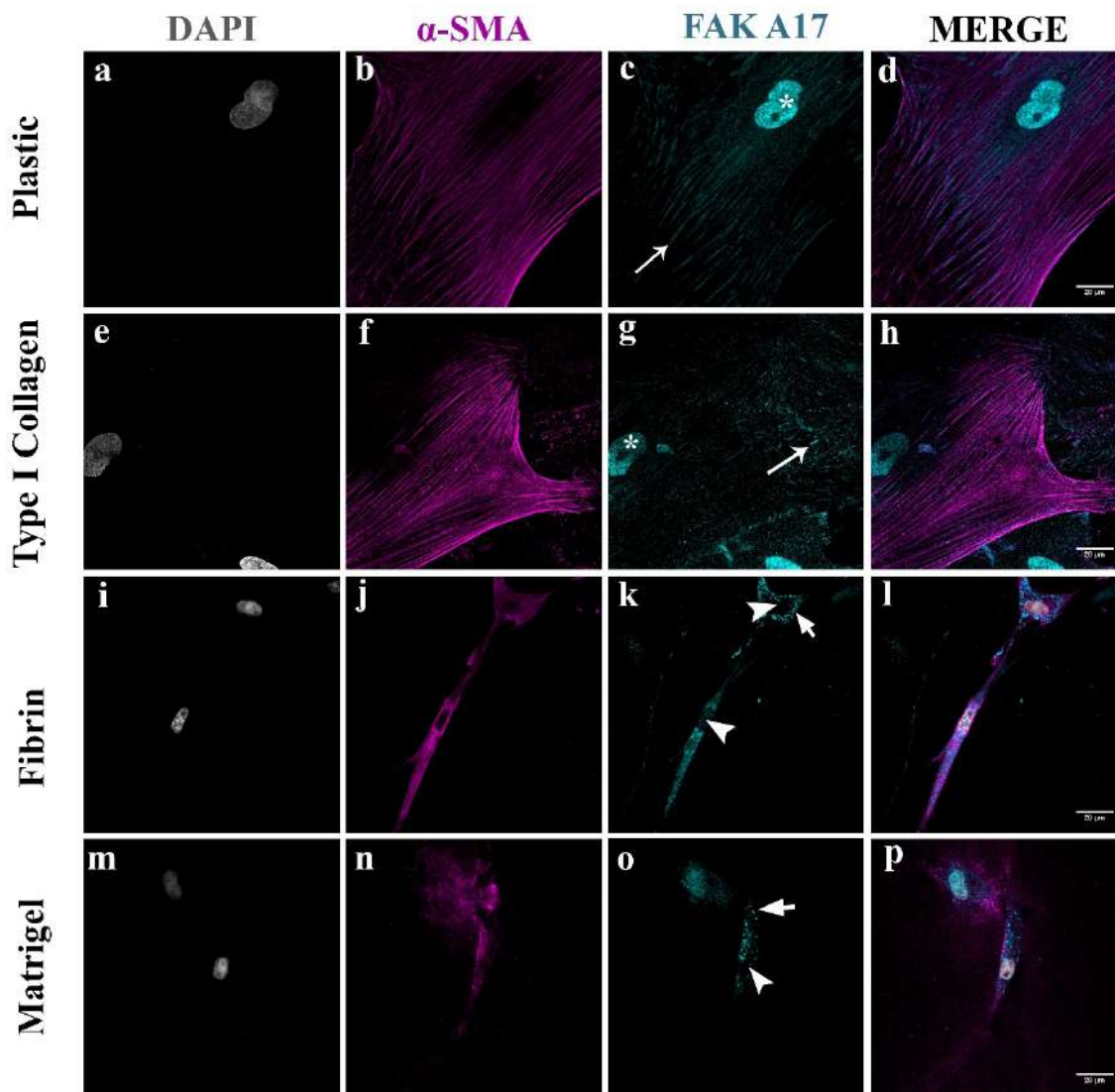
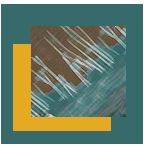


Figure. Immunofluorescence staining against α -SMA and FAK A17. SMC were positive for α -SMA (b, f, j, n). SMCs seeded on plastic (a-d) and type I collagen (e-h) showed FAK at the focal adhesions (arrows) and in the nucleus (asterisk), whereas on fibrin (i-l) and matrigel (m-p) it was predominantly in cytoplasmic dots (small arrows). Some cells seeded on fibrin and matrigel did not show nuclear staining for FAK (k, o) (arrowheads). Scale bar: 20 μ m.



Biological Activity of the Compound Synthetic 4-[(2e)-N-(2,2'-bithienyl-5-methylene)hydrazinecarbonyl]-6,7-dihydro-1-phenyl-1h-pyrazolo[3,4-d]pyridazin-7-one in Promastigotes of *Leishmania infantum*

Hélito Volpato¹, Danielle Lazarin-Bidóia¹, Débora Botura Scariot¹, Andrey Petita Jacomini², Fernanda Andreia Rosa², Tânia Ueda-Nakamura¹, Adley Forti Rubira², Edna Filipa Pais Soares³, Maria do Céu Souza³, Olga Borges³ and Celso Vataru Nakamura¹

1. Laboratório de Inovação Tecnológica no Desenvolvimento de Fármacos e Cosméticos, Departamento de Ciências Básica da Saúde, Universidade Estadual de Maringá (UEM), Maringá, Paraná, Brazil

2. Departamento de Química, Universidade Estadual de Maringá (UEM), Maringá, Paraná, Brazil

3. Faculdade de Farmácia da Universidade de Coimbra (FFUC), Coimbra, Portugal

*Email: cvnakamura@gmail.com

Visceral leishmaniasis (VL) is a neglected disease caused by some species of the protozoan *Leishmania* sp. About 500,000 new cases are reported worldwide, mainly in Bangladesh, Brazil, Ethiopia, India and Sudan. In the new world, VL is caused by the protozoan parasite *L. infantum*, with an incidence of 1.9 cases per 100,000 inhabitants and 90% mortality rate if there is no adequate treatment [1-3]. Currently, the drugs used in the treatment of patients with VL have shown several limitations, for example, long treatment times, severe side effects, high cost, and some resistance cases. These drawbacks reveal the urgent need to develop new therapeutic agents for the treatment of leishmaniasis. Recently, our research group reported the antileishmanial activity of synthetic compound 4-[(2e)-n'-(2,2'-bithienyl-5-methylene)- hydrazinecarbonyl]-6,7-dihydro-1-phenyl-1h-pyrazolo[3,4-d]pyridazin-7-one (C6) against *L. amazonensis* [4]. Thus, the objective of this study was to evaluate the biological activity and mechanism of action of C6 involved in the cell death of *L. infantum*. To evaluate the biological activity, promastigotes were treated with different concentrations of C6 for 72 h. After treatment, MTT (5 mg/mL) was added, incubated for 2 h and the absorbance was evaluated at 530 nm. Morphological and ultrastructural analysis was performed in promastigotes treated with IC₅₀ and 2xIC₅₀ of C6 for 72 h at 25 °C. After, the parasites were fixed in 2.5% glutaraldehyde in 0.1 M cacodylate buffer for 24 h at 4 °C. For SEM, the sample were adhered in poly-L-lisine, dehydrated in increasing concentrations of ethanol, critical-point-dried in CO₂, sputter-coated with gold and observed in Shimadzu SS-550 SEM. For TEM, the parasites were post-fixed with in a solution of 0.1% osmium tetroxide and 1% uranyl acetate, dehydrated in increasing acetone gradient, incorporated in molten agar (2%), re-hydrated with acetone, embedded in Epoxy resin. Ultrathin sections were then obtained, contrasted with 0.2% lead citrate, and observed in FEI-Tecnaï G2 Spirit Bio Twin. In order to elucidate the mechanism of action, promastigotes treated with IC₅₀ and 2xIC₅₀ of C6 for 24 h were analyzed by flow cytometry to evaluate cell volume, phosphatidylserine exposure (annexin-V/FITC) and plasma membrane integrity (propidium iodide; PI). Our results demonstrated that C6 exhibited promising activity against promastigotes of *L. infantum*, presenting IC₅₀ of 2.5 µg/mL. Analysis by SEM demonstrated reduction of the cell body and evident alteration in the plasma membrane. Analysis by TEM revealed alteration in the nuclear envelope, presence of concentric membrane structures and autophagic vacuoles. Moreover, by flow cytometry, was observed a decrease in cell volume, increased phosphatidylserine exposure and maintenance of plasma membrane integrity. In conclusion, our results show that C6 synthetic compound is also active on *L. infantum*, and this activity may be related to morphological and biochemical events that are characterized in cell death by apoptosis and autophagy.



DOI: **INSERIR ENDEREÇO DO DOI AQUI.**

Caderno de Resumos do 26º Congresso Brasileiro de Macroscopia da SBMM – ISSN: **INSERIR AQUI.**

Acknowledgement: This study was supported through grants from CAPES, CNPq, FINEP, PRONEX/Fundação Araucária.

REFERENCES

- [1] F. CHAPPUIS et al. *Nature Rev Microbiol* 5 (11) (2007) S7-16.
- [2] H. W. MURRAY et al. *The Lancet* 366 (2005) 1561-1577.
- [3] WHO. *Leishmaniasis* (2016) 1-5.
- [4] A. P. JACOMINI et al. *Eur J Med Chem* 124 (2016) 340-349.

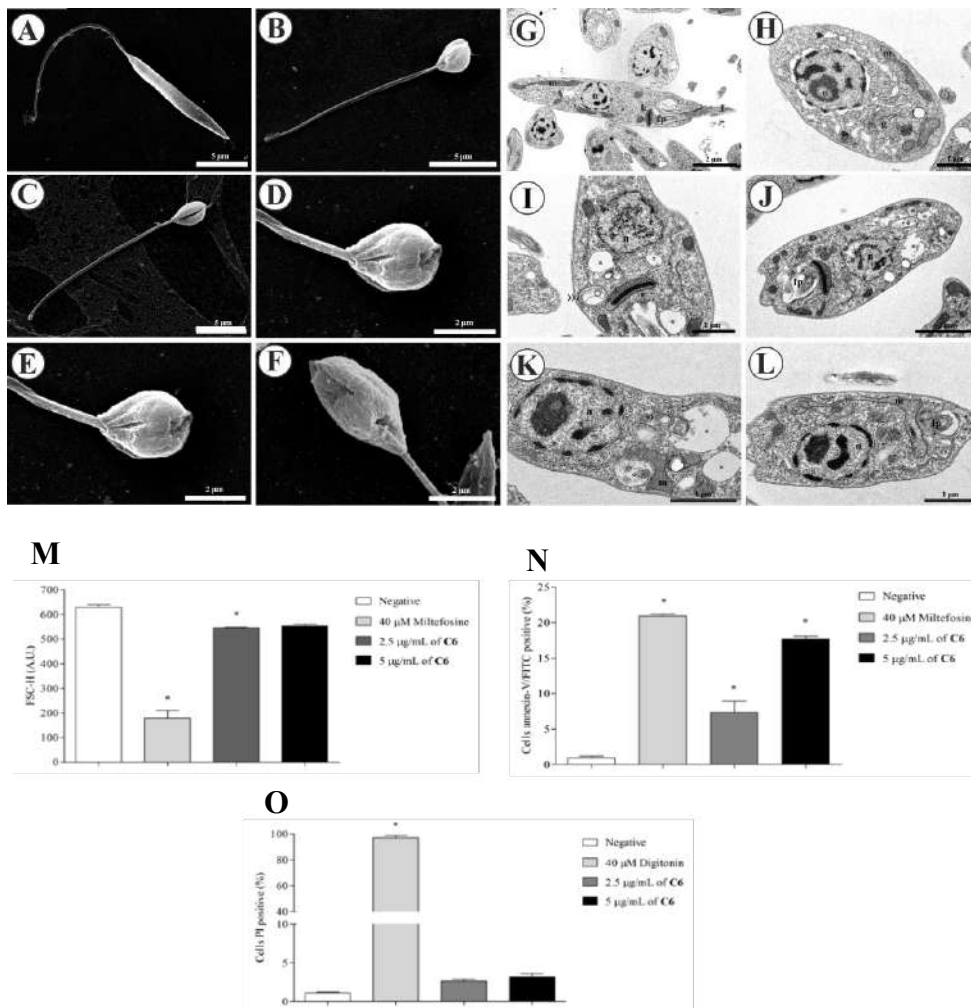
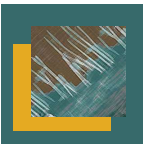


Figure 01. Electron microscopy and mechanism of action in C6-treated *L. infantum*. (A-C) SEM of C6-treated promastigotes for 72 h: (A) untreated, (B-C) 2.5 μ g/mL and (D-F) 5.0 μ g/mL. (G-L) TEM of C6-treated promastigotes for 72 h: (G) untreated, (H-I) 2.5 μ g/mL, (J-L) 5.0 μ g/mL. (n) nucleus, (m) mitochondria, (k) kinetoplast, (fp) flagellar pocket, (g) Golgi complex, (») concentric membrane structures and (*) autophagic vacuoles. (M) Cell volume in C6-treated promastigotes for 24 h. (N) Phosphatidylserine exposure in C6-treated promastigotes for 24 h using annexin-V/FITC. (O) Plasma membrane integrity in C6-treated promastigotes for 24 h using PI.



In vitro Anti-Leishmania Activity of a Synthetic Compound Loaded in Glucan Particles Extracted from the Cell Wall of *Saccharomyces cerevisiae*

Hélito Volpato¹, Danielle Lazarin-Bidóia¹, Débora Botura Scariot¹, Andrey Petita Jacomini², Fernanda Andreia Rosa², Tânia Ueda-Nakamura¹, Adley Forti Rubira², Edna Filipa Pais Soares³, Maria do Céu Souza³, Olga Borges³ and Celso Vataru Nakamura¹

1. Laboratório de Inovação Tecnológica no Desenvolvimento de Fármacos e Cosméticos, Departamento de Ciências Básica da Saúde, Universidade Estadual de Maringá (UEM), Maringá, Paraná, Brazil

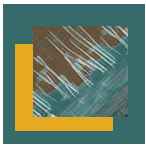
2. Departamento de Química, Universidade Estadual de Maringá (UEM), Maringá, Paraná, Brazil

3. Faculdade de Farmácia da Universidade de Coimbra (FFUC), Coimbra, Portugal

*Email: cvnakamura@gmail.com

Leishmania infantum is a protozoan parasite that causes visceral leishmaniasis (VL), a neglected disease that affects several countries, including Brazil. The current treatment of patients infected with *L. infantum* is based on inefficient drugs that present several restrictions, such as toxicity, high costs, and long-term treatment [1–3]. Thus, an urgent need exists to develop new drugs and therapeutic strategies. Our research group demonstrated, in preliminary studies, the antileishmanial effect of the synthetic compound 4-[(2e)-N'-(2,2'-bithienyl-5-methylene)hydrazinecarbonyl]-6,7-dihydro-1-phenyl-1h-pyrazolo[3,4-d]pyridazin-7-one (C6) against promastigotes of *L. infantum* (IC₅₀ of 2.5 µg/mL). However, this compound showed toxicity in RAW macrophages (CC₅₀ of 2.8 µg/mL). Based on this problem, the objective of this study was to perform the microencapsulation of C6 in glucan particles (GPs) extracted from the cell wall of *Saccharomyces cerevisiae*. GPs are hollow and porous particles composed mainly of β-1,3-D-glucan. Phagocytic cells (e.g. macrophages) can readily recognize GPs due to the presence of glucan receptors on the plasma membrane: dectin-1 and complement receptor 3 [4,5]. To evaluate the activity against intracellular amastigotes, peritoneal macrophages were infected with promastigotes, treated with different concentrations of C6-loaded for 48 h, and stained with May-Grunwald Giemsa. The percentage of infected cells and the number of parasites per cell were determined by counting 100 cells. The survival index (%) was obtained by multiplying the percentage of infected cells by the mean number of amastigotes per infected macrophages. The survival index observed in the control without treatment was considered as 100% and the results for treated groups were comparatively evaluated. The cytotoxicity was performed on RAW macrophages treated with different concentrations of C6-loaded for 48 h, incubated with MTT and the absorbance was evaluated at 530 nm. Additionally, the GPs were processed and analyzed in TEM and SEM. For TEM, the samples were resuspended in MilliQ water, an aliquot was added on the grid support film of formvar/carbon (300 mesh), dried at room temperature and observed in FEI-Tecnaï G2 Spirit Bio Twin. For SEM, the samples were dehydrated in increasing concentrations of ethanol, sputter-coated with gold and observed in Shimadzu SS-550 SEM. Our results demonstrated anti-leishmanial activity of C6 (IC₅₀: 1.23 µg/mL) and C6-loaded (IC₅₀: 8.20 µg/mL) against intracellular amastigotes. Interestingly, C6-loaded showed no toxicity in RAW macrophages (CC₅₀ > 152.3 µg/mL), even at the highest concentration tested. In conclusion, our results demonstrated that C6 was effective against intracellular amastigotes of *L. infantum*, and the microencapsulation of C6 in GPs may be a promising strategy for drug development, since it exhibited a reduction of the toxicity in mammalian cells.

Acknowledgement: This study was supported through grants from CAPES, CNPq, FINEP, PRONEX/Fundação Araucária.



REFERENCES

- [1] F. CHAPPUIS et al. Nature Rev Microbiol 5 (11) (2207) S7-16.
[2] H. W. MURRAY et al. The Lancet 366 (2005) 1561-1577.
[3] WHO. Leishmaniases (2016) 1-5.
[4] H. HUANG et al. J Immunol 2012 (189) (2012) 312-317.
[5] G. D. BROWN et al. Nature 413 (2001) 36-37.

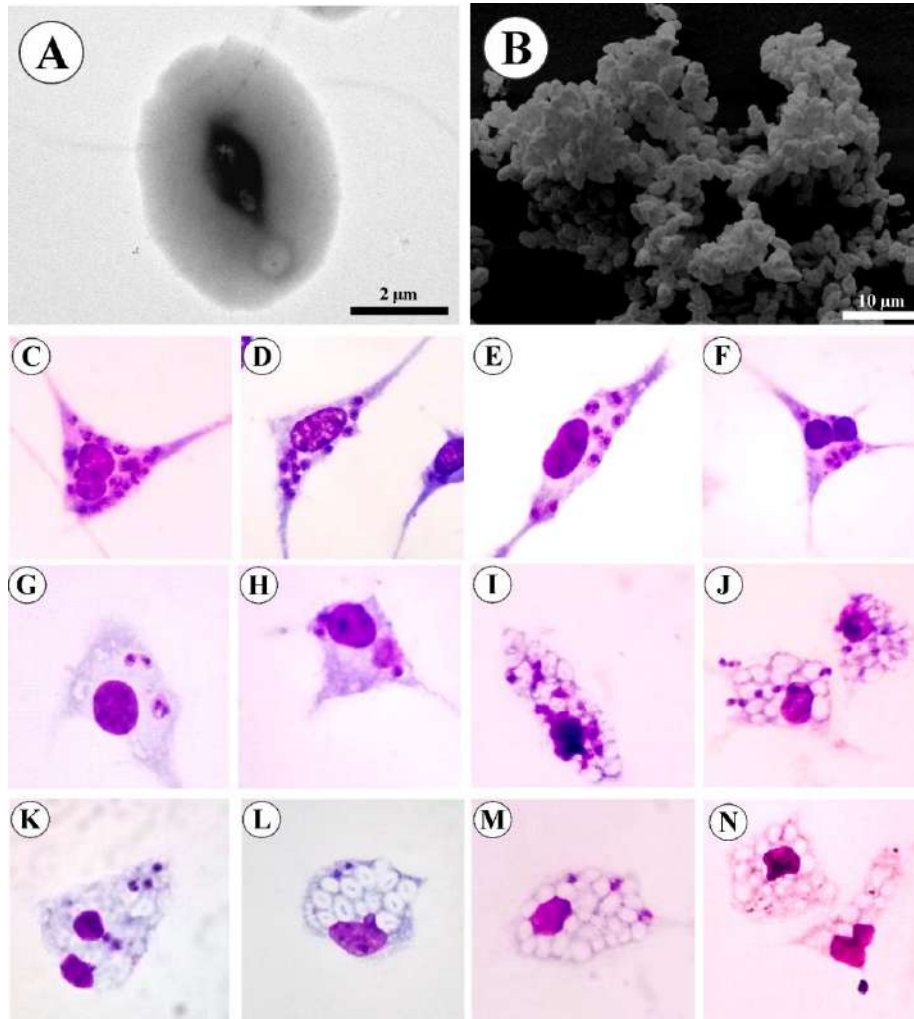
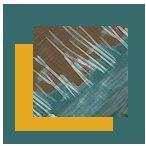


Figure 01. (A) TEM and (B) SEM of the GPs. (C-H) Biological activity of C6 against intracellular amastigotes of *L. infantum*: (C) infected and untreated cells (negative control), (D) treated cells with 0.1 μg/mL, (E) treated cells with 0.5 μg/mL, (F) treated cells with 1.0 μg/mL, (G) treated cells with 2.5 μg/mL, (H) treated cells with 5.0 μg/mL. (I-N) Biological activity of C6-loaded in GPs against intracellular amastigotes of *L. infantum*: (I) infected and treated cells with GPs (negative control), (J) treated cells with 0.4 μg/mL, (K) treated cells 1.6 μg/mL, (L) treated cells with 2.9 μg/mL, (M) treated cells with 8.6 μg/mL and (N) treated cells with 15.2 μg/mL.



Mammary Adenocarcinoma Cells Diminished Functional Activity of RAW264.7 Macrophages

Débora Mares Silvestro¹, José Renildo de Carvalho¹, Thiago Albuquerque¹, Toshie de Camargo Konno¹, Leoni Bonamin¹, Maria Anete Lallo¹ and Elizabeth Cristina Perez^{1*}

1. Programa de Pós-Graduação em Patologia Ambiental e Experimental, Universidade Paulista, São Paulo, Brazil.

*Email: elicristin@hotmail.com

Breast cancer is the leading cause of cancer death in women worldwide with high morbidity and mortality [1]. Macrophages are the major cells of the immune system found in the tumor microenvironment. They have high plasticity and are polarized into two phenotypically distinct groups: M1 and M2 correlating with anti and pro-tumoral responses, respectively [2]. Considering that anti-tumor response is correlating with increase of phagocytic and microbicidal capacity of macrophages, the aim of the present study was to evaluate in vitro the influence of 4T1 mammary adenocarcinoma cells on the phagocytic and microbicidal ability of macrophages. For this, phagocytosis assays in vitro were performed using RAW 264.7 macrophages cultured alone or with 4T1 breast adenocarcinoma cells or its supernatant. After 48 hours, macrophages were collected and cultivated overnight on glass coverslips in a 24 well plates. The heat inactivated bread yeast particles were added at a 1:10 effector target ratio and incubated for two hours. After removed non-ingested yeast particles, coverslips were collected at 0, 24 and 48 hours and submitted to Giemsa stained. Phagocytic index (PI) was calculated considering % of macrophages that internalized at least yeast X the average number of fungal cells in these macrophages. To evaluate the microbicidal capacity of macrophages, Griess assay was performed to quantify the release of nitrite as an indirect method of NO₂ production. Profile of Th1/Th2/Th17 cytokine was evaluated by CBA technical. Light microscopy analyzes shown decrease in the phagocytic index of macrophages after culture with mammary adenocarcinoma cells or its supernatant. In addition, significant morphological alterations were observed in the macrophages after culture with tumor cells. CBA analyses revealed increase of IL-10 and TNF levels in culture of macrophages with mammary cells or its supernatant. Together, these results indicate that mammary adenocarcinoma cells or soluble factors released by latter can modulate phagocytic activity of RAW 264.7 macrophages in an in vitro model.

REFERENCES

- [1] B.Weigelt et al., Breast cancer metastasis: markers and models. *Nat Rev Cancer*. (8) 2005,591-602.
- [2] R.B.Leite et al., Macrófagos e sua relação com o carcinoma de células escamosas orais. *Revista eletrônica Unimep. Faculdade de Odontologia de Lins* (25) 2015. 37-46.
- [3] This research was supported by Universidade Paulista - UNIP (Brazil).

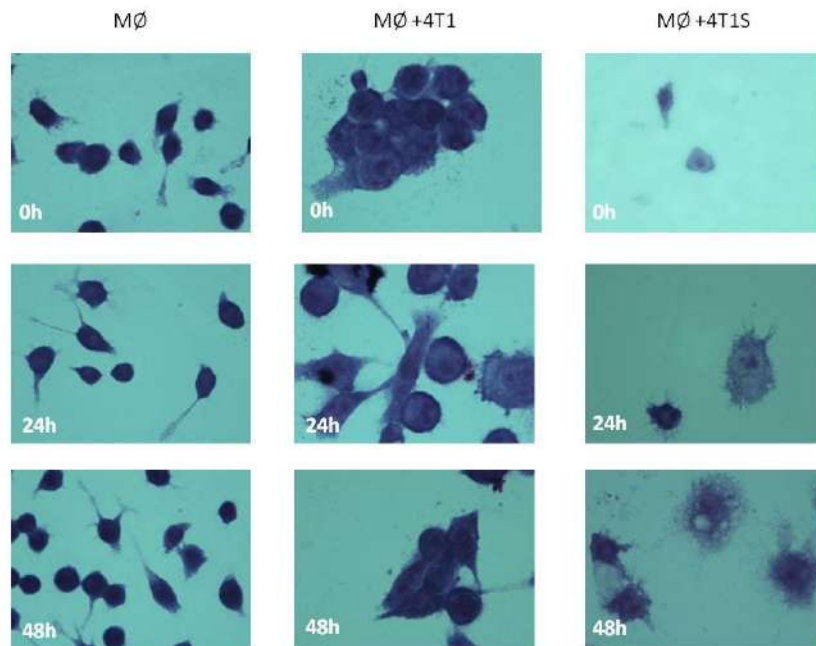
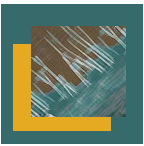


Figure 1. Morphological changes in macrophages induced by 4T1 mammary carcinoma cells interaction. RAW264.7 macrophages (2×10^6) were cultured alone (MØ) or with mammary adenocarcinoma cells (MØ + 4T1) or its supernatant (MØ + 4T1s). After 48h macrophages were collected and cultivated overnight on cover glass in 24-wells plates. Cover glass were collected and submitted to Giemsa stained at 0, 24 and 48h. All images showed 1000x of magnification.

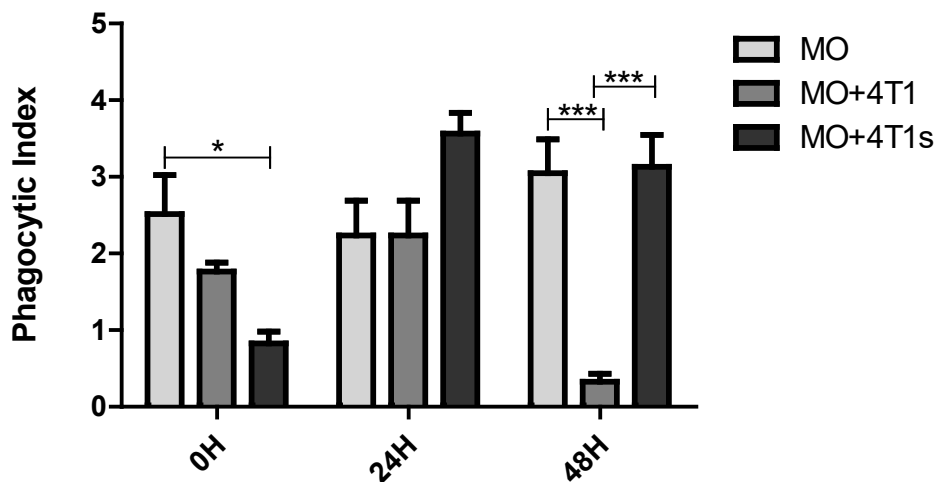
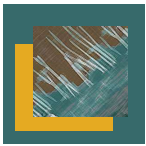


Figure 2. Phagocytic index. Macrophages previously cultured alone (MØ), or with 4T1 mammary adenocarcinoma cells (MØ + 4T1) or its supernatant (MØ + 4T1s) were cultivated overnight on cover glass in 24-wells plates. After this, *Saccharomyces cerevisiae* yeast were added in the proportion 1:10, respectively (macrophages:yeast). After 2 h of culture, adherent cells were washed 3X with PBS and coverslip collected (0 h) or re-cultured for 24 and 48 with new/free of yeast-medium. After each period, coverslips were stained with Giemsa for phagocytic index determination (% of macrophages that internalized at least one yeast X the average number of fungal cells in these macrophages). Two-way ANOVA * P0.05 *** p<0.0001.



3D study of the evolution of the tachyzoite form of *Toxoplasma gondii* inside the host cell

Diana Dolzani Motta^{1*}; Marcia Attias^{1,2}

1. Instituto de Biofísica Carlos Chagas Filho, Universidade Federal do Rio de Janeiro, Rio de Janeiro, Brazil
2. Instituto Nacional de Ciência e Tecnologia em Biologia Estrutural e Bioimagens, UFRJ, RJ. Brazil

Toxoplasma gondii is a protozoan parasite of all warm blooded animals, including humans. It can infect virtually any nucleated cell of all of hosts where it replicates by endodyogeny. The RH strain of *T. gondii* is the most used to study de acute phase of toxoplasmosis. The purpose of this study was to analyze the intracellular development of the tachyzoites of the RH strain and the relation of the parasites with the residual body (RB) that connect them. The interaction of the tachyzoites harvested from the peritoneal cavity of CF1 mice with the LLC-MK2 cells (ATCC® CCL-7™) was observed at 7, 24 and 48 hours post infection (hpi). Samples were chemically fixed [1] and observed by transmission electron microscopy and 3-D models were built from slice and view FIB series [2]. At 7hpi (Figs. A and B) the first endodyogenic division has already started and we observed that the apical complex of the mother cell was conserved almost until the end of the process. At 24hpi (Figs. C and D) the rosette is fully assembled and we counted 32 parasites attached to the RB. Some parasites seemed to be leaving the PV, but 3D models (Fig. D) showed that they were still connected to the RB. At 48hpi (Figs. E and F) tachyzoites were already scattered and the RB was disrupted, but three of the parasites were still attached to each other. In conclusion, the observation of series obtained using FIB slice and that the RB is formed at the end of the first division by endodyogeny. In a series of a rosette at 24hpi all the parasites remained connected to the RB, although some parasites appeared already leaving. In the third series, 48hpi, the parasites were disconnected from the RB that was filled with vesicles that were fusing. This seems to be the fate of the RB: self destruction by fusion of acidocalcisomes accumulated inside it as the parasite division cycles progress. These observations only were possible with the modeling of large volumes allowed by slice and view FIB-SEM series.

Acknowledgements: CNPq, CAPES, and FAPERJ.

REFERENCES:

- [1] Magno RC ET AL., Microsc Microanal. 2005 Apr;11(2):166-74.
- [2] Paredes Santos ET AL., J Struct Biol. 2012 Feb;177(2):420-30

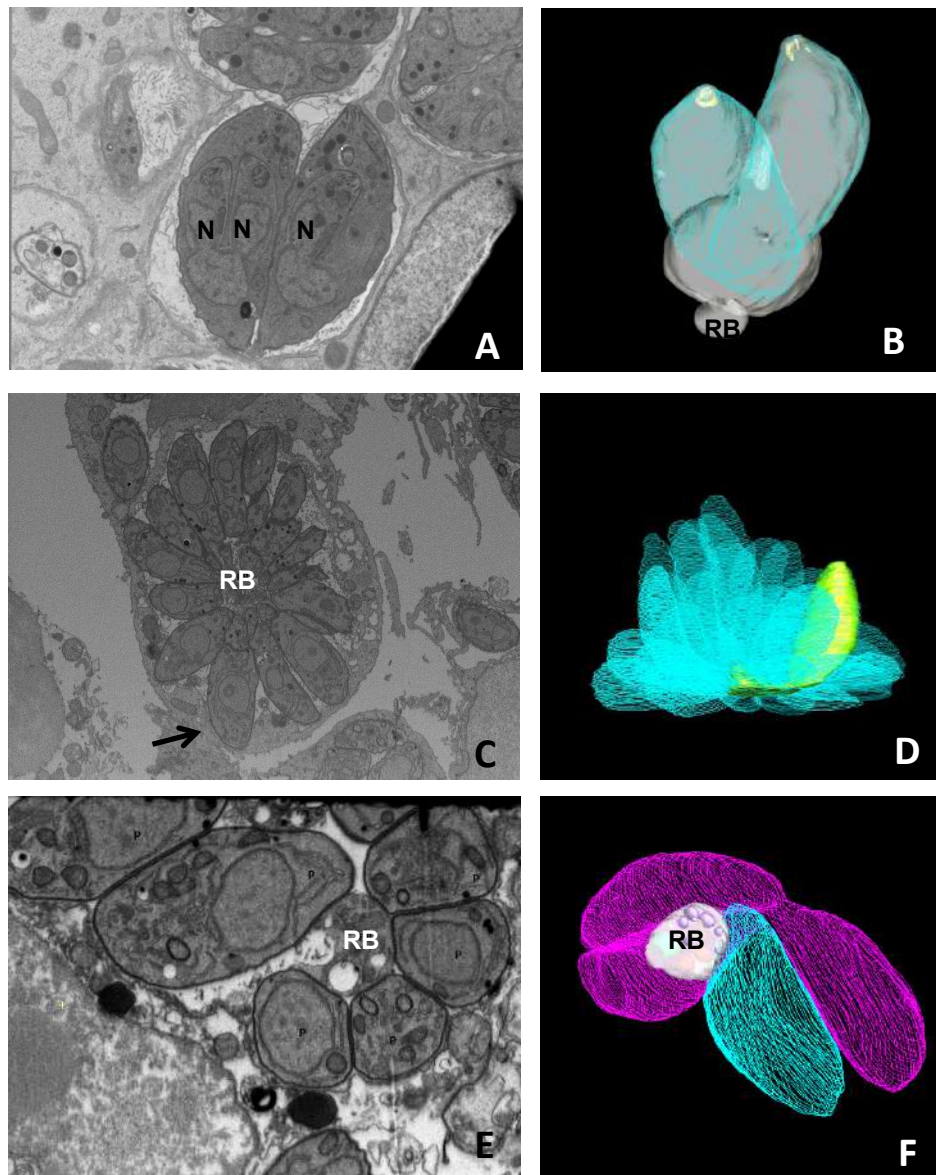
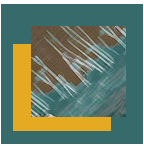


Figure A: Ultrathin section of parasites at the two tachyzoites stage. A second division cycle has already started (N) nucleus. Figure B: 3D model from a FIB slice and view series of two parasites attached to the RB. The daughter cells are outlined in blue, the pellicle and the RB are transparent and the conoids are in yellow. Figure C: Slice view from a 24hpi vacuole. Some parasites seem to be leaving the vacuole (arrow). Figure D: Model rendered from the series represented in C. 32 parasites were counted and are outlined in blue. One of the parasites that seemed to be in egress was shown to be attached to the RB (yellow). Figure E: Representative slice from a FIB series 48hpi. Parasites (P) are already individualized and the RB is in process of disaggregation. Figure F: Model rendered from the FIB series in E. The RB is shown in transparent white. An isolated parasite is outlined in blue and 3 parasites that are still linked are outlined in magenta.



Biological evaluation of lapachones derivatives as the new mitochondrial probes for cellular imaging

Douglas C. Brandão¹, Fabíola dos Santos³, Gleiston G. Dias³, Rossimiriam P. de Freitas³, Lucas S. Santos³, Guilherme F. de Lima³, Hélio A. Duarte³, Carlos A. de Simone⁴, Lidia M. S. L. Rezende¹, Monique J. X. Vianna¹, Brenno A. D. Neto², Eufrânio N. da Silva Júnior³ and José R. Correa¹

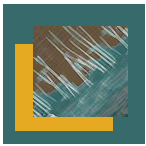
1. Institute of Biological Sciences, University of Brasilia, Brasilia, DF, Brazil.
2. Institute of Chemistry, University of Brasilia, Brasilia, DF, Brazil
3. Institute of Exact Sciences, Department of Chemistry, Federal University of Minas Gerais, Belo Horizonte, MG, Brazil.
4. Department of Physics and Informatics, Institute of Physics, University of São Paulo, São Carlos, Brazil.

*Email: douglasbrandao10@hotmail.com

Lapachol is a natural phenolic compound isolated from the bark of *Handroanthus impetiginosus*, this compound can undergoes to several chemical modifications, which produce structural diversity increasing its applications^{1,2}. Fluorescent phenazines and their complexes may be used to stain different cell organelles as well fluorescent imidazoles³. The objective of this study was the *in vitro* evaluation of new fluorescent imidazole and phenazine derivatives from lapachone toward selective mitochondrial staining in live cells. The fluorescent imidazole and phenazine lapachone derivatives (Lch 1 and Lch 2) were evaluated against the tumoral cells MCF-7, Caco-2, PANC-1 and T47D, and also against the normal cells HUVEC. The stained samples were analyzed in confocal laser scanning microscope, Leica, modelo TCS SP5. It was used the MTT assay (tetrazolium salt) in order estimate the cellular cytotoxic effect. The compounds Lch 1 and Lch 2 aldehyde-bearing dyes afforded intense dual fluorescence signals in the ranges of 420-450 nm (blue) and 510 - 560 nm (green) with low background signal noise (figure 1). In order to confirm the lapachone derivatives as mitochondria markers, it was used Mitotracker® cells staining as positive control (Mitotracker is comercial fluorescent dye widely used to stain the mitochondria). It was observed cytotoxic effects only in samples incubated with Lch1 solution at 10 μ M (figure 4). The compound Lch1 produced more accentuated cytotoxic effect than those observed in samples treated with the compound Lch2. The differences related to cytotoxic effects obtained by microscopy analyses and MTT results could be explained by the time of incubation. Our results suggest that it is necessary much more than 30 minutes for both compound start to induce cytotoxicity. Finally, the two tested compounds were very efficient to selectively stain mitochondria (figures 2 and 3). Here we described the azoles prepared from a natural product with highlighted luminescence properties and able to selectively stain mitochondria. This work opens a new avenue for the synthesis and application of fluorescent dyes produced from natural compounds.

REFERENCES

- [1] S. G. C. Fonseca, R. M. C. Braga, D. P. Santana, Rev. Bras. Farm. 2003 ,84, 9-16.
- [2] S. L. de Castro, F. S. Emery, E. N. da Silva Júnior, Eur. J. Med. Chem. 2013, 69, 678-700.
- [3] L. Huang, B. Gu, W. Su, P. Yin, H. Li, RSC Adv.2015, 5, 76296-7630.



Physalis angulata promotes death of promastigotes and amastigotes of *Leishmania (Leishmania) infantum chagasi*

PEREIRA, S.W.G.¹, SILVA, B.J.M.^{1,2*}, RODRIGUES, A.P.D.^{2,3}, SILVA, E.O.^{1,2*}

¹ Federal University of Pará, Institute of Biological Sciences, Laboratory of Parasitology and Laboratory of Structural Biology, Belém, Pará, Brazil

² National Institute of Science and Technology in Structural Biology and Bioimaging, Rio de Janeiro, Rio de Janeiro, Brazil

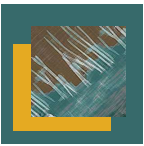
³ Laboratory of Electron Microscopy, Evandro Chagas Institute, Department of Health Surveillance, Ministry of Health, Belém, Pará, Brazil

*E-mail: edilene@ufpa.br

Leishmania (Leishmania) infantum chagasi is the protozoan that causes visceral leishmaniasis in Brazil [1]. The disease affects viscera such as liver, spleen, intestines and bone marrow. It is considered the clinical forms most severe and its treatment are limited, presenting many side effects and high cost [2]. Thus, search for new medicaments from natural origin and high efficacy against the parasite without toxicity are needed. In this context, *Physalis angulata* plant, a natural product widely used in folk medicine, is considered an important alternative source of a new leishmanicidal agent.[3,4,5]. In the present study it was evaluated the effects of aqueous extract of *Physalis angulata* root (AEPa), on promastigotes and amastigotes of *Leishmania (Leishmania) infantum chagasi*. Promastigotes of *Leishmania (L.) i. chagasi* were obtained from the Evandro Chagas's Institute and subjected to treated with AEPa by 96 hours at concentrations of 50, 100 and 200 µg/mL and analyzed by light microscopy and fluorimeter. For transmission Electron Microscopy analysis (TEM), promastigotes treated with AEPa (50 and 100 µg/mL for 72 hours) were fixed with 2.5% glutaraldehyde and 4% paraformaldehyde in 0.1M sodium cacodylate buffer, post-fixed in 1% osmium tetroxide and 0.8% potassium ferricyanide for 1 hour, subsequently, cells were dehydrated in graded acetone and embedded in Epon® resin. Thin sections were stained with uranyl acetate and lead citrate and finally analyzed using a Zeiss LEO 906E TEM. In addition, peritoneal macrophages (J774 cell line) were used for anti-amastigote and viability assays. Treatment with AEPa promoted a reduction in the number of promastigotes (IC₅₀= 67.2 µg/mL, SI= 21.7- Fig. 1A) and amastigotes (IC₅₀= 37.9 µg/mL, SI= 38.5- Fig. 1C) of *L. (L.) i. chagasi*. AMPB reduced 100% the promastigotes number after 96 hours of treatment at concentrations of 0.25, 0.5 and 1 µg/mL (IC₅₀= 0.13 µg/mL) (Fig. 1B). AEPa also induced several morphological changes, indicative of cell death by apoptosis (Fig 2B-D), increase of reactive oxygen species production (Fig. 2E) and apoptosis death (Fig. 2F) in promastigotes treated for 72 hours. In addition, AEPa showed no cytotoxic effect to J774-G8 cells (CC₅₀> 1000- Fig. 1D). These results show that AEPa presented antileishmanial activity against promastigotes and amastigotes of *L. (L.) i. chagasi* without cytotoxicity for macrophages.

REFERENCES

- [1] E.M. Michalsky, et al., Phlebotominae distribution in Janaúba, an area of transmission for visceral leishmaniasis in Brazil. Memórias do Instituto Oswaldo Cruz, 104, (2009).
- [2] J ALVAR, et al., Leishmaniasis Worldwide and global estimates of its incidence. PLoS One, 7, (2012).
- [3] A.M MAHALAKSHMI & B. N. RAMESH. *Physalis angulata*: an ethanopharmacological review. Indo American Journal of Pharmaceutical Research, 4, (2014).
- [4] H.I. MAGALHÃES, et al., *In-vitro* and *in-vivo* antitumour activity of physalins B and D from *Physalis angulata*. *Journal of Pharmacy and Pharmacology*, 58, (2006).



[5] Da Silva et al., *in vitro* biological action of aqueous extract from roots of *physalis angulata* against *Leishmania (Leishmania) amazonensis*. BMC Complementary and Alternative Medicine. 15, (2015).

[6] This research was supported by CNPq (Brazil), CAPES (Brazil), INBEB (Brazil) and FAPESPA.

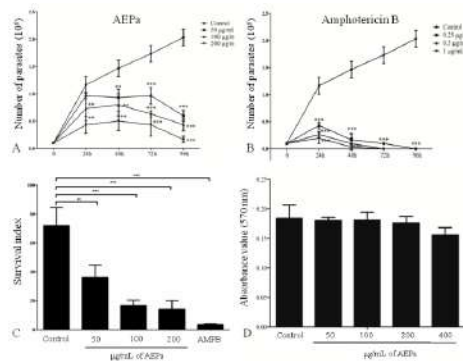


Figure 1: Leishmanicidal action of AEPa. A) Antipromastigote assay on *L. (L.) i. chagasi* treated with 50, 100 and 200 µg/mL AEPa for 4 days. Note that AEPa reduce the parasite number when compared to the control. B) Promastigotes treated with 0.25, 0.5 and 1 µg/mL of Amphotericin-B (AMPB) for 4 days. AMPB was able to reduce in 100% the number of *Leishmania*. C) AEPa action on amastigotes of *L. (L.) i. Chagasi*. Note that AEPa reduced the number of intracellular parasites when compared to the untreated control, AMPB (0.5 µg/mL) was used as a positive control. D) Viability of macrophages treated with AEPa for 3 days. AEPa showed no cytotoxic effect for J774-G8 cells. ANOVA, followed by Tukey test, (**) $p < 0.01$, (***) $p < 0.001$.

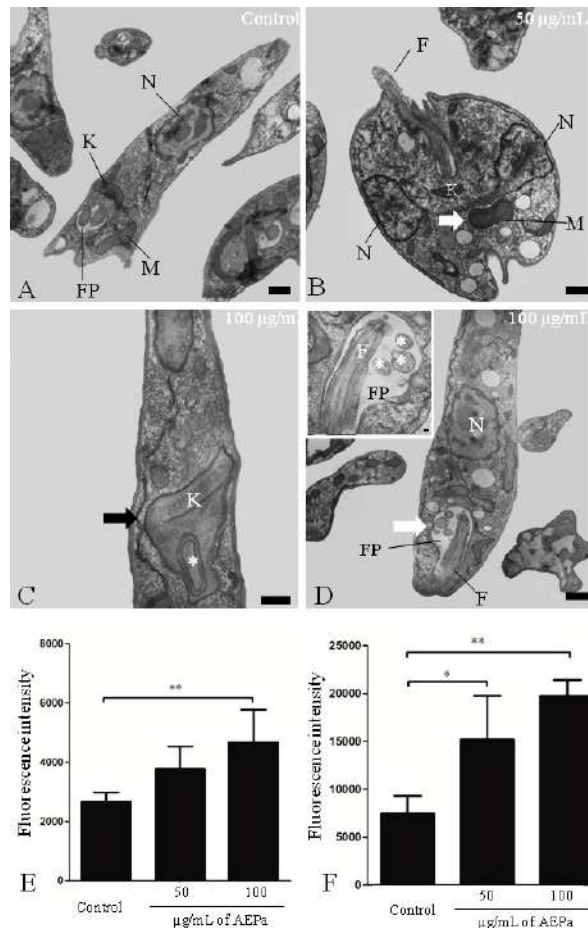


Figure 2: Effect of AEPa on promastigotes of *L. (L.) i. chagasi*. Transmission electron microscopy analysis. A) Untreated control, parasite showing a typical morphology. B) Promastigotes treated with 50 µg/mL AEPa, note parasite with two nuclei and only one kinetoplast, observe also the presence of myelin-like figures in the mitochondria (white arrow). C) Promastigotes treated with 100 µg/mL, note atypical morphology of kinetoplast, observe alterations in shape and swelling (arrow) and the appearance of concentric membrane (*). Promastigotes treated with 100 µg/mL AEPa, note the presence of vesicles in the flagellar pocket and in the mitochondria (white arrow). Inset of figure 2D showing the presence of vesicles in the flagellar pocket (*). N-nucleus; FP-flagellar pocket; K -kinetoplast; F-flagellum; M - Mitochondria. Bars (A, B, C and D): 2µm, inset: 0.2 µm. E-F) Mechanism leishmanicidal activity AEPa on *L. (L.) i. chagasi* promastigotes. Detection of reactive oxygen species (ROS) production by CellRox assay in treated and untreated *L. (L.) i. chagasi* promastigotes for 72 hours with AEPa (50 e 100 µg/mL). Note the high production of ROS in the protozoa after 72 hours of treatment (100 µg/mL) with AEPa. Apoptosis detection (Annexin V), fluorescence intensity of the cells labeled with Annexin V. AEPa causes death by apoptosis in promastigotes of *L. (L.) i. Chagasi*. ANOVA, followed by Tukey test (*) $p < 0.05$, (**) $p < 0.01$.



DOI: [INSERIR ENDEREÇO DO DOI AQUI.](#)

Caderno de Resumos do 26º Congresso Brasileiro de Microscopia da SBMM – ISSN: [INSERIR AQUI.](#)

Epifluorescence And Laser Scanning Confocal Microscopy Applications at Universidade Federal De Lavras – UFLA

Eduardo Alves^{1*}, Silvino Intra Moreira¹, Fabiano França Silva¹, Eduardo Mateus Nery¹, Lucas Silveira Lopes¹, Elisa de Melo Casto¹, Aline Norberto Ferreira¹.

1. Laboratório de Microscopia Eletrônica e Análise Ultraestrutural – LME, Depto de Fitopatologia – Anexo I, Universidade Federal de Lavras – UFLA, Lavras MG, Brazil.
*Email: ealves@dfp.ufla.br.

Created in 2002, the Electron Microscopy and Ultrastructural Analysis Lab (LME) helps many UFLA Departments and other Institutions with research, extension and teaching activities, with equipment to carry out Bright field microscopy, Scanning and Transmission electron microscopy, and Epifluorescence and Laser scanning confocal microscopy. To perform fluorescence microscopy assays the LME uses the Epifluorescence microscopes: Inverted Zeiss Axio Observer Z1 with Apotome system (Axio Vision Software) and the Vertical Leica DM2000 (LAS v.4.5 Software); Stereoscope fluorescence microscope Nikon SMZ1500 (NIS Elements D3.2 Software); and the Laser scanning confocal Zeiss LSM780. Several studies have been developed at the Lab using fluorescence techniques, mainly in detection and localization of plant pathogens, such as viruses, fungi and bacteria; beneficial agents, such as nitrogen-fixing bacteria and fermentative yeasts; and also plant components. Microorganisms have been studied through genetic transformation for fluorescent proteins expression, such as the Green Fluorescent Protein (GFP) (Figure 1 A and B) and Red Fluorescent Protein (RFP) (Figure 1 C), or by the use of fluorochromes. The fluorochromes Alexa Fluor® 488 (Figure 1 D) or Calcofluor White can be used for fungi. Plant cellular components are marked with fluorochromes for location and or relative quantification by fluorescent intensity analysis. Some examples are lignin marked with Auramine-O (Figure 1 E), callose with Aniline Blue (Figure 1 D), and cellulose with Calcofluor White (Figure 1 F) and pectin with Coriphosphine O (Figure 1 G). Emulsions in food have been characterized with Rhodamine-B for locating proteins (Figure 1 H), Nile Red for lipids (Figure 1 I) and Fluorescein-5-isothiocyanate for carbohydrates (Figure 1 J). Tests to verify the cell mortality are done with Propidium Iodide, as in the wine fermentative yeasts assay (Figure 1 K). This fluorochrome can be used also to mark the fungal nucleus, such as *Rhizoctonia* (Figure 1 L). As a nucleus marker, 4',6-Diamidine-2'-phenylindole dihydrochloride (DAPI) is widely utilized, and it can be useful to visualize chromosomes in the condensation phase (Figure 1 M). During the hands-on classes and calibrations it is common to have autofluorescence observations with *Convallaria* rhizome slides (Figure 1 N) and the palm caterpillar *Opsiphanes invirae* (Figure 1 O), as well as bovine muscle cell slide (Figure 1 P) with markers for nucleus (DAPI), and immunostaining for tubulin (Rabbit mAb, green) and actin (Alexa Fluor® 555, red). Thus, several fluorescence microscopy techniques are routinely used in the LME and contribute to the teaching and research projects of various fields of Agrarian and Biological Sciences.

Financial Support: CAPES, CNPq, FAPEMIG and FINEP.

Key words: Fluorescence, Confocal, Laser Scanning Confocal Microscopy.

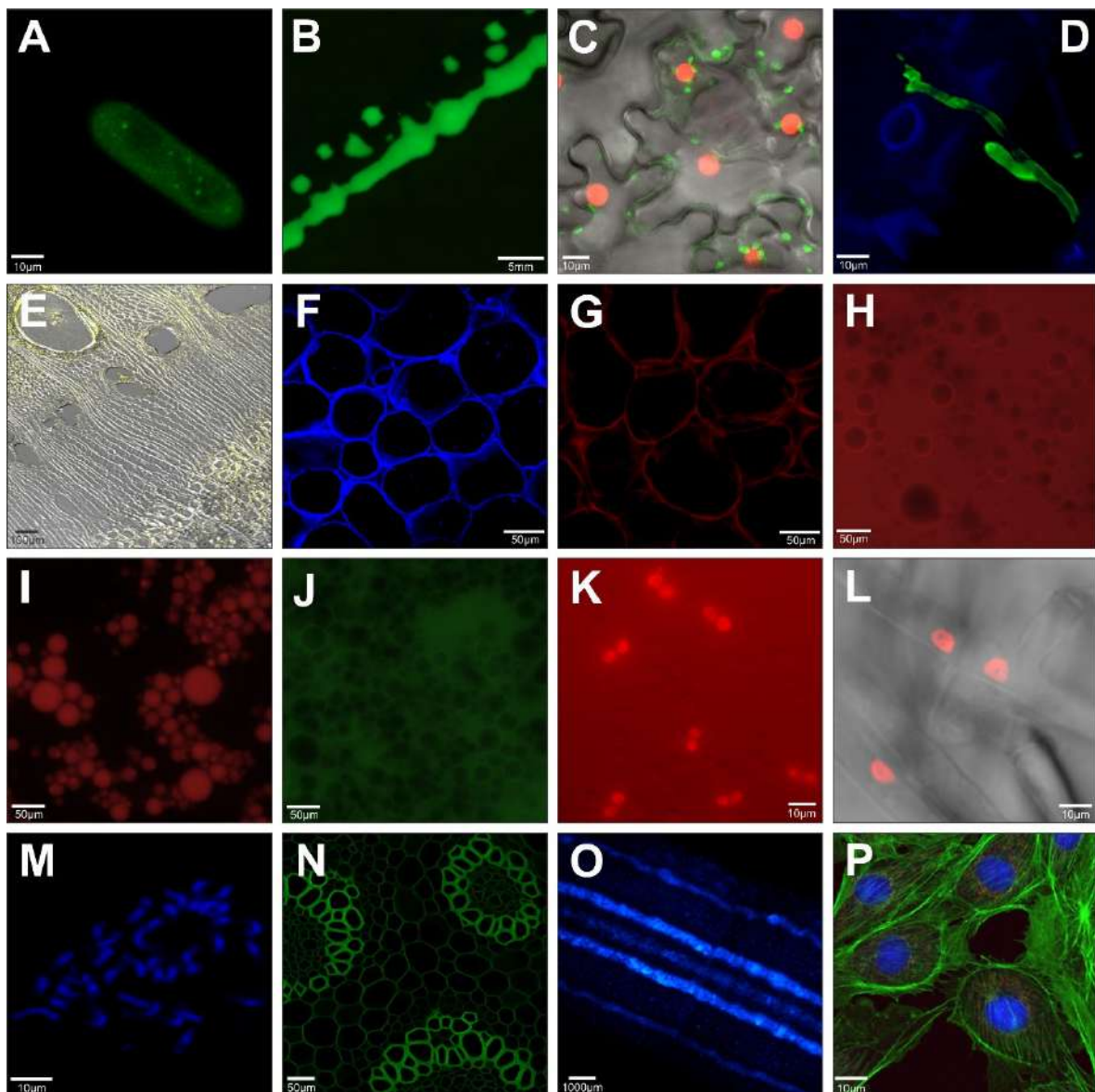
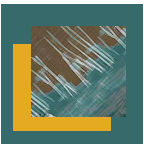


Figure 1: Organisms transformed for GFP expression: *Colletotrichum gloeosporioides* conidium (A) and a *Rhizobium* sp. culture stria (B). Leaf adaxial surface of a tobacco transformed for RFP expression associated with a Coffee ringspot virus (CoRSV) protein (C). *Alternaria alternata* marked with the Alexa Fluor® 488 fluorochrome (D, green) at the tangerine leaf abaxial surface marked for callose localization with Aniline Blue (D, blue). Lignin localization at the *Eucalyptus* cambium with Auramine-O (E). Peach fruit pulp cut stained with Calcofluor White for cellulose (F) and Coriphosphine O for pectin (G). Rhodamine-B for locating proteins (H), Nile Red for lipids (I), and Fluorescein-5-isothiocyanate for carbohydrates (J) in food emulsions. Propidium iodide evidencing died wine fermentative yeasts (K) and *Rhizoctonia* nucleus (L). *Brachiaria* chromosomes stained with DAPI in the condensation phase (M). Autofluorescence in *Convallaria* rhizome (N) and in the palm caterpillar *Opsiphanes invirae* back (O). Bovine muscle cell (P) with nucleus marked by DAPI, and immunostaining for tubulin (Rabbit mAb, green) and actin (Alexa Fluor® 555, red). The images A, C–G, L–N, and P were acquired with Laser scanning confocal microscopy; B and O: Stereoscope fluorescence microscopy; H – K: Epifluorescence microscopy.



Preliminary studies on the localization and ultrastructural characterization of processing bodies in *Trypanosoma cruzi*

Eduardo Glejzer¹, Wendell Girard-Dias^{1,2}, Wanderley de Souza^{1,3}, Kildare Miranda^{1,3}

1. Laboratório de Ultraestrutura Celular Hertha Meyer, Instituto de Biofísica Carlos Chagas Filho and Instituto Nacional de Ciência e Tecnologia em Biologia Estrutural e Bioimagens – Universidade Federal do Rio de Janeiro, Rio de Janeiro, Brazil.

2. Plataforma de Microscopia Eletrônica Rudolf Barth – IOC / Fiocruz.

3. Instituto Nacional de Biologia Estrutural e Bioimagem, INBEB.

*Email: kmiranda@biof.ufrj.br

Trypanosoma cruzi is the causative agent of Chagas disease which is a worldwide spread disease, specifically in some regions such as Latin American countries, including Brazil. The functional correlation between structures found in this parasite and biochemical and molecular processes, such as post-transcriptional control by RNA-binding proteins (RBP) is of paramount importance to the understanding of *T. cruzi* biology [2]. Some sites of mRNA metabolism regulation have been recently described, among them some known as Processing Bodies (P-bodies). They are aggregates of ribonucleoprotein (RNP), a complex of mRNA molecules and RBPs, usually seen as cytoplasmic granules, when analysed by fluorescence microscopy. Interestingly, they have been associated with the regulation of mRNA metabolism especially during stress conditions such as starvation, heat shock, pH stress and osmotic stress when it is possible to identify differences in protein content, number and size of those granules [3,4]. It is assumed that P-bodies act as storage or degradation sites of mRNA. Despite being extensively studied from the biochemical and molecular point of view, the fine structure of the P-bodies complexes is still not completely understood in this parasite. Here, we present preliminary data on the attempt to characterize the ultrastructure of the P-bodies of *T. cruzi* epimastigotes by fluorescence microscopy and and electron microscopy analysis of high pressure frozen and freeze substituted samples [5]. Immunolocalization analysis by super-resolution fluorescence microscopy of cells incubated with antiserum against the protein DHH1, a helicase normally found in protein content of P-bodies and often used as a reporter to identify them, showed clearer and specific distribution of granules through cell body (figure 1). In contrast to chemically-fixed cells, samples prepared by high-pressure freezing (HPF) and freeze substituted (FS) showed several clusters of ribosomes (figure 2), possibly representing the P-bodies. Further analysis using correlative microscopy approaches will be carried out to establish the possible functional correlation between the P-bodies and the ribosome clusters found in HPF cells.

REFERENCES

- [1] Wanderley de Souza (2002) *Current Pharmaceutical Design*, 8: 269-285.
- [2] Sandra M. Fernández-Moya et al (2010) *Wiley Interdisciplinary Reviews RNA*, 1: 34-46.
- [3] Lysangela Ronalte Alves et al (2016) *World J Biol Chem*, 7(1): 78-87.
- [4] Fabíola Barbieri Holetz et al. (2007) *Biochemical and Biophysical Research Communications*, 356: 1062-1067.
- [5] Girard-Dias W, Alcantara CL, Cunha-e-Silva N, De Souza W, Miranda K (2012) *Histochem Cell Biol* 138:821–831.
- [6] This research was supported by CNPq, FAPERJ, FINEP and CAPES (Brazil).

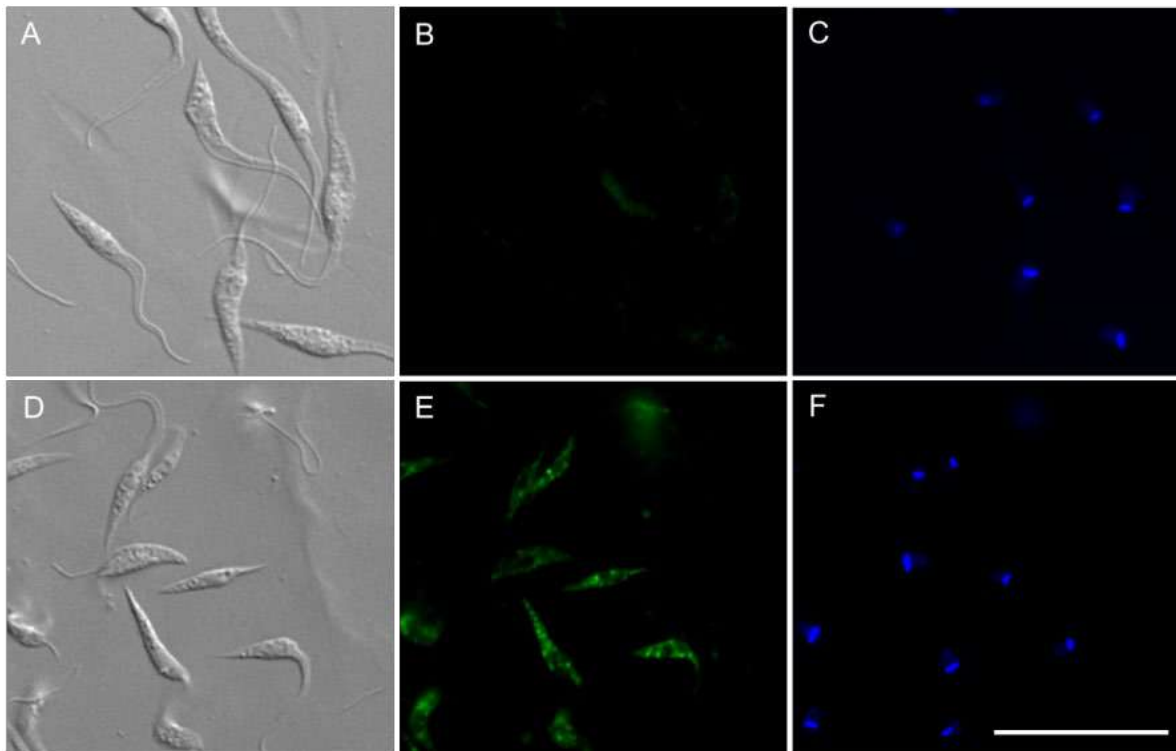
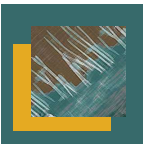


Figure 1. Immunolocalization of P-bodies. (a,d) Differential interference contrast microscopy of control and incubated with antiserum against DHH1 cells, respectively. (b,e) Conjugated Alexa-488 imaging showing clear and specific granules through cell body. (c,f) Nuclear staining by DAPI. Scale bar 20 µm for all images.

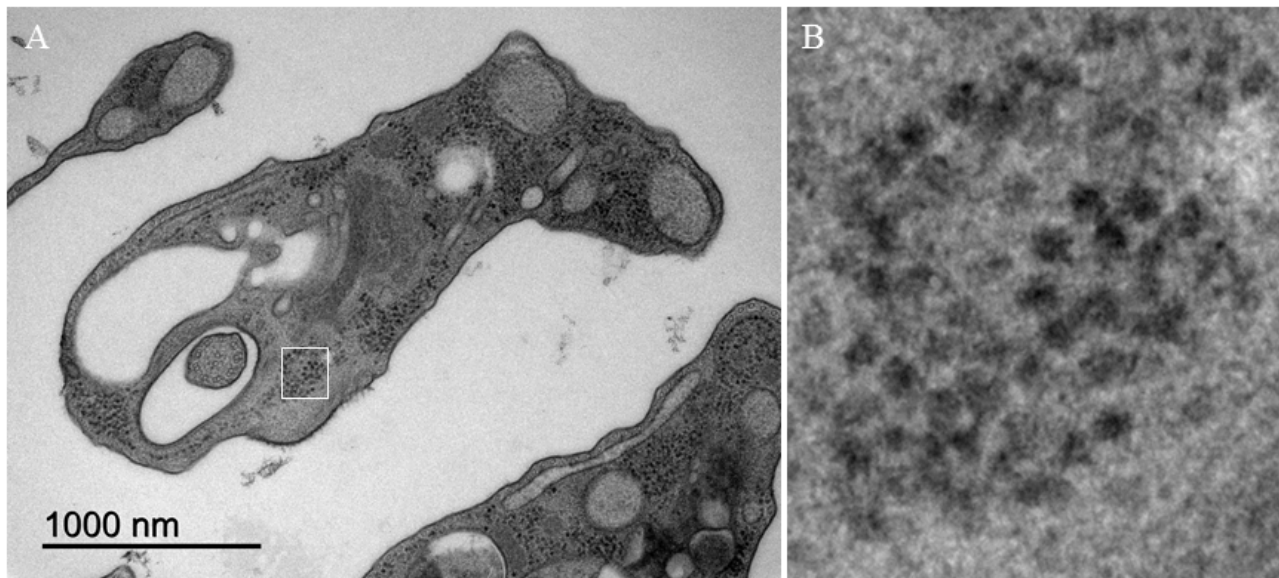


Figure 2. Transmission Electron Microscopy of cryofixed cells. (a) Epimastigotes processed by high pressure freezing and freeze substitution. (b) Amplification of square box area on image A.



Antifungal Activity of Lectin from *Alpinia purpurata* Inflorescence against *Candida*

Gustavo Ramos Salles Ferreira¹, Jéssica de Santana Brito¹, Thamara Figueiredo Procópio¹, Bárbara José Rocha Cardoso de Lima², Elinaldo Francisco de Lima Bento^{2,*}, Luana Cassandra Breitenbach Barroso Coelho¹, Patrícia Maria Guedes Paiva¹, Tatiana Soares², Maiara Celine de Moura¹ and Thiago Henrique Napoleão¹

1. Departamento de Bioquímica, Universidade Federal de Pernambuco, Recife, Brazil.

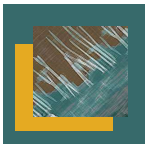
2. Centro de Tecnologias Estratégicas do Nordeste, Universidade Federal de Pernambuco, Recife, Brazil.

*Email: tinhoxp1@gmail.com

The genus *Candida* comprises a group of fungi that belong to the microbiota of the oral cavity as well as of the vaginal and intestinal tracts of humans. However, they can cause local and systemic infections, mainly in situations where the immune system is compromised [1] [2]. More than 17 species of *Candida* are recognized as etiological agents of diseases, but more than 90% of the invasive infections are caused by *Candida albicans*, *Candida parapsilosis*, *Candida tropicalis*, *Candida glabrata* and *Candida krusei* [3]. The abilities to evade host defenses, to form biofilms (both in host tissues and medical devices), and to produce hydrolytic enzymes that damage tissue structures are the main virulence factors of the pathogenic species of *Candida* [4]. The increase in the number of patients with decreased immunity, submitted to invasive procedures, and users of intravenous catheters and parenteral nutrition, as well as the reports on the resistance of *Candida* strains to the antibiotics currently used, have led to an increase in the number of infections caused by these fungi [5]. The lectins are proteins that bind carbohydrates and are broadly distributed in nature. [6]. In plants, they can be found in seeds, leaves, roots, inflorescences, rhizomes, barks and other tissues [6] and have presented several biological activities such anti-inflammatory [7], antitumor [8] and antimicrobial [9] effects. Thus, lectins possess a broad biotechnological potential. *Alpinia purpurata* (Viell.) K. Schum. is an ornamental plant from the Family Zingiberaceae, native from Pacific islands and currently broadly cultivated in Brazil due to its ability to bloom all year long and the exuberance and durability of the flowers [10]. The inflorescences of this plant contain an essential oil with larvicidal and antimicrobial activities [11]. The present work describes the evaluation of antifungal activity of a lectin isolated from the inflorescences of *Alpinia purpurata* (ApuL) against *Candida albicans* e *Candida parapsilosis*, by determining the minimal inhibitory (MIC) and fungicidal (MFC) concentrations as well as by analysis through scanning electronic microscopy (SEM). ApuL was obtained following a purification protocol previously established in the *Laboratório de Bioquímica de Proteínas* from the *Universidade Federal de Pernambuco*. The MIC and MFC values were determined as described by Procópio et al. [12]. ApuL showed fungistatic and fungicidal properties against *C. albicans* with MIC of 195 µg/ml and MFC of 390 µg/ml and for *C. parapsilosis* with MIC and MFC of 390 µg/ml. For the microscopic characterization of the microorganisms before and after the exposition to ApuL at previously concentrations; those were freeze-dried and prepared with an Au coating for the Scanning Electron Microscopy (SEM) analysis. From SEM images, it was possible to observe alterations on cell walls caused by the presence of ApuL in experiments performed with *C. albicans* and *C. parapsilosis* (Figure 1 and 2). The SEM images obtained for treatments at the MIC demonstrated that the incubation of the lectin resulted in damage to cell wall (Figure 1) as well as interfered in the separation after cell division and caused agglutination (Figure 2). In conclusion, ApuL is a bioactive agent against the tested *Candida* species, inhibiting their growth and causing structural damages.

REFERENCES

[1] L.C. Shao et al., Acta Pharm Sin B., 42 (2007) 1129-1136.



- [2] J.C.O. Sardi et al., J. Med. Microbiol. 62 (2013) 10-24.
- [3] M.A. Pfaller et al., J. Clin. Microbiol. 45 (2007) 3522-3528.
- [4] M. Ortega et al., J. Hosp. Infect, 77 (2011) 157-161.
- [5] S. Silva et al., FEMS. Microbiol. Rev. 36 (2011b) 288-385.
- [6] P.M.G Paiva et al., Bioprocess Sci. Technol. (2011) 269-264.
- [7] M.N Napimoga et al., Int. Immunopharmacol. 7 (2007) 824-835.
- [8] L.P. Albuquerque et al., Acta Trop. 138 (2014a) 23-27.
- [9] M.C. Moura et al., J. Appl. Microbiol. 119 (2015) 666-676.
- [10] C.P. Victório et al., J. Essent. Oil. Res. 22 (2010) 22-24.
- [11] G.K.N. Santos et al., Ind. Crops Prod. 40 (2012) 254-260.
- [12] T.F. Procópio et al., Int. J. Biol. Macromol. 98 (2017) 419-429.

Acknowledgments: CNPq, FACEPE, Centro de Tecnologias Estratégicas do Nordeste (CETENE), CAPES.

Figure 1. SEM images of the *Candida parapsilosis* (a) in the absence and (b) in the presence of ApuL in MIC and MFC concentration of 390 $\mu\text{g mL}^{-1}$.

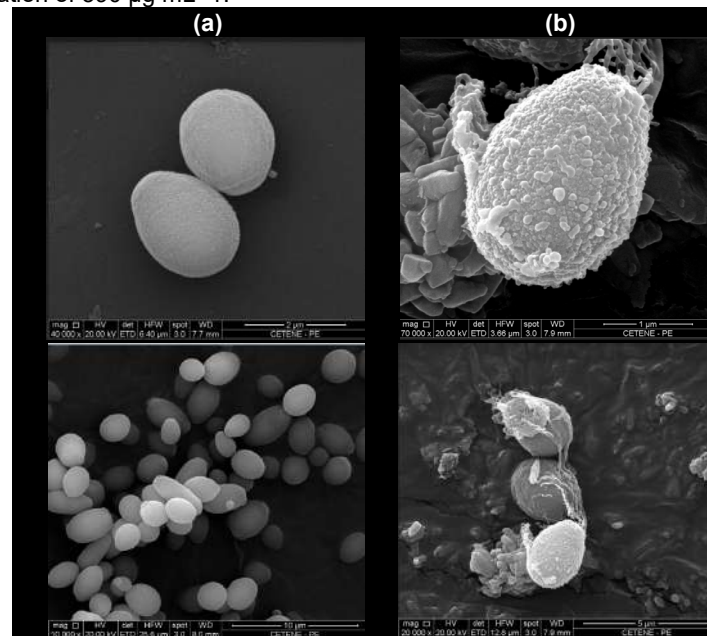
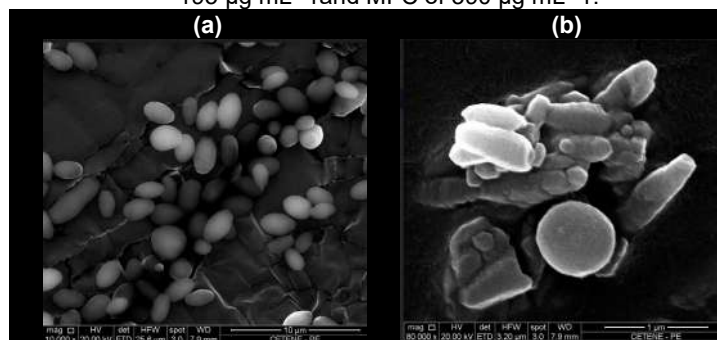
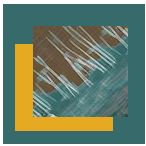


Figure 2. SEM images of the *Candida albicans* (a) in the absence and (b) in the presence of ApuL in MIC 195 $\mu\text{g mL}^{-1}$ and MFC of 390 $\mu\text{g mL}^{-1}$.





Trypanosoma cruzi Reservosomes Change In Number And Volume Before Cell Division

Felipe S. Gama¹, Aline A. Alves¹, Carolina L. Alcantara¹, Narcisa L. Cunha-e-Silva^{1*}

1. Laboratório de Ultraestrutura Celular Hertha Meyer, Instituto de Biofísica Carlos Chagas Filho, UFRJ, Rio de Janeiro/Brazil

Reservosomes are organelles found at the posterior region of the epimastigote form of *T. cruzi*. They were named due to their ability to accumulate lipids and proteins. These structures also contain proteases and an acidic pH, similar to pre-lysosomes [1]. Previous evaluation showed that reservosomes are organelles with a diameter of 400-600 nm [2], which would correspond to a volume of 0.3-0.9 μm^3 considering an approximately round form. The purpose of this new study is to apply a novel methodology and assess data on the number and volume of reservosomes per cell during G1 and G2 phases of the cell cycle. Three dimensional reconstruction can show both parameters of the cell, including if it is preparing for mitosis by analyzing other structures of the cell, such as the presence of one or two basal bodies/flagella. Epimastigotes incubated with Transferrin-Au as an endocytic tracer were processed for electron microscopy, associating thiocarbohydrazide [3] with osmium post fixation to enhance contrast, embedded in Epon and then ultrathin sections of 100 nm were obtained using SBF-SEM (Serial Block Face Scanning Electron Microscope) in collaboration with Dr. Sue Vaughan at the Oxford Brookes University. Alternatively, epimastigotes were incubated with horseradish-peroxidase, processed for electron microscopy, with cytochemical development of the enzyme. Series of images with a step size of 30 nm were obtained using FIB-SEM (Focused Ion Beam Scanning Electron Microscope). Using the software 3dmod, developed by Mastronarde *et al.*[4], whole cells were reconstructed (Figure 1) and had their reservosomes counted. Preliminary results showed that reservosomes of parasites in G2 are bigger and more abundant when compared to parasites in G1 (Table 1). More cells will be reconstructed to test our hypothesis that epimastigotes enlarge their endocytic compartments before mitosis. Moreover, our preliminary results showed that data obtained using 3D reconstruction of whole cells from FIB-SEM or SBF-SEM preparations are comparable with those obtained by stereology of aleatory ultrathin sections [2].

REFERENCES

- [1] M.J. Soares *et al.*, Journal of Cell Science 102: 157-167 (1992)
- [2] Soares & De Souza, Journal of Submicroscopic Cytology and Pathology 20 (2): 349-361(1988)
- [3] Willingham, M. C. and Rutherford, A. V., J. Histochem. Cytochem. 32, 455-460 (1984)
- [4] Mastronarde *et al.*, University of Colorado (1994)
- [5] This research was supported by CNPq and FAPERJ (Brazil)

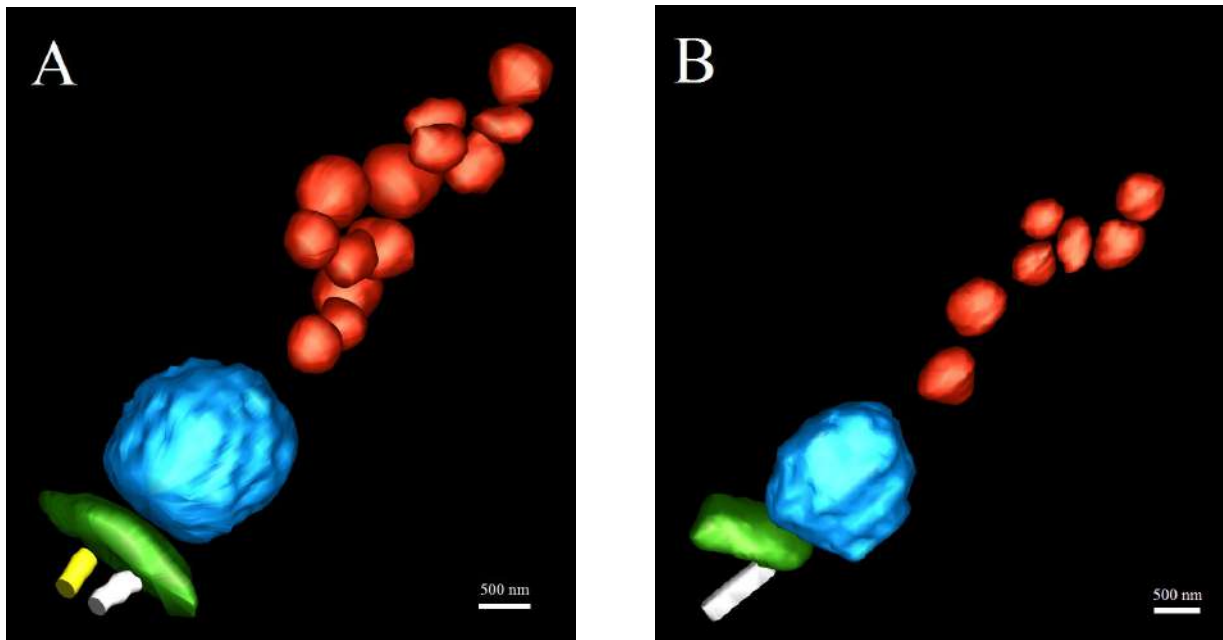
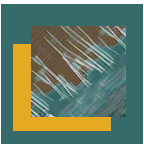


Figure 1 - 3D Reconstruction of *T. cruzi* epimastigotes during G2 (A) and G1 (B), showing Reservosomes (Red), Nucleus (Blue), Kinetoplast (Green) and Old Flagellum (White) and New Flagellum (Yellow).

Table 1 - Comparison of reservosomes of G1 and G2 epimastigotes, showing their quantity, volume and diameter.

Cell cycle phase	Reservosomes per cell ³	Mean Reservosome Volume ³ (µm ³)	Mean Reservosome Diameter ³ (nm)
G1 ¹	7	0.65 ± 0.07	540 ± 20
G2 ²	11 ± 2	1.40 ± 0.07	700 ± 55

¹ N = 2 ; ² N = 7; ³ Mean ± standard deviation



Microscopy of Light and Confocal Laser Scanning of *Gelidium floridanum* Tetraspores Germination Treated with EGTA

Fernanda Bouvie^{1*}, Débora Tomazi¹, Marianne Kreuch¹, Nandara de Bortoli¹, Elisa Filipin¹, Deonir Batista¹, Luciane Ouriques¹, Zenilda Bouzon¹ and Carmen Simioni¹.

1. Plant Cell Biology Laboratory, Department of Cell Biology, Embryology and Genetics, Federal University of Santa Catarina, Florianópolis, SC, Brazil

*Email: fernanda.bouvie@gmail.com

Gelidium floridanum, a species of red alga, it presents great economic importance due to the ficoloid compound, found in its cell wall, the agar. Its pattern of spore germination is the "Gelidium" type, presenting tetraspores that when released do not have cell wall. After its establishment, it undergoes a polarized disorganization of the cytoplasmic content, which allows the cellular expansion, allowing the rapid formation of a protuberance, denominated germ tube. In macroalgae, the role of inorganic ion Ca^{2+} is fundamental in the polarization of zygotes of fucoid algae, as well as in the formation of the germ tube of spores [1]. In order to inhibit Ca^{2+} , many studies use EGTA (ethylene glycol-bis (b-amino-ethyl ether) N, N', N', N'-tetra-acetic acid) which acts as a chelating agent for bivalent ions. This study aimed to characterize the action of extracellular Ca^{2+} during the initial development of macroalga *G. floridanum* by treatment with EGTA 1 mM. Fertile tetrasporophytic thalli were selected and placed for release of the tetraspores. After release, tetraspores were cultivated on slides in petri dishes for a period of 6 hours, during this time the germ tube formation occurred. After the treatments, light microscopy analyzes were used to verify the formation of the germ tube and analyzes with confocal laser scanning microscopy to observe the cell wall formation, actin filaments and chloroplast organization. Rhodamine-phalloidin was used to label the actin filaments, which were observed at a laser excitation wavelength of 500 to 580 nm (green) and Calcofluor to label the cell wall and its fluorescence was observed at the 405 nm laser wavelength with an emission spectrum of 410 to 480 nm. The autofluorescence of chloroplasts was observed at a 488 nm (violet) laser excitation wavelength with an emission spectrum of 510 to 750 nm. The samples were observed in a DMI6000B Confocal Laser Scanning Microscope (Leica TCS SP-5, Germany) of the Central Laboratory of Electronic Microscopy (LCME). After 6 hours of culture, the tetraspores of *G. floridanum* begin to form the germ tube (Fig. a), where fine filaments of actin and presence of a cell wall are visualized (Fig. b, c). At this time, migration of the chloroplasts also occurs towards the tip of the germ tube. When treated with EGTA, chelating the extracellular Ca^{2+} , the tetraspores were not visualized with tube formation, but the majority presented reddish cytoplasmic staining and it was considered viable (Fig d). These tetraspores showed actin filaments only at the periphery of the cytoplasm (Fig e), and did not form cell wall (Fig. f). The elliptic chloroplasts remained in the central region of the tetraspores. We conclude that at the beginning of germination of *G. floridanum* tetraspores, Ca^{2+} is essential for the polymerization of actin filaments, which help the migration of cytoplasmic contents and formation of the germ tube, as well as the formation of the cell wall.

REFERENCES

- [1] Z. L. Bouzon et al., Ultrastructure of tetraspore germination in the agar-producing seaweed *Gelidium floridanum* (Gelidiales, Rhodophyta). *Phycology*. (2005) v. 44: 409-415.
- [2] This research was supported by CAPES (Brazil).

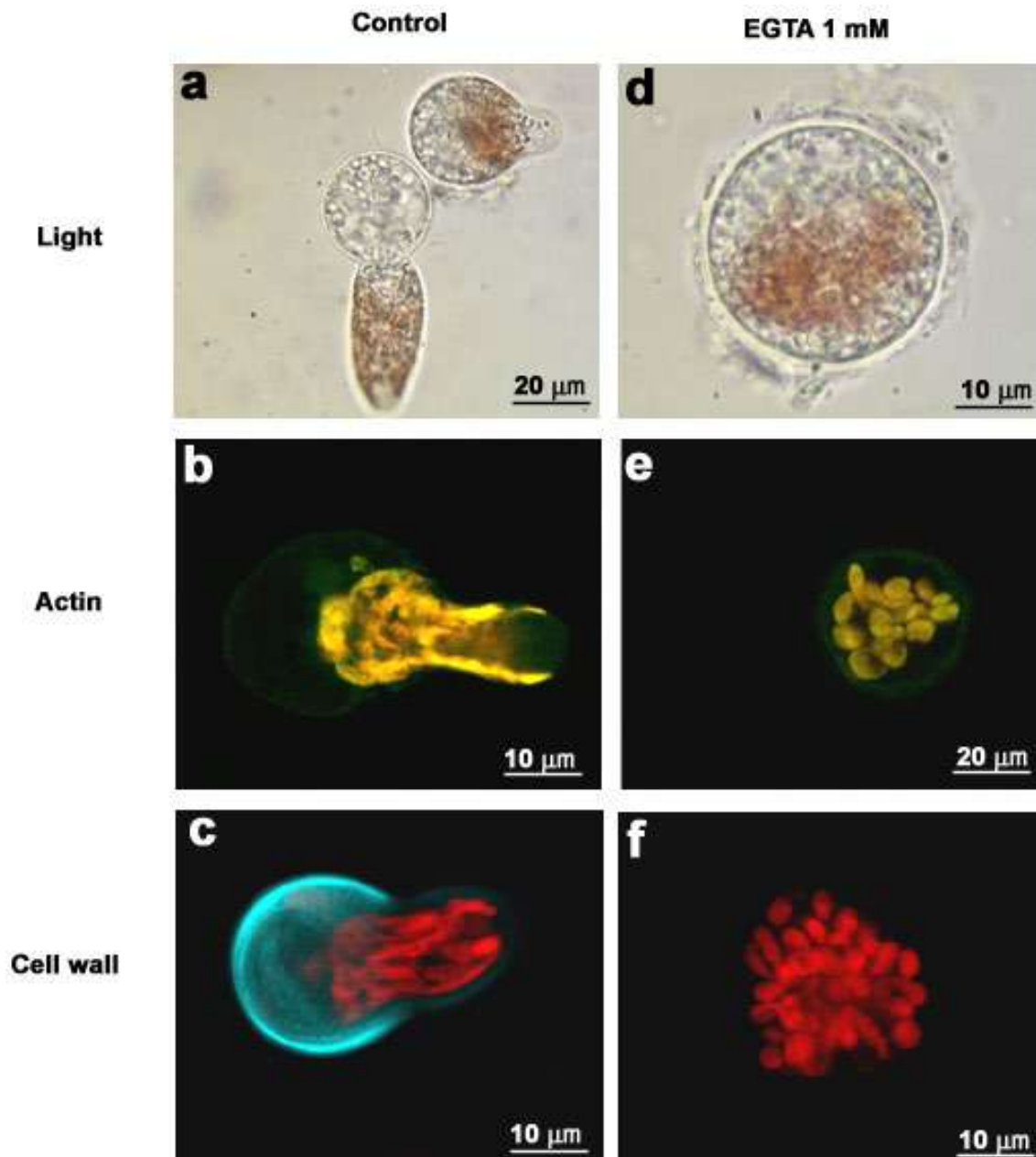
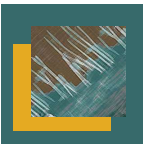


Figure 1 – Microscopy of light and confocal laser scanning of tetraspores of *Gelidium floridanum*; a-c: Tetraspores control, with formation of the germinative tube (a), presence of filament of actin (b) and cell wall (c). Perceive the movement of chloroplasts towards the germ tube d-f: Tetraspores treated with EGTA, without formation of the germ tube, presence of actin filaments only in the periphery of the cytoplasm and without formation of the cell wall. Perceive that chloroplasts are elliptical and remain in the central region. Actin filaments (green). Cell Wall (blue). Chloroplasts (red and yellow).



Histopathological Analysis of livers of *Danio rerio* Exposed to Manganese

Gabriela Zimmermann Prado Rodrigues^{1*}, Bruna Graziela Zwetsch¹, Günther Gehlen¹

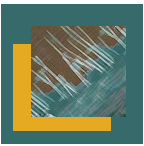
1. Laboratory of Comparative Histology, Feevale University, Novo Hamburgo, Brazil

*Email: gabizpr@gmail.com

Environmental impacts of anthropogenic origin are constantly increasing and interfere with the quality of water resources, which are daily polluted by the incorrect disposal of numerous substances. Studies indicate that environmental exposure to manganese and its mixtures pose threats to public and animal health [1] because even when performing essential functions in humans and animals [2], higher concentrations can affect the brain and liver of organisms [3], resulting in motor behavioral changes [4]. In this context, the objective of the present study was to evaluate the tissue damage caused in the liver (indicating the nutritional and toxic state of the animal) in fishes exposed to manganese, through the histopathological analysis that reflects the health of the organ [5]. For this, specimens of *Danio rerio* (n= 3) were exposed for 96 hours at concentrations of 0.5 mg/L, 2.0 mg/L, 4.0 mg/L, 8.0 mg/L and 16.0 mg/L, in addition to these concentrations, a control group was kept under the same conditions in the water from the dechlorinated tap. At the end of the exposure, the animals were immediately sacrificed for liver removal. The samples were fixed in Formol, embedded in paraffin, cut in a 5 micron rotating microtome, and stained with hematoxylin and eosin. Fifteen fields were analyzed per animal under optical microscopy (400x magnification), where the degree of cell vacuolation was classified as 1 (non-pathological), 2 (mild to moderate) and 3 (severe alterations), according to Schwaiger and collaborators in 1997 (Figure 1). The number of hepatocytes per field (0.25 x 0.18 mm), and the area of 35 cells per group were also recorded through ImageJ Software. Statistical analysis was performed using the Kruskal-Wallis test, followed by the Dunn post-test, and differences were considered significant when $p < 0.05$. Regarding the analysis of cell vacuolation, the 16 mg/L group presented a significantly higher number of cells with grade 3 histopathological lesions if compared to the control group and the concentration of 0,5 mg/L; the group of 4, 0 mg/L also presented a higher number of grade 3 lesions when compared to 0,5 mg/L (Figure 2). Concerning the hepatocyte count, the 16 mg/L group had a higher amount of cells than the animals exposed to the concentrations of 0,5 mg/L and 4,0 mg/L, as can be observed in figure 3, which also presents the data of the cellular areas analyzed, where the 16 mg/L group had a higher mean cell area than the 0,5 mg/L and 4,0 mg/L groups. Like this, it was observed that the number of hepatocytes and the area of these cells increased in the three highest concentrations tested, but for a better interpretation of these data, it is necessary to analyze the rest of the animals from this acute exposure. In addition, the presence of vacuolation, which indicates cellular degeneration, may be associated with the fact that in biological media, manganese in any oxidation state can spontaneously give rise to infinitesimal amounts of Mn 3+, leading to the formation of reactive species of Oxygen, lipid peroxidation and subsequent cell death [7]. According to Van Dyk and collaborators (2007), this cellular response suggests the presence of regions with accumulation of lipid and glycogen inclusions, or the combination of toxic agents with intracytoplasmic lipids. These data, despite of being partial, corroborate with the literature that elects the liver as one of the organs most affected by metals such as manganese. This fact can be explained due to the number of mitochondria of the tissue, since this is the organelle where the accumulation of manganese occurs in the cell [7]. As future prospects, these analyzes will be done in a larger number of animals and the histopathological lesions caused by manganese in *Danio rerio* brains will also be evaluated.

REFERENCES

- [1] A.P. Sanders et al. Current Environmental Health Reports., 2 (2015), p. 284.
- [2] I. Thornton. Metal and Environmental., (1995).
- [3] S.C.T. Silva. Monografia Centro Federal de Educação tecnológica., (2015).



- [4] J.A. Roth. Neurotoxicology., 44 (2014) p. 314.
- [5] S. Zimmerli et al., Aquatic Sciences., 69 (1) (2007) p.11.
- [6] J. Schwaiger et al. J. of Aquatic Ecosystem Stress and Recovery., 6 (1)(1997) p. 75.
- [7]D. Hamai et al., Free Radical Biology and Medicine., 31(6) (2001) p.763.
- [8] J.C. Van Dyk et al., Ecotoxicology and Environmental Safety., (66) (2007) p. 432.
- [9] WHO. World Health Organization. Environmental Health Criteria 17 (1981).

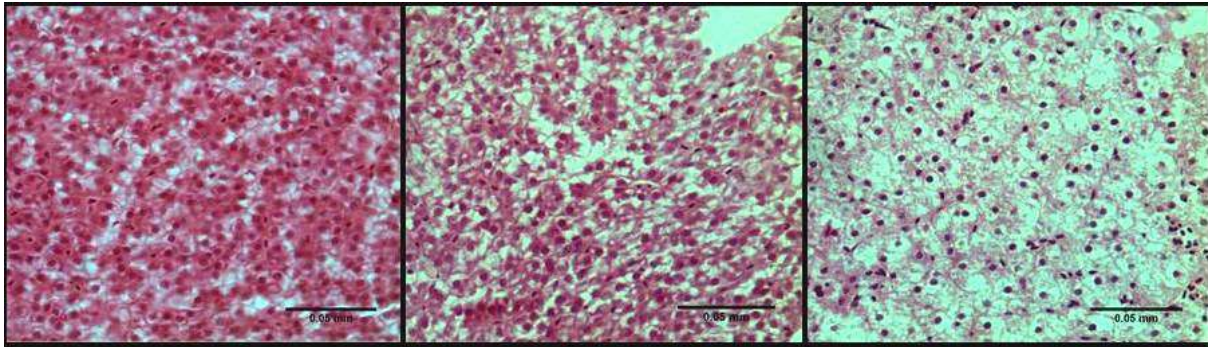


Figure 1: Representation of cell vacuolization. Grade 1, 2 and 3, respectively.

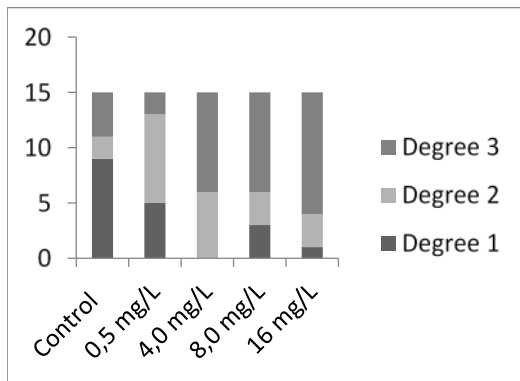


Figure 2: Cell vacuolization of hepatocytes.

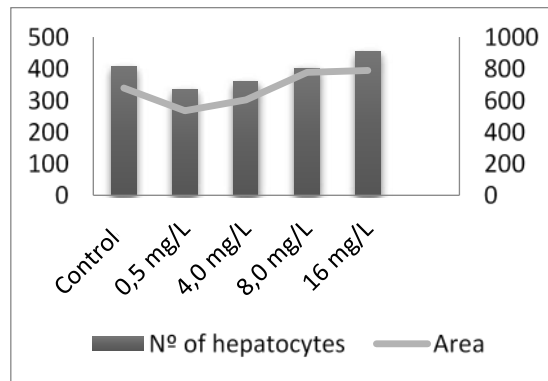


Figure 3: Hepatocyte count X cell area.



Analysis of Nuclear Morphology for Evaluation of Manganese Induced Genotoxicity in *Danio rerio*

Gabriela Zimmermann Prado Rodrigues^{1*}, Jenifer Panizzon¹, Gunther Gehlen¹

1. Laboratory of Comparative Histology, Feevale University, Novo Hamburgo, Brazil

*Email: gabizpr@gmail.com

Manganese is a widely distributed element on the earth's crust, water and atmosphere [1] and occurs in almost all soil types [2]. It is a widely used substance for the manufacture of iron and steel alloys, its compounds are used in the manufacture of batteries, glasses, fireworks [3] and also fertilizers, fungicides, varnishes and animal supplementation [4]. In addition, it is among the heavy metals commonly found in sewage, making it one of the metals of most interest in terms of public health [5]. The contamination by metals causes concern mainly because they are not removed from aquatic ecosystems by autopurification [6] and accumulate in suspended particles and sediments [7], damaging organisms in aquatic environments [8]. In this context, the objective of the present study was to evaluate the genotoxic potential of different concentrations of manganese, since this element has been found along the Sinos River Basin, located at the Rio Grande do Sul state, in Brazil. For this, specimens of *Danio rerio* (n = 5) were exposed for 96 hours at concentrations of 0.5 mg/L, 2.0 mg/L, 4.0 mg/L, 8.0 mg/L and 16 mg/L, in addition to these concentrations, a control group was maintained under the same conditions in dechlorinated tap water. At the end of the exposition the animals were immediately sacrificed to obtain the blood sample for the blood smear, and then stained with Giemsa 5%. For the micronucleus test, 3000 erythrocytes were counted per fish (optical microscopy in 1000x magnification) where the number of nuclear and micronuclei abnormalities were recorded. The criteria for identification of the micronucleus were followed by Fenech and collaborators (2003), where the micronucleus should correspond to approximately 1/3 of the area of the main nucleus, not be connected to the nucleus and have the same intensity of staining. Budding differs from the micronucleus precisely because it has a size larger than 1/3 of the nucleus. Statistical analysis was performed using the Kruskal-Wallis test, and differences were considered significant when $p < 0.05$. No significant differences were found in the number of nuclear and micronuclei abnormalities in the slides analyzed (Table 1). However, two abnormalities (invagination and binucleate cells) (Figure 1) appeared more frequently at all concentrations used. These abnormalities are related to errors occurring during cell division [10], and it is known that heavy metals can interfere in the mitotic index, inducing nuclear alterations and formation of micronuclei [10]. In humans, the genotoxicity of manganese has been studied for a long time: Brega and collaborators (1998) evaluated agricultural workers exposed to pesticides containing manganese, and assert that the metal has a long-term mutagenic potential. Dutta and collaborators (2006) state that manganese can cause DNA breakage, chromosomal aberrations and micronuclei in human peripheral lymphocytes. However, no other previous study has evaluated the genotoxicity of manganese in *Danio rerio* cells, even though it is a commonly species used for aquatic ecotoxicology trials. The data are still partial, more samples of this acute exposure and a chronic exposure of 30 days are being analyzed for a better genotoxic characterization of this element, and will provide a better interpretation of the data.

REFERENCES:

- [1] I. Mena. Manganese. In: Waldron, H.A. Metals in the environment. (1980) 199.
- [2] D.G. Barceloux, Clinical Toxicology., 37 (2) (1999) p. 293.
- [3] D.S. Patil et al., Journal of Environmental Chemical Engineering., 4 (2016) p. 468.
- [4] HSDB. National Library of Medicine., Hazardous Substances (2001).
- [5] M.M.F. Peirano. Revista de Gerenciamento Ambiental., 24 (2003) p.51.



- [6] P.S. Harikumar et al., *Ecotoxicology and Environmental Safety.*, 73 (7) (2010) p. 1742.
[7] R.H. De Jonge., *Proceedings of the National Academy of Sciences.*, 109 (13) (2012) p. 510.
[8] C. Protano et al., *Bulletin of Environmental Contamination and Toxicology.*, 92 (1) (2014) p. 75.
[9] M. Fenech et al., *Mutation Research.*, 534 (2003), p.65.
[10] N.S. Corrêa et al., *Ciência e Saúde Coletiva.*, 14 (6) (2009) p. 2251.
[11] S. Chandra et al., *Science of the Total Environment.*, 346 (2005) p.56.
[12] S.M. Brega et al., *Public Health Reports.*, 14 (1998) p. 109. [13] D. Dutta et al., *Biomedical and Environmental Sciences.*, 19 (6) (2006) p. 487.

	Micronucleus	Nuclear Abnormalities
Control	0,40 ± 0,54	5,80 ± 4,81
0,5 mg/L	0 ± 0	6,16 ± 5,81
2,0 mg/L	0,80 ± 0,44	8,60 ± 2,70
4,0 mg/L	0 ± 0	4,2 ± 3,42
8,0 mg/L	0,20 ± 0,44	4,20 ± 4,10
16,0 mg/L	0,80 ± 1,30	6,20 ± 4,14
p	0,057	0,4598

Table 1: Micronucleus frequency and nuclear abnormalities. (Mean ± Standard Deviation).

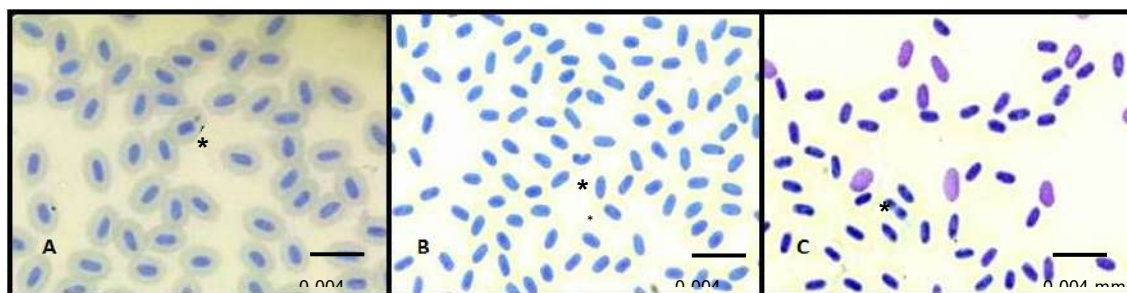


Figure 1: Erythrocytes of *Danio rerio*. A: asterisk signaling a cell with micronucleus. B: asterisk signaling a cell with invagination. C: asterisk signaling a binucleate cell.



HRTEM and STEM Tomography of Nano-sized Magnetic Crystal Produced by Bacteria.

Vargas, G.^{1*}; Cypriano, J.¹; Vieira, D. G. I.²; Leão, P.¹; Abreu, F.¹; and Lins, U. G. C.^{1,2}.

1. Laboratório de Biologia Celular e Magnetotaxia (LabMax) – Instituto de Microbiologia Paulo de Góes – UFRJ

2. Centro Nacional de Biologia Estrutural e Bioimagem (CENABIO) – UFRJ

*Email: gabriele@micro.ufrj.br

Biom mineralization is a process in which organism concentrate metal ions and synthesize crystalline structures [1, 2, 3]. One group of organisms capable of biom mineralization is the magnetotactic bacteria (MTB), the prokaryotic cells that respond to magnetic fields due to the presence of iron-rich intracellular nano-particles called magnetosomes. Each magnetosome is formed by a magnetic crystal composed of magnetite (Fe_3O_4) or greigite (Fe_3S_4) enveloped by a lipoprotein membrane [4]. The alignment of crystal chain along the geomagnetic field together with motility of flagella is named magnetotaxis [5]. The aim of this work is to have a better understand of the crystal chain structure of magnetotactic bacteria analysing the: microstructures, three-dimensional morphologies and positions of Fe-sulfide crystals in air-dried cells of magnetotactic bacteria. A better knowledge of the three-dimensional shapes, positions, and orientations of magnetosomes is important for comprehension of their magnetic properties [6]. Samples were collected at Macaé – Rio de Janeiro, and magnetically concentrated using a magnet, some part were deposited and air-dried directly on formvar-carbon film supported by a copper TEM grid, and another part were fixed with 2.5% glutaraldehyde (2.5% GA, 0.1M Cacodylate buffer) and embedded with epoxy resin for ultrathin sections. Followed by contrast with uranyl acetate and lead citrate. The samples were analyzed by HRTEM (High Resolution Transmission Electron Microscopy) and STEM (Scanning Transmission Electron Microscopy) tomography using a FEI TECNAI G2 F20 Transmission Electron Microscope operating at 200 kV. HRTEM, enables us to observe crystal structure in an atomic scale, while STEM associate with tomography allow to do the image with contrast by atomic number using a high angle detector annular dark field and subsequent reconstruction of the 3D model. All types of TEM showed prismatic magnetite magnetosome (Figure 1). The bacterium isolated is a vibrio with a crystal chain containing around thirteen magnetosomes aligned (Figure 1A), which are surrounded by a membrane (Figure 1B, black arrow). HRTEM image of crystal (Figure 1C), and FFT (Fast Fourier Transform) (on the top right), show a pattern compatible with magnetite, elongated in a direction [111]. The STEM (Figure 1D) and 3D model based on STEM tomography (Figure 1E) demonstrated the nano cracks in the both extremities of magnetosome. More details in Figure 1E inset. This type of imperfection is describe in other magnetotactic bacteria and possibly associated with the biom mineralization process of magnetosome [7]. Our data suggest that STEM is suited to better visualize crystalline structure and defects at nanometric scales of magnetosomes.

REFERENCES

- [1] Sogin, ML et al. (2006). Proc Natl Acad Sci USA 103: 12115–12120.
- [2] Pedrós-Alió, C. (2012). Ann Rev Mar Sci 4: 449–466.
- [3] Prozorov, T (2015). Semin Cell Dev Biol. Oct;46:36-43.
- [4] Lefèvre CT and Bazylinski DA. (2013). Microbiol Mol Biol Rev. 77(3):497-526.
- [5] Blakemore, R. (1975). Science 190(4212):377-9
- [6] Kasama, T et al. (2006). American Mineralogist 91:1216-1229.
- [7] Faivre, D. and Schuler, D. (2008) Chem. Rev. 08, 4875–4898 4875

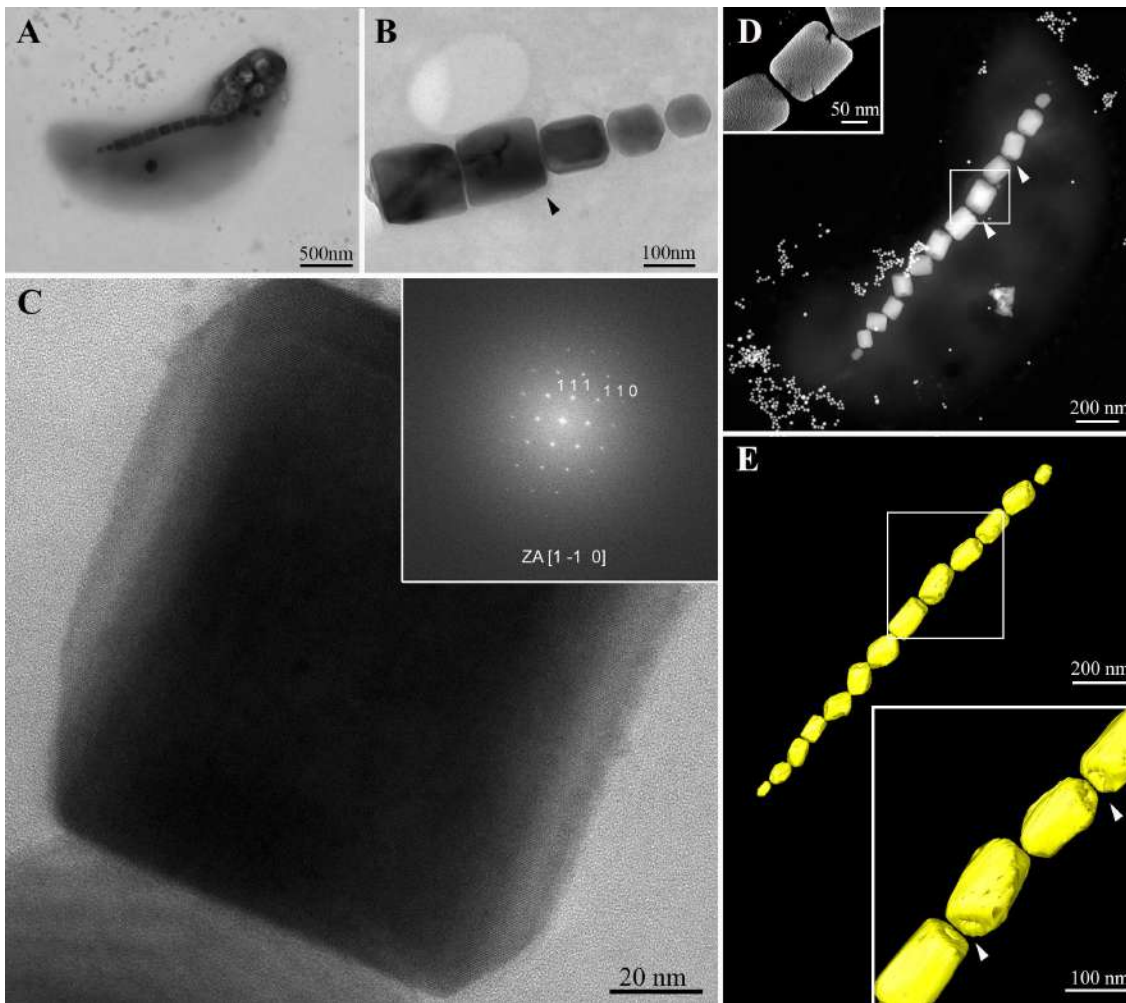
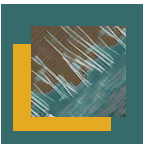
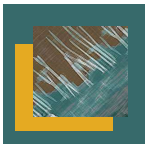


Figure 1. (A) Whole-mount uncultivated magnetotactic bacterium showing a single chain of prismatic magnetosomes. (B) Ultrathin section TEM of the same morphotype of MTB showing the membrane (arrow) around magnetosomes FEI – Morgagni. (C) HRTEM image of crystal showing a prismatic morphology and Fast Fourier Transform crystal pattern (at the top right), showing family of magnetite planes $\{111\}$ and $\{110\}$ indexed in $[1, -1, 0]$ zone axis. (D) STEM of a magnetotactic bacterium cell showing a chain of magnetosomes; the round dots are gold particles used for tomography alignment; FEI – Tecnai G2 F20. At (D) the top left is a high magnification of one slice of image in the boxed region shown in D. (E) 3D model of the same magnetosomes chain shown in D using IMOD – 3dmod software. Inset is a high magnification image of the boxed region shown in E.



Histopathological Evaluation of Gills from *Astyanax jacuhiensis* Exposed to Water from Different Stages of a Water Treatment Process.

Günther Gehlen^{1*}, Gabriela Zimmermann Prado Rodrigues¹, Bruna Graziela Zwetsch¹, Mateus Santos de Souza¹

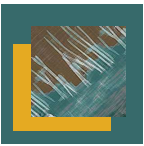
1. Laboratory of Comparative Histology, University Feevale, Novo Hamburgo, Brazil.

*Email: guntherg@feevale.br

Water is a natural resource essential to maintaining life. However, poor handling, lack of basic sanitation and incorrect disposal of several pollutants (agrochemicals, heavy metals, domestic sewage and others) lead to the poor quality of this resource, which poses risks to human and animal health [1]. The importance of the ecotoxicology tests, which are laboratory tests performed under specific and controlled experimental conditions, are used to estimate the toxicity of substances, industrial effluents and environmental samples (water or sediments) [2]. Fishes are among the organisms used in these tests, and the gills reflect the health of the animal because they come in direct contact with the external environment [3]. In this context, the objective of the present study was to evaluate the histopathological changes of gills in fish exposed to water from different stages of the process of a water treatment plant. For this, fishes of the species *Astyanax jacuhiensis* (n = 10) were obtained from a commercial supplier of the region. Exposed for 96 hours to the following water samples: collected water from the Sinos River which supplies the city (raw water); collected after Sand filtration in the middle of the process (filtered); from the end of the conventional processes of water treatment (supply), and water captured at the place of origin of the fish, being considered as a control group. After the exposure the animals were sacrificed for removal of the first arch of the left operculum, which was fixed in Bouin's solution. The material was embedded in paraffin, were sectioned in a rotatory microtome (Leica®, Germany) in 5 µm of thickness, and stained with Hematoxylin and Eosin. Eight fields were analyzed per animal under optical microscopy (400x magnification), and the frequency of normal and altered lamellae was recorded according to Dalzochio et al. (2016). Statistical analysis was performed using the Kruskal Wallis test, followed by the Dunn test, and differences were considered significant when $p < 0.05$. The main lamellar alterations were cell hypertrophy and hyperplasia, epithelial lifting and lamellar fusion (Figure 1). No significant differences were found between the number of normal and altered lamellae (Figure 2); however, animals exposed to raw water had a higher incidence of epithelial lifting than the control animals ($p = 0.001$). These morphological changes, besides providing qualitative evidence of a functional adaptation to the external environment, evaluating the quantitative relations between the structure and the physiological processes [5], since all the mentioned changes cause damages in the life of the fish and can take it to death, especially epithelial lifting, which can cause disturbances in osmoregulation [6]. However, the absence of difference between normal and altered lamellae indicates that the fish used was not sensitive enough to evaluate the treatments tested. A fact that may be related to the peculiar characteristics of the genus *Astyanax*, such as its ability to adapt to abrupt changes in the environment, characterized as a generalist organism [7].

REFERENCES

- [1] S.S. Sousa et al. *Ciência e Natura.*, 38 (3) (2016) p.1615.
- [2] C.R. Costa et al. *Química Nova.*, 31 (7) (2008) p. 1820.
- [3] M.F. Luvizotto. Dissertação: Efeito de diferentes salinidades sobre as células de cloreto e as células secretoras do epitélio branquial do peixe antártico *Nototheniops nudifons* (1994).
- [4] T. Dalzochio et al. *Biotemas.*, 29 (1) (2016) p. 75.
- [5] C. Lupi et al. *Revista Fafibe Online.*, 3 (2007) p.1.
- [6] D.J. Nogueira et al. *Ciência et Praxis.*, 1 (1) (2008). P.15.



[7] U.H. Schulz. Brazilian Journal of Biology., 61 (4) (2001) p.615.

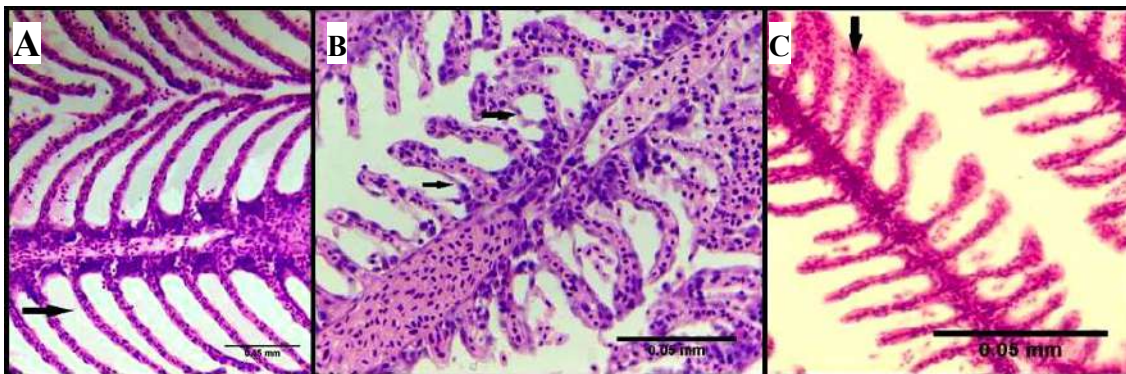


Figure 1: Observe in A: Normal lamellae (arrow). B: Epithelial lifting (arrows). C: Hyperplasia (arrow).

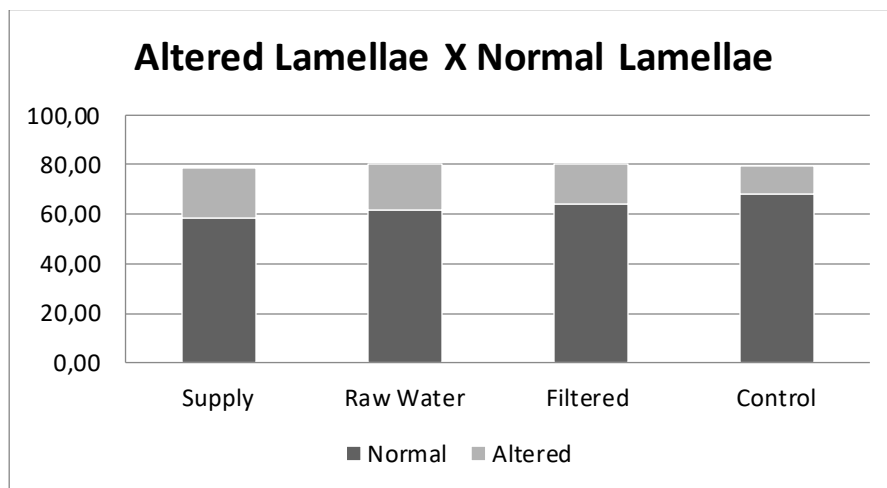
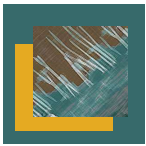


Figure 2: Representative graph of normal and altered lamellae from the fishes exposed to different water treatment stages.



Virtual Reconstruction and Three-Dimensional Printing of Blood Cells as a Tool in Cell Biology Education

Augusto I², Monteiro D², Girard-Dias W², Guimarães MCC¹, Miranda K^{2*}

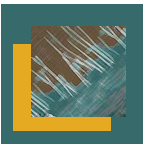
1. Laboratório de Ultraestrutura Celular Carlos Alberto Redins, UFES, Vitória, Brazil;
2. Instituto de Biofísica Carlos Chagas Filho e Centro Nacional de Biologia Estrutural e Bioimagem, UFRJ, Rio de Janeiro, Brazil.

*Email: kmiranda@biof.ufrj.br.

The Electron Microscope (EM) emerged as a cell biology tool in the late 1930s [1] and has since enormously contributed to our understanding of cell structure and function [2]. Amongst the main obstacles to the introduction of new cell biology concepts to students, it is their general lack of affinity with traditional teaching methods [3]. Some specialized tools, however, are usually far from the reality of majority of life sciences schools. In this work, we propose a strategy to increase the engagement of students into the world of cell and structural biology by combining 3D electron microscopy and 3D printing to generate 3D physical models. We introduce three strategies for 3D imaging, modeling and prototyping of cells: (1) 3D reconstruction from a single thin section in the Transmission Electron Microscope (TEM) (2) from serial sections using a classical (low resolution) approach (available in most electron microscopy labs) and (3) 3D reconstruction at high resolution by Serial Electron Tomography. In total, 10 ml of venous blood was extracted from two healthy rats. Once the leucocyte pellet formed after centrifugation, cells were fixed in 2.5% glutaraldehyde for 1 hour, post-fixed in 1% osmium tetroxide plus 0.8% potassium ferrocyanide for 30 min; dehydrated in acetone series and embedded in epoxide resin. In the first strategy, we image a neutrophil in a single ultrathin section (70 nm thick) acquired with a 120 kV Transmission Electron Microscope (JEM 1400, JEOL, Inc., USA) and artificially increased the height (z scale) of each structure. The 3D reconstruction from serial sections was made through 30 serial slices. Images of profiles of a neutrophil in consecutive sections were obtained and aligned with the use of AMIRA (FEI Company, USA). Finally, to 3D reconstruction at high resolution by Serial Electron Tomography a 200 kV Transmission Electron Microscope (Tecnai G2, FEI Company, Eindhoven) was used to record approx. 25 consecutive tomograms of a monocyte from a series of 200 nm thick sections. Alignments were applied using IMOD software package (University of Colorado, USA). 3D virtual reconstructions were obtained from all approaches (Fig. 1-3) revealing the mainly internal structures of each cell type. The 3D model from a single slice and serial electron tomography (Fig. 1B, 3H) were then printed at a 3D printer (FELIX 3.0 Dual Extruder, FELIXprinters, Netherlands) using Repetier-Host software (FELIXrobotics bv, Netherlands) to generate a physical prototype (Fig. 1C, 3I). The use of these technologies, that have gained a lot of attention among young students, may represent a step forward in the teaching process. In addition, introduction of printed prototypes presenting a close-to-the native structure of the cell structure may also shorten the gap between the information through experimental work and learning it in the textbook. Regarding the vectorization and 3D printing of thin sections, we believe that this may have potential when applied to visually impaired students. Lastly, we propose the establishment of a virtual platform where different digital models can be deposited by EM groups and subsequently downloaded and printed by anyone, thereby increasing the accessibility to modern approaches in basic science. This research was supported by CNPq, CAPES, FAPERJ, FAPES, FINEP.

REFERENCES

- [1] Ruska E. The development of the electron microscope and of electron microscopy. *Biosci Rep.* 1987; 7: 607-629.



[2] McIntosh JR. Electron Microscopy of Cells: A New Beginning for a New Century. 2001; 153: 25-32.

[3] Buabeng-Andoh C. Factors influencing teachers' adoption and integration of information and communication technology into teaching: A review of the literature. Int. J. Educ. Dev. Using Inf. Commun. Technol. 2012; 8: 136-155.

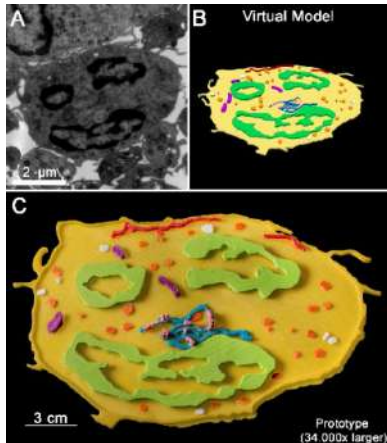


Fig 1. 3D representation of the neutrophil used on 3D printing. (A) Transmission electron microscopy of a thin section of a neutrophil. (B) virtual model resulted from image vectorization (artificial increase in the z scale). Primary granules (orange), secondary granules (white), nucleus (green), rough endoplasmic reticulum (blue), endoplasmic reticulum (red), mitochondria (purple). (C) Printed prototype of the neutrophil 34,000 times larger than the virtual model.

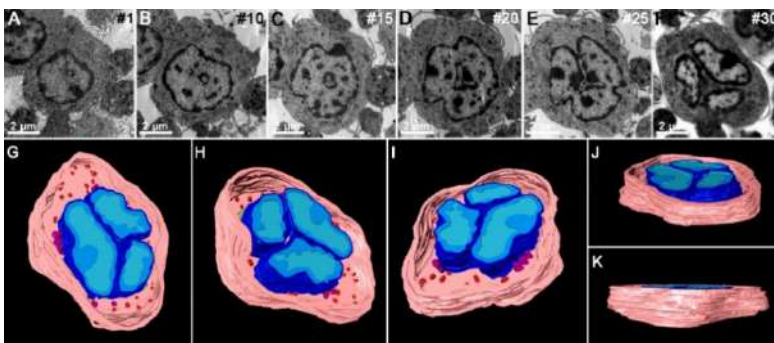


Fig 2. 3D reconstruction of the whole volume of a neutrophil by serial section. (A-F) Images from 70 nm-thick serial sections of a neutrophil. (G-K) 3D model showing the cell nucleus (blue) with heterochromatin (dark blue) and euchromatin (light blue), plasma membrane (light pink) and primary (red) and secondary granules (purple).

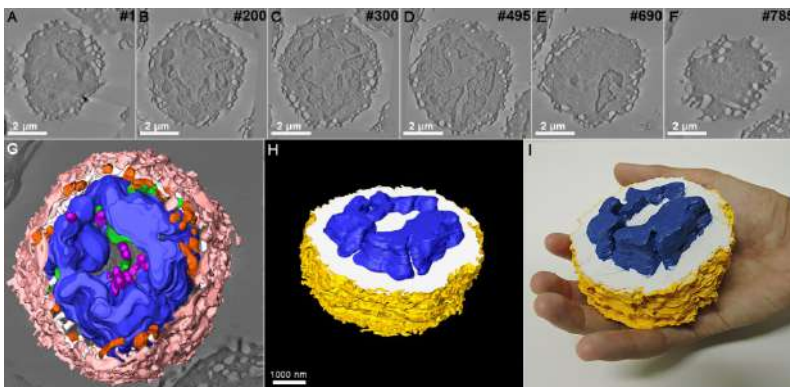
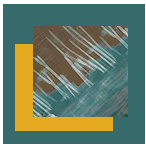


Fig 3. 3D representation of the monocyte used on 3D printing. (A-F) Virtual sections from a serial tomogram of a monocyte obtained from serial electron tomography. Bar 2 µm. (G) 3D representation of the model, showing the cell nucleus (blue), plasma membrane (light pink), mitochondria (green), lysosomes (purple) and phagosomes (orange). (H) Virtual model of a monocyte generated by serial electron tomography. (I) Printed prototype (15,000 times larger) being manipulated by a student and on a table.



Ultramorphological Characteristics of Immature Stages of *Piophilidae* (Diptera: Piophilidae)

Karine B. Barros-Cordeiro^{1,2}, *Ingrid Gracielle², Andre G. Savino¹, Welinton R. Lopes¹, José R. Pujol-Luz¹ and Sônia N. Bão²

1. Laboratório de Entomologia 2-Diptera, Dpto. Zoologia, IB. UnB. Brasília, Brazil

2. Laboratório de Microscopia Eletrônica, Depto. Bio. Celular. IB. UnB. Brasília, Brazil

*Email: gracilias@gmail.com

Piophilidae (Linneus, 1758), known as the cheese skipper fly, is a sarcosaprophagous diptera as it has a wide range of feeding habits (e.g. proteins, animal and vegetable decaying matter, and feces). *P. casei* biological aspects can be applied in several fields of knowledge, including i) forensic entomology, in which it can be used to determine post mortem interval (PMI), ii) veterinary medicine, since it may cause gastrointestinal, nasal and urinary myiasis, and iii) medicine, acting as a vector of several pathogens. Larvae of first and second instar have never been described, specially using scanning electron microscopy (SEM). This work presents ultramorphological characteristics of *P. casei* by the comparison of the structures along the development using SEM [1-4]. Colonia adults were used previously maintained in the laboratory (3 generation). Preparation of samples for SEM: Larvae (n=55) from the three instars were fixed in Karnovsky (2.5% glutaraldehyde, 4% paraformaldehyde, 3% saccharose 5 mM CaCl₂ buffered with sodium cacodylate 0.1 M, pH 7.2) for 24 hours. The samples were removed from the buffer and immersed in osmium tetroxide for one hour, washed in distilled water and dehydrated in different acetone concentrations (30-100%), for 1 minute in each concentration. Next, the material was submitted to critical-point drying process with CO₂, mounted on stubs, metallized with gold and viewed under a scanning electron microscope JEOL JSM 7001 F. The use of SEM allowed the identification of structures with great morphological changes along the larval instars: face mask (horizontal or vertical position), oral comb (quantity) (Fig. 1 A, D, G), maxillary palp (Fig. 1B, E, H), respiratory slit and trichoid sensilla of the posterior spiracle (quantity) (Fig. 1 C, F, I). In this way, structures as face mask, oral comb and maxillary palp develop from the first (L1) to the third (L3) larval instar. The posterior spiracle of L1 presents two respiratory slits intercalated by trichoid sensilla. The second instar, presents three respiratory slits intercalated by four trichoid sensilla and may present undeveloped sensilla in each respiratory slit. On the other hand, the posterior spiracle of L3 resembles L2, but it can be distinguished by the presence and development of trichoid sensilla in each respiratory slits. Sukontason *et al.* (2001) morphological description of the third instar of *P. casei* is similar to the one reported here, but this is the first time that the presence of the trichoid sensilla in the posterior spiracle of L3 has been described. Scanning electron microscopy enabled the recognition of some morphological characters, making the identification viable which is not possible with light microscopy due to the small size of morphological structures.

REFERENCES

- [1] Greenberg, B. Flies and disease (1971)
- [2] Martín-Vega, D. For Sci International (2011) 212
- [3] Papavero, N. & Pimentel, T.J. Fauna da Amazônia Brasileira, Belém (2002) 15
- [4] Zumpt, F. Myiasis in man and animals in the old world. (1965) 267
- [5] Sukontason, K.L. *et al.* J Med Entomol (2001) 38 (5)
- [6] Financial Support: CAPES, CNPq, FAPDF, FINEP

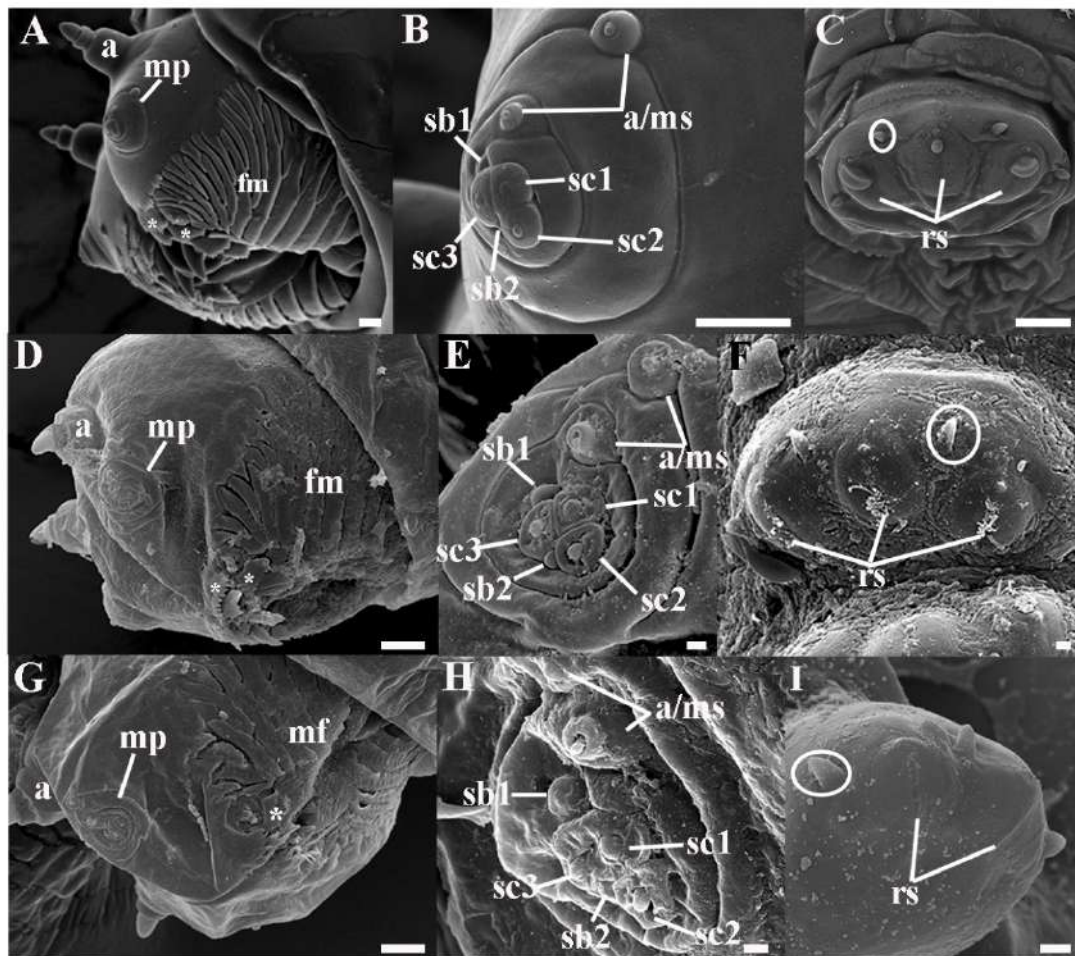
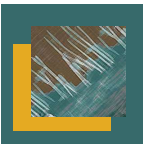


Figure 1. SEM micrographs of *Piophila casei*. Third instar: (A) cephalic region, (B) detail of sensilla in maxillary palpus and (C) detail of posterior spiracle. Second instar (D) cephalic region, (E) detail of sensilla in maxillary palpus and (F) detail of posterior spiracle. First instar (G) cephalic region, (H) detail of sensilla in maxillary palpus and (I) detail of posterior spiracle. Abbreviations: a, antenna; a/ms, antennal or mandibular sensilla; fm, face mask (oral ridge); mp, maxillary palpus sensilla; *, oral comb; rs, respiratory slit; sb 1-2, basiconic sensilla of maxillary palpus; sc1-3, coeloconic of maxillary palpus; circle, trichoid sensilla. Scales: (A, B, C, D, G) 10 μ m; (E, F, H, I) 1 μ m.



Anatomy and Ultrastructure of *Barbacenia purpurea* Hook. (Velloziaceae) Leaves

Izabella Fontenelle de Andrade^{*,2*}, Laura Jane Moreira Santiago¹, Ricardo Pereira Louro²

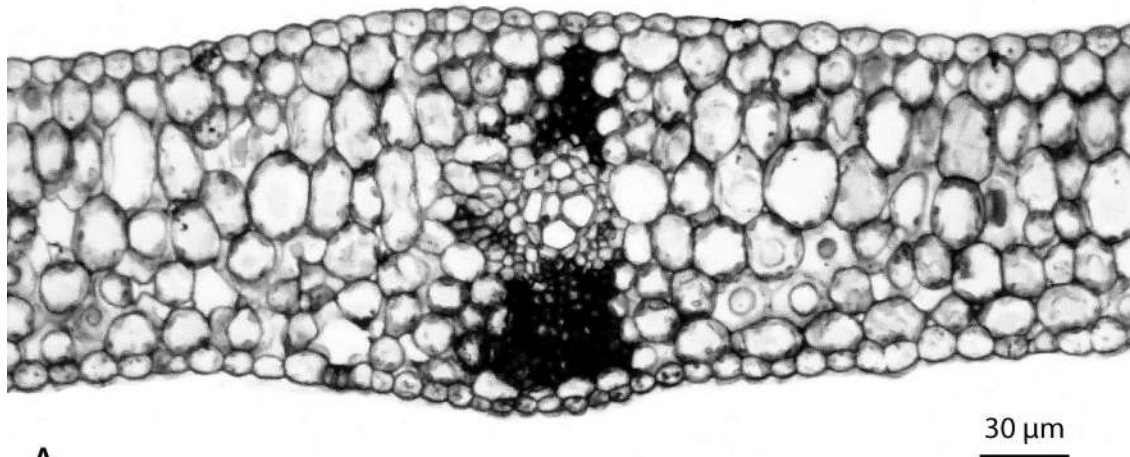
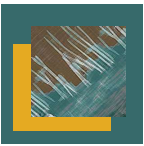
1. Laboratório de Biodiversidade e Biotecnologia, Departamento de Botânica, Instituto de Biociências, UNIRIO, Rio de Janeiro, RJ, Brazil.

2. Laboratório de Ultraestrutura Vegetal, Dep.de Botânica, UFRJ, Rio de Janeiro, RJ, Brazil.
*izabellafontenelle@gmail.com

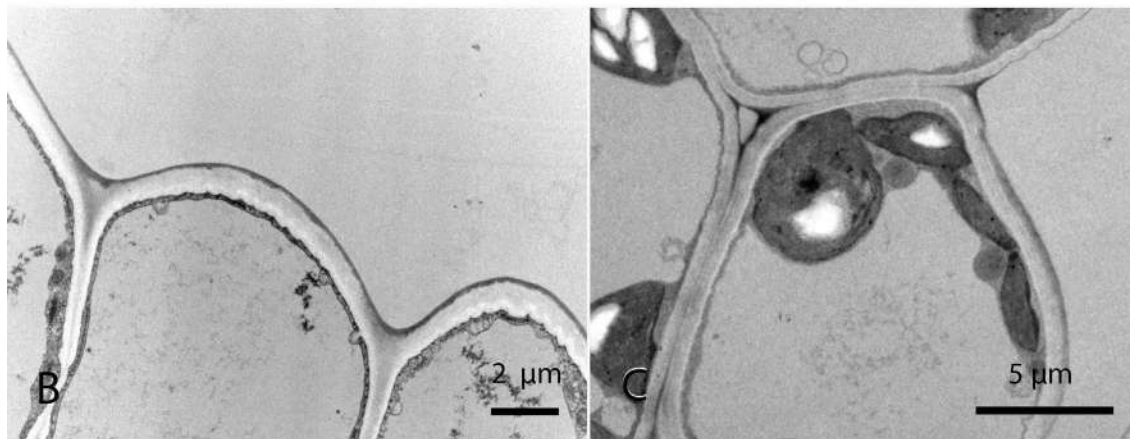
Barbacenia purpurea Hook. is a herbaceous rupicolous plant involved in successional processes on inselbergs such as the Sugarloaf and Urca Natural Monument in Rio de Janeiro [1]. Even though part of its physiological features is already described, there is no data on anatomical and ultrastructural leaf attributes of this pioneer plant [2]. This work aims to elucidate the structural and subcellular characteristics of this species. For this purpose, seeds of *B. purpurea* were collected from Morro da Urca, germinated and cultivated for one year. For light and electron microscopy analysis, leaf samples were fixed with 4 % paraformaldehyde and 2.5 % glutaraldehyde in 1.25 % PIPES buffer at pH 7.3, postfixed with 1 % osmium tetroxide in 1.25 % PIPES buffer and embedded in Spurr's resin [3]. The semithin sections were stained with 0.05% toluidine blue and viewed with a Zeiss 900 microscope, and the ultrathin sections were stained with 1 % uranyl acetate in absolute ethanol and lead citrate and the studies were performed with a Morgagni 286 transmission microscope [4]. In cross section, *Barbacenia purpurea* leaves have uniseriate epidermal cells, with rectangular shape in the adaxial surface and rounded in the abaxial surface (Fig. 1.A). The cell walls are thin and there are few plastids in the cytoplasm, and one large vacuole (Fig. 1.B). The chlorophyll parenchyma cells present an isodiametric shape and increase size towards the median mesophyll of the leaf (Fig. 1.A, 1.C). In the cytoplasm chloroplasts are lens-shaped (Fig. 1.D) with well-developed grana formed by up to 15 thylakoids, from 2 to 3 starch grains and small plastoglobules in the stroma (Fig. 1.E). Mitochondria are round-shaped or elongated and have well defined cristae (Fig. 1.D). Peroxisomes are rare and the endoplasmic reticulum is generally associated to the cell wall. A large vacuole occupies the center of the cell. Each vascular bundle (Fig. 1.F) has a sclerenchymal cell sheath forming extensions that are more significant by the abaxial surface of the leaf. These results represent new information for *Barbacenia purpurea* and contribute to structural data on this important species of inselbergs in Rio de Janeiro.

REFERENCES

- [1] S. T. Meirelles et al., Environ. Conserv. 26 (1) (1990) 10.
- [2] S. T. Aidar et al., Photosynthetica 52 (1) (2014) 124.
- [3] A. R. Spurr, J. Ultrastruct. Res. 26 (1969) 31.
- [4] R. P. Louro and L. J. M. Santiago, Protoplasma 253 (1) (2016) 77.

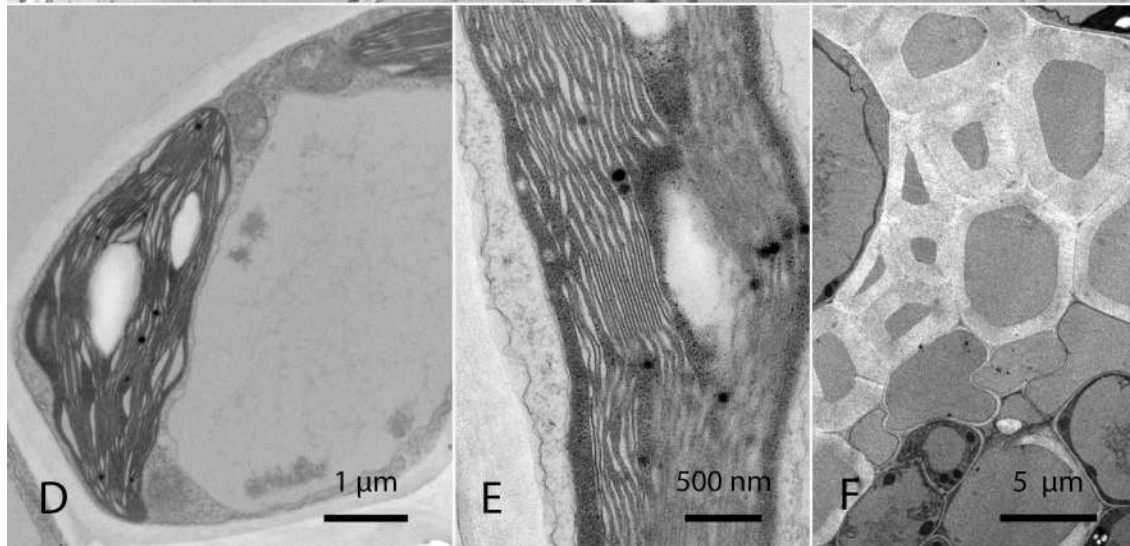


A



B

C



D

E

F

Fig. 1. Structural aspects of *Barbacenia purpurea* Hook. leaves. A- Leaf blade cross section, B- Adaxial epidermal cells with vacuole containing phenolic compounds, C- Parenchymal cell showing a large central vacuole and organelles in a parietal position, D- Chloroplast and mitochondria adjacent to the cell wall, E- Thylakoids and grana arrangement and few plastoglobules in the stroma, F- Vascular bundle cells.



In vitro Antileishmanial Activity of a New Synthetic β -carboline Compound Against *Leishmania amazonensis*

Jéssica Carreira de Paula^{1*}, Talitha Fernandes Stefanello¹, Danielle Lazarin-Bidóia¹, Tania Ueda-Nakamura¹, Paula Baréa², Maria Helena Sarragiotto², Celso V. Nakamura¹.

1. Laboratory of Technological Innovation for the Development of Pharmaceuticals and Cosmetics, State University of Maringá, Maringá, Brazil

2. Department of Chemistry, State University of Maringá, Maringá, Brazil

*Email: jessicacarreira123@gmail.com

Leishmaniasis is a complex of diseases caused by protozoa of the genus *Leishmania* that has an endemic character in 98 countries. Although it affects approximately 12 million people worldwide and is responsible for 20,000-40,000 deaths annually, the current treatments for leishmaniasis, based mainly in antimonial drugs, have many drawbacks, such as toxicity, resistance, high cost, and long-term treatment. In this context, the development of new alternatives of treatment is highly necessary. Several β -carboline compounds have been described as potential antileishmanial agents [1,2], and here we studied the *in vitro* antileishmanial activity of the compound *N*-{2-[(4,6-bis(isopropylamino)-1,3,5-triazin-2-yl)amino]ethyl}-1-(4-methoxyphenyl)- β -carboline-3-carboxamide (β -CC) against *Leishmania amazonensis*. β -CC was active against promastigote and intracellular amastigote forms, exhibiting 50% inhibitory concentrations (IC₅₀) of 4.5 μ M and 1.2 μ M, respectively. Cytotoxicity was assessed in J774A1 macrophages and 50% cytotoxic concentration (CC₅₀) of 145.7 μ M was observed. These results demonstrate that β -CC is highly selective for the parasite, exhibiting selective index (SI) of 32 and 121 for promastigote and intracellular amastigote forms, respectively. Morphological and ultrastructural alterations in promastigotes caused by β -CC were assessed by scanning and transmission electron microscopy, respectively (Figures 1 and 2). It was observed rounding and shrinking of parasites in a time-dependent manner (24, 48 and 72 h post-treatment), as well as mitochondrial swelling (24-72 h post-treatment) with presence of lipid-storage bodies 48 h post-treatment and intense exocytic activity in the flagellar pocket 72 h post-treatment. Lipid-storage bodies were observed 24 h post-treatment in promastigotes treated with IC₉₀ (9.9 μ M), but not with IC₅₀, evaluated by Nile Red method, corroborating the results of microscopy analyses. Also, increase of total reactive oxygen species (ROS) was observed in promastigotes 24 h post-treatment with β -CC, assessed using the fluorescent probe H₂DCFDA. Are necessary others biochemical analysis for determine the mechanism of action of compound, but we know that the alterations generated can indicate primary oxidative stress, followed of mitochondrial stress causing the death of the protozoan.

REFERENCES

[1] T.F.Stefanello et. al., AAC, 58 (2014) 7112.

[2] L.T. Tonin et. al., Biomed. Pharmacother. 64 (2010) 386.

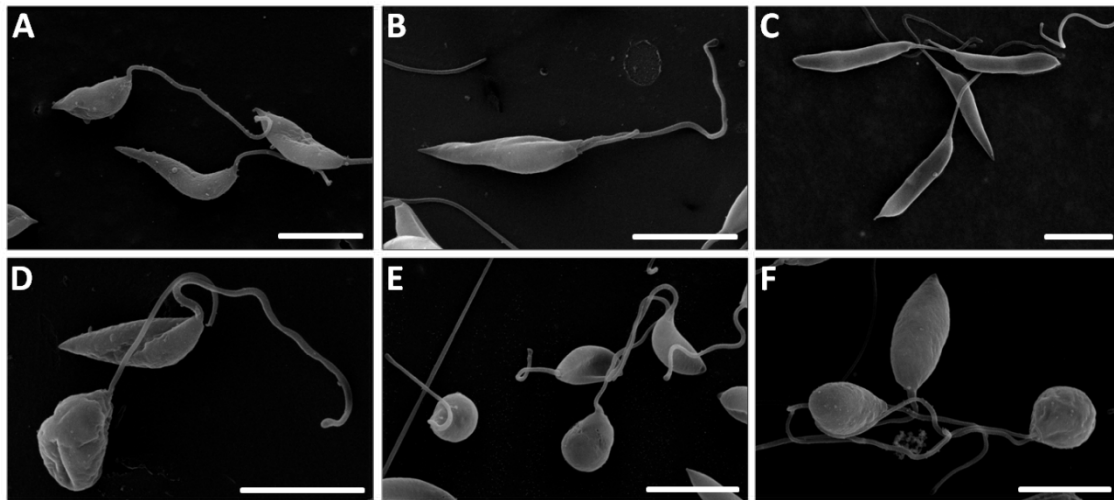
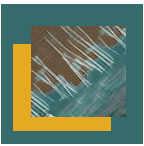


Figure 1. Morphological alterations in promastigotes of *Leishmania amazonensis* treated with p-anisal-RCC-iso, visualized by scanning electron microscopy. Control cells (A-C) and parasites treated with IC₅₀ (4.5 µM) (D-F) for 24 h (A;D), 48 h (B; E) and 72 h (C;F). Bars = 5 µm.

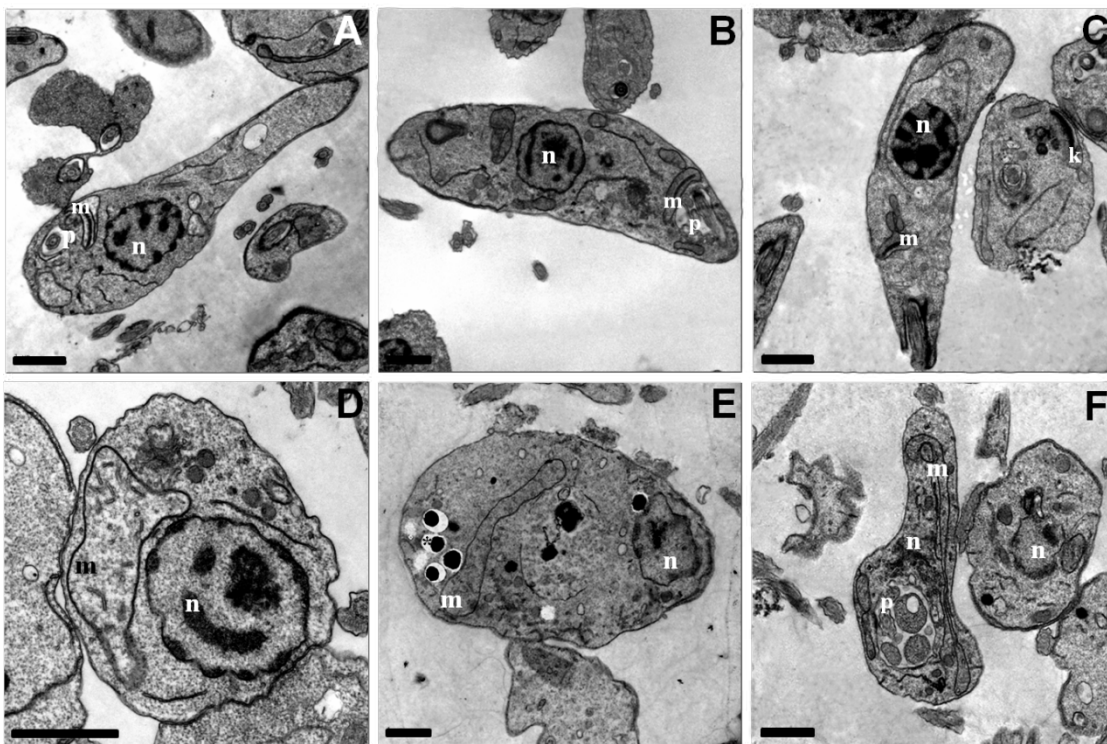
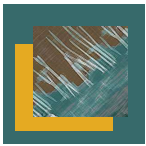


Figure 2. Ultrastructural alterations in promastigotes of *Leishmania amazonensis* treated with p-anisal-RCC-iso, visualized by transmission electron microscopy. Control cells (A-C) and parasites treated with IC₅₀ (4.5 µM) (D-F) for 24 h (A;D), 48 h (B; E) and 72 h (C;F). (n) nucleus; (m) mitochondrion; paraflagellar pocket; (*) lipid-storage bodies. Bars = 1 µm.



The Role of Sonic Hedgehog Signaling During Chick Muscle Differentiation

John Douglas de Oliveira Teixeira^{1*}, Ivone Rosa de Andrade¹, José Brito², Claudia Mermelstein¹.

1. Laboratório de Diferenciação Muscular e Citoesqueleto, Instituto de Ciências Biomédicas, Universidade Federal do Rio de Janeiro.

2. Laboratório de Proliferação e Diferenciação Celular, Instituto de Ciências Biomédicas, Universidade Federal do Rio de Janeiro.

* Email: teixeira.john@gmail.com

Skeletal muscle fibers are multinucleated cells that have striations that enable them to contract. These cells are involved by connective tissue, composed mainly of fibroblasts. The fusion of several myoblasts gives rise to muscle fibers. The molecular events that control myoblast fusion are not fully understood. Sonic hedgehog (Shh) is a morphogen produced that has been implicated in the regulation of muscle differentiation. It has been shown that Shh stimulate myoblast proliferation [1] and mice Shh^{-/-} shows a reduction in muscle mass [2]. In this study we evaluated the role of Shh during chick myogenesis. Myoblast cell cultures were obtained from 11 day-old chick embryos (Granja Tolomei, RJ). Cells were plated at an initial density of 1×10^5 on 24 well culture plates previously coated with collagen. In chick culture, myoblast fusion occurs after 24 hours of cell plating [3], and at this time we treated cells with different concentrations Shh recombinant protein. 48 hours after treatment, cells were fixed and analyzed by immunofluorescence microscopy using anti-desmin (muscle cell marker) antibody and DAPI (DNA binding probe). Cell cultures were quantified in relation to: (i) total number of nuclei; (ii) number of nuclei in desmin positive cells; (iii) number of fibroblasts; (iv) number of myoblast and (v) muscle cells area. The results show Shh recombinant protein increased the muscle cell area and reduced number of fibroblasts. Our data suggest that Shh pathway is involved in the regulation of chick muscle differentiation. The study was approved by CEUA-DAHEICB092-05/16. Support: CNPq and FAPERJ.

REFERENCES

- [1] D. DUPREZ *et al.* Sonic Hedgehog induces proliferation of committed skeletal muscle cells in the chick limb. *Development*, 1998.
- [2] M. KRÜGER *et al.* Sonic hedgehog is a survival factor for hypaxial muscles during mouse development. *Development*, 2001.
- [3] Y. SHIMADA. Electron microscope observations on the fusion of chick myoblasts in vitro. *J Cell Biol*, 1971.

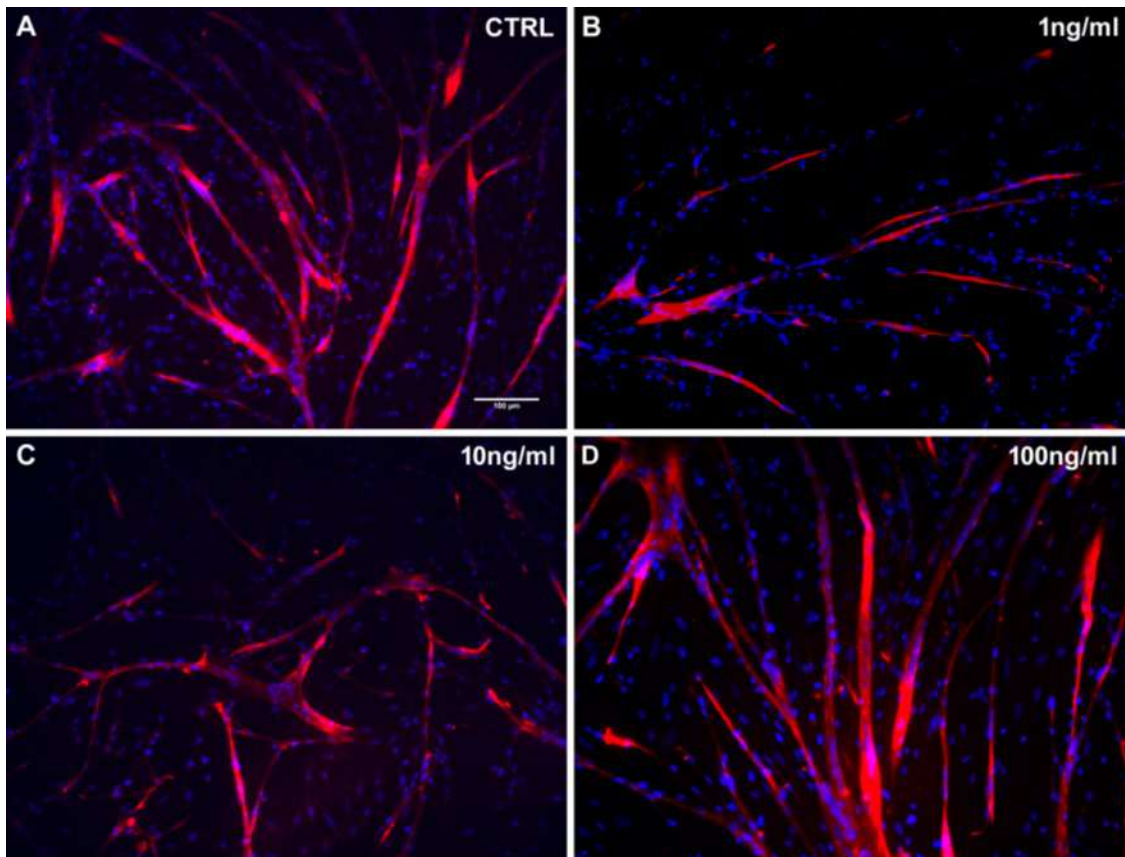
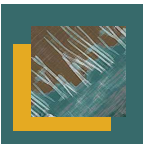


Figure 1. Effect of recombinant sonic protein in muscle cells. In A control, in B muscle cells treated with 10ng/ml Shh, in C treated with 10ng/ml and in D with 100ng/ml. Immunofluorescence to desmina (red) and DAPI (blue).

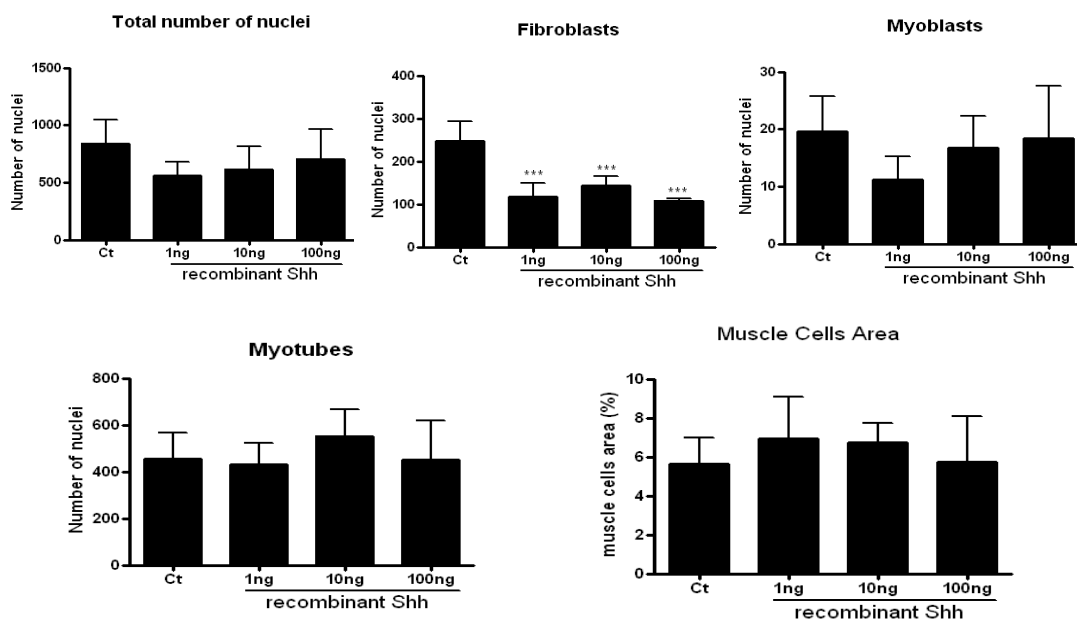
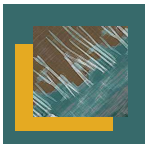


Figure 2. Statistical analysis of the sonic effect of fusion and muscle differentiation. In A total number of nuclei per field, in B number of fibroblast, in C number of muscle cells undifferentiated, in D number of nuclei in myotubes and E Area occupied by muscle cells. The number of fibroblast is reduced with sonic recombinante protein. The statistical test: ANOVA with pos-test Tukey.



Jurona Virus Induces Encephalitis in BALB/c Adult Mouse Model by Sequential Intranasal Inoculations

Diniz JAP¹, Araújo LM¹, Vasconcelos PF²

1. Instituto Evandro Chagas - Laboratório de Microscopia Eletrônica ²Instituto Evandro Chagas - Seção de Arbovirologia e Febres Hemorrágicas

Previous report using Jurona virus intranasal inoculation (1:10 titration) revealed subsequent encephalitis and inflammatory CNS host response in albino Swiss neonate mouse [1] model but not in adults. Here we hypothesized that intranasal sequential inoculations with same titration could induce an encephalitis in adult mice. To test this hypothesis, we injected intranasally 10µl of virus infected brain homogenate once a day, during three days. Control subjects received equal volumes of saline. Animals were euthanized at 4th, 8th, 12nd and 16th days post infection (d.p.i.) and had their brains processed for histopathology and selective immunolabeling for virus antigens and microglia. Animals were anesthetized with Ketamine and xylazine and perfused intracardially through the left ventricle with 0.9% saline and 4% formaldehyde in PBS. After craniotomy, the brains were cut into 70µm thick sections with a vibratory microtome. Alternatively, fixed tissue was processed for gross histopathology after paraffin embedding. Blocks were cut into 5µm thick sections with a rotary microtome, mounted on electrostatic slides and stained with hematoxylin-eosin. For immunohistochemistry assay free-floating sections were rinsed once PBS and the sections were incubated 3% hydrogen peroxide solution in methanol, rinsed in Tris-buffer saline/Tween solution, and incubated with 10% normal horse serum and Ig blocked according to the instructions of the Mouse-on-Mouse Immunodetection Kit (M.O.M kit) and incubated with the primary antibody overnight. Next, the sections were washed and incubated for 1 h with the biotinylated anti-mouse secondary antibody (M.O.M. kit). The slides were rinsed again and incubated with the avidin/biotin/peroxidase complex (M.O.M. kit) according to manufacturer instructions. The sections were then rinsed and the reaction was developed with diaminobenzidine tetrahydrochloride dihydrate according to manufacturer instructions. Color was detected and sections were rinsed in PBS, embedded in Entelan and coverslipped [2]. Clinical signs including hunched posture, ruffled fur, progressive and 13% weight loss, start at 4th d.p.i. and aggravate as disease progresses, with a peak at 8 d.p.i., disappearing at 16th d.p.i. Histopathology (Figure 1B) revealed focal neuronal degeneration, chromatolysis, picnosis, apoptotic and necrotic cell deaths, satellitosis, focal gliosis, neuronophagia, lymphocytic infiltrate, and polymorphonuclear leukocytes around vessels as a perivascular cuffing and perivascular edema. These focal lesions were detected mainly in olfactory bulb, striatum, hippocampus and cerebral cortex from 4^o d.p.i. onwards, with a peak at 8^o d.p.i. Virus antigens (Figure 1D) and morphological activated microglia (Figure 1F) colocalized with histopathological damage. These lesions characterize an acute virus encephalitis with progressive and regressive CNS inflammatory host response, which is spontaneously resolved in adult immunocompetent mice model.

REFERENCES

[1] Gomes-Leal et al., Acta Tropica 97: 126–139, 2006.

[2] Diniz et al. Plos One 3 (3): e1733, 2008.

This research was supported by IEC/SVS/MS and CAPES

Key words: Virus encephalitis, Jurona virus, microglia, immunolabeling, BALB/c

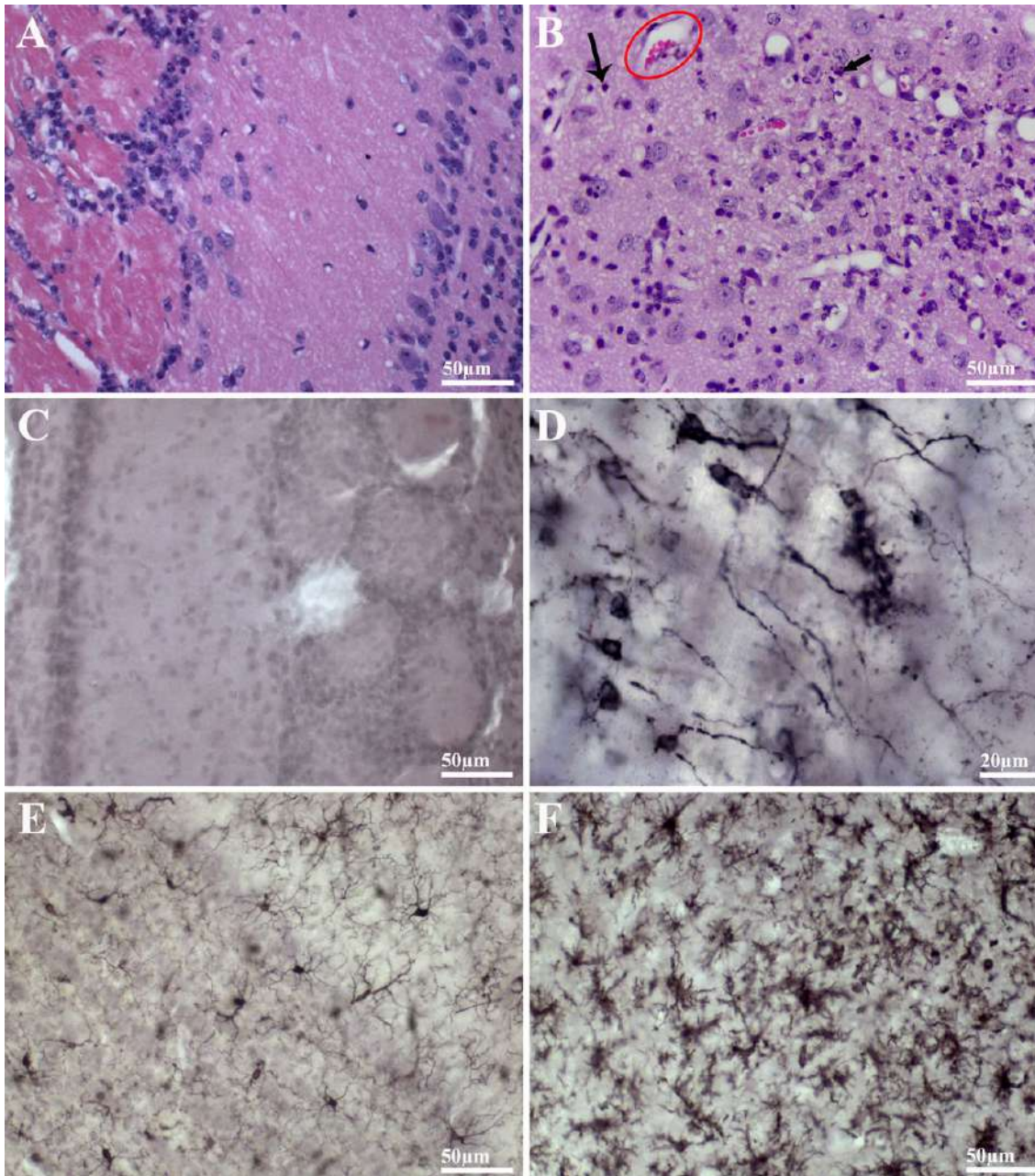
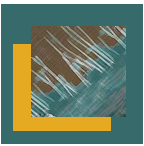
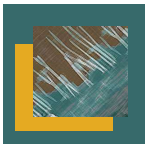


Figure 1. Photomicrographs from control (A, C and E) and infected (B, D and F) olfactory lobes at 8th days post infection. Hematoxylin/eosin stained sections (A and B). Virus antigens immunolabeling (C e D) and selective immunolabeling of microglia (E and F). Healthy tissue of control animal (A). Infected brain tissue illustrating apoptotic cells (Small Arrows) , picnotic nuclei (Large arrows) and focal vascular congestion (Ellipse) (B). Control brain section (C) does not show virus antigens immunolabeling. Virus immunolabeling in the neurons of olfactory bulb (D). Morphologically non-activated microglia (E). Morphologically activated microglia (F).



Structural Changes And Apoptosis In The Submandibular Gland Of Rat Following Fluoxetine Treatment

José Paulo de Pizzol Júnior^{1*}, Luciana Guilherme Navarro², Estela Sasso-Cerri², Paulo Sérgio Cerri²

1. Department of Morphology and Genetics - UNIFESP, São Paulo, SP, Brazil

2. Laboratory of Histology and Embryology – Dental School-UNESP, Araraquara, SP, Brazil

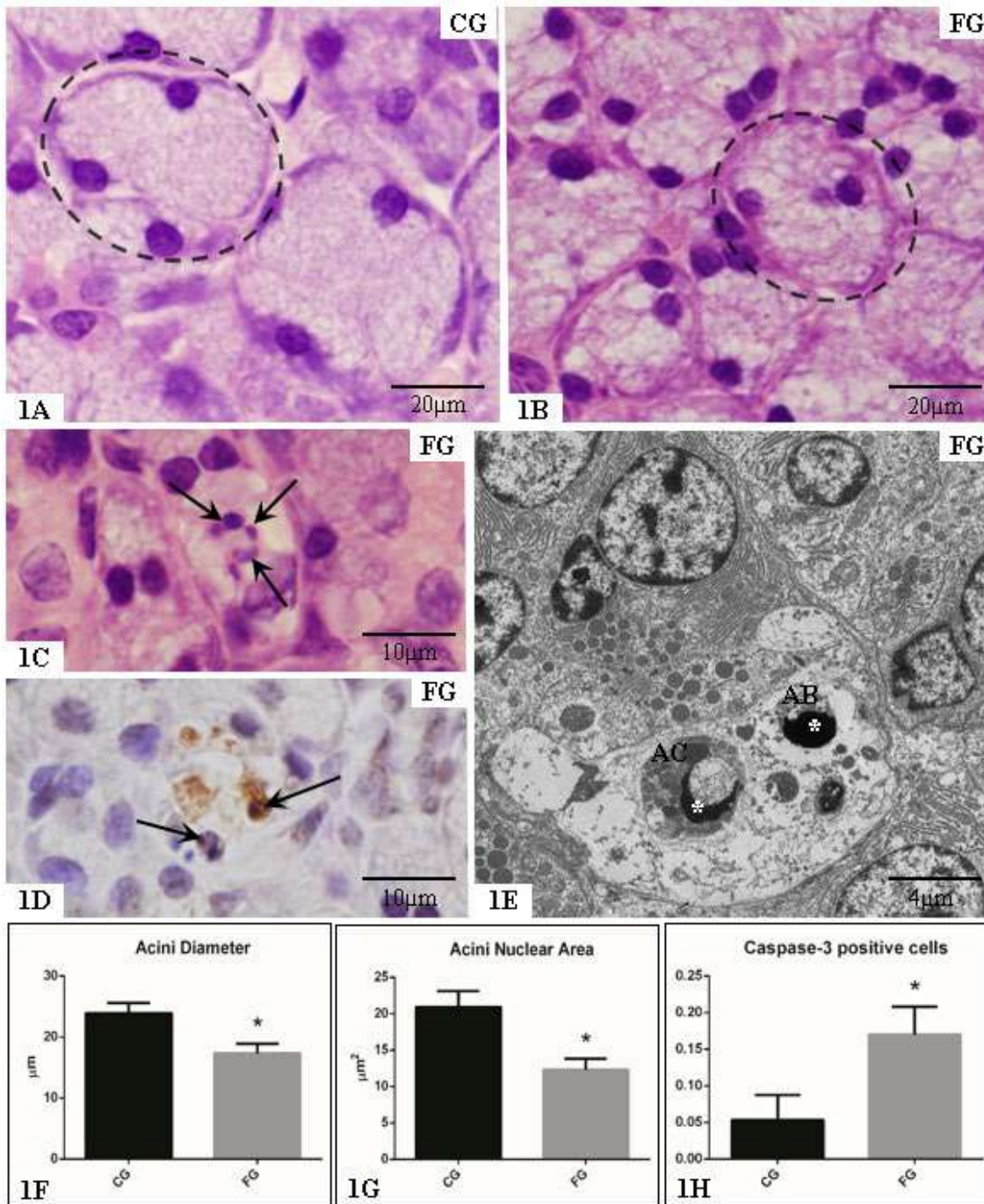
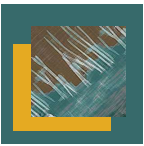
*Email: jpaulopizzol@gmail.com

As depression is a health problem with worldwide repercussions, several pharmacological agents have been associated with psychotherapy treatment. Among them, the selective serotonin reuptake inhibitors, such as fluoxetine hydrochloride, have been widely prescribed [1]. These drugs selectively and potently block the serotonin transporters and receptors in the central nervous system, and effectively increase the extracellular levels of serotonin, reducing depression symptoms [2]. The salivary glands are under sympathetic and parasympathetic input; thus, a wide range of drugs can interfere in their secretory activity [3]. Dry mouth has been a severe side effect in patients treated with antidepressants, and the reduction in the salivary flow lead to loss of taste sensation, increase in the incidence of caries and periodontal disease [4]. In this study, we investigated the morphological and ultrastructural changes promoted by fluoxetine in submandibular (SBM) gland of adult rats. Ten adult male rats were distributed into two groups: fluoxetine (FG) and control (CG). The rats from FG (n=5) received daily 20mg/kg of fluoxetine hydrochloride for 11 days; the animals from CG received saline. After 24 hours of the last injection, the animals were killed and the right SBM gland were fixed in 4% formaldehyde, dehydrated and embedded in paraffin. The sections were stained with hematoxylin/eosin (HE) and picosirius; the acini diameter and nuclear area were measured. The number of caspase-3-immunolabeled acinar cells was also quantified. Data were statistically evaluated using one-way analysis of variance (ANOVA) followed by t-student post-test; $p < 0.05$ was considered statistically significant. Fragments of SBM glands were immersed in glutaraldehyde/formaldehyde solution and processed for Araldite embedding. The ultrathin sections were examined in Tecnai transmission electron microscope (TEM). Significant reduction in the acini diameter and in the nuclear area of the acinar cells was observed in the rats of FG (Figs. 1A, 1B, 1F and 1G). In FG, round/ovoid structures with masses of chromatin strongly stained by hematoxylin as well as cleaved caspase-3 immunolabeled cells were usually found in the acini of SBM glands (Figs. 1C and 1D). The number of caspase-3-immunolabeled acinar cells increased significantly in the FG in comparison with CG (Fig. 1H). Under TEM, acinar cells showing nuclear portions containing electron dense masses of condensed chromatin were observed (Fig. 1E). Our findings indicate that fluoxetine induces apoptosis in the acinar cells and subsequent reduction in the acini size of SBM glands. Since reduction in the nuclear area of acinar cells indicates low secretory activity of these cells, the structural changes induced by fluoxetine in the submandibular glands may be responsible at last in part for the high incidence of oral dryness reported by patients treated with fluoxetine.

REFERENCES

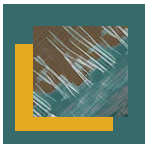
- [1]- Jimenez-Solem E. et al. *BMJ Open* 2012; 18, 2(3).
- [2]- Chau K. et al. *J Osteoporos.* 2012;2012:323061.
- [3]- Scully C. *Oral Dis.* 2003; 9(4):165-76.
- [4]- Javed F. et al. *J Periodontol.* 2007; 78(11):2112–9.

This research was supported by CNPq and CAPES.



Figures

1A-1D – Light micrographs of sections of submandibular glands stained with HE (1A-1C) and subjected to immunohistochemistry for detection of caspase-3 and counterstained with hematoxylin (Fig. 1D). Fig. 1A (CG) – Typical serous acini (outlined). Figs. 1B and 1C (FG) – acini showing reduced size (outlined) and round/ovoid basophilic structures (arrows) are observed (Fig. 1C). Fig. 1D – caspase-3 immunolabeled acinar cells (arrows) are observed. Fig. 1E (FG) – Electron micrograph shows a shrunken acinar cell (AC) exhibiting nucleus with electron opaque masses of peripheral condensed chromatin (asterisk), typical of apoptosis. Adjacent to this apoptotic cell “AC”, a small structure (AB) with conspicuous block of condensed chromatin (asterisk) is also observed.



Central Nervous System and Oncosis

Juçara Loli de Oliveira¹, Maria Ivone Mendes Benigno², Rejane Maria Cirra Scaff¹, Marcio Alvarez-Silva³.

1. Departamento de Ciências Morfológicas, Universidade Federal Santa Catarina, Brazil

2. Departamento de Morfologia, Universidade Federal Piauí, Brazil

3. Departamento de Biologia Celular, Embriologia e Genética, Universidade Federal de Santa Catarina, Brazil.

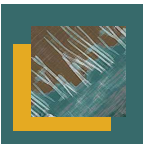
*Juçara Loli de Oliveira¹, Departamento de Ciências Morfológicas, Universidade Federal de Santa Catarina, Campus Universitário, Trindade, 88040-900, SC, Florianópolis, Brazil (Email: jucara.oliveira@ufsc.br)

Brain function is impaired immediately after the blood flow drops below one fourth of normal values. If the reduction blood flow condition persists for a prolonged period of time, primary neuronal death appears rapidly in the core areas, and is accompanied by multiple morphological cell alterations [1, 2]. These reduce hypoxic-ischemic brain injury in various animal models have been applied for clinical research [2, 5]. During injury and ischemia of the central nervous system (CNS) mediators like glutamate, free fatty acids, or high extracellular potassium compounds are released or activated, which cause secondary oncosis and damage of nerve cells [2, 3, 5, 6, 7]. In cerebral hypoxia, the molecular cascade includes the loss of membrane ionic pumps and cell swelling, in the literature, namely, oncosis (onkos, meaning swelling) [4]. The aim of our study was verified the cellular oncosis in brain injury in adult mice. Material and Methods: Directa Middle cerebral artery occlusion (MCAO) was performed in the animals C57/BL6 mice [3]. The animals were divided experimental groups: Group 1 (control normal, n=6) and Group 2 (experimental occlusion, n=6). Experiments were performed in accordance with the guidelines by Colégio Brasileiro de Experimentação Animal (Cobea) and were approved in Universidade Federal de Santa Catarina Animal Care Committee (CEUA PP00943). The samples of cerebral cortex were submitted to Nissl staining and to immunohistochemistry were incubated overnight at 4°C with GFAP Monoclonal Mouse Anti-Glial Fibrillary Acidic Protein, at a concentration of 1:50, as well as NeuN Monoclonal Mouse Anti-Neuronal nuclear protein, at a concentration of 1:100 overnight. Biotinylated secondary antibody and streptavidin-peroxidase were incubated for 40 minutes, followed with 3,3'-diaminobenzidine (DAB). Results: The reduction of the blood flow resulted in irreversible brain damage (Figures 1A, B, D), neurons and astrocytes in infarcted tissue (Figures 1A, B, D, F) submitted hypoxic conditions leading to interruption of ionic function with intracellular accumulation of sodium and water. Histopathological results in the brains (Figures 1A, B, D, F) demonstrated vacuolation and eosinophilic (Figures 1A, D), oncosis neuronal cells (Figures 1A and B), with glial cell reactions (Figure 1F) in compare to control group (Figures 1C, E) by immunohistological method [6, 7]. Conclusions: The cerebral injury predisposed neurons alteration size, meanly in the nuclei, denominated as cell oncosis or cell swelling and GFAP immunoreactivity within the hemisphere affected compared to the unaffected hemisphere of the control animal.

Keywords: Histology, immunohistochemistry, structural biology

REFERENCES

- [1] Garman, R. H. Histology of the central nervous system. Toxicologic pathology, 39(1) (2011) 22-35.
- [2] Jha, S. K. "Cerebral edema and its management." Medical Journal, Armed Forces India 59(4) (2003): 326.



- [3] Kuraoka, Mutsuki, et al. "Direct experimental occlusion of the distal middle cerebral artery induces high reproducibility of brain ischemia in mice." *Experimental Animals*, 58(1) (2009) 19-29.
- [4] Majno, Guido, and Isabelle Joris. "Apoptosis, oncosis, and necrosis. An overview of cell death." *The American journal of pathology* 146(1) (1995): 3.
- [5] Nag, S., Manias, J. L., & Stewart, D. J. Pathology and new players in the pathogenesis of brain edema. *Acta neuropathologica*, 118(2) (2009) 197-217.
- [6] Wagner, D. C., Scheibe, J., Glocke, I., Weise, G., Deten, A., Boltze, J., & Kranz, A. Object-based analysis of astroglial reaction and astrocyte subtype morphology after ischemic brain injury. *Acta neurobiologiae experimentalis*, 73(1) (2013) 79-87.
- [7] Won, Seok-Joon, Doo-Yeon Kim, and Byoung-Joo Gwag. "Cellular and molecular pathways of ischemic neuronal death." *BMB Reports* 35(1) (2002): 67-86.

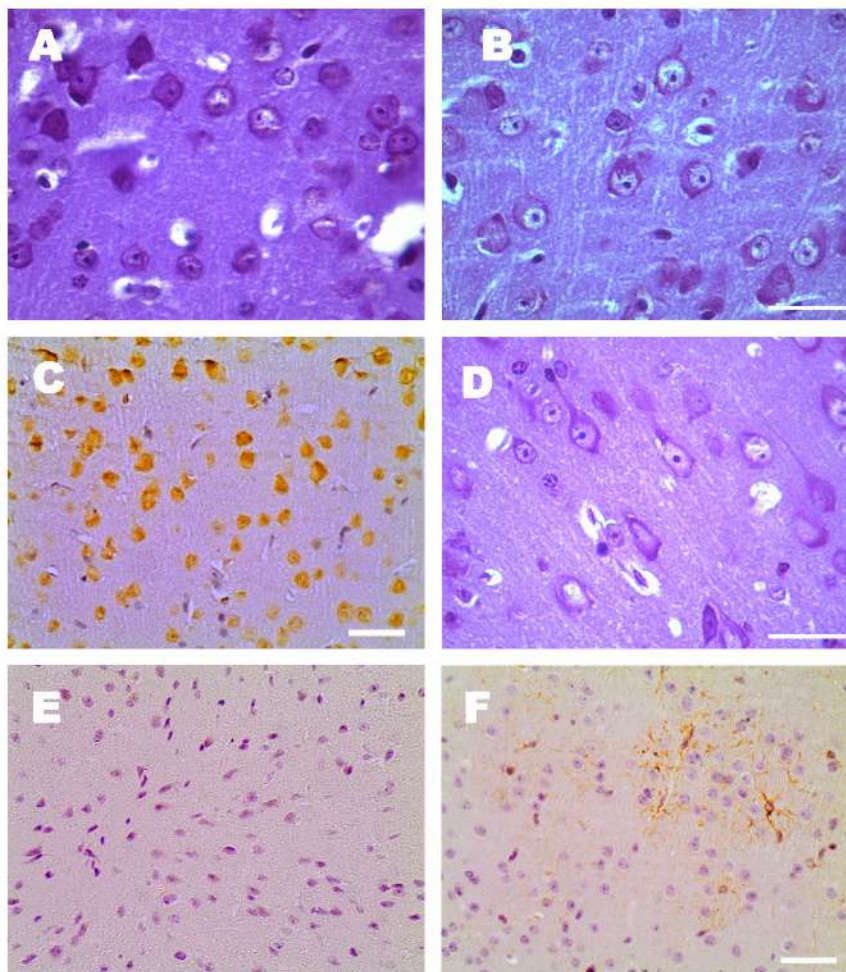
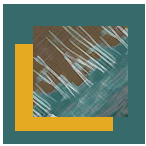


Figure 1. Nissl staining and Immunohistochemical peroxidase staining in mouse cortex. NeuN immunostaining of the normal morphology in the control group (C) and neuropil vacuolation, cell oncosis neuronal, eosinophilic neurons after vessel occlusion (A, B, D). GFAP negative immunostaining of the control group (E) and GFAP positive after occlusion (F) Increase cell volume nuclear and cytoplasm of the neurons was observed in occlusion area (A, B). Scale Bars = 50 μ m (C, E, F) and 20 μ m (A, B, D).



Expression Of HER2 Oncogene In Feline Mammary Carcinomas

Simone C. S. Cunha¹, Kassia V. G. C. Silva^{1*}, Franciele B. F. Silva², Ana Maria R. Ferreira^{1,2,3}

1. Programa de Pós-Graduação em Clínica e Reprodução Animal. Faculdade de Medicina Veterinária. Universidade Federal Fluminense, Niterói-RJ, Brazil.

2. Programa de Pós-Graduação em Patologia. Faculdade de Medicina. Universidade Federal Fluminense, Niterói-RJ, Brazil.

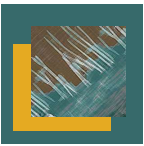
3. Departamento de Patologia e Clínica Veterinária. Laboratório de Anatomia Patológica Veterinária. Universidade Federal Fluminense, Niterói-RJ, Brazil.

*Email: kassiavet@yahoo.com.br

Mammary neoplasms are very frequent in felines, and in this species, most have a highly malignant behaviour, being not only locally aggressive but also with high metastatic potential [1-3]. Proto-oncogenes have been investigated in human breast cancer because of its relevant role in mammary carcinogenesis, as well as its prognostic value [4-8]. The epidermal growth factor receptor 2 (HER2) proto-oncogene has been worldwide studied within the context of breast neoplasms, since its amplification occurs mainly in this tumour class [4-8, 9]. Since few studies are conducted on feline mammary neoplasms, this study aimed to evaluate the immunoexpression of the HER2 oncogene in feline mammary carcinomas. Fifteen paraffin-embedded (FFPE) feline mammary samples diagnosed with mammary carcinomas (MC) were selected from the archives of the Veterinary Anatomic Pathology Laboratory of the Institution, regardless of race, sex or reproduction status. Feline MCs were classified according to the histological grading proposed by Elston and Ellis [10], which evaluates the tubular formation, number of mitoses and nuclear pleomorphism. Immunohistochemical evaluation (IHC) was performed using the polymer method (Advance™ / HRP, Dako) for the detection of the anti-HER2 primary antibody (polyclonal, 1:200, Dako). HER2 immunostaining intensity was classified according to the scoring system HerceptTest, as described by Dutra et al (Table 1) [11]. The established score was 0 to 3+ according to the staining intensity and quantity, where tumour cells were considered HER2 positive when with scores 2+ or 3+. A descriptive statistical analysis was performed. The histopathological diagnosis of malignant neoplasms was simple adenocarcinoma. The most frequent histological grade was grade II (8/15, 53.3%), followed by grade III (5/15, 33.3%) and grade I (2/15, 13.3%). Regarding HER2 expression, 33.3% (5/15) of the feline neoplasms were classified as positive for HER2 (13.3%, 2/15 score 2+ and 20%, 3/15 score 3+), and 66.7% classified as negative for HER2 (27%, 4/15 score 0 and 40%, 6/15 score 1+). Considering HER2 expression and histological grade of tumours, among grade I tumours, 50% (1/2) were HER2 1+ and HER2 2+, respectively. In grade II tumours, 25% (2/8) were HER2 0, 37.5% (3/8) were HER2 1+ and HER2 3+, respectively. In the case of grade III tumours, 40% (2/5) were HER2 0 and HER2 1+, respectively, and 20% (1/5) were HER2 2+. It is concluded that HER2 expression was present in all histological grades of feline mammary carcinomas.

REFERENCES

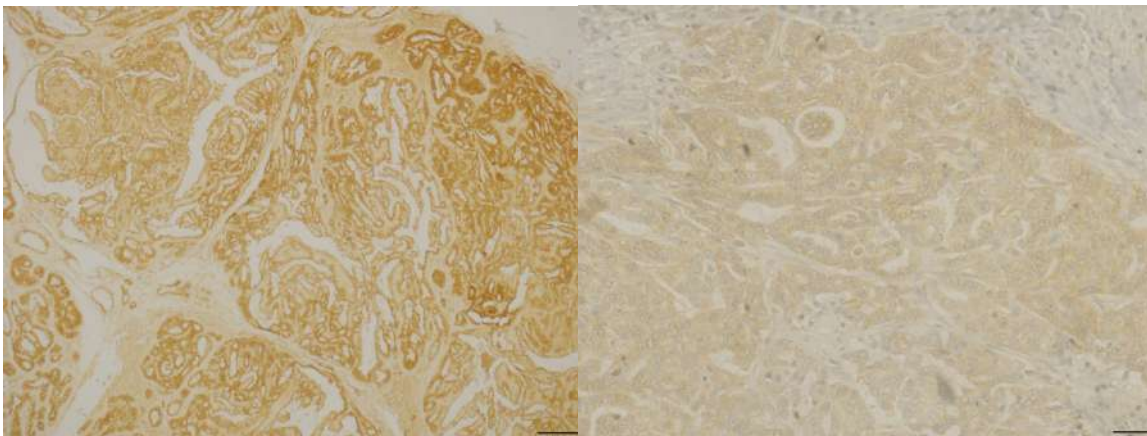
- [1] K.U. Sorenmo et al. Small animal clinical oncology. Saunders, St.Louis, 2013.
- [2] M.N.Silva et al. J. Feline Med. Surg. 19 (4) (2016) 445.
- [3] A.C. Figueira et al. BMC Vet. Res. 10 (2014) 270.
- [4] R. De Maria et al. Cancer. Res.65 (n.3) (2002) 907.
- [5] K. Hughes et al. Vet. J. 194 (n.1) (2012) 19.
- [6] F. Millanta et al. Vet. Pathol. 42 (n.1) (2005) 19.
- [7] J. Ordás et al. BMC. Cancer.7 (2007) 179.
- [8] R. Rasotto et al. J. Comp. Pathol. 144 (2011) 170.
- [9] M. Yan et al. Cancer Metastasis Rev. 34 (2015) 164.



- [10] C.W. Elston, I.O. Ellis, *Histopathology*. 19 (1991) 403.
- [11] A.P. Dutra et al. *Braz. J. Med.Biol. Res.*37 (n.11) (2004) 1673.
- [12] This research was supported by CAPES (Brazil).

Table 1. Classification of HER2 imunoexpression according to the scoring system HerceptTest.

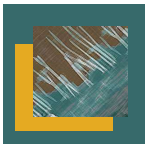
Scores	Evaluation of imunoexpression	HER2 Labelling Pattern
0	Negative	No staining is observed, or membrane staining is observed in less than 10% of cells
1+	Negative	Weak and incomplete membrane labelling in more than 10% of tumour cells
2+	Positive	Complete poor to moderate membrane labelling in more than 10% of tumour cells
3+	Positive	Strong membrane labelling in more than 10% of tumour cells



A

B

Figure 01. Photomicrograph of feline mammary grade II carcinoma. A. Immunohistochemical labelling for HER2 3+ in the plasma membrane of neoplastic feline mammary epithelial cells, showing intense membrane labelling; Bar = 161µm. B. Immunohistochemical labelling for HER2 1+ in the plasma membrane of neoplastic feline mammary epithelial cells, showing weak and incomplete membrane labelling; Bar = 32µm.



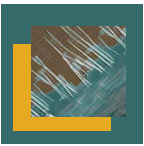
Relation Of HER2 And KI67 Expression To Histologic Graduation In Canine Mammary Carcinomas

Franciele Basso Fernandes Silva^{1*}, Kassia Valéria Gomes Coelho da Silva², Juliana da Silva Leite³, Simone C. S. Cunha², Ana Maria Reis Ferreira^{1,2,3}

1. Programa de Pós-Graduação em Patologia, Faculdade de Medicina. Universidade Federal Fluminense, Niterói-RJ, Brazil.
2. Programa de Pós-Graduação em Clínica e Reprodução Animal. Faculdade de Medicina Veterinária. Universidade Federal Fluminense, Niterói-RJ, Brazil.
3. Departamento de Patologia e Clínica Veterinária. Laboratório de Anatomia Patológica Veterinária. Universidade Federal Fluminense, Niterói-RJ, Brazil.

*Email: francibasso2@hotmail.com

Mammary tumours are the most common tumour type in both women and in female dogs [1]. The study of cell dynamics through molecular markers has been fundamental for the understanding of the behaviour of tumour biology [2]. Thus, this study evaluated the involvement of KI67 cell proliferation protein and epidermal growth factor receptor 2 (HER2) in canine mammary carcinomas, considering the histological grade. Twenty samples of canine mammary carcinomas (CMC) fixed in formalin and embedded in paraffin were selected from the records of the Department of Veterinary Pathology Anatomy of the Institution. The CMCs were classified according to the histological grading proposed by Elston and Ellis [3], which evaluates tubular formation, number of mitoses and nuclear pleomorphism. Immunohistochemical evaluation (IHC) was performed using the polymer method (Advance™ / HRP, Dako) for the detection of the anti-HER2 primary antibody (polyclonal, 1: 200, Dako) and the streptavidin-biotin-peroxidase method (LSAB™ / HRP kit, Dako) for the detection of the primary anti-KI67 antibody (monoclonal, 1:25, MIB-1, Santa Cruz Biotechnology). Two analysts counted the cells that were immunopositive for each antibody. For KI67 evaluation counting of positive and negative cells was performed and the percentage of positive cells was established. The percentage of immunolabelled cells for KI67 was classified as low when <10%, intermediate when 10% - 25%, and high when > 25% [4]. The immunostaining intensity of HER2 was classified according to the scoring system described by ASCO/CAP [5]. The latter establishes a score of 0 to 3+ according to staining intensity and quantity, where tumour cells are considered HER2 positive (3+ score) only if the strong and complete staining of the cell membrane is observed in > 10% of neoplastic cells [5]. For statistical analysis, the comparison between variables was performed using Pearson's chi-square. Statistical significance was set at 5% using statistical software SPSS, version 20.0 (SPSS Inc.). The most frequent histological grade was grade II (11/20, 85%), followed by grade I (6/20, 30%) and grade III (3/20, 15%). Regarding HER2 expression, 25% of CMCs were classified as positive for HER2. For the expression of KI67, 10% presented high cell proliferation index, 40% intermediate index and 50% low index. The HER2 IHC label was observed mainly in the epithelial cells of the mammary ducts of the CMCs, and in some cases there was cytoplasmic marking (Figure 01-A). Regarding the labelling of KI67, intense marking was observed in the nucleus of epithelial and myoepithelial cells and there was sometimes a change in the intensity of the marking (Figure 01-B). There was a statistically significant association between HER2 expression and histological grade of tumours ($p < 0.05$). It was observed that all grade III CMCs were HER2 positive whereas less aggressive grade CMCs (I and II) showed a high frequency of HER2 negative status (Graph 1-A). Taking into account the KI67 expression, even without presenting a statistically significant association ($p > 0.05$), there is a tendency for grade I CMCs to have low rates of cell proliferation, while the more aggressive grade III CMCs have intermediate or high indices for KI67 (Graph 1-B). Thus, it can be concluded that the high activity of HER2 activator protein of cellular signalling



pathways and the high cellular proliferation evaluated by the KI67 protein are associated to the increase in aggressiveness in CMC, evaluated by the decrease in tubular formation, greater number of mitoses and accentuated nuclear pleomorphism.

REFERENCES

- [1] O. Ozmen et al., *Vet Comp Oncol.* doi:10.1111/vco.12293. [Epub ahead of print] (2017).
- [2] M. Paoloni, C Khanna, *Nat Rev Cancer.* 8 (2008) 147-56.
- [3] C.W. Elston, I.O. Ellis, *Histopathology.* 19 (1991) 403–410.
- [4] L.L. Peña et al., *J. Vet. Diagn. Invest.* 10 (1998) 237–246.
- [5] A.C. Wolff et al., *J. Clin. Oncol.* 31 (2013) 3997–4013.
- [6] This research was supported by CAPES (Brazil).

Graph 1. Evaluation of the HER2 (A) and KI67 (B) proteins compared to the histological grade of canine mammary carcinomas.

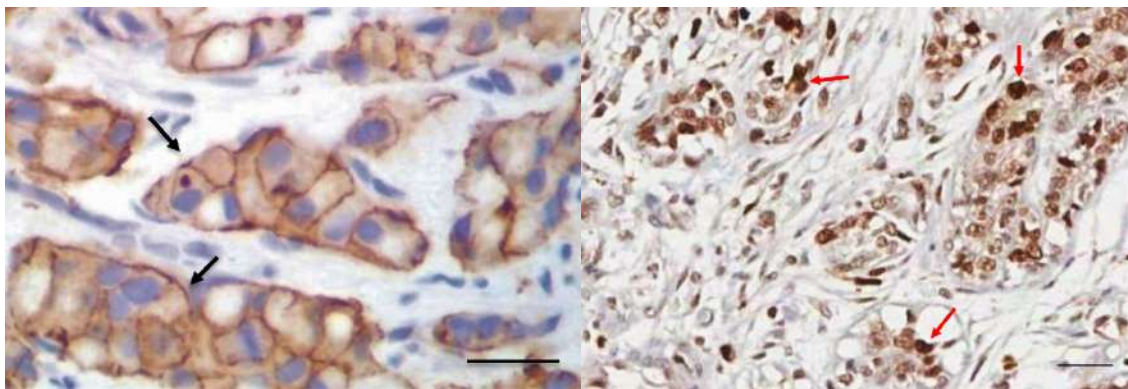
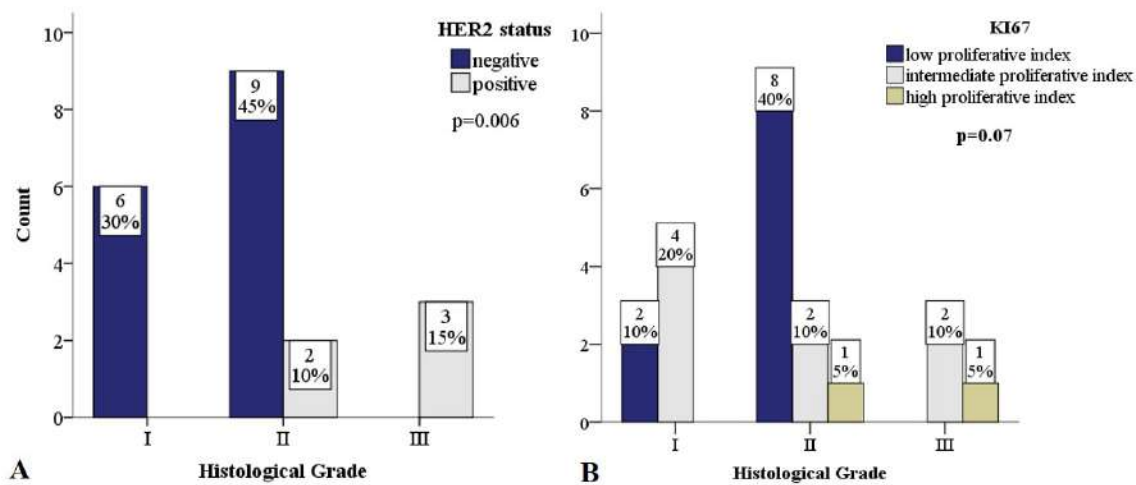


Figure 01. Photomicrograph of canine mammary carcinoma grade III. A. Immunohistochemical labelling for HER2 protein in the plasma membrane of neoplastic canine mammary epithelial cells; note cytoplasmic marking in some cells (black arrows). B. Immunohistochemical labelling for KI67 protein in the nucleus of canine mammary neoplastic cells (red arrows), showing high rate of cell proliferation. Bar = 20µm.



Differential Effects Of Lemon Grass (*Cymbopogon citratus*, *Lippia alba* And *Melissa officinalis*) Ethanolic Extracts On The Nucleolar Activity In Ehrlich Ascites Cells

Letícia de Souza Giordano^{1,2*}, Marilanda Ferreira Bellini^{1,2}, Wilson Aparecido Orcini², Rita Luiza Peruquetti^{1,2,3}.

1. Centro de Ciências da Saúde, University Sagrado Coração, Bauru, Sao Paulo, Brazil.
 2. Laboratório de Biologia Molecular e Citogenética, University Sagrado Coração, Bauru, Sao Paulo, Brazil.
 3. Programa de Pós-graduação em Odontologia – Saúde Coletiva, University Sagrado Coração, Bauru, Sao Paulo, Brazil.
- Email: llegiordano@hotmail.com

Chronotherapy consists of restricting the administration of therapies to certain periods of the day based on the different levels of cell activity within this 24 hours period[1]. It is promising cancer therapy due to the circadian effects on the progression of the cell cycle[2]. It has been also shown that nucleolar activity is increased in cancer cells due to the high synthetic levels on those cells[3]. The aim of this study was to identify if the timing of the administration of three different ethanolic Lemon grass extracts (*Cymbopogon citratus*, *Lippia alba*, and *Melissa officinalis*) have influence on the (1) tumor progression; (2) nucleolar activity. 40 male mice were divided into two control groups and six experimental groups (n = 5 / per group). Control groups received water at different times of the day (light phase - TC-L; and dark phase - TC-D). Each experimental group received 100 mg/kg of ethanolic extracts from the three natural products mentioned at different times of the day (light phase – EECc-L, EELa-L, and EEMo-L; and dark phase - EECc-D, EELa-D, and EEMo-D). On the seventh day of experiment, it was proceeded the inoculation of Ehrlich ascites tumor cells (1×10^3 cells) in the animals, which continued to receive extracts and deionized water in the same system for another 7 days. At the end of the experiment slides with smear tumor fluid were prepared and they went through the following analysis: (1) Impregnation by Ions Silver, to check parameters such as number of organized nucleoli and number of fragmented nucleoli; position of distribution of nucleolar fragments in the nucleus; and nucleolar area in the cells that showed evident nucleolus; (2) HE staining (hematoxylin-eosin) and labeling of nuclear DNA by Dapi dye (blue color), both techniques to confirm that the cells seen in the impregnation by silver ions technique were the cells of interest. EELA-D group presented: (a) increased nucleolar area of organized nucleoli; (b) reduction in the number of tumor cells when compared to its tumor control (TC-D). EECc-D demonstrated a reduction of the nucleolar area when compared to the administration of the same extract performed in the clear phase of the day. Taking into consideration that nucleolar activity is a factor related to the growth and tumor aggressiveness it can be conclude that the administration of different ethanolic extracts (Cc, La and Mo) at different times of the day seem to possess differential activity in the control of development of Ehrlich tumor *in vivo*.

REFERENCES

- [1] S. Sahar and P.Sassone-Corsi. Nat. Rev.: Cancer, 9 (2009) 886.
- [2] C.G. Lis et al., Int. Can. Therap. 2 (2003) 105.
- [3] C.V. Ribeiro et al., Braz. J.Otorhino. (2015). doi:<http://dx.doi.org/10.1016/j.bjorl.2014.12.003>
- [4] This research was supported by CNPq (Brazil).

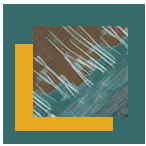


Figure 1: Standard counting of the number of nucleoli evident in tumor cells of the different groups.

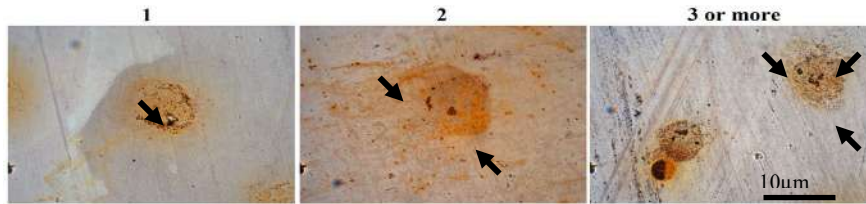


Figure 2: Pattern of analysis of the type of nucleolus observed in tumor cells of the different groups: evident nucleolus; fragmented nucleolus; and extranuclear fragmentation.

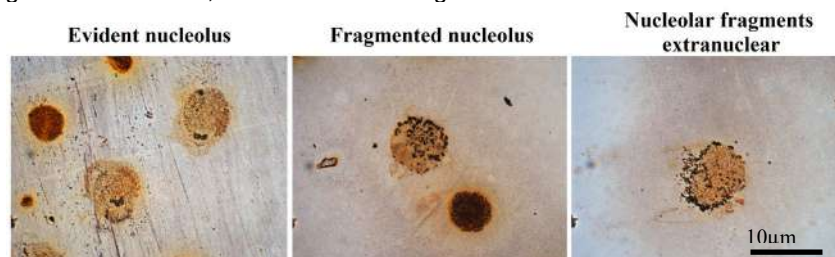


Figure 3: Comparison among area of evident nucleoli of the tumor cells in the different groups. The letters (a and b) represent statistical differences in the groups that ingested different extracts at the same time of day. The asterisks (*, **) represent statistical differences between the groups that consumed the same extract at different times of the day. A: Lemon grass ingestion in the light period; B: Lemon grass ingestion in the dark period.

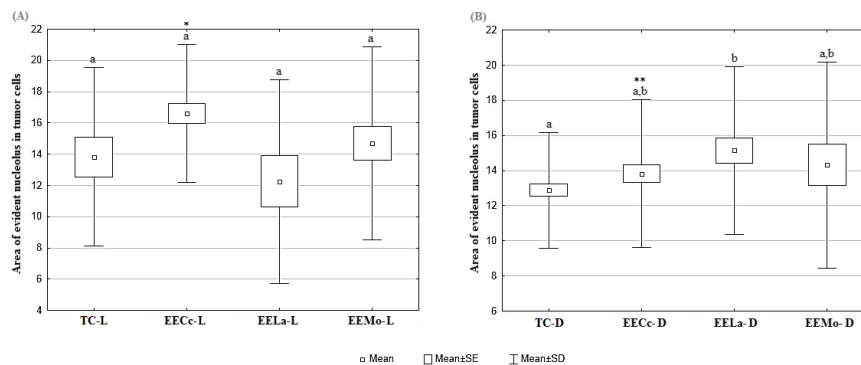
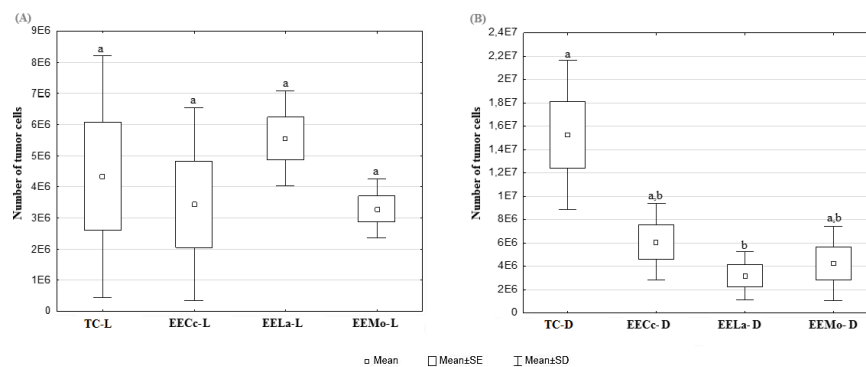


Figure 4: Counting the number of tumor cells at the end of the 15 days of treatment with the different extracts. The letters (a and b) represent statistical differences in the groups that ingested different extracts at the same time of day. A: Lemon grass ingestion in the light period; B: Lemon grass ingestion in the dark period.





Method of Inclusion with Microwave of Cashmere Fiber for Characterization by Transmission Electron Microscopy

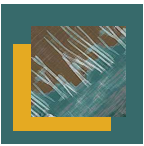
Lia Souza Coelho^{1*}, Noemia Rodrigues Gonçalves²

1. Federal Rural University of Rio de Janeiro, Seropédica, Brazil.
2. Federal University of Rio de Janeiro, Rio de Janeiro, Brazil.

Cashmere is a fine fiber produced by goats used in the production of extremely soft yarns valued by the fashion industry. The Brazilian cashmere fine fiber has an average diameter of 8.46 μm [1]. Characterization of internal cashmere structures is important to certify textile labeling more precisely [2]. The characterization of the internal structures of the cashmere fiber is important to certify the textile labeling more accurately [2]. Transmission electron microscopy (TEM) has already been used [3], although the technique developed presents difficulties in resin infiltration. The technique with microwaves for the preparation of protozoan samples was used with efficiency in the infiltration of resin [4]. The objective of this work was to develop a technique and laboratory procedures to improve the efficiency of resin infiltration, making it possible to identify animal fibers, specifically cashmere. In this work, different microwave pulse times were used with the aim of improving the inclusion of the Spurr resin of the cortex and cuticle regions. The fibers were pre-fixed for 30 minutes in 2.5% Glutaraldehyde in 0.1 M Cacodylate buffer. For the inclusion, the samples were submitted to 3 microwave time pulses (5, 10 and 15 seconds) and control, without the use of microwaves. Ultra-fine sections (60-70 nm) was obtained by Leica EM UC 7000 ultramicrotome and were observed in a JEOL 1200 EX Transmission Electron Microscope (TEM) operating at 80 kV. The sections were mounted on slotted copper grids on Formvar film and contrasted with 5% Uranyl Acetate and Lead Citrate. Figure 1 shows TEM images from a cross section of cashmere fiber. Total fixation and infiltration of the material on the resin were observed with the 3-pulse times of 10 "and 3 pulses of 15". The presence of samples preserved and adhered to the resin in TEM images demonstrates the efficiency of the microwave infiltration technique. The micrographs of the morphological structures of the cuticle and the cortex allowed the recognition of fine fiber cashmere.

REFERENCES

- [1] L.S. Coelho, Modesto E.C., J. Text. I., (2016).
- [2] B.A. McGregor, R. Postle, Int. J. Cloth. Sci. Technol. 16 (2004) 119.
- [3] D.P. Harland, J. A. Vernon, R. J. Walls, J. L. Woods, 243, 184–196 (2011).
- [4] M. Benchimol et al., Microsc. Res. Tech, 25 (1993) 286.
- [5] This research was supported by CAPES (Brazil).



DOI: [INSERIR ENDEREÇO DO DOI AQUI.](#)

Caderno de Resumos do 26º Congresso Brasileiro de Microscopia da SBMM – ISSN: [INSERIR AQUI.](#)

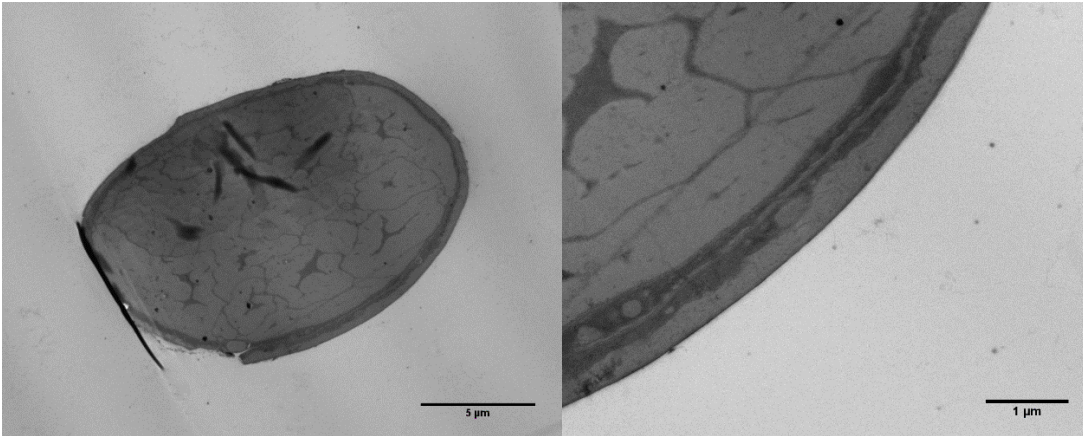


Figure 3. TEM micrograph of cross-sectional cashmere showing the resin attached to the surface of the fiber, enabling future analyzes on cashmere samples.



Ultrastructural Characterization of EGTA Effects on Calcium Signaling During Early Development of Tetraspores of *Palisada flagellifera* (Ceramiales, Rhodophyta)

Luciane Cristina Ouriques^{1*}, João Pedro Krauspenhar Barros¹, Fernanda Bouvie, Zenilda Laurita Bouzon¹, Carmen Simioni²

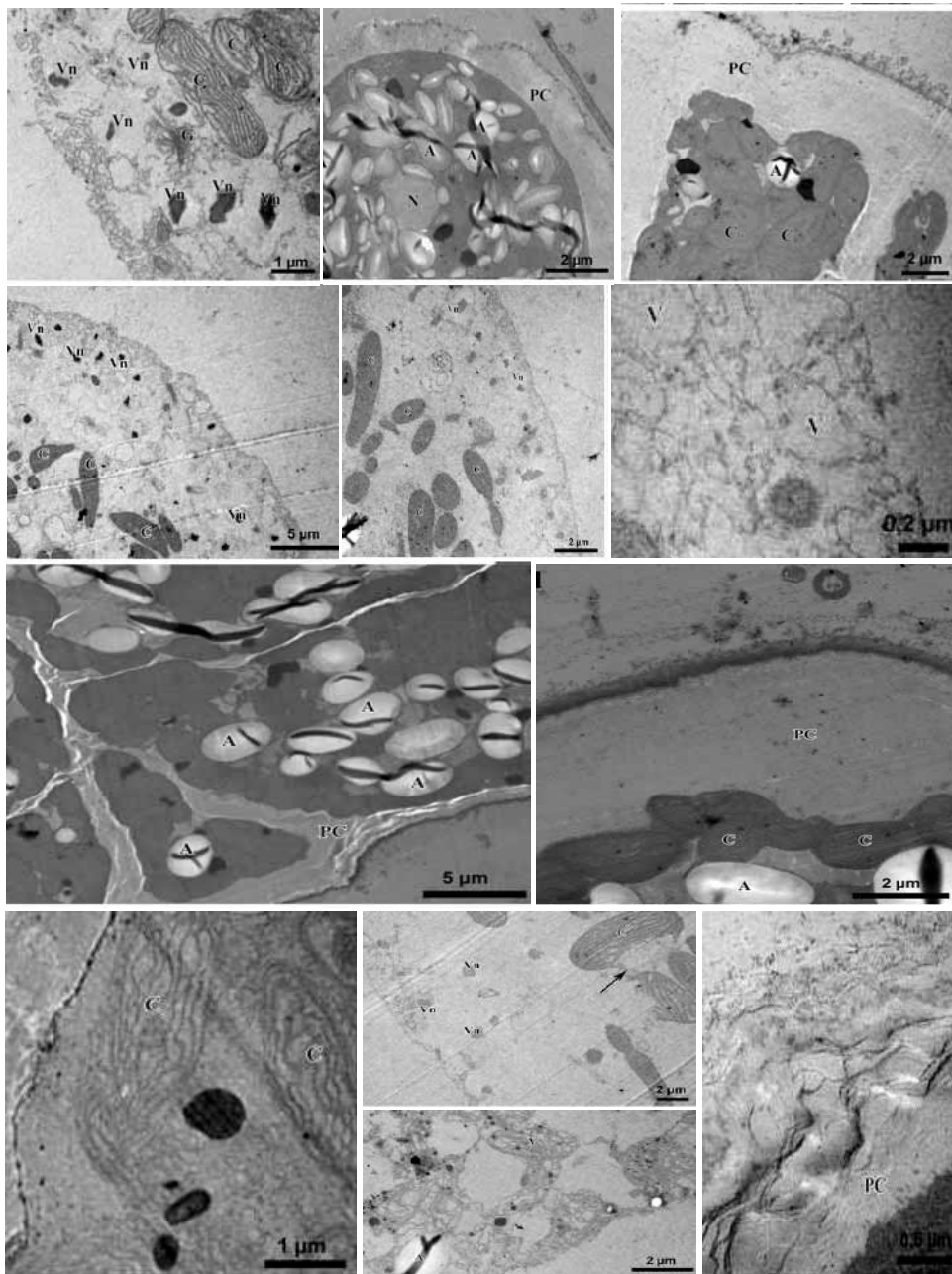
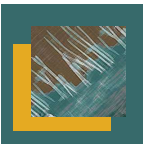
1. Laboratory of Plant Cell Biology, Department of Cell Biology, Embryology and Genetics, Federal University of Santa Catarina, 88049-900, CP 476, Florianópolis, SC, Brazil. luciane.ouriques@ufsc.br

2. Post-Graduate Program in Cell Biology and Development, Department of Cell Biology, Embryology and Genetics, Federal University of Santa Catarina 88049-900, CP 476, Florianópolis, SC, Brazil

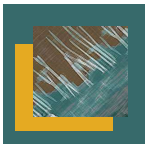
Calcium has an essential signaling role in polarizing the extension of most tip-growing plant cells [1]. EGTA buffers reduce the free Ca^{2+} concentration in sea water and in high concentration can completely block rhizoids germination and elongation. The aim of this study was to determine changes in cellular organization during early development of tetraspores of *P. flagellifera* in tetrasporophytic plants treated with EGTA calcium chelator. The control plants were placed on slides in Petri dishes with sterilized sea water and the treated samples were incubated with two different EGTA concentrations (1.0 mM and 2.0 mM). Both control and treated samples were incubated in their respective treatments during two distinct periods (12 and 24 hours). Subsequently, all samples were analyzed by transmission electron microscopy (TEM) according the methodology described by [2]. The analyses with 12 hours showed that the control tetraspores were surrounded by adhesive mucilage. Prior to cell wall synthesis we observed that chloroplasts, Golgi bodies and nucleated vesicles were at the cell periphery (Fig.1). Following adhesion, a thin cell wall was synthesized. At this stage, the chloroplasts and floridean starch granules became randomly distributed within the tetraspore. The nucleus was located in the central region (Fig. 2). After cell wall formation, the tetraspore germinated (Fig. 3). Interesting, the majority of tetraspores treated with 1.0 mM and 2.0 mM of EGTA in this time, didn't present cell wall. A large quantity of nucleated vesicles was detected at these cell peripheries (Fig. 4 and 5). With 2.0 mM of EGTA was observed electron-transparent vesicles near to the plasma membrane (Fig. 6). After the 24 hours, the tetraspores of the control samples proceeded to germination. The daughter cells from these tetraspores became gradually smaller due to successive divisions and were compacted by organelles (Fig. 7), as well as, their cell wall showed a microfibrillary organization (Fig. 8). In this same time, in the treated samples, the chloroplast thylakoids were disrupted (Fig. 9 and 10). The cell wall showed disorganized in microfibrils (Fig. 11). Numerous electron-transparent vesicles were observed near the cell periphery (Fig. 12). These results demonstrated that the cell organization during early development of tetraspores of *P. flagellifera* is calcium dependent. This research was supported by UFSC/CNPq.

REFERENCES

- [1] L. Lin et al., Journal of Experimental Botany, 12 (2009), 3477-3489.
[2] L.C.Ouriques, Z.L. Bouzon, Plant Biosystems, 137 (2003), 193-202.



Figs. 1-6. MET of early development of tetraspores of *P. flagellifera* after 12 hour period. Figs. 1-3 Control tetraspores. Fig. 1. Attached tetraspore without cell wall, with chloroplasts, Golgi bodies and nucleated vesicles at cell periphery. Fig. 2. Nongerminated tetraspore with cell wall. Observed in the cytoplasm the chloroplast, floridean starch granules and nucleus. Fig. 3. Detail of tetraspore germinated. Figs. 4 and 5. Tetraspores treated with 1.0 mM and 2.0 mM EGTA without cell wall. Fig. 6. With 2.0 mM EGTA, showing electron-transparent vesicles near to the plasma membrane. Figs. 7-12 MET of early development of tetraspores of *P. flagellifera* after 24 hour period. Figs. 7 and 8 Control tetraspores. Fig. 7. Sporeling showing daughter cells that become gradually smaller. Fig. 8. Detail of the cell wall. Figs. 9 and 10. The treated samples. Observed of disrupted chloroplast (arrow). Fig. 11. With 1.0 mM EGTA. Detail of disorganized microfibrils. Fig. 12. With 2.0 mM EGTA. Note numerous electron-transparent vesicles. Nucleated vesicles (Vn), cell wall (CW), chloroplast (C), starch grains (S), Golgi bodies (G) and nucleus (N).



The ultrastructure of *Malassezia furfur* and *Malassezia pachydermatis* and their interactions with macrophages

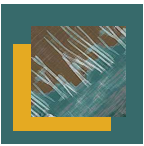
Rossana Teotônio de Farias Moreira¹, Maria Anete Lallo², Diva Denelle Spadacci-Morena³, José Guilherme Xavier², Elizabeth Cristina Perez Hurtado², Luciane Costa Dalboni^{2*}, Selene Dall'Acqua Coutinho²

1. Escola de Farmácia e Enfermagem da Universidade Federal de Alagoas, Maceió, Brazil
2. Pós-Graduação em Patologia Ambiental e Experimental, Universidade Paulista, São Paulo, Brazil. Email: selene@uol.com.br
3. Instituto Butantan, Laboratório de Fisiopatologia, São Paulo, Brazil

Malassezia pachydermatis and *Malassezia furfur* are lipophilic yeasts of the cutaneous microbiome, living in an interface between pathogenic and commensal organisms. These organisms are occasionally responsible for serious invasive infections in humans, especially in preterm infants undergoing supplemental lipid nutrition. In invasive infections little is known about the pathogenesis and the innate or adaptive immune response triggered by the *Malassezia* species. A unique characteristic of *Malassezia* sp is the cell wall, which is multilamellar [1] and very thick compared to other yeasts [2]. The cell wall is surrounded by a lipid-rich capsule-like structure, involved in the interactions of this yeast with the host [1, 2, 3]. Probably the cell wall plays a critical role in infection conditions [4]. The aim of this research was to study the fine structure of *M. furfur* and *M. pachydermatis* and their interaction with macrophages. RAW-264.7 (ATCC) lineage murine macrophages (3×10^5 cells) were challenged with *M. furfur* CBS-1878 and *M. pachydermatis* CBS-1696 in concentrations of 5:1 (yeasts:macrophages ratio), and incubated at 37°C with 5% CO₂. After 24h following the challenges, cover glasses were collected, submitted to Giemsa stain and it was calculated the average number of fungal cells in the macrophages. For transmission electron microscopy (TEM), suspensions of the macrophages infected with *M. furfur* and *M. pachydermatis* were fixed in 2% glutaraldehyde in 0.2 M cacodylate buffer (pH 7.2) at 4°C for 10 h, post-fixed in 1% OsO₄ buffered for 2 h and routinely processed. Both species induced high uptake of *Malassezia* spp. by the macrophages. In *M. furfur*-infected macrophages the average number of fungal cells was 2.2 and in *M. pachydermatis*-infected macrophages was 3.4 (statistically significant). In this assay, *M. pachydermatis* generated a higher phagocytic capacity than *M. furfur*. There is no available data in the literature comparing the phagocytic capacity for these species. TEM showed the uptake of *Malassezia* spp. by the macrophages (Fig. 1A). Several macrophages internalized more than one yeast (Fig. 1B). It was observed intracellular multiplication of *Malassezia*, buds formed on a very broad base from the mother cells (Fig. 1C). TEM showed the characteristic multilamellar cell wall of *Malassezia* sp, with two layers, inner and outer coated with a diffuse microfibrillar like-capsule (Fig. 1D). Notice the characteristic corrugated inner surface and the collarette formed by bud scars (Fig. 1D). We suggest that lipids of multilamellar cell wall interfere on the phagocytosis and could protect the yeast from the innate immunity [5]. We conclude the high phagocytic capacity verified in this research, reinforces the character of the relationship between these yeasts and the host, acting as a commensal in the cutaneous microbiome and causing infections when an imbalance in the parasite-host relationship occurs.

REFERENCES

- [1] J. Guillot et al., J. Med. Mycol. 5 (1995) 86.
- [2] Gioti et al., mBio, 4 (2013) e00572-12.
- [3] Guého et al., Ant. Leewenhoek, 69 (1996) 337.
- [4] Kim et al., Ann. Dermatol., 21 (2009) 130.
- [5] Kesavan et al., Med. Mycol., 38 (2000) 239.



Financial support: FAPESP no. 2015/25948-2

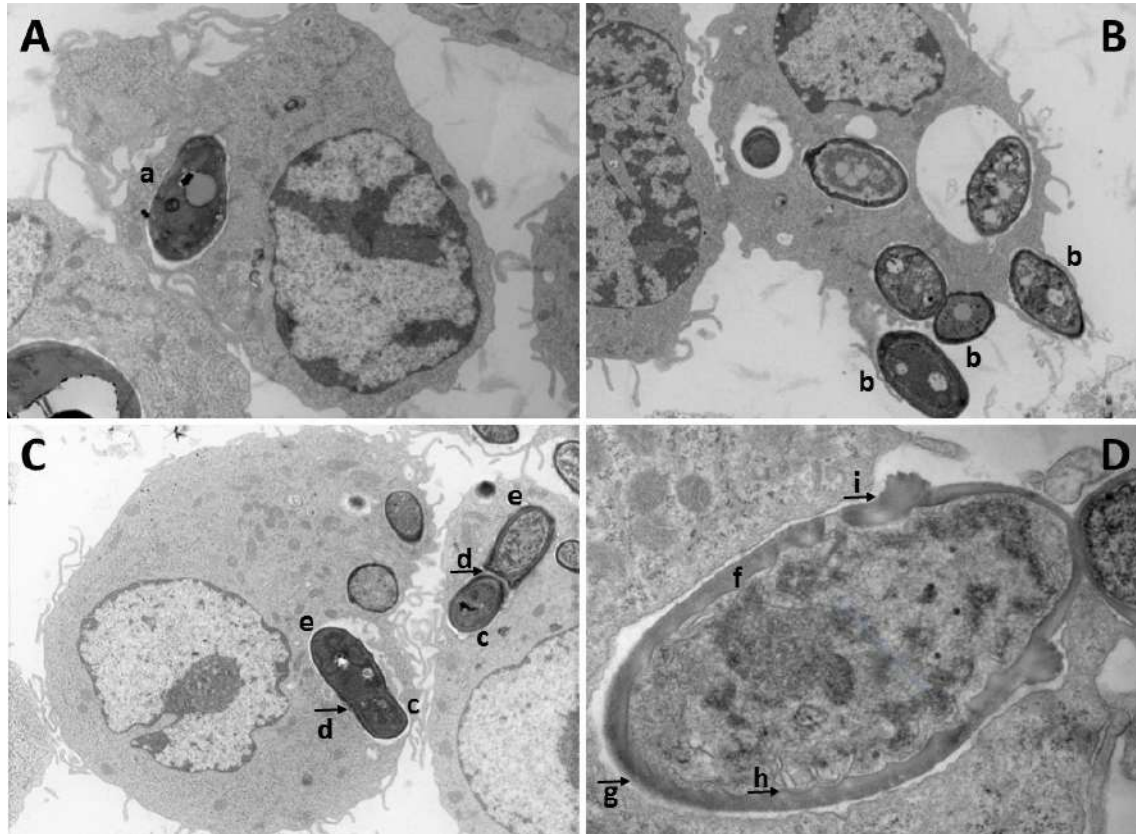
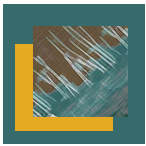


Figure 1. A. *Malassezia pachydermatis* ingestion by macrophage RAW 264.7 (a). B. *M. pachydermatis* internalized or in process of internalization (b) by macrophage RAW 264.7. C. Intracellular multiplication of *M. furfur* buds (c) formed on a very broad base (d) from the mother cells (e). D. Cell wall of *M. pachydermatis* with two layers: the inner one (f) and the outer with a diffuse microbrillar aspect (g). Notice the corrugated inner surface (h) and the collarette formed by bud scars (i).



In Vitro Phagocytosis of *Encephalitozoon cuniculi* by Adherent Peritoneal Cells

Adriano Pereira^{1,2*}, Luciane Costa Dalboni¹, Diva Denelle Spadacci-Morena³, Anuska Marcelino Alvares-Saraiva¹, Elizabeth Cristina Perez¹, Maria Anete Lallo^{1,2}

1. Pós-Graduação em Patologia Ambiental e Experimental, Universidade Paulista, São Paulo, Brazil
2. Curso de Biomedicina, Centro Universitário São Camilo, São Paulo, Brazil
3. Instituto Butantã, Laboratório de Fisiopatologia, São Paulo, Brazil

*Email: biomedadriano@yahoo.com.br

Microsporidia are intracellular and opportunistic pathogens, causing serious diseases in immunodeficient individuals. We recently demonstrated that XID mice are more susceptible to encephalitozoonosis caused by intraperitoneal infection by *Encephalitozoon cuniculi* and the role of B-1 cells in resistance to infection was evidenced [1]. Studies by Popi and collaborators suggest the regulatory activity of B-1 cell on the function of other cell types, for example, macrophages [2]. In this way, the objective of this study was to evaluate *in vitro* the participation of B-1 cells in the process of phagocytosis of *E. cuniculi* by peritoneal macrophages in order to collaborate with the understanding of the involvement of this cell in the response against this microorganism and also corroborate in the elucidation of participation in the defense against other pathogens. Adherent peritoneal cells (APC) were obtained from BALB/c by peritoneal lavages performed with RPMI medium. The cell volume was adjusted to 1×10^7 cells which were transferred to 25 cm² bottles and incubated in the same medium plus 10% fetal bovine serum (R 10) at 37°C with 5% CO₂ for 40 min. After this time, the culture medium was removed and new R10 medium containing *E. cuniculi* spores (2:1) was introduced into the bottles. After 1h, the cultures were collected and fixed in 2% glutaraldehyde in 0.2 M cacodylate buffer (pH 7.2) at 4°C for 10 h, post-fixed in 1% OsO₄ buffered for 2 h and routinely processed for transmission electron microscopy (TEM). In the APC of BALB/c mice we observed phagocytosis, intact spores inside macrophages and in the process of lysis (Fig. 1A,B). Phagocytic cells, especially macrophages, showed membrane extensions with free pseudopodia or adhered to the wall of extracellular spores (Fig. 1C). It was very evident the communication between the cells present in the cultures, being identified the adhesion of lymphocyte to the macrophage or mast cell with macrophage and lymphocyte (Fig. 1D,E). The internalized spores in the lytic process were surrounded by a vacuolar membrane, forming a typical phagosome. Fewer numbers of non-lysed spores were observed, sometimes without any vacuolar structure around them. The spore ultrastructure of *E. cuniculi* was typical of non-germinated mature spores and consisted of a triple membrane, with an outer layer (exospore), a middle layer (endospore) and an inner layer (plasma membrane) (Fig. 1F). The results presented here show that phagocytic cells, especially macrophages, communicate intimately with B-1 cells, other lymphocytes and with mast cells present in the peritoneal lavage, significantly interfering with phagocytic function.

REFERENCES

- [1] L.F.V da Costa et al. Immunobiology, 222 (2017) 218-227.
- [2] A.F. Popi et al. Microbes Infec. 10 (2008) 817-824.

This research was supported by CAPES and FAPESP (Brazil)

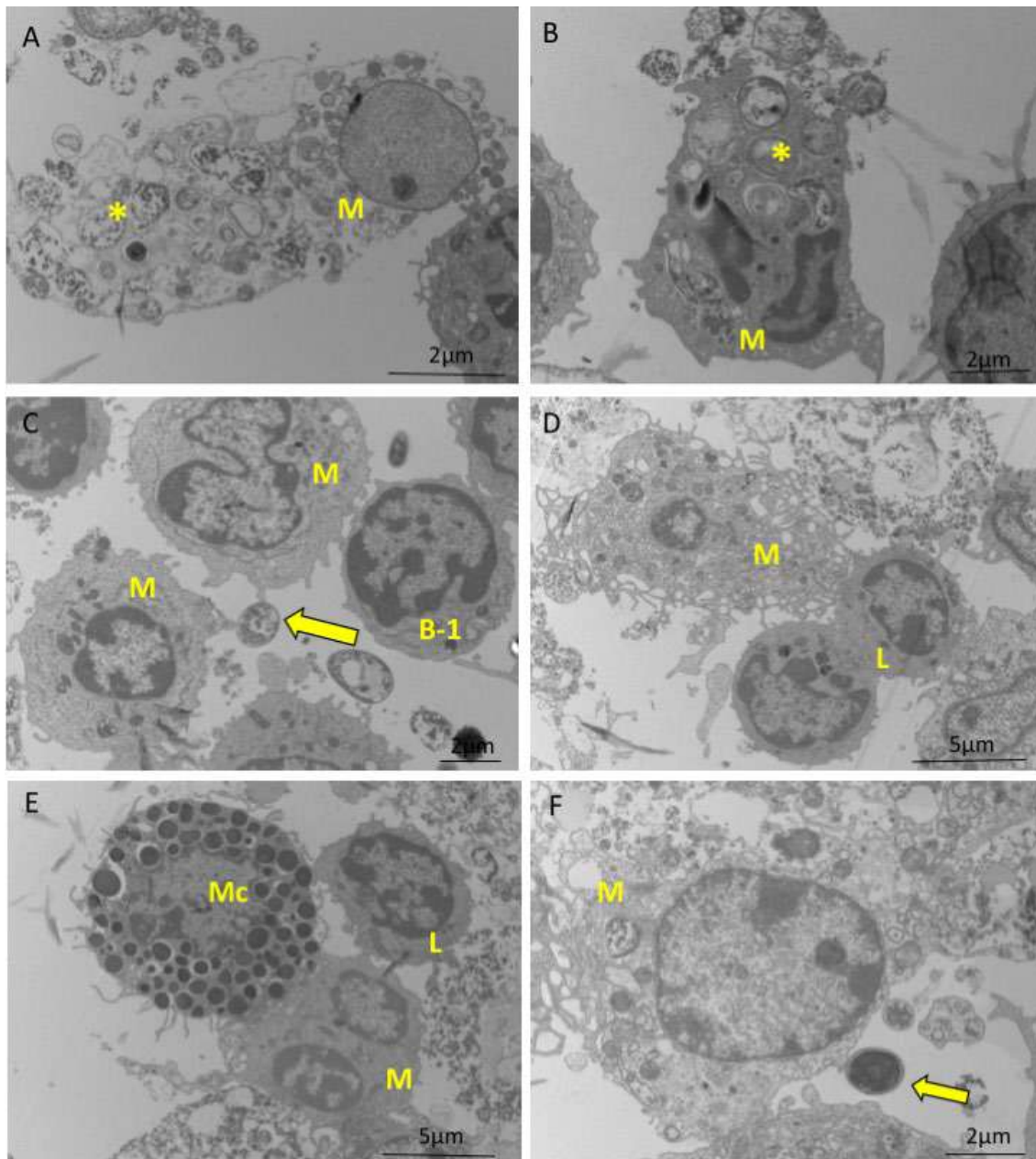
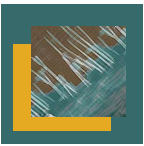
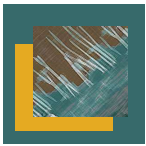


Figure 1: TEM of adherent peritoneal cells (APC) obtained from BALB/c mice. (A) Intact spores (asterisk) and (B) spores in the process of lysis (asterisk) inside phagocytic cells. (C) Macrophages showed membrane extensions adhered to the wall of extracellular spores (arrow). (D) Intercellular communication between macrophages (M) and B-1 cell and (E) between mast cells (Mc) with macrophages and lymphocytes (L). (F) A typical non-germinated mature spore of *E. cuniculi* (arrow) in contact with a phagocytic cell.



Structural Chraterization of the *Trichuris muris* egg and

Lima L R¹, Miranda, K.,^{2,3} Torres E J L^{1*}

1. Laboratório de Helminologia Romero Lascasas Porto – FCM – UERJ. 2- Laboratório de Ultraestrutura Celular Hertha Meyer-UFRJ and 3- CENABIO-UFRJ

*Email: eduardo.torres@uerj.br

Soil-transmitted helminths are among of the most common infections worldwide, affecting mainly developing countries children's [1]. Its transmission is performed through eggs in the human faeces, thus contaminating the soil. It is estimated that more than 270 million pre-school and more than 600 million school-aged children live in regions with risk of helminth transmission. It is estimated that more than one million people are infected with *Trichuris trichiura*, being considered one of the most successful parasitic nematodes [1,2]. *T. muris* species is used as an experimental model for a better understanding of medical and veterinary trichuriasis. This work aims to investigate the egg structure, including the shell and larva, that is responsible for establishing the infection and is recovered naturally in eggs presents in the soil. In this work we used light microscopy (bright field and confocal), Cryo-scanning electron microscopy (CSEM) and transmission electron microscopy (TEM) of the unfixed samples and submitted of the high-pressure freezing/freeze-substitution (HPF/FS). Using LM we observed the not embryonated egg (Fig. A), the fully developed larva L1, the polar pugs and the three layers that forming the shell of the egg are identified (Fig. B and inset). By confocal microscopy, we observed the larva cells and structures inside of the egg (Fig. C-E). HPF/FS samples were analyzed using TEM, we identified the larva cuticular folds (Fig. F and H), stylet (Fig. F and G), fibers that forming the egg shell and polar plug without fiber shell structures. The structure of the polar plug exhibits a fibrillar appearance with low electron density (Fig. I). Details of the eggshell, observed by TEM and CSEM showed that this structure is divided in different layers, organized in three main regions: the outer layer (vitelline), cuticular layer medium and the inner lipidic layer (Fig. J-M). Our results showed details of the egg shell and larval structures, the preservation of the samples enabled to explore the ultrastructural aspect with biological implications not yet described. The egg-shell structures, the larva cuticle and the stylet observation are important information for understand the resistance of the egg in soil, larval molting and the tissue invasion of the parasite in their hosts. These results are directly associated with the elucidation of parasitism developed by *Trichuris* species.

REFERENCES

- [1] WHO, Media centre Soil transmitted helminth (2014) 366
- [2] Cliffe e Grecis. Adv. Parasitol. 57 (2004) 255-307.
- [3] This research was supported by CNPq (Brazil) ; FAPERJ and UFRJ -CENABIO

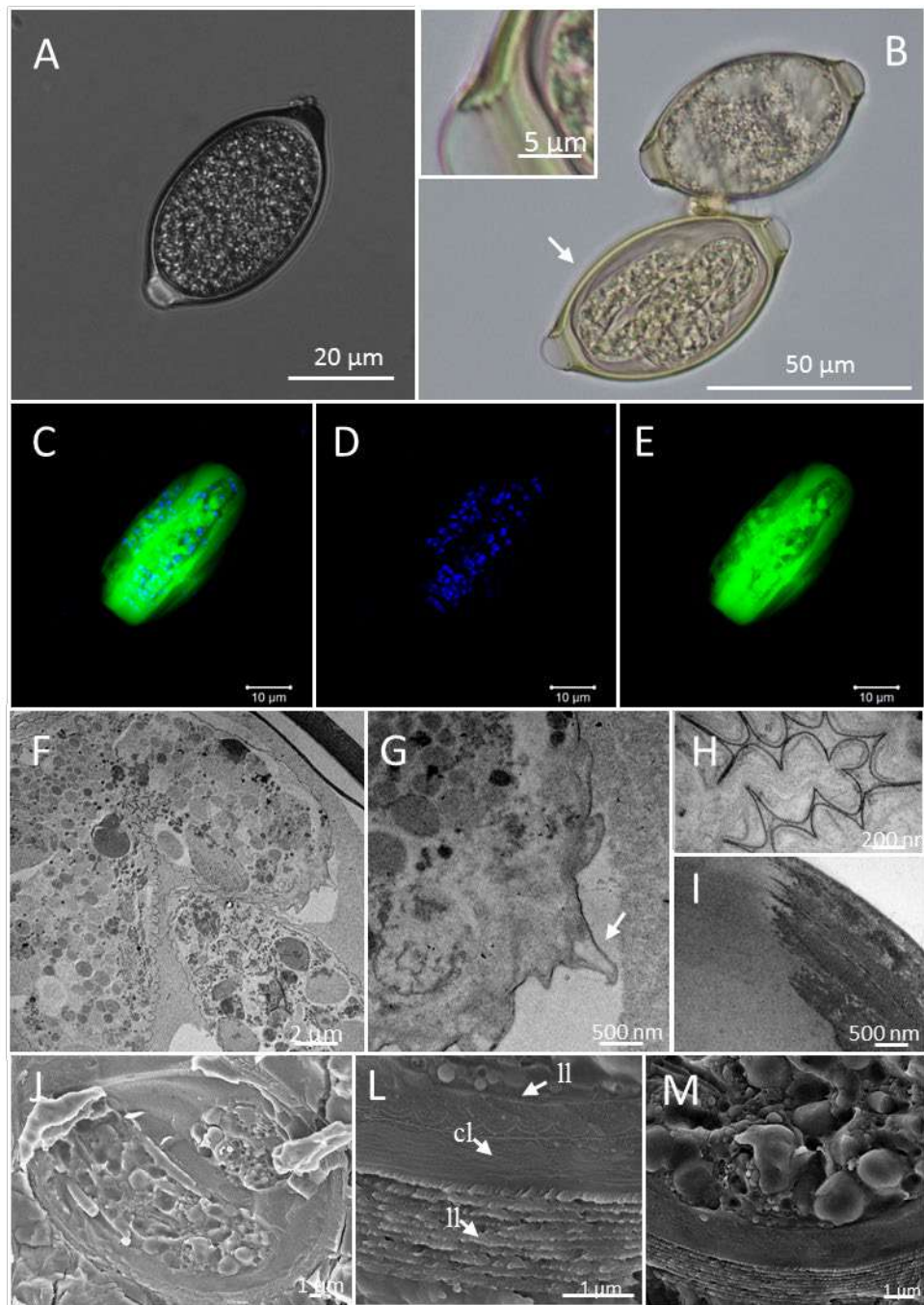
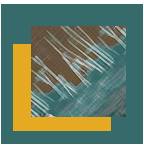
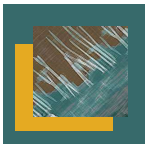


Image 1: Light microscopy in Normasky-A interferential contrast mode: Non-embryonic egg; Microscopy of light: B- Eggs embryonated with a larva L1 (L) inside, the three layers of eggshell (); Confocal microscopy: C- Double labeled egg, D- Labeled with DAPI, E - Calcein-labeled ; Transmission electron microscopy: F: Egg with the larva inside it, electron-dense granules forming the larva, G- The posterior region of the larva, expressing its stilet, H- Tegument folds, I- Insertion of the polar plug in the layers of the shell Of the egg; Cryo-Scanning Electron Microscopy: J- Embryonated egg, L- Egg shell layers: ll- Lipid layer, cl- cuticular layer, vl- vitelline layer, M- granules in the pre-vitelinic space.



Morphology Characterization of Nematodes associated of Parasitic Otitis in Bovines

Makoto Enoki Caracciolo¹, Eduardo José Lopes Torres^{1*}

1. Laboratório de Helmintologia Romero Las Casas Porto, FCM-UERJ, RJ. Brazil.

*Email: lopestorresej@gmail.com

The parasitic otitis presents veterinary impact due to infection caused by bacterial and nematode species, resulting in an intense inflammatory process, which may affect both the external and internal ear [1]. Several cases have been reported in hot and humid countries [2]. The species *Metarhabditis freitasi* and *M. costai* have been described as being responsible for creating the parasitic otitis in Gir cattle (*Bos taurus indicus*) [3]. The objective of this work is to identify the nematodes that cause otitis using scanning electron microscopy (SEM). Inflammatory exudate samples collected from four Gir cattle ear canals with otitis clinical signals. These animals are from an experimental farm of EPAMIG - Empresa de Pesquisa Agropecuária de Minas Gerais, in the municipality of Itabira, MG, Brazil. Nematodes were recovered of the exudate using swabs and immediately washed in PBS, fixed with Karnovsky's solution (Glutaraldehyde 2,5%, freshly prepared formaldehyde 4,0% in sodium cacodylate buffer 0,1M, pH 7,2), adhered on glass coverslips and post-fixed in osmium tetroxide and 1% potassium ferrocyanide 0,8%. The samples were then dehydrated in ethanol series, critical point dried (Leica EM CPD300), mounted in a metal stub, coated with gold (15-20 nm) and analyzed using a conventional SEM FEI-Quanta 250 and a field emission SEM Zeiss Auriga Compact. Our results by SEM identified three species: *M. freitasi* (Fig. 1-2), *M. costai* (Fig. 3-4) and *Rhabditis* sp. (Fig. 5-6). All species presented in the anterior end, a triangular oral opening surrounded by three lips, two latero-ventral and one dorsal (Fig. 1, 3 and 5). Each latero-ventral lip presents three papillae and one phasmid. The dorsal lip presents four papillae. The differences between these species are observed in the posterior end of males, mainly in the length of the tail and the morphology and spicule size (Fig. 2, 4 and 6). We conclude that nematodes *Metarhabditis costai* and *M. freitasi* are the main cause of the parasitic otitis in Brazil, and this parasitosis promoted by *Rhabditis* sp. and according to our data, this nematode may be a new parasite species. Molecular analysis are in progress.

REFERENCES

- [1] E.R.Duarte, J. S. Hamdan, J. Vet. Med. B Infect. Dis. Vet. Public. Health, 51 (2004) 1.
- [2] P. V. B.Leite et al *Pesq. Veterinária Brasileira*.32 (2012) 855.
- [3] W.Jr.Martins, *Mem. do Inst. Oswaldo Cruz*. 80 (1985) 11.
- [4] This research was supported by CNPq (Brazil), FAPERJ (Brazil).

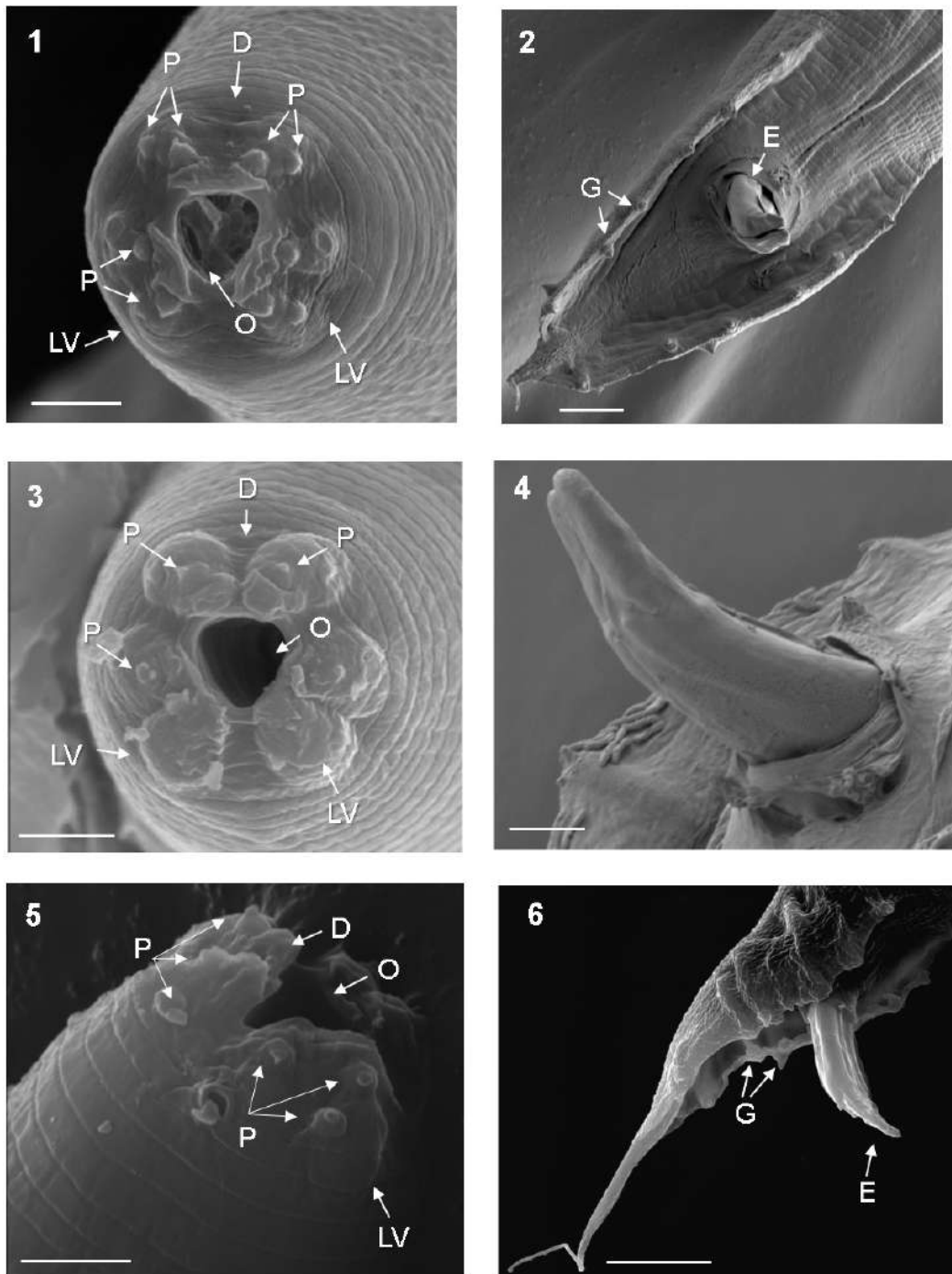
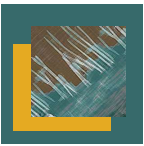
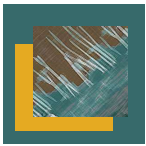


Fig. 1 - *M. freitasi* anterior end, showing the oral opening [O], dorsal lip [D], latero-ventral lips [LV] and cefalic papillae [P] (Bar = 5 μ m); Fig. 2 - Posterior end of *M. freitasi*, showing genital papillae [G] and spicules [E] (Bar = 10 μ m); Fig. 3 - *M. costai* anterior end, showing oral opening [O], cefalic papillae [P], dorsal lip [D] and latero-ventral lips [LV] (Bar = 5 μ m); Fig. 4 - *M. costai* spicules (Bar = 5 μ m); Fig. 5 - *Rhabditis sp.* anterior end, showing the oral opening [O], dorsal lip [D], latero-ventral lip [LV] and cefalic papillae [P] (Bar = 2 μ m); Fig. 6 - *Rhabditis sp.* posterior end, showing genital papillae [G] and spicules [E] (Bar = 20 μ m).



Relationship Between Aging And Structural Alteration On Chromatoid Bodies

Elisa Gomes Santos¹, Maraisa Alves^{2*}, Wilson Aparecido Orcini³ and Rita Luiza Peruquetti^{1,2,3}

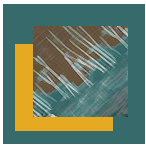
1. Programa de Pós-graduação em Odontologia – Saúde Coletiva, University Sagrado Coração, Bauru, Sao Paulo, Brazil.
2. Centro de Ciências da Saúde, Universidade Sagrado Coração - USC, Bauru, Sao Paulo, Brazil.
3. Laboratório de Biologia Molecular e Citogenética, University Sagrado Coração, Bauru, Sao Paulo, Brazil.

*Email: maraiiisa@yahoo.com.br

The chromatoid body (CB) is cytoplasmic male germ cell structure, which has a role in the regulation of mRNA transcription during spermatogenesis[1,2,3]. Complete proteomic analysis of this structure identified the abundant presence of its classical molecular markers (MVH, MIWI, DDX25, TDRD6, and TDRD7), but also identified a large number of transient proteins[4], such as CLOCK (circadian locomotor output cycles protein kaput) and BMAL1 (brain and muscle ARNT-like 1), which are molecular components of circadian control. The aim of this study was to find out whether the morphological changes previously observed in CBs of BMAL1 KO mice spermatids are produced due to BMAL1 ablation in these models or if they are related to the aging process caused by this ablation. 30 male mice were divided into 3 groups: young (45 days old), adults (120 days old), and old (180 days old). Viability and sperm count analysis as well as testosterone dosage were carried out for aging confirmation. Squash slides were prepared using seminiferous tubules fragments of stage IV-VI, which were immunostained with antibodies MVH, MIWI, BMAL1 and CLOCK. In young animals single round CBs were observed by discrete MVH / BMAL1 and MIWI / CLOCK signals. Chromatoid bodies in round spermatids of adult animals showed few morphological and numerical alterations when compared to young animals. In the old animals many CBs displayed numerical and morphological alterations as well as an increase in the interaction between MVH / BMAL1 and MIWI / CLOCK. It was also possible to observe a reduction in the expression of the proteins analyzed in the present study (BMAL1, MVH, CLOCK and MIWI) in seminiferous tubules of the old animals. Changes of CBs morphology coupled with increased interaction of the proteins analyzed as well as a decrease in the amount of those proteins may indicate that aging can have influence on the organization and also on the physiology of CBs, which may affect the determination of the fertility of the organisms.

REFERENCES

- [1] N. Kotaja et al., *Nat. Rev. Mol. Cell. Biol.* 8 (2007), 85.
- [2] I. Nagamori et al., *J. Cell Sci.* 124 (2011) 4346.
- [3] O. Meikar et al., *Reproduction.* 142 (2011), 195.
- [4] O. Meikar et al., *RNA.* 20 (2014) 1.
- [5] This research was supported by FAPESP and CNPq (Brazil).



MVH x BMAL1

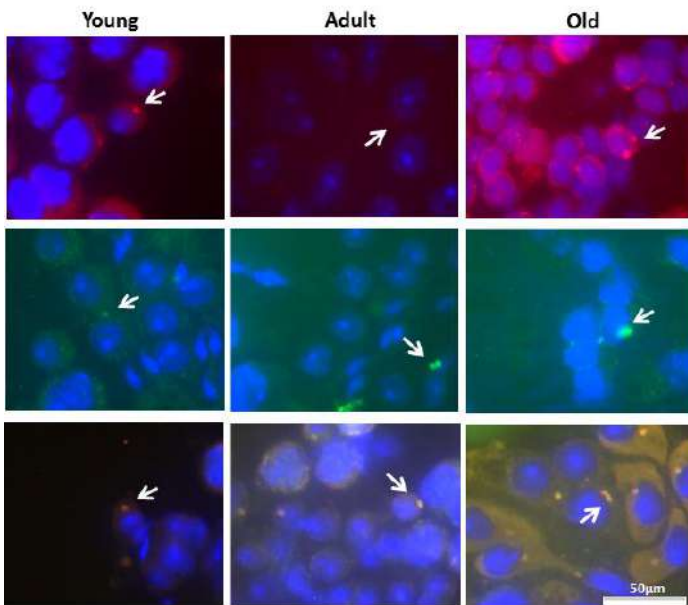


Figure 1: Immunofluorescence analyzes (MVH and BMAL1) in round spermatids of young, adult and old animals. Observe the numerical and structural changes pointed out in the round spermatids of old animals.

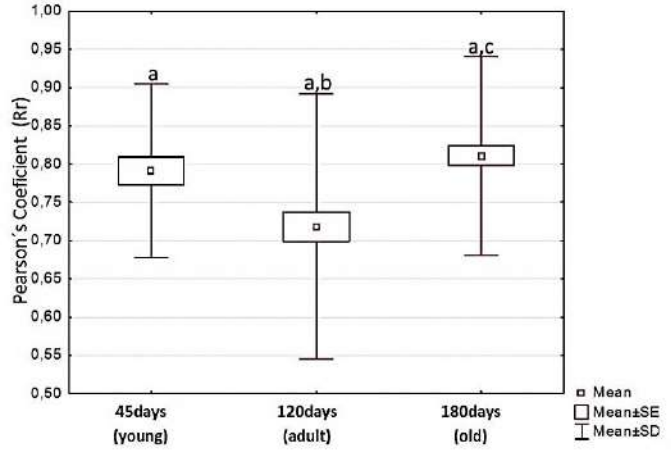


Figure 2: Overlap coefficient between the immuno-stainings of MVH and BMAL1 in round spermatids of young, adult and old animals. The coefficients were obtained using the Pearson's Coefficient.

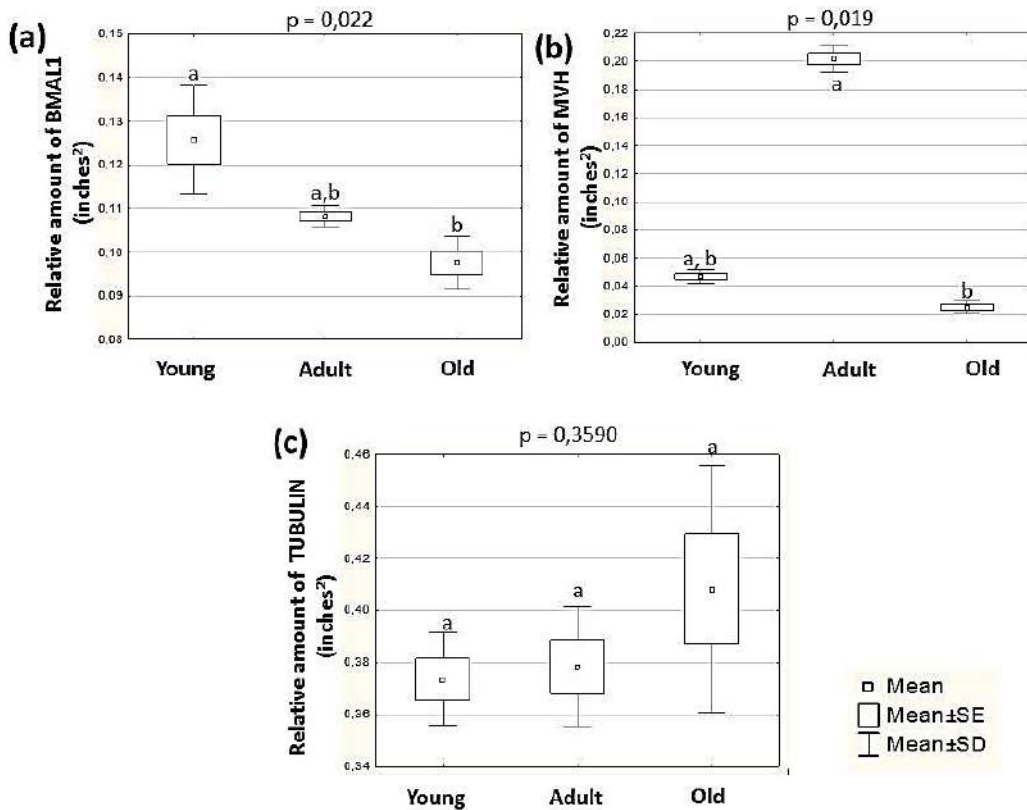
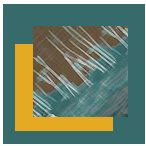


Figure 3: Relative amount of MVH and BMAL1 obtained by Western blot analyzes of total proteins extracted from seminiferous tubules of young, adult and old animals.



Outbreak of encephalitis caused by human herpesvirus type 1 (HSV-1) in nonhuman primates. Diagnosis by transmission electron microscopy

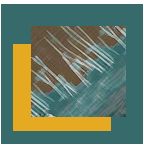
M.H.B. Catroxo^{1*}, A.M.C.R.P.F. Martins¹, F.F. Queiróz¹, G.P. Oliveira Júnior¹

^{1*} Electron Microscopy Laboratory, Biological Institute, São Paulo, SP, Brazil

Human herpesvirus type 1 (HHV-1), a member of the *Alphaherpesvirinae* subfamily, has a broad range of cross-species infectivity with considerable variation in expression and disease severity among different hosts. Infection in humans, the natural host, most commonly results in mild disease characterized by recurrent mucocutaneous lesions. In some species of nonhuman primates, however, the infection can be lethal [1]. Transmission occurs through food contaminated by humans with labial herpes, offered to monkeys, constituting an important anthroozoonosis [1,2]. The disease affects the neurological system of the monkeys, causing prostration, lingual ulcers, and loss of balance, apathy and death [1]. HSV-1 shows 79% nucleotide sequence identity with monkey B virus, a zoonosis that results in encephalitis or neurological problems in humans, with the majority of monkeys being asymptomatic carriers [3]. This study describes an outbreak of encephalitis in nonhuman primates, occurred in October 2016. The animals were kept in captivity at a breeding located in São José dos Campos, SP, Brazil, with 40 animals. Ten marmosets (*Callitrix aurita*) were found dead suddenly in the enclosure without presenting symptoms or clinical signs. During the necropsy pulmonary and intestinal congestion was evidenced and the presence of free sero-sanguinolent liquid in the thoracic cavity. Were sent to Electron Microscopy Laboratory of the Biological Institute of São Paulo, SP, Brazil, organ fragments samples of the animals to investigate the etiological agent. The samples were processed for transmission electron microscopy utilizing, negative staining (rapid preparation), immunoelectron microscopy and immunocytochemistry (immunolabeling with colloidal gold particles) techniques. In the negative staining the samples were suspended in phosphate buffer 0.1 M, pH 7.0, placed in contact with metallic grids, and negatively stained at 2% ammonium molybdate, pH 5.0 [4]. In the immunoelectron microscopy, the screens were incubated with a virus-specific antibody and with viral suspension. Upon the screens were contrasted at 2% ammonium molybdate, pH 5.0 [5]. At the immunocytochemistry technique [6], the screens were placed in contact with viral suspension and with specific monoclonal antibody drops. After the screens were incubated in protein A in association with 10 nm gold particles (secondary antibody) and contrasted at 2% ammonium molybdate, pH 5.0. At the transmission electron microscopy all the samples were analyzed by negative staining technique and a great number of particles with similar morphology to isometric herpesvirus exhibits enveloped (fig. 1, arrow) and non-enveloped particles (figs. 2 and 3) and showing nucleocapsids stain penetrated (fig.2, big arrow) and non-stain penetrated (fig.2, minor arrow), measuring 120-200 nm of diameter was observed. The presence of aggregates formed by antigen-antibody complex, characterized the positive result obtained at the immunoelectron microscopy technique for herpesvirus type 1 (HSV1) (fig. 2). In the immunocytochemistry technique, the antigen-antibody reaction was strongly enhanced by the dense colloidal gold particles (fig. 3, arrow). The viral identification through the use of transmission electron microscopy techniques allowed the characterization of encephalitis caused by human herpesvirus type 1, as well as promoting the rapid implementation of prophylactic measures and control of the disease at the breeding, preventing the occurrence of new deaths, considering that the Buffy-tufted-ear marmoset (*Callitrix aurita*) is a species framed in the category endangered to extinction by the IBAMA list.

REFERENCES

- [1] JA Landolfi, JFX Wellehan, AJ Johnson, MJ Kinsel, J Vet Diagn Invest, 17 (2005) 369-71.
- [2] BK Tischer, N Osterrieder, Vet Microbiol, 140 (2010) 1-5.
- [3] JL Huff, PA Barry, Emerging Infect Dis, 9 (2003) 246-50.



- [4] MA Hayat, SE Miller, *Negative Staining*. Mc. Graw-Hill Publ. Company. New York, (1990).
[5] D Katz, A Kohn, *Adv Virus Res*, 29 (1984) 169-94.
[6] S. Knutton, *Methods Enzymol*, 253 (1995) 145-58.



Fig. 1 - Negatively stained of enveloped herpes virus particles, showing envelope covered by spikes (arrow). Bar: 85 nm.

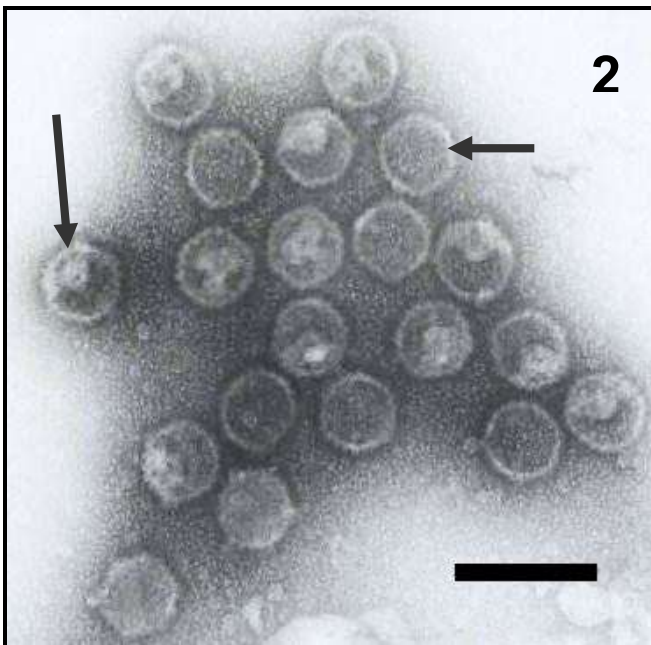


Fig. 2: In the immunoelectron microscopy technique the type 1 herpesvirus particles were aggregated by antigen-antibody complex. Observe nucleocapsids stain penetrated (big arrow) and non-stain penetrated (minor arrow). Bar: 260 nm.

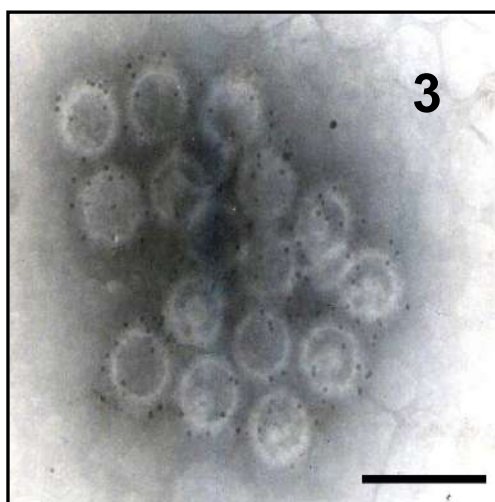


Fig. 3: Antigen-antibody interaction strongly enhanced by the dense gold particles over the type 1 herpesviruses (arrow). Bar: 200 nm.



Morphological Evaluation of the Expression and Distribution of Collagen Type I, Fibronectin and Laminin Glycoproteins in Human Placenta at Term

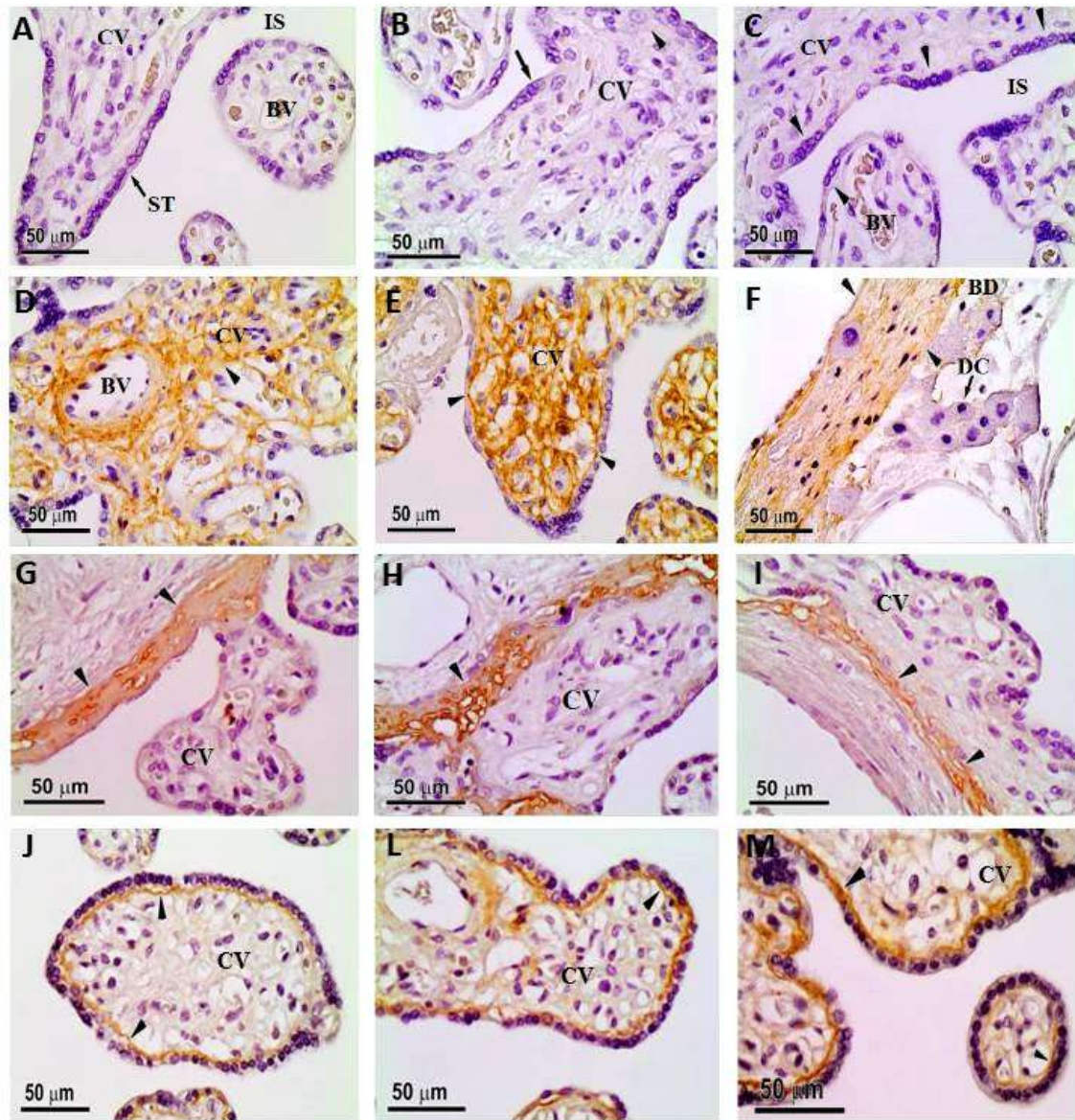
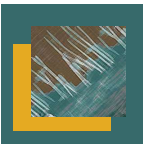
Rogério Gargioni¹, Márcio Ferreira Dutra^{1*}, Marcio Alvarez-Silva¹

1. Laboratory of Stem Cells and Bioengineering. Department of Cellular Biology, Embryology and Genetics. Center of Biological Sciences. Federal University of Santa Catarina. Florianópolis – Brazil. marcio.dutra@ufsc.br

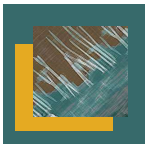
The placenta is a highly-specialized organ of maternal-fetal origin. It is responsible for the exchange of molecules and substances between the pregnant and the fetus [1]. As in other organs, the basic histological organization of the placenta is composed of cells and the extracellular matrix (ECM). The constitution of the ECM is extremely varied, being composed by different families of structural proteins, adhesion molecules, growth factors and other components [2]. In this context, the objective of this study was to investigate the expression and distribution of constitutive ECM glycoproteins collagen type I (collagen I), fibronectin and laminin in human placenta at term. For this purpose, three placentas at term were obtained in the Department of Obstetrics from the University Hospital of the Federal University of Santa Catarina. All procedures were approved by the Human Being Research Ethics Committee of the university (Protocol Number 198/03). The material was processed using routine preparation techniques for microtomy and 5 µm serial sections were performed on the microtome. Control slides were stained with hematoxylin while other slides were processed with immunohistochemical techniques for each of the glycoproteins of interest. The results obtained from the control slides showed the general organization of the placenta, with the typical structural characteristics of the chorionic villi (CV) and basal decidua (BD) (Figures A, B and C). The results of immunohistochemistry demonstrated a profile of collagen I expression in all areas of CV and BD (Figures D, E and F). Fibronectin has been shown to be stained in the BD region bordering the CV tissue (Figures G, H and I) and laminin was found with greater intensity in the basal trophoblastic membrane of CV (Figures J, L and M). As conclusions regarding the results of the control slides (Figures A, B and C), it was possible to analyze the general conditions of the tissue as well as the morphological and structural characterization of the placenta. From the analysis of the immunohistochemical images for collagen I (Figures D, E and F) it was possible to confirm the wide distribution of this glycoprotein on tissues of the CV and the BD, which confirms that collagen I is the basic structural unit of the placenta human at term [3]. Regarding the immunohistochemical results for fibronectin, interestingly its presence was clearly more intense in the region of BD bordering to the tissue of the CV. We concluded that laminin had a dispersed distribution in the CV, with greater intensity in the region of the basal trophoblastic membrane, which corroborates with the role of this glycoprotein as one of the main components of the basal membranes in different tissues [4]. However, due to the complexity of the MEC organization, more studies will be needed to better characterize the human placenta at term.

REFERENCES

- [1] K. Moore et al. *The Developing Human*, 6th Edition, Elsevier, 2015.
- [2] B. Alberts et al., *Molecular Biology of the Cell*, 6th Edition, Garland Science, 2015.
- [3] P.S. Amenta et al., The ECM is integrated unit. *Coll. Rel. Res.*, 6 (1986) 125.
- [4] H. Colagnato et al., From and function: the laminin family of heterotrimeres. *Dev. Dyn.*, 2 (2000), 213.



Photomicrographs of histological sections of human placenta at term. Figures A, B and C: negative controls, staining with hematoxylin. **Figures D, E and F:** immunostaining for type I collagen. **Figures G, H and I:** fibronectin immunolabeling. **Figures J, L and M:** immunostaining for laminin. Contracolloration: hematoxylin. Chorionic villi (CV), intervillous space (IS), blood vessel (BV), syncytiotrophoblast (ST), basal decidua (BD), decidual cells (DC). Arrowheads indicate the regions of immunohistochemical reaction for the glycoproteins of interest.



Transfection of placenta-derived mesenchymal stem cells with green fluorescent protein

Rodrigo Lucas Pérez¹, Márcio Ferreira Dutra^{1,2*}, Marcio Alvarez-Silva^{1,2}

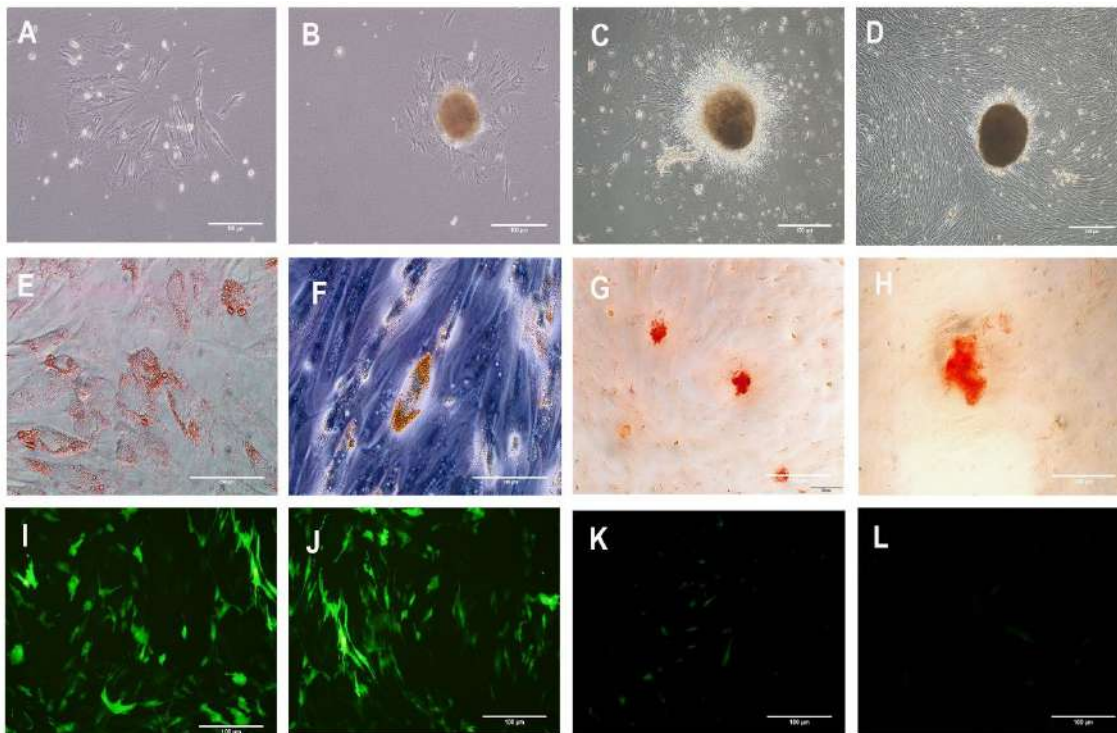
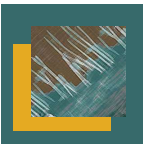
Postgraduate Program in Cellular Biology and Development. Center of Biological Sciences. Federal University of Santa Catarina. Florianópolis – Brazil.

Laboratory of Stem Cells and Bioengineering. Department of Cellular Biology, Embryology and Genetics. Center of Biological Sciences. Federal University of Santa Catarina. Florianópolis – Brazil. marcio.dutra@ufsc.br

The human placenta is a complex fetal-maternal organ. It is a very attractive source of mesenchymal stem cells (MSCs) [1]. The placenta-derived chorionic villi are able to harbor a hematopoietic niche composed by MSCs [2]. In this context, the objective of this study was to evaluate the capacity of MSCs from chorionic villi to be transfected with the green fluorescent protein (GFP) gene. In this study, two full-term health human placentas were collected in the Department of Obstetrics from the University Hospital of the Federal University of Santa Catarina. All procedures were approved by the Human Being Research Ethics Committee of the university (Protocol Number 198/03). To establish primary cell culture, fragments of 0.5 cm thickness from the fetal side of the placenta were digested with trypsin-EDTA 0.25%. Subculture P5 was used to carry out all the experiments. Proliferation, characterization, and morphology of MSCs cultures were assed with conventional phase-contrast microscopy, plastic adherence, and the ability to undergo mesodermal differentiation using previously standards differentiation protocols [3]. Electroporation protocol provided by Neon[®] Transfection System (Invitrogen, America), was used to introduce a plasmid with GFP construct gently given by Dr. Megumi Okawa. Transfected cells were scored by fluorescent microscopy until the GFP expression failed. The results from the morphological analyses of MSCs cultures showed that individual cells migrated and proliferated from explants and that cells attached to the culture flasks and acquired a fibroblastic-like shape (Figures A, B, C and D). The results with differentiation protocols confirmed the ability of these cells to undergo differentiation into adipose and osteogenic lineage respectively (Figures E, F, G and H). In electroporation assays we observed that these cells had the competence to incorporate the plasmid, expressing the GFP gene (Figures I, and J). The GFP expression was maintained for 7 days, when the fluorescence staining dropped 22-fold as compared to maximum GFP expression (24hs after transfection) (Figures K, L, and M). We concluded that the cells isolated form the chorionic villi represent a subpopulation of MSCs that reside in the human placenta. Furthermore, these cells could express elevated levels of the GFP gene in electroporation assays. The expression was detectable until 7 days after transfection of MSCs with GFP plasmid.

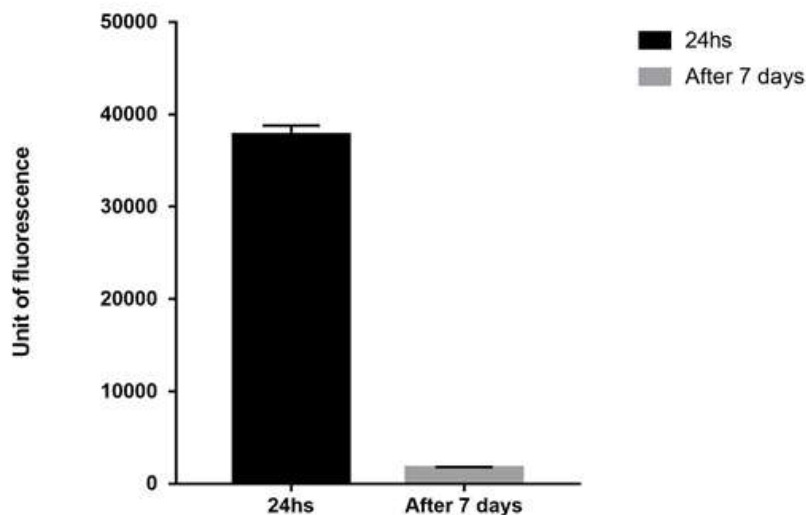
REFERENCES

- [1] Pipino, C., et al. Placenta as a reservoir of stem cells: an underutilized resource? *British Medical Bulletin* 2013;105(1):43-68.
- [2] Castrechini, N.M., et al. Mesenchymal stem cells in human placental chorionic villi reside in a vascular Niche. *Placenta* 2010;31(3):203-212
- [3] Pittenger M.F., et al. Multilineage potential of adult human mesenchymal stem cells. *Science* (New York, NY). 1999; 284(5411):143–7
- [4] This research was supported by CAPES (Brazil).

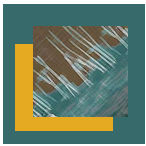


M

Level of green fluorescent protein after electroporation the MSCs with pcx-EGFP plasmid



Photomicrographs of primary and experimental cultured cells from human placenta chorionic villi tissue. **Figures A, B, C and D:** Culture of cells at 5, 9, 15 and 25 days respectively. **Figures E and F:** adipogenic differentiation assays stained with Oil Red. **Figures G and H:** osteogenic differentiations assays stained with Alizarin Red. **Figures I and J:** Electroporation of cultured cells after 24 hours. **Figures K and L:** Electroporation of cultured cells after 7 days. **Figures M:** Graphic shows the unit of fluorescence in electroporation experiments after 24 hours and after 7 days of GFP transfection respectively.



Comparison of Two Strains of *Toxoplasma gondii* by Scanning Electron Microscopy and Transmission Electron Microscopy

Marco Antonio Ferreira Mota^{1*}; Aline C.A. Moreira-Souza¹; Marcia Attias^{1,2}

1. Instituto de Biofísica Carlos Chagas Filho, Universidade Federal do Rio de Janeiro, Rio de Janeiro, Brazil

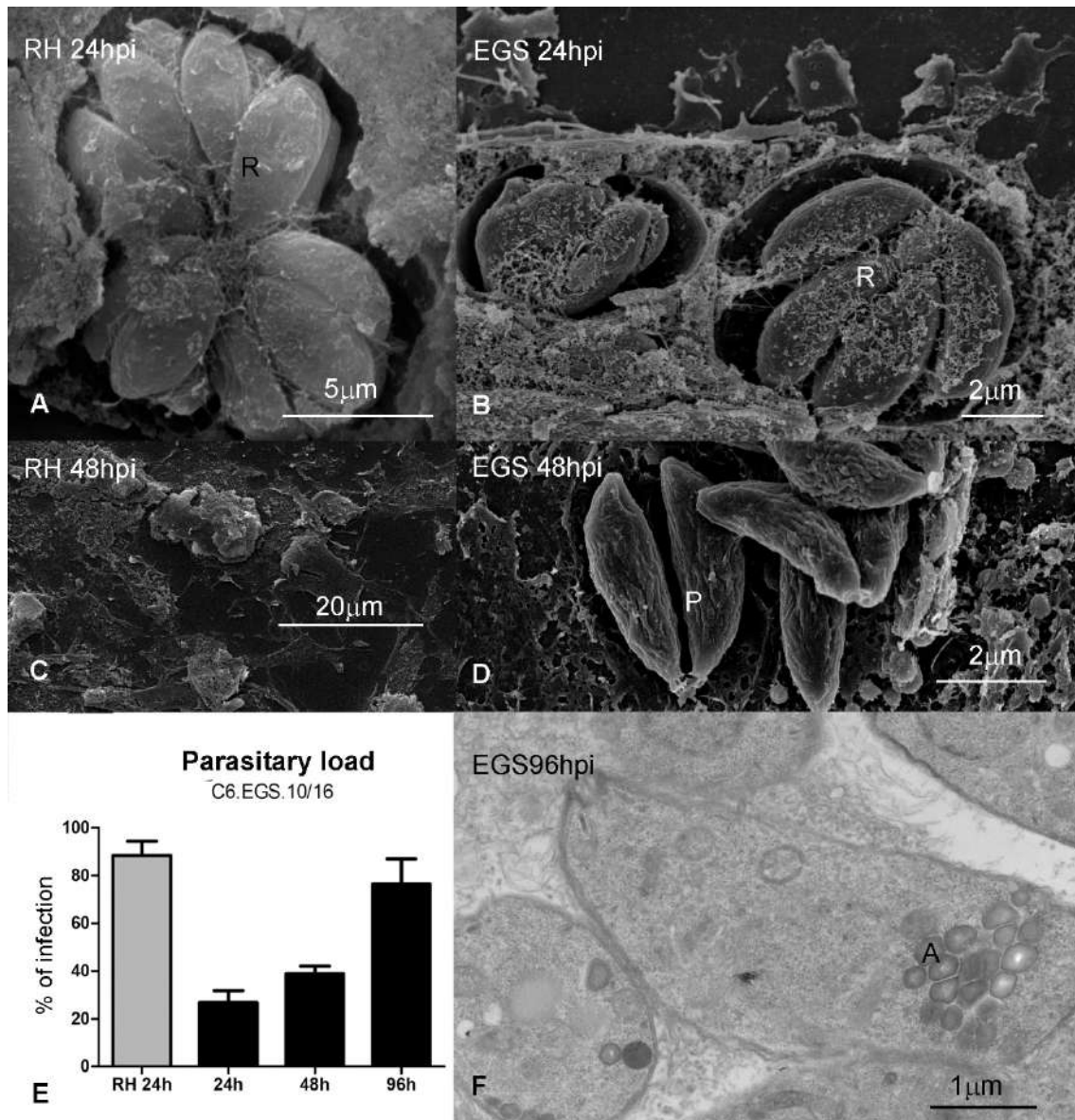
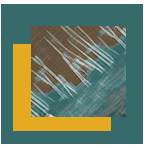
2. Instituto Nacional de Ciência e Tecnologia em Biologia Estrutural e Bioimagens, UFRJ, RJ. Brazil

Toxoplasma gondii is an obligate intracellular parasite capable of infecting and multiplying in any nucleated cell of all warm-blooded animals, including humans. It is a protozoan belonging to the phylum Apicomplexa, being the etiological agent of toxoplasmosis. Among the models studied in the literature, we highlight the RH strains of *T. gondii*, which presents virulent trait (Type I), and EGS, a hybrid (Type I-III) strain that spontaneously encysts [1]. In this work, we proposed to compare characteristics of the above-mentioned *T. gondii* strains in central nervous system cells of the C6 line by scanning (SEM) and transmission (TEM) electron microscopy. To obtain SEM images, glia derived-C6 cells were plated at a density of 2×10^5 in 13 mm round coverslips for 24 hours in DMEM medium plus 5% fetal calf serum. Then the cells were infected with *T. gondii* (RH and EGS) in the ratio of 5 parasites per cell. After 1, 2 or 4 days of infection, the samples were fixed in 2.0% glutaraldehyde in 0.1M sodium cacodylate buffer pH 7.2, post-fixed in 1% osmium tetroxide and 1.25% potassium ferrocyanide, progressively dehydrated in ethanol and dried by the CO₂ critical point method in the CPD chamber. The specimens were then mounted on specific stubs, stripped with adhesive tape to expose the inside of the cells and vacuoles and then sputtered with gold. The samples were observed either in the Quanta 250 - FEI scanning electron microscope or in the JEOL 6340 Fe-Sem. To obtain the images by TEM the samples were fixed, scraped from falcon bottles, and the same protocol described above was followed. However, after the dehydration step, the samples were infiltrated in epoxy resin, distributed in silicon molds, polymerized for 48h at 60°C to make ultrathin sections and observed in a FEI-120-Tecnaï Spirit TEM. In the virulent RH strain, 24hpi several vacuoles containing rosettes of parasites were observed (Figure A) and after 48hpi there was an intense destruction of the monolayer of C6 cells, indicative of a massive egress of tachyzoites (Figure C). On the other hand, 24hpi, the cells infected with the EGS strain contained several rosettes that seemed to bear less parasites than in the RH strain (Figure B). Later, at 48hpi, the EGS vacuoles contained several doublets of parasites (Figure D) and at 96hpi, the parasites inside the cell showed already amylopectin granules, indicative of the conversion to bradyzoites (Figure F). Comparing the parasitary load of EGS infected cells with the RH strain, we concluded that in the EGS strain the initial multiplication of parasites takes longer than in the RH strain (Figure E).

Acknowledgements: CNPq, CAPES, FAPERJ

REFERENCE

- [1] Paredes-Santos TC et al. Parasitol Int. 2013; 62(2):181-8.



Figures A and B: SEM of parasitophorous vacuoles 24hpi. (A) in the RH strain 13 parasites can be counted in this rosette (R). (B) two parasitophorous vacuoles of the EGS strain, the larger contains a rosette (R) with four parasites. Figures C and D: SEM of Parasitophorous vacuoles 48hpi. (C) In the RH strain only lysed host cells were observed, after egress of parasites. (D) In the strain EGS parasites are in doublets, not forming a rosette. Figure E Comparison of the parasitary load of EGS infected cells with the RH strain. Figure F A parasite containing amylopectin granules (A), indicative of conversion to bradyzoites.



Cell-scale Biomaterial Topography Influences the Organization of Epithelial Monolayers

Pablo Rougerie^{1*}, Laurent Pieuchot², Naiara Sgambato¹, Thaís Canuto¹, Maxence Bigerelle³,
Marcos Farina¹, Karine Anselme²

1. Instituto de Ciências Biomédicas, Universidade Federal do Rio de Janeiro, Brazil,
2. Institut de Science des Matériaux de Mulhouse, Université de Haute-Alsace, Mulhouse, France,
3. Département de Mécanique, Université de Valenciennes et du Haut Cambresis, Valenciennes, France

*Email: pablrougerie@gmail.com

Cells not only interact with their environment through the well-known chemosensing and mechanosensing but also through the perception of substrate topography [1]. The notion that the local geometry is also a carrier of information for the cells has thus great consequences for regenerative medicine and tissue engineering. Nanometric topographies have already been shown to cause various effects on cell morphology and behavior, from cell elongation to stem cells differentiation. The transduction of nanometric topography seems mostly mediated by spatial restrictions on focal adhesion formation [2]. On the contrary, cell-scale micrometric features impose morphological constraints over the entire cell body and thus present a different challenge of topography reading by the cells. Many studies have investigated the cell response to micrometric topographies with sharp surface features (edges, angles) [3]. However, little is known about the effect of cell-scale, smoothly curved, micrometric features presenting no edges or discontinuities. In particular, the effect of cell-scale substrate curvature on the collective behavior of epithelial colonies cannot be extrapolated from single cells because of the presence of intercellular mechanical tensions. As the local topography of the substrate has to be taken into account, global approaches such as flow cytometry or biochemistry cannot be used. In situ microscopy-based techniques are thus necessary. We managed to generate thin PDMS substrates with controlled cell-scale surface topographies compatible with cell culture, photonic and electronic microscopy. Our model topographies are anisotropic, present edges or continuous smooth curves (figure 1) and are compatible with formation of epithelial monolayer (figure 2). We showed that smoothly curved grooves and ridges were able to induce the alignment of the epithelial cells from unconfined, expanding monolayers, albeit to a lesser extent than angular, edge-containing substrate. This is the first demonstration that cells can detect edge-free topographies and react to them, whereas the presence of edges strongly potentiates the cell reaction. Interestingly, the preferential alignment of epithelial cells along the grooves and ridges axis is lost in confined, not-expanding monolayers. This indicates that the topography sensing is allowed by a certain state of cytoskeleton organization and dynamics, lost in the course of epithelial maturation. Importantly, we detected a collective supracellular contact guidance where several neighboring cells at the border of a monolayer align to follow the same groove. As a result, the whole epithelial monolayer elongates and grows along the grooves and ridges axis. We thus concluded that the reaction of epithelia to micrometric topographies is conserved from the cell scale to the millimetric scale of whole colonies [4].

REFERENCES

- [1] H. Miyoshi, T. Adachi, *Tissue Eng Part B Rev*, 20 (2014), 609-627
- [2] M. Ventre et al., *J R Soc Interface*, 9 (2012), 2017-2032
- [3] M. Nikkhah et al., *Biomaterials*, 33 (2012), 5230-5246
- [4] This research was supported by CNPq, FAPERJ and CNRS

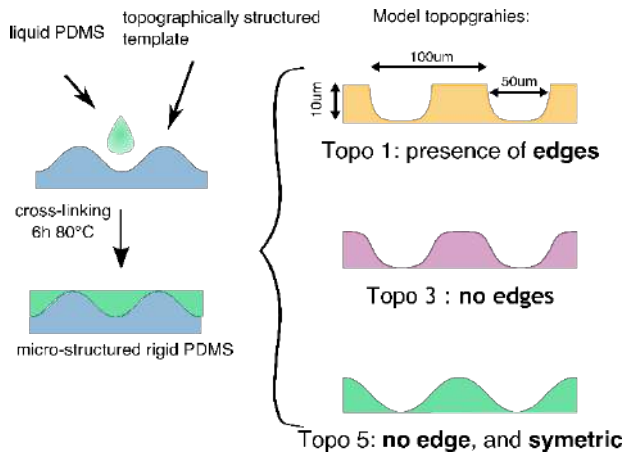
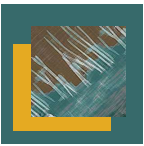


Figure 1: Production of microscopy-compatible PDMS surface with controlled anisotropic cell-scale topography. Liquid PDMS is layered between a topographically structured steel template and a glass coverslip and cross-linked. After cross-linking, the separation of the sandwich yields a glass-PDMS conjugate thin and transparent enough for photonic imaging. Three anisotropic (grooves and ridges) topographies are used, presenting either edges (topo 1) or smooth curves (topo 3 and 5)

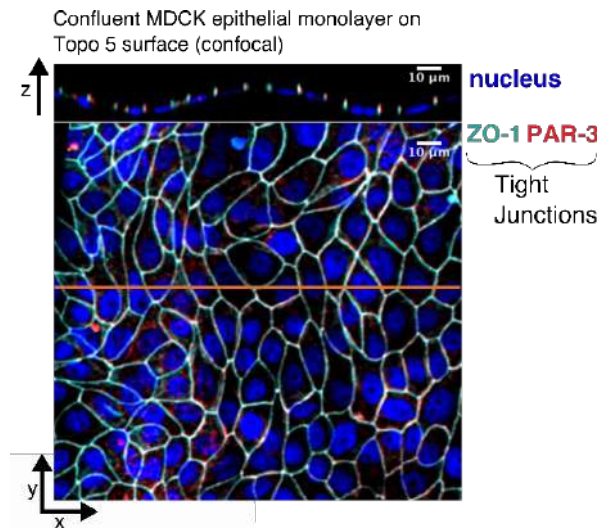
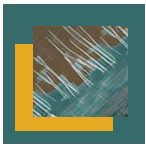


Figure 2: epithelial cells form coesive and differentiated monolayers on top of the biomaterial. Vertical projection from confocal imaging z-stack. ZO1 and PAR3 indicate the tight junctions, illustrating the coesiveness of the monolayer. The z section highlights that the monolayer follow the topographical curves of the substrate.



In vivo compatibility of PLGA membranes produced by electrospinning

Ana Chor¹, Raquel Pires Gonçalves¹, Beatriz Guerra^{1,2}, Christina Maeda Takiya², Marcos D. Lopes³, Marcos Farina¹, Leonardo R. Andrade¹

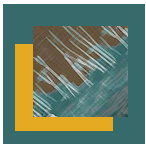
1. Laboratório de Biomineralização, Instituto de Ciências Biomédicas, CCS, UFRJ
2. Instituto de Biofísica Carlos Chagas Filho, CCS, UFRJ
- 3]. Laboratório de Polímeros, IMA, UFRJ

Several biodegradable polymers have been produced and tested as cell substrates in the field of tissue engineering. The poly-lactic-co-glycolic acid (PLGA) is a synthetic polyester approved by the FDA that has been used as sutures, bone screws and particles for drug delivery. In vivo hydrolysis of PLGA-based biomaterials results in byproducts that are naturally eliminated from the body. The time required for PLGA biodegradation depends on the monomers proportion [1,2]. Higher lactide monomer amounts in the blend means a lower biodegradation. PLGA scaffolds have been suggested for dermal or oral mucosa substitutes due to its biocompatibility. PLGA membranes can be produced by the electrospinning technique. Briefly, this technique is based on the application of an electrical potential between a capilar end of a syringe-like device filled with a polymeric solution, and a metallic plate, causing the deposition of thin fibers of the polymer onto the plate [3,4]. This is widely used by being a simple, versatile and effective method for obtaining ultrafine fibers from a wide range of materials with controlled diameters and compaction. Our goal was to produce PLGA membranes and to study its interactions with biological tissues for its future use in the repair of oral mucosa ulcers.

PLGA membranes containing randomly deposited nanofibers were produced by electrospinning using PLGA (85/15) powder at a concentration of 5% (w/v) in a solution containing CHCl₃ (80%) and DMF (20%), and voltages 15kV. The spinning flow rate was kept constant at 0.6 ml/h and the distance between the needle and the collector plate was 15 cm. The membranes were sterilized by 15 kGy of gamma irradiation and surgically inserted subcutaneously in the dorsal region of 09 Golden Syrian hamsters for 7, 15 and 30 days. All the procedures followed international rules for the use and care of experimental animals and approved by local animal care committee. After each period, dorsal tissues with the membranes were removed and immediately immersed in Karnovsky fixative for 2 h, post-fixed in 1% OsO₄, dehydrated in ethanol series, and embedded in paraffin or Spurr resin for histological (HE staining) and TEM observations, respectively.

After 7, 15 and 30 days in vivo, bright field and polarized microscopy showed that the fibers were still structurally forming the membranes. The membranes were undulated and transparent. No lymphocytic infiltrate was observed at the three time periods. In 7 days, we observed numerous cells adjacent to the membranes. These cells resembled fibroblasts and macrophages due to its morphology. In 15 and 30 days, these cells invaded the membrane mesh but also formed a peripheral cell layer. The amounts of collagen fibers seemed to increase along the time by polarized microscopy. Many multinucleated giant cells were seen interacting with the PLGA membrane surface. These cells are often seen in foreign body reaction and indicated the conventional process of material degradation. We concluded that our electrospun PLGA membranes were biocompatible and stimulated local cell adhesion. We didn't observe clear membrane degradation due to the presence of fibers after 30 days in vivo; however TEM observations might show different perspectives of cell-biomaterial interface.

Financial support: Brazilian Agencies Faperj and CNPq.



DOI: [INSERIR ENDEREÇO DO DOI AQUI.](#)

Caderno de Resumos do 26º Congresso Brasileiro de Microscopia da SBMM – ISSN: [INSERIR AQUI.](#)

REFERENCES

- [1] K.A. BLACKWOOD, et al., *Biomaterials*, 29 (2008) 3091.
- [2] J-M. LÜ, et al. *Expert Rev Mol Diagn* 9 (2009) 325.
- [3] A.J. HASSIBA J, et al. *Nanomedicine* 11 (2016) 715.
- [4] JIA, J; LIU, G; GUO, Z-X; YU, J; DUAN, Y. Preparation and Characterization of Soluble Eggshell Membrane Protein/PLGA Electrospun Nanofibers for Guided Tissue Regeneration Membrane. *Journal of Nanomaterials*, 7:45-49. 2012.



In vitro evaluation of Carbon C-Dot produced from coffee waste

Mariane V. Vilioni¹, Carime Vitória da Silva Rodrigues², Marcelo Oliveira Rodrigues², Brenno A. D. Neto², José R. Corrêa¹

1. Institute of Biological Sciences, University of Brasilia, Brasilia, DF, Brazil.

2. Institute of Chemistry, University of Brasilia, Brasilia, DF, Brazil.

*Email: mariane_v10@hotmail.com

Carbon quantum dots are nanoparticles that can be employed in several applications including cell imaging and as drug delivery systems^{1, 2}. They can be synthesized from a variety of unconventional sources by using cheap or waste material on a direct and simple chemical oxidation methodology^{3, 4}, which is a great advantage. Cellular selection is one of the most attractive attributes of new fluorescent probes; therefore, this represents a limiting gap between tangible successful applications of C-dots⁵. The objective of this study was an *in vitro* evaluation of a new CDOT derived from coffee grounds as a potential fluorescent carrier. The CDOT-CA compound was evaluated in living and pre-fixed samples of tumor cell lines MCF-7 (human breast adenocarcinoma cells), Caco-2 (human epithelial colorectal adenocarcinoma cells), MDA-MD-231 (invasive human mammary adenocarcinoma cells), T47D (human ductal breast epithelial tumor cells line), and also in normal cells HUVEC (human umbilical vein epithelial cells). All samples were incubated with de CDOT-CA for 30 minutes. The cell samples were analyzed in confocal laser scanning microscope, Leica, model TCS SP5. After 24 hours of C-DOT samples incubation, the cells viability was evaluated by 3-(4,5-dimethylthiazol-2-yl)-2,5-diphenyltetrazolium bromide (MTT) assay. Our preliminary results showed that C-Dot was capable to cross the cellular membrane and to produce fluorescence emission in cellular environment at two different wavelength ranges (550-565, green and 645-720, red) in all tested samples. The fluorescence signal detected was distributed throughout the cytoplasm with a mild accumulation near to cells membrane; however, no nuclei staining could be detected (figure 1, images A, B, D and E). The C-DOT-CA showed no cytotoxic effect through MTT assay for all tested cells (figure 2). Finally a normal cells morphological aspect was observed by phase contrast microscopy (figure 1 images C and F). The C-DOT-CA showed be permeable to cellular membrane, reach the cytoplasm without enter into the cell nucleus. Moreover, the C-DOT-CA was capable to emit fluorescence at cellular environment, which make it traceable, and was no toxic to the tested cells. All these features are very important for qualify potential carriers structures.

REFERENCES

- [1] Probst, C. E.; Zrazhevskiy, P.; Bagalkot, V.; Gao, X. H.; Adv. Drug Deliv. Rev. 2013,65,703.
- [2] Jin, Y. D.; Gao, X. H.; Nat. Nanotechnol. 2009,4,571.
- [3] P. J. G. Luo, S. Sahu, S. T. Yang, S. K. Sonkar, J. P. Wang, H. F. Wang, G. E. LeCroy, L. Cao, Y. P. Sun, J. Mater. Chem. B 2013, 1, 2116 – 2127.
- [4] H. P. Liu, T. Ye, C. D. Mao, Angew. Chem. Int. Ed. 2007, 46, 6473 – 6475; Angew. Chem. 2007, 119, 6593 – 6595.
- [5] B. A. D. Neto, J. R. Correa, R. G. Silva, RSC Adv. 2013, 3, 5291 – 5301.

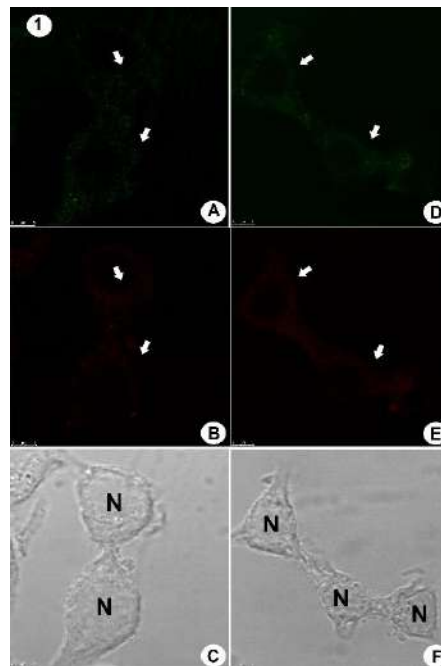
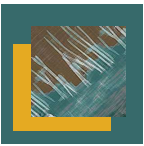


Figure 1. (1) Fluorescent profile of Caco-2 cells, incubated with compost CDOT-CA live (A, B and C) and fixed (D, E and F). The images C and F show the normal morphological aspects of these samples by phase contrast microscopy. The arrowheads (white) show the distribution of fluorescence in cells cytoplasm. The “N” letter was used to identify the nuclei. Reference bar: 5 µm.

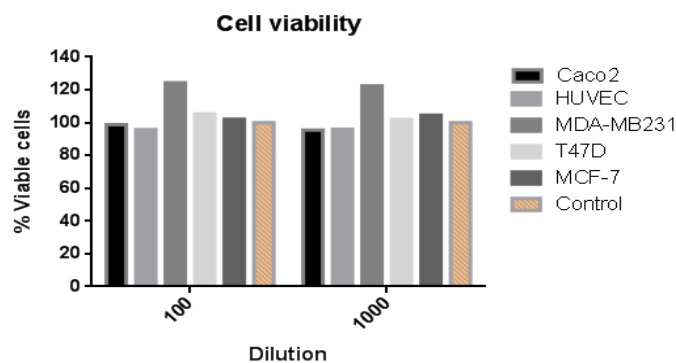


Figure 2. Cell viability assay after 24 hours of samples incubation with CDOT-CA. No cytotoxic effects could be detected to all tested C-DOT-CA concentration.



Expression of proteins fibronectin and laminin by rhodium (II) citrate-coated maghemite nanoparticles in breast tumor

Márcia Rocha^a, Marina Radicchi^b and Sônia Bão^b

^aP.h.D student of Nanoscience and Nanotechnology postgraduate program, University of Brasília, Brasília, DF, Brazil. *marcia.cristinaor@gmail.com

^bInstitute of Biological Sciences, University of Brasília, Brasília, DF, Brazil.

Degradation of extracellular matrix (ECM) is one of the important processes related to breast cancer progression. Tumor cells have the ability to obtain the necessary conditions for growth and survival, promoting the degradation processes of extracellular matrix proteins, such as laminin (LN) and fibronectin (FN) [1]. Drug Delivery Systems, in nanometer scale, can improve the effectiveness of cancer treatments. These systems have advantages when compared to conventional therapies. Maghemite nanoparticles ($\gamma\text{-Fe}_2\text{O}_3$), are one the most widely used in biological applications. A compound that has being used for surface modification of nanoparticles is the rhodium (II) citrate ($\text{Rh}_2(\text{H}_2\text{cit})_4$), an analogue of cisplatin, has cytotoxic, cytostatic and antitumor activity in mammary carcinoma cells. Thus, the association of rhodium (II) citrate with maghemite nanoparticles (Magh- $\text{Rh}_2(\text{H}_2\text{cit})_4$) is a strategy employed in the attempt to reduce toxicity in the organism and increase specificity in the target tissue during cancer treatment [2]. In this study, the FN and LN expression was correlated with the efficacy of treatments after intratumoral administration. Female BALB/c mice were injected with 2×10^4 4T1 mammary carcinoma cells for tumor establishment. After 14 days, animals were treated with $\text{Rh}_2(\text{H}_2\text{cit})_4$ (8 mg/kg), Magh- $\text{Rh}_2(\text{H}_2\text{cit})_4$ (8 mg/kg / 216 mg/kg of iron) and maghemite nanoparticles (Magh-Cit) (216 mg/kg of iron) by intratumoral administration. Treatments were carried out every two days. Afterwards, tumors were measured daily with digital caliper to verify the antitumor activity. As shown in figure 1-A, the Magh- $\text{Rh}_2(\text{H}_2\text{cit})_4$ -treated group had a large statistically significant reduction in tumor volume of about 83%. The survival curve showed that the treatments used did not influence the survival of the animals (Figure 1-B). The tumors were prepared for immunohistochemical analyses in order to evaluate the FN and LN expression after the treatments. We observed that the groups which received treatment Magh- $\text{Rh}_2(\text{H}_2\text{cit})_4$ had a significant reduction of 25.8% of FN (Figure 2-D) and 23% of LN (Figure 2-H) when compared to the control group. Studies have shown that increased FN and LN contributes to metastasis and tumor aggressiveness [3, 4]. Western blotting analysis was made as a complementary test to evaluate the FN and LN expression (Figure 3). In the groups that received treatment, the data corroborated with those found in immunohistochemistry. Significant reduction of the expression levels of FN and LN in the group treated with Magh- $\text{Rh}_2(\text{H}_2\text{cit})_4$ was 76.1% and 73.3%, respectively. In conclusion, our results suggest that treatments based on Magh- $\text{Rh}_2(\text{H}_2\text{cit})_4$ compound significantly reduced tumor volume. Consistently the technique used shown treatments also downregulate the expression of FN and LN proteins and correlate expression of these proteins are directly related to tumor progression.

REFERENCES

- [1] K. Wang et al., *Biomaterials*. 54 (2015).
- [2] Z.G.Lacava et al., *J. Nanobiotechnology*. 11 (2013).
- [3] K.C. Clause et al., *Opin. Biotechnol.* 24 (2013).
- [4] H. Kumra et al., *Drug Deliv. Rev.* 97 (2016).
- [5] This research was supported by CAPES, CNPq, FAPDF e FINEP (Brazil).

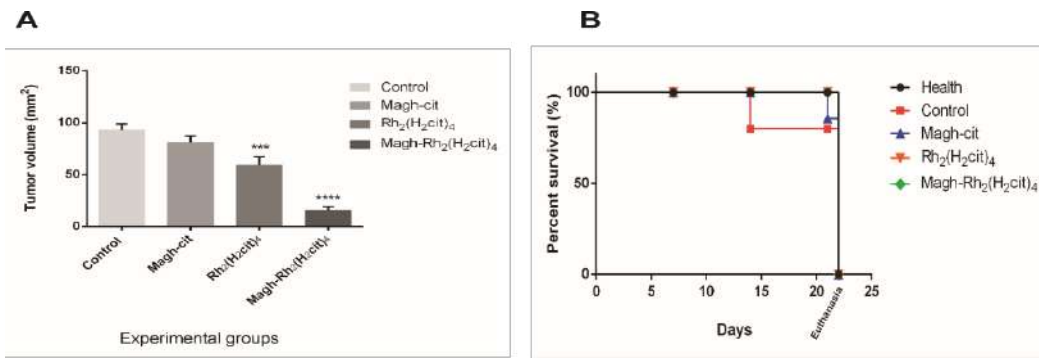
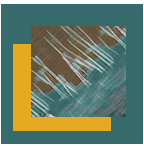


Figure 1: Antitumor effect in tumor bearing mice and survival indices. The mice were treated with five doses of Rh₂(H₂cit)₄ or Magh-cit or Magh-Rh₂(H₂cit)₄ until 21st day after tumor inoculation. A) Regression of tumor volume of experimental groups mice. B) Survival curve for tumor-bearing mice. The days are referenced from the beginning of the experiment to euthanasia. The values shown are the mean ± SEM ***p<0.001, ****p<0.0001. GraphPad Prism 6.0.

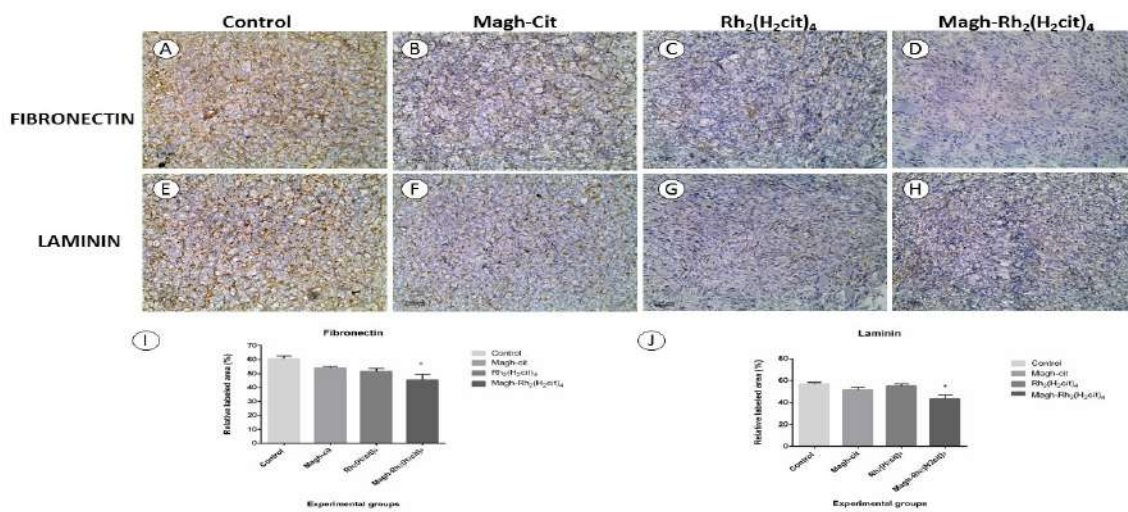


Figure 2: Representative images of fibronectin and laminin immunohistochemical detection in tissue of Balb/c mice from each experimental group. A; E) Control, B; F) Magh-Cit, C; G) Rh₂(H₂cit)₄, D; H) Magh-Rh₂(H₂cit)₄, I; J) Quantification of FN and LN staining decreased markedly after Magh-Rh₂(H₂cit)₄ treatment when compared to control mice. The data represent the average of 10 photos of each group. Original magnification 200x. Data represent mean values ± standard error and different letters indicate statistical difference among treatments (p<0.05). Scale bars: 50 µm.

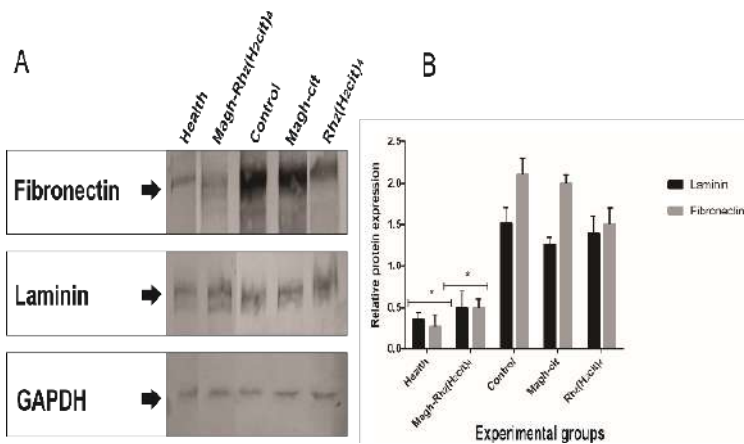
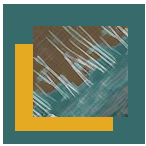


Figure 3: Analysis of FN and LN proteins expression of Balb/c mice bearing 4T1 breast tumor. The animals were treated with Magh-cit or Rh₂(H₂cit)₄ or Magh-Rh₂(H₂cit)₄. A) western blotting analysis shows a band of approximately 250 kDa (FN) and 225 kDa (LN) in the total protein extracts from normal and tumor tissues from mice. B) Quantification of relative protein expression of LN and FN found in western blotting analysis. GAPDH was used as internal control. The healthy and Magh-Rh₂(H₂cit)₄ treated groups showed markedly statistically significant reduction when compared to the control group. The values shown are the mean ± SEM *p<0.05 and analyzed by an ANOVA; Tukey's post hoc test



Decalcification of fish scales for histological processing in biomonitoring studies

Mateus Santos de Souza^{1*}, Marina Zimmer Correa¹ and Günther Gehlen¹

1. Comparative histology laboratory, Feevale University, Novo Hamburgo, Brazil.

*Email: mateusssouza@yahoo.com.br

Bioindicators integrate environmental quality assessment studies because they are able to provide information on the way in which environmental variables and their variations, in the course of time, can affect organisms. In aquatic environments, fish are widely used as bioindicators due to factors such as their ecological importance and their sensitivity to pollutants [1]. A great variety of organs and tissues of these animals, like gills, liver, brain and blood, for example, can be used as biomarkers on this type of study, methodologies that require the sacrifice of the animal. Recently, a non-lethal method of biomonitoring was proposed, using epithelium of fish scales as a biomarker [2]. The objectives of the present study were to define the best decalcifier and the most appropriate decalcification time for the histological processing of scales, in order to standardize the methodology for biomonitoring studies developed in our laboratory. Scales from juveniles of *Prochilodus lineatus*, previously fixed in Bouin were used. We tested decalcification with 5% nitric acid solution and with 5% EDTA solution during the following periods: 14, 17, 21, 28 and 36 days. The solutions were renewed every three days. After these periods, samples were processed in order to produce histological slides. The scales were dehydrated in a graded ethanol series, clarified in chloroform, embedded in paraffin, sectioned in a rotatory microtome (5 µm) and stained with Hematoxylin-Eosin. The integrity of the tissue and the quality of the staining were analyzed in an optical microscope, in 100X and 400X magnifications. The decalcifiers presented different effects on the analyzed tissue. Scales immersed in nitric acid showed, in all periods tested, a faint staining of the epithelial cells nuclei, a well-known consequence of this decalcifier [3], in addition to a similar staining tone between the collagen plate and the adjacent epithelial tissue (Figure 1), making it difficult for evaluating the epithelium details. Therefore, nitric acid is not an appropriated decalcifier for our studies. Scales decalcified in EDTA showed better results. Epithelial cells nuclei were well stained, and the cytoplasm staining tone was different from the collagen plate staining tone, allowing the identification of the limit between these structures (Figure 2). Differences between scales exposed at distinct decalcification periods were not seen, probably due to the small volume of this structure, which facilitates decalcification. Therefore, 5% EDTA solution is the best decalcifier for scales and 14 days of immersion are enough for this process. The next step of the study will be the assessment of the scale epithelium of fish exposed to different environmental conditions, in order to analyze specifically the thickness of the tissue and the frequency of cells related to defense processes, like goblet and club cells.

REFERENCES

- [1] R. Oost et al., Environ. Toxic. And Pharm. 13 (2003) 57.
- [2] R.M.S. Alves et al., Ecotox. And Environ. Saf. 129 (2016) 43.
- [3] L.C.U. Junqueira et al., Técnicas básicas de citologia e histologia, Santos, São Paulo, 1983.

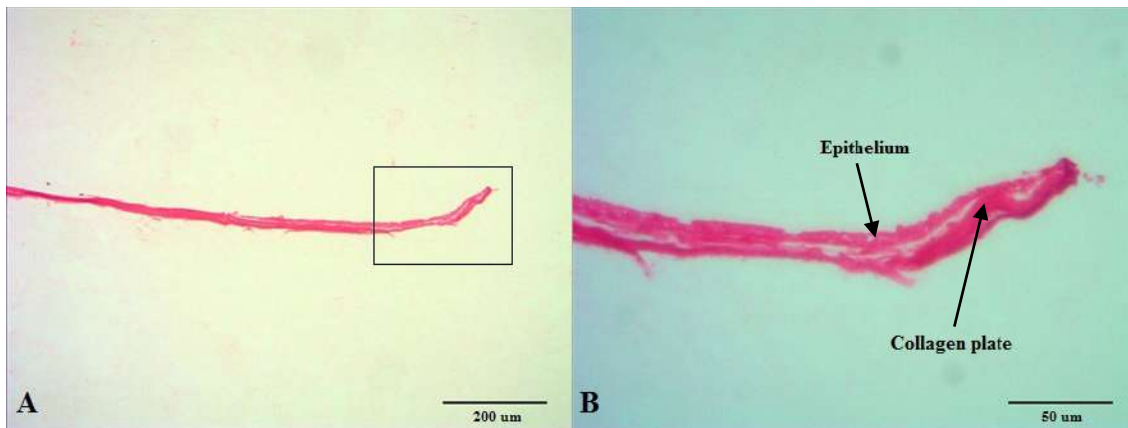
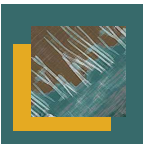


Figure 1. A: General overview of a scale decalcified during 21 days with 5% nitric acid solution (100X magnification). B: The region delimited in A is showed in 400X magnification. Note that collagen plate and the epithelium (arrows) have a very similar staining and they are discernible only because a detachment between them occurred. Nuclei are not perceptible.

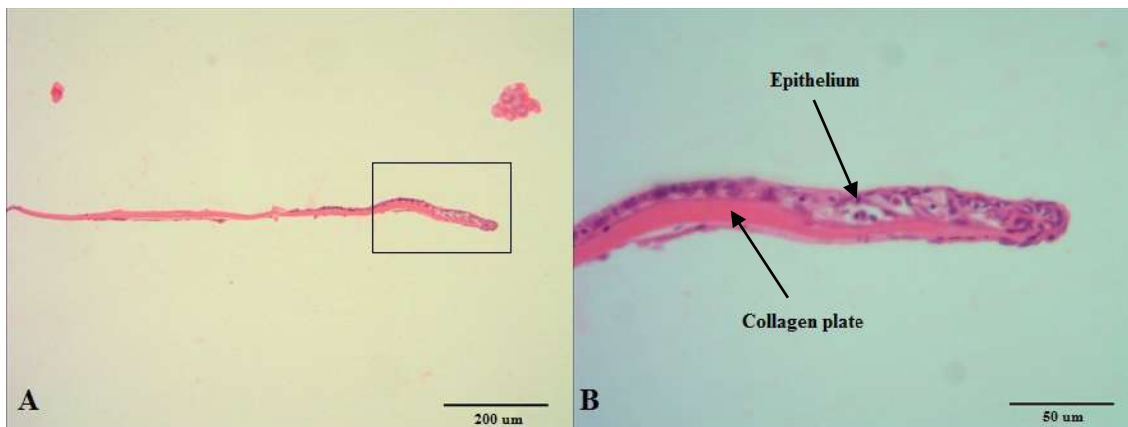
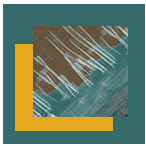


Figure 2. A: General overview of a scale decalcified during 21 days with 5% EDTA solution (100X magnification). B: The region delimited in A is showed in 400X magnification. The collagen plate and the epithelium (arrows) have different staining and nuclei are well stained.



Effects of a Model of Cerebral Palsy on the Intramuscular Collagen in *Wistar* Rats

Matheus Felipe Zazula¹, Pâmela Buratti*¹, Caroline Covatti¹, Dafne Strozake Maximo¹, Lígia Aline Centenaro¹, Marcia Miranda Torrejais¹

1. Universidade Estadual do Oeste do Paraná - Unioeste, Cascavel, Paraná, Brasil.

*Email: pamela_buratti@hotmail.com

For the skeletal striated muscle function to be adequately performed, it is important to maintain the composition and arrangement of the connective tissue, which may undergo changes in disorders, affecting the musculature [1]. Cerebral palsy (CP) is considered a group of permanent developmental and postural disorders that cause activity limitation, resulting from non-progressive disorders that occur during brain development [2]. The treatment of CP symptoms is commonly performed at a muscular level. To understand the muscular alterations present in this encephalopathy, this study had as objective to evaluate the implications of an experimental model of CP on the intramuscular collagen in the plantaris muscle of *Wistar* rats. All procedures adopted were submitted and approved by the Ethics Committee in the Use of Animals (CEUA) of Unioeste, number 24/16. CP was induced with the use of prenatal infection by lipopolysaccharide (LPS), perinatal anoxia and sensorimotor restriction. Initially, adult pregnant rats were submitted to intraperitoneal injections of lipopolysaccharide (LPS) (200 µg/kg LPS in 100 µl of sterile saline) or vehicle (100 µL of sterile saline). Both injections were performed from the 17th gestational day until the end of gestation (21st gestational day), every 12 hours. The offspring obtained was used to form the experimental groups, and the control group (CG, $n = 5$) was composed by the offspring of rats injected with saline solution during gestation; and CP group (CPG, $n = 5$) composed by the offspring of rats injected with LPS during gestation. For the induction of perinatal anoxia, on the day of birth, the animals of the CPG were placed in a closed chamber, partially immersed in water at 37 ° C, with a flow of 9 L/min of nitrogen (100%) for 20 minutes. From the first postnatal day (P1) to the 30th postnatal day (P30), the CPG animals were submitted to sensorimotor restriction 16 hours/day, with immobilization of the pelvic limbs through the use of epoxy mold and adhesive microporous tape. After euthanasia, at 48 days of age, the plantaris muscle was collected and the right muscle antimere was frozen in liquid nitrogen. Histological sections were performed in a cryostat (7 µm thick) and later submitted to the Masson's Trichrome to evidence and study intramuscular collagen. This material was photodocumented in a 20X objective, and three images were captured per animal. The results showed that connective tissue collagen was present in the perimysium involving the muscle fibers fascicles (Figure 1A and 1B). The analysis of collagen percentage showed a 27% increase in CPG in relation to GC ($p = 0.038$) (Figure 1C). The animal model of CP used increased the intramuscular collagen, which leads to the loss of extensibility and limitation of movement by the installation of muscular rigidity.

REFERENCES

- [1] M.A. Mathewson & R.L. Lieber, Phys. Med. Rehabil. Clin. N. Am. 26 (2015).
- [2] P. Rosenbaum et al., Dev. Med. Child Neurol. 109 (2007).
- [3] This research was supported by CAPES (Brazil).

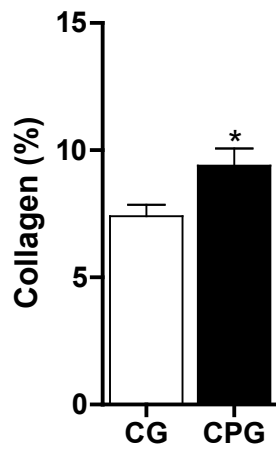
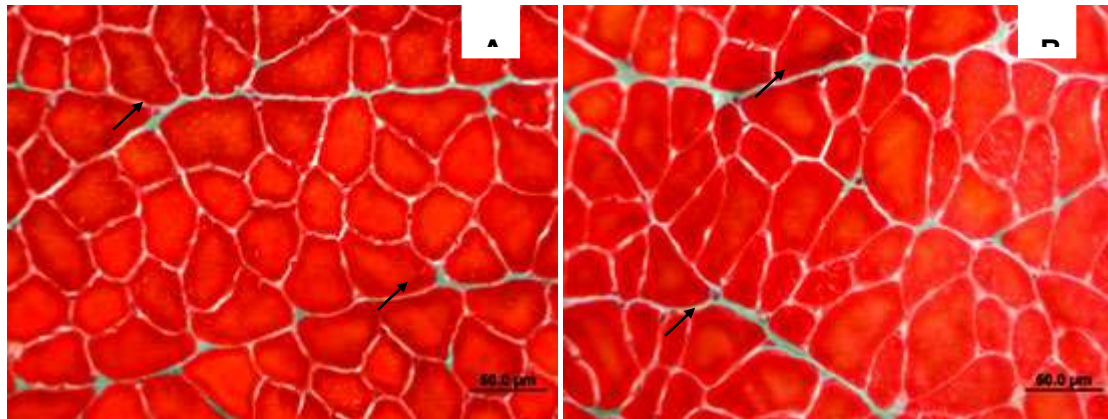
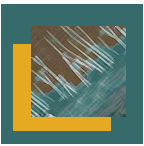
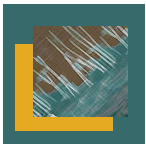


Figure 1 - Photomicrographs of the plantaris muscle of Wistar rats at 48 days of age. Cross section. Masson's trichrome. A and B: Connective tissue in the perimysium (arrow) of the control (CG) and cerebral palsy (CPG) groups, respectively. C: Percentage of intramuscular collagen in CG and CPG. Values expressed as mean \pm standard deviation. Student's t-test. * Represents $p < 0.05$.



Cerebral Palsy Affects Nuclei/Fiber and Capillary/Fiber Relations in Striated Skeletal Muscle

Matheus Felipe Zazula¹, Pâmela Buratti*¹, Camila Kuhn¹, Caroline Covatti¹, Dafne Strozake Maximo¹, Lígia Aline Centenaro¹, Marcia Miranda Torrejais¹

1. Universidade Estadual do Oeste do Paraná - Unioeste, Cascavel, Paraná, Brasil.

*Email: pamela_buratti@hotmail.com

Cerebral palsy (CP) is a sensorimotor disorder involving disorders of muscle tone, posture and movements, caused by brain injury during the period of structural and functional encephalic maturation [1]. Commonly observed symptoms in CP are motor disorders [2]. Thus, it is important to evaluate the muscular changes present in this encephalopathy. This study aimed to evaluate the effects of a CP animal model on the nuclei/fiber and capillary/fiber relations in the plantaris muscle of *Wistar* rats. All the procedures adopted were submitted and approved by the Ethics Committee in the Use of Animals (CEUA) of Unioeste (number 24/16). Adult pregnant rats were separated into rats injected intraperitoneally with sterile saline (100 µl) and rats injected intraperitoneally with LPS (200 µg/kg LPS in 100 µl of sterile saline). The injections were performed every 12 hours, from the 17th gestational day until the end of gestation (21st gestational day). The male offspring were separated into two groups: Control group (CG, $n = 5$) - offspring of rats injected with saline during pregnancy, and CP group (CPG, $n = 5$) - offspring of rats injected with LPS during pregnancy, submitted to perinatal anoxia and sensorimotor restriction. For perinatal anoxia, the offsprings were placed in a closed chamber, partially immersed in water at $37\text{ }^{\circ}\text{C} \pm 1$, with a flow of 9 l/min of nitrogen (100%) for 20 minutes, on the day of birth (postnatal day 0, P0). From the 1st to the 30th postnatal day (P1 to P30), CPG animals were submitted to sensorimotor restriction 16 hours/day. At 48 days of age, the plantaris muscle was collected and the right muscle antimere frozen in liquid nitrogen. This material was sectioned in a cryostat at seven µm thickness and stained with Hematoxylin-Eosin (HE). The histological sections obtained were photodocumented and used to study the nuclei/fiber and capillary/fiber relations. The analyzes were carried out in 10 microscopic fields, obtained with the objective of 40X. The results showed that the muscle fibers had polygonal aspect, multinucleated with peripheral nuclei. Capillaries were observed streaky to the connective tissue that surrounds the muscle fibers (Figures 1A and 1B). There was a 33% reduction in the nuclei/fiber relation ($p = 0.002$; Figure 1C) and a 34% reduction in the capillary/fiber relation ($p = 0.002$; Figure 1D) in CPG compared to CG. Therefore, this experimental model of CP affected the amount of nuclei per fiber and capillarity, influencing fiber composition due to the importance of nuclei in protein synthesis and muscle metabolism, since the reduction of capillaries leads to a decrease in the supply of oxygen in the muscle.

REFERENCES

- [1] R.C. Lima et al., R.U.V.R.V. 12 (2014).
- [2] ABPC, 2014
- [3] This research was supported by CAPES (Brazil).

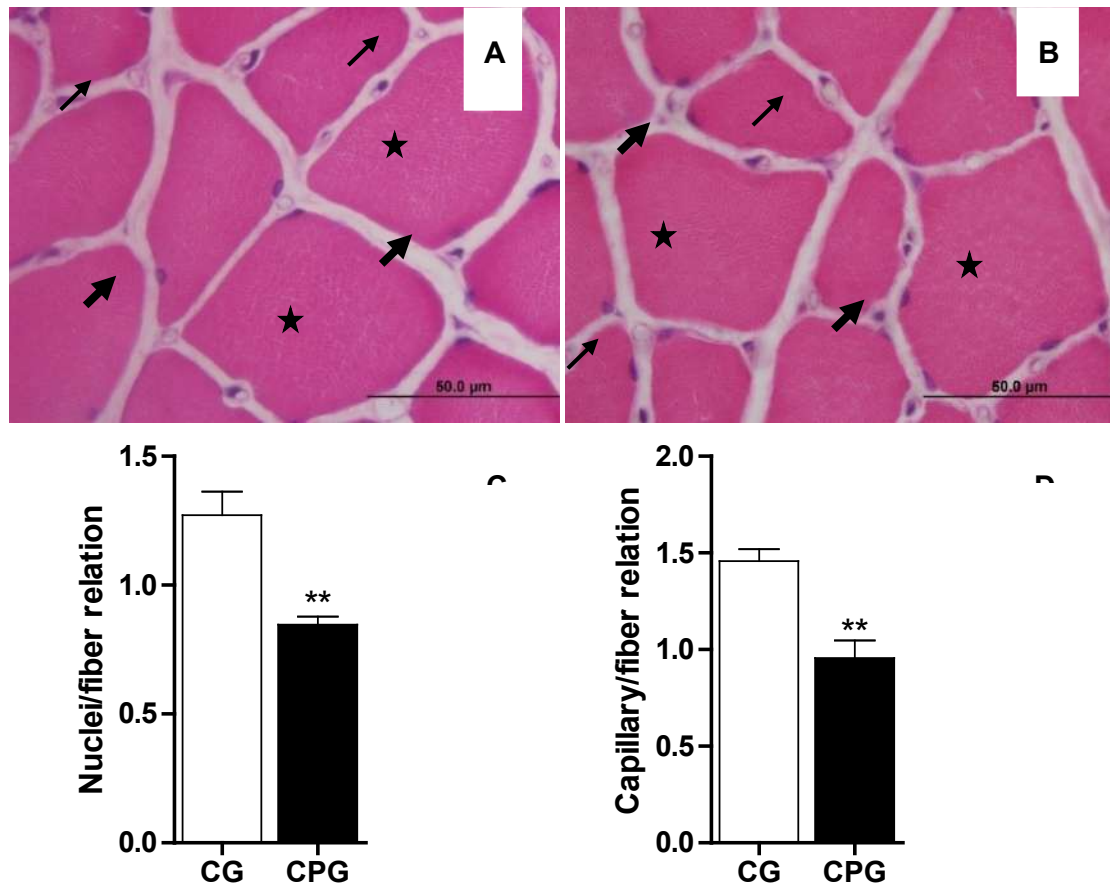
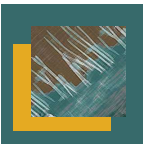


Figure 1 - Photomicrographs of the plantaris muscle of *Wistar* rats at 48 days of age. Cross section. HE. **A and B**: Muscle fibers (star), peripheral nuclei (thick arrow) and capillaries (thin arrow) of the control (CG) and cerebralpalsy (CPG) groups, respectively. **C and D**: Nuclei/fiber and capillary/fiber relations in CG and CPG. Values expressed as mean \pm standard deviation. Student's *t*-test. ** Represents $p < 0.01$.



Evaluation of the Muscular Fiber Area of the Extensor Digitorum Longus in Wistar Rats Submitted to Duodenojejunal Bypass

Mylena de Campos Oliveira^{1*}, Pâmela Buratti¹, Caroline Covatti¹, Ariadne Barbosa¹, Leslie Cazetta Jeronimo¹, Maria Lucia Bonfleur¹, Márcia Miranda Torrejais¹.

1. Universidade Estadual do Oeste do Paraná - Unioeste, Cascavel, Brasil.

*Email: mylenac.oliveira@hotmail.com

Obesity has been considered the disease of modern civilization and may become a worldwide epidemic in the future [1]. It results from the accumulation of body fat, which brings health risks and increases mortality due to its relation with other metabolic diseases [2]. Obesity complications increase the demand for health resources [3] and a modality of bariatric surgery known as duodenojejunal bypass (DJB) has been studied as a treatment strategy for obesity and associated comorbidities [4]. Considering that the implications of this procedure on the skeletal musculature have not been clarified yet, the present study aimed to evaluate the effects of DJB on the muscular fiber area of the extensor digitorum longus (EDL) of obese rats. All procedures involving the use of animals were approved by the Ethics Committee in the Use of Animals (CEUA) of UNIOESTE. Newborn Wistar rats were randomly distributed into control group (CTL; n = 6), which received saline solution (1,25 mg/g body weight/day), and monosodium glutamate group (MSG, n = 12), which received MSG injections in the cervical region (4 mg/g body weight/day), both during the first five days of age. The rats were weaned after 21 days of age and kept on standard diet and water *ad libitum*. At 90 days of age, obese animals from MSG group were randomly distributed into two subgroups: MSG group submitted to false operation (MSG FO, n = 6) and MSG group submitted to DJB (MSG DBJ, n = 6). Six months after surgery, the animals were killed and the EDL muscle was collected. The right antimere muscle was frozen in liquid nitrogen and subsequently submitted to cross sections (seven μm thick) in a cryostat. Histological sections were stained using the Hematoxylin-Eosin technique. These samples were photo documented and used to analyze the cross-sectional area through 10 microscopic fields (40x objective). Statistical analysis was performed by One-way ANOVA and Tukey post-test ($p < 0,05$). Skeletal muscular fibers were organized into fascicles, showing the regular architecture preserved (Figures 1A, 1B and 1C). The muscular fibers area was reduced 48 % in the MSG FO group, in relation to CTL. When comparing the MSG FO group to the MSG DJB, no significant changes were observed (Figure 1D). These results lead us to infer that the surgery did not interfere in the morphological characteristics of the muscle fibers and that obesity was the most influential factor, causing atrophy that could impair the muscle function.

REFERENCES

- [1] M.A.S.B. Azevedo & C. Spadotto, *Temas em Psicologia*. 12 (2004).
- [2] WHO, World Health Organization (2016).
- [3] W.C. Le Roux et al. *Annals of Surgery*. 243 (2006).
- [4] B. Geloneze et al. *Annals of Surgery*. 256 (2012).
- [5] Research supported by the Program PIBIC/UNIOESTE.

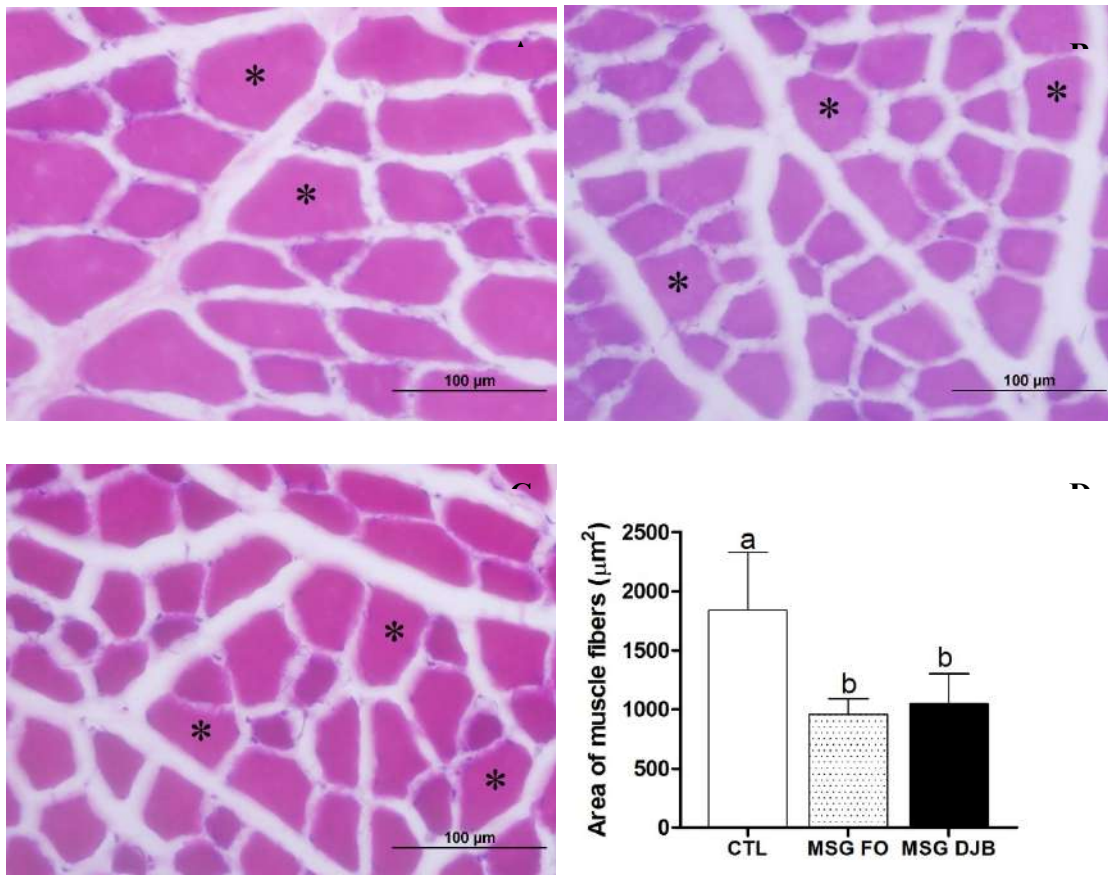
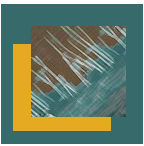
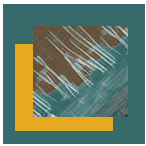


Figure 1 - Photomicrographs of the extensor digitorum longus of Wistar rats. Cross-section, HE staining. **A, B** and **C**: Organization of muscular fibers in fascicles (asterisks) in the control groups (CTL), MSG submitted to false operation (MSG FO) and MSG submitted to duodenojejunal bypass surgery (MSG DJB), respectively. **D**: Cross-sectional area of muscle fibers in the groups CTL, MSG FO and MSG DJB. Values expressed as mean ± standard deviation. Different letters indicate significant differences. One-way ANOVA ($p < 0,05$).



Effects of a Cerebral Palsy Model on the Skeletal Muscular Fiber in *Wistar* Rats

Mylena Campos de Oliveira¹, Pâmela Buratti*¹, Caroline Covatti¹, Dafne Strozake Maximo¹, Lúgia Aline Centenaro¹, Marcia Miranda Torrejais¹

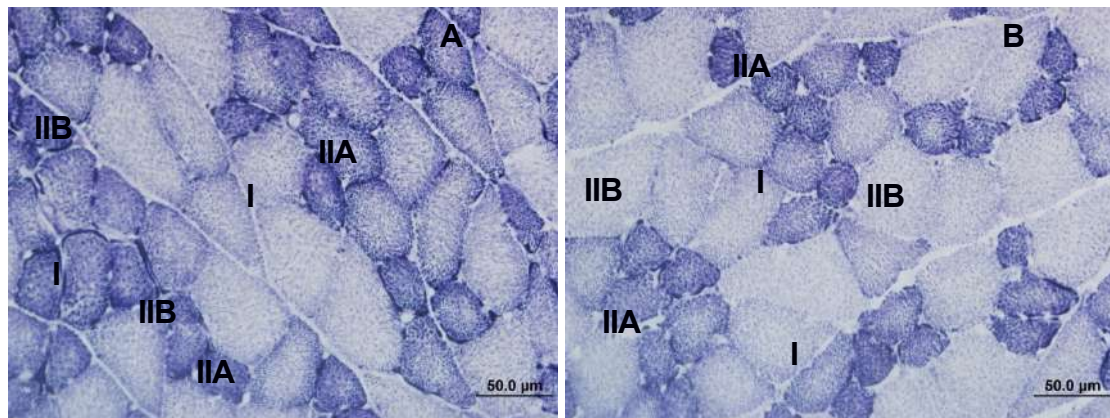
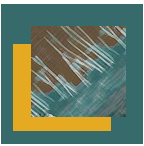
1. Universidade Estadual do Oeste do Paraná - Unioeste, Cascavel, Brasil.

*Email: pamela_buratti@hotmail.com

Cerebral palsy (CP) corresponds to a group of permanent disorders developmental and posture attributed to non-progressive disorders that occur during brain development [1]. This condition is manifested by an imbalance of strength and alteration in muscle tone, which may be associated with musculoskeletal disorders [2]. The striated skeletal muscle is composed of muscle fibers, which have contractile capacity [3]. The present study investigated the implications of an animal model of CP on muscle fibers in the plantaris muscle of *Wistar* rats. All procedures involving the use of animals were submitted and approved by the Ethics Committee in the Use of Animals (CEUA) of Unioeste (number 24/16). To obtain the litters, pregnant *Wistar* rats were injected intraperitoneally with vehicle (100 µL of sterile saline solution) or lipopolysaccharide (LPS) (200 µg/kg LPS in 100 µl of sterile saline solution). The injections were performed every 12 hours, from the 17th gestational day until the end of gestation. The male offspring were separated into Control group (CG) - offspring of rats injected with saline solution, and CP group (CPG) - offspring of rats injected with LPS. CPG was also submitted to perinatal anoxia and sensorimotor restriction. For perinatal anoxia, the offspring was placed in a chamber partially immersed in water at 37 °C ± 1, with a flow of 9 L/min of nitrogen (100%) for 20 minutes, at the day of birth (P0). The sensorimotor restriction was performed from P1 to P30, by immobilizing the pelvic limbs of the animals for 16 h/day. At 48 days of age, the plantaris muscle was collected and the right muscle antimere frozen in liquid nitrogen. This material was sectioned in a cryostat (seven µm thick) and subjected to the NADH-TR reaction. The sections obtained were photodocumented and used to study the cross-sectional area and quantification of the different types of fibers. The analyzes were performed in three images, obtained with a 20x objective. The muscle fibers were classified according to the proposition of Brooke and Kaiser [3]. The reaction to demonstrate the activity of NADH-TR evidenced type I muscle fibers (small diameter and intense oxidative activity), type IIA (intermediate diameter and moderate oxidative activity) and type IIB (large diameter and low oxidative activity) in the two groups studied (Figures 1A and 1B). It was observed that the mean area of type I fibers had a 20% decrease in CPG in relation to CG (p = 0.024), There was no statistically significant difference in types IIA and IIB (Figure 1C). Regarding muscle fiber counts, there was a 35% increase in the number of type I fibers in the CPG when compared to the CG (p = 0.034), whereas the types IIA and IIB fibers did not present any difference between the groups evaluated (Figure 1D). It was concluded that the animal model resulted in atrophy of the type I muscle fibers, with consequence on muscle contraction due to the importance of the fibers for the performance of this function.

REFERENCES

- [1] M. Bax et al., Dev. Med. Child Neurol. 47 (2005).
- [2] P. Rosenbaum et al. Dev. Med Child Neurol. 109 (2007).
- [3] M.A. Mathewson & R.L. Lieber, Phys. Med. Rehabil. Clin. N. Am. 26 (2015).
- [4] M.H. Brooke & K.K. Kaiser, J. Histochem. Cytochem. 18 (1970).
- [5] This research was supported by CAPES (Brazil).



C

D

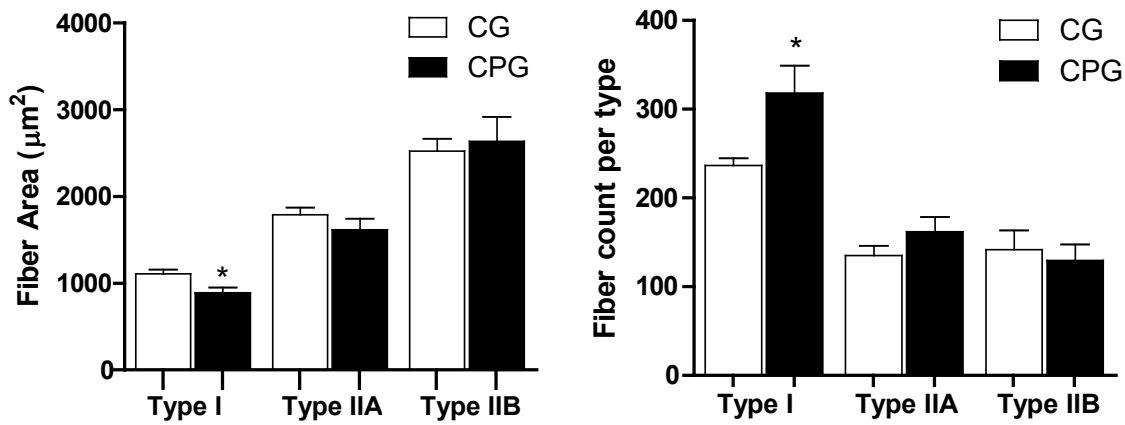
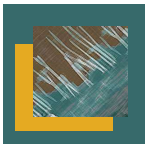


Figure 1 - Photomicrographs of the plantaris muscle of *Wistar* rats at 48 days of age. Cross section. NADH-TR reaction. **A and B:** Muscle fibers of types I, IIA and IIB in the control (CG) and cerebral palsy (CPG) groups, respectively. **C and D:** Mean area and count of different types of muscle fibers in CG and CPG animals. Values expressed as mean ± standard deviation. Student's *t*-test. * Represents $p < 0.05$.



A C-type Lectin from *Bothrops leucurus* Venom Forms Amyloid Aggregates In Culture Medium And Are Efficiently Phagocytosed By Peritoneal Macrophages

Aranda-Souza, MA¹, Lorena, VMB², Correia, MTS³, Pereira-Neves, A¹, Figueiredo, RCBQ1*

1. Departamento de Microbiologia, Instituto Aggeu Magalhães (IAM-FIOCRUZ), Recife, Brasil;
2. Departamento de Imunologia, Instituto Aggeu Magalhães (IAM-FIOCRUZ), Recife, Brasil;
3. Departamento de Bioquímica, Universidade Federal de Pernambuco (UFPE), Recife, Brasil.

Lectins are proteins that specifically recognize and bind to carbohydrate domains of diverse glycosylated molecules, including cell-surface receptors on effector cells such as macrophages. Upon their recognition, these proteins usually trigger signaling events leading to an effective cell response [1]. In this context, the conformational state of lectins has an important role for their biological functions. Previous works have demonstrated that under some environmental conditions lectins, as Concanavalin A, may undergo unfolding and/or aggregation process [2]. However the effects of these conformational/aggregation changes on the lectin-cell interactions is still unclear. In this work, we analyzed the effects of aggregation state of C type lectin, purified from *Bothrops leucurus* snake venom on the lectin-macrophage interaction. To investigate whether BLI are able to form amyloid-like structures in culture medium, the aggregation state of BLI was monitored spectrophotometrically at ratio 450 nm/750 nm, in presence of Congo Red, an specific marker of amyloid aggregates with β -sheet structures [3]. The BLI was also incubated at 37°C in RPMI and negatively stained for Transmission Electron Microscopy (TEM). To analyze the effects of BLI treatment on macrophages morphology, peritoneal macrophages were plated at 10⁶ cells/mL (37°C, 5% CO₂) and treated with BLI or BLI bound to galactose for 24h, and analyzed by TEM. Additionally, control and treated macrophages were stained with Thioflavin S (ThS), a marker of amyloids, and observed by confocal laser scanning microscope at 488 nm. Our results showed that BLI forms aggregates with amyloid-like properties in RPMI medium at 37°C, as observed by Congo Red and TEM (Figs 1-2). This aggregation state of BLI was inhibited by addition of the lectin specific carbohydrate, galactose (Figs 1A and 2C). TEM of BLI-treated macrophages revealed the presence of fibrillar structures in vesicular compartments in the cytoplasm (Fig. 2B). To investigate whether those structures internalized by macrophage are amyloid fibrils of BLI, macrophages were treated with BLI or BLI-Gal for 24 hours and submitted to staining with ThS. Our results showed that cells treated with BLI are strongly positive for ThS. No staining was observed in control or cells treated with cytochalasin B, an inhibitor of phagocytosis (Fig. 3). The cytochemical analysis, using antibody against amyloid fibrils coupled to colloidal gold, showed an intense labeling localized in fibrils inside intracellular compartments as well as extracellularly (Fig. 4). Our results suggest that BLI forms amyloid aggregates in culture medium, which are efficiently phagocytosed by macrophages. Once inside the macrophages BLI amyloid aggregates are able to trigger an inflammatory response, as demonstrated by a significant increase in the production of proinflammatory cytokines IL-1 β , INF- γ and TNF α (data not shown).

REFERENCES

- [1] R.G. Lichtenstein and G.A. Rabinovich, *Cell Death Differ.*, 20 (2013), 976–986.
- [2] Picone P. et al., *Biophys. J.* 96 (2009).
- [3] H. LeVine III, *Methods Enzymol.* 309 (1999) 274–284.
- [4] supported by CAPES, CNPq and FACEPE

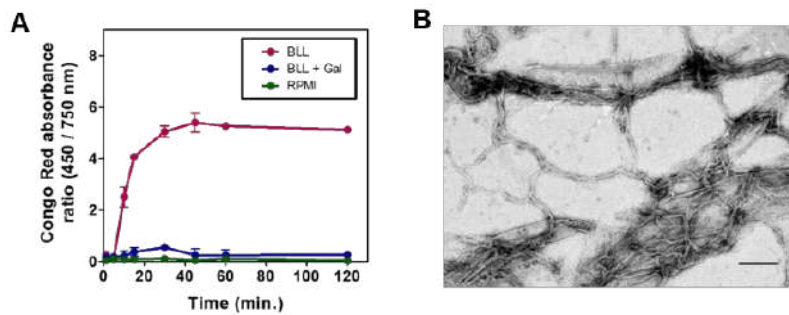
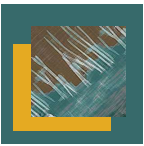


Figure 1. Characterization of aggregates of BLI in RPMI at 37°C. (A) Aggregation kinetics monitored by Congo Red fluorescence; (B) Negatively stained samples of BLI fibrils after 15 min of incubation in RPMI medium. Bar = 500 nm.

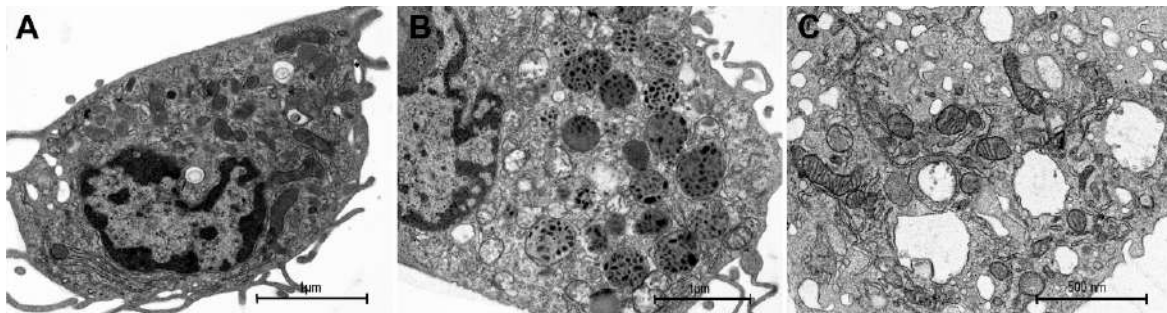


Figure 2. TEM of macrophages. (A) Control cell (B) Cell treated with BLI or (C) with BLI bound to galactose. Bars: A and B = 1µm; C = 500 nm.

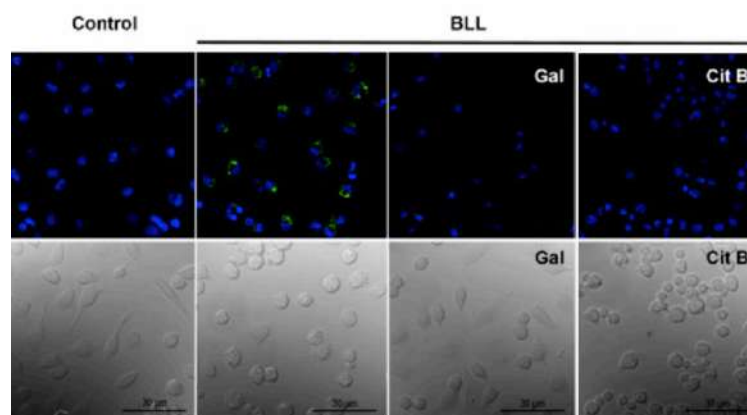


Figure 3. Representative micrographs of macrophages treated with BLI or BLI-Gal and double stained with Thioflavin S (green) and Hoechst 33258 (Blue). The cells were also previously incubated with Cytochalasin B (CitB).

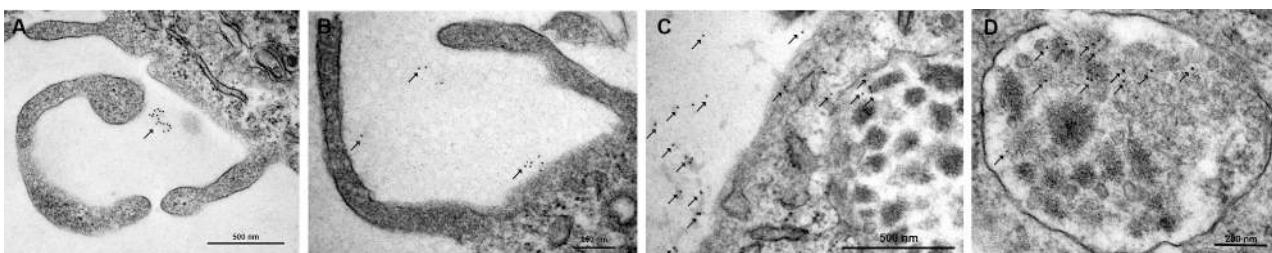


Figure 4. TEM of macrophages treated with 1 µM BLI and labeled with anti-amyloid fibrils antibody coupled to colloidal gold (arrows). (A-B) Detail of extracellular fibrils labeled with colloidal gold. (C-D) Detail of intracellular fibrils labeled with colloidal gold. Bars: A and C = 500 nm; B and D = 200 nm.



Ontogeny and Calcification Process in Coralline Algae *Lithophyllum corallinae* (Corallinophycidae, Rhodophyta)

Rodrigo Tomazetto de Carvalho¹, Maria Julia Pinto da Fonseca Fernandes Willemes¹, Gustavo Miranda Rocha², Ricardo da Gama Bahia¹, Marcos Farina de Souza³, Gilberto Menezes Amado Filho¹, Leonardo Tavares Salgado¹

1. Laboratório de Algas. Instituto de Pesquisas Jardim Botânico do Rio de Janeiro. Jardim Botânico. Rio de Janeiro, Brazil.
2. Laboratório de Física Biológica. Instituto de Biofísica Carlos Chagas Filho. Universidade Federal do Rio de Janeiro. Ilha do Fundão. Rio de Janeiro, Brazil.
3. Laboratório de Biomineralização. Instituto de Ciências Biomédicas. Universidade Federal do Rio de Janeiro, Brazil.

Coralline algae are one of the most abundant organisms in the hard-bottom of marine photic zone where they provide settlement substrates, structure and shelter on rocky substrates. Coralline algae also play important roles in tropical reefs, both cementing corals together and producing substantial amounts of calcium carbonate [1]. The ecological roles of coralline algae in the marine environment are related to the biomineralization process that occurs in the cell walls, which became heavily calcified [2]. Currently, this group of algae is receiving renewed attention from researchers from different fields, especially due to possible effects of climate changes in seawater chemistry, like temperature rise and ocean acidification [3]. Despite this renewed attention, we still have poor information regarding the first steps of coralline algae ontogeny and calcification. The aim of this study was to describe the earlier steps of development and calcification process in *Lithophyllum corallinae*. Spores from incrustated algal specimens collected in Rio de Janeiro were released in laboratory for settlement over microscope laminules. The germinating spores were analysed by polarizing optical, scanning electron and atomic force microscopies and also by energy dispersive spectroscopy. Results revealed the differences among cell walls from initial division spores (with 2 and 4 cells) to subsequent division spores (16 and 32 cells), with changes in elemental composition and hardness that allowed us to affirm that the biomineralization process begins in some moment after the third cell division and is restrict to the cell walls of the innermost part of the spore. The beginning of the process could be related to spore size and availability of organic matrix and energy from photosynthesis. Taking together, the results presented in this work represents an advance in the knowledge of the ontogeny of the biomineralization process and the development of germinating spores and can be useful for comparison in future studies on the effects of climate change in early coralline algae development.

REFERENCES

- [1] W.A. Nelson, Mar. Fresh. Res. 60 (2009) 787-801.
- [2] J. Cabioch , Biomineralization in Lower Plants and Animals. Oxford (1986).
- [3] S.J. McCoy & N.A. Kamenos, J. Phycol. DOI: 10.1111/jpy12262 (2015).

Acknowledgements

We thank CENABIO for the SEM facilities; Lab. de Biomineralização for Light and PLM facilities and Lab. de Física Biológica for AFM facilities. Authors also thank FAPERJ, CNPq, CAPES and BRASOIL for financial support. G.M.A.F., M.F. and L.T.S. would like to thank CNPq and FAPERJ for research fellowships.

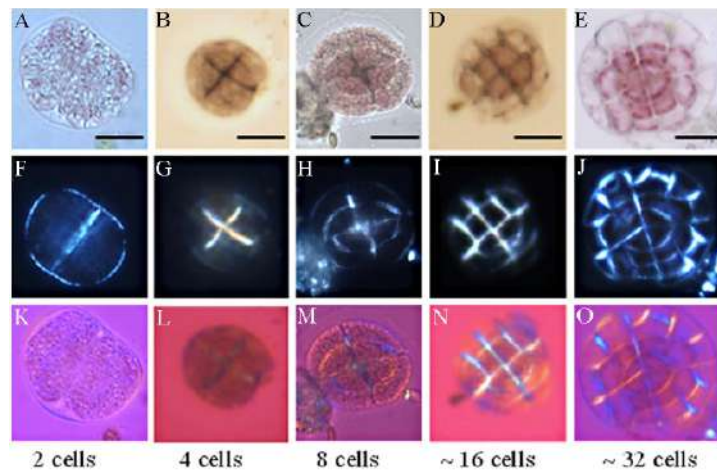
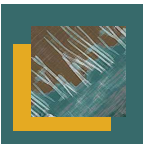


Figure 1. Light and polarized light microscopy of *L. corallinae* germinating spores in different development stages. It is noticeable the change of cell wall composition from two cells to 4 cells, with the appearance of an opaque material and polarization changes. Polarized microscopy images (Figures 1F – 1J) showing the presence of polarizing material inside the cell walls since the 2 cells stage. Polarized microscopy images with the utilization of a compensator (Figures 1K – 1O), where an increase of polarized light since the 8 cells stage can be observed. Figures 1A– 1C, scale bar = 10 μm ; Figures 1D and 1E, scale bar = 20 μm .

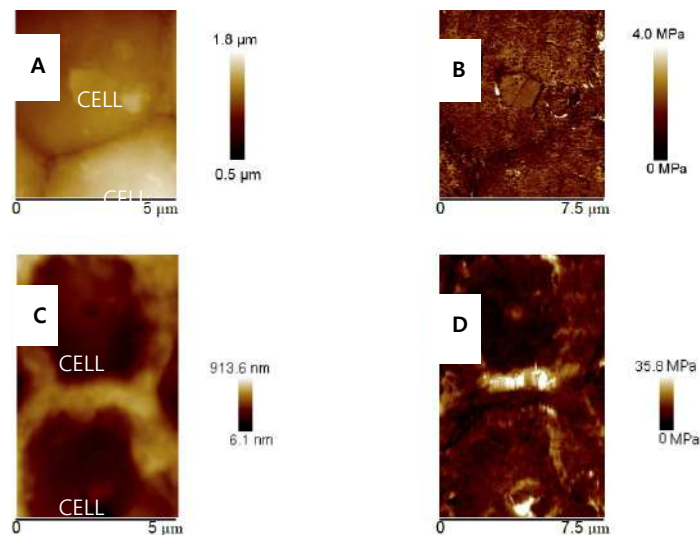


Figure 2. Topographical and elasticity images of 4 cells (Figs. 2A and 2B) and 16 cells (Figs. 2C and 2D). While in the 4 cells stage the cells are more turgid, with the central part of the cell higher than the lateral cell walls and cell regions presenting the same elasticity, older spores superficial cells presented the central part of the cell lower than the surrounding and cell walls with higher hardness.

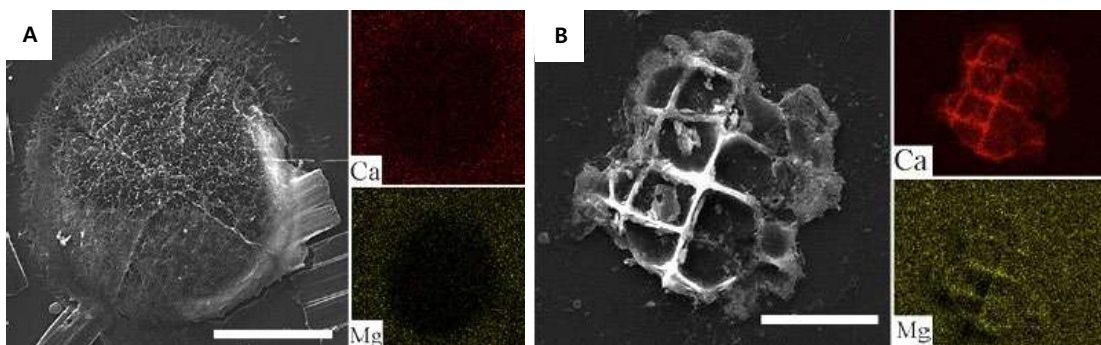


Figure 3. SEM images and their respective EDS maps of Ca and Mg of *L. corallinae* germinating spores with 4 cells (3A) and 16 cells (3B) settled over the microscope laminules. (Fig. 3A, scale bar = 10 μm ; Fig. 3B, scale bar = 20 μm). EDS maps clearly shows the higher concentration of Ca and Mg in



Ultrastructural analysis of *Rhodnius prolixus* metasternal gland

Rosane L. Lopes^{1*}, Suzete A. O. Gomes², Cátia F. Barbosa³, Denise Feder², Carolina N. Spiegel⁴

1. Programa de Pós-graduação de Ciências e Biotecnologia, UFF, Niterói; 2. GBG, Instituto de Biologia, UFF, Niterói; 3. GEO, Instituto de Química, UFF, Niterói; 4. GCM, Instituto de Biologia, UFF, Niterói

*Email: rosanelopes90@hotmail.com

Pheromones are chemical signals used by animals to communicate with their co specific and can represent an alternative tool for monitoring and control of insect vectors [1]. Adults of triatomines have a pair of exocrine gland located ventrally on the metathorax called, Metasternal Gland (MG) [2]. MGs are known as main source of sex pheromones in *Triatoma infestans*, *Triatoma brasiliensis* and *Rhodnius prolixus*. The bloodsucking triatomine *R. prolixus* is a vector of Chagas' disease [3]. The chemical compounds released by *Rhodnius prolixus* MG are alcohols and ketones [2]. Those volatiles when released by females stimulate the activation of sheltered males and subsequent approximation of couples [4]. In this study we analyzed ultrastructural aspects of MG in *R. prolixus*. The MG opening is small and droplet shape, located beside the coxal cavity (Figs: 1 A, C). The cuticle around the opening has a protuberant shape with a smooth appearance and with several pores, called metacetabular callus (MetCal) (figs:1 A, B). In the lateral margin of the metacoxa there is a row of setae, known as metacoxal comb (Fig 1B). Internally, our data corroborates with Brindleys' MG description [4]. The secretory portion presenting a marked central duct interconnected to the elongated base of a pear shaped reservoir with rough appearance (Fig: 1 D). Muscle is associated with the reservoir (Fig: 1 D). Transmission electron microscopy showed that the gland cells from these secretory portion present well developed rough and smooth endoplasmic reticulum (Figs: 2 A, C), indicating intense protein and lipid synthesis. The gland cell contains a large number of mitochondria, glycogen granules and vacuoles which are similar to lipid droplets (Figs: 2 B, C). We also observed innumerable canaliculi inside the GM (Fig 2 D). These structures probably conduce the individual cell gland secretion to the central duct. Further studies should be carried out to better elucidate the ultrastructure of the MG gland and correlates it with the pheromone biosynthesis in *Rhodnius prolixus*.

REFERENCES

- [1] Tilman JA et al Insect pheromones—an overview of biosynthesis and endocrine regulation. *Insect Biochemistry and Molecular Biology*. 1999; 6:481-514
- [2] Ponte SG et al. Female odours promote the activation of sheltered kissing bug *Rhodnius prolixus* males and modulate their orientation. *Medical and Veterinary Entomology*, 2014; 28: 257–263
- [3] Chagas C. Nova tripanozomíase humana. Estudos sôbre a morfologia e o ciclo evolutivo de *Schozotrypanum cruzi* n. gen., n. sp. agente etiológico de nova entidade mórbida do homem. *Memórias do Instituto Oswaldo Cruz*. 1909; 1: 159-218
- [4] Brindely. Scent glands of certain heteropteras. 1930

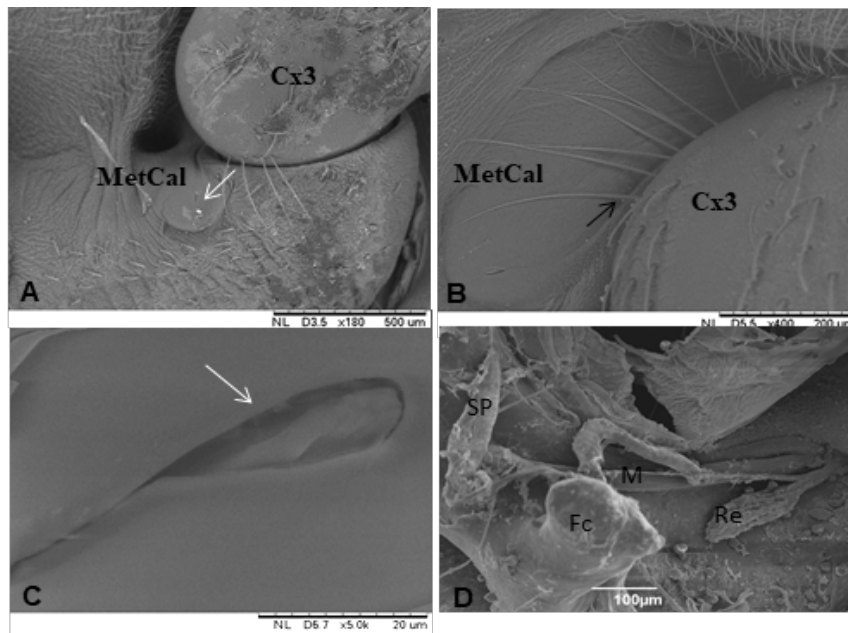
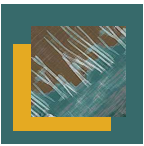


Figure 1: SEM of *R. prolixus*. A: Insertion of the opening of the MG (arrow) into the third coxal cavity (Cx3); Apophysis of furca (Ap) and metacetabular callus (MetCal); B: Metacetabular callus (MetCal) and metacoxal comb (arrow); C: Opening of MG (arrow); D Glandular apparatus around the furca (Fc), secretory portion (SP), reservoir (Re) and musculature (M).

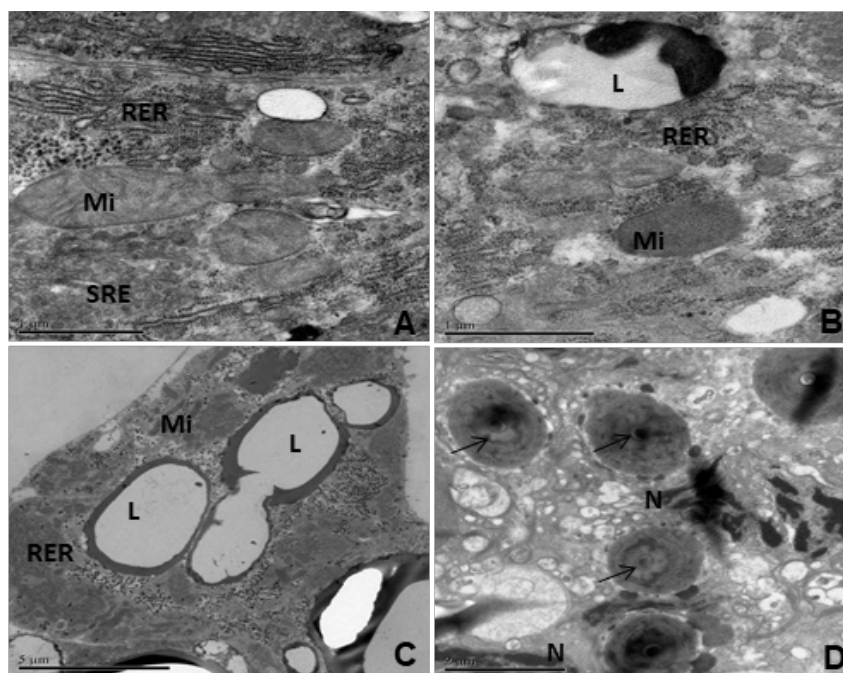


Figure 2: TEM of MG in *R. prolixus*. A: Observe the presence of mitochondria (Mi), rough (RER) and smooth endoplasmic reticulum (SER) in the gland cell; B: Lipid inclusions (L) can be observed admits the mitochondria (Mi) and the rough endoplasmic reticulum (RER); C: Glycogen granules (circle) are abundant as well as the rough endoplasmic reticulum (RER), the mitochondria (Mi) and lipid inclusions (L). D: Note the presence of multiple cuticular canaliculi (arrows) and nuclei (N)



Morphological Characterization Of A *Eucalyptus* Soil *Aspergillus* Strain

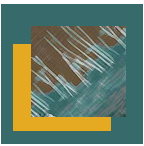
Vanessa Maria Pereira¹, Sirlei Cristina de Souza¹, Silvino Intra Moreira², Sarah da Silva Costa Guimarães³, Gláucia Mara Moreira⁴, Wesley de Oliveira Mendes¹, Eduardo Mateus Nery¹, Eduardo Alves¹, Sara Maria Chalfoun de Souza⁵, Luis Roberto Batista^{1*}.

1. Laboratório de Micotoxinas e Micologia, Dept Ciência dos Alimentos, Universidade Federal de Lavras – UFLA, Lavras MG, Brazil.
2. Laboratório de Microscopia Eletrônica e Análise Ultraestrutural, Dept Fitopatologia, UFLA, Lavras MG, Brazil.
3. Laboratório de Sistemática e Ecologia de Fungos, Dept Fitopatologia, UFLA, Lavras MG, Brazil.
4. Laboratório de Epidemiologia, Dept Fitopatologia, Universidade Federal de Viçosa – UFV, Viçosa MG, Brazil.
5. Empresa de Pesquisa Agropecuária de Minas Gerais – EPAMIG, Unidade Sul, Campus UFLA, Lavras MG, Brazil.

*E-mail: luisrb@dca.ufla.br.

Aspergillus species identification is done by a polyphasic approach, based on colony characteristics, micromorphology, phylogeny, and in some cases metabolites production [1]. The goal of this work was to characterize the micro-morphology of a soil *Aspergillus* strain. The isolate was obtained from a soil dilution plate (10^1x to 10^4x) on dichloran glycerol agar (DG18) and dichloran rose bengal chloramphenicol agar (DRBC) with 20 cm depth soil from an *Eucalyptus* cultivation located in Ferriferous Quadrangle, Minas Gerais State, Brazil. The isolate was grown on malt extract agar 2 % (MEA) and yeast extract sucrose agar (YES) at 25 °C for 14 days in darkness to evaluate the micromorphology [2]. The bright field images were acquired with a stereoscope Nikon SMZ1500 (NIS Elements D3.2 software) and an inverted Zeiss Axio Observer Z1 with differential interference contrast (DIC) (Zen 2012 software). The biometrical data were determined with around 30 units from each morphological structure, with bright field microscopy and Zen software. The preparation of samples for scanning electron microscopy (SEM) was done with colony fragment fixation in Karnovsky solution (pH 7.2) and dehydration in acetone series [3]. A Critical Point Bal-tec CPD 030 Balzers and a Sputter Coater Bal-tec SCD 050 Balzers were used for drying and gold coating, respectively. The images were acquired with a SEM Zeiss LEO EVO 40 XVP (Smart SEM software) at 20kV and 6 mm distance work. The purified fungus presented more typical morphological structures in the YES medium, for this reason it was chosen for the microscopic analysis. Two different growing lines of sporulation were observed, green and white (Figure 1 A–D). The white conidiophores were taller than the green one (Figure 1 D). The microscopic analysis revealed three types of conidiophores. The green conidial heads (Figure 1 E–H) were radiate, biseriate, stipes uncolored to pale brown, smooth-walled, usually non-septate, (3–) 5 (–8) × (55–) 90 (–120) μm, vesicles pyriform to subclavate, (5–) 14 (–25) μm long and (5–) 12 (–19) μm wide, metulae (5–) 6 (–8) μm long, phialides (5–) 6 (–7) μm long, conidia green, echinulate and globose to subglobose, (3–) 4 (–5) μm, without echinules. White conidial heads (Figure 1 I–L) were radiate, biseriate, stipes uncolored, smooth walled, usually non-septate, (320–) 510 (–740) μm, vesicles clavate, (19–) 23 (–25) μm long and (13–) 16 (–20) μm wide, metulae (6–) 8 (–10) μm long, phialides (7–) 8 (–10) μm long, conidia hyaline, smooth and globose to subglobose, aliptical or ovoid, (2–) 3 (–4) μm diameter. Finally, the accessory conidia (Figure 1 M–P) on short, hyaline and micro- to semi-macronematous conidiophores were globose to subglobose, (3–) 4 (–6) μm diameter. No ascomata, ascospores or Hülle cells present. Thus, the presence of these three types of conidiophores is typical of the *Aspergillus* species Section *Jani*, with differences between the known species [2]. The new species description will be confirmed using phylogenetic analysis and colonial morphology.

Key words: SEM, Differential Interference Contrast Microscopy.

**REFERENCES:**

[1] R.A. Sanson et al., *Studies in Mycology*, 78 (2014) 141.

[2] V. Hubka et al., *Mycologia*, 107 (2015) 169.

[3] J.J. Bozzola, L.D. Russell, *Electron Microscopy*, Jones and Bartlett, Boston, 1999.

Financial Support: FAPEMIG, CAPES, CNPq and FINEP.

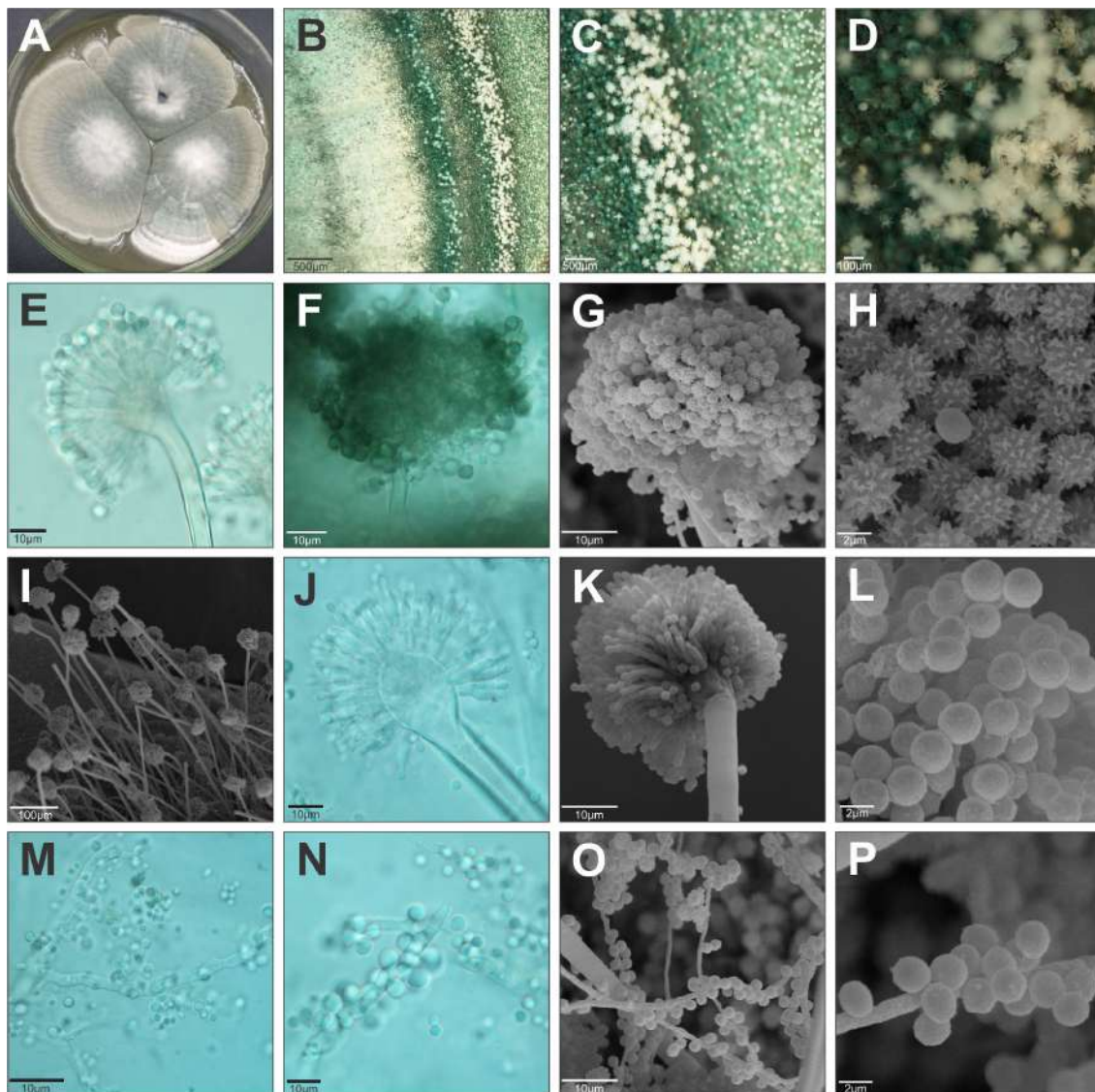


Figure 1: Morphological characters of *Aspergillus* sp. isolated from *Eucalyptus* soil incubated at 25 °C on YES medium in darkness for 14 days. **A–D:** Colony morphology. **E–H:** Green and echinulate sporulation in biserial conidiophores. **I–L:** White and smooth sporulation in long stipe biserial conidiophores. **M–P:** Micro- to semi-macronematous conidiophores producing accessory conidia. **B–D:** Stereoscope microscopy; **G–I, K–L, O–P:** Scanning electron microscopy; **E, J, M–N:** Bright field microscopy with DIC. **G, K and O:** 3kx magnification. **H, L and P:** 10kx magnification.



Characterization and Evaluation of the Cytotoxic Effect of Solid Lipid Nanoparticles Containing Docetaxel in Ovary Carcinoma *in vitro*.

Barbara Y. G. Andrade^{1*}, Márcia C. O. Rocha², João Paulo F. Longo³, Sônia N. Bão³

1. Animal Biology Master Student - University of Brasília, Brazil.
 2. Nanoscience and Nanobiotechnology Ph.D. Student - University of Brasília, Brazil.
 3. Science Biology Institute Professor - University of Brasília, Brazil.
- *Email: barbarayasmi@gmail.com

Ovarian epithelial cancer is the gynecological cancer that most causes death in women worldwide [1]. Docetaxel (DTX) is an important drug with antimetabolic action and acts to promote the hyper-stabilization of the microtubules, interrupting their dynamics. It is currently used as a chemotherapeutic agent in several types of solid tumors, but its systemic toxicity is high due to the main solvent used [2]. Solid lipid nanoparticles (SLN) are shown as an option to improve the problems related to the biological application of docetaxel [3]. Three formulations were made: white SLN, SLN-DTX-1 (1mg/ml DTX) and SLN-DTX-2 (2mg/ml DTX). The SLN were prepared by the hot homogenization method using the Ultra turrax T-25 stirrer and ultrasonic homogenization apparatus with high power probe. SLN morphology was evaluated with transmission electron microscopy (TEM). All formulations have similar morphology (Figure 1), demonstrating that the association with the drug does not alter the shape of the SLN. The hydrodynamic diameter and polydispersity index (Pdl) of the SLN were evaluated by dynamic light scattering and electrophoretic light scattering in Zetasizer Nano ZS. The Pdl measured for the three formulations was on average $0,338 \pm 0,04$. The mean size of nanoparticles associated with DTX is less than a white nanoparticle (Figure 2). A2780 cells (ovary carcinoma) were treated with increasing volumes of the formulations (125, 250, 375 e 500 $\mu\text{L/mL}$) then cell viability was measured by the MTT assay. The cellular viability values of the treatment are shown in Figure 3, and it is possible to observe that only the SLNs associated with DTX had reduced viability with increasing concentration. In order to verify if the action of DTX on microtubules is maintained when associated with NLS, A2780 cells were treated with NLS-DTX (400 $\mu\text{g/mL}$) and DTX (130 $\mu\text{g/mL}$), and then fixed and incubated in anti- α -tubulin antibody followed with fluorescein-labeled secondary antibody. The nucleus labeling with DAPI and analyzed by laser confocal microscopy. In Figure 4 it is possible to observe the cytoskeletal disorganization of cells treated with NLS-DTX similar to that observed in the treatment with free DTX. It is possible to conclude that the association of DTX with the NLS nanosystem is promising because the formulations have the appropriate size and morphology, and the cytotoxicity and antimetabolic action of the drug has not been altered by association with the nanosystem.

REFERENCES

- [1] L. A. TORRE *et al.*,. A Cancer Journal for Clinicians, 2015.
- [2] H. J. CHO *et al.*, International journal of nanomedicine, 2014.
- [4] M. NARVEKAR *et al.*, AAPS PharmSciTech, 2014.
- [5] Financial Support: CAPES, CNPq, FAPDF, FINEP.

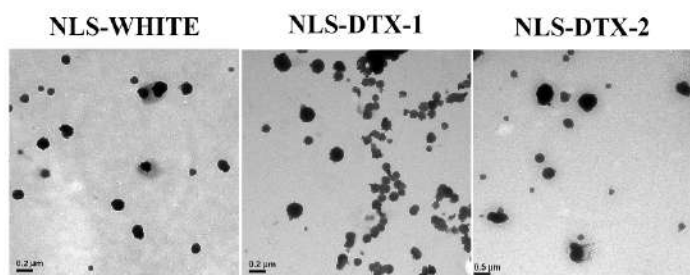


Figure 1. Morphology of the NLS-WHITE, NLS-DTX-1 and NLS-DTX-2 formulations analyzed by TEM. Samples were diluted 1:1000 in water and dried, were incubated in the osmium vapor for five minutes. Micrographs were made at 50.000 fold increase. Bar: 500 nm.

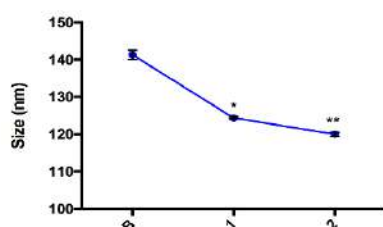


Figure 2. Mean size of NLS-WHITE [B], NLS-DTX-1 [1] and NLS-DTX-2 [2]. Samples were diluted 1:20 and then analyzed on Zetasizer Nano ZS. *P <0.05 and ** P <0.001.

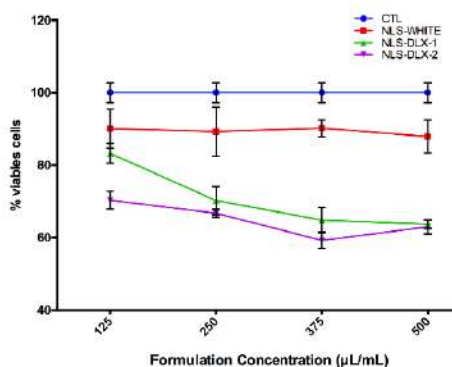


Figure 3. Effect of NLS-WHITE, NLS-DTX-1 and DLX-2 on the cellular viability of A2780 in 3h of exposure. A2780 cells were treated with the formulations at concentrations and cell viability was determined by the MTT assay. Data represent the mean ± SEM of three independent experiments in triplicate.

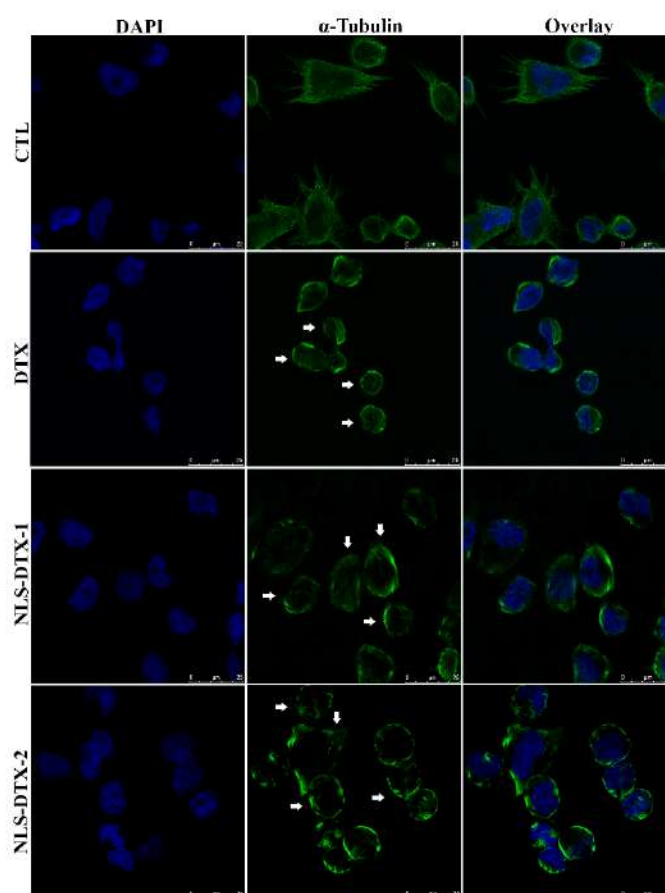
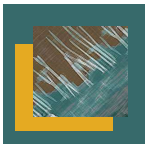


Figure 4. The docetaxel-associated SLNs promote a disorganization of the microtubules in A2780 cells. A2780 cells were treated for 3 hours with either DTX (130 μg/ml - positive control), NLS-DTX-1 and NLS-DTX-2 (400 μg/ml) or received no treatment (CTL). Cells were immunolabelled with anti- α -tubulin antibody followed with fluorescein-labeled secondary antibody (green) and nucleus from cells was stained with DAPI (blue). The analyzes were performed in a laser scanning confocal microscope and show the atypical organization of monoastrous spindles (arrows) induced by the treatments with NLS-DTX, reproducing the effect already described by the DTX. Micrographs were made at 1.200 fold increase. Bar: 25 μm.



Leishmania amazonensis infection induces migration of fibrocytes

¹Camila Guerra, ¹Roger Magno Macedo-Silva, ¹Paolla Roberta de Paula Pereira , ¹Mariana Yazeji Lanzelote, ¹Suzana Côrte-Real*

1. Oswaldo Cruz Institute/ Fiocruz

*Email: scrif@ioc.fiocruz.br

The bone marrow harbors the hematopoietic system being responsible for the origin of different cell types found in peripheral blood [1]. Fibrocytes originate in the marrow, express the pan-leukocyte CD45 protein and produce matrix proteins, such as type I collagen [2]. The presence of parasites of the *Leishmania* genus in the dermis of the mammalian host may lead to an intense inflammatory reaction with infiltration of blood-derived cells into infected tissues according to the genetic background of the host [3]. From this information, we suggest that the fibrocytes correspond to one of the migratory groups in the skin, composing the inflammatory set in the response to *Leishmania amazonensis*. In order to analyze the behavior of fibrocytes in the dermis of BALB/c mice during infection, fragments of the central ear skin were removed, included in OCT and immediately frozen in liquid nitrogen for analysis by fluorescence microscopy. Cryostat sections were obtained, fixed with 2% PFA and incubated with the anti-CD45 and anti-HSP47 antibodies, they were developed with secondary antibodies complexed to fluorochromes and analyzed under a microscope equipped with epifluorescence - Zeiss Axioplan 2. For analysis by transmission electron microscopy, fragments of the skin of the ears were fixed at 2.5% GA and post-fixed 1% OsO₄, then dehydrated in acetone series and included in PolyBed 812 resin. After that, ultrathin sections were collected in grids and analyzed in transmission electron microscope/Jeol JEM-1011. Analyzes showed, from 15 days of infection, an inflammatory cellular infiltrate and internalized amastigotes (Fig. 1A-B). Fibrocytes identification in the infected tissue was performed using a double labeling for anti-CD45 and anti-HSP47. Fluorescence microscopy analyzes showed the presence of three distinct cell groups: leukocytes / non-fibrocytes (CD45 + / HSP47-); Fibroblasts (CD45- / HSP47 +) and fibrocytes (CD45 + / HSP47 +) after 15 days of infection (Figure 1C-H). With these analyzes, we detected the progressive fibrocytes migration in the inoculum areas of *Leishmania amazonensis*. Initial evaluations of the production of inflammatory mediators by fibrocytes lead us to assume the probable action of this cell on the immune response in Leishmaniasis.

Supported by Faperj, IOC / Fiocruz

REFERENCES:

- [1] I. Godin and A. Cumano, Nat. Ver. Immunol. 2 (2002) 593.
- [2] R. Bucala et al., Mol. Med. 1 (1994) 71.
- [3] J. Ji et al., Infect. Immun. 71(8) (2003) 4278.

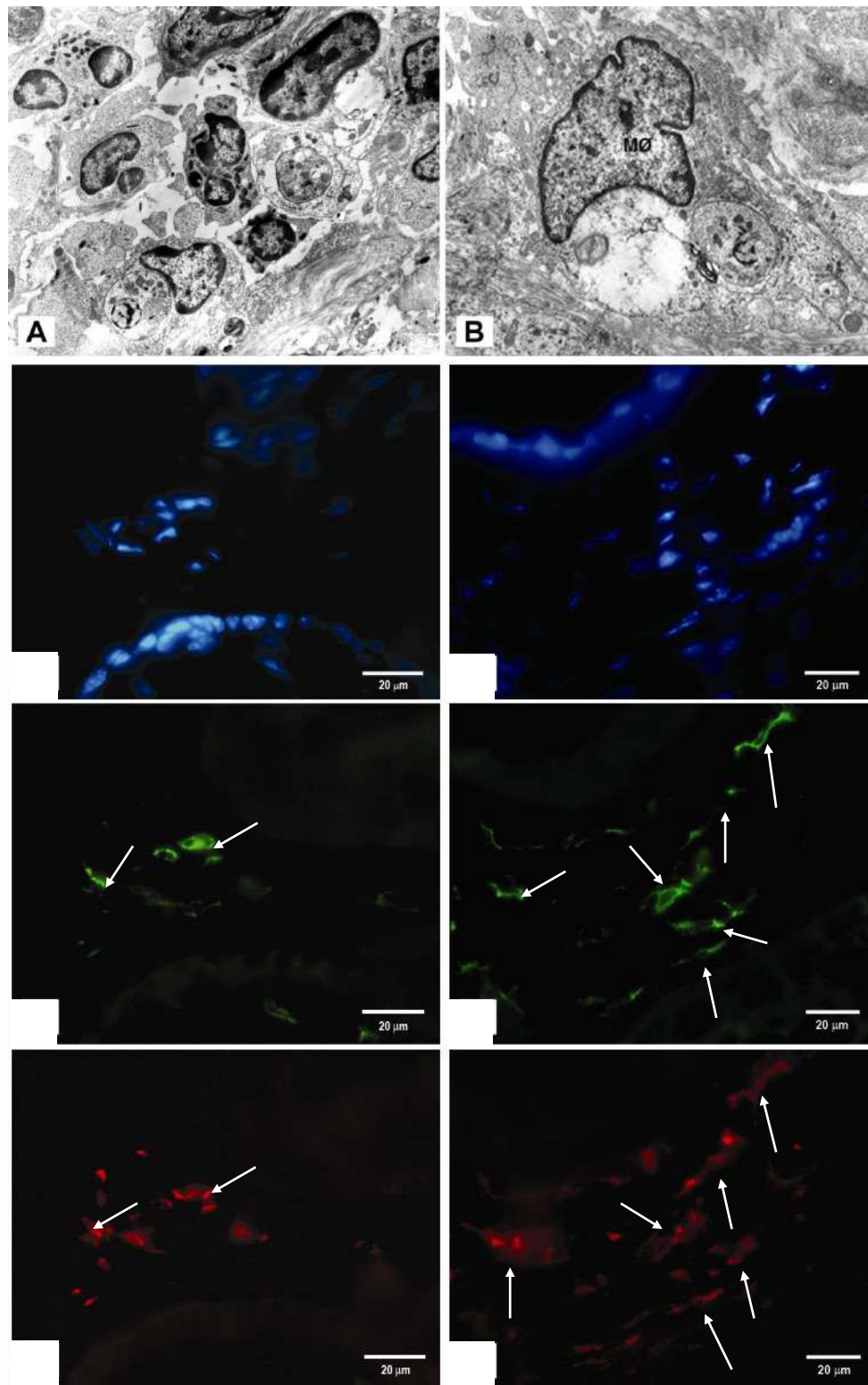
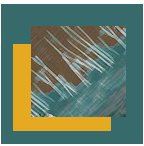


Figure 1 (A-B) - Transmission electron microscopy of the inoculum area dermis of the ears of BALB/c mice with 15 days of infection with *Leishmania amazonensis*. A- Inflammatory infiltrate cells and internalized amastigotes. B- Macrophage with amastigote within the parasitophorous vacuole. (C-H) Immunofluorescence. C-D: Dermal cell identification of nuclei labeled with DAPI (★). E-F: Leukocytes identified (CD45 +) in the dermis of the ears. G-H: Fibroblasts (▶) marked with HSP47-TRITC only. E-F and G-H: arrows indicate cells that have the same markings for CD45+ and HSP47+ indicating the fibrocytes.



DOI: [INSERIR ENDEREÇO DO DOI AQUI.](#)

Caderno de Resumos do 26º Congresso Brasileiro de Macroscopia da SBMM – ISSN: [INSERIR AQUI.](#)

In Vitro Activity of *Dysidea avara* Extract Against *Helicobacter pylori*

Martins, T.K.^{1*}, Lancheros, C.A.C.², Stefanello, T.F.², Retamiro, K.M.², Paula, J. C.², Ribeiro, S.M.³, Ueda-Nakamura, T.², Dias Filho, B.P.², Nakamura, C.V.^{1,2}

1. Department of Microbiology, State University of Londrina, Paraná, Brazil.
 2. Department of Basic Health Sciences, State University of Maringá, Paraná, Brazil.
 3. Department of Marine Biology. Federal Fluminense University. Niterói, RJ, Brazil.
- *Email: tkmuem@gmail.com

Helicobacter pylori is a Gram-negative, curve or helical bacterium that colonizes the gastric mucosa inducing chronic gastritis and plays an important role in gastric ulcer, lymphoma and gastric cancer [1]. The treatment of infections related to this bacterium as well as its eradication is the subject of several studies worldwide. Conventional therapies such as triple therapy of proton pump inhibitor, amoxicillin and clarithromycin have been avoided because of increased bacterial resistance. To avoid this resistance the use of natural products becomes an effective alternative. Marine sponges exhibit many biological activities and important pharmacological potential due to their secondary metabolites, which make them strong candidates for the treatment of various diseases [2]. The present work evaluated the *in vitro* activity of the *Dysidea avara* (*D. avara*) extract against *H. pylori* using the broth microdilution technique to determine the minimum inhibitory concentration (MIC). It was also observed the effect of this extract on the morphology and ultrastructure of *H. pylori* through scanning and transmission electron microscopy. *H. pylori* strain used for the experiment was ATCC 43504. The species of the *Dysidea* marine sponge was collected on the Spanish marine coast in the Mediterranean, and the extract was obtained with acetone. The stock solution was made by dilution in DMSO. For scanning microscopy *H. pylori* were exposed to 0.5x MIC (62.5 µg/mL), MIC (125 µg/mL) and 2x MIC (250 µg/mL) and for transmission microscopy the bacterial were exposed at the same concentration except 2 x MIC of *D. avara* extract and without extract (control cells) for 48 h at 37°C in microaerophilic conditions and fixed for 2 h with 2.5% glutaraldehyde in 0.1 M sodium cacodylate buffer. For Scanning electron microscopy samples were placed on a glass support with poli-L-lysine, dehydrated with graded ethanol, subjected to critical point drying in CO₂, coated with gold and observed in a Quanta 250 FEI. For transmission electron microscopy cells were fixed in glutaraldehyde, postfixed for 2 h at room temperature in 1.0% osmium tetroxide plus 2.0% potassium ferrocyanide. Then, its were dehydrated in acetone and embedded in Epon®. Ultrathin 65-nm-thick sections were then prepared, stained with uranyl acetate and lead citrate and observed in a JEM-1400 microscope, operated at 80 kV. *D. avara* was active against *H. pylori* exhibiting minimum inhibitory concentration (MIC) of 125 µg / mL as determined by the broth microdilution method. Morphological and ultrastructural alterations were observed at different concentration by scanning and transmission electron microscopy, respectively (Figure 1 and 2). After 48 h of treatment, rounded cells and different cellular density were observed. This was dose dependent, at highest concentration, such 250 µg/mL, this rounding became more evident. At 0.5x MIC and MIC, damages of the cell wall and decrease in its content were observed. These results have proved that *D. avara* extract has a strong inhibitory effect on *H. pylori*, being an alternative to the development of strategies to the treatment of *H. pylori* infection.

REFERENCES

- [1] WU T.S. et al. Kaohsiung Journal of Medical Sciences, 30 (2013) 167.
- [2] DE PAULA, J.C. et.al. Journal Brazilian of farmacognosy, 25 (2015) 651.

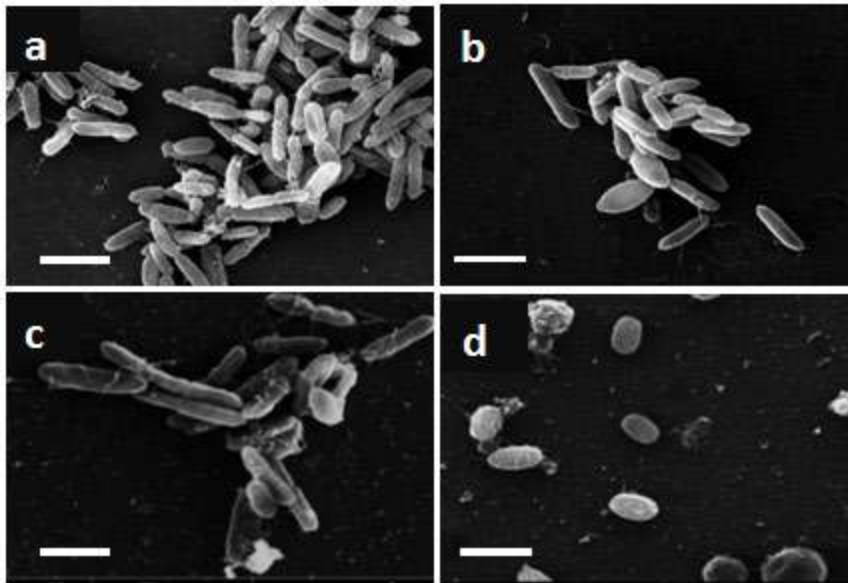
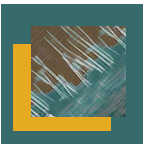


Figure 1. Scanning electron micrographs of *H. pylori* treated with different concentrations of *D. avara* extract. (a) Control cells; (b) 62.5 µg/mL (0.5x MIC); (c) 125 µg/mL (MIC); (d) 250 µg/mL (2x MIC). Bars = 2,5 µm.

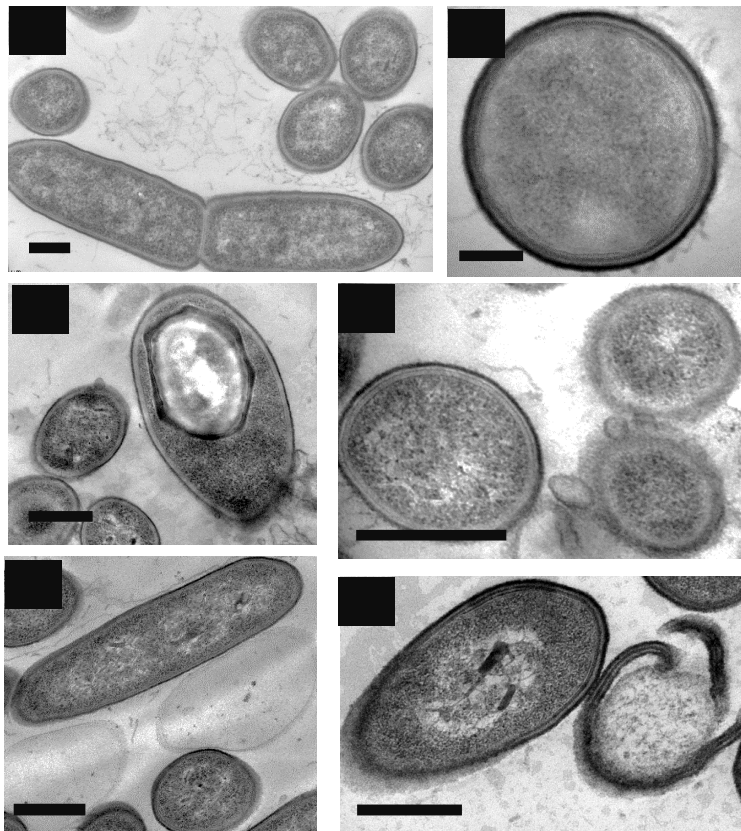
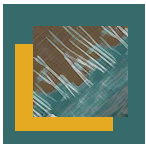


Figure 2. Transmission electron micrographs of *H. pylori* treated with different concentrations of *D. avara*. (a and b) Control cells; (c and d) 62.5 µg/mL (0.5x MIC); (e and f) 125 µg/mL (MIC). Bars a, c and e = 0.2 µm; b = 100 nm; d and f = 200 nm. (d) damages of cell wall; (c) decrease in its content.



DOI: [INSERIR ENDEREÇO DO DOI AQUI.](#)

Caderno de Resumos do 26º Congresso Brasileiro de Macroscopia da SBMM – ISSN: [INSERIR AQUI.](#)

PARTE 5

**PÔSTERES
- MATERIAIS**



Self-assembly of Gold Nanoparticles for Nanoscale Devices

Adilson R. Prado¹; Luis Guilherme L. Nunes¹, Luiz Felipe C. Del Caro¹, J. P. Oliveira²; R. H. A. Pereira²; Marco. C. C. Guimarães²; Breno V. Nogueira²; Moisés R. N. Ribeiro³; Maria J. Pontes³

1. Federal Institute of Espírito Santo, Serra, Brazil

2. Dept. of Morphology, Federal University of Espírito Santo, Vitória, Brazil

3. Dept. of Electrical Engineering, Federal University of Espírito Santo, Vitória, Brazil

*Email: adilsonp@ifes.edu.br

Introduction

Gold nanoparticles motivate various researches in nanotechnology with the purpose of applying their potential in different areas of science. The search by integration between electronic and optical devices promotes lots of attention in nanostructures metal as gold nanoparticles, since such systems have properties that manifest interesting electrical and optical behavior. Several studies showed that gold nanoparticles (AuNPs) can be used as biosensors [1], nano-antennas [2], phototherapy [3], among other applications [4].

Thus, this paper explores the cluster formation phenomenon with nanoparticles that can help understanding the mechanism involved in such process. The investigation considers two possible chemical agents with ability to organize the gold nanoparticles in different ways, thiocyanate ions (SCN^{-1}) and sulfide ions (S^{-2}). Cluster formation is of great validity, since it can aid in building nanodevices as optical and electric integrated devices. Among this phenomenon one can highlight the Localized Surface Plasmon Resonance (LSPR).

Therefore, it becomes necessary to study and understand the behavior of gold nanoparticles when they coalesce [5,6] in contact with ionic coordinating as the sulfide ion. Such study may help to develop methods that promote direct guidance on specific substrates.

Experimental

The AuNPs were synthesized using Turkevich's method [7]. All glassware were cleaned with a solution of aqua regia ($\text{HCl}:\text{HNO}_3 = 3:1$) and washed with deionized water. The synthesis procedure considered the citrate reduction method, thus the Dihydrate of Trisodium Citrate solution was added to the gold precursor when the phase reached the boiling point. It were used sodium thiocyanate (NaSCN) and ammonium sulfide ($(\text{NH}_4)_2\text{S}$) as suppliers of SCN^{-1} and S^{-2} ions. Figure 1 shows an illustration of how the samples were prepared. Although the two experiments were produced exactly in the same manner, each sample had its own AuNP spatial organization due to ionic electrostatic imbalance.

Results and Discussion

After concluding the synthesis of gold nanoparticles, the process of characterization was carried out by UV-visible spectrometry, where it was checked the absorption band at 521 nm due to the localized surface Plasmon resonance. The result obtained by UV-visible spectrometry is normally obtained when following the Turkevich's method.

In order to perform the analysis by Transmission Electron Microscopy two samples of 2 mL colloid of gold nanoparticles were used. A quantity of 80 μL of SCN^{-1} and S^{-2} was added in each one. The obtained results can be observed in Figure 2 that shows nanoparticles with and without addition of the mentioned chemical substances. Figure 2(a) shows gold nanoparticles characterized by TEM. Clusters obtained by adding thiocyanate nanoparticles that are characterized by TEM are shown in Figure 2(b). Moreover, cluster formed with sulfide nanoparticles also characterized by TEM can be observed in Figure 2(c). A significant difference could be found in gold nanoparticles' samples with and without sulfide ions. It means this specific ion have high capacity for coating gold nanoparticles, effect not observed when the ion thiocyanate is considered. This characteristic makes the



nanoparticles involved by sulfide present energetic connection, generating patterns of resonance or characterized by the form and size of arrays [8]. This fact allows manifestation of nonlinear effects. In some situations the electromagnetic fields generated among gold nanoparticles can have high magnitudes, being a very important tool for applications and manufacturing of nanodevices.

REFERENCES

- [1] B. Zargar et al., *Sensors and Actuators B: Chemical*, 182 (2013) 706.
- [2] T Schumacher et al., *Nature Communications*, 2 (2011) 1.
- [3] G. S. Terentyuk et. al., *J. Biomed Opt.*, vol. 14, no. 2, p. 021016, April 2009.
- [4] Y. Zhou et. al., *Sensors and Actuators B: Chemical*, 196 (2014) 106.
- [5] A. S. BARNARD et. al., *Accounts of Chemical Research*, 45 (2012) 1688.
- [6] O. C. Compton et al., *J. AM. CHEM. SOC.*, 129 (2007) 7793.

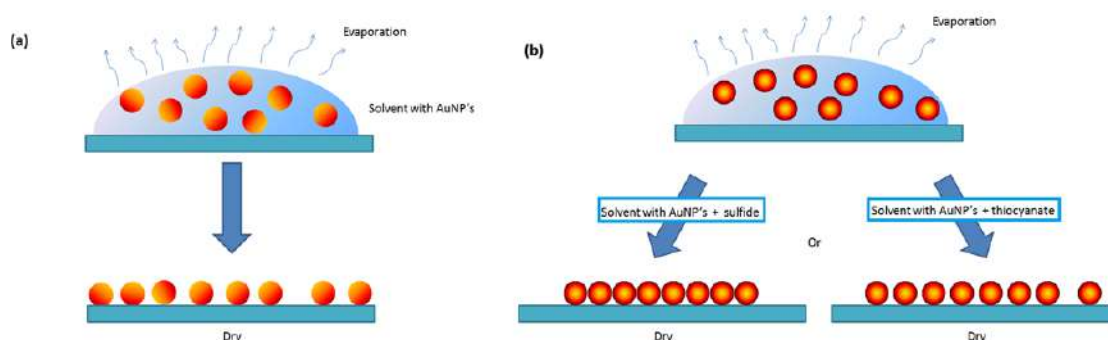


Figure 1. Sample preparation process. Coupling of gold nanoparticles with sulfide and thiocyanate.

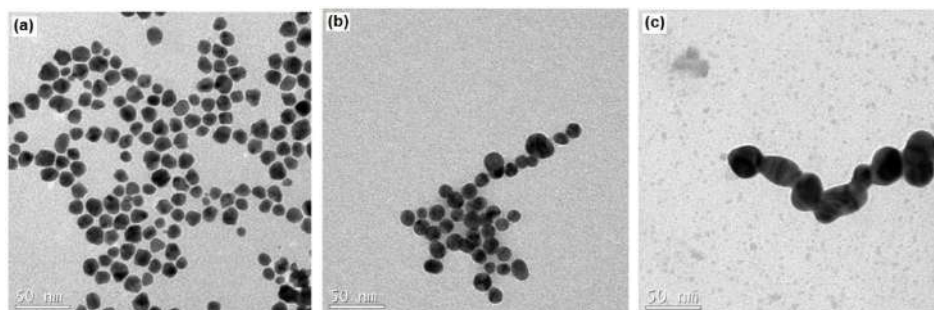
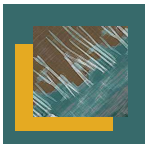


Figure 2. (a) Gold nanoparticles by TEM; (b) Cluster with thiocyanate nanoparticles by TEM; (c) Cluster with sulfide nanoparticles by TEM.



DOI: **INSERIR ENDEREÇO DO DOI AQUI.**

Caderno de Resumos do 26º Congresso Brasileiro de Macroscopia da SBMM – ISSN: **INSERIR AQUI.**

MATERIALS LIFE: Publication of Images That Explain Behaviors

Annelise Zeemann ^{1*} Gustavo Zeemann ²

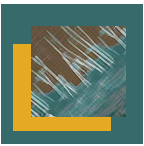
¹ Editor of www.materials.life site. Email: annelise@materials.life

² Designer of www.materials.life site.

The understanding of materials characteristics and its relation with the expected behavior of a specific product, to be applied in a specific condition, is the key for selecting and specifying materials. It is, for instance, very important to understand that a carbon steel presents limits of use in terms of strength and toughness, depending on the product manufacturing (casting, forging, plate), possible fabrication treatments and dimensions. And the best way to understand what are the limits to be applied in an engineering design for this cheaper material, is through a search in the literature looking for similar conditions. But this search is not easy because who will present specific conditions for a carbon steel? Although it is the most used material due to the low cost, carbon steel applications, or failures, are seldom of research interest. The MATERIALS LIFE site, www.materials.life, was created to be the reference of engineering materials, not only carbon steel but any material, presenting actual characteristics of donated samples that were removed from operation, or that were adopted to be qualified for specific operations, or that failed in fabrication, assembling, commissioning or operation. It presents a page of a material (called ML in the site, illustrated in figure 1) and all actual characteristics of chemistry, microstructure and properties are published for a specific application of a specific product. If the material failed it is also presented a short history of the failure, since the focus is about how the material behave and not in defining the failure root cause. The site is an image database that was designed to present materials pages, organized and searchable by categories. The page of RESULTS is dynamically filled after any searching of a specific condition by using a keyword or by selecting one of the four categories: material alloy (ferrous, non ferrous or composites), product (that can be a raw material, a finished product or a welded joint), application (pipeline, refinery, automotive), condition (sound, damage or used). Figure 2 presents the HOME page where the selection is conducted and figure 3 presents the RESULTS page. The site is independent and is mainly supported by people donation and sponsoring.

ACKNOWLEDGMENT:

The authors thank the UFRJ Materials Department Microscopy Laboratory.



DOI: INSERIR ENDEREÇO DO DOI AQUI.

Caderno de Resumos do 26º Congresso Brasileiro de Metalografia da SBMM – ISSN: INSERIR AQUI.

Seamless Composite Tube

M Material
Carbon Seal/
Seamless Steel

C Chemistry (% in weight)
Seam Tube Production Analysis
0.0000 0.0000 0.0000 0.0140 0.0000 0.0000
Cladding Tube Production Analysis
0.0000 0.0000 0.0000 0.0000 0.0000 0.0000

Mc Microstructure
Ferritic ferritic
Carbon Seal Tube
Juxtaposed
Seamless Steel
Clad

P Product
Seamless tube
Cladding
3.1416 ID Tube
14.1416 ID Wall
Clad

Pr Properties
Carbon Seal Tube
140 HV0.05
Seamless Steel
160 HV0.05

Ap Application
Pulp and Paper
Wack liquor used
in Kraft process

Obs
The composite seamless tube corresponds to a solid solution welding process by a co-diffusion process of iron, carbon and steel elements. The interface shows a decarburized layer in the carbon seal side and a strain hardened layer in the seamless steel side, with carbide precipitation around the interface. The hardness of the post-welding microstructure is high enough to create fine grains.

Associated Images

CI1 - Longitudinal Section
CI2 - Welding Interface
CI3 - Steel Tube Cross Section
CI4 - Metallographic Image

Figure 1 – The materials page (called ML), containing all actual information.

your Brand

Search by MATERIAL, PRODUCT, APPLICATION and CONDITION

MATERIAL LIFE

Search by MATERIAL, PRODUCT, APPLICATION and CONDITION

your Brand

Preferential Dissolution and Cracks in 2024

Vibration Induced Fatigue in 2024

Ring Corrosion in 2168 Pipe

Fragmentation Corrosion of 2024 Pipe

SCC in Free Cutting 2024

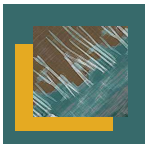
Casting Defects in 2168 Pipe

Suspension of 2024 Tube in

Corrosion in Tubular 2024

Subsea Tubular Fatigue in 2168 Pipe

Figure 2 – Pages HOME (for searching) and RESULTS.



Characterization of Hydrogen-Induced Cold Cracks in a Thick C-Mn Welded Steel Plate

Aline Raquel Vieira Nunes^{1*}, Annelise Zeemann², Luiz Henrique de Almeida¹.

1. PEMM-COPPE/UFRJ, Caixa Postal 68505, Rio de Janeiro, RJ, CEP 21945-970, Brazil.
*alineraraquel@metalmat.ufrj.br
2. TECMETAL/RJ, Estrada dos Bandeirantes, 28.000 – Vargem Grande, Rio de Janeiro, RJ, 22785-092, Brazil

The adoption of suitable parameters, such as preheating temperature and heat input magnitude, for welding thick plates of carbon steel, is necessary to avoid hydrogen-induced cracking (HIC). HIC is also referred to as “cold cracking” because the cracks form near room temperature after welding [1-4]. The internal cracking observed in a 6”-thick carbon-manganese steel plate after welding in this study is discussed with respect to the presence of material impurities. The microstructure of the center of the plate, as shown in Figure 1a, contains segregation bands. The morphology and location of the cracks detected during fabrication of a large, heavy structure are typical of HIC (Figure 1b), associated with intergranular cracks, at previous austenite grain boundaries of the coarse-grained HAZ. For this work, thin slices were cut at the segregated regions of the plate. Test pieces were machined and polished, and subjected to various hydrogenation conditions. After hydrogenation, the test pieces underwent an autogenous GTAW cycle, creating a liquid pool. The adopted welding parameters for the thin slices were suitable to create a low hardness HAZ with the same characteristic of the original microstructure of the SAW 6” plate HAZ. Similar intergranular cracking was observed in the test piece welded immediately after hydrogen charging (Figure 2) in the bainite region of the coarse-grained HAZ, indicating that even softer steels may crack if the hydrogen content is high. The microstructure of the weld metal, which has a similar composition to the base metal due to the 100% dilution, is bainitic with interdendritic martensitic islands and some micropores, as shown in Figure 3a. Voids associated with the small sulfide inclusions at austenite grain boundaries, Fig. 3b, were observed in the bainite regions, suggesting that the base material impurities create regions at the coarse grains boundaries near the fusion line with low melting points. In this study, it is clear that the hydrogen embrittlement is not associated with the movement of hydrogen atoms from the weld metal into the HAZ. Instead, there is clear evidence that the welding cycles create a condition at the fusion line, that results in the entrapment of hydrogen in the coarse grain boundaries. This region remains liquid during solidification of the weld pool due to the high concentration of impurities, causing a local reduction of the liquid temperature. Upon cooling, the diffusion of hydrogen from these traps becomes more difficult, creating intergranular voids and cracks when the material reaches ambient temperature.

REFERENCES:

- [1] H. W. Lee, S. W. Kang, D. S. Um., *Welding Research Supplement* (1988) 503–10.
 - [2] J. C. Lippold., John Wiley & Sons, Inc., Hoboken (2013) 421.
 - [3] S. Kou., *Welding Metallurgy*, (2003) 410–417.
 - [4] R. P. Gangloff, B. P. Somerday (Eds.), Woodhead Publishing Limited (2012) 840.
- Financial support by CNPq and TECMETAL, who also provided the materials for this study, is gratefully acknowledged.

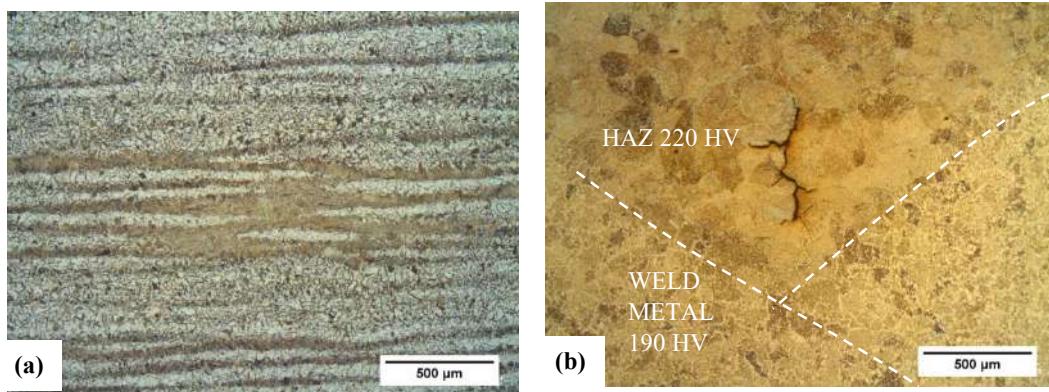
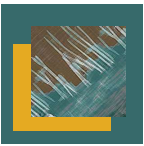


Fig.1: Optical micrograph (a) of the center of the steel plate after etching with Nital showing base metal segregation bands and (b) of the cracked region in the center of the 6" steel plate showing intergranular cracking at the HAZ

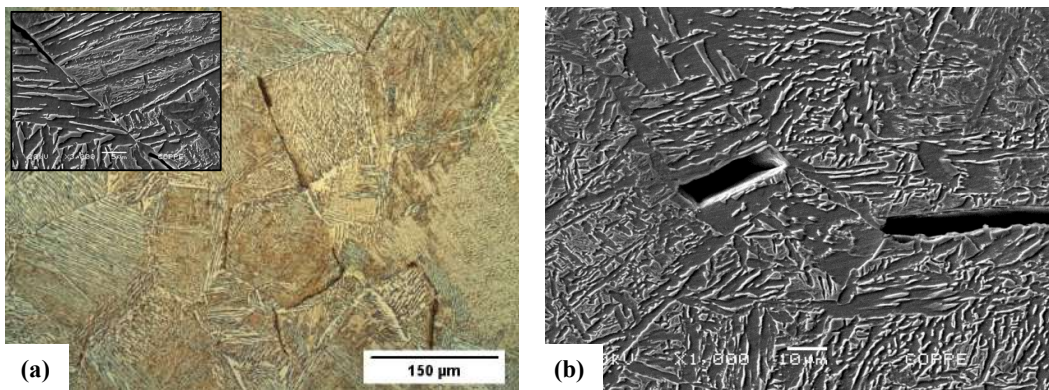


Fig.2: (a) Optical micrograph showing the crack location at the HAZ produced by autogenous GTAW. Detail of the bainite structure and intergranular cracking at the (previously austenite) coarse-grained HAZ; (b) Intergranular crack opening in a bainite structure with a hardness of only 280 HV1. The sample was etched with 2% Nital.

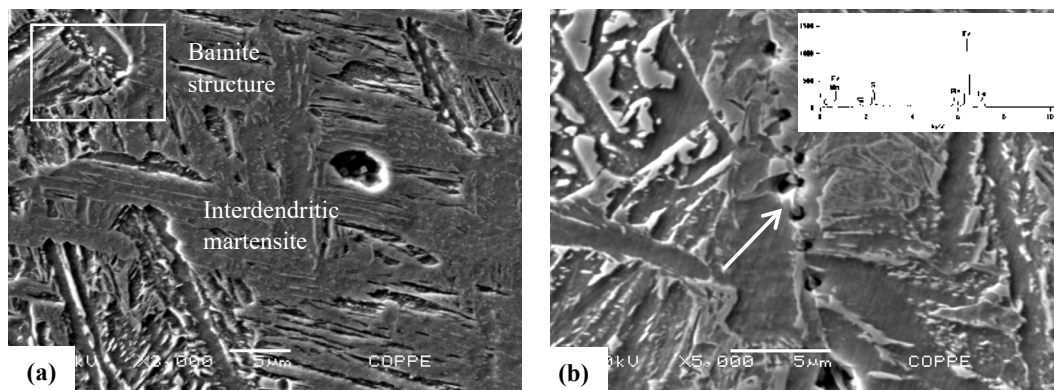


Fig.3: (a) Metallographic cross-section cut transverse to the weld bead showing the typical microstructure of the weld metal, which has the same chemical composition as the base metal (autogenous weld). High magnification; (b) SEM image of the interdendritic regions of the weld metal. SEM micrograph of the voids created by hydrogen entrapment near the fusion line between regions of partial melting at grain boundaries. Detail of the grain boundary spectrum of the HAZ, showing evidence of sulfide impurities. The sample was etched with 2% Nital



Laves Phase Identification in Inconel 625 Produced by 3D Laser Melting

C. Labre^{*1,2}, A.L. Pinto¹ and I.G. Solórzano²

1. Brazilian Center of Research in Physics (CBPF), Rio de Janeiro, Brazil

2. Department of Chemical and Materials Engineering, PUC-Rio, Rio de Janeiro, Brazil

* clabre@cbpf.br

Additive manufacturing (AM) or rapid prototyping is a technique based on layer-by-layer growth by selectively melting and consolidating thin layers of loose powder with a scanning laser beam, for building three-dimensional (3D) shaped objects [1]. Among the various methods of additive manufacturing techniques selective laser melting (SLM) has grown quickly as an alternative manufacturing route to produce components because of its high process speed, easy processing and production of complex shaped metallic components. Here, it is reported the investigation on an AM produced Alloy 625 sample. Alloy 625 is a solid-solution and precipitation strengthened nickel-base superalloy (Cr 21,29wt%, Mn 0,20wt%, C 0,015wt%, Si 0,17wt%, Mo 8,77wt%, Ti 0,14wt%, Al 0,18wt%, Nb 3,67wt%, Fe 3,05wt% and Ni (bal.)). This alloy is extensively used in industrial applications, such as chemical and petrochemical industries, that require a combination of excellent creep and high corrosion resistance at temperatures below 800 °C [2]. This investigation focused on the microstructural characteristics of a SLM consolidated alloy 625 sample. Details of the processing are reported by others [2]. Microstructural characterization was performed by SEM (JEOL JSM-7100F) and TEM (JEOL 2100F) both coupled to X-ray energy dispersive spectroscopy (EDS). The TEM was operated at 200 kV accelerating potential under conventional and diffraction modes. In addition the instrument was operated in STEM mode alloying analytical information through EDS spectroscopy and elemental mapping. A lamella containing specific precipitates was prepared by focused ion beam (TESCAN LYRA 3 FIB/SEM).

Figure 1a shows a SEM image of the as-received SLM sample containing a colony of lamellar-like precipitates growing together with some kind of block-type precipitates. In Figure 1b a bright field TEM image of a FIB sample is shown where the lamellar-type precipitates are indicated by arrow. In Figure 2 a bright field/centered dark field (BF/DF) pair image of a lamellar-type precipitates developed during manufacturing process is shown. DF image was obtained with the diffracted beam indicated by the red circle of diffraction pattern shown in the insertion. Elemental EDS mapping of lamellar-type precipitates are rich in Nb, Cr and Mo, and depleted of Ni and Fe. This precipitate is thus identified as Laves phase. The elimination of Laves phase through thermal treatment will be crucial for improvement of mechanical properties in components produced in this route.

REFERENCES

- [1] Y.J. Zhang, Y.J. Huang, L. Yang, J.G. Li, *J. Alloy Comp.* 570 (2013) 70-75.
- [2] J. Hernandez, L. E. Murr, et al. *Journal of Materials Science Research* 1 (2012) n3 124-144.
- [3] The authors are grateful to CBPF for providing full access to the LABNANO Electron Microscopy facilities and to the Brazilian Funding agencies CNPq, FINEP and FAPERJ.

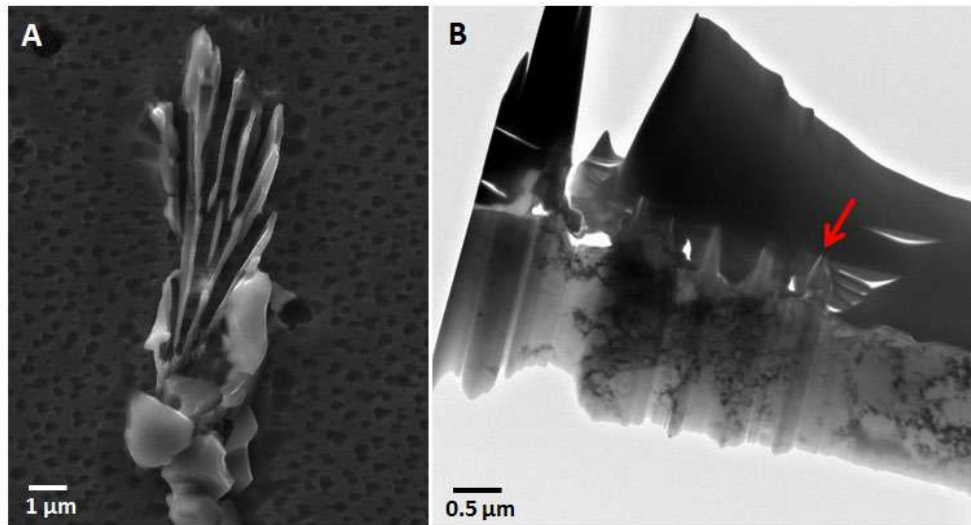
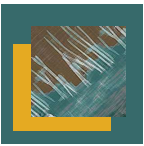


Figure 1 - (a) SEM image of the SLM consolidated alloy 625 sample showing precipitates with different morphologies and (b) TEM image showing lamellar-type precipitates indicated by arrow.

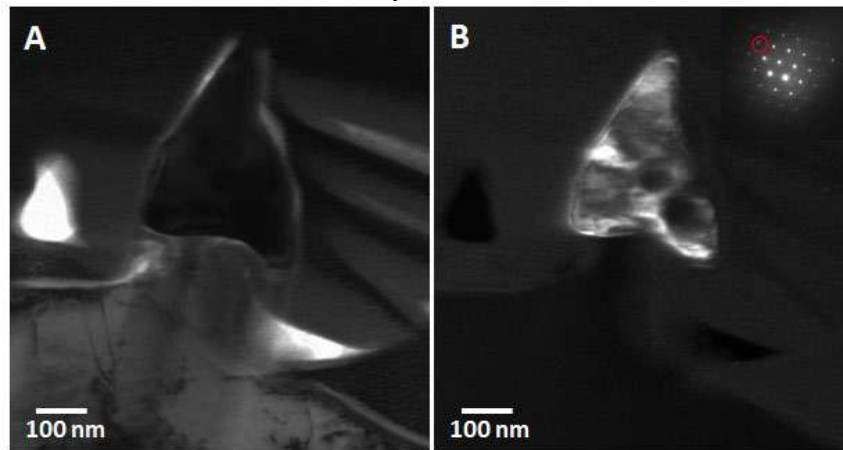


Figure 2 - BF/DF pair image of a Laves precipitate.

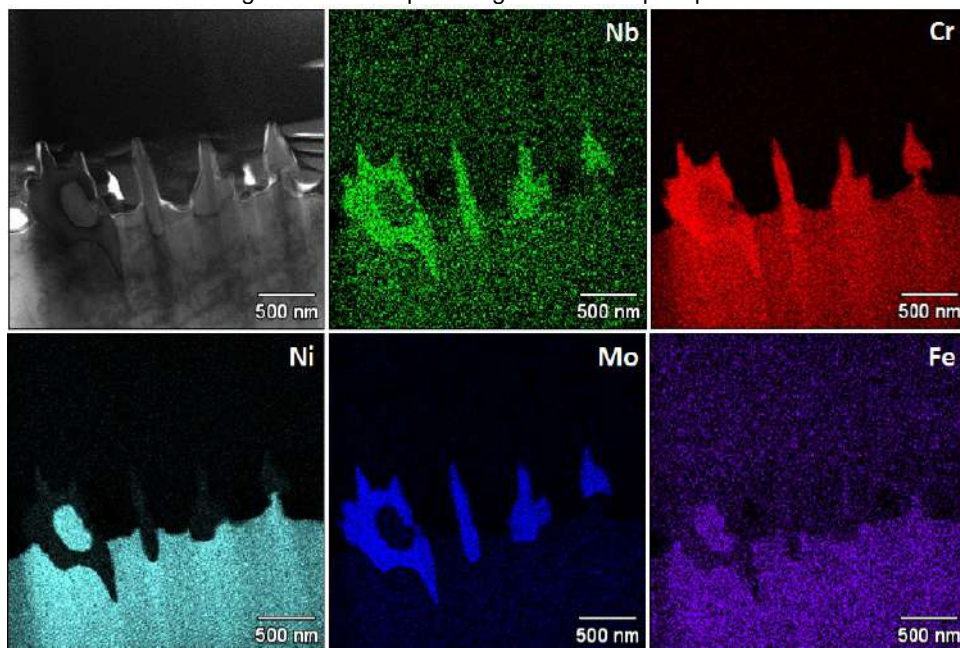


Figure 3 - SEM image and EDS elemental mapping of a lamellar-type precipitate containing Nb, Cr and Mo, and depleted of Ni and Fe.



Structural and electronic properties of NiO catalyst

Corinne Arrouvel^{1*}, Jacques Werckmann², Sabrina G. Sanches² and Jean-Guillaume Eon²

1. UFSCar, DFQM/CCTS, Sorocaba, SP, Brazil, ²UFRJ, Rio de Janeiro, Brazil

*Email: corinne@ufscar.br

NiO is an antiferromagnetic (AFM) p-type semiconductor which shows interesting catalytic properties at the nanoscale. It is well-known that controlling the shape and the size of the nanostructures is important for the development of a good catalyst.

This work is based on the study of the surface chemistry using experimental and first-principle methods, aiming in particular at improving the catalytic performances for low temperature alkane oxidative dehydrogenation (ODH) [1] or hydrogen production [2]. Different solvothermal synthesis of NiO particles were prepared from nickel acetate precursor ($\text{Ni}(\text{CH}_3\text{COO})_2 \cdot 4\text{H}_2\text{O}$), nickel nitrate precursor and using five types of solvent (P: Propanol, E: Ethylglycol; M: Methanol; U: Urea and T: Trimethylamine). NiO (T) has a hexagonal shape, presents a higher conversion of propane (48.9 %) and has smaller particle sizes (size 107 Å with BET of 106 m²/g). The theoretical comparison of two surfaces, the apolar (100) and the polar (111) surfaces, aims to better understand the reactivity of nanocatalysts under various temperatures and partial pressures of gases such as H₂, H₂O and O₂ adsorbed on clean and defective surfaces. Some magnetic anomalies and redox chemistry will be detailed upon the adsorption of the species. A further analysis is performed to correlate theoretical results to available DRX, TPD, XPS, IR, STM and HRTEM data, taking into account the difference between experimental measurements and catalytic working conditions. We show that the clean (001) surface is stable and not catalytically reactive. While it is possible to observe hydroxyl groups on NiO (001) surfaces from IR spectroscopy (at ambient T and P), under XPS conditions (vacuum at $P = 6 \times 10^{-12}$ atm) and under ODH conditions, no OH group is observed, the clean (001) surface being dehydroxylated. However, the (111) surface is a reactive surface. Hydrogen and water molecules are dissociated on the surface at low temperature leading to tricoordinated hydroxyl groups having a calculated O(1s) surface core-level binding-energy shift of 1.72eV. This is consistent with XPS experimental results and it explains the high reactivity of this surface towards oxidative dehydration of alkanes. We predict then that synthesizing NiO nanoparticles with higher (111) surface areas (i.e. hexagonal shapes rather than cubic shapes exhibiting only (001) surfaces) will increase the catalytic activity. **Acknowledgment:** CENAPAD for computing resources

REFERENCES

- [1] Zhaorigetu, B.; Li, W. Z.; Kieffer, R.; Xu, H. Y. *Reaction Kinetics and Catalysis Letters* (2002) 75, 275.
[2] Gallon, H. J.; Tu, X.; Twigg, M. V.; Whitehead, J. C. *Applied Catalysis B-Environmental* (2011) 106, 616.

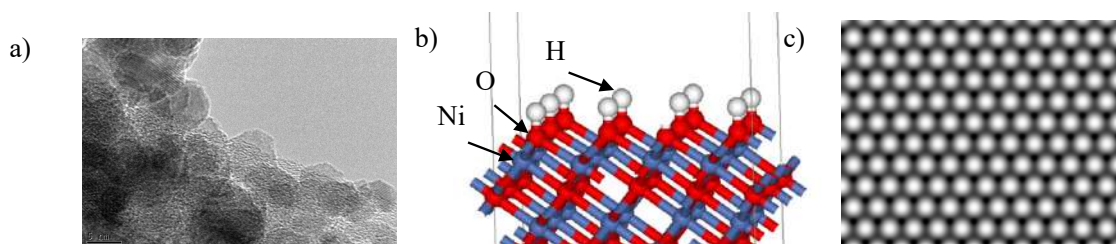
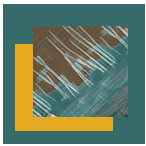


Fig: a) HRTEM of NiO obtained by hydrothermal synthesis with trimethylamine, b) fully hydrated (111) surface at 0.5ML from DFT calculations, c) simulated STM at 2eV below VB (OH in white).



Analysis by Optical Microscopy and X-ray Diffraction of Composite Cu-Cr-Ag-Al₂O₃ Synthesized Using Powder Metallurgy

Daniela Passarelo Moura da Fonseca^{1*}, Waldemar Alfredo Monteiro¹

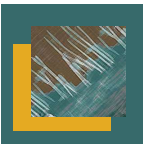
1. Instituto de Pesquisas Energéticas e Nucleares, IPEN–CNEN/SP, São Paulo, Brazil

*Email: danipassarelo@hotmail.com

The use of Nature's materials in favor of human beings has been present in its daily life for a long time, copper and its alloys have been used in function of the high thermal and electrical conductivity, good mechanical properties, resistance to corrosion, ease of fabrication and also by the high value of scrap [1]. Metal alloys can also be combined with other classes of materials in order to obtain new properties, superior to the original alloy, this union of two or more materials forms a composite [2]. The studied composite has a ternary metal alloy (copper, chromium and silver) as a matrix and a ceramic oxide (alumina) as the reinforcing phase. The addition of chromium, silver and small amounts of finely dispersed metal oxides in copper improves their mechanical properties and increases the operating temperature, causing little loss of conductivity. A possible application of this composite is in electrical contacts, electronic devices that break the passage of current in electrical circuits [1]. The objective of this study was the microstructural characterization by optical microscopy and X-ray diffraction of the composite Cu-Cr-Ag-Al₂O₃ processed by powder metallurgy. The samples used were fabricated in laboratory scale of 25 mm diameter, 3,5 mm $\geq h \geq$ 4,0 mm of height and 6,5 g of mass, with the following chemical compositions: (a) 85% Cu – 15% Al₂O₃; (b) 90% Cu – 5% Cr – 2% Ag – 3% Al₂O₃; (c) 90% Cu – 5% Cr – 5% Al₂O₃; (d) 90% Cu – 7% Cr – 3% Al₂O₃; (e) 85% Cu – 5% Cr – 5% Ag – 5% Al₂O₃; (f) 90% Cu – 5% Cr – 3% Ag – 2% Al₂O₃; (g) 90% Cu – 3% Cr – 7% Al₂O₃. In order to obtain the samples, the powders were weighed on a precision balance (according to each composition), mixed manually and cold-compacted in uniaxial press with 450 MPa pressure and sintered in an EDG furnace under 10⁻³ torr of mechanical vacuum and 650 °C in 6 h. The samples were prepared metallographically and observed in an optical microscope, the micrographs indicated coalescing of the copper particles and other metallic elements and formation of porosity (figure 1). The X-ray diffraction data were collected for samples (a) and (e) using graphite monochromator, copper tube, 25° $\leq 2\theta \leq$ 90° and $\Delta 2\theta = 0,02$, from the diffractograms the mean crystallite size (*D*) and microdeformation (ϵ) were calculated using the Williamson-Hall graphical method where the approximate line has a linear coefficient equal to 1/*D* and the angular coefficient is equal to 4 ϵ/λ [3]. In both samples were identified the expected phases, in agreement with the composition, and an undesirable phase of copper oxide (figure 2). The Williamson-Hall method was not used for all phases because it requires the identification of at least three peaks. Optical micrographs indicated presence of porosity inside the structure and partial homogeneity, due to the non-dissolution of the elements involved in the metal alloy, it is necessary to do further special thermal treatments. In some samples, a third phase was recognized, whose composition demands microanalyses to be properly identified. Through the diffractograms it was possible to identify the phase of copper oxide possibly coming from the sintering stage, this phase is not desirable or this composite because it negatively influences its electrical and mechanical properties. The Williamson-Hall method obtained a straight line with good correlation and suitable values of mean crystallite size and microdeformation for the copper phase.

REFERENCES

- ASM International. Specialty Handbook – Copper and Copper Alloys. 2001.
ASKELAND, D.; PHULÉ, P. Ciência e Engenharia de Materiais – Uma introdução. São Paulo: Cengage Learning, 2008.



SANTOS, R. L. P.; RIBEIRO, P. C.; VIEIRA, D. A.; SANTOS, P. T. A.; SASAKI, J. M.; COSTA, A. C. F. M. Difração de raios X e refinamento por Rietveld de ferritas $Mn_{0.65}Zn_{0.35}Fe_2O_4$ sintetizada por reação de combustão. Revista Eletrônica de Materiais e Processos, v.6.3 (2011), p. 145-150, ISSN 1809-8797.

This research was supported by Universidade Presbiteriana Mackenzie, Instituto de Pesquisas Energéticas e Nucleares and Coordenação de Aperfeiçoamento de Pessoal de Nível Superior.

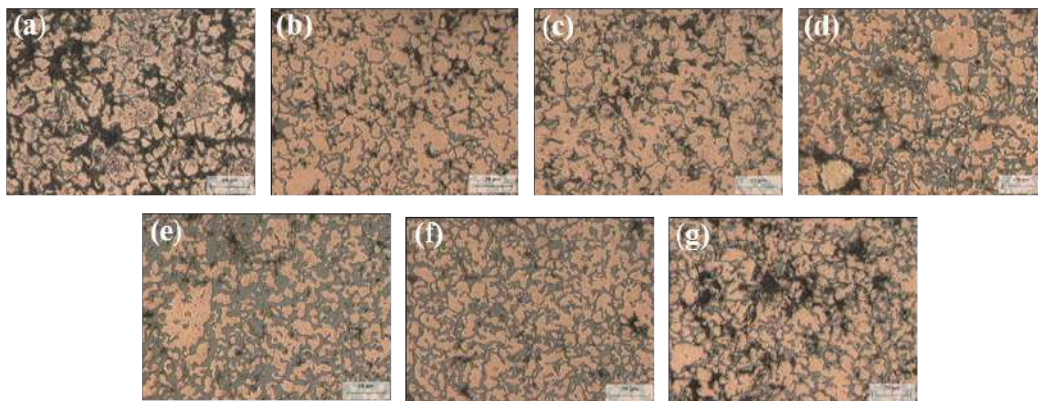


Figure 1: Optical micrographs of the composites Cu-Cr-Ag- Al_2O_3 , as polished (20 μm scale). It was observed porosity, coalescence of the copper particles and partial homogenization.

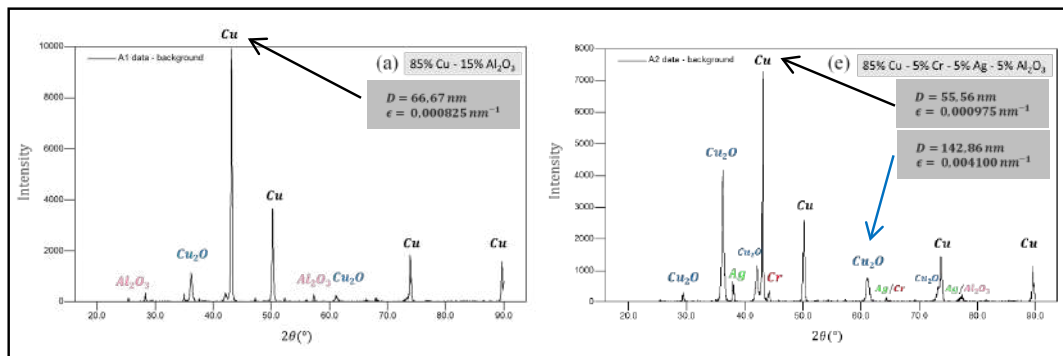
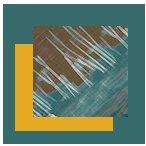


Figure 2: Diffractogram and results of the Williamson-Hall method for sample (a) and (c). The phases of copper and copper oxide were identified with greater intensity, some phases were not possible to identify due to the overlapping of peaks. A suitable crystallite size was found for the copper phases in both samples.



Microstructural Analysis of Composite Cu-Cr-Ag-(CeO₂, Al₂O₃) Processing by Powder Metallurgy

Daniela Passarelo Moura da Fonseca^{1*}, Waldemar Alfredo Monteiro¹

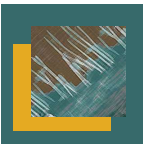
1. Instituto de Pesquisas Energéticas e Nucleares, IPEN-CNEN/SP, São Paulo, Brazil

*Email: danipassarelo@hotmail.com

Copper has long been used by mankind, since the 20th century they have gained industrial and technological importance [1]. They can be combined with ceramic materials in the synthesis of modern composites, optimized and with balanced properties [2]. The studied composite has a metal as a matrix (copper or copper, chromium and silver), the ceramic oxide as the reinforcing phase (ceria or alumina) and was synthesized by powder metallurgy. A possible application of this material is like anodes in Solid Oxide Fuel Cells (SOFC), cermets based on rare earth oxides and metals such as copper, silver and nickel have been studied in this component [3]. The objective of this work was the analysis of the particle size by SEM and chemical composition by EDS of the starting material (powders of copper, chromium, silver, ceria and alumina) and the microstructural characterization by MO of copper composites with four compositions: (a) 80% Cu – 8% Cr – 4% Ag – 8% CeO₂; (b) 80% Cu – 20% CeO₂; (c) 80% Cu – 8% Cr – 4% Ag – 8% Al₂O₃; (d) 80% Cu – 20% Al₂O₃. For analysis in the SEM/EDS the powders were fixed in the sample port with carbon paint, for the powders of ceria and alumina was made gold coating for 2 min. The copper powder presented nodular agglomerates; the chromium powder presented large particles with coarse contours and irregular shape; the silver powder presented a dendritic shape; the ceria powder presented very small particles and it was not possible to observe them due to the limitation of the SEM and the alumina powder presented flake-shaped agglomerates, figure 1. The EDS microanalysis results for copper, silver, ceria and alumina powders were adequate, for chromium powder indicated silicon and iron (manufacturer predicted) and calcium impurities (not predicted but with low percentage), figure 1. The powders were weighed on a precision balance (according to each composition), mixed manually and cold-compacted in uniaxial press with 180 MPa pressure and sintered in a tubular furnace with vacuum of 10⁻⁷ torr, temperature of 750 °C and time of 6 h. The samples were obtained in laboratory scale with a 31x12x 3.5 mm parallelepipedal shape, hot mounting, grinded (240, 320, 400, 600, 800) and polished (3µm and 1µm diamond and 0.02 µm silica). The optical micrographs indicated coalescence of copper particles, homogeneity, porosity and an unknown (black) phase, possibly related to ceramic materials, figure 2. The sample (c) was the only one that presented different microstructure between the normal and transverse directions, possibly due to segregation of the powders during mixing. It was possible to make an adequate analysis of the particle formats of the copper, chromium, silver and alumina powders; however, the ceria powder needs to be analyzed again in SEM with higher capacity of increase. The results of EDS microanalysis were promising for all powders. The optical micrographs suggest a good adequacy of the compaction and sintering parameters, forming a homogeneous microstructure and with the desired porosity, except for sample (c), that the mixture was not suitable. In order to study the formed phases it is necessary to perform an X-ray mapping on SEM and X-ray diffraction in the samples after sintering.

REFERENCES:

- [1] ASM International. Specialty Handbook – Copper and Copper Alloys. 2001.
- [2] ASM International. Metals Handbook: Volume 21 - Composites. 2001.
- [3] CIMENTI, M. HILL, J. M. Direct Utilization of Liquid Fuels in SOFC for Portable Applications: Challenges for the Selection of Alternative Anodes. *Energies* 2009, 2, 377-410; doi: 10.3390/en20200 377.



This research was supported by Instituto de Pesquisas Energéticas e Nucleares and Coordenação de Aperfeiçoamento de Pessoal de Nível Superior

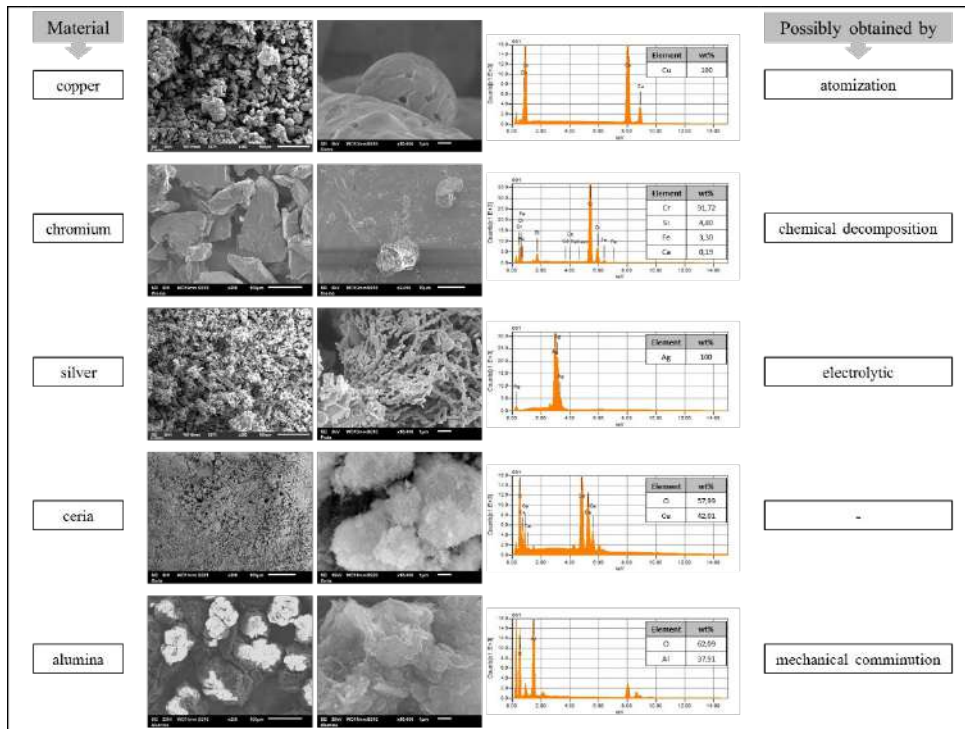


Figure 1: SEM micrographs by secondary electrons and EDS results of copper, chromium, silver, ceria and alumina powders (100 µm and 1 µm scale).

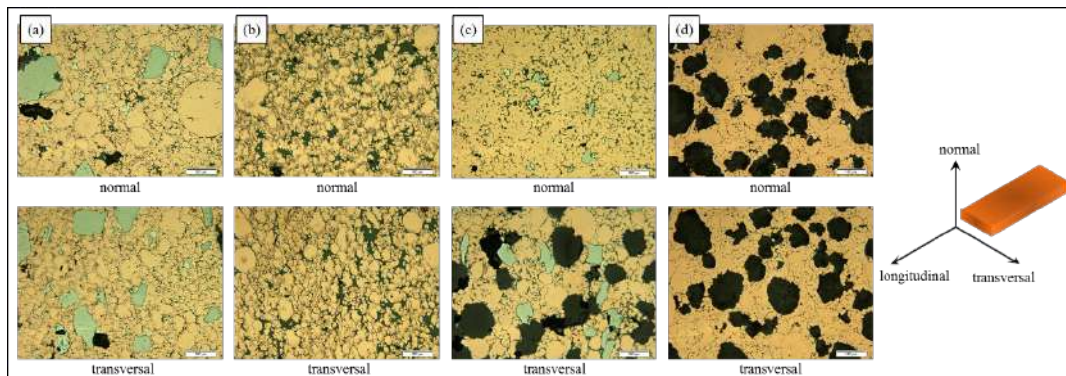
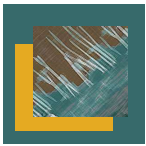


Figure 2: Optical micrographs of the composites Cu-Cr-Ag- (CeO₂, Al₂O₃) in normal and transversal directions, as polished (100 µm scale).



Microstructural Features of Intermetallic Phases of Recycled 6061 Aluminum Alloy Processed by Different Techniques

Leandro Henrique Pereira^{1*}, Lucas Barcelos Otani¹, Diego Davi Coimbrão¹, Claudio Shyinti Kiminami², Claudemiro Bolfarini² and Walter José Botta²

1. Programa de Pós-Graduação em Ciência e Engenharia de Materiais (PPGCEM), CCET, UFSCar, São Carlos, Brazil.

2. Departamento de Engenharia de Materiais, DEMa, UFSCar, São Carlos, Brazil.

*Email: leandrohp@ppgcem.ufscar.br

Controlling of chemical composition is one of the main concerns during recycling of aluminum alloys. Cycles of recycling may lead to increase in the impurity content and consequently affect the final properties of the material. The most common impurity in aluminum alloys is iron, which (because its low solubility in aluminum matrix) leads to the formation of brittle intermetallic phases. The presence of these phases in the microstructure is generally associated with the decrease in mechanical properties not only because of its brittle nature, but due to its morphology as well [1, 2]. Among the alloying elements of the 6061 aluminum alloy, iron and silicon are the most important regarding the mechanical properties. Because of its importance for aluminum alloys, many studies on the Al-Si-Fe system has been done and at least twelve stable intermetallic phases have been reported for this system. Moreover, other metastable phases, that may arise from processing techniques involving high cooling rates, have also been reported. The main intermetallic phases present in the microstructure of recycled 6061 alloy are the cubic α -Al₁₅(Fe,Mn)₃Si₂ and orthorhombic β -Al₉Fe₂Si₂. When the α -Al₁₅(Fe,Mn)₃Si₂ is formed as primary phase, it presents a polyhedral morphology. On the other hand, when this phase is formed during the last stages of solidification it presents a Chinese script-like morphology. The β -Al₉Fe₂Si₂ phase is always formed with a platelet-like morphology, which is detrimental for the mechanical properties. For this reason, many efforts are done to avoid the formation of β -intermetallic [3, 4]. The objective of this work is to compare the microstructure of recycled 6061 aluminum alloy processed by different techniques, named: conventional casting in graphite mold, rapid solidification technique using a wedge type copper mold and spray forming. Microstructural characterization was performed by scanning and transmission electron microscopy (SEM and TEM). STEM-EDX mapping and TEM phase mapping using new ASTAR technique were also carried out. Figures 1, 2 and 3 show phase mapping obtained by ASTAR of the conventionally cast alloy, rapidly solidified-alloy (in wedge cooper) and the spray-formed alloy, respectively. The results show that both conventionally cast and rapidly solidified samples presented the α intermetallic with Chinese script-like morphology that is formed during an eutectic reaction with aluminum. However, spray-formed 6061 alloy presented α intermetallic with polyhedral morphology characteristic of primary phase. It was shown that the solidification features of the spray forming technique changes the solidification path of the 6061 alloy, resulting in a different morphology of the α -Al₁₅(Fe,Mn)₃Si₂ phase. This might be interesting from the point of view of recycling.

Acknowledgements: This work was supported by CNPq, CAPES and FAPESP via Projeto Temático - process number 2013/05987-8 (Brazil).

REFERENCES

- [1] B. Kulunk et al., *Fundação e Serviços*, São Paulo, n. 89, p. 32-41, 2000.
- [2] R. Ferro; A. Saccone. In: R. W. Cahn; P. Haasen. (Org.). *Physical Metallurgy*. part. 1, cap. 4, 4. ed. Amsterdam: North Holland, 1996.
- [3] A. Gorny et al., *Journal of Alloys and Compounds*, v. 577, p. 103–124, 2013.
- [4] N. Krendelsberger et al., *Metallurgical and Materials Transactions A*, v. 38, n. 8, p. 1681–1691, 2007.

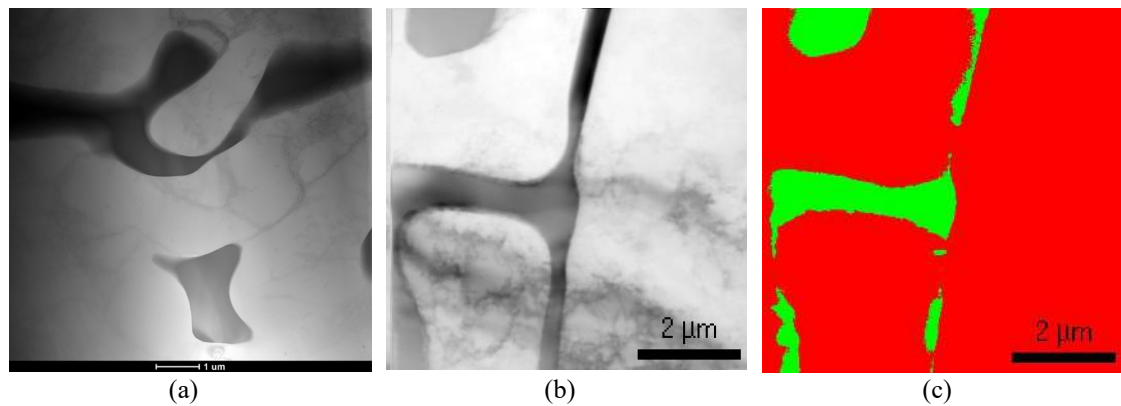
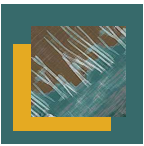


Figure 1: Conventionally cast sample. (a) TEM-Bright field, (b) ASTAR -Virtual Bright field and (c) ASTAR phase mapping (Red: α -Aluminum; Green: α -Al₁₅(Fe,Mn)₃Si₂).

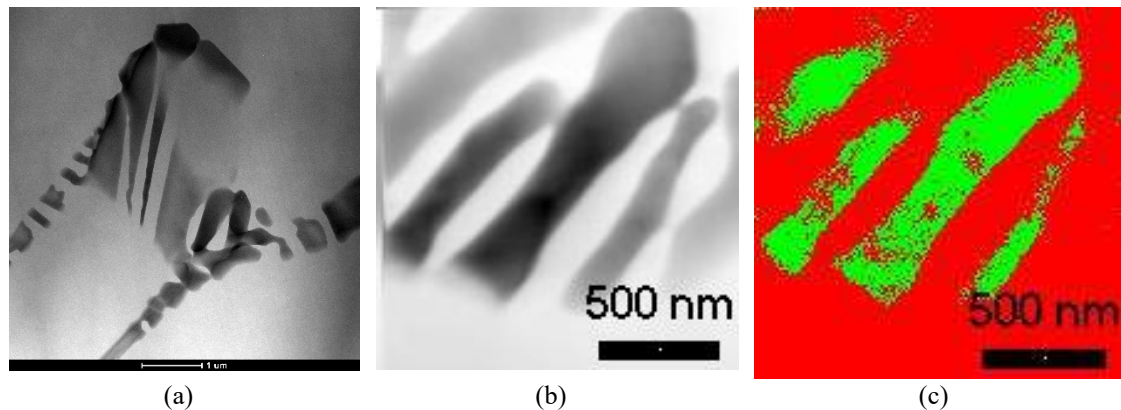


Figure 2: Rapidly solidified sample (wedge-type cooper mold). (a) TEM-Bright field, (b) ASTAR -Virtual Bright field and (c) ASTAR phase mapping (Red: α -Aluminum; Green: α -Al₁₅(Fe,Mn)₃Si₂).

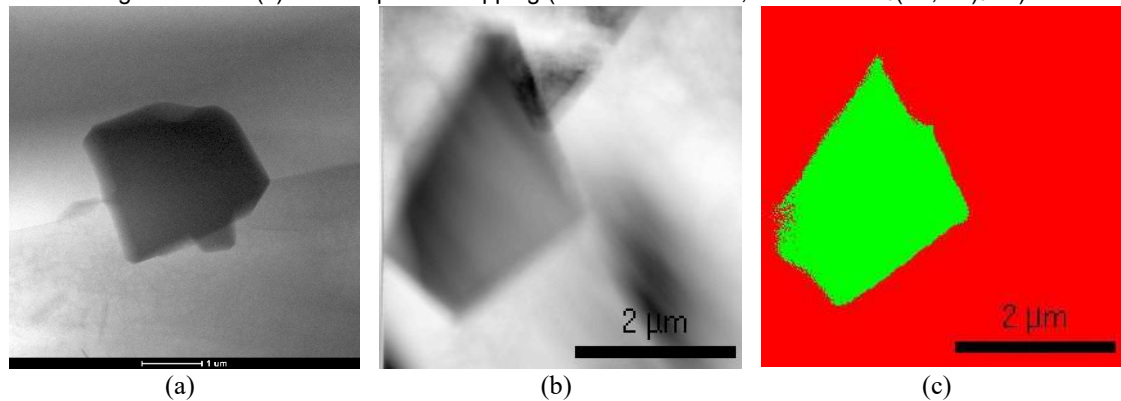


Figure 3: Spray-formed sample. (a) TEM-Bright field, (b) ASTAR -Virtual Bright field and (c) ASTAR phase mapping (Red: α -Aluminum; Green: α -Al₁₅(Fe,Mn)₃Si₂).



Characterization of Al-Cu-Fe-Cr Quasicrystals by Means of EDX Mapping and Electron Diffraction Analysis

W. Wolf¹, E. Segantin^{2,*}, C. Bolfarini², C.S. Kiminami², and W. J. Botta²

1. Programa de Pós-Graduação em Ciência e Engenharia de Materiais, Universidade Federal de São Carlos, São Carlos, SP, Brazil

2. Universidade Federal de São Carlos, DEMa, São Carlos, SP, Brazil

Quasicrystals (QC's) exhibit interesting and very complex atomic structures. They present an aperiodic, however, highly ordered atomic structure. These phases exhibit a variety of interesting properties for application as protective coatings, including high hardness, low friction coefficient, high corrosion resistance in acid medium, high resistance to oxidation and low thermal conductivity. In the present work, Al-Cu-Fe based alloys were produced with addition of Cr in order to assess the influence of Cr addition on the formation of the quasicrystalline phase observed in the ternary alloy. Although there are studies of quasicrystalline phase formation on the Al-Cu-Fe-Cr system, the compositional range of QC formation is not well established as it is for the Al-Cu-Fe system. Master alloys of 5 to 10 g were fabricated by arc melting of high purity (>99.99%) elements. The following atomic compositions were produced: $Al_{65}Cu_{22.5}Fe_{12.5}$, $Al_{65}Cu_{22}Fe_{10}Cr_3$ and $Al_{67}Cu_{20}Fe_5Cr_8$. The choice of chemical composition was based on the average electron concentration per atom (e/a) of the ternary Al-Cu-Fe quasicrystal, which is about 1.8. The as-cast ingots were then melt-spun under argon atmosphere. The velocity of the cooper-wheel used was 30 m/s. The microstructures were characterized by transmission electron microscopy TEM with a TECNAIG2 F20 200kV, coupled with EDX detector. TEM analyses were performed in conventional TEM mode and in STEM mode. The conventional mode was used to obtain crystallographic information of the phases, whereas the STEM mode was used to collect EDX mapping of the phases. Two quasicrystalline phases were observed in the Al-Cu-Fe-Cr system, one is icosahedral and the other decagonal. With increasing Cr content, the decagonal phase appears as the major phase in this system. The results from this assessment of potential quaternary quasicrystalline alloys indicated a promising way of tailoring new quasicrystalline compositions with improved properties such as corrosion and oxidation behavior, by the addition of corrosion resistant elements such as Cr.

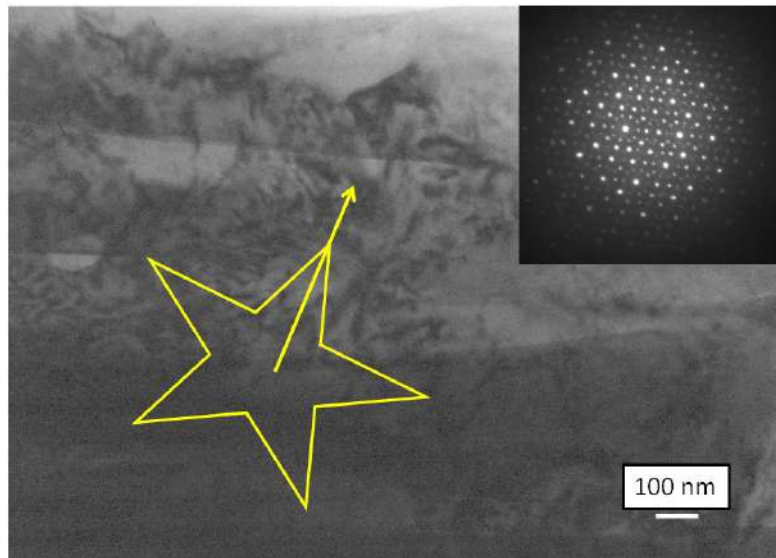
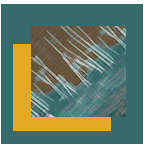


Fig1. TEM micrograph showing the icosahedral phase from the $Al_{65}Cu_{22.5}Fe_{12.5}$ alloy.

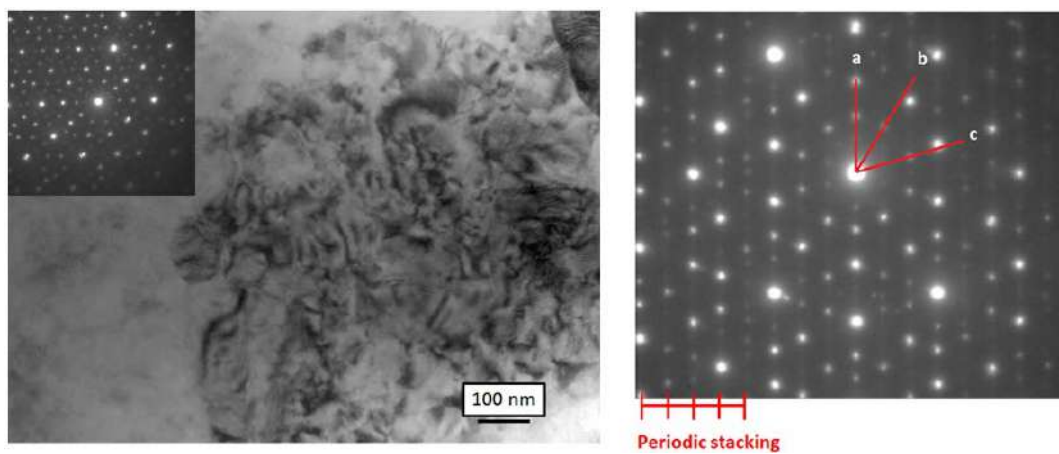


Fig2. TEM micrograph showing the icosahedral and decagonal quasicrystalline phases in the $Al_{65}Cu_{22}Fe_{10}Cr_3$ alloy.



SEM-EDS Characterization of Precipitates in *Eucalyptus* and Sugar Cane Biochars Used in Processes to Decontaminate Water

Erica Martini Tonetto¹, Ricardo Perobelli Borba¹

1. Department of Geology and Natural Resources, Institute of Geosciences, University of Campinas.

In an attempt to evaluate *Eucalyptus* and sugar cane biochar as a reactive material, studies of competitiveness absorption were conducted with polymetallic solutions (Cd, Cu, Cr, Ni, Pb e Zn) within a range of concentrations and pH values [1, 2]. Besides that, experiments with acid mine drainage were also performed [3]. The biochar was mixed, in diverse proportions, with sand to increase porosity and with iron to increase reactivity [1,2]. To characterize the biochar one sample of each, before the experiments, were imaged (Figure 1). After the column experiments [1,2] biochar samples of interest were dried, disaggregated and fractionated. A small fraction of each was deposited in Pelco Tabs (9 mm dia.) in aluminum stubs (12.9 mm dia.). In order to prevent surface charging, samples were coated with 5 nm of carbon (rod carbon coating with a Quorum QT-150T ES). They were then submitted to SEM Zeiss LEO 410i coupled with an EDS Oxford model 7059 (detector area 10mm², res at 5,9 keV of 133 eV). The working distance was 19 mm, EHT 20 kV, and i_{probe} varied from 500 to 3000 pA for images and qualitative EDS analysis, respectively. In the images for the biochar before the experiments (Figure 1) some morphological differences, as well as the presence of silica structures are visible; chemically the EDS spectrum indicates only the presence of C and O. It's worth of mention the considerable number of porous and the significant surface area of the biochar, important features for the experiments. After the experiments it is possible to identify visual differences and qualitative chemical changes in the biochar, for instance: (i) iron oxide crust with metals (Figure 2A); (ii) crystalline structures with the presence of Pb and other metals (Figure 2B); (iii) dispersed fragments of different compounds (Figure 2C); (iv) sand grains with crusts of iron oxide + metals (Figure 2D) and (v) qualitative changes in the biochar composition (Figure 2E). To sum up, the experiments allowed metals to be retained in the columns either in the biochar or in the materials added to it. SEM-EDS technique (images + qualitative microanalyses) were effective to visualize and qualify the particles that showed up to the biochar surface, as well as the presence of metals in the biochar itself.

REFERENCES

[1] Barbosa, P. R. C. ; Borba, R. P. ; Luiz-Silva, W. ; Coscione A. R ; Camargo, Otávio Antônio . Uso do biocarvão de bagaço de cana na remoção de metais pesados de água sob diferentes condições de pH's. In: III Congresso Internacional de Meio Ambiente Subterrâneo, 2013, São Paulo. [2] Barbosa, P. R. C. ; Borba, R. P. ; Luiz-Silva, W. ; Coscione AR ; Camargo, Otávio Antônio . Eficiência do biocarvão na remediação de água contaminada. In: 14 Congresso Brasileiro de Engenharia e Ambiental, 2013, Rio de Janeiro. [3] Relatório de Iniciação Científica de Camila Sayuri Vasconcelos Shibata "Remediação de drenagem ácida de mina com barreira reativa permeável em escala de laboratório"

Acknowledgements: R. P. Borba is thankful to Fapesp (Proc. 2012/02619-5). Images were kindly ceded by Barbosa, P.R.C., Shibata, C.S.V. and Souza, C. C.

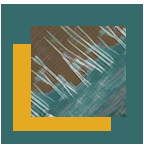


Figure 1 - General aspects of the biochar, *Eucalyptus* (A) and sugar cane (B) biochar before experiments

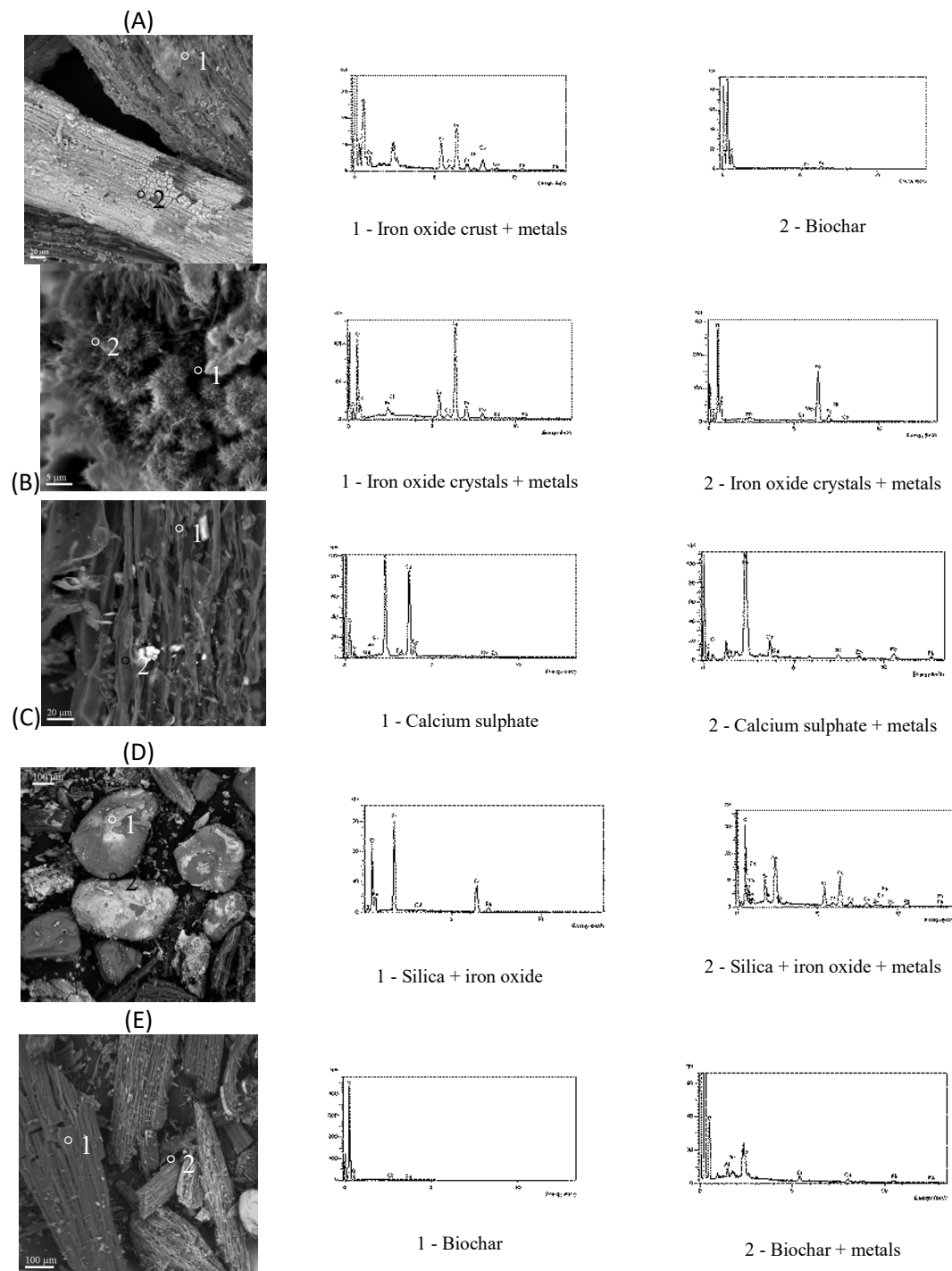


Figure 2 - Biochar images and EDS spectra of the biochar, particles and crystals that showed up after experiments. Note their distinct aspect according to the composition.



An SEM Study of a Low-Temperature Mineral Assemblage Associated With Native Copper Mineralization in the Serra Geral Formation, Nova Prata do Iguaçu, State of Paraná, Brazil

Gianna Maria Garda^{1,*}, Diego Arruda Figueira², Isaac Jamil Sayeg³

1. Dept. Mineralogy and Geotectonics/Geosciences Institute, São Paulo University, São Paulo, Brazil. giagarda@usp.br

2. LiGeA Undergraduate Student/Geosciences Institute, São Paulo University, São Paulo, Brazil

3. Dept. Sedimentary and Environmental Geology/Geosciences Institute, São Paulo University, São Paulo, Brazil

Native copper occurs in the Serra Geral Formation (Paraná Basin, Southern Brazil), both as films in fractures and as blebs in amygdaloids of the basalt flows. In the Vista Alegre district, north of the State of Rio Grande do Sul, native copper is associated with dioctahedral and trioctahedral smectites, zeolites (heulandite and clinoptilolite), quartz, and calcite, which is a typical low-temperature (100–150 °C) hydrothermal alteration assemblage [1]. A similar occurrence, in the region of Nova Prata do Iguaçu (west of the State of Paraná), is the focus of our present study. Minerals filling amygdaloids of the basalt were identified by x-ray diffractometry as cuprite, quartz, goethite, malachite, calcite, feldspar and analcime [5]. Analcime was also recognized in hand specimen by its trapezohedral shape (Fig. 1). Chrysocolla, which was not detected by x-ray diffractometry, is usually blue or green and forms botryoidal masses or coats analcime (Figs. 1 and 2), as described in [2].

A semi-quantitative analysis of both minerals was possible by means of a LEO 440I scanning electron microscope. Operating conditions were 20 kV and 80 seconds of interaction time. The basalt sample containing the minerals to be analyzed was previously coated with carbon.

Figure 3 shows the EDS spectra for analcime 4 and 5 in Figure 2. The intensity of the Na peaks is much lower than the expected for analcime, which is a Na-Al silicate ($\text{NaAlSi}_2\text{O}_6 \cdot \text{H}_2\text{O}$). Table 1 presents the EDS analysis for analcime 1 in Figure 1, which is the closest to that in ref. [3], despite the higher SiO_2 content. An excess of SiO_2 and Al_2O_3 and lower CuO contents were observed in chrysocolla 3 and 6 of Figure 2, when compared to the chrysocolla $[(\text{Cu},\text{Al})_2\text{H}_2\text{Si}_2\text{O}_5(\text{OH})_4 \cdot n\text{H}_2\text{O}]$ composition in ref. [4]. Interestingly, EDS detected Mn in chrysocolla, which may explain the darker tints observed in botryoidal masses (Fig. 1).

Petrography of polished thin sections to be used in future microprobe and LA-ICP-MS analyses has shown that analcime is either replaced or intergrown with feldspar, and was affected by both hydrothermal and supergene alteration.

REFERENCES

- [1] VM Pinto, LA Hartmann and W Wildner, *International Geology Review* 53 (2011), p. 1163–1179.
- [2] MJ Crane, JL Sharpe and PA Willi, *Microsc. Microanal.* 22 (Suppl. 3) (2016), p. 446-448.
- [3] <http://www.handbookofmineralogy.org/pdfs/analcime.pdf>
- [4] <http://www.handbookofmineralogy.org/pdfs/chrysocolla.pdf>

The authors wish to thank Dr. Flávio Machado de Souza Carvalho for obtaining and interpreting the x-ray diffraction data.

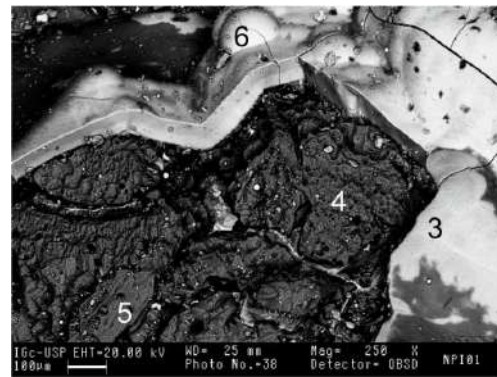
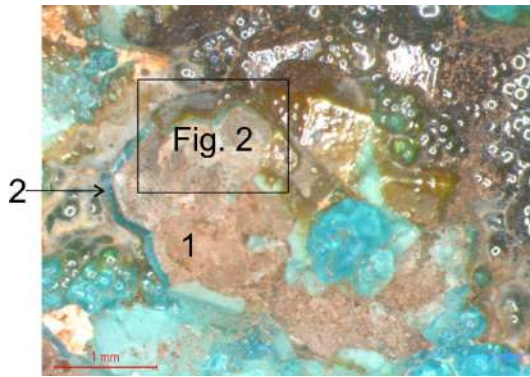
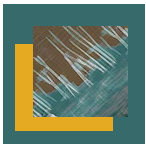


Figure 1. Photograph of an amygdale filled with analcime (1) and blue chrysocolla (2). Observe that chrysocolla can also precipitate around analcime.

Figure 2. BSE image of detail labeled 'Fig. 2' in Figure 1. EDS analyses of chrysocolla 3 and 6 are listed in Table 1 and EDS spectra for analcime 4 and 5 are shown in Figure 3.

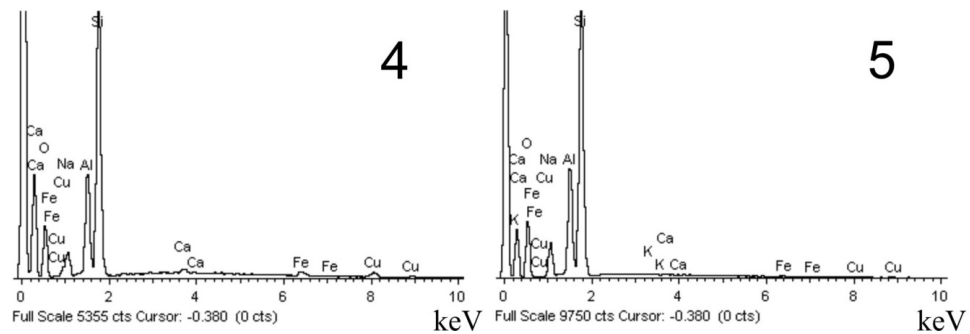


Figure 3. EDS spectra for analcime 4 and 5 in Figure 2. The intensity of the Na peak is much lower than the expected for the ideal $\text{NaAlSi}_2\text{O}_6 \cdot \text{H}_2\text{O}$ formula.

Table 1. EDS analysis of analcime 1 in Figure 1 and chrysocolla 3 and 6 in Figure 2.

analcime	1	ref. [3]	chrysocolla	3	6	ref. [4]
Na ₂ O	10.78	11.08	MgO	0.77	1.04	0.47
MgO		0.1	Al ₂ O ₃	5.13	6.92	1.91
Al ₂ O ₃	21.62	23.12	SiO ₂	48.12	55.90	39.48
SiO ₂	66.71	54.19	K ₂ O	0.18		
K ₂ O		1.62	CaO	1.56	2.07	0.52
CaO		1.54	MnO	2.74	9.47	
Total 1	99.11	91.65	Fe ₂ O ₃			0.13
H ₂ O+		8.2	CuO	26.39	27.70	46.93
Total 2		99.85	Total 1	84.89	103.10	89.44
			H ₂ O+			8.29
			H ₂ O-			1.31
			Total 2			99.04



Effect of Surface Irregularity in the SEM-EDS Analysis of Ca-Mg Carbonates

Hannah Larissa Siqueira Matos^{1*}, Ivan Mendes Caixeta de Pamplona Araújo¹, José Affonso Brod¹, Jesiel Freitas Carvalho¹.

1. Centro Regional para o Desenvolvimento Tecnológico e Inovação (CRTI), Universidade Federal de Goiás (UFG), Goiânia – Brazil.

*Email: hannah.matos@gmail.com.

The microanalysis of mineral phases on irregular surfaces by Energy Dispersive X-ray Spectroscopy (EDS) may be subjected to interference in the detection of X-ray photons that may compromise the accuracy of the results. In some cases, due to the position of the analyzed surface relatively to the detector, signal suppression of light elements may occur. If the analyzed sample has an irregular topography and the detector is mounted obliquely, it is likely that some portion of the sample will be in the path of the X-rays, thus resulting in signal absorption and consequently low analytical results. The intensity of absorption follows an exponential attenuation law given by [1]:

$$I = I_0 e^{-\left[\frac{\mu}{\rho}\right]x}$$

where (μ/ρ) is the mass attenuation coefficient, ρ is the sample density, and x the mass thickness, obtained by multiplying the density (ρ) by the sample thickness (t). In the case of irregular surfaces, adjustments can be made by changing the working distance, tilt or rotation of the specimen relatively to the EDS detector, in order to compensate for the effects of topography in signal detection [2]. In the present case-study we observed a dolomite rhombohedron (Figure 1) analyzed by EDS compositional mapping and line scan in a JEOL *JSM-IT300* scanning electron microscope, equipped with an OXFORD *X-MaxN* X-ray detector. The sample composition appeared to vary from one face to the other (Figure 2) with no otherwise indication of compositional zoning. The crystal face pointed to the detector yielded a typical dolomite $[\text{CaMg}(\text{CO}_3)_2]$ composition, but the face opposite to the detector showed a composition closer to calcite $[\text{CaCO}_3]$, a carbonate that often occurs associated with dolomite in nature. Figure 3a shows that this was produced by a strong suppression of the Mg signal, whereas the Ca signal was mostly unaffected. In fact, the apparent difference in composition is topography-related, due to that the mass attenuation coefficient of dolomite for the energy of Mg K_α line (1.253 keV) being about 10 times greater than that of Ca (3.690 keV). So, the effect of the optical length path for the characteristic X-ray from Mg is more prominent, resulting in the apparent compositional difference. The mass attenuation coefficients of dolomite for both energies were calculated using the values of corresponding coefficients for individual atoms [1] and their weight fractions in dolomite. The effect of a 20° tilt in favor of the detector is illustrated in Figure 3b, where the difference between signals from both cations is smaller, confirming the topographic effect. This case-study illustrates how drastic the effect of surface irregularities on the results of SEM-EDS compositional analysis can be.

[1] <http://physics.nist.gov/PhysRefData/XrayMassCoef/>

[2] K.P. Severin, *Energy Dispersive Spectrometry of Common Rock Forming Minerals*, Kluwer Academic Publishers, Netherlands, 2004.

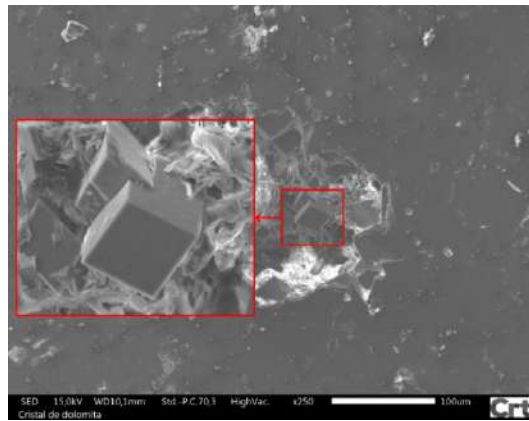
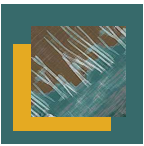


Figure 1. Secondary electron image of the dolomite crystal.

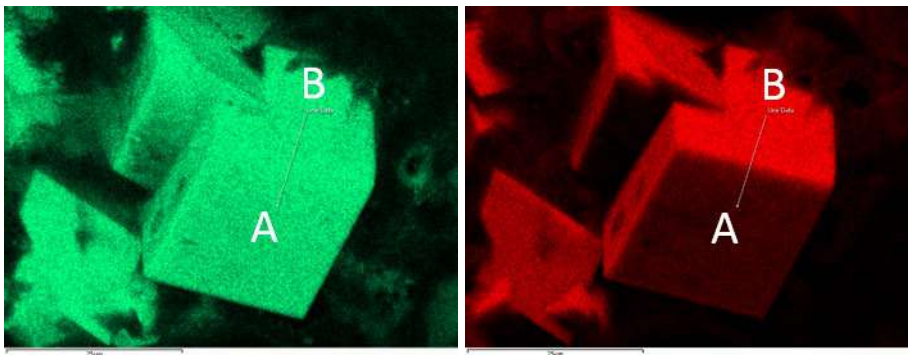
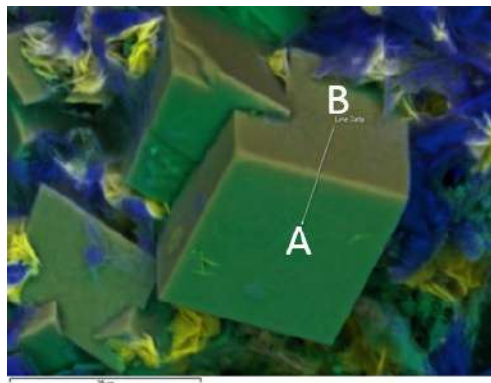


Figure 2. Compositional map on a dolomite crystal (Ca green and Mg red).

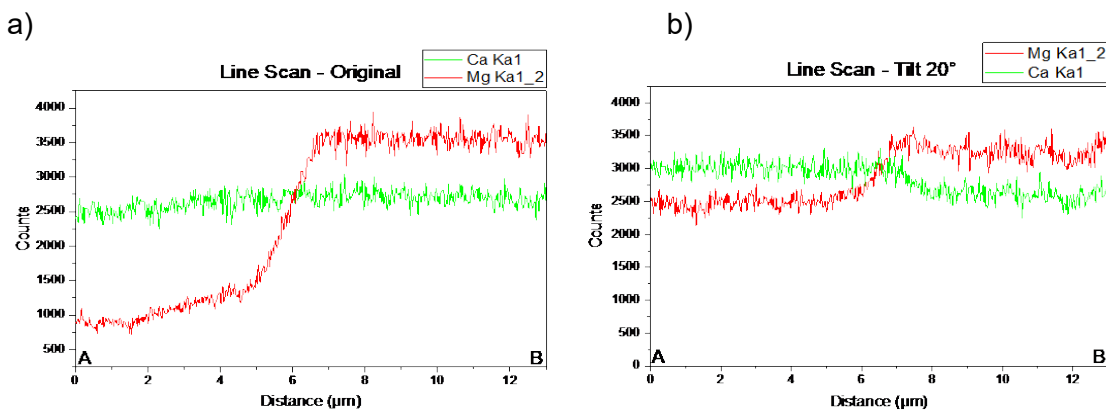


Figure 3. EDS Line Scan of dolomite crystal in original position (a) and 20° northward tilt (b).



Investigation of PBAT/TPS Compatibilized Blend Morphology

Hugo C. Loureiro^{1*}, Laura C. E. da Silva¹, Maria do Carmo Gonçalves¹

1. Institute of Chemistry, University of Campinas (UNICAMP), Campinas, Brazil

*Email: hugo@iqm.unicamp.br

Blending thermoplastic starch (TPS) with poly(butylene adipate-co-terephthalate) (PBAT) provides mechanical stability to thermoplastic starch while reducing the overall costs of PBAT based materials[1]. However, these blends are immiscible and incompatible due to TPS hydrophilic character in contrast to PBAT hydrophobic character. In order to obtain blends with improved mechanical properties, compatibilization is required[2]. Therefore, the aim of this work is to investigate the PBAT/TPS blend compatibilization, through reactive extrusion using citric acid (CA) and triphenyl phosphite (TPP) as compatibilizers. The effects of processing time and screw speed on the blend morphology were also evaluated. Before extrusion, starch was mixed with glycerol (35 wt%), citric acid and triphenyl phosphite (1 wt% and 0,5 wt% total blend, respectively) and left to sit at 60 °C for 16 hours. PBAT/TPS (70/30) blends were prepared in a DSM Xplore twin screw extruder at 130 °C. The morphology of the cryogenically fractured blends was examined in a Jeol JSM6340 field emission scanning electron microscope. Blends showed bimodal domain size distributions with larger domains corresponding to partially plasticized starch (starch granule core and TPS shell) as well as TPS nanodomains (Figure 1). These results indicate that, during extrusion, the starch plasticization was carried out from outside to inside the granules, forming TPS shells that were sheared and broken up into smaller domains. In addition, a low adhesion between TPS and PBAT phases was observed in the non-compatibilized blends, indicated by starch granules detachment during sample fracture (Figure 1a). This lack of adhesion can be attributed to the low affinity between TPS and PBAT. An increase in the extrusion processing time and screw rotation speed improved plasticization. As a consequence, the non-compatibilized blend showed increased disruption of the starch granules, while the compatibilized blends presented smaller TPS domains. Furthermore, the screw speed increase promoted a good interphase adhesion in the compatibilized blends, indicated by the presence of large TPS deformed domains. To conclude, blends prepared by reactive extrusion in the presence of citric acid and triphenyl phosphite showed a finer morphology with good phase adhesion, indicating that the combination of them can promote improved compatibility between the PBAT and TPS phases.

REFERENCES

- [1] J. B Olivato *et al.*, *Carbohydr. Polym.* 90 (2012) 159
- [2] J. B. Olivato *et al.*, *Int. J. Food Sci. Technol.* 46 (2011) 1934
- [3] This research was supported by CNPq and FAPESP (Brazil).

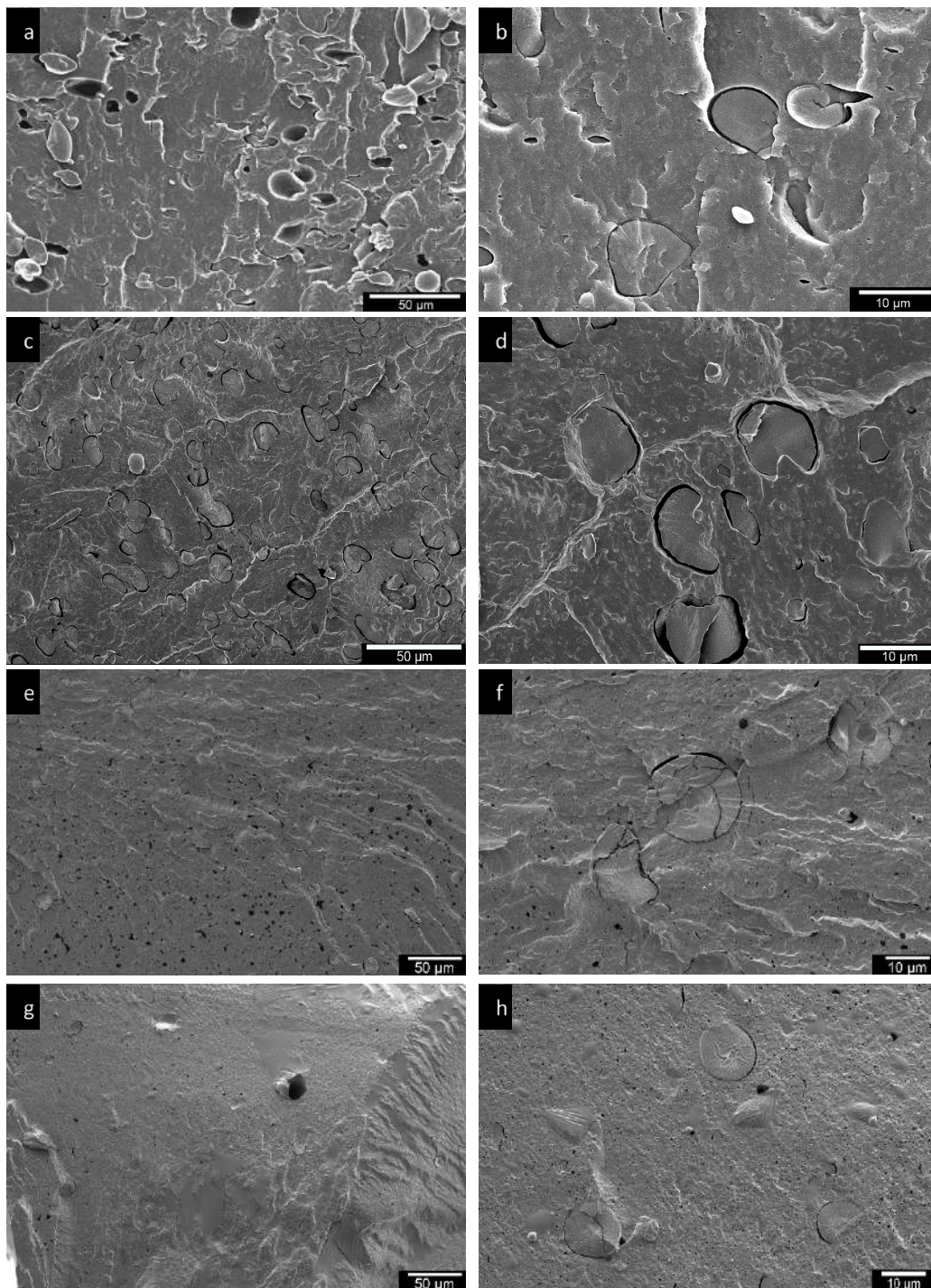
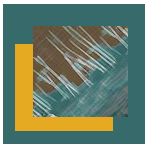


Figure 1: FESEM micrographs of cryogenically fractured cross sections. **a** and **b** PBAT/TPS – 100 rpm, 3min; **c** and **d** PBAT/TPS – 200 rpm, 6min; **e** and **f** PBAT/TPS/TPP/CA – 100 rpm, 3min; **g** and **h** PBAT/TPS/TPP/CA – 200 rpm, 6min



A new protocol for quantification of inter-particle spacing caused by thiol self-assembled monolayers using transmission electron microscopy

Jairo P. Oliveira¹, Adilson R. Prado², Wanderson J. Keijok¹, Rafaela Spessemille Valotto¹, André R. Silva³, Breno V. Nogueira¹, Marco C. C. Guimarães^{1*}

1. Federal University of Espírito Santo, Av Marechal Campos 1468, Vitória, ES 29.040-090, Brazil

2. Federal Institute of Espírito Santo, km 6.5 ES 010, Serra, ES 29173-087, Brazil

3. Federal Institute of Espírito Santo, Av. Morobá, 248 - Morobá, Aracruz, ES, 29192-733, Brazil.

*Email: marco.guimaraes@ufes.br

Nano-*surface modification* techniques have been increasingly reported in a multitude of applications. However, the metal-ligand interface can be difficult to characterize, mainly due to the inadequacy of analytical methodologies. Here, we analyse this interface using transmission electron microscopy, which can determine the thickness of the linkers. This work presents a comprehensive physical characterization of gold nanoparticles with modified surfaces using conventional transmission electron microscopy. We have successfully demonstrated a simple and reliable protocol for the quantification of inter-particle spacing caused by SAM thiol ligands bound onto AuNPs. This approach is based on the linear correlation of the distance between the gold nanoparticles and the length of 3-mercaptopropionic acid (MPA), 11-mercaptoundecanoic acid (MUA) and 16-mercaphexadecanoic acid (MHA). We have shown how the thickness of the monolayer of nanomaterials can be determined by conventional transmission electron microscopy. Moreover, the method of preparation for TEM was also discussed, taking into account the influence of the drying mechanisms to improve the distribution of the colloids in the grid. Finally, our results open new perspectives for the study of the functionalization of nanomaterials with different chain sizes using conventional TEM for quantification, encouraging the study of such modified surface nanomaterials for a plethora of applications.

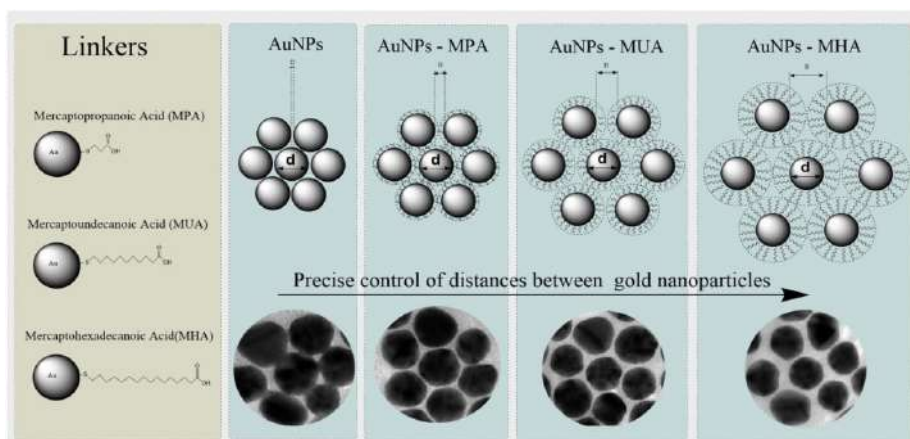


Figure 1. Scheme showing the particle diameter (d) and the distance between the metal cores (D) promoted by the thickness of the coordination sphere as the ligand length increases; From left to right: AuNPs without ligands; AuNPs-MPA with 3-carbon spacing; AuNPs-MUA with a spacing of 11 carbons and AuNPs-MHA with a spacing of 16 carbons

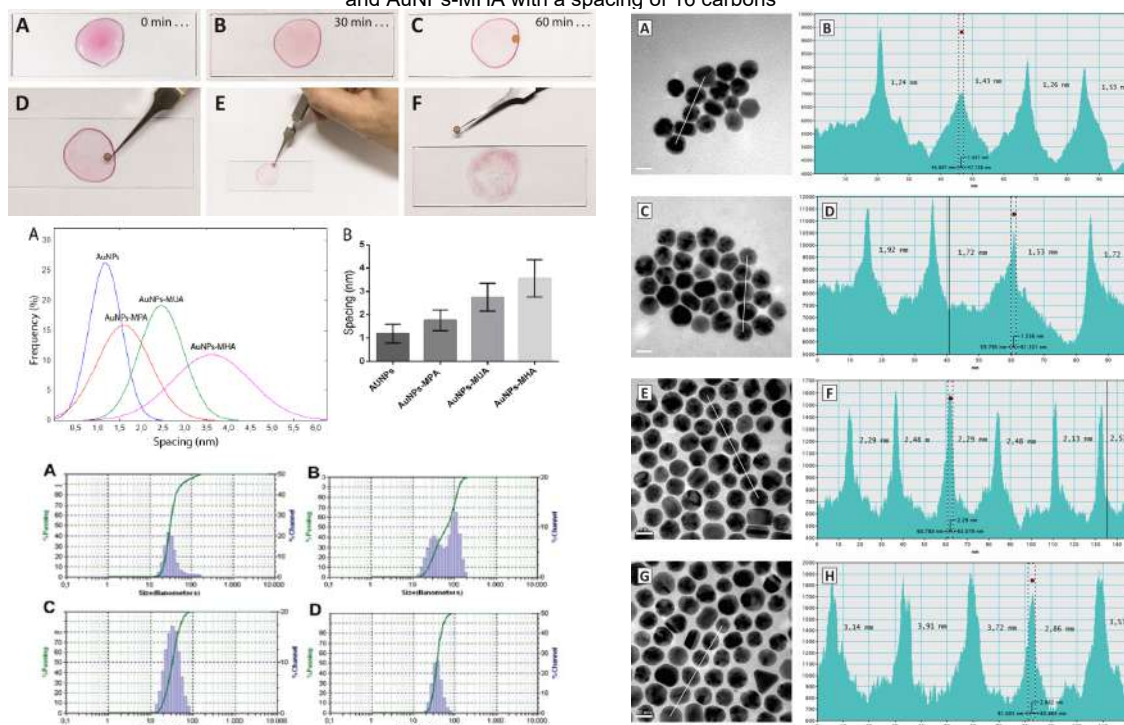


Figure 2. Images showing the sequence of the grid preparation. The first step is demonstrated in A, where the colloidal suspension of AuNPs was dripped on the centre of a glass slide; after a resting time, the formation of the coffee ring at the edge of the droplet (B-C) is observed; a grid previously covered with a hydrophobic formvar polymer is placed on the drop (C); the grid is carefully passed over the entire ring formed to recover as many AuNPs as possible (E); the final drying can be observed in F. **Figure 3.** Histogram showing the spacing between functionalized gold nanoparticles with different spacers: AuNPs (A); graph showing the deviations found for each spacer (B), mercaptopropionic acid (MPA), mercaptoundecanoic acid (MUA) and mercaptohexadecanoic acid (MHA) and gold nanoparticles without ligands (AuNPs). **Figure 4.** Distribution histogram from DLS of gold nanoparticles with different ligands. On the abscissa, we have the sizes of the nanoparticles (in nm), and on the ordinate, we have the percentages (relative frequency) of particles in the respective size bands. AuNPs (A); AuNPs-MPA (B); AuNPs-MUA (C); AuNPs-MHA (D). **Figure 5.** Examples of images obtained by transmission electron microscopy to determine the spacing between the particles using Digital Micrograph software. The white line shows where the spacing data were obtained in each image. The histograms show the regular spacing between the particles for all assays in the corresponding order. AuNPs without binders (A, B); AuNPs functionalized with mercaptopropionic acid (AuNPs-MPA) (C



Hydrothermal Synthesis of Magnesium Silicates

J. F. Carvalho^{1,2*}, E. M. R. Bosco¹, S. P. Marcondes¹, I. M. C. P. Araújo¹, L. J. Q. Maia², and J. A. Brod¹

1. Centro Regional para o Desenvolvimento Tecnológico e Inovação (CRTI), Universidade Federal de Goiás (UFG), Goiânia, Goiás, Brazil. carvalho@ufg.br.
2. Instituto de Física, Universidade Federal de Goiás, Goiânia, Goiás, Brazil.

The aim of this work was the study of formation conditions and stability of Mg-silicates, like talc and stevensite, in various systems with carbonatic compositions under hydrothermal conditions, and characterize the synthetic product concerning their chemical and crystallographic properties. Stevensite is a Mg-silicate with general composition $(Ca,Na)_xMg_{3-y}(Si_4O_{10})(OH)_2$ [1], and talc has general formula $Mg_3Si_4O_{10}(OH)_2$ [1]. The synthesis of interest materials was carried out by the hydrothermal synthesis method, at temperatures in the interval of 90 to 170 °C during 5 hours. A microwave heated commercial equipment *CEM Mars 6*, equipped with hermetic vessels with *Teflon*[®] internal walls was used. Different chemical environments were tested during the synthesis procedures, like Mg/Si ratio, concentrations of Ca and Na, solution salinity (NaCl), and pH values (8-14). The best results concerning the synthesis of the target phases were obtained for the Mg : Si : Ca : Na molar ration of 3.3 : 4.0 : 0.2 : 0.4, pH values between 8 and 9, and temperature in the interval of 130 to 170 °C. The temperatures closer to 130 °C favor the formation of stevensite, while the formation of talc is preferred in higher temperature conditions. Calcite crystals were grown for pH higher than 9, like those shown in Figure 1(B). Also, for high salinity solution (2.4 wt%) halite crystals were formed. The microstructures of the Mg-silicates synthesized in different physico-chemical conditions were analyzed by using a field-emission scanning electron microscope (FEG-SEM) *JEOL JSM-7100 FT*, with samples prepared by direct deposition of dilute suspension on a flat conducting substrate, dried at room temperature and coated with conductive film. Figure 1 shows the secondary electron images of four samples. WDS analysis was carried out in the sample SC00026 using a *JEOL JXA 8230 Electron Microprobe*. The material was dried, compacted, embedded into a disc and coated with Carbon prior the measurements. The results indicate a Mg-silicate with composition close to talc. WDS analysis also indicated that the material has a humidity of approximately 8% and elevated concentrations of Na and Cl. When calculating the structural formula considering 22 oxygens, there is an excess charge of interlayer cations (Na basically) not expected in Talc structure. This was interpreted as the presence of a Sodium Chloride (NaCl) crystals microscopically associated with the synthetic Mg-silicate. Similar analysis was done in stevensite samples. X-ray powder diffraction was done to characterize the crystal phases using a *Bruker D8 Discover* diffractometer, equipped with a *Johansson* monochromator for $K\alpha_1$ radiation of a copper tube, and a unidimensional *Lynxeye*[®] detector. Figure 2 shows the diffractograms of two characteristics samples of synthetic Mg-silicates and calcite crystals formed during the hydrothermal synthesis.

[1] Anthony, J. W., Bideaux, R. A., Bladh, K. W., Nichols, M. C., Handbook of Mineralogy, Mineralogical Society of America, Chantilly, VA 20151-1110, USA. <http://www.handbookofmineralogy.org/>.

Acknowledgements: This work was supported by the project Silcarb/ANP/Petrobras (Brazil).

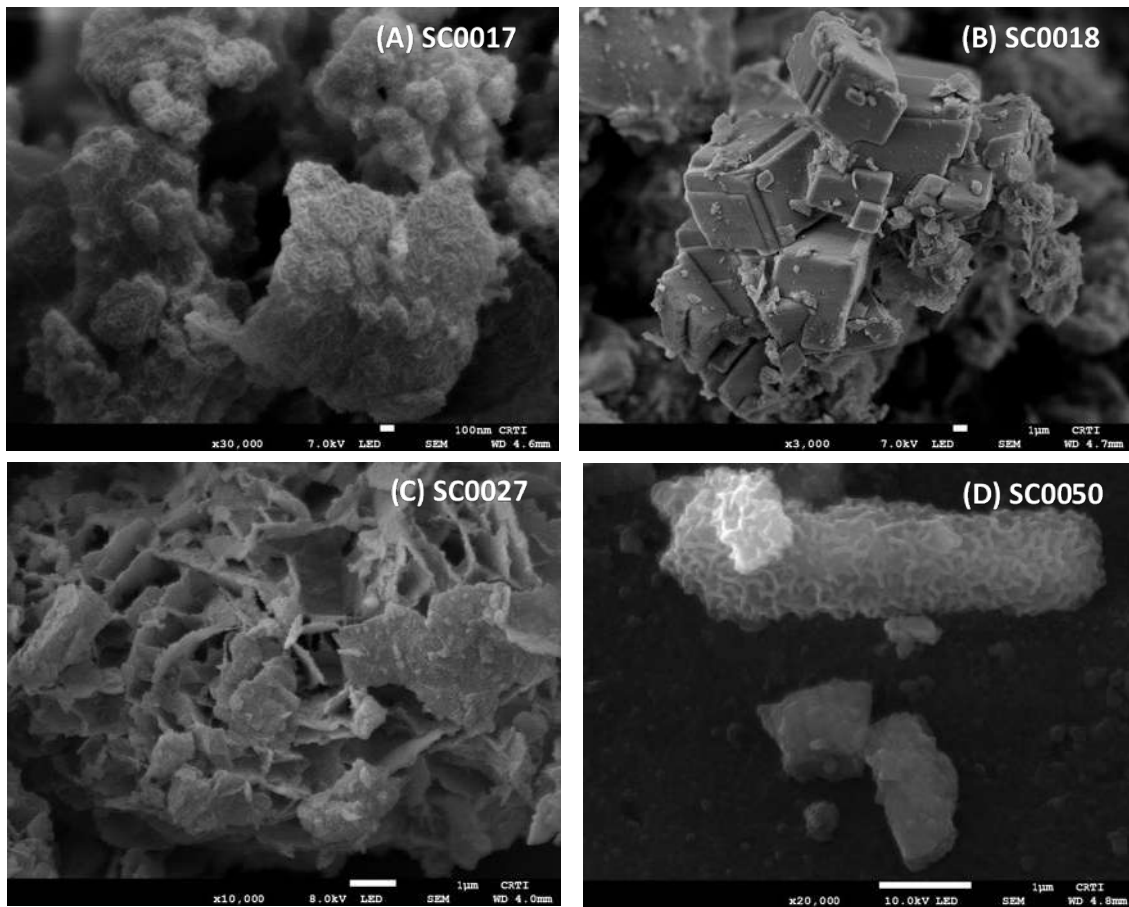
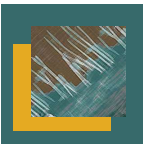


Figure 1 - Secondary electron images showing microstructural characteristics of synthesized samples. (A) Lamellar agglomerates with elongated structures of dimensions in the order of 100 nm, with composition of Mg-silicate; (B) Calcite microcrystals with deposit of small Mg-silicate plates; (C) Lamellar agglomerates of Mg-silicates; (D) Cylindrical agglomerate of elongated nanometric structures with Mg-silicate composition.

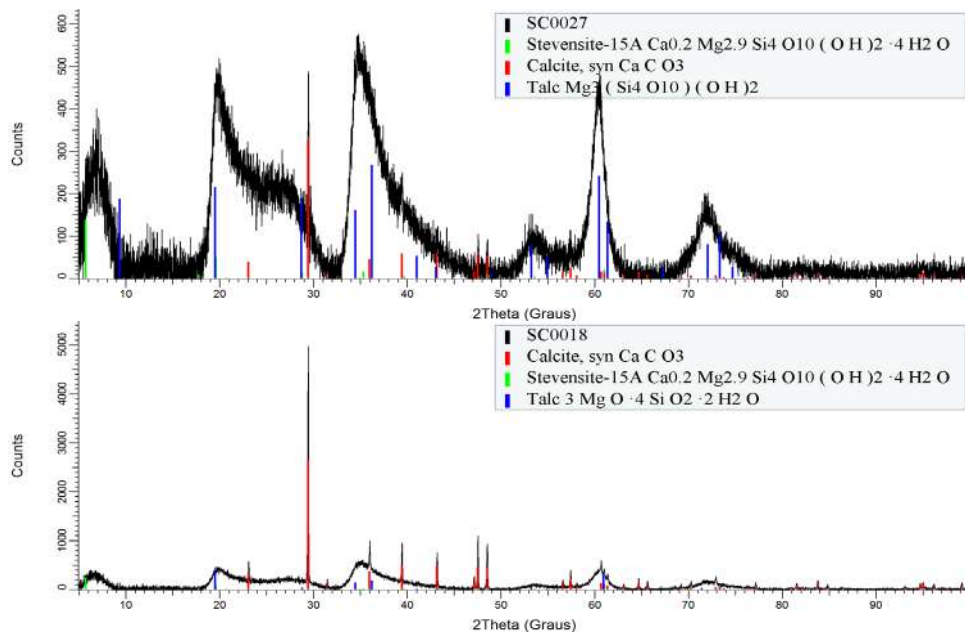
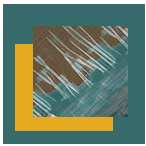


Figure 2 - Diffractograms of SC0018 and SC0027 samples of synthetic Mg-silicates with calcite crystals formed during the hydrothermal synthesis.



Internal Structure And Morphology Of Zircon Grains On Recent Sediments From The Amazon River Mouth: SEM (Back Scattered and Cathodoluminescence) images and Implications On LAICPMS Technique

Juliana Fernandes Bonifacio^{1*}, Armando Dias Tavares¹, Mauro Cesar Geraldes¹, Letícia Muniz da Costa Cardoso¹, Marcio Inácio Alves¹.

1. Universidade do Estado do Rio de Janeiro, Faculdade de Geologia, Rio de Janeiro, Brazil.

*Email: juliana_bonifacio@hotmail.com

The scanning electron microscope (SEM) is one of the most versatile instruments available for the examination and analysis of the microstructure morphology [1]. It is used on analysis of structures, microfractures, inclusions and zoning in mineral crystals. Usually, the magnification for mineral analysis is around 10,000 times. In this technique, an area is targeted by an electron beam, and as a result of the interaction with the surface of the sample, several radiations are emitted: secondary electrons, backscattered electrons, characteristic X-rays, Auger electrons, among others. Such radiations, when captured correctly, will provide information regarding the material being analyzed. In the present study, recent sediment samples were collected at the mouth of the Amazon River with the purpose of identifying main rock formation events from the Amazonian Craton. The isotopic studies and definition of geochronological provinces are useful for providing a basis for the understanding of crustal evolution processes and their tectonic implications on a continental scale [2]. In summary, this work aims to apply U-Pb analytical techniques on zircon grains for the investigation and understanding of Amazonian Craton crustal provinces. Therefore, the laboratorial procedures start with sediments granulometric classification by sieving (100 mesh), followed by dense liquid separation with bromoform (2.89 g/cm³) in which the heavy portion is later processed using hand magnet and Frantz magnetic separator. The amperages used for zircon magnetic separation were 0.1 A; 0.2A; 0.4A; 0.5A; 0.6A; and over 0.6A (which means the grain was not attracted). Approximately 5g of zircon were obtained and then quartered until around 500 grains were fixed in epoxy and formerly polished. Five images of 50 zircon grains each were taken (figure 1) and the cathodoluminescence imaging in Electronic Microscope allowed the characterization of a large diversity of types of zircon grains. The main groups selected (figure 2) according to their morphology and texture is described as follows: (i) Grains with well defined internal oscillatory zoning (in which layers vary in thickness) were interpreted as a typical growth texture in magmatic processes; (ii) Grains with irregular zoning pattern were interpreted as a result of growth during a metamorphic event; (iii) Grains with convoluted zoning and boundaries between light and dark zones, curved and irregular were interpreted as a result from metamorphic or hydrothermal alteration; (iv) Rounded homogeneous grains were interpreted as formed during a metamorphic (granulitic) event; (v) Grains with core and rim were interpreted to characterize their crystallization in two events. As conclusion, the use of Electronic Scanning Microscopy and the definition of zircon grain types is crucial in LA-ICP-MS analysis, given that the selection of best targets through the incidence of the laser beam (with spatial resolution of 25-30µ) can influence isotopic results and geological interpretations.

[1] W. Zhou et al. Fundamentals of Scanning Electron Microscopy (2007)

[2] C. C.G. Tassinari, M. J.B. Macambira. Geochronological provinces of the Amazonian Craton (1999)

This research was supported by FAPERJ (Brazil)

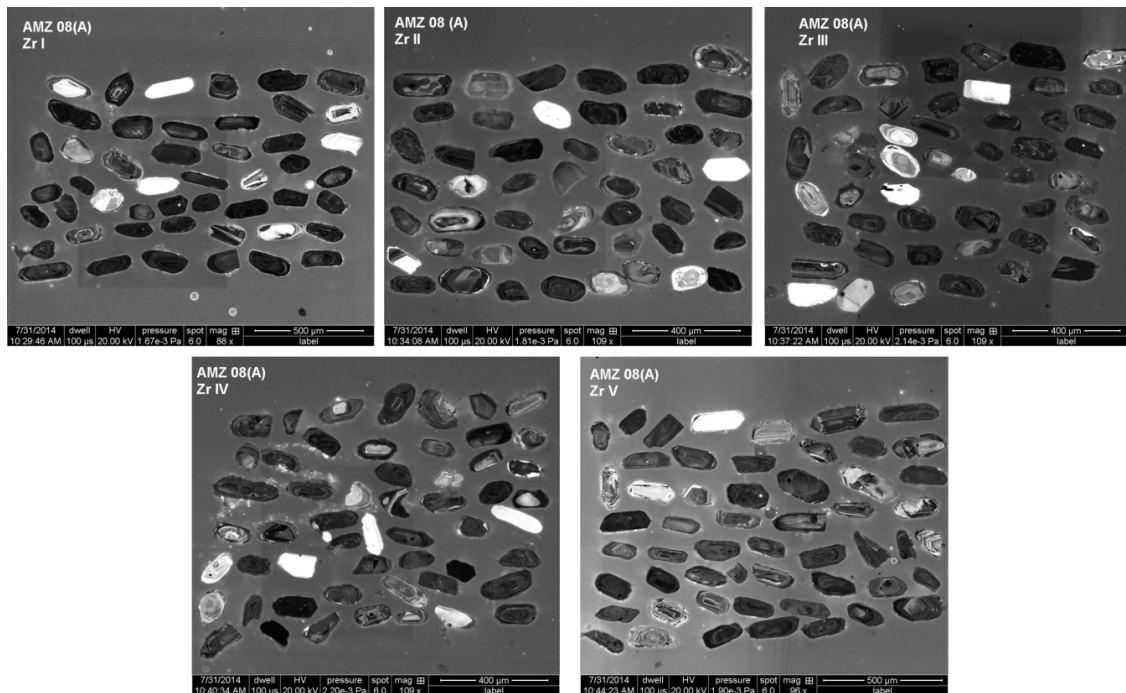
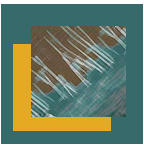


Figure 1 – Cathodoluminescence images of zircon grains using SEM.

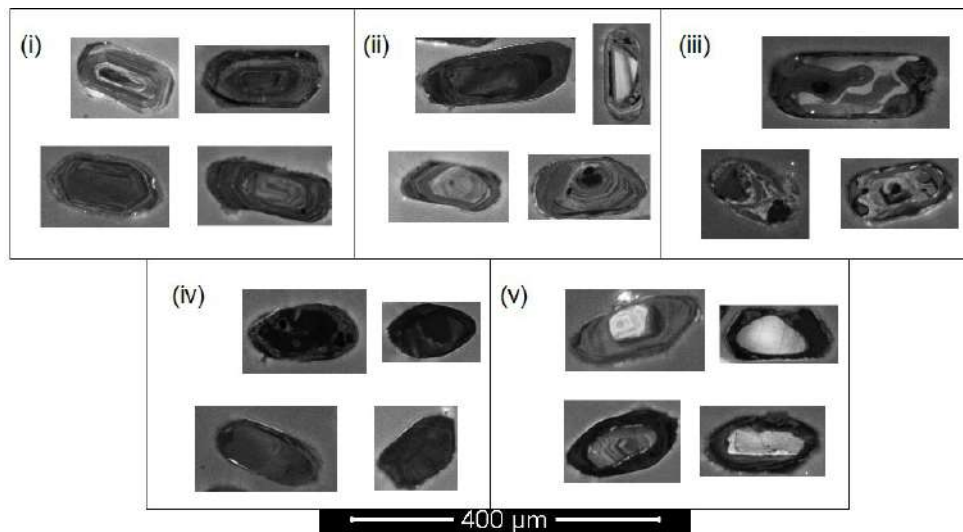
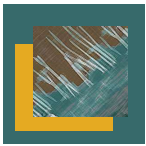


Figure 2 – Groups selected to U-Pb analysis. Morphology description, texture, shape and internal structure are important in order to characterize their formation event ages.



Microscopy Study of Conventional Together with Discontinuous Precipitation in a High Cr-Ni Superalloy

Spadotto, J.C*. and Solórzano, I.G.

Department of Chemical and Materials Engineering, PUC-Rio, Rio de Janeiro, Brazil

*Email: juliofspadotto@gmail.com

Precipitation processes in materials are widely studied because of its direct effect on properties. In addition to conventional precipitation (homogeneous and heterogeneous), discontinuous precipitation (DP) phenomena may simultaneously occur in some alloy systems [1]. While conventional precipitation is a diffusional process through the crystalline lattice, DP in multicomponent system is a grain boundary diffusion-controlled acting as fast reaction path under the action of chemical and capillary forces, leaving behind a regularly spaced array of lamellar precipitates growing cooperatively from the supersaturated matrix [2]. In this study, a DP phenomenon is focused, which takes place in a high performance super alloy 33 with austenitic matrix and chemical composition (wt.%) of 32,75Cr-32,53Fe-31,35Ni-1,49Mo-0,54Cu-0,4N-0,012C-0,63Mn-0,30Si during pre-determined heat treatments. Figure 1A shows the triple point after aging at 700 °C for 10 h where it is possible to observe that the density of precipitates is not the same at all grain boundaries. It is also observed that a boundary with less prominent precipitation allotriomorphs, whereas in the two adjacent boundaries besides grain boundary precipitation occurs the formation of DP colonies, which are indicated by the arrows. This different precipitation behavior is due to individual structural grain boundary structural characteristics, which results in different precipitation kinetics. In Figures 1B and 1C a bright field/centered dark field (BF/DF) pair image of a DP colony developed upon aging at 700 °C for 100 h is shown. The DF image was obtained from the diffracted beam indicated by the red circle of diffraction pattern shown in the insertion. Figure 2 shows DP colony generated during direct-aging at 700 °C for 100 h, which are at an advanced stage of precipitation as compared with the DP colonies shown in Figure 1A. Figure 2A shows a DP colony growing on both sides at the grain boundary, however, in Figure 2B, the colony develops only at one side of the boundary. In both cases, copious conventional grain boundary precipitation also occurred. In the DP colonies, grain boundary migration towards the supersaturated matrix has generated precipitates with several morphologies as well as well-defined lamellae. Such morphological variations indicate the precipitation of more than one phase within the same DP colony, which was confirmed by XEDS microanalysis. The precipitation of more than one phase within the same colony, besides the occurrence of non-lamellar precipitates, is in contradiction with the classical characteristics of the PD phenomena in both binary and multicomponent systems containing substitutional and interstitial atoms so far reported in the literature [2,3,4].

REFERENCES

- [1] P. A. Carvalho et al., *Philos. Mag.*, pp. 1–30, 2007.
- [2] I. Manna et al., *Int. Mater. Rev.*, vol. 46, no. 2, pp. 53–91, 2001.
- [3] R. D. Knutsen et al. *Acta Mater.*, vol. 52, no. 8, pp. 2407–2417, 2004.
- [4] The authors acknowledge are grateful to CBPF for the access to the LabNano Electron Microscopy facilities and to the Brazilian Funding agencies CAPES and CNPq.

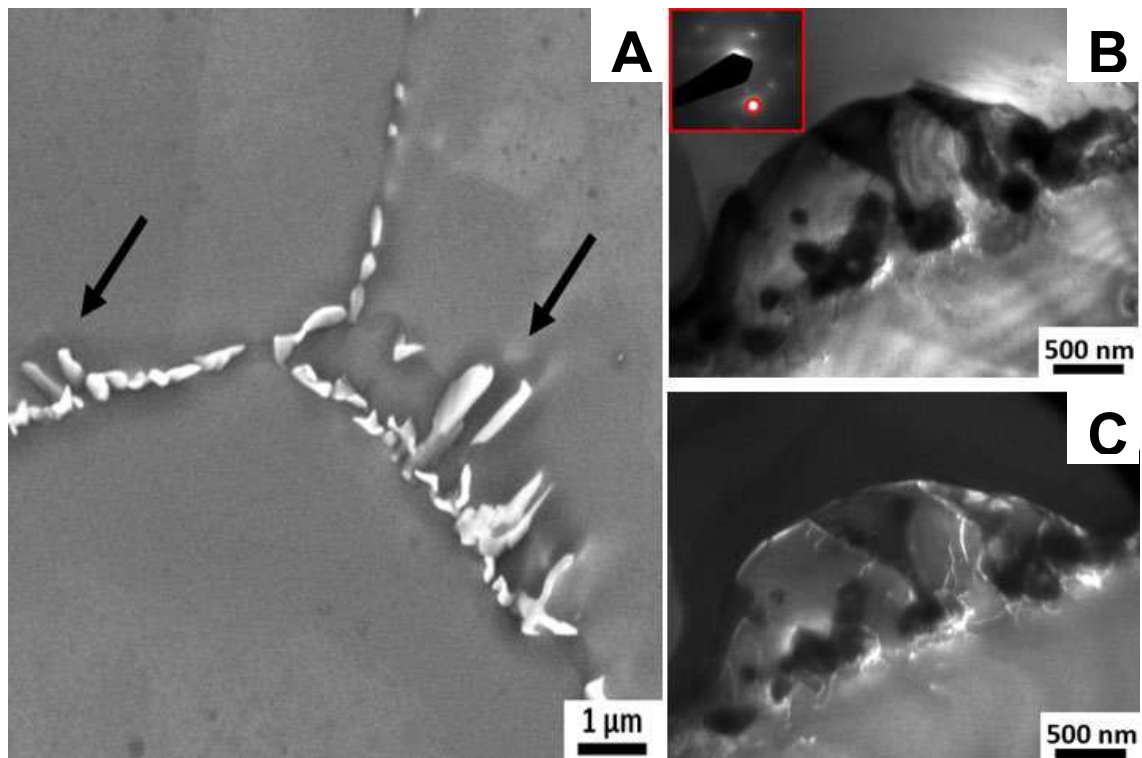
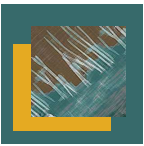


Figure 1 – SEM images of DP colonies resulting of the direct-aging at 700 °C for 10h. (A) Triple point with allotriomorphs in the upper boundary and PD colonies growing to one of the sides of the adjacent boundaries; (B) BF/DF pair image of a DP colony developed upon aging at 700 °C for 100 h.

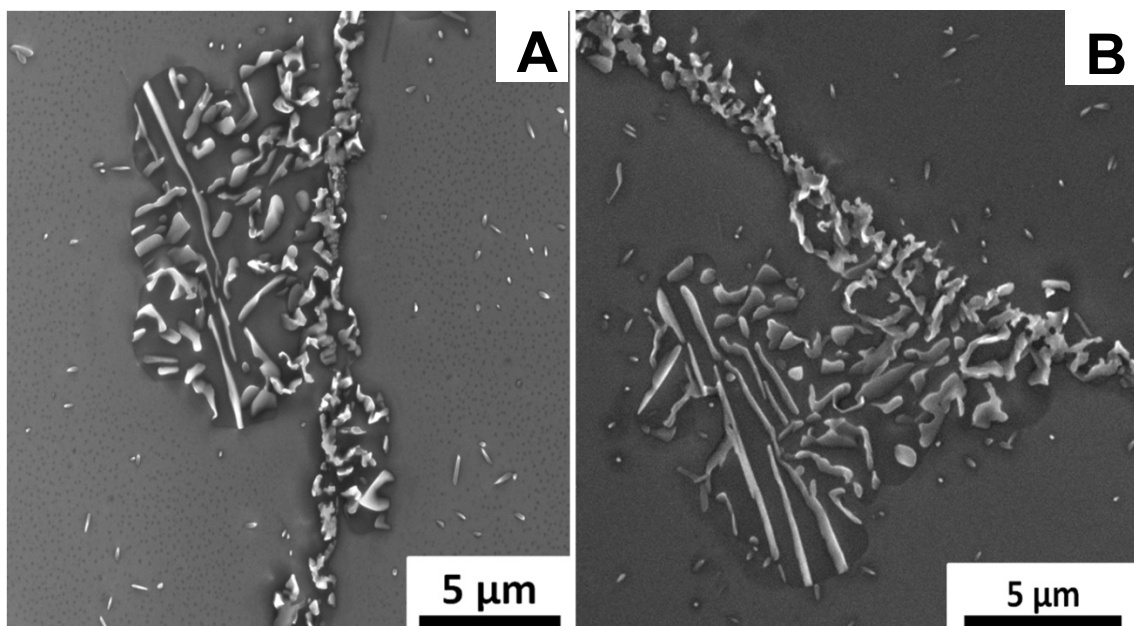


Figure 2 – SEM images of DP colonies resulting of the direct-aging at 700 °C for 100 h. (A) DP colony growing on both sides of boundary and (B) DP colony growing only to one of the sides of the adjacent grain.



Oxidation of Iron Catalyst (ZVI) for Removal of Organic Matter in Present in Surface Water

Santos, N.O.*¹, Spadotto, J.C.¹, Lacombe, M.¹, Solórzano, I.G.¹, Teixeira, L.A.C.^{1,2}

1. Department of Chemical and Materials Engineering, PUC-Rio, Rio de Janeiro, Brazil

2. Peróxidos do Brazil Ltda (Solvay Group)

*Email: naiara.pucRio@gmail.com

Natural organic matter (NOM) may pose a significant impact on the treatment of drinking water, such as odor and taste problems, and the need for a greater dosage of active chlorine-based disinfectants (resulting in the formation of harmful chlorinated organic by-products) [1]. In this work, the oxidative removal of NOM in water was investigated using the application of a solid catalyst (iron), simultaneously to the dosage of a liquid non-chlorinated oxidant. The main advantages of this process are the reduction of costs by the type of catalyst used [2] and the lack of need of special equipment rather than the usual open tanks. The efficiency of the process is dependent on the action of the oxidizing agent on the solid Fe catalyst to form during the chemical reaction highly reactive radicals that can oxidize the target NOM compounds. Studies on iron sheets [3] have shown that the pH, oxidant, and concentration of organic substances are responsible for corrosion of the iron surface. This suggests that the control of iron corrosion in an appropriate range is vital for the development of this water treatment system. In this context, the objective was to evaluate the action of the oxidizing agent on the surface of elemental iron (as steel wool) in acid pH, in order to obtain the removal of the organic matter present in surface waters. To verify the possible oxidation of the Fe catalyst, steel wool was characterized by analytical Scanning Electron Microscopy SEM (JEOL JSM-7100F) in the forms of untreated metal and post-reaction metal. The SEM image shown in Figure 1a presents several wires of steel wool in the untreated condition. In Figure 1b it is observed that the wire surface in this condition does not show prominent oxidation. After the reaction of the steel wool only with the solution containing deionized water was verified the appearance of a small amount of oxidation on the surface of the wire, as shown in Figure 1c. On the other hand, the reaction between steel wool with deionized water together with the oxidizing agent led to almost total oxidation of the material surface, Figure 1d. From 3 regions indicated by the red boxes in Figures 1b, 1c and 1d, representing the 3 different conditions of the samples studied in this work, the elemental compositions have been obtained by means of Energy dispersive X-ray spectroscopy EDS in the SEM. The EDS results confirm the effective action of the reagent (hydrogen peroxide) on the oxidation of steel wool, as shown in the spectra and in the table of Figure 2 [4].

REFERENCES

- [1] Sillanpää, M., 2015. Natural Organic Matter Characterization and Treatment Methods First Edit. IWA, ed., Finland.
- [2] Bremner, D.H. et al. Applied Catalysis B: Environmental, 63(1–2), pp.15–19, 2006.
- [3] Namkung, K.C. et al. Environmental technology, 26(3), pp.341–352, 2010. [4] The authors acknowledge are grateful to Peróxidos do Brazil Ltda (Solvay Group), to CBPF for the access to the LabNano Electron Microscopy facilities and to the Brazilian Funding agencies CNPq.

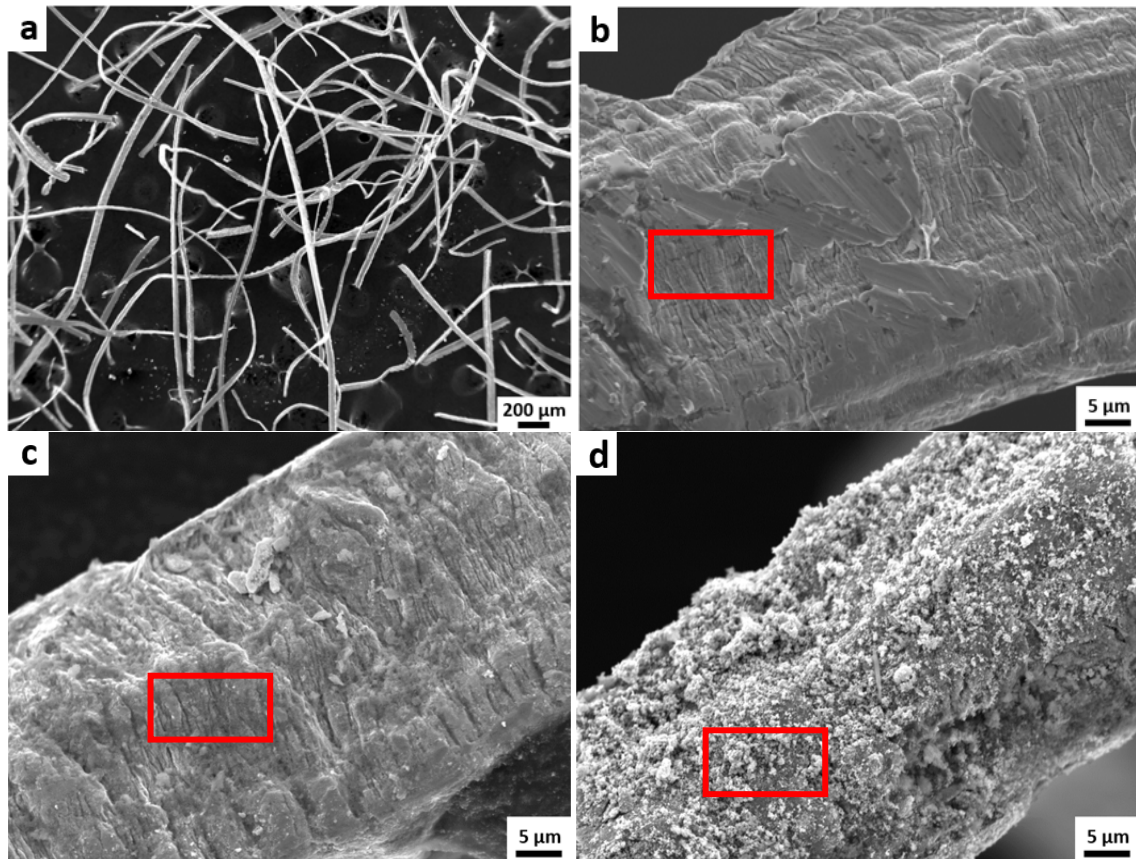
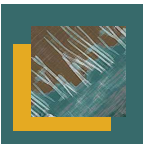


Figure 1 – SEM images of steel wool. (a) and (b) in the as-received condition; (c) post-reaction process with H₂O; (d) post-reaction process with H₂O + oxidizing agent. The red boxes indicate the region of EDS microanalysis.

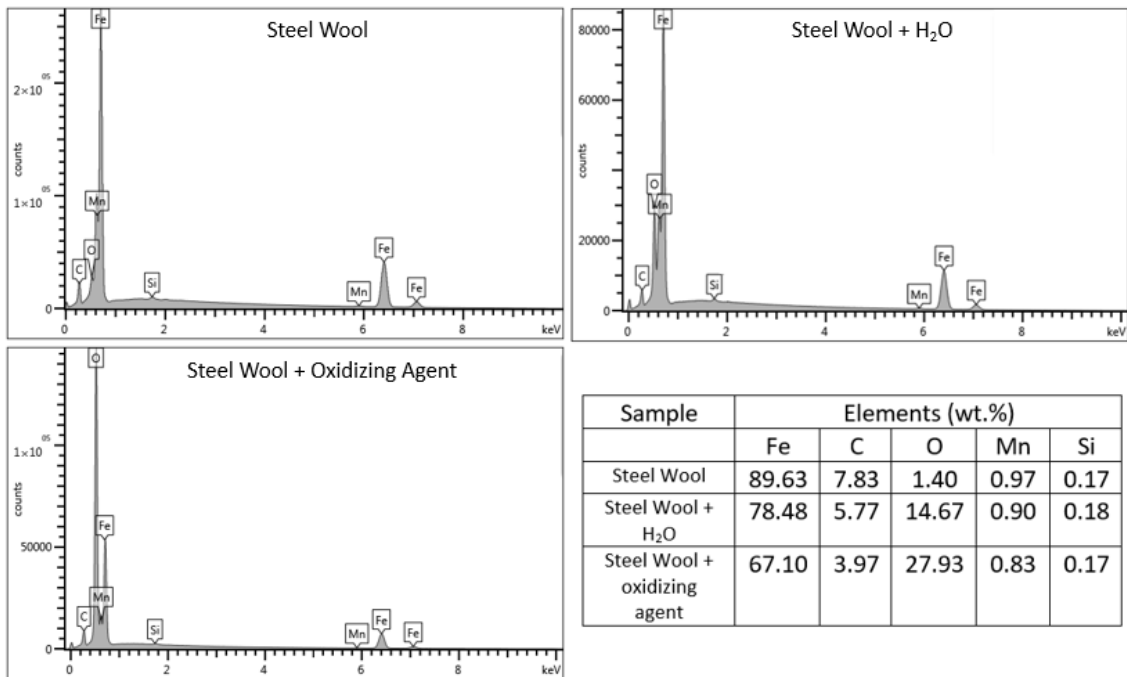
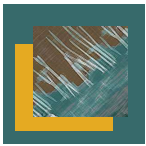


Figure 2 – A set of EDS spectrum obtained from the 3 conditions of samples studied and a table with the mean values of three results obtained from different steel wool wires for each condition.



Microscopy Analysis of a Biocorrosion Degradation of C-Mn Steel

Júnia Ananias^{1*}, Flávio Sandro Lays Cassino², Paulo Henrique Vieira Magalhães³ and Vicente Braz Trindade²

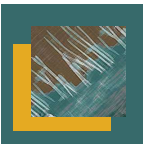
1. Universidade Federal de São João Del Rei, Departamento de Química, Biotecnologia e Eng. de Bioprocessos, Ouro Branco-MG, Brazil. Email: juniananias@gmail.com
2. Universidade Federal de Ouro Preto, Departamento de Engenharia Metalúrgica, Ouro Preto, Brazil.
3. Universidade Federal de Ouro Preto, Departamento de Engenharia Mecânica, Ouro Preto, Brazil.

Since the year of 1991 it was recognized that the huge presence of golden mussel at Rio da Prata in Argentina was causing serious environmental impact on the biodiversity. Since then, its presence was detected in several countries within South America, including Brazil [1]. Several studies have been conducted in order to understand the dynamics of its proliferation as well as strategies to avoid its growing and degradations [2]. One of deleterious effect of the golden mussel is the corrosion of steel structures. Systems such as energy power generation by hydropower as well as ship's hulls are severely affected by the corrosion caused by golden mussel, causing a huge economical losses and safety risks of those components. Therefore, studies aiming to understand the corrosion mechanism of steel in this complex environment are essential for the economy and safety of structures working in presence of this kind of biocorrosion environment.

In order to study the phenomenon of biocorrosion caused by golden mussel, systematic laboratory experiments were carried out using a C-Mn steel exposed to the golden mussel environment to different times, such as 1 month and 6 months, as well as samples from in-service conditions were investigated (exposure of approximately 12 months). The steel used was a ASTM A36 type. All the samples were analyzed using Scanning Electron Microscopy (SEM) combined with EDS. Surface analysis using secondary electrons (SE) and polished cross section observation using back-scattered electrons (BSE) were performed in order to investigate the morphology and the nature of the corrosion products formed in different exposure conditions. Figure 1 shows the macroscopic condition of the samples studied.

On the sample 1 (exposure after 1 month), the surface of a biofilm formed in the presence of the bacteria and others microorganisms can be observed. However, the exposure time (1 month) was not enough for the development of the golden mussel. In this case, the corrosion was homogeneous in the entire surface of the sample. The corrosion mechanism is governed by electrochemical characteristics. On the sample 2 (exposure after 6 months), the golden mussel was developed and reached a size up to 30mm, but in small amount of colonies. The corrosion was more heterogeneous and been more severe in the regions where the golden mussels were present. On the sample 3 (in-service condition, 12 months), a severe corrosion was observed.

Figure 2 shows the different stages of the corrosion process. Figure 2a shows that even without the presence of the golden mussel, the corrosion is driven by the aquatic micro-organisms causing severe corrosion with different corrosion product morphologies. The corrosion product seems to growth by the coalescence of small tubercles, which is typical from the action of iron bacteria also called iron-depositing bacteria that produce orange iron oxide deposits and iron hydroxides. Figure 2b shows the severe corrosion with the presence of iron hydroxide of type $\text{Fe}^{3+}\text{O}(\text{OH})$ [3]. Figure 2c shows the presence of diatomaceous within the corrosion film. Figure 2d shows cross section observation forming different layers of corrosion products as well as the interface steel/corrosion film. The morphological analysis of the corrosion products caused by the golden mussel allowed understanding the basic mechanisms of corrosion process. A synergetic action of at least three types of bacteria was observed, such as sulphate reducing bacteria, iron-depositing bacteria and Fe^{3+} reducing anaerobic bacteria, which produces hydroxide carbonate from magnetite. Cross section



observations have been shown how the steel is corroded, firstly by a kind of internal corrosion followed by complete deterioration of the whole substrate forming a thick corrosion film.

REFERENCES

- [1] G. Darrigran, in Monitoring and Control of Macrofouling Mollusks in Fresh Water Systems, Gerald L. Mackie and Renata Claudi, Editors, 2nd Ed, CRC Press, 2010.
- [2] O.S.M. Neto, Controle da Incrustação de Organismos Invasores em Materiais de Sistema de Resfriamento de Usinas Hidrelétricas, Dissertação de Mestrado, Universidade Federal do Paraná (2001).
- [3] R.A. Antunes et al, Materials Research 6 (suppl. 6) (2003).



Figure 1: Example of the surface condition of the steel ASTM A36 after different exposure conditions.

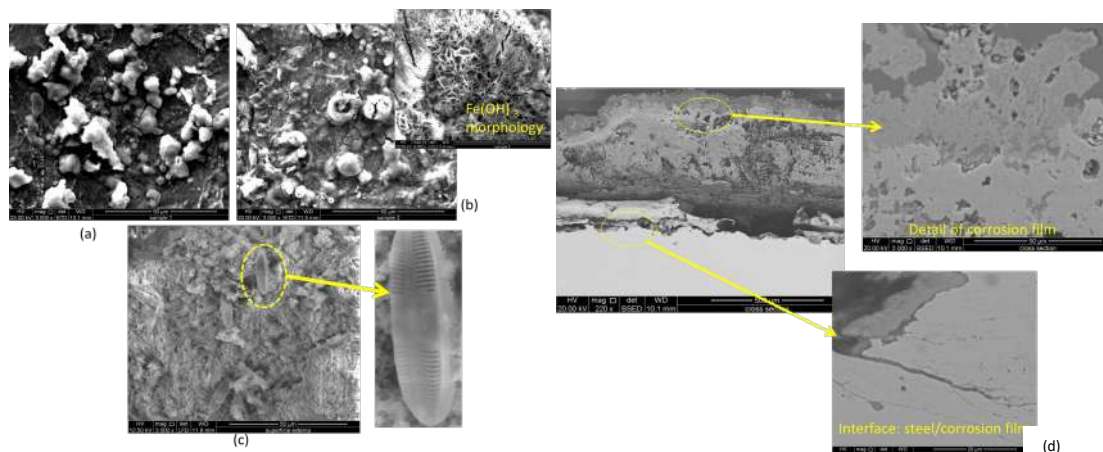
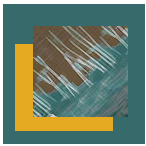


Figure 2: Surface analysis using SEM. (a) after 1 month, (b) after 6 months and (c) after 12 months, (d) cross section observation of the corrosion film using SEM showing the multilayer characteristics and severe attack of the steel surface.



Interdiffusion Zone Evaluation of the System Steel/Inconel 625 Thermal Spray Coating

Júnia Ananias^{1*} and Vicente Braz Trindade²

1. Universidade Federal de São João Del Rei, Departamento de Bioprocesso, Ouro Branco-MG, Brazil. Email: juniananias@gmail.com
2. Universidade Federal de Ouro Preto, Departamento de Engenharia Metalúrgica, Ouro Preto, Brazil.

In the petroleum industry the application of piping is mandatory in many part of the project for the production of oil and gas (upstream) as well as transportation and refining (downstream). Common materials used to produce those pipes are C-Mn steels. However, there are some parts of the project that C-Mn steels are not complying with the project requirements, mainly regarding corrosion due to CO₂, H₂S, chlorides, etc. [1] as well as strong wear and elevated temperature in some cases [2-4]. Therefore, most noble materials are demanded, such as austenitic steels, super alloys and/or composites ultra-high resistant materials. On the other hand, the manufacture of the entire pipe body using those noble materials can affect strongly the cost, since these materials are very expensive compared to C-Mn steels. Therefore, a possible solution is to develop appropriate coatings using these noble materials on surface of C-Mn steel pipes. Thermal spraying is widely used to provide corrosion protection to ferrous metals or to change the surface properties of the sprayed items, such as improve the wear resistance or thermal conductivity. Thermal spray is defined as applying these coatings takes place by means of special devices/systems through which melted or molten spray material is propelled at high speed onto a cleaned and prepared component surface.

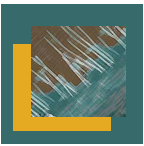
In this study, Inconel 625 was deposited on a C-Mn steel substrate using thermal spray process. Interdiffusion heat treatment were performed in order to improve the adherence of the coating. The temperature used was 900°C and the diffusion time varied from 1h to 10h. The Microstructural characterizations were performed using light microscope and scanning electron microscope (SEM) integrated with energy-dispersive X-ray spectroscopy (EDS). Transversal cuts were done in order to investigate the cross section of the coating and interface coating/substrate (steel). The specimens were prepared by grinding down to 1200 mesh SiC paper followed by polishing in diamond paste of 1 µm and 0.5 µm size, respectively. Etching in Nital 2% was used to observe the substrate microstructure and electrolytic etching (current of 2A and voltage of 10V) with a solution of 10 vol % of oxalic acid (C₂H₂O₄.2H₂O) was used to observe the coating microstructure.

A thinner and uniform Inconel 625 coating was observed as shown in Figure 1. Some contamination of tungsten was observed (white phase in Figure 1). However, the coating can be considered as good quality in terms of phase homogenization and adherence. Furthermore, diffusion treatment was performed in order to improve the coating adherence. As shown in Figure 2, the interdiffusion zone increases as the diffusion time increased.

It can be observed in the Figure 2 that as the interdiffusion time increases, the interdiffusion zone increases, that means the diffusion of Fe in the coating and Ni/Cr in the steel substrate increases. This process shall improve the coating adherence enhancing the in-service life of the component working in harsh environment, e.g. in the oil&gas industry.

REFERENCES

- [1] M.W. Joosten, Corrosion of carbon steels by H₂S in CO₂ containing oilfield environments – 10 year update. Nace Corrosion Conference (2015).
- [2] T. Lin et al., Evaluation of casing integrity defects considering wear and corrosion – application to casing design. Journal of Natural Gas Science and Engineering 29 (2016) p. 440-452.



[3] D. Gao et al., Prediction of casing wear in extended-reach drilling. *Petroleum Science* 7 (2010), p. 494-501.

[4] M.A.L.H. Rodriguez et al., Corrosive wear failure analysis of a material gas pipeline. *Wear* 263, (2007), p. 567-571.

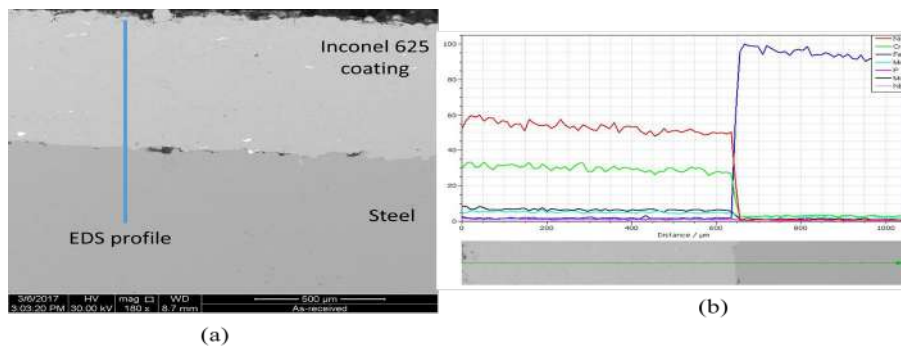


Figure 1: SEM observation of the Inconel 625 coating on the C-Mn steel. (a) macroscopic observation and (b) EDS element profiles.

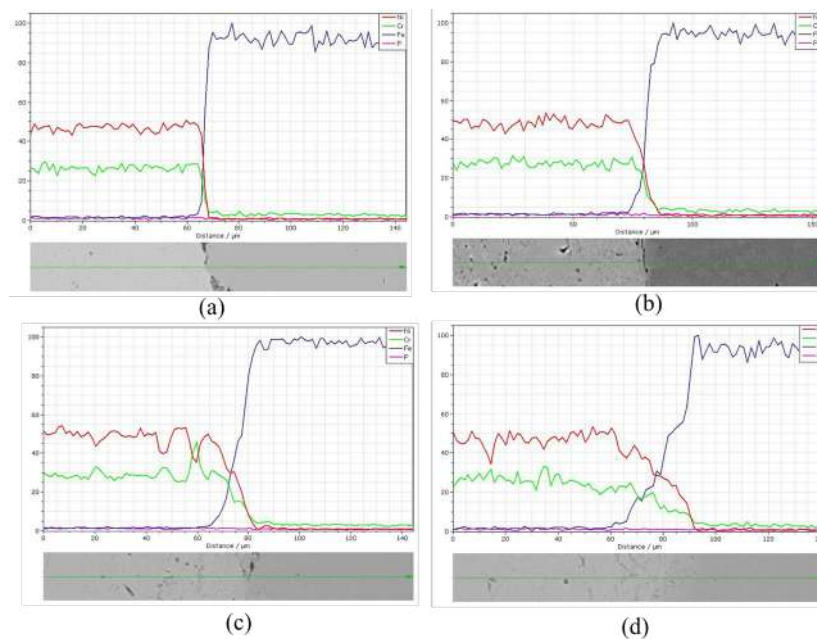


Figure 2: EDS element profiles after diffusion treatment at 900°C for different diffusion time. (a) as-deposited condition, (b) 1h of interdiffusion, (c) 4h of interdiffusion and (d) 10h of interdiffusion.



Quantitative EDS analysis of metallic alloys

K. Balzuweit^{1,2*}, W. N. Rodrigues^{1,2}, M.C.C.Souza², R. C. Ribeiro, P. Alves, B. B. Moreira, I. Delben, W. T. Soares, M.A. Flores, L.R. Garcia²

1. Physics Department, ICEX, Federal University of Minas Gerais, Belo Horizonte, MG, Brazil

2. Center of Microscopy, Federal University of Minas Gerais, Belo Horizonte, MG, Brazil

*Email: karla@fisica.ufmg.br

The last decades have seen an astonishing evolution of the electron microscopes, at the same time they are much more versatile, more stable, easier to use, with higher resolution and magnification, more sensitive detectors and much better signal to noise relation.

Historically scanning electron microscopes were always more a visualization tool where low current, of the order of pA are key for high resolution imaging. On the other side were the microprobes with their specific stable optics which allows currents of the order of nA and stability throughout the magnification range combining EDS and WDS detectors. The versatility of the current scanning electron microscopes (SEM) is slowly turning them into both visualization and analytical tools. There is a growing need for better, faster and higher magnification quantitative analytical data combined with imaging, especially on heterogeneous samples.

The Center of Microscopy of the University of Minas Gerais (CM-UFMG) has been working in order to increase the reliability of the results obtained at the microscopes, and lately had the opportunity of participating at a national project: project Modernit as part of SisNaNo from the Ministry of Science, Technology, Innovation and Communication, as an Associate Laboratory. One of the aims is to work towards accreditation of some methodologies performed at CM-UFMG. In that mainframe, an EDS inter and intralaboratory test is being performed. Unknown thin wires were received and are being tested for composition on a SEM and on a microprobe.

The thin wires were cross-section prepared: embedded in resin, prepared with conventional polishing, and carbon coated. Measurements are being performed on a Quanta 3D –dual FIB from FEI with a Bruker Quantax 800 SDD Energy Dispersive Spectrometer (EDS) and on a Jeol 8900 Microprobe with a Thermo-Noran EDS and four Wavelength Dispersive Spectrometers (WDS).

An initial survey was performed and both standardless as well as with standards were performed at the SEM. Also measurements on the microprobe are being performed. Preliminary results show a quite reasonable agreement between data.

REFERENCES

- [1] J.I. Goldstein et al., Scanning Electron Microscopy and X-ray Microanalysis, Plenum, New York, 1992
- [2] L. Reimer, Scanning Electron Microscopy, Springer, 1988.
- [3] A. J. Tousimis and L. Marton, Electron Probe Microanalysis, Academic Press 1969.
- [4] We acknowledge the support of Fapemig and Finep, this work was funded through project Modernit –SisNaNo from MCT (Brazil).

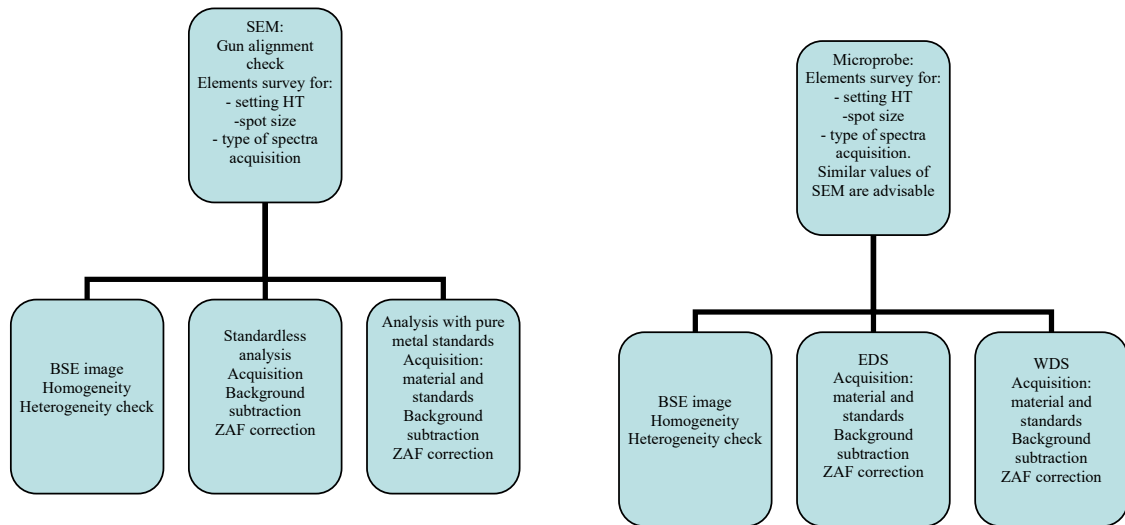
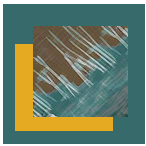


FIG. 1. SEM and microprobe workflow.



Phase and Elemental Mapping by STEM-EELS Spectrum-Image

Erico T. F. Freitas¹, Karla Balzuweit ^{2*}, Clauson de Souza³, Claudia L. Caldeira³, Virgínia T. S. Ciminelli³

1. Universidade Federal de Minas Gerais, Centro de Microscopia, Belo Horizonte, Brazil. freitas.eric@gmail.com

2*. Universidade Federal de Minas Gerais, Departamento de Física – ICEX / Centro de Microscopia, Belo Horizonte, Brazil. karla@fisica.ufmg.br

3. Universidade Federal de Minas Gerais, Departamento de Engenharia Metalúrgica, Escola de Engenharia, Belo Horizonte, Brazil.

Electron energy loss spectroscopy (EELS) performed under the (scanning) transmission electron microscope (STEM) have been successfully applied in a wide range of studies both in materials and life sciences [1, 2]. The EELS spectra provide chemical and structural information of solids such as elemental composition, phase, chemical bond, oxidation state [3]. In modern (S)TEM one can fully characterize a given sample in terms of composition and phase with high spatial and energy resolutions by combining EELS and energy dispersive X-ray spectroscopy (EDS). The STEM-EELS analysis can be performed by collecting many spectra while the electron beam rasters the sample thus forming what is called a spectrum-image (SI). An electron energy loss spectrum image (EELS-SI) is essentially a matrix where x and y are spatial coordinates of the area of the sample scanned by the electron beam, and to each (x,y) pixel corresponds a whole EEL spectra. Elemental and phase mapping can then be performed by post-data processing with the help of some scripts available for the Digital Micrograph (Gatan) software. In this present work a sample from the tailings of a gold mine plant in Minas Gerais state, Brazil, was characterized by punctual STEM-EDS and STEM-EELS-SI to map different oxide phases that may contain Sb. The analysis was carried out in the Center of Microscopy at the Universidade Federal de Minas Gerais, by using a FEI Tecnai G2-20 (200kV) (S)TEM, with a LaB6 electron source, coupled with a Si-Li EDS detector (EDAX) and a GIF Quantum SE System (Gatan). EELS analysis were performed by using dispersions of 0.05 and 0.25 eV/channel at low and high energy losses, respectively. A relatively fast mapping (approximately 3 minutes) was performed to avoid drifting. The results show Sb associated with Fe-(hydr)oxides and CaCO₃ (not shown here). Figure 1 shows the EELS mapping for Fe M-, Al L-, and Sb N- Edges performed from the SI data cube. The Sb M-Edge at 528 eV was not used for mapping because it overlaps with the pre-peak at the O K-Edge for Fe-(hydr)oxides, but the presence of Sb was confirmed by the EDS analysis (not shown).

REFERENCES

[1] C.Collix, Ultramicroscopy, (2017). In press.

[2] R. Leapman, Ultramicroscopy, (2017). In press.

[3] R. Egerton, Reports on Progress in Physics Plenum, 72:1 (2008).

[4] This research was supported by Center of Microscopy of UFMG, FAPEMIG and FINEP (Brazil).

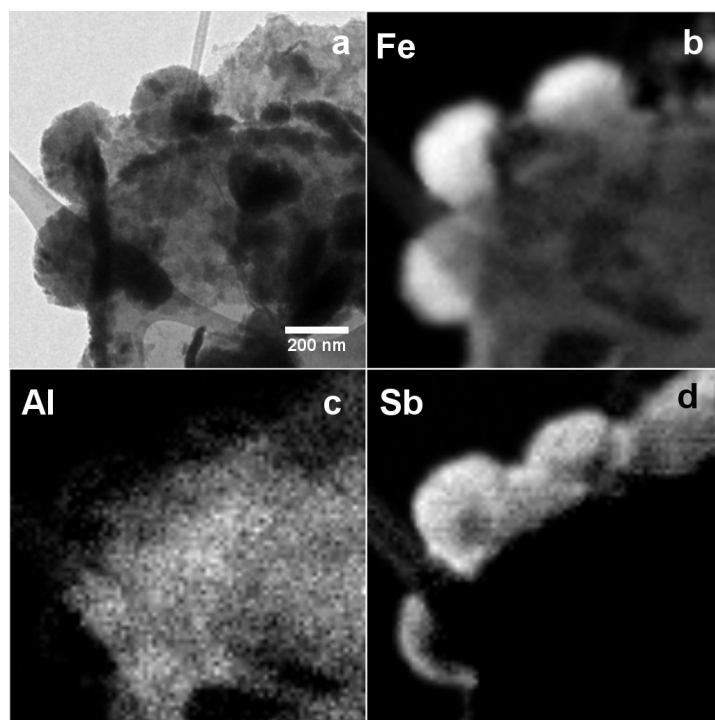


Figure 1: (a) Bright Field TEM image of a clay mineral sample; (b-d) EELS maps for Fe M-, Al L-, and Sb N-Edges generated from the STEM-EELS-SI performed in the area shown in (a)



3D X-ray microscopy analysis of lignocellulosic fibers used as reinforcement in composite materials of polymer matrix

L.O.L Gontijo^{1*}, M.H.P. Mauricio¹, S. Paciornik¹ and J. R. M d'Almeida¹

1. Dept. of Chemical and Materials Engineering, PUC-Rio, Rio de Janeiro - RJ, Brazil.

*Email: layneglucas@gmail.com

The use of natural fibers to reinforce composite materials has been gaining considerable notice in many industrial fields. This is mainly due to environmental restrictions, which impose legal requirements related to the use of synthetic products, aiming at the reuse and replacement of non-renewable raw materials, which cause less damage to the environment. Natural fibers are biodegradable, renewable resources with very attractive properties and morphology. One of characteristics of lignocellulosic fibers is to have a non-uniform structure along their major axis. This feature makes any 2D analysis, like optical or even scanning electron microscopy, incomplete. In this context, 3D X-ray microscopy (XRM), also known as X-ray microtomography (microCT), can be applied to better understand the microstructure of these lignocellulosic materials. It is a non-destructive analysis that gives real 3D information about the material. It uses x-rays to create a stack of cross-sections images of a material, which is used to recreate a 3D model [1]. Among several natural fibers, *luffa cylindrical* and piassava (*Atallea funifera*) are interesting examples and the focus of the present work. Both can be used as reinforcement in polymer matrix composites. Luffa is particularly interesting due to its three-dimensional layout, which can contribute to the composite toughness [2]. Piassava presents mechanical properties similar to coir fibers, widely used by the automotive industry [3]. One of the challenges in the use of lignocellulosic fibers as reinforcement in composite materials is to improve the interaction between fiber and polymer matrix, once natural fibers are hydrophilic and matrices are hydrophobic, leading mostly to weak interfaces. In some cases, specific chemical treatments (e.g the mercerization method) can improve this interface by removing part of lignin and cellulose from fibers, roughening their surface. In this work, the microstructure of piassava and luffa fibers were evaluated through microCT before and after mercerization in 10 wt% NaOH aqueous solution. Figure 1 shows the result for piassava. No significant surface change is visible, apart from the removal of silica protrusions. In the luffa case, Figure 2, the change is more visible in the form of a contraction of the fiber network although the fiber thickness distribution (color coded in the images) did not change substantially.

REFERENCES

- [1] E.N. Landis, D.T. Keane, *Materials Characterization* 61 (2010) 12, 1305-1316.
- [2] C.A. Boynard and J.R.M. d'Almeida, *Polymer-Plastics Technology and Engineering*, 39 (2000) 489–499.
- [3] R.C.M.P. Aquino, J.R.M. d'Almeida, S.N. Monteiro, *Journal of Materials Science Letters*, 20 (2001) 1017–1019.
- [4] This research was supported by FINEP (Brazil).

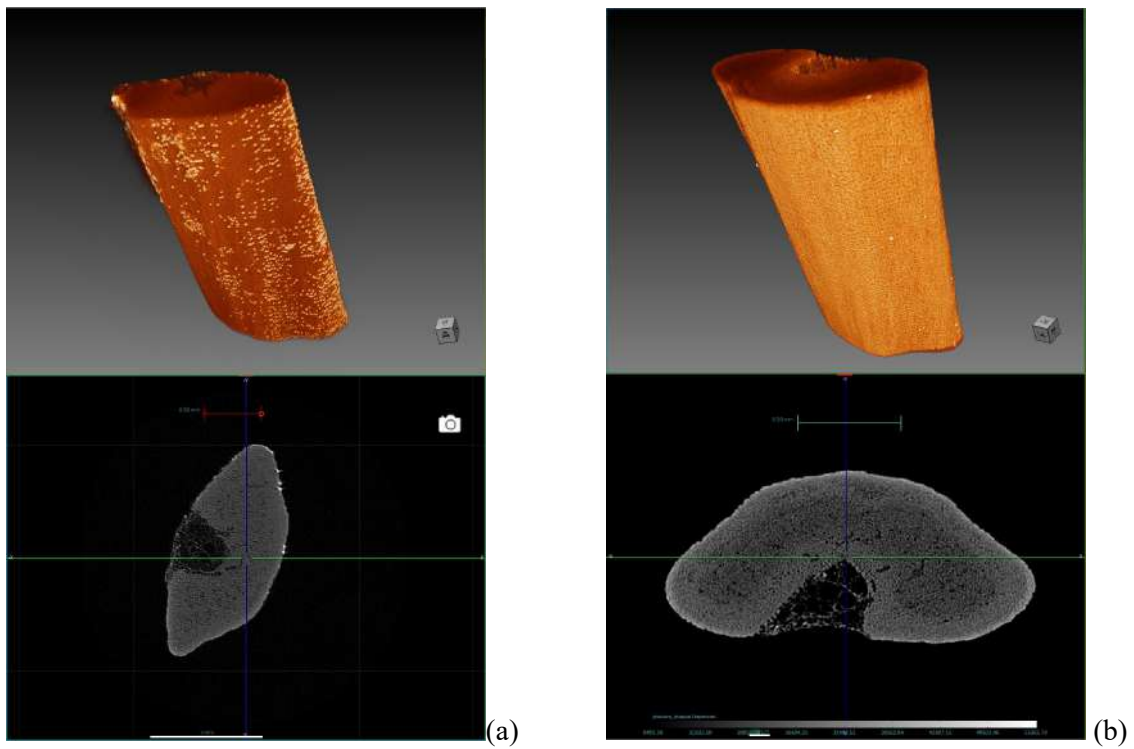
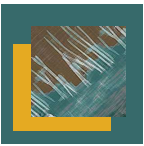


Figure 1 – 3D and 2D images of piassava fiber: (a) before and (b) after chemical treatment.

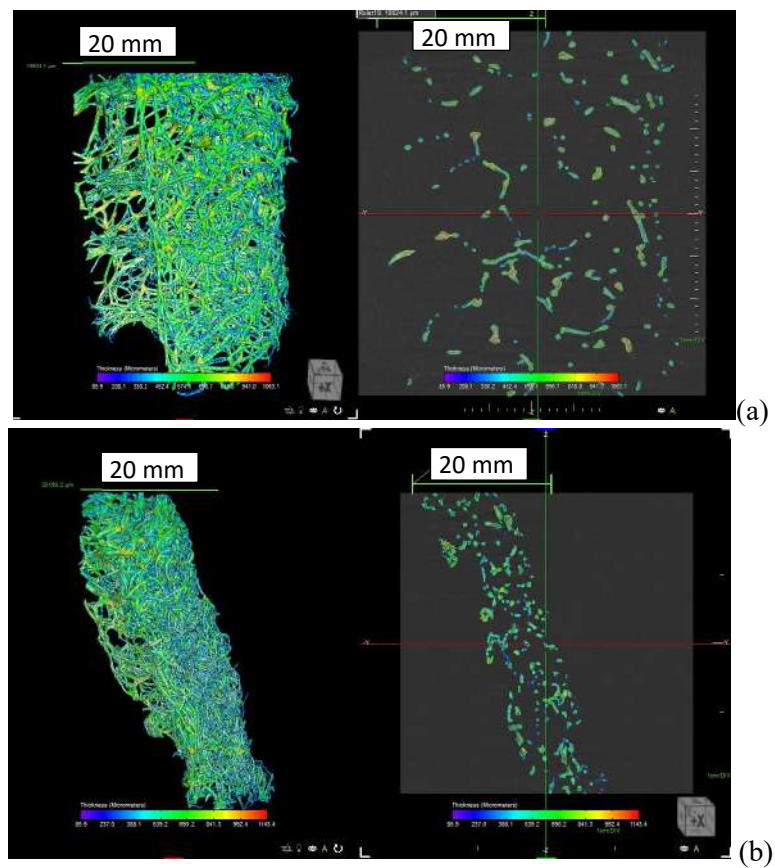
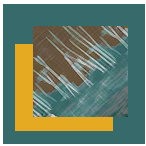


Figure 2 - 3D and 2D images of luffa fiber: (a) before and (b) after chemical treatment.



Tridimensional Characterization of Epoxy Matrix Glass-Fiber Reinforced Composites

De La Hoz Alford, Lorenleyn^{1*}; Paciornik, Sidnei¹; Moraes D'Almeida, José Roberto¹; Lopes Alves, Haimon Diniz²; Mauricio, Marcos H. P.¹.

1. Dept. of Chemical and Materials Engineering, Catholic University of Rio de Janeiro (DEQM/PUC-Rio), Rio de Janeiro - RJ, Brazil.

2. University of the State of Rio de Janeiro (UERJ), Rio de Janeiro – RJ, Brazil.

*Email: lorenfisica@gmail.com

Composites are typically non-homogeneous and anisotropic materials, both from the microstructural point of view and in terms of mechanical properties. The failure mechanisms are affected by the spatial distribution and quality of the adhesion at the interface between matrix and reinforcement. The traditional techniques of microscopic characterization are limited to characterize this type of material since sections or two-dimensional projections may not fully reveal the anisotropic microstructure. When the goal is to understand the origin of failure mechanisms, these limitations are even more important, as voids and cracks can appear anywhere in the 3D sample and be missed by specific 2D cross sections. These defects can have their origin in the material manufacture or be caused by mechanical stress. In the present work, a three-dimensional characterization methodology based on X-ray microtomography (microCT) was developed. The material evaluated was a composite with an epoxy matrix reinforced with unidirectionally aligned glass fibers. Samples were submitted to bending tests at increasing loads and tomographed as-received and after each test. To discriminate between preexisting defects and those created during the tests the 3D images were registered in 3D and compared both visually and quantitatively. An assessment of the uncertainty of the procedure was performed doing more than one tomography of the as-received samples, registering and comparing the resulting 3D images. Figure 1 shows 3D views of Sample 1 as-received and after the bending test. Both preexisting and defects created during bending are visible. Figure 2 depicts the segmentation of defects in Sample 2. After segmentation of defects in different conditions, their true 3D volume fraction can be automatically measured, as shown in Table 1. The results are consistent with a strong increase in defect volume due to the mechanical stress.

REFERENCES

- [1] BUFFIÉ J., et al., Characterization of internal damage in composites material using x-ray synchrotron phase contrast microtomography. ElsevierScience, 1:7, 1998.
- [2] SCHELL J.S.U., et al., Micro-computed tomography determination of glass fibre reinforced polymer meso-structure. Composites Science and Technology, 66:7, 2006.
- [3] SHILLING, P., et al., X-ray computed microtomography of internal damage in fiber reinforced polymer matrix composites. Composites science and technology, 8:7, 2005.
- [4] This research was supported by CNPq and FAPERJ (Brazil).

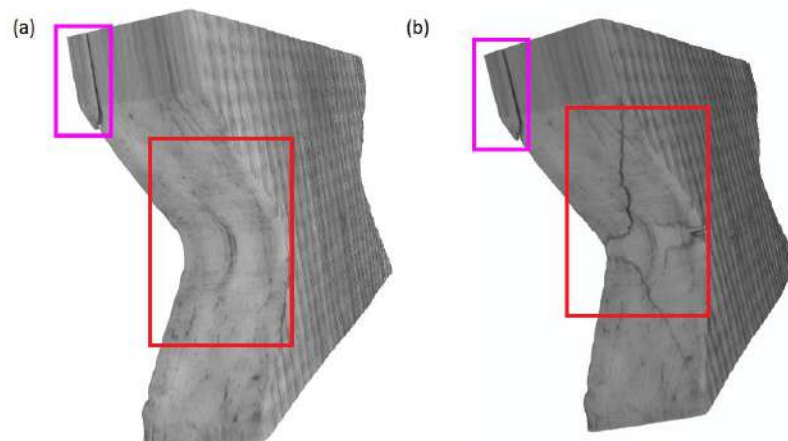
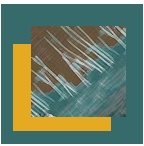


Fig. 1. Sample 1 - 3D Visualization of defects in the as-received (a) and tested (b) conditions. The pink rectangle shows a preexisting crack while the red rectangle shows a crack created during the bending test.

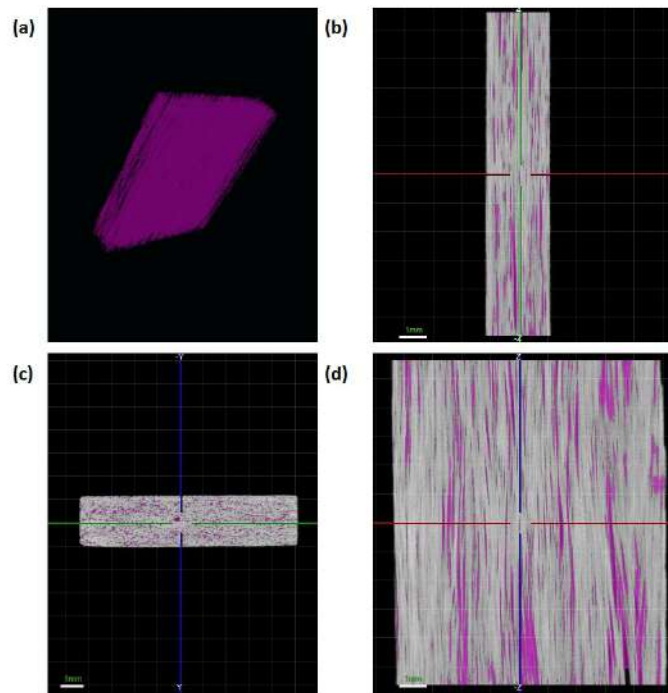
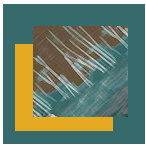


Fig. 2. 3D segmentation of defects in Sample 2. The pink regions correspond to voids and cracks in the material, that can be quantified. See Table 1.

Table 1 – Defect Volume Fraction

Samples	Volume Fraction (%)
Sample 1 – As-received	1.0
Sample 1 – After bending test	3.0
Sample 2 – As-received	7.8
Sample 2 – After bending test	14.0



Identification of Quaternary Phases With Mg of Alloy B390.0 (Al-Si-Cu) by Electrons Backscattering Coefficients (η)

Marcelo da Cruz Costa de Souza^{1*}, Karla Balzuweit²

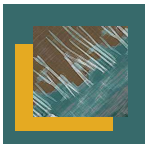
1. Microscopy Center of UFMG, Belo Horizonte, Brazil . mccsouza@sga.pucminas.br

2. Microscopy Center of UFMG, Belo Horizonte, Brazil. karla@fisica.ufmg.br

The aluminum alloy B390.0 (16.94Si, 4.52Cu, 1.03Fe, 0.68 Zn, 0.36Mg, 0.26Mn) % Wt is manufactured by melting process ($T = 1033\text{K}$) and cast under pressure.[4] From the manufacturing process, the formation of microstructures such as dendrites and undissolved solutes occurs. Because it is an alloy of great chemical diversity in its composition, many microstructures occur, in addition to a large variety of phases.[2] The objective of this study is to identify the quaternary Al-Si-Cu-Mg and Fe-Mg-Si-Al phases using the backscattered electron (BSE) signal; Correlating the backscatter coefficients (η) generated by the interaction of the electron beam, of each phase of the alloy, with the gray tones generated by the image; Backscattered electron signal (BSE) micrographs have the so-called Z contrast, containing information on the chemical compositions of the phases.[1][3] The intensity of a particular region of the backscattered electron micrography is proportional to the backscatter coefficient (η) of electrons in this region. In the preparation of the sample, a fine polishing was performed on the surface, a carbon film was deposited by evaporation in order to make it more conductive, facilitating the generation of a micrography with a minimum amount of load loading, which could generate artifacts that made difficult The identification of phases.[1] The hypereutectic aluminum alloy B390.0 has the following quaternary phases with the presence of the Mg element, which can be identified ($\text{Cu}_2\text{Mg}_8\text{Si}_6\text{Al}_5$, $\text{CuMg}_5\text{Si}_4\text{Al}_4$, $\text{FeMg}_3\text{Si}_6\text{Al}_8$).[4] The equipment used was Quanta 3D FEI + EDS Bruker SEM-FEG and ImageJ microscopy imaging software. For a uniformity of gray tones generated by the backscattered electron signal (BSE), the standardization of the voltage of 20kV and spotsize 7.0 was adopted, electric current of 53 nA and tilt = 0° ; The brightness / contrast function was adjusted in such a way that all the micrograph forming pixels were restricted to the 254 grayscale that an 8-bit image can generate was made using the histogram function of the microscope image acquisition software. For an initial identification of the distribution of the elements in the alloy matrix, an image was made by mapping X-rays and associating the regions where there was simultaneous presence of (Al-Si-Cu-Mg) and (Fe-Mg-Si-Al) to be associated with the gray contrasts of electron backscatter coefficients (η). To determine the backscatter coefficient values of the phases, the Casino software was used for Monte Carlo Method simulation. Using the ImageJ software, brightness / contrast threshold filters were applied, delimiting the grayscale cut to identify the phases more effectively. The technique was shown to be efficient in determining the phases by electron backscattering coefficients (η), The $\text{CuMg}_5\text{Si}_4\text{Al}_4$ phase was easily identified, the $\text{CuMg}_8\text{Si}_6\text{Al}_5$ and $\text{FeMg}_3\text{Si}_6\text{Al}_8$ phases had more difficulty in separating them, due to the near gray contrast values. With more accurate image processing it is possible to define and quantify them.

REFERENCES

- [1] F. Zupanič, *Materials Characterization* . 61 (Suppl. 12) (2010) 1335-134
- [2] J. Hatch, *Aluminum: properties and physical metallurgy*, ASM International, 1984
- [3] J.I. Goldstein et al., *Scanning Electron Microscopy and X-ray Microanalysis*, Springer, New York, 2003.
- [4] N. Belov, D. Eskin, A. Aksenov. *Multicomponent phase diagrams: applications for commercial aluminum alloys*, Elsevier, 2005
- [5] R. Gauvin, *Software Casino for Simulation Monte Carlo Method*. Quebec, Sherbrooke University, Version 2
- [6] W. Rasband, *Software ImageJ, NIH*, Version 1.51
- [7] This research was supported by Fundep (Brazil) and Fapemig (Brazil)



Phase	Backscattering electrons	Backscatter coefficient (η)- Monte Carlo Method[5]	Grayscale value (8 bits 0 - 255 tones)[6]
[I] $\text{CuMg}_8\text{Si}_6\text{Al}_5$		0,160	210 - 255
[II] $\text{CuMg}_5\text{Si}_4\text{Al}_4$		0,149	90 - 110
[III] $\text{FeMg}_3\text{Si}_6\text{Al}_8$		0,154	130 - 200

Table 1 - Correlation of the gray tones of the studied phases with the backscatter coefficient

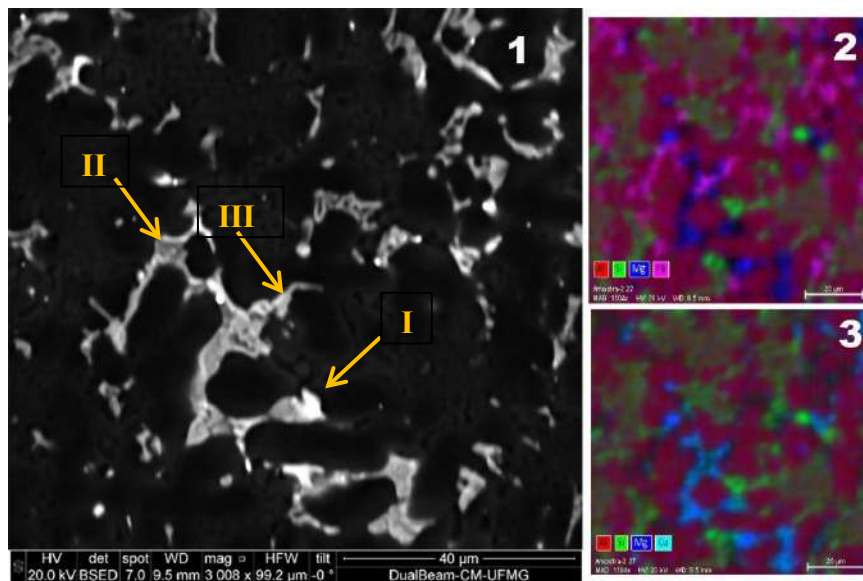
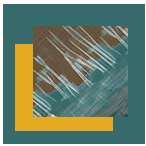


Image 1 – (1) Microstructures and phases of alloy B390.0. (2) Al-Si-Mg-Fe (3) Al-Si-Mg-Cu



STEM Study of Cu-Ni Matrix Nanocomposites Reinforced with Al₂O₃ Nanoparticles After heat Annealing at 600 for 300min.

M.I Ramos, E. Brocchi, I.G Solórzano.

Department of Chemical and Materials Engineering, PUC- Rio de Janeiro, Brazil

Metal ceramic composites (CerMet) have been successfully applied in engineering materials. Recently nanocerments have been produced through different methods aiming at achieving properties superior to those in traditional bulk materials [1]. In this context, the present work focuses on a production and evolutional microstructural study characterization by transmission electron microscopy (TEM) and measure of mechanical properties of two different nanomaterials. First 89wt%Cu-10wt%Ni/1wt%Al₂O₃ nanocomposite and the other is the same Cu-Ni composition without ceramic phase (Al₂O₃). Both nanomaterials were prepared by a chemical-route based in co-formed oxides followed by selective hydrogen reduction. The produced nanoparticles were compacted to pellets and, finally, the pellets were 80% cold rolled followed by annealing at 600°C for 300 minutes [2].

Microstructural characterization was conducted by transmission electron microscopy (TEM) using LaB6 Jeol 2010 instrument under 200 kV accelerating potential operating in diffraction and phase contrast modes. TEM specimens were prepared by typical mechanical thinning down to about 100µm. The thickness of the thinned sample was decreased to 5 µm using a dimpling machine (South Bay Technology model 515) and, finally, submitted to ion milling at low incident angle (Gatan PIPS 691).

The instrument operating in STEM mode allowed to complement the fine structures identification. In particular, grain growth was confirmed to happen in heat treated samples at 600°C for 300 minutes. A typical micrograph illustrating the concurrency of this phenomenon is shown in Figure 1a, bright field STEM micrograph. While fine grained fully recrystallized structure, with average size of 50 nm, is observed in the lower left of the image, the remaining of the micrograph is occupied by larger grains having grown one order of magnitude in size. Figure 1b shows a detail of large grain, in growing process, consuming smaller grains.

A fully recrystallized Cu-Ni grain matrix containing a fine dispersion of Al₂O₃ is observed in Figure 2. It is well known that dispersion of stable nanoparticles causes a pinning effect on dislocation and grain boundary migration, thereby preventing more prominent thermally activated grain growth and so improving the mechanical properties of the composite material. While Figure 2a shows some dislocation and grain boundary activity with pinning nanoparticles, in Figure 2b the homogenous dispersion and volume fraction of Al₂O₃. In fact, Vickers micro hardness indentation in both materials, dispersion-free and containing ceramic Al₂O₃ nanoparticles, were measured, showing an increase in 22% hardness in the nanocomposite material, in despite of having undergrown significant grain growth

REFERENCES

[1] Han, S. Z et al. Sci. Rep. 5, 17364 (2015)

[2] Ramos, M.I et al. Metall Mater Trans A, *in press*.

[3] The authors are grateful to the Brazilian funding agencies CNPq, CAPES and FAPERJ for financial support. The access to the electron microscopy facilities at the LabNano/CBPF, Rio de Janeiro, is gratefully acknowledged. Particular appreciation is due to Dr. Andre Pinto.

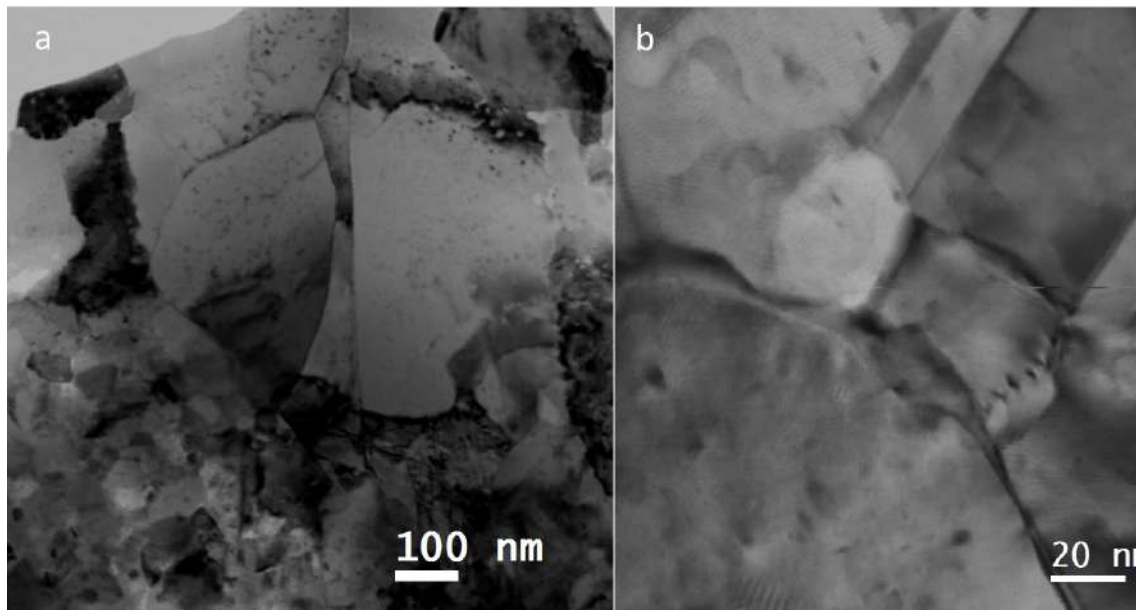
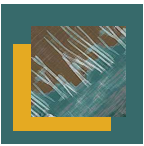


Figure1. STEM bright field image of cold rolled and annealed sample exhibiting grain growth. a) shows the transition boundary and in b) a detail of the moving boundary consuming smaller grains.

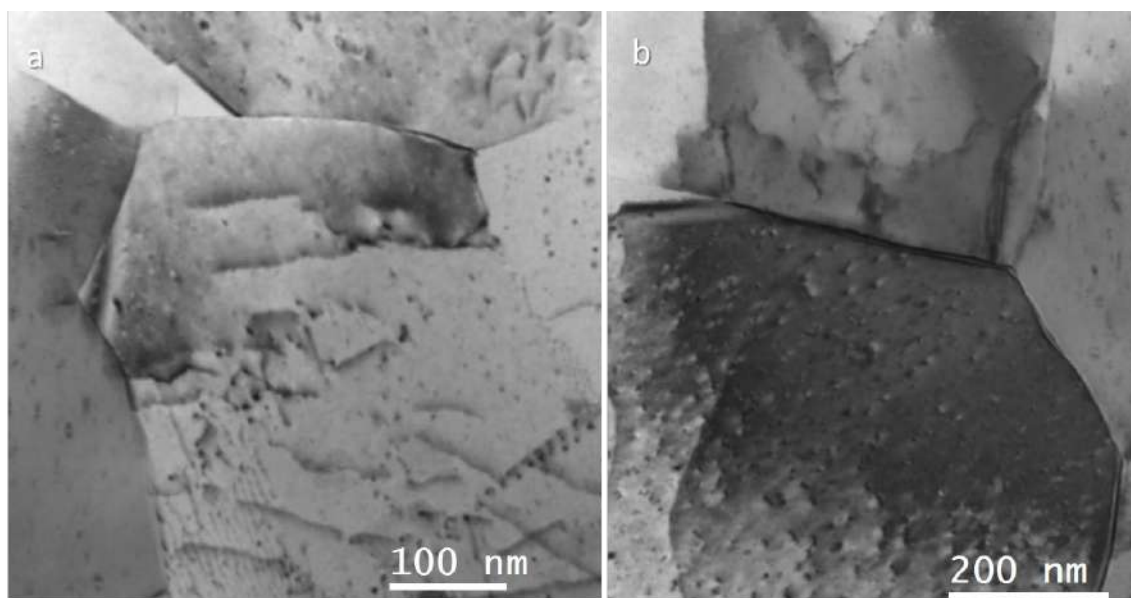


Figure2. STEM bright field images a) of cold rolled and annealed composite showing Al_2O_3 nanoparticles interaction with dislocations and (occasionally) with grain boundaries b) showing homogeneous dispersion of Al_2O_3 nanoparticles throughout the Ni-Cu matrix.



Niobium Carbide Morphology in HP-Modified Steel Reformer Tubes as an Indicator of Temperature Surges

Mario Nascimento^{1*}, Matheus Campolina², Laudemiro Nogueira Jr³, Luiz Henrique de Almeida¹, Iain Le May⁴.

1. PEMM-COPPE/UFRJ, Caixa Postal 68505, Rio de Janeiro, RJ, CEP 21945-970, Brazil
2. CEFET/RJ, Av. Maracanã, 229 - Maracanã, Rio de Janeiro - RJ, CEP 20271-110
3. PETROBRAS-CENPES, Cidade Universitária, Rio de Janeiro - RJ, CEP 21040-000
4. Metallurgical Consulting Services Limited, P.O.Box 5006, Saskatoon, Canada S7K4E3

Bulk hydrogen is currently produced inside reforming furnaces at temperatures above 900°C within centrifugally cast HP grade austenitic stainless steel tubes, modified by additions of Nb (HP-Nb). Service aging at these temperatures causes, among other microstructural modifications, the transformation of primary NbC to G phase, an Ni-Nb based silicide [1], whose interface with the matrix is quoted in literature as a preferential site for creep damage nucleation [2]. More recently, titanium has been microalloyed to these steels (HP-NbTi), inhibiting the (NbTi)C→G phase transformation [3]. Frequently premature failure of the tubes, designed for a minimum service life of 110,000 hours, occurs due to “temperature surges”, overheatings occurring in a few minutes because of operational problems [4]. Despite the financial and operational character of this problem, little is known about the fitness for service of tubes which have undergone a temperature surge and present no visible damage. This work presents a microstructural analysis carried out by means of scanning electron microscopy (SEM) with energy dispersive X-ray spectroscopy (EDS) of two tubes, one microalloyed with Ti and the other not, which cracked due to a temperature surge. Results suggest the reprecipitation of NbC and (NbTi)C in the morphology of small particle clusters from pre-existing G phase, according to the following sequence of events: (i) Regions of tubes exposed to surge overheating reached temperatures above 1000°C for approximately 12 min before shutdown; (ii) G phase thus dissolved, forming Nb saturated interdendritic regions; (iii) High NbC/(NbTi)C nucleation rates in these regions resulted in small particle cluster morphology, maintained during cooling upon furnace shutdown. These transformations are summarized with SEM micrographs in Figure 1 and schematically presented in Figure 2. NbC/(NbTi)C with this morphology thus serve as a microstructural indicator of the occurrence of temperature surges, both characterizing the microstructure and determining the extension of the region affected by this phenomenon.

REFERENCES:

- [1] C. J. Liu, Y. Chen., Mater. Des. 32 (n. 4) (2011) 2507.
- [2] L. H de Almeida, F. C. Ferraz, I. Le May., Microstruct Sci 24 (1996) 193.
- [3] L. H de Almeida, A.F. Ribeiro, I. Le May., Mater Charact, 49 (n. 3) (2003) 219.
- [4] I. U. Perez, L. N. Júnior, L. de Oliveira Bueno, L. H. de Almeida, T. L. da Silveira, JFAP.13 (n. 6) (2013) 779.

Financial support by CNPq and Petrobras, who also provided the materials for this study, is gratefully acknowledged.

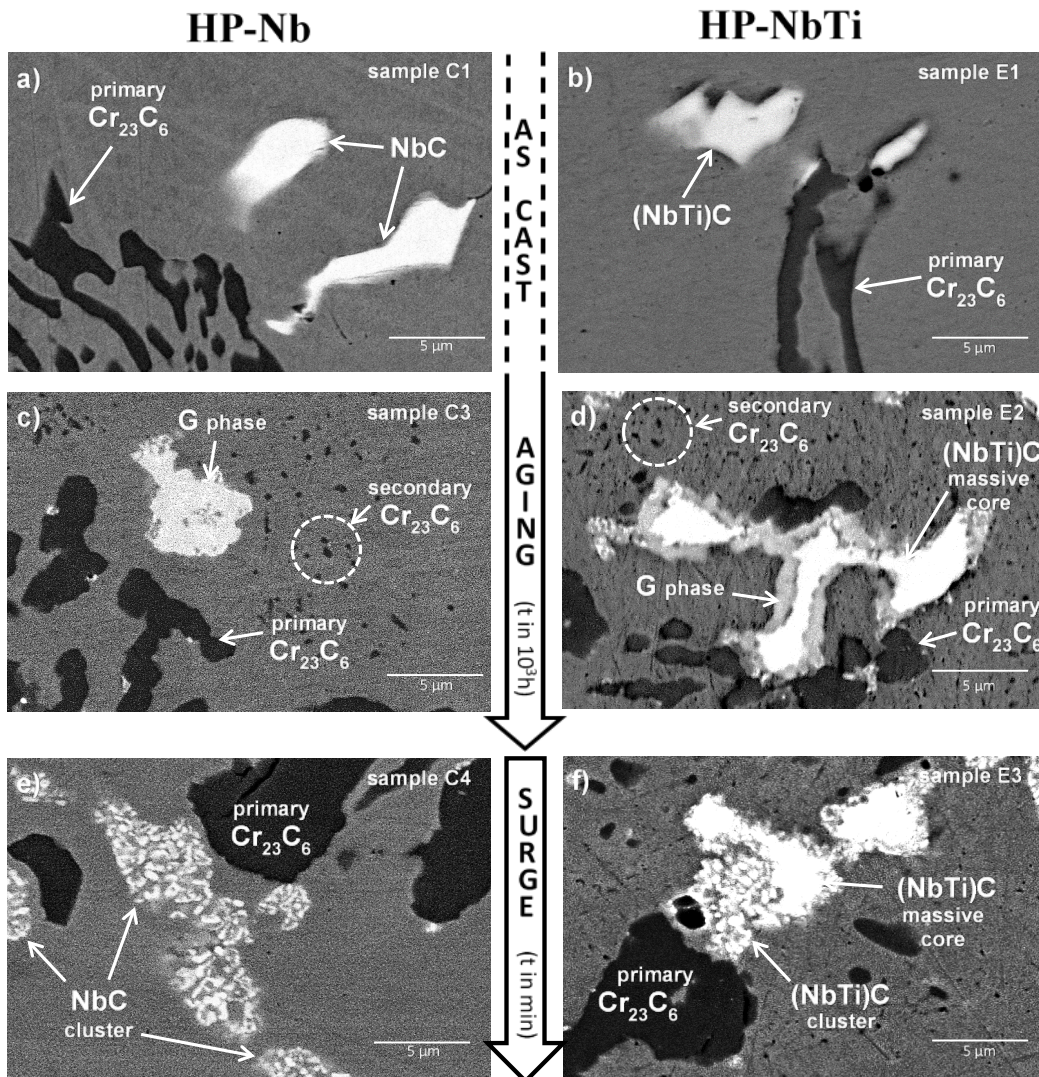
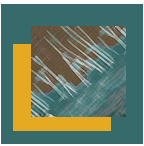


Fig.1: SEM images of samples from differently aged and surge exposed regions of the analyzed tubes. (a) and (b): AS CAST meaning no significant aging; (c) and (d): service aged; (e) and (f): surge overheated regions.

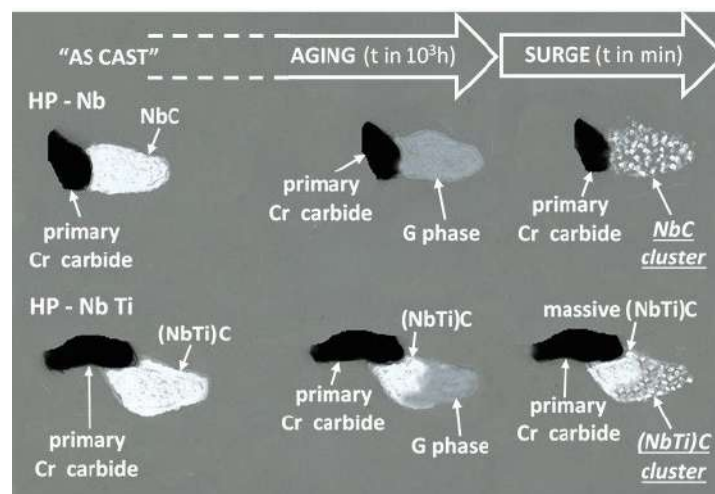
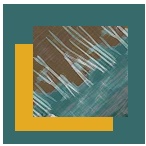


Fig.2: Diagram representing the formation of NbC and (NbTi)C small particle cluster morphology due to a temperature surge. "AS CAST" meaning no significant aging.



Microstructural effects of aging after a temperature surge event on Centrifugally Cast HP-Steels Used in Steam Reformer Furnaces

M. C. Mendes^{1,2,*}, L. H. de Almeida², J. Dille³

1. Federal Center for Technological Education of Rio de Janeiro (CEFET-RJ), Maracanã, Rio de Janeiro/RJ, Brazil, CEP: 20271-110, campolinamendes@gmail.com
2. Federal University of Rio de Janeiro (UFRJ), C.P. 68505, Ilha do Fundão, Rio de Janeiro, Brazil, matheus@metalmat.ufrj.br, lha@metalmat.ufrj.br
3. Free University of Brussels, C.P. 194/03, Av. F. D. Roosevelt, 50, B-1050, Brussels, Belgium, jdille@ulb.ac.be

Reformer furnaces have been largely applied in the petrochemical industry to produce hydrogen gas from a mixture of hydrocarbons and steam at high temperatures which can, under operational conditions, reach 950°C at about half the length of the radiant tubes [1]. The use of centrifugally cast stainless steels in radiant tubes, particularly HP grade, has been well-established due its high creep resistance. However, the decrease in creep resistance after long-term aging has motivated an improvement on the performance of HP steels in recent years. In this context, Nb and Ti were added to the chemical composition of the normal grade to increase microstructural stability, resulting in the micro-alloyed HP steels. Service conditions lead to the gradual deterioration of the catalyst inside the radiant tubes, possibly resulting in a restricted feedstock flow, leading to a quick increase in temperature to above 1000°C, in localized regions along the tubes' length, a phenomenon known as a temperature surge [2]. Micro-alloyed HP steels, in the "as cast" condition, have a fully austenitic matrix with primary chromium, niobium and niobium/titanium carbides along the interdendritic region. During aging, fine secondary precipitation in the matrix and partial transformation of the primary NbC and (Nb,Ti)C to a G-phase ($\text{Ni}_{16}\text{Nb}_6\text{Si}_7$) occur [3]. After a temperature surge, some uncertainties remain as to the possibility of reusing the tubes that didn't collapse during the event, as their integrity may have been compromised by the extensive microstructural changes suffered when compared to normally aged tubes. In this context, the aim of this work is to characterize, by means of scanning (SEM) and transmission electron microscopy (TEM) with energy-dispersive X-ray spectroscopy mapping (EDS), the effect of aging time at 900°C on the microstructures of samples that have undergone a temperature surge. SEM samples were prepared by conventional grinding and polishing techniques without chemical etching while TEM samples were prepared by Focused Ion Beam (FIB) technique. After the temperature surge, besides the expected coalescence of the primary interdendritic carbide network, an apparent dissolution of the secondary precipitation, Fig.1 (a), can be observed. Fig.1 (b), shows an EDS mapping of the "as received" condition, the massive presence of NbC in interdendritic regions may indicate G-phase dissolution, as a result of the temperature surge. The artificially aged samples showed that 1000 hours were sufficient to reprecipitate the secondary carbides and promote a new NbC/(Nb,Ti)C to G-phase transformation, Fig.2. TEM analysis of a 1000h artificially aged sample showed, besides a partial transformation to G-phase, two morphologies of primary (Nb,Ti)C carbides, which present the titanium content as their main difference, Fig.3. This fact broadens the discussion on the possibility of reutilizing, under normal service conditions, radiant tubes which have undergone a temperature surge, mainly due to the microstructural evolution that succeeded the overheating event.

[1] F.C. Nunes et al., *Mater Charact.* 58 (2007) 132.

[2] G.D.A. Soares et al., *Mater Charact.* 29 (1992) 387.

[3] R.A.P. Ibañez et al., *Mater Charact.* 30 (1993) 243.

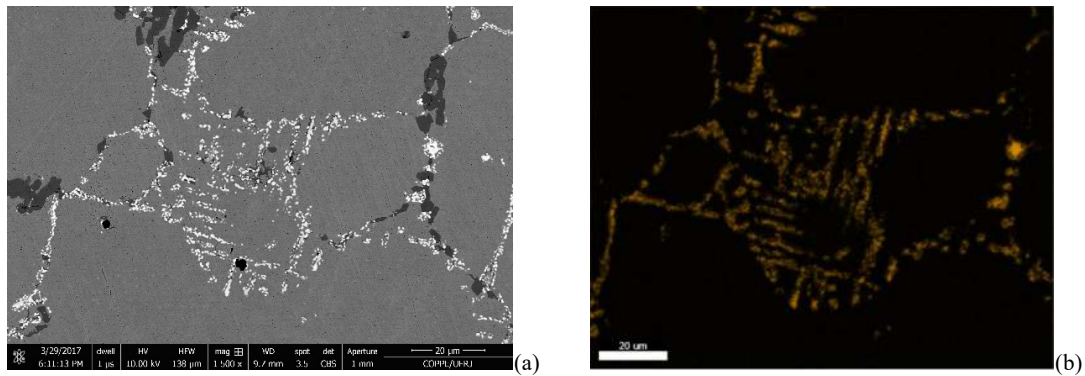
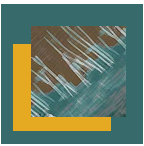


Fig.1. (a), SEM image of the microstructure a temperature surge condition, (b) EDS mapping of Nb (orange) showing a massive fragmented NbC carbides a temperature surge condition

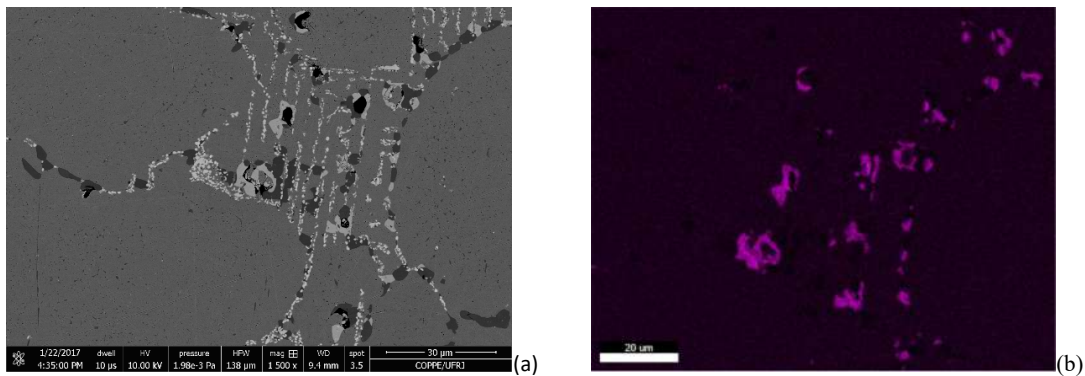


Fig.2. (a) SEM image of the sample aged for 1000hs at 900°C. (b) EDS mapping of Si (purple) showing a massive presence of G-phase after aging.

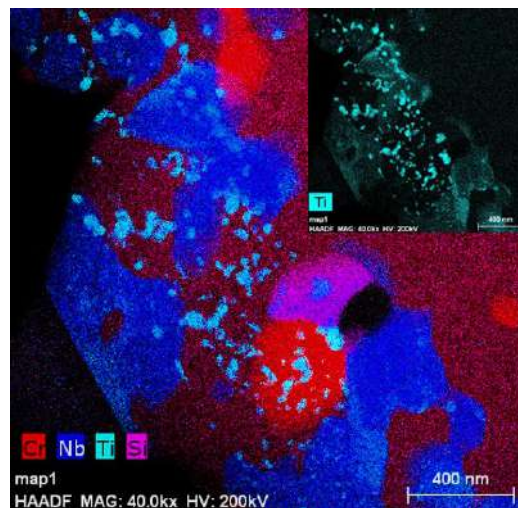
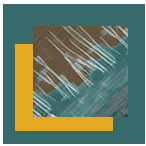


Fig.3. TEM EDS mapping of the sample aged for 1000hs at 900°C. In detail, a Ti (cyan) mapping showing a presence of TiC in a interdendritic region due the influence of Ti on NbC to G-phase transformation.



Microstructural characterization of the interface between CuAg/Cu joint brazed with SnCu_{0,7}Ni alloy

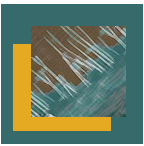
O. R. Bagnato^{1,2}, C. Ambrósio¹, F.E. Silva¹, M. M. Capovilla¹, P. M. Pimentel³

1. Universidade São Francisco, Campinas, SP - Brazil, osmar.bagnato@Inls.br
2. Brazilian Synchrotron Light Laboratory, Campinas, SP - Brazil,
3. Universidade Federal Rural do Semi-Árido/CMA, Angicos, RN, Brazil.

CuAg/Cu joint brazed with SnCu_{0,7}Ni alloy stabilized with germanium are being used in vacuum chamber of electron accelerators [1]. The brazing system in copper and tin alloys as the filler metal is known; however, each alloy has a different behavior in its compositions and a difference in the microstructure when they are subjected to different temperature conditions. Therefore is necessary to perform complementary tests for a microstructural analysis of these materials. This work presents the preparation and microstructural study of a CuAg/Cu joint brazed with a SnCu_{0,7}Ni alloy stabilized with germanium, aiming to evaluate the influence of base materials, thermal cycle and process variables in order to improve the mechanical resistance of the brazed joint. Seven samples were submitted to different temperatures and exposure time, and were subjected to microhardness test, metallography, scanning electron microscopy and X-ray diffraction techniques to metallurgical and mechanical evaluation. Metallography tests, microhardness and SEM images allowed the identification of phases, possibly Cu₃Sn e Cu₆Sn₅[2] in the analyzed microstructures. The analyzed samples had enough thermal cycling to study the growth of the intermetallic compounds phases, whereas the ones with lower temperatures presented only two phases. Moreover, at higher temperatures, it was observed the presence a new phase, Kirkendall'effect [3] and the weakening of the union. Figure 1 shows some fractures present in the piece with thermal cycling 250°C to 500 hours and also shows the phases lengths. Microhardness test demonstrated the increase in hardness in one of the intermediates compounds by about 3400% when compared to a brazing sample and another with the cycling temperature at 100°C for 250 hours. Although there is a brittle brazing of these parts they support an estimated life of up to 400 hours under 250 ° C cycles.

REFERENCES

- [1] CNPEM. *Projeto Sirius: a nova fonte de luz síncrotron brasileira*. Campinas. 2014.
- [2] L. M. LEE, et al., *Adv. Mater. Sci. Eng.*, 2013 (2013) 1.
- [3] LIN, J.-A, et al. "Crystals, 6 (1) (2012) 12.
- [4] This research was supported by LNLS (National Synchrotron Light Laboratory)



DOI: [INSERIR ENDEREÇO DO DOI AQUI.](#)

Caderno de Resumos do 26º Congresso Brasileiro de Macroscopia da SBMM – ISSN: [INSERIR AQUI.](#)

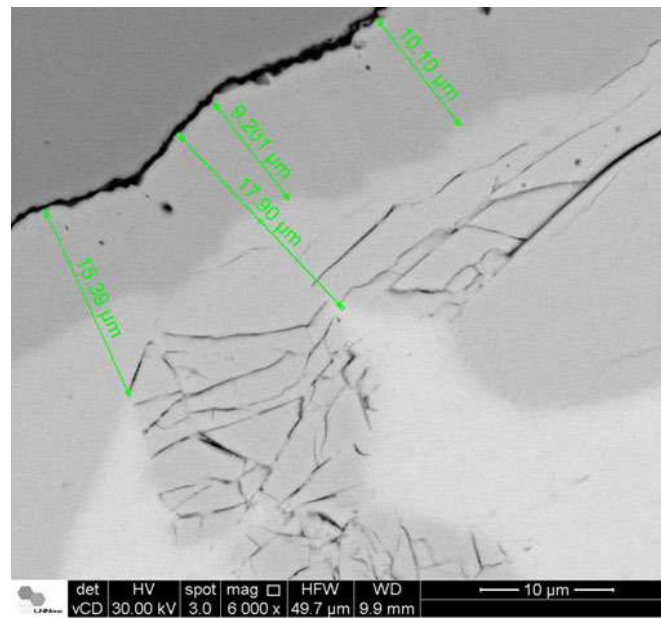
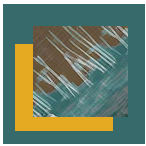


Figure 1- SEM image of three different intermetallic regions after thermal cycling, is possible to observe fractures inside a specific region and another fracture between the filler metal and the base metal (superior left corner)



Evaluation of the shot peening effect on the resistance of SAE 9254 steel springs and analysis of failure by scanning electron microscopy

O. R. Bagnato^{1,2,4}, M. C. Filho¹, R. L. Brescanci¹, R.S.Silva¹, P. M. Pimentel³

1. Universidade São Francisco, Campinas, SP - Brazil, osmar.bagnato@lnls.br

2. Brazilian Synchrotron Light Laboratory, Campinas, SP - Brazil,

3. Universidade Federal Rural do Semi-Árido/CMA, Angicos, RN, Brazil.

4. FAE, Curitiba, Pr, Brazil

The use of thermal or mechanical processing tools to increase the fatigue life of a particular part is very common in the industries. When it comes to automotive helical springs, the importance of the surface blasting process becomes even greater, since they are parts that undergo several "stress tests" and their failure can cause car accidents. In this context, the shot peening process becomes essential to get better results in the production of springs. [1]. This work aims to investigate the presence of failures in the microstructure of the spring after mechanical treatment and thermal treatment. They were manufactured 42 SAE 9254 steel helical springs used in passenger cars, following the standard for the development of durability tests. Fatigue tests, metallographic tests and failure analysis were performed through scanning electron microscopy and the chemical composition was obtained through EDS. The use of SEM in microstructural analysis is an essential tool for investigating the cause of failure in this type of component. After the steps of tempering and annealing, the steel samples have their own microstructure transformed from perlite + ferrite to martensite, as shown in figure 1. According to results, it was observed that there was a predominance of ruptures generated by fatigue, except for a spring with rupture at 57600 cycles, which presented a defect coming from raw material. In this sample, mechanical properties tests, fracture analysis by electron microscopy and metallographic analyzes were performed. SEM images revealed the connection between the defect and the beginning of the fracture, as well, the presence of oxides inside the defect, as shown in figure 2 and figure 3, respectively.

REFERENCES

[1] M. L. AGGARWAL, et al., Indian J. Engg. & Mat. Sci., 12(6) (2005) 515.

[2] This research was supported by LNLS (National Synchrotron Light Laboratory)

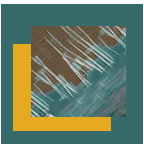


Figure 1. Martensitic microstructure obtained by tempering and annealing in SAE 9254 steel samples.

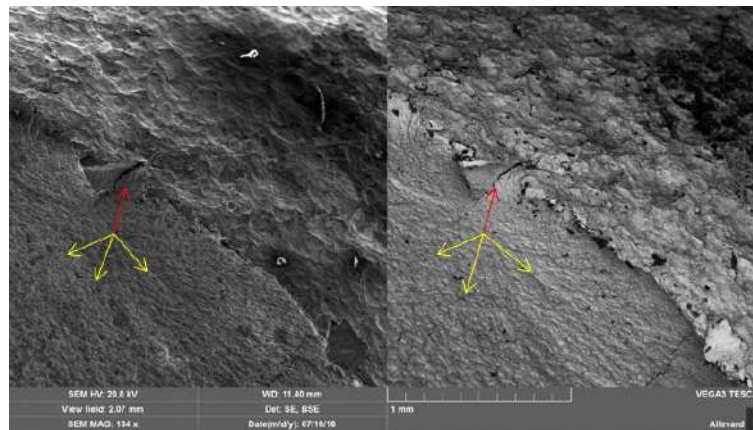


Figure 2. SEM images of the beginning of the fracture, red arrows indicate an initial crack and the yellow arrows, the direction of rupture propagation.

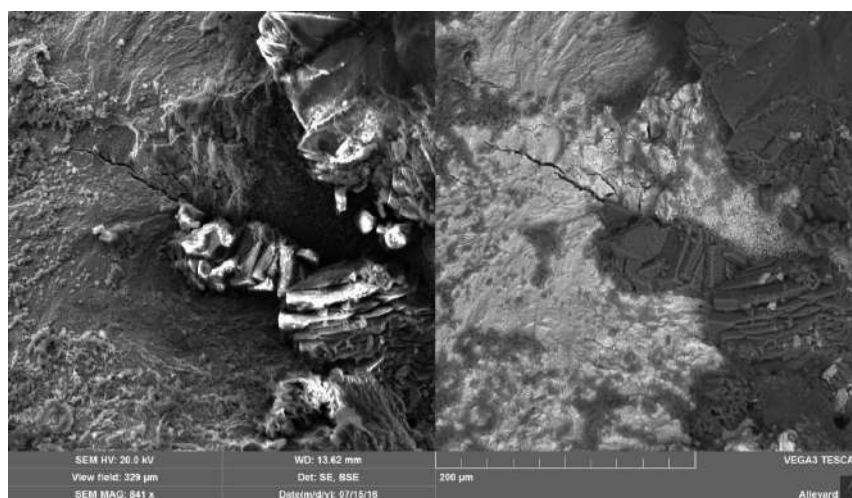


Figure 3 SEM images of the beginning of the fracture, red arrows indicate the presence of oxides inside the defect.



DOI: INSERIR ENDEREÇO DO DOI AQUI.

Caderno de Resumos do 26º Congresso Brasileiro de Microscopia da SBMM – ISSN: INSERIR AQUI.

Size And Polydispersity Trends Found In Gold Nanoparticles Synthesized By Coconut Water

Rafaela S. Valotto¹, Wanderson J. Keijok¹, Danilo S. Costa¹, Jairo P. Oliveira¹ and Marco C. C. Guimarães^{1*}

1. Universidade Federal do Espírito Santo, Av. Maruípe, s/n, 29053-360 Vitória, ES.

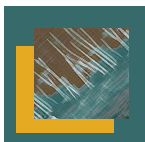
* Email: marco.guimaraes@ufes.br

This study reports a green route to produce gold nanoparticles using coconut water. The aqueous solution of tetrachloroauric hydrogen (HAuCl_4) was exposed to coconut water *in natura* and lyophilized (150 mg.mL^{-1}) (Table 1). The nanoparticles were characterized by UV–Visible spectroscopy (UV–Vis) (Image 1) and Transmission Electron Microscopy (TEM) (Image 2 and 3). The solution presented purple and deep pink coloration, indicating high amounts of shapes and sizes [1]. The UV–Vis spectra of the gold nanoparticles gave surface plasmon resonance at 540 nm while the TEM nanoparticles analyses revealed the particles distribute polydispersely. Although the coconut water presents a substantial reducing potential, their stabilize activity are low. Therefore, in order to obtain a monodisperse distribution, with well-defined shapes and sizes, we believe that be suitable the utilization of stabilizing agents during the synthesis. Furthermore, the reducing potential of coconut water lyophilized shows more efficient than *in natura*.

REFERENCE

[1] J. Turkevich, G. Garton, P. C. Stevenson, The color of colloidal gold. 9 (1954) 9.

Thanks to Laboratório Multiusuário de Análises Biomoleculares CCS/UFES (LABIOM), Universidade Federal do Espírito Santo (UFES) and Laboratório de Ultraestrutura Celular Carlos Alberto Redins (LUCCAR).



Assays	Processing	Concentration of lyophilized coconut water (mg.mL ⁻¹)	Reaction time (min)	Agitation (rpm)	Temperature (°C)	pH
1	<i>In natura</i>	-	15	400	80	5
2	<i>In natura</i>	-	15	400	95	5
3	Liofilized	150	30	100	80	5
4	Liofilized	150	30	400	90	5

Table 1. Synthesis conditions of gold nanoparticles with coconut water. The HAuCl₄ concentration utilized in all syntheses was 2,5 x 10⁻⁴ M.

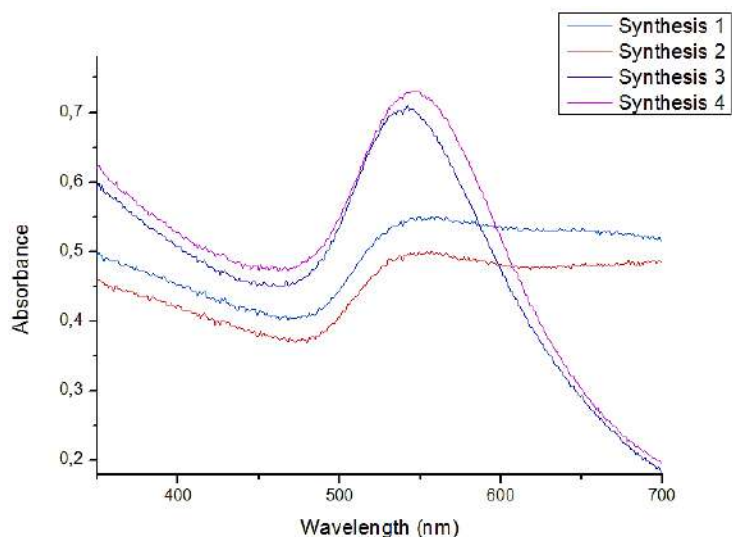


Figure 1. UV-visible spectra of gold nanoparticles at different conditions.

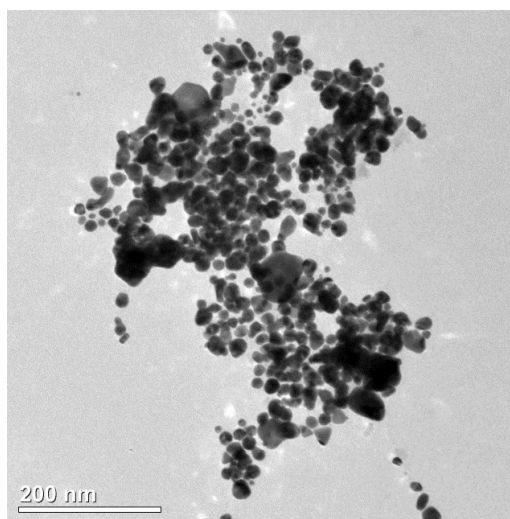


Image 2. TEM image of synthesis 1. Magnification of 120,000.

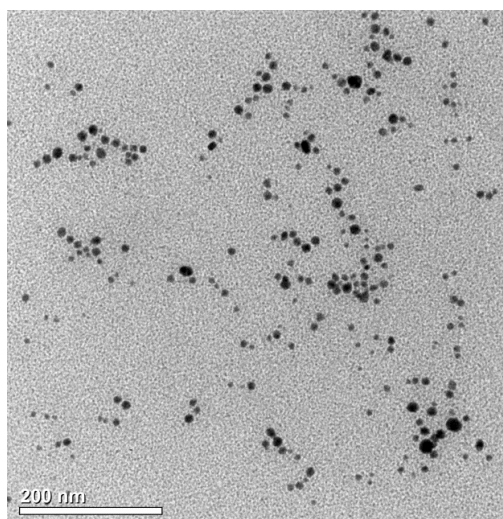
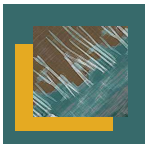


Image 3. TEM image of synthesis 3. Magnification of 120,000.



Non-destructive, microstructural and mechanical performance evaluation of metal-polymer hybrid structures

Pereira Pinto, R.1; Paciornik, S.1 *; Etzberger Feistauer, E.2; Manente Andre, N.2; Zocoller Borba, N.2; Mauricio, M. H. D P1; dos Santos, J. F.2, Amancio-Filho, S. T.2,3, **

1. Department of Chemical and Materials Engineering, PUC-Rio, Rio de Janeiro, Brazil.
2. Helmholtz-Zentrum Geesthacht, Centre for Materials and Coastal Research, Institute of Materials Research, Materials Mechanics, Solid State Joining Processes, Geesthacht, Germany.
3. Hamburg University of Technology, Institute of Polymer Composites, Hamburg, Germany

*Email: sidnei@puc-rio.br (NDT), **Email: sergio.amancio@hzg.de (joining processes)

The transportation industry has been facing stringent environmental regulations to decrease the fuel consumption and CO₂ emissions. A promising solution to fulfill these demands is decreasing the structural weight of vehicles by combining lightweight alloys and fiber-reinforced polymers in hybrid structures. However, the physical and chemical material dissimilarities are a challenge for the joining process of such hybrid structures. Conventional joining technologies are usually inadequate to produce high performance metal-polymer hybrid joints. Thus, advanced joining technologies are under development to overcome these limitations. In the present work, metal-polymer/composite hybrid joints were produced using three new friction-based joining techniques: Ultrasonic Joining (U-Joining) [1] (Fig. 1), Friction Spot Joining (FSpJ) [2] (Fig. 2) and Friction Riveting (FricRiveting) [3] (Fig. 3). Two joining conditions with different heat input levels (low and high) were selected to produce hybrid joints for each joining technology. The joint formation along with process-related microstructural changes of the joints and their influence on mechanical performance were studied. Process temperature, thermomechanical-induced flaws, microstructural features and interface quality were correlated with the quasi-static mechanical performance of the joints. The failure mechanisms were also evaluated and correlated with the microstructural features and the mechanical performance of the joints. Microscopy techniques (*i.e.* optical, confocal laser and scanning electron), X-ray micro-computed tomography (μ CT), lap shear and T-Pull testing were chosen for this purpose. The current abstract focuses on the microstructural characterization – mechanical testing results will be reported elsewhere. In this context, high-resolution tridimensional μ CT characterization of the hybrid joints' internal features (*i.e.* voids, metallic fragments, agglomerates, process-related joint geometrical changes) was performed to evaluate joint feature shape, size, and distribution. Therefore the understanding of the joint formation, process-related changes of internal features and their correlation with joint mechanical performance were established by combining μ CT tri-dimensional volumetric rendering, optical and electron microscopy, and quasi-static mechanical testing.

REFERENCES

- [1] AMANCIO-FILHO, S. T.; FEISTAUER, E. E.; DOS SANTOS, J. F. European Patent Application EP3078480A1, 2015.
- [2] AMANCIO-FILHO, S. T.; DOS SANTOS, J. F. European Patent 2329905B1, 2012.
- [3] AMANCIO-FILHO, S. T.; BEYER, M.; DOS SANTOS, J. F. European Patent DE102005056606A1, 2005.

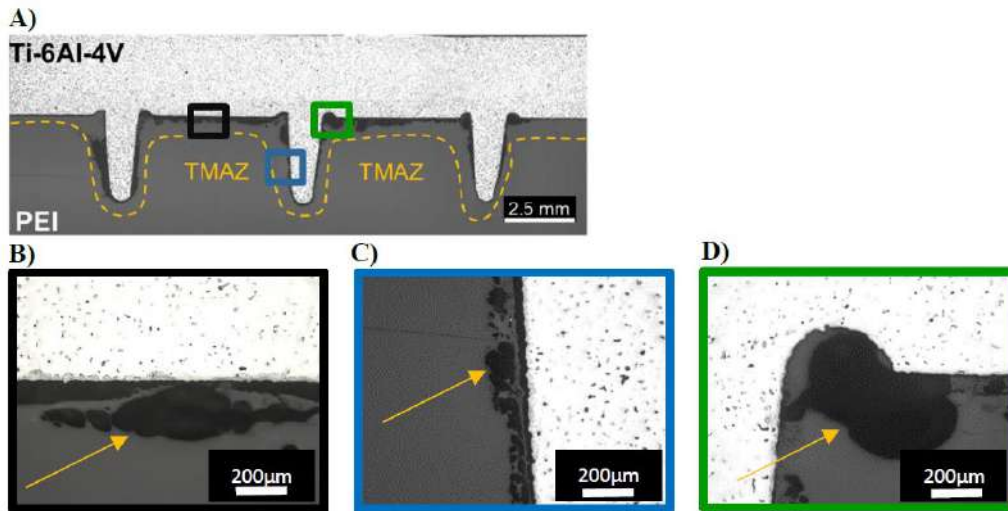
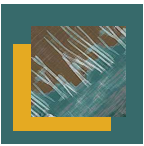


Figure 1. Cross-sectional view of ultrasonically joined Ti-6Al-4V/PEI joint obtained by optical microscopy (A) and detailed images of process-induced flaws in the Thermo-mechanically affected zone, TMAZ (B) (C) (D).

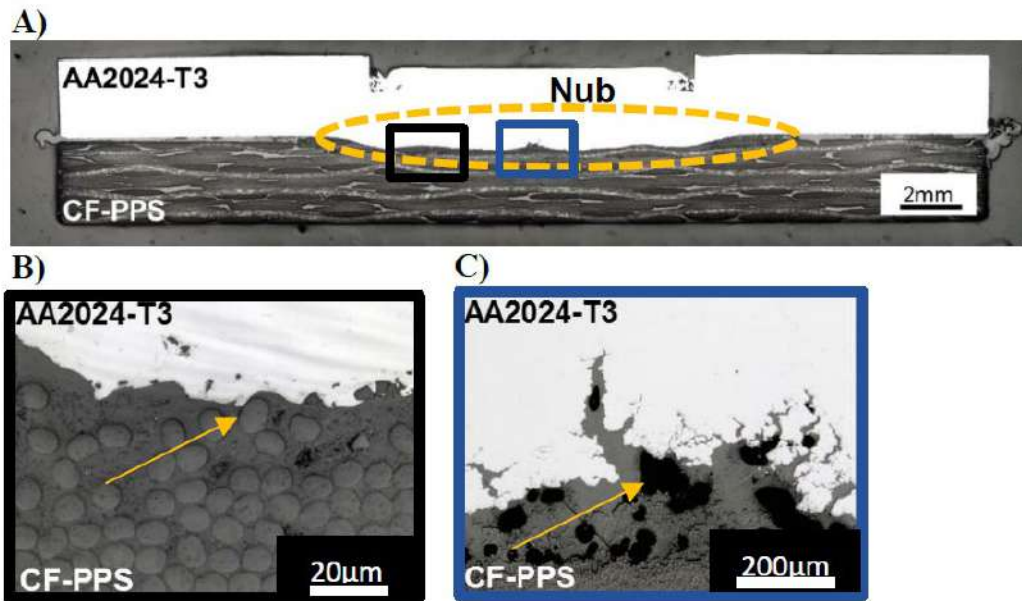


Figure 2. Cross-sectional view of an AA2024-T3/CF-PPS friction-spot joint obtained by and optical microscopy (A). (B) Entrapment of polymer matrix and fibers into the irregularities of the metal surface. Detail view of the metal-composite interface showing process-induced volumetric flaws (C).

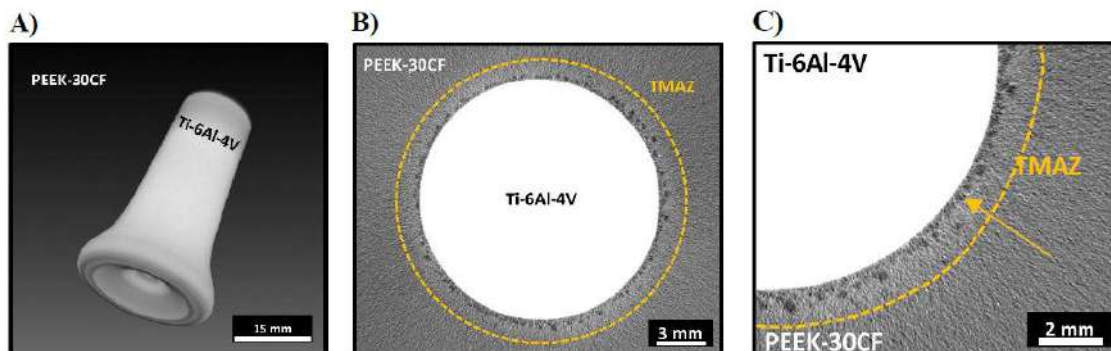


Figure 3. 3D view of a Ti-6Al-4V/PEEK-30CF friction-riveted joint obtained by μ CT (A). Process-induced flaws in the TMAZ (B), magnified view (C).



Characterization by X-ray Computed Tomography of Class G Oil Well Cement Paste Exposed to Elevated Temperature

R. Lorenzoni^{1*}, M. H. D. P. Mauricio¹, S. Paciornik¹ and F. A. Silva²

1. Dept. of Chemical and Materials Engineering, PUC-Rio, Rio de Janeiro - RJ, Brazil.

2. Dept. of Civil Engineering, PUC-Rio, Rio de Janeiro - RJ, Brazil.

*Email: renata_lorenzoni@hotmail.com

Class G oil well cement is used in oil and gas well cementing procedures. During the life cycle of an oil well the cement paste is subjected to various forms of deterioration which affect its durability. One of these forms of deterioration is due to the effect of elevated temperatures that can reach 350°C [1]. Therefore, studies to analyze the deterioration of cement paste by the effect of elevated temperatures are of utmost importance. In the present study, cement paste cylindrical specimens with dimensions of $\varnothing 1 \times 2$ in were subjected to temperatures of 100°C, 450°C and 650°C for one hour. The temperature of 100°C was chosen because it is usual in oil well operation. The temperatures of 450°C and 650°C were chosen from the results of the thermal analysis of previous studies [1]. The temperature of 100°C indicates the beginning of the decomposition of C-S-H while the dehydroxylation of $\text{Ca}(\text{OH})_2$ occurs at 450°C. At 650°C the degradation of CaCO_3 takes place. X-ray computed tomography (microCT) was used to generate three-dimensional images to visualize the internal structure of the samples before and after the high temperature tests, and to quantitatively assess the evolution of pore structures and cracking. The results of the qualitative and quantitative analysis of the sample submitted to 100°C showed the appearance of small cracks (Figure 1), but the pore structures did not change (Figure 2). In the sample subjected to 450°C the appearance of several cracks was visualized (Figure 3). The specimens submitted to 650°C were completely degraded (Figure 4), making it impossible to scan them in microCT. As a partial conclusion, the Class G Oil Well Cement Paste can be used for operations with service temperatures up to 100°C, as it showed small amounts of narrow cracks. Finally, the dehydroxylation of $\text{Ca}(\text{OH})_2$ and the degradation of CaCO_3 led to a high deterioration of the studied cement paste.

Keywords: x-ray computed tomography, class G oil well cement Paste, elevated temperature.

REFERENCES:

[1] ZHU, H., WU, Q., ZHANG, C., DENG, F. Thermal stability and structural characterization of class g oil well cement paste exposed to elevated temperature. *Journal of Materials in Civil Engineering*, V.27 No.11, 201.

[2] Research with the support of FAPERJ and CNPq.

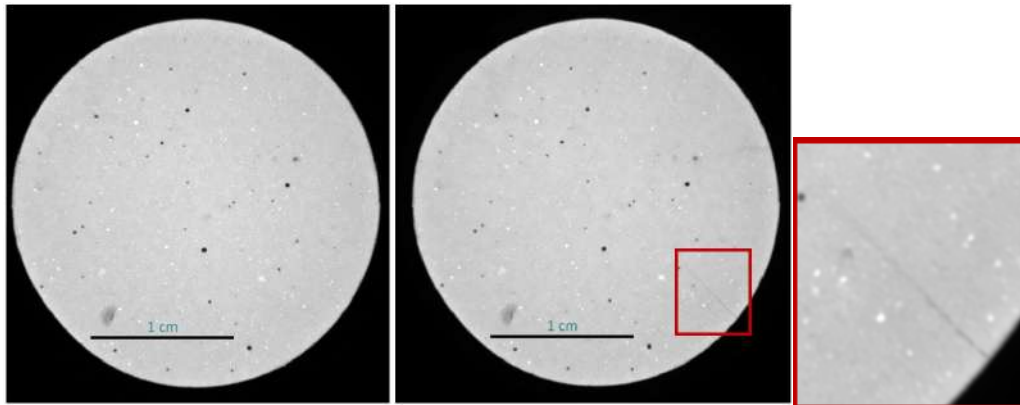
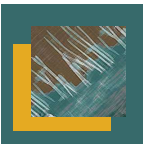


Figure 1 - Appearance of small cracks after 100°C test.

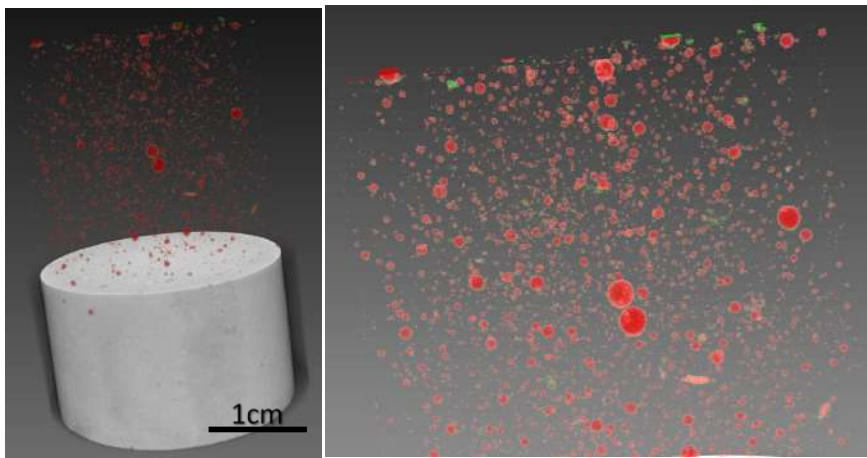


Figure 2 - Overlapping of the pores structures before (red) and after (green) 100°C test.

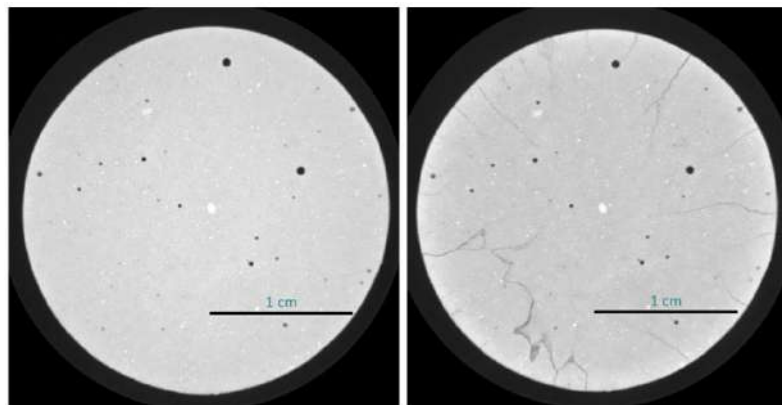


Figure 3 - Appearance of several cracks after 450°C test.



Figure 4 – Picture after 650°C test.



Nanostructures based in TiO₂ on titanium

Renata Santos Seixas, Isabela da Rocha Silva, Juliana do Nascimento Lunz, Paula Mendes Jardim

Department of Materials and Metallurgy Engineering, Federal University of Rio de Janeiro (UFRJ), Rio de Janeiro, Brazil.

Email: pjardim@metalmat.ufrj.br

Titanium oxide (TiO₂) has attracted great attention from the scientific community due to its chemical stability, non-toxicity, low cost, photocatalytic potential, biomedical applications, among other properties. This paper's materials of interest are 1D nanostructures of sodium titanate (after synthesis), hydrogen titanate (after acid washing) and nanostructures based on TiO₂ (after calcination). The 1D sodium titanate nanostructures were grown on a metallic titanium plate, and obtained by the alkaline hydrothermal route [1, 2, 3, 4]. Thus, this work aims to elucidate the effect of synthesis conditions on the morphology and crystal structure of these 1D nanostructures, before and after the washing, and calcination treatments. For this purpose, we used X-ray diffraction, scanning electron microscopy and transmission electron microscopy. The nanostructured films were synthesized on metal Ti disks of degree 4 purity by hydrothermal route using NaOH solution in a Berghof reactor model BR500. For the acid washing step, 5% HNO₃ solution was used. The samples were also heat treated for 2h at 550 °C. Different synthesis conditions were tested to evaluate the most appropriate method of obtaining the material of interest. For all the synthesis conditions the temperature was fixed at 150°C. Three NaOH solution molarity (1M, 3M and 5M) and three time of synthesis (2h, 6h and 10h) were investigated. Through the XRD results of the materials produced by alkaline hydrothermal synthesis, the crystalline structure of sodium trititanate (Na₂Ti₃O₇) were identified (before to acid washing). SEM images (figure 1) shows samples obtained with different synthesis conditions after washing with distilled water. Figures 1c (3M, 6h) and 1d (5M 2h) showed the formation of 1D nanostructures (nano nest-like structure). When the most extreme condition was tested (5M NaOH for 10 hours of synthesis), cracks were observed in the film and poor adhesion to the substrate. However, using milder conditions, such as 5M NaOH for 2 hours of synthesis (Figure 1d), cracks were not visualized on the material surface. The sample synthesized with 3M NaOH for 6 hours of synthesis (Figure 1c) also showed good results without cracking in the film. However, the samples produced with 1M NaOH for 2 or 6 hours of synthesis (Figures 1a and 1b respectively) did not present structures with well-defined scaffold structure as the samples previously mentioned. Modification of the surface of titanium substrates for biomedical applications plays a significant role in the integration of bone tissue at the interface of the material. Therefore, this preliminary study of the growing of nanostructures on titanium surface is of great importance since it will help to determine the adequate synthesis conditions to optimize the process of osseointegration of titanium implants.

REFERENCES

- [1] R. YOSHIDA et al., J. Solid State Chem. 178 (2005) 2179.
- [2] J. XIE et al., J. Mater. Sci. Technol. 28 (Suppl. 6) (2012) 488.
- [3] L. LIN et al., J. Orthop. Translat. 2 (2014) 35.
- [4] R. CAMPOSECO et al., Catal. Today (2015) 1.

This research was supported by CNPq (Brazil).



DOI: [INSERIR ENDEREÇO DO DOI AQUI.](#)

Caderno de Resumos do 26º Congresso Brasileiro de Macroscopia da SBMM – ISSN: [INSERIR AQUI.](#)

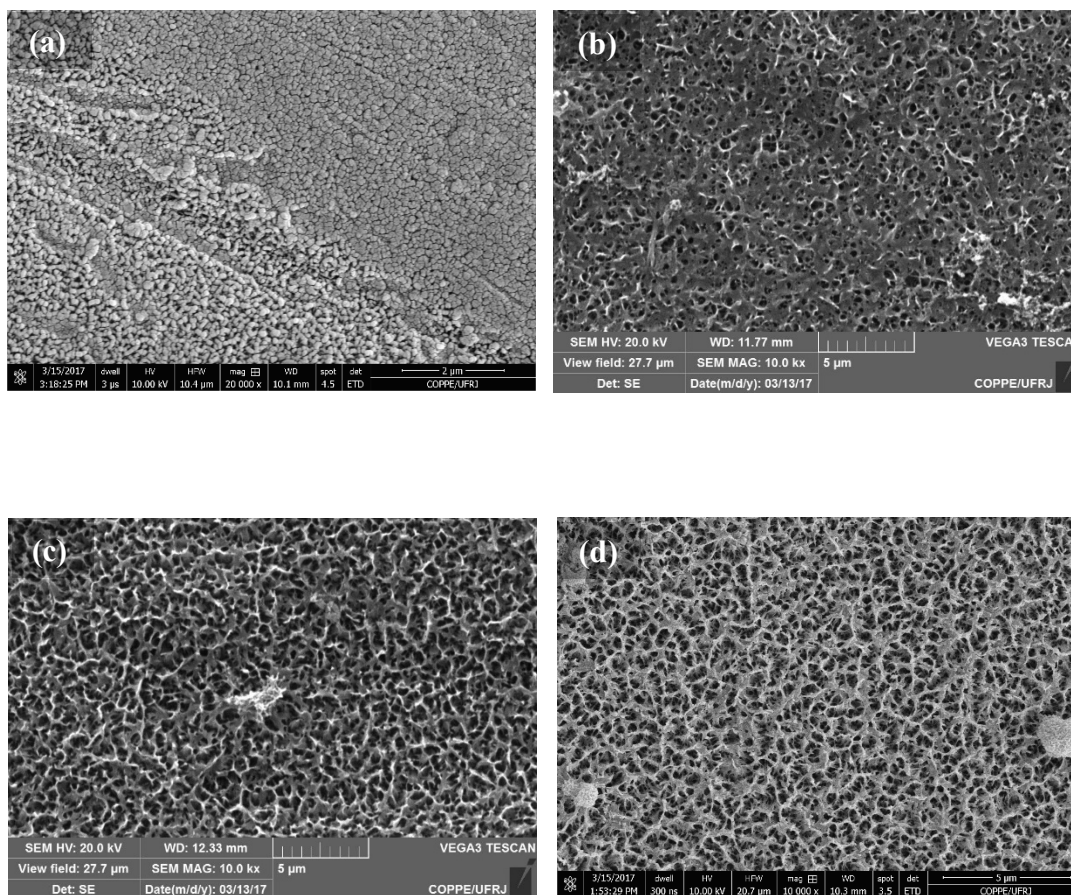


Figure 1: Shows the growth of nanostructures on titanium using hydrothermal synthesis, after washing with distilled water: (a) synthesized with 1M NaOH for 2 hours; (B) synthesized with 1M NaOH for 6 hours duration; (C) synthesized with 3M NaOH for 6 hours; (D) synthesized with 5M NaOH for 2 hours.



Characterization of Oxide Layer Formed on External Surface from Steam Reformer Furnaces Tubes

Rosa Maria Sales da Silveira^{1*}, Luiz Henrique de Almeida¹, Adriana da Cunha Rocha¹ e Carlos Bruno Eckstein²

1. PEMM-COPPE/UFRJ, Caixa Postal 68505, Rio de Janeiro, CEP 21945-970, Brazil.
2. PETROBRAS-CENPES, Cidade Universitária, Rio de Janeiro – RJ, CEP 21040-000

*Email: rosasilveira@metalmat.ufrj.br

Steam reforming furnaces are used in the petrochemical industry to produce bulk hydrogen. These furnaces consist of counterweight suspended columns disposed in a sequence of rows, manufactured with Nb-modified centrifugally cast HP-Type stainless steel tubes, in some cases microalloyed with Ti. The burners, localized on the roof of combustion chamber, are disposed in rows on both sides of the columns [1]. The furnace configuration generates temperatures, which vary between 600 and 1000 ° C along the height of the columns, causing diverse microstructural modifications associated to the different stages of aging [2]. Depending on the operational conditions of the furnace, these alloys may suffer premature damages caused mainly by creep, which reduces the service lives of the columns. Studies are therefore being carried out to develop advanced eddy current non-destructive inspection techniques, aiming at characterizing the aging state along the heights of the columns [3-4]. The external surface of the tubes is however, exposed to severe oxidizing conditions, causing the formation of an oxide layer with ferromagnetic characteristics that severely hinders eddy current measurements. The objective of the present work is to characterize the oxide layer formed on the external surface of service exposed reformer tubes, in order to correlate their microstructural characteristics and composition to their aging state. The morphological characterization of the oxide layer at different heights of the reforming columns was carried out via high-resolution scanning electron microscopy (SEM) in backscattered electron mode, with a VERSA 3D Dual Beam scanning electron microscope. The elements present in the oxide layer as well as their distribution were identified through EDS chemical composition mapping with an EDAX EDS3 spectrometer. The results showed that the external surface of the samples is composed of a subsurface layer depleted in chromium and chromium carbides, Figure 1. The oxide layer is composed of sublayers of oxides SiO_2 , MnCr_2O_4 , Cr_2O_3 , Fe_3O_4 e NiFe_2O_4 , identified by X-ray diffraction, whose distribution defines a sequence which is repeated for different columns and heights submitted to different skin temperatures, Figure 2. Average thickness measurements showed that both the oxide, and the chromium depleted layers grow with temperature exposure.

REFERENCES

- [1] T.L. da Silveira et al., Arab. J. Sci. Eng. 31 (2006) 99–119.
- [2] I. Le May et al., Int. J. Press. Vessel. Pip. 66 (1996) 233-241.
- [3] M. Arenas, In: XIV Brazil MRS Meet., SBPMat (2015) 3-5.
- [4] M.P.C. Arenas, Dissert. MSc., UFRJ, Rio de Janeiro, 2013.

The authors would like to thank CAPES for the financial support and Petrobras for supplying the samples.

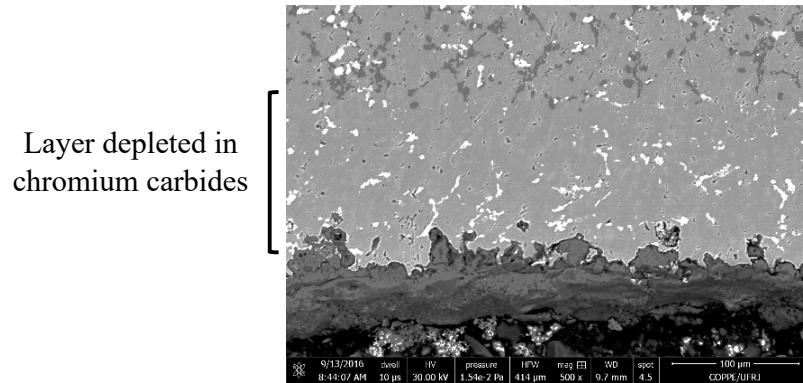
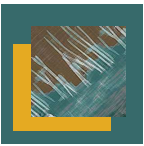


Figure 1 – SEM image in backscattered electron mode showing the morphological characteristics of the external surface of the HP tube sample taken from a Nb-Ti modified HP tube, located in the exposed region at temperatures of 800 to 900°C for 90.000 hours.

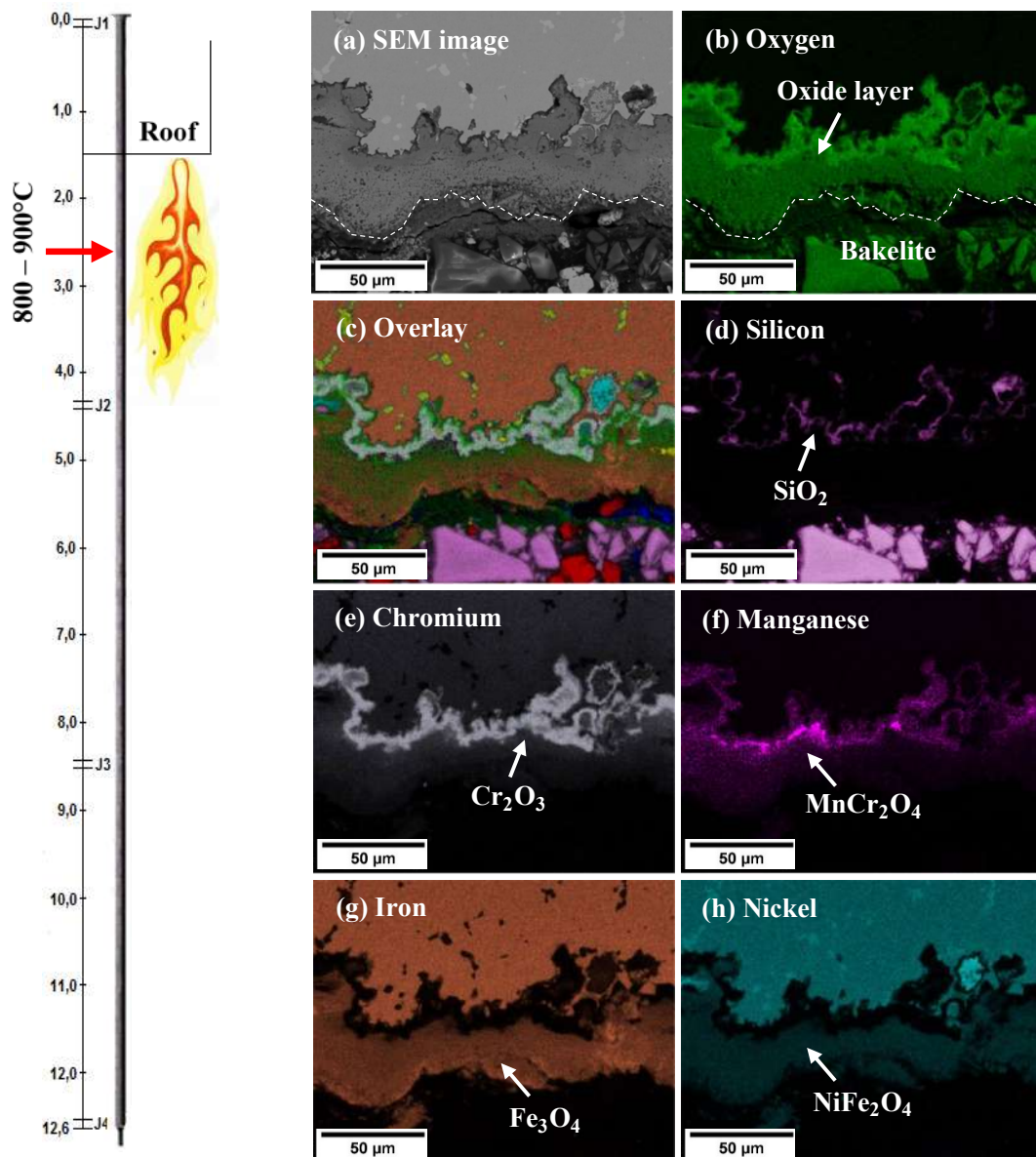
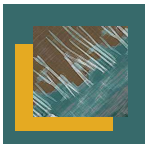


Figure 2 – Chemical composition mapping of the external surface of sample located in the exposed region at temperatures of 800 to 900°C. The oxides distribution from (a) to (h) describes a standard sequence which is repeated for different heights (exposed to different temperatures) and columns that operated for 90.000 to 135.000 hours.



Study and analysis of failures in multilayer ceramic capacitors by mechanical stress

Fonseca R. T.^{1,2*}, Antonelli E.², Matos C. P.¹

1. Integration and Testing Laboratory – LIT/National Institute for Space Research – INPE, São José dos Campos – SP, Brazil.

2. Federal University of São Paulo – UNIFESP; São José dos Campos – SP, Brazil

*Email: tatiana.hazine@gmail.com, antonelli.eduardo@gmail.com

The use of multilayer ceramic capacitors in electronics projects has been growing due to the high product reliability and the high energy storage in a small area. These components are built as monolithic chips consisting of a multilayer structure of electrodes and dielectric ceramics (Figure 1a). The multilayer structure allows the use of very thin ceramic dielectric layers of approximately 20 μm (Figure 1b). In general, the constructions are inner electrode nickel plates and arranged in a pattern with adjacent plates extending to a barium titanate ceramic block (Figure 1c). The exposed ends of the electrodes are electrically interconnected with a copper conductor by means of an externally applied metallized coating, called termination, consisting of tin-lead alloy [1, 2]. Often these devices fail, which impairs the performance of their function. Failures occur on the ceramic surface in the form of macro cracks or between layers [3]. Failures in capacitors originate from mechanical and thermal stresses. Mechanical failure occurs because of bending during the handling of the printed circuit board (PCB) with the capacitor mounted. In general, a small degree of board warping in this process already exceeds the resistance limit value of the capacitor, and the crack begins at the junction of the capacitor with the PCB [3]. A component failure is usually checked by microscopy of the sectioned sample. This work aims to verify and analyze the occurrence of cracks in ceramic capacitors by means of non destructive tests using the technique of impedance spectroscopy, and to confirm the analysis results by microscopy. Type X7R ceramic capacitors, composed by BaTiO_3 , were submitted to 3-point bending tests to simulate mechanical failure, and their capacitance values monitored in the fixed frequency of 1 kHz. The tests allowed verifying a decrease of the capacitance or even the lack of electrical response (Figure 2). Scanning electron microscopy was used to evaluate the component construction and to analyze the failures.

Keywords: multilayer ceramic capacitors, scanning electronic microscope and impedance spectroscopy

REFERENCES

- [1] Prevallet M, Bagdy S, Prymak J, Randall M. High voltage considerations with MLCS [abstract]. 2004 [Presented at Power Modulator Symposium, 2004 and 2004 High-Voltage Workshop. Conference Record of the Twenty-Sixth International, 2004 May; 42-45; San Francisco-CA
- [2] Chien PL, Yen FL, Chang HL, Hung CC, Yi CK, Jeng YL, et al.. A novel decapsulation technique for failure analysis of epoxy molded IC packages with Cu wire bonds. *Microelectronics Reliability*. 2012; 52: 725–734
- [3] Bergenthal J. Ceramic Chip Capacitors “Flex Cracks” Understanding & Solutions. Kemet Electronics Corporation. F-2111/98

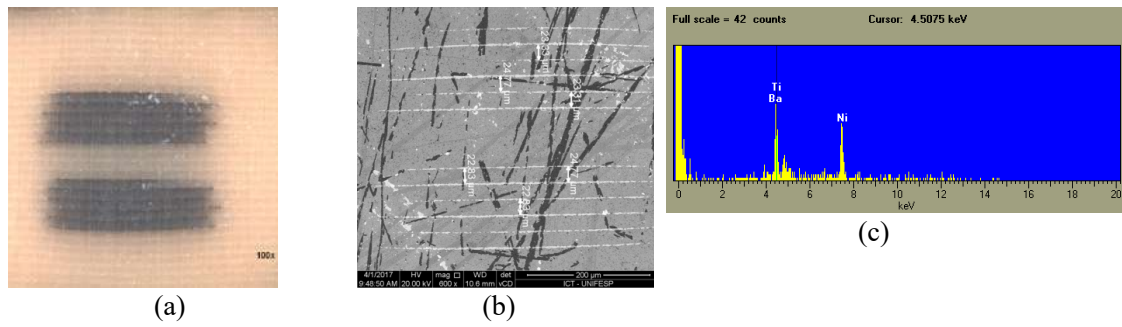
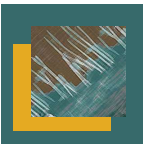


Figure 1 – Microscopic images: a) with optical microscope, b) with backscattered SEM beam and c) EDS analysis

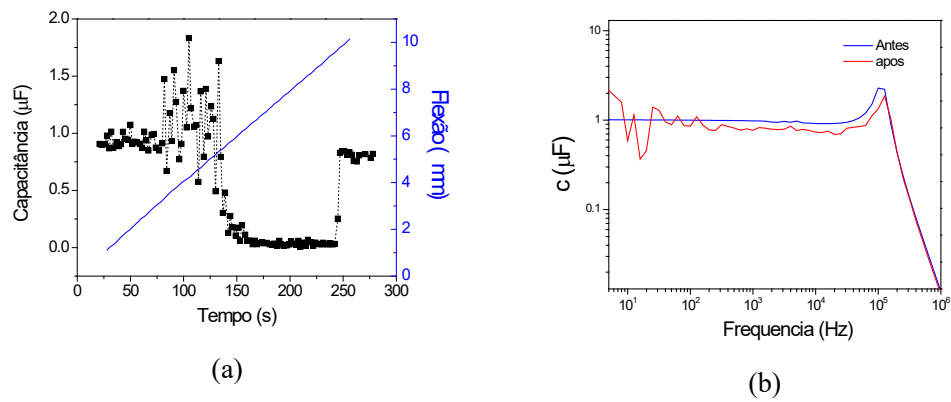


Figure 2 – Sample 22091605: a) Deflected sample deflection capacitance and b) Impedance capacitance before and after the bending test



Artifacts on the Characterization of Copolymer Micelles by TEM Using Phosphotungstic Acid for Negative Staining

I. S. de Oliveira¹, R. A. Bernardo¹, T. O. Santos^{2*} and E. C. D. Lima¹.

1. Instituto de Química da Universidade Federal de Goiás, Goiânia, GO, Brazil.

2. Instituto de Física da Universidade Federal de Goiás, Goiânia, GO, Brazil.

*Email: tatiane_oliveira@ufg.br

Polymeric systems have been proposed as strategy to overcome the constraints related to the applications of hydrophobic drugs. The solubility and bioavailability of these drugs can be increased if they were conjugated to the water-soluble polymers and their toxicity can be reduced, once the polymeric system allow the drug to be preferentially delivered at specific sites [1]. In this context we have used micelles of poly(ethylene glycol)–poly(caprolactone) (PEG–PCL) copolymer [2] and thiolated chitosan (TC) microspheres [3] for delivery of amphotericin B (AB). AB is a macrocyclic polyene extracted from *Streptomyces nodosus*. It has an amphiphilic character and presents very low solubility in water. In spite of having good antifungal activity, AmfB present high toxicity [4]. In this communication we present results related to tentative of characterizing the size and morphology of PEG-PCL micelles and CT microspheres loaded with AB by conventional transmission electron microscopy (TEM) using phosphotungstic acid (PTA) as negative staining. The morphological characteristics and the particle size of PEG–PLA micelles and CT microspheres were examined in a transmission electron microscope (JEOL JEM-2100) operated at 100kV accelerating voltage. The PEG–PLA micelles and the CT microspheres were diluted from its respective suspensions with distilled water and one drop of each diluted suspension was deposited on carbon-coated copper grids and dried at room temperature. Sample was negatively stained with 2% PTA solution by applying a drop of solution over each grid, which were let to dry by evaporation, at room temperature. The mean sizes of the PEG-PCL micelles and CT microspheres were also measured by dynamic light scattering (DLS) using a Malvern, Nano-ZS equipment. Figure 1 (A-1 and A-2) present the images of the AB loaded PEG-PCL micelles. The images confirm the expected spherical shape of the micelles and the mean size obtained from a histogram was 17 nm. These images are very similar to the image presented by Gong *et al.* (2013) for curcumin loaded PEG-PCL micelles [2]. The mean size of the AB loaded PEG-PCL micelles measured by DLS was 26 nm, and the difference between the size measured by TEM was attributed to the dehydration of the sample. On the other hand, the images obtained from AB loaded CT microspheres (Figure 2 B-1 and B-2) present structures and size very similar to the images of PEG-PCL micelles presented in figure 1. As the size of the CT spheres measured by DLS was 500 nm, we started to speculate if the images of both samples would be artifacts of the staining process. Then, we have examined carbon-coated copper grid, without sample, treated with PTA. The results presented in figure 3 (C-1 and C-2) show that the evaporation of PTA solution over the carbon grid lead to the formation of structures with shape and mean size very close to that observed in the images of micelles and microspheres. The mean diameter in these structures was 18 nm. In conclusion, negative staining with phosphotungstic acid can introduce artifacts with the shape and size with magnitude similar to that of AB PEG-PCL loaded micelles, which makes not reliable the characterization of the system by this methodology.

REFERENCES

- [1] Ulrich et al. *Chem Rev.*, 99 (1999).
- [2] Gong C. et al. *Biomaterials.*, 34 (2013).
- [3] He et al. *Int. J. Pharm.*, 166 (1998).
- [4] Les K.A. et al. *Polym. Chem.*, 5 (2014).
- [5] This research was supported by CNPq (Brazil).

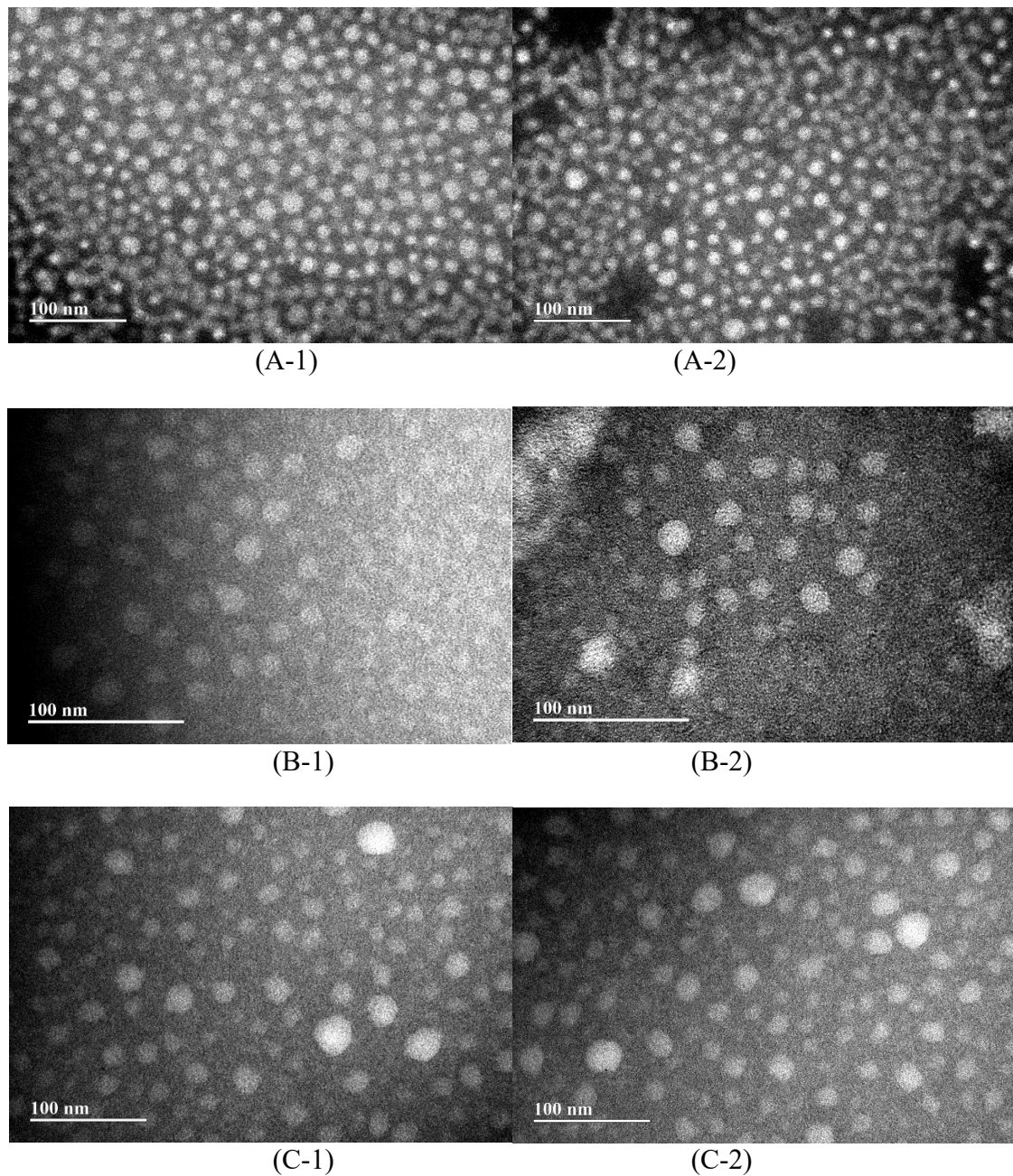
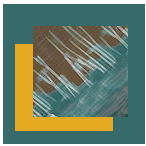


Figure 1 – A-1 and A-2, PEG-PCL micelles negatively stained with 2% PTA; B-1 and B-2, CT microspheres negatively stained with 2% PTA and C-1 and C-2, carbon-coated copper grid without sample negatively stained with 2% PTA.



DOI: [INSERIR ENDEREÇO DO DOI AQUI.](#)

Caderno de Resumos do 26º Congresso Brasileiro de Macroscopia da SBMM – ISSN: [INSERIR AQUI.](#)

Study of Physicochemical Properties of a Hybrid Coagulant Used in Potable Water Treatment

Valquíria Campos^{1,*}, Jhoan Sebastian Jaramillo Peralta², Isaac Jamil Sayeg³

São Paulo State University (UNESP), Institute of Science and Technology, Sorocaba, Brazil¹
University of Valladolid (UVA), Environmental Engineering, Valladolid, Spain²
University of São Paulo (USP), Institute of Geoscience, São Paulo, Brazil³

*Email: vcampos@sorocaba.unesp.br

Some companies produce commercial gamma-polyglutamic acid (γ -PGA) for different sectors of the economy. Nippon Poly-Glu Co. Ltd. produces PG α 21Ca for water treatment. Aluminum sulfate and polyaluminum chloride (PAC) are coagulants widely used in water treatment plants (WTP), but the use of these products containing aluminum salts has been questioned because they are harmful to human health and have even been linked to Alzheimer's disease. Another disadvantage is the generation of nonbiodegradable sludge, which must be discarded in landfills, increasing operating costs and polluting the environment. Thus, biopolymer has attracted increasing attention, given its biodegradability and innocuousness, and because it generates little residual sludge. Campos et al. (2016), who carried out coagulation-flocculation tests and separated solids from liquid phase by sedimentation with PG α 21Ca, achieved better results in the removal of both apparent color and water turbidity in the Salto de Pirapora WTP than with PAC and aluminum sulfate coagulants. An essential process in most water treatment technologies is the coagulation of raw water, which is aimed at ensuring adequate levels of quality such as turbidity of less than 1 NTU and absence of pathogens. Gamma-polyglutamic acid can be extracted from soybeans. γ -PGA is naturally present in the mucilage of fermented soy products consumed in Asian countries, and soy and soybean derivatives are potential substrates for biopolymer production. The use of γ -PGA in water treatment increases flocculation, among other properties. The purpose of this work is to produce γ -PGA using different soybean cultivars and a new formulation, comparing its removal efficiency of apparent color and water turbidity against that of PG α 21Ca. The PG α 21Ca was characterized to determine its chemical composition, thermal stability, and morphology by means of X-ray fluorescence spectrometry (XRF), X-ray diffraction (XRD), elemental analysis, infrared spectroscopy, thermal analysis and scanning electron microscopy. Before subjecting the PG α 21Ca to physicochemical characterization, it was sifted through a stainless steel sieve (Tyler, 200 mesh) with 0.075 mm sieve opening size, placed in stoppered flasks, and stored in a desiccator. Structural information about PG α 21Ca was obtained using a conventional scanning electron microscope (SEM). The micrograph was magnified by up to 5000 X after coating the surface of the sample with Au. The analysis was performed using a scanning electron microscope (LEO 440i) coupled to an energy dispersive X-Ray spectrometer (EDS) (Oxford Si (Li) detector). The microstructure of the sample was examined by SEM. To this end, the powder sample was spread on an adhesive, double-stick carbon tape which was then pressed onto a 0.5 inch diameter stub. Various areas of the sample spread on the stub were examined, and after ensuring that its morphology and morphometry did not vary, images were recorded with a secondary electron detector. The SEM micrographs and X-ray diffraction patterns (Table 1) revealed morphologies typical of gypsite (Figure 1). The mineral sometimes appeared in the form of thick platelets ranging in size from 10 to 30 μ m, and at others, as aggregates of up to 30 μ m in size, composed of particles of approximately one micron. The representativeness of the sample can be shown in other micrographs. Chemical mapping of the composition of PG α 21Ca by EDS revealed the presence of Ca, S, Si and Al. The results of these analyses of PG α 21Ca indicate that it is essentially inorganic, containing high levels of calcium sulfate (87%) and 5% of γ -polyglutamic acid, among other chemical compounds. PG α 21Ca was highly efficient in the removal of turbidity and apparent color, with a residual value of 1.93 NTU of turbidity and a removal efficiency



of 96.89% of apparent color and little change in the pH level of the medium, indicating its effectiveness for public water supply treatment.

[1] V. Campos et al., J. Environ. Chem. Eng. 4 (2016) 3753.

[2] This research was supported by FAPESP (grant 2015/02650-8) and CNPq (grant 400040/2016-6).

Table 1 Interlayer spacing d_{hkl} on dried basis (nm).

PG α 21Ca	d/l	d/l	d/l
Gypsum	0.426/100	0.755/88.21	0.266/36.27
Anhydrite	0.349/100	0.285/60.16	0.220/38.88

Note: d-spacing and I-intensity

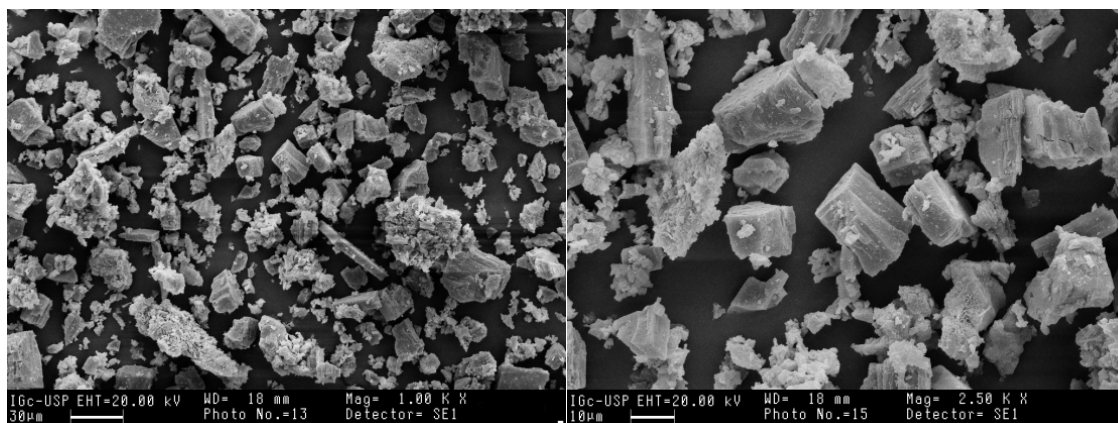
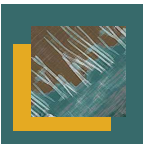


Figure 1. SEM images of PG α 21Ca (1000 and 25000x magnification).



DOI: [INSERIR ENDEREÇO DO DOI AQUI.](#)

Caderno de Resumos do 26º Congresso Brasileiro de Microscopia da SBMM – ISSN: [INSERIR AQUI.](#)

PARTE 6

PÔSTERES
- OUTROS



Evaluation of the Cytotoxicity of Graphene Oxide Nanosheets Associated with Aluminum Chloride-Phthalocyanine as an Agent for Photodynamic and Photothermal Therapies Combined

Ana Luisa Gouvêa^{1*}, Mayara Simonelly^{1,2}, Ludmilla D. Moura¹, Leonardo G. Paterno³, Paulo Eduardo de Souza⁴, Ricardo B. de Azevedo¹ and Sônia N. Bão¹.

¹Institute of Biological Sciences, University of Brasilia, Brasilia, Brazil, ²Boston Children's Hospital/Harvard Medical School, Boston, MA, ³Institute of Chemistry, University of Brasilia, Brasilia, Brazil, ⁴Institute of Physics, University of Brasilia, Brasilia, Brazil

* Email: iza_gouvea@hotmail.com

Breast cancer is the second most common cause of death in women worldwide [1]. The main treatments that are currently used against to this disease are surgery, chemotherapy, radiotherapy, and hormonal treatment. However, they do not promote the complete tumor ablation and present an invasive nature and high systemic toxicity [1,2]. In this context, photodynamic (PDT) and photothermal therapies (PTT) are suggested as an alternative approach as result to their specificity, low toxicity, and low invasiveness [3]. On PDT, the photosensitizer produces reactive oxygen species when irradiated with visible light of specific wavelength. On PTT, the photothermal agent suffers temperature increase when irradiated with near-infrared (NIR) visible light. Both therapies can cause irreversible cell damage and then cell death [3]. The present work suggests the association of the photosensitizer Aluminum Chloride-Phthalocyanine (AlFtCl) to the photothermal agent graphene oxide nanosheets (NanoGO-AlFtCl) for use in combined PDT and PTT in the treatment of human mammary carcinoma (MCF-7) *in vitro*. On dynamic light scattering, NanoGO-AlFtCl presented a hydrodynamic diameter of 128.5 ± 2.2 nm, a polydispersity index of 0.2 and a surface charge of -19.9 ± 0.5 mV. The sheet-like structure of NanoGO-AlFtCl sheets was visualized by transmission (TEM) and scanning (SEM) electron microscopy. NanoGO photothermal properties were assessed placing 200 μ L of the suspension at a concentration of 50 μ g/mL under irradiation using an 808 nm NIR laser light at a power density of 2 W/cm². There was a temperature increase on NanoGO of approximately 20 °C, whereas the temperature variation of deionized water was only 4 °C. NanoGO and free AlFtCl dark toxicity were determined by standard MTT screening assay using MCF-7 and mesenchymal stem cell isolated from dental pulp (MSCP). The viability of MCF-7 and MSCP cells were assessed during NanoGO-AlFtCl treatment (NanoGO at 50 μ g/mL and AlFtCl at 0,078 μ M) under irradiation with a 660 nm LED light and an 808 nm NIR laser light for three minutes each for PTT, PDT and PDT-PTT combined. The different treatments assessed exhibit statistical significance between the two different cells studied, MCF-7 and MSCP, respectively. NanoGO-AlFtCl when irradiated with the NIR laser and LED light for three minutes promoted a cell viability reduction in tumor cells, preferably. Therefore, with the data obtained, NanoGO-AlFtCl showed to be a potential nanosystem for the treatment of human mammary carcinoma *in vitro*.

REFERENCES

- [1] R. Siegel et al., "Cancer Statistics, 2014," vol. 64, no. 1 pp. 9-29, 2014.
- [2] A. M. Gonzalez-Angulo et al., Overview of Resistance to Systemic Therapy in Patients with Breast Cancer. *Adv. Exp. Me. Biol.*, 7(608):1-22, 2007.
- [3] A. Sahu et al., Graphene Oxide Mediated Delivery of Methylene Blue for Combined Photodynamic and Photothermal Therapy. *Biomaterials*, 34(26): 6239-6248, 2013.
- [4] D. Dolmans et al., "Photodynamic Therapy for Cancer.", *Nat. Rev. Cancer*, vol.3, no 5, pp. 380-7, May 2003.
- [5] This research was supported by CNPq (Brazil).

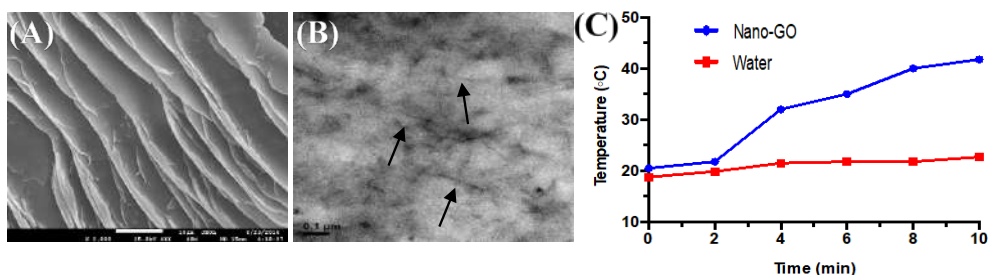
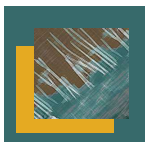


Fig. 1. NanoGO-AIFtCl ultrastructure and NanoGO photothermal properties upon irradiation with 808 nm NIR laser. **A.** SEM image of NanoGO-AIFtCl reveals the sheet-like shape, magnification 2000x (scale bar= 10 μ m); **B.** On TEM image arrows indicate the boundaries of the graphene oxide nanosheets, magnification of 120.000x (scale bar= 0,1 μ m); **C.** Sharp temperature increase in NanoGO (blue) when irradiated with an 808 nm NIR laser while deionized water (red) remains almost invariable.

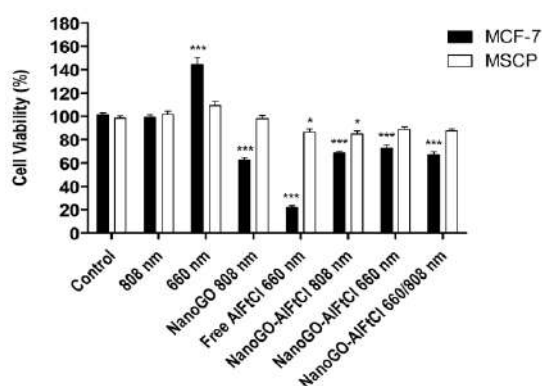


Fig. 2. NanoGO, free AIFtCl and NanoGO-AIFtCl (NanoGO 50 μ g/mL and AIFtCl 0,078 μ M) cell viability assay of MCF-7 and MSCP cells upon 660 nm LED and 808 nm laser light irradiation. Mean \pm SD of three independent experiments, *** $p < 0.001$. There was no statistical significance between PDT only, PTT only and PDT-PTT combined.

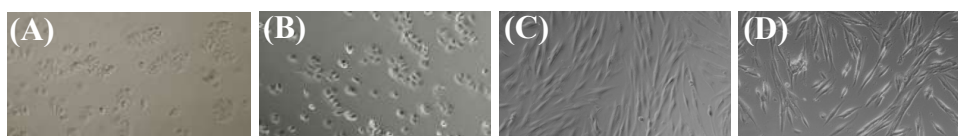


Fig. 3 Morphology of MCF- 7 and MSCP cells after treatment with NanoGO-AIFtCl under PDT and PTT combined. Phase contrast microscopy of **A.** MCF-7 cells before treatment; **B.** MCF-7 cells after treatment with NanoGO-AIFtCl and PDT-PTT combined; **C.** MSCP cells before treatment; **D.** MSCP cells after treatment with NanoGO-AIFtCl and PDT-PTT combined.



TEM Study on Size and Morphology of TiO₂ Nanorods Within a MgH₂-TiO₂ Nanocomposite Produced Via High Energy Ball Milling

Anderson de Farias Pereira^{1*}, Paula Mendes Jardim¹

¹ Department of Metallurgical and Materials Engineering, Federal University of Rio de Janeiro, COPPE/UFRJ, Rio de Janeiro, Brazil.

*Email: anderso.n@poli.ufrj.br

Magnesium hydride is highly attractive for solid state hydrogen storage technologies due to its high storage capacity (7.6 wt% of H₂) and low specific mass (1.7 g/cm³). However, its low sorption kinetics and high desorption temperature are the main obstacles for its application [1]. One of the strategies used to improve these properties is through the production of nanocomposites of MgH₂ with catalysts via reactive ball milling. In this aspect, previous works suggest that the addition of TiO₂-based nanomaterials with 1D morphology improves significantly its sorption properties, even superior to 0D nanoparticles [2,3]. Nevertheless, reactive ball milling is a high energy process and can additionally promote nanoparticle's fragmentation and hence lead to the loss of its previous morphology. Consequently, an investigation on the effects of the milling process on the size and morphology of the nanomaterials is of paramount importance to confirm and better understand the effect of additives with 1D morphology on the sorption properties of MgH₂. The present study's objective is to evaluate the integrity of unidimensional nanomaterials as a function of milling energy. To this purpose, TiO₂-anatase nanorods (NR-550) produced via thermal treatment of hydrogen trititanate nanotubes at 550°C were used as additives to MgH₂. MgH₂ was previously milled for 24h at 300 rpm and later mixed with 5 wt% of NR-550 in a planetary ball mill for 20 minutes at 100rpm for the production of the MgH₂-TiO₂ nanocomposite. X-Ray Diffraction (XRD) was used to characterize crystal structure and Transmission Electron Microscopy (TEM) was used to evaluate catalyst's size and morphology and its dispersion within MgH₂. To analyze the milling effect on particles' integrity, the additives were observed as synthesized and within the nanocomposite. This evaluation was done through the measure of particle size and aspect ratio distribution of the samples previous and after milling. For this analysis, TEM images on Bright Field associated with Dark Field images produced through the positioning of the objective's aperture on different regions from (101) diffraction ring of TiO₂-anatase were used to better identify individual particles. Figure 1 presents an image of NR-550 before milling in bright and dark field mode and Figure 2 the corresponding electron diffraction. From Figure 1 it is possible to observe that the samples consist of a mixture of nanoparticles and nanorods, where nanoparticles showed mean size around 40 nm while nanorods presented an average length around 70nm. For the nanocomposite, XEDS mapping of the element Titanium within MgH₂ matrix was also used as a mean of identifying TiO₂ nanoparticles. The milling process was effective to disperse the nanoparticles within the hydride matrix and no significant difference was observed on catalysts' morphology due to the milling at 100rpm. The overall results show that the technique employed is a successful tool for identifying individual particles among agglomerates and within a nanocomposite matrix.

REFERENCES

- [1] I.P. Jain et al., Int. J. Hydrogen Energy, 35 (2010) 5133.
- [2] P.M. Jardim et al., Int. J. Hydrogen Energy, 40 (2015) 17110.
- [3] A.F. Pereira et al., Brazil MRS Meeting 15 (2016) 720.
- [4] The authors thank the Brazilian agencies CNPq, FAPERJ, FINEP and CAPES for its financial support.

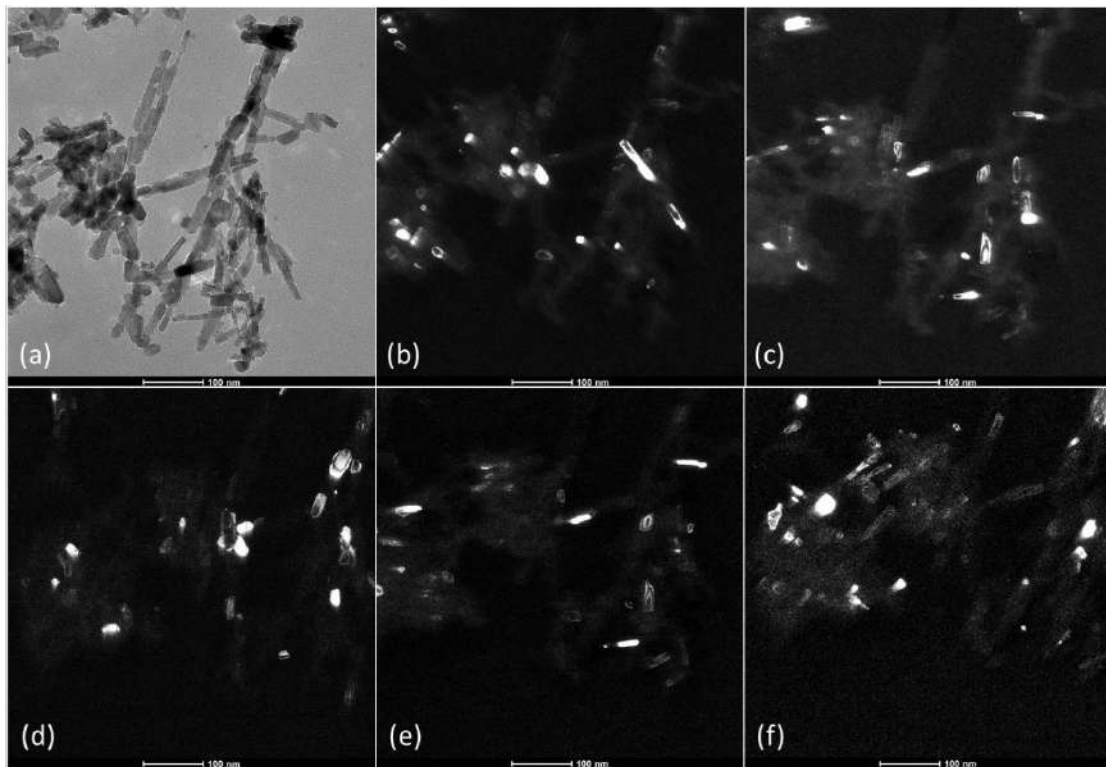
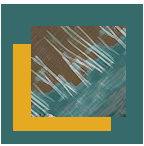


Figure 1 – Bright (a) and Dark field (b-f) TEM images of TiO₂-nanorod sample (NR-550) before milling. Dark field images were generated through selection of different regions from (101) diffraction ring of TiO₂-anatase.

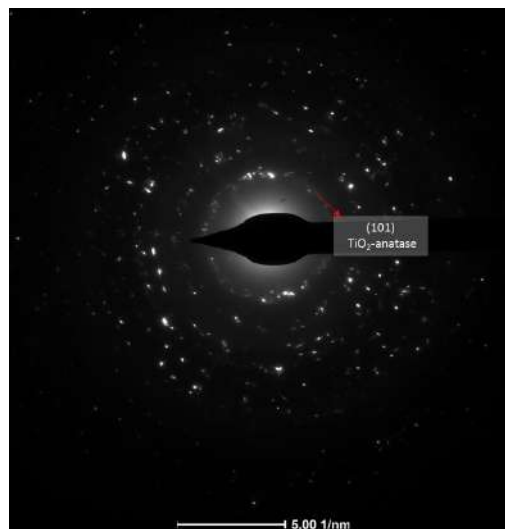


Figure 2 – Selected Area Diffraction of region on Figure1 highlighting (101) diffraction ring of TiO₂-anatase.



Analytical TEM study of calcium phosphate nanoparticles in an intracellular environment

Andre Linhares Rossi^{1*}, Mariana Longuinho¹, Marcelo Tanaka² and Marcos Farina²

1. Centro Brasileiro de Pesquisas Físicas, Rio de Janeiro, Brazil.
2. Universidade Federal do Rio de Janeiro, Centro de Ciências Biomédicas, Rio de Janeiro, Brazil.

Internalization of hydroxyapatite nanoparticles in osteoblast SAOS-2 cells was investigated *in vitro* for 2 and 24h using 5 and 50 µg/mL of nanoparticles in culture medium. No cytotoxic effect was observed by the Presto Blue viability assay. Dual-Beam (Focused Ion Beam-Scanning Electron Microscopy) and transmission electron microscopy were used to study the traffic of nanoparticles inside cells and to characterize the physico-chemical properties of the material during this process. Nanoparticles were actively internalized by cells and were maintained in membrane bound compartments in the intracellular environment [1,2]. Dissolution of hydroxyapatite were observed inside lysosome compartments in all samples. After 24h of internalization in cell culture assays, reprecipitation of calcium phosphate minerals were observed in membrane bound compartments in 5 and 50 µg/mL samples. Comparing to the original nanoparticles, the new reprecipitated calcium phosphate phase presented different morphology, structure and chemical composition. Physico-chemical characteristics were investigated by analytical transmission electron microscopy techniques (EELS and EDS Spectrum Imaging; and SAED) using high spatial resolution. Two methods of sample preparation were performed to confirm that reprecipitation of the calcium phosphate crystallites occurred in the intracellular environment and not during the sample preparation for electron microscopy. Reprecipitation of calcium phosphate prevented the release of high amounts of calcium and phosphate ions inside the cells. This phenomenon may correspond to a strategy to overcome the cytotoxic effect of calcium ions which is highly controlled by cells [3,4].

REFERENCES

- [1] F. Qing et al., J. Mater. Sci. Mater. Med. 23 (2012) 2245.
- [2] J.M. Chen et al. Nanotechnology. 22 (2011) 1.
- [3] Y. Yuan et al. Biomaterials. 31 (2010) 730.
- [4] M Motskin et al. Biomaterials. 30 (2009) 3307. [1] H.G. Hansma et al., Microsc.
- [5] This research was supported by CNPq and FAPERJ (Brazil).



Quasi-spherical and monodisperse synthesis of *Virola oleifera*-capped gold nanoparticles

Andressa dos Santos Corrêa¹, Jairo Pinto de Oliveira² and Marco C C Guimarães^{1,2}

1. Programa de Pós-Graduação em Bioquímica e Farmacologia, Universidade Federal do Espírito Santo

2. Departamento de Morfologia, Universidade Federal do Espírito Santo, Av. Maruípe, s/n, 29053-360 Vitória, ES.

*Email: marco.guimaraes@ufes.br

The greener synthesis of gold nanoparticles using plant extracts are usually non-reproducible [1-3]. For this reason, we choose to synthesize capped citrate gold nanoparticles using *Virola oleifera* extract. The extract, rich in phenolic and flavonoid compounds, exhibits high inherent antioxidant property [4, 5]. Here, we report the interaction between gold nanoparticles and *Virola oleifera* extract and the optimal capping conditions. The synthesized AuNPs were characterized by UV-Vis spectroscopy, transmission electron microscopy (TEM), x-ray diffraction (XDR), and Fourier transform infrared (FTIR) spectroscopy, RAMAN spectroscopy and zeta potential measurements. The best capping time was 5 minutes, because no significant changes were observed in absorbance of supernatant from that time before the nanoparticles were centrifuged at 14000 rpm for 10 minutes (Figure 1A). Subsequently, the optimum pH range was determined, evaluating the adsorption of *Virola* extract on the nanoparticles surfaces at pH 3, 5, 7, 9 and 11. As can be seen in Figure 1B, the adsorption was most intense between pH 3 and 5. Based on this information, we use a 3² factorial design with 3 levels and 2 variables (pH and extract concentration) to verify the optimal capping conditions. The UV absorption spectra of each capping condition was assessed, and 0,1 mg/mL and pH 4 shows higher concentration of nanoparticles (Figure 1C). The capping of flavonoids on the citrate gold nanoparticles surface was confirmed by charge inversion (Figure 1D). The TEM images shows the citrate gold nanoparticles with the mean size 14, 92 ± 2,12. Furthermore, the aspect ratio was 0,936 confirmed quasi spherical aspects (TEM). The interaction is confirmed by different biophysical techniques, such as Fourier-Transform InfraRed (FTIR) and RAMAN. This study indicates that gold clusters are covered by organic compounds present in the extract by the aromatic characteristic bands (664,57 and 1575, 96 cm⁻¹, Raman and 1516 cm⁻¹, FTIR in Figure 2E)[6], as well as the TEM images (Figure 2: A, B, C e D). The DRX confirmed the face-centered cubic structure of citrate AuNPs (Figure 2F). The result of this study shows the synthesis of monodisperse AuNPs, with potential biological activities by confirmed adsorption of flavonoids and other biocompounds. Furthermore, we show a reproducible and simple methodology of synthesis and capping.

REFERENCES

- [1] DURÁN, N.; SEABRA, A.B. Metallic oxide nanoparticles: State of the art in biogenic syntheses and their mechanisms. *Appl. Microbiol. Biotechnol.* 2012, 95, 275–288.
- [2] SEABRA, A.B.; HADDAD, P.S.; DURAN N. Biogenic synthesis of nanostructured iron compounds: Applications and perspectives. *IET Nanobiotechnol.* 2013, 7, 90–99.
- [3] RAI, M. *et al.* Diversity in synthesis and bioactivity of inorganic nanoparticles: Progress and pitfalls. *Nanotechnol. Rev.* 2014, 3, 281–309.
- [4] Barata, L.E.S.; Baker, P.M.; Gottlieb, O.R.; Rúveda, E.A., 1978. *Phytochemistry.* 17(4), 783-786.
- [5] Konya, K.; Vargas, Zs.; Antus, S., 2001. *Phytomedicine.* 8(6), 454-459.
- [6] SILVERSTEIN, Robert M.; WEBSTER, Francis X.; KIEMLE, David J. Identificação espectrométrica de compostos orgânicos. In: Identificação espectrométrica de compostos orgânicos. LTC, 2007.

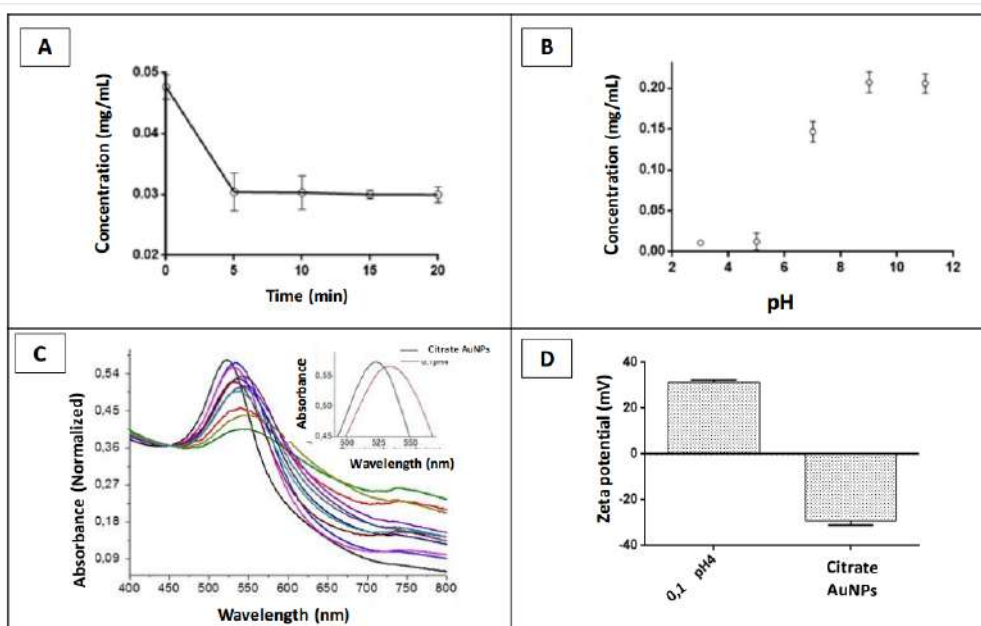


Figure 1. Time and pH in *Virola* adsorption (A and B), UV-Vis spectra of capped AuNPs under different conditions (C), and AuNPs and *Virola* capped AuNPs zeta potential (D).

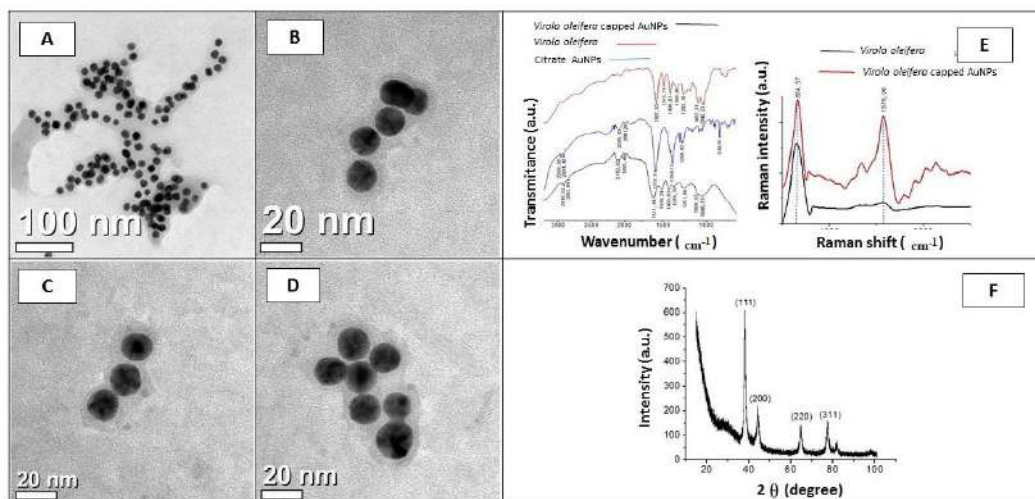


Figure 2. TEM images of AuNPs used to determine the monodispersity of *Virola oleifera* capped AuNPs (A, B, C and D). FTIR spectra of the citrate gold nanoparticles in blue, *Virola oleifera* extract in red and *Virola oleifera* capped AuNPs (0,1 mg.mL⁻¹ and pH 4). Raman spectra of *V. oleifera* is in black, and the *Virola oleifera* capped AuNPs are in red (E), and XDR patterns confirmed the face-centered cubic structure (F).



Sodium Niobate Nanostructure Synthesized Over Metallic Niobium by Alkali Hydrothermal Route

Beatriz R. Canabarro^{1*}, Paula M. Jardim¹

1. Federal University of Rio de Janeiro

*Email: bicanabarro@yahoo.com.br

Alkali niobates have gained scientific and technological interest due to their properties as a piezoelectric, non-toxic, pyroelectric, photocatalytic material among others, and their wide range of possible applications [1]. The method of hydrothermal synthesis has shown promise in manufacturing niobates, both from metal oxides or from the metal itself. This route requires much lower temperatures than the solid-state reaction and also enable obtaining crystals of nanometric size [2]. The objective of this study is to observe how the synthesis variables influence the formation of sodium niobate crystals from the metallic niobium, by the reaction of these with aqueous NaOH solution. In this study, There are some synthesis variables that influence the sodium niobate layer, some of them are temperature, time of synthesis, and base concentration [3], and these variables were chosen to complete a factorial experimental plan of 2^3 with four central points. The temperature was varied from 40°C to 120°C, time from 12 to 36 hours, and caustic soda concentration from 0,25 M to 0,75 M. So that, the central point conditions chosen were the same of Yu *et al.* [4]. After synthesis, the samples were heat treated at 400°C for 30 minutes in a vacuum furnace. The morphology of the crystals was analyzed by Scanning Electron Microscopy (SEM) and by Transmission Electron Microscopy (TEM), their crystalline structure was analyzed by Electron Diffraction (SAED) and Low-Angle X-Ray Diffraction (LAXRD). The niobate produced, in all synthesis' conditions, showed a wire form with nanometric diameter, even after heat treatment, forming a porous network (Figure 1). Its composition was then evaluated by energy-dispersive X-ray spectroscopy (EDX) analysis, showing that all of the samples were composed only by Na, Nb and O. After synthesis, the nanowire have monoclinic crystal structure ($\text{Na}_2\text{Nb}_2\text{O}_6 \cdot \text{H}_2\text{O}$, $a=17.114 \text{ \AA}$, $b=5.0527 \text{ \AA}$, $c=16.5587 \text{ \AA}$, $\beta=113.947^\circ$, with spatial group C2/c). After heat treatment, they suffered a phase transformation and became orthorhombic (NaNbO_3 , $a=5.567 \text{ \AA}$, $b=7.764 \text{ \AA}$, $c=5.515 \text{ \AA}$, with spatial group Pbm_n). It was observed that higher temperature, reaction time and base concentration result in thicker wire layers with worse adhesion to the substrate (Figure 2), forming cracks and sodium niobate detachment from the niobium plate.

REFERENCES

- [1] R.D. Kumar et al., J. Phys. Chem. Solids 101 (2017) 25.
- [2] S.Y. Wu et al., J. Mater. Sci.-Mater. Electron. 21 (Suppl. 5) (2010) 450.
- [3] R. Grange et al., Intech (2011).
- [4] A. Yu et al., Appl. Surf. Sci. 258 (2012) 3490.
- [5] This research was supported by CNPq (Brazil).

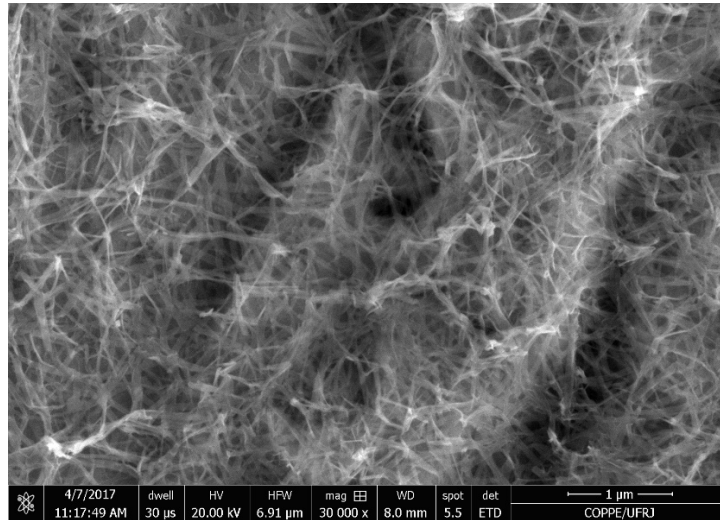
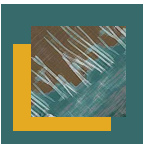


Figure 1 – Sodium niobate synthesized from metallic niobium under 0,75M of NaOH, 12 hours and 40°C.

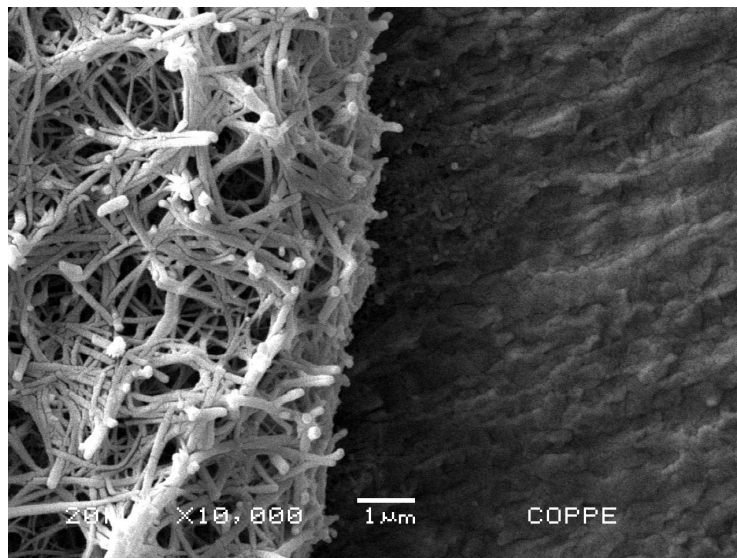


Figure 2 – Sodium niobate detachment observed at the sample synthesized under 24 hours, 0,5M of NaOH and 80°C, after heat treatment.



Phenolic Lipid 2-(3,5-Dimethoxy-2-Octanoyl Phenyl) Acetic Acid Effects in The MCF-7 Breast Adenocarcinoma Treatment

Débora Rojas de Figueiredo Gomes^{1*}, Lucas Roberto Pessatto², Juliana Jorge¹, Adilson Beatriz¹, Rodrigo Juliano de Oliveira², Marco Antonio Utrera Martines¹

1. INQUI - Institute of Chemistry, Federal University of Mato Grosso do Sul, Campo Grande, Brazil.
2. CETROGEN – Center of Studies in Stem Cell, Cell Therapy and Toxicological Genetics, Campo Grande, Brazil.

*Email: deborarofi@hotmail.com

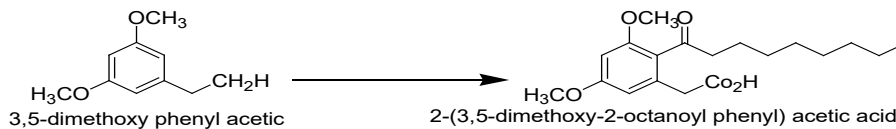
Increases of life longevity over the last decades have been followed by an increase of cancer cases around the world. This, lead to development of new therapeutic strategies for prevention and treatment. Therefore, studies have shown the importance of phenolic lipids, which are important agents of apoptosis, especially in tumour cell culture, also inhibiting cell proliferation. Then, this work synthesized the phenolic lipid 2-(3,5-dimethoxy-2-octanoyl phenyl) acetic acid and analysed the effects in the MCF-7 cells. Firstly, synthesis of the phenolic lipid was performed following the described synthetic route by Zamberlam et al. (2012) [1]. Biological assays were performed in MCF-7 breast cancer cell line with doses 2.5, 5, 10, 15, 30, 50, 100, 150 and 200 µg/mL, as well the apoptotic assays with doses 20.91, 43.65 and 91.11 µg/mL. Results analysis shows that 2-(3,5-dimethoxy-2-octanoyl phenyl) acetic acid is cytotoxic in 24, 48 and 72 h, and doses above 100 µg/mL is lethal in 100% of tumour cells. Studies of cell death shows that doses 20,91, 43,65 and 91,11 µg/mL increases apoptosis index significantly in MCF-7 cells. Thus, it considered that this compound has desired properties for drugs prospection of breast cancer treatment.

Synthesized product is the 2-(3,5-dimethoxy-2-octanoyl phenyl) acetic acid. Then, using 3,5-dimethoxy phenyl acetic and dichloromethane as solvent. The starting material was 3,5-dimethoxy phenyl acetic, and dichloromethane as solvent. After 8 h, was observed the appearance of aimed compound with 80% yield [1].

The apoptosis and MTT assays showed that the phenolic lipid 2-(3,5-dimethoxy-2-octanoyl phenyl) acetic acid has a cytotoxic effect and cell death is caused by apoptosis (Figure 1).

REFERENCE

- [1] C. E. M. ZAMBERLAM; A. MEZA.; C.B.; LEITE, M.R. MARQUES; D.P. LIMA; A. BEATRIZ., Total Synthesis and Allelopathic Activity of Cytosporones A-C, J. Braz. Chem, Brazil, 2012.



Scheme 1: Synthesis of 2-(3,5-dimethoxy-2-octanoyl phenyl) acetic acid having as key step Friedel-Crafts acylation, according to Zamberlam et al., 2012, adapted.

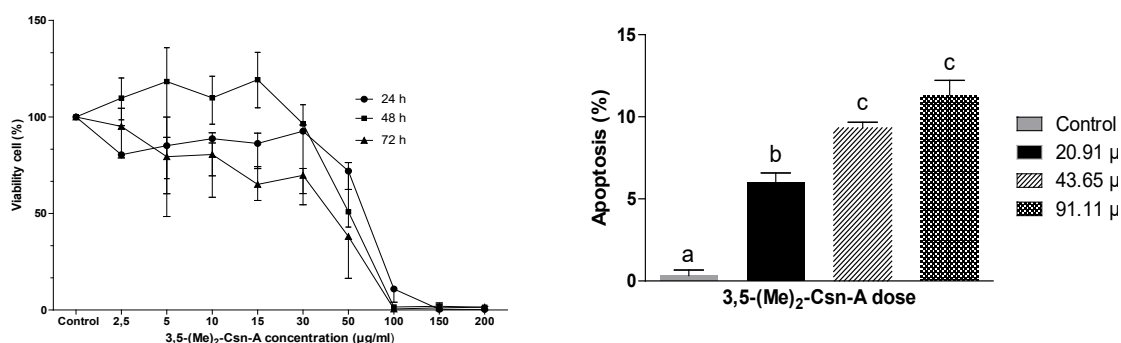


Figure 1. Cell viability values obtained by MTT assay after 24, 48 and 72 h of treatment, and average frequency of apoptosis in MCF-7 cell line culture using phenolic lipid as treatment (Statistical Test: ANOVA/Tukey, $p < 0,05$). Different letters indicate significant statistical differences.

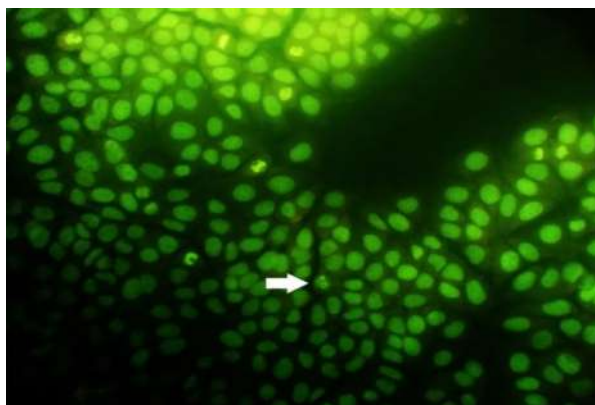
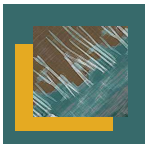


Figure 2. Frequency of apoptosis in MCF-7 cell line culture observed after 24 h of treatment with cytosporone B precursor. It was analysed 100 cells for sample, classified by morphological feature and differential colour by ethidium bromide and acridine orange (Figure 2). (A) In the graphics, the average and \pm standard error are presents (Statistical Test: ANOVA/Bonferroni, $p < 0,05$). (B) Photomicrography of MCF-7 cell line culture with dye acridine orange and ethidium bromide in 40x magnification. Arrow indicates a cell apoptosis.



Application of Calcium Phosphates: *In Vivo* Test in Sheep

G.M.L. Dalmônico^{1,2*}, N.H.A. Camargo¹, A.L. Rossi², A.L. Dallabrida³, O. Cambra-Moo⁴, M.A. Rodríguez⁵

¹Santa Catarina State University (UDESC), Joinville, Brazil

²Brazilian Center for Physics Research, Rio de Janeiro, Brazil.

³Department of Veterinary Medicine, Santa Catarina State University, Lages, Brazil

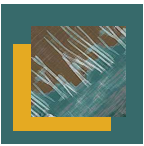
⁴Laboratorio de Poblaciones del Pasado (LAPP), Universidad Autónoma de Madrid.

⁵Instituto de Cerámica y Vidrio - CSIC, Madrid, Spain.

*Email: gidalmonico@gmail.com

Treatments for bone loss are research topics and involve different areas of scientific knowledge, engineering, physics, chemistry, biology and biomedicine. The biomaterials that stand out as replacement in bone structure treatments are hydroxyapatite, β and α calcium phosphate, biphasic hydroxyapatite/calcium phosphate β and α and hydroxyapatite matrix nanocomposite biomaterials. These biomaterials stand out as bone substitutes because they present a crystallography similar to that of human skeleton bone apatite, being bioactive and biocompatible. Nanostructured biphasic bioceramics are researched and show potential to be bone substitutes in surgical repairing procedures and reconstruction of bone tissue [1-4]. This project was developed based on research of granular biomaterials of HA, β -TCP and biphasic composition HA/ β -TCP=20/80% [4]. All biomaterials were characterized by different techniques: scanning electron microscopy, atomic force microscopy, confocal microscopy, optical microscopy, polarized light microscopy. The interest of this research was to evaluate the performance of biomaterials in *in vivo* tests for the time period of 180 days, in relation to osseointegration and the formation of neoformed bone tissue and determine which biomaterials presented potential as bone replacement for biomedical applications. The study was conducted on sixteen healthy half-breed Texel sheeps with 12 months old. Two 4-mm non-critical defects were produced on the medial tibial diaphyseal of each tibia with the aid of a dental drill. For the adequate implantation of the biomaterials, initially the granulated material was deposited in a sterile vat and hydrated with the animal's own arterial blood. The animals were euthanized 180 days after implantation and implanted bone fragments were collected. The results (figure 1) found are encouraging and demonstrate that the granulated microporous biomaterials of calcium phosphate proves to be ability to repair and bone reconstruction for the test *in vivo* evaluated, revealing the osseointegration and bone formation. The apparent color change of the granules could be related with a possible phase change over time (figure 1c, 1f, 1i). The results obtained from the biopsies containing the biomaterials revealed similar osseointegration behaviours, with excellent biomaterial/bone tissue interface and greater bone formation, presenting smaller amounts of remaining biomaterial. It is due to the contribution of porosity and phase composition parameters to the biodegradation process. Figures 1a, 1d shows the projections of osteoblast cells performing the deposit and biomineralization of bone tissue.

Keywords: β -calcium phosphate, hydroxyapatite, *in vivo* testing, bone neoformation.



REFERENCES

- [1] Granjeiro, J.M; Soares, G.D.A. 1a ed. VM Cultural Editora Ltda., 2011. [2] Dorozhkin, S.V. Acta Biomat. 8 (2012) 963–977.
- [3] N.Levandowski Jr., N.H.A.Camargo, D.F. Silva, G.M.L.Dalmônico, P.F.Franczak. Ad Mat Res 936 (2014) 695-700.
- [4] G.M.L. Dalmônico, D.F. Silva, P.F. Franczak, N.H.A. Camargo, M.A. Rodríguez. Bol Soc Esp Ceram Vidrio 54 (2015) 37–43.

Acknowledgments: The financial support of the Coordenação de Aperfeiçoamento de Pessoal de Nível Superior (CAPES-BRAZIL); the Ministry of Economy and Competitiveness from the Spanish Government (MAT2013-48426-C2-1R) and the Brazilian Center for Physics Research for a financial congress.

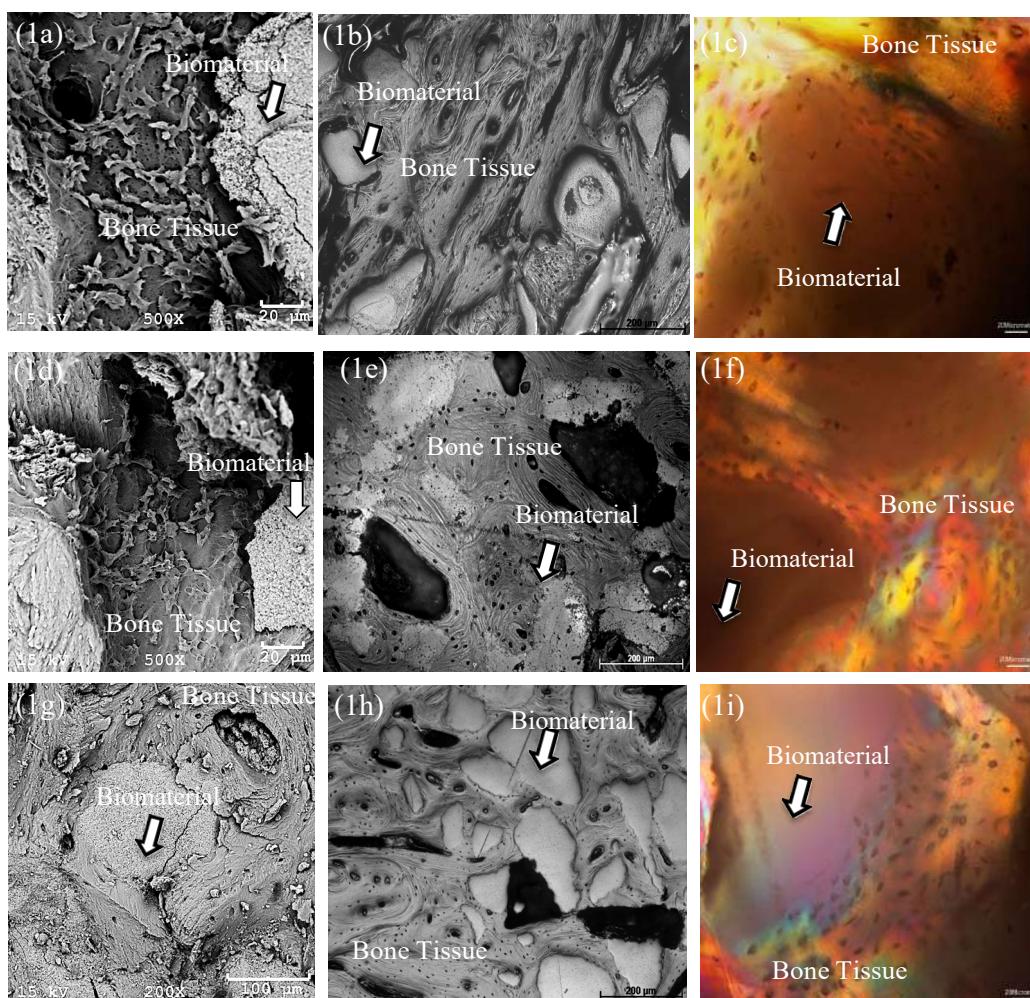


Figure 1. Characterization of biopsies by: scanning electron microscopy HA (1a), β -TCP (1d), 20/80%(1g); optical microscopy HA(1b), β -TCP (1e), 20/80%(1h); polarized light microscopy HA(1c), β -TCP (1f), 20/80%(1i): biomaterial, new bone tissue, osseointegration, biomaterial/bone tissue interface at 180 days.



Micromorphology and Composition of Bioconstructions of Sessile Gastropods from the Brazilian Coast

Thiago Freitas Toniolo^{1*}, Paulo César Fonseca Giannini¹, Isaac Jamil Sayeg¹, Rodolfo José Angulo², Maria Cristina de Souza², Luiz Carlos Ruiz Pessenda³

1. Instituto de Geociências – Universidade de São Paulo; 2 Departamento de Geologia – Universidade Federal do Paraná; 3 Centro de Energia Nuclear na Agricultura – Universidade de São Paulo

*Email: thiago.toniolo@usp.br

Throughout the Brazilian coast north of Laguna, Santa Catarina (28°S), remains of vermetid (Gastropoda) bioconstructions are common. These animals live in the coastal zones, in colonies fixed on the rocky shores and their fossils dated by ¹⁴C are widely used as indicators of the sea level variation in the Holocene [1] [2] [3] [4]. More recently, attempts have been made to use the variation of the geochemical and isotopic composition of these fossils over time as an indication of changes in the coastal circulation [4]. For this purposes, it is important to know the purity and homogeneity of the analyzed material, which demands the use of SEM-EDS. This work analyzes by SEM-EDS samples of fossil bioconstructions from Santa Catarina (SC), Paraná (PR) and Pernambuco (PE). The analyzed bioconstructions are basically composed of vermetid (30%), primary porosity (30%), terrigenous grains (30%) and cement/ matrix (8%). Other minor constituents are bryozoans (formed *in situ*) and bioclasts (mainly of bivalves). Vermetid shells are tubular in shape and formed by several concentric layers consisting of prismatic/fibrous crystals of aragonite (mineral previously identified by X-ray diffractometry) whose orientation can be radial (most common) (Fig. 1), inclined or tangential to the circumference of the tube. In thin sections, vermetid tubes walls often show intercalation between layers with orange color and others with white or beige color (Fig. 2), being the last predominant. SEM-EDS analysis reveal that in the orange layers (Fig. 3, points 2 and 3) S is present and the O/Ca ratio is lower than in the white layers (Fig. 3, point 1), whose O/Ca ratio is closer to the stoichiometric value of pure CaCO₃ (1.20). This result suggests that the color of the orange layers is possibly due to the presence of organic pigments. In the compositional mapping by EDS, bryozoans and micrite show higher Mg contents than the vermetid shell, what was already expected, once they are composed of calcite, which can take on more Mg in its lattice than aragonite [5]. In addition to the micrite calcite, other cement commonly found in the bioconstructions is smectite (Fig 5), that coats the internal and external walls of the vermetid tubes and also terrigenous grains.

REFERENCES

- [1] J. Laborel, in: Sea Level Research, 12 (1986) 281-310.
- [2] R.J. Angulo et al., Quaternary Science Review 25 (2006) 486-506.
- [3] P.C.F. Giannini et al., in: 14º Congresso da ABEQUA, Natal, RN (2013).
- [4] T.F. Toniolo et al., in: 48º Congresso Brasileiro de Geologia, Porto Alegre, RS (2016).
- [5] D.J.J. Kinsman & H.D. Holland, Geochim Cosmochim Acta 33 (1969) 1-17.
- [6] This research was supported by by CNPq (307055/2013-2) and FAPESP (09/54232-4).

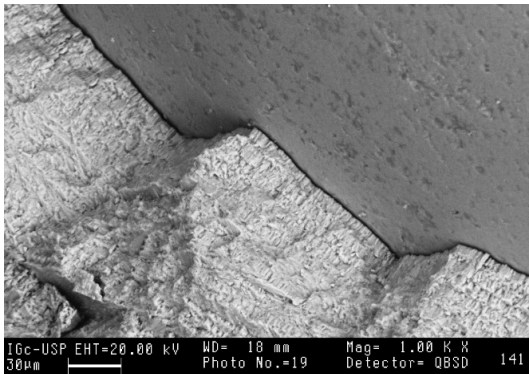
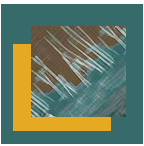


Fig. 1. SEM Photomicrography, using backscattered electron detector, of cross section of vermetid shell, showing its structure of concentric layers of aragonite crystals radially disposed. On the upper right, micrite calcite filling inside the tube. Sample from Caiobá (PR).

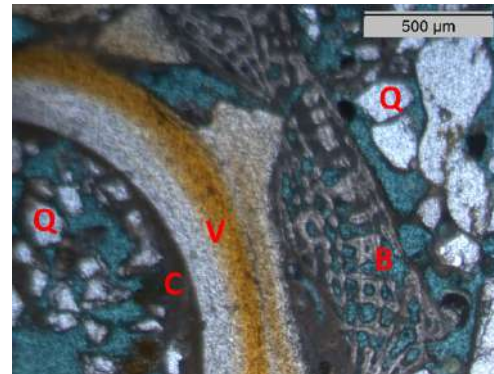
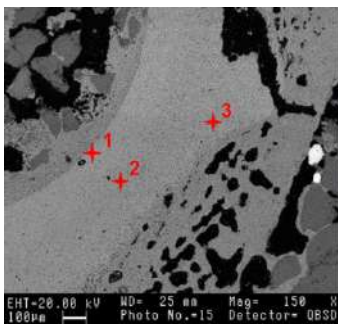


Fig. 2. Photomicrography under the petrographic microscope with uncrossed polarizers. B: bryozoans, Q: quartz, C: micrite cement. Bioconstruction from Gaibu (PE) in thin section. Notice color variation on the vermetid shell (V).



Elements (weight %)	1	2	3
O	53.56	48.10	51.41
Ca	46.07	51.52	48.43
Sr	0.38	-	-
Na	-	0.38	-
S	-	-	0.16
Total	100.00	100.00	100.00

Fig. 3. SEM Photomicrography, using backscattered electron detector of Sample of Fig. 2 with indication of spots analyzed by EDS (quantitative results detailed in the table to the right). Carbon was excluded from the computation, since it is the element used in the sample coating.

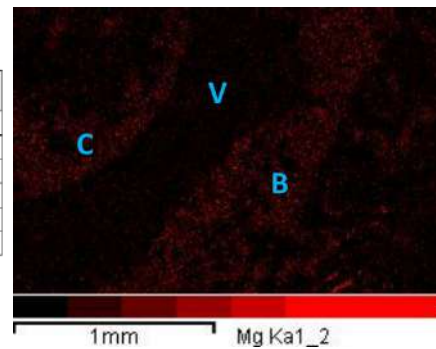


Fig. 4. EDS compositional map of sample of Fig. 2, revealing slight differences in the Mg content of the carbonates that compose the vermetid shell (V), the bryozoans (B) and the cement (C).

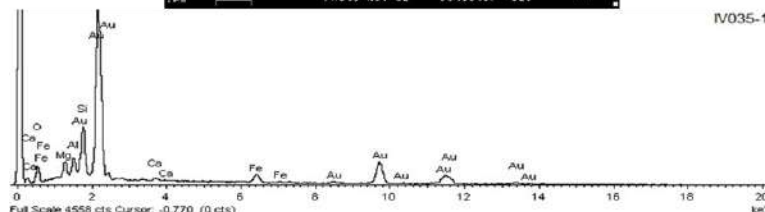
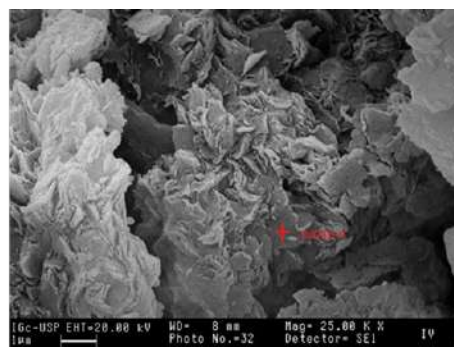


Fig. 5. SEM Photo-micrography, using secondary electron detector, of clay mineral cement found inside a tube of vermetid from São Francisco do Sul (SC). SEM image reveal habit indicative of smectite. Below, the EDS spectrogram reveals composition (rich in Si, Al, with presence of Mg, Fe and Ca) consistent with smectite.



Evidences of Bioclast Pseudomorphous Replacement in the Eolianites of Fernando de Noronha Archipelago, Northeast Brazil

Valentina Espinel Arias^{1*}, Paulo César Fonseca Giannini¹, Isaac Jamil Sayeg¹, Renata Cagliariani¹, Rodolfo José Angulo², Maria Cristina de Souza²

1. Instituto de Geociências – Universidade de São Paulo; 2 Departamento de Geologia – Universidade Federal do Paraná

*Email: geovalespa@gmail.com

The eolianites of the Fernando de Noronha Archipelago (FNA) are being studied to understand the responses of Quaternary eolian sedimentation in the region of the Intertropical Convergence Zone (ITCZ) to climatic factors such as winds, humidity, swell waves and relative sea level (RSL). For this, about 300 measurements of azimuth and dip angle of cross stratifications were obtained and more than 70 samples were collected for sedimentological, chronological and petrographic analysis. Thin sections of 44 samples show the predominance of biomicrosparite calcarenites, whose framework consists mainly of red algae and benthic foraminifera (mainly miliolids). The porosity varies between 15 and 40% and the spar and microspar cements show fabrics indicative of early origin. Ten ¹⁴C AMS datings were performed, being two in total rock (about 9.8 and 13.7 ky BP) and eight in paired aliquots which were obtained from the previous separation under stereomicroscope between cement and red algae bioclasts in four samples. The dating of these paired cement-bioclast aliquots aimed to know the minimum and maximum age of the calcarenites, respectively. The obtained set of ages presents two modes, between 41 and 18 ka BP and from 13.7 to 9.8 ka BP, and the time hiatus between them, from 18 ka to 13.7 ka BP, coincides with moment of RSL more than 90 m below the present and Heinrich Stadial event 1 (HS1), when the increasing of precipitation in the region must have led to the stabilization of the eventual existing eolian dunes. However, the four pairs of bioclast and cement samples showed an apparent age inversion, that is, cement older than bioclast, which motivated the SEM analysis of both the dated bioclasts and rock samples, in search of evidences of red algae bioclasts recrystallization and / or pseudomorphosis. The electromicrographs evidenced the generalized occurrence of moldic porosity generated by the total or partial dissolution of bioclasts. This porosity appears rimmed by an anisopachous fringe of micrite carbonate cement (Fig. 1), sometimes forming meniscus, a association of fabrics which is indicative of early origin under vadose conditions. The existence of larger calcite crystals (microspar) as partial or total filling of the moldic pores (Fig. 2) suggests the occurrence of a second cementation event, with crystallization slower than the first, which implies conditions of lower solutes concentration in interstitial water. This second event must have been responsible for the possible replacement of the calcite-Mg of the red algae by diagenetic low-Mg calcite. SEM results show that great caution is required with the interpretation of the FNA eolianite ¹⁴C datings. Considering that fringe and meniscus cement is early and incorporates the carbon from the red algae themselves as well from the soil existing on the time just after deposition, the ages obtained from this cement can be a good approximation of the age of eolian deposition. In contrast, the ¹⁴C content of the bioclasts replaced by the second generation of diagenetic calcite should reflect the combined influence of the carbon from the dissolved bioclasts and first cement with the carbon from interstitial waters and soils which have existed thousands of years after.

REFERENCES

[1] This research was supported by CNPq / Ministério da Marinha (457714-2013-1) and CNPq (307055/2013-2)

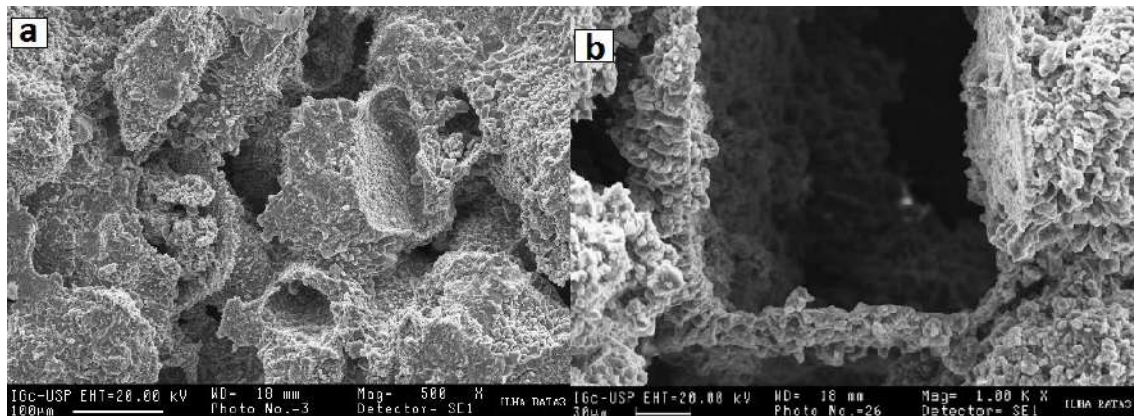
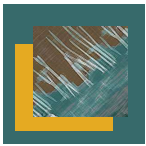


Fig. 1. Moldic secondary porosity created by red algae bioclasts dissolution: **a:** general view of the pores rimmed by carbonate anisopachous fringe and meniscus; **b:** detail of a moldic pore rimmed by fringe cement. Eolianite sample from Ilha Rata, FNA. SEM image, secondary electrons detector.

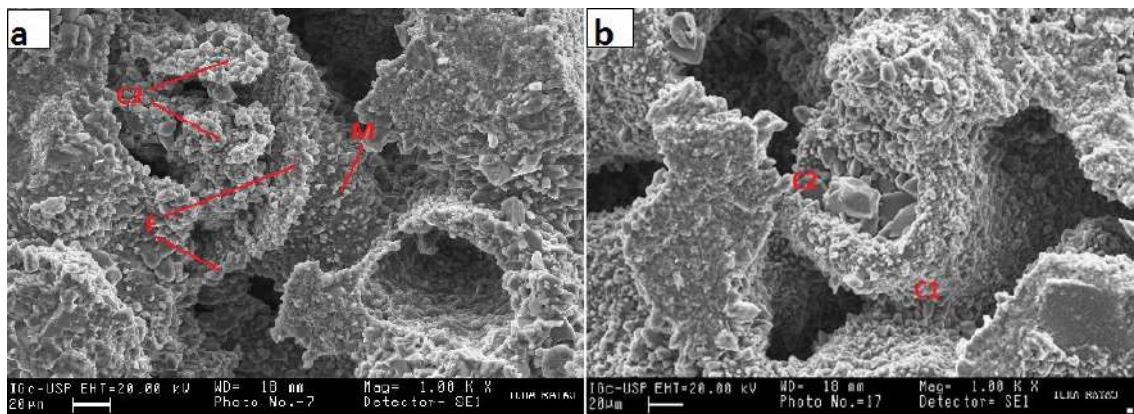
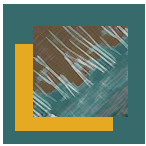


Fig. 2. Evidences of at least two generations of carbonate cement: **a:** first generation, occurring as meniscus (M) and fringes (F), and second generation (C2) filling partially a moldic pore; alternatively, C2 here can be also interpreted as bioclast remains, after partial dissolution; **b:** first cement generation (C1), appearing as micrite fringe rim around moldic pore, and second generation (C2), with microspar texture, filling a moldic pore; here, C2 is an example of pseudomorphous replacement of the red algae bioclast. Eolianite sample from Ilha Rata, FNA. SEM image, secondary electrons detector.



Crystallographic orientation of spicules from the sponge *Sycettusa hastifera*

Lia Souza Coelho^{1*}, Mariana Moreira Longuinho², Marcos Farina³, Andre Linhares Rossi²

1. Universidade Federal Rural do Rio de Janeiro.
2. Centro Brasileiro de Pesquisas Físicas.
3. Universidade Federal do Rio de Janeiro, Instituto de Ciências Biomédicas.

Sponges are morphologically simple organisms and their systematics is mainly based on their skeleton^[1,2]. In calcareous sponges (phylum Porifera, Calcarea class) the skeleton is formed by Mg-calcite spicules ranging from approximately 10 to 2000 μm in length and usually composed of two, three or four (rarely five) conics rays joined at the base^[1].

The class Calcarea is subdivided into two subclasses: Calcinea and Calcaronea. Several characteristics support this deep division. One of these characteristics is the shape of the spicules. In Calcinea, triactine and tetractine spicules are always regular, which means that they have identical angles (120°) between their basal actines that are in the same plane. In the subclass Calcaronea, triactines and tetractines are irregular, i.e., they have a larger angle ($>120^\circ$) between their paired actines and a have bilateral symmetry (the plane of symmetry contains the unpaired actine).

In this work, the crystallographic orientation of the spicules of the sponge *Sycettusa hastifera* inside the aquifer tube was investigated. The sponge was dehydrated and included in epoxy resin. Several cross-sections were made along the length of the sponge tube and then each cut was polished with 1 μm alumina solutions and 0.25 μm diamond paste. The sample was coated with a thin carbon layer and analyzed by SEM-FEG (Field Emission Gun Scanning Electron Microscopy) to observe the mineral structure and by EBSD (Electron Back Scattered Diffraction) (Oxford, Inc.) The EBDS was used to determine the orientation of the calcite crystals of the spicules relative to their location within the body of the sponge. The analyzes were performed using an acceleration voltage of 20 kV. Kikuchi patterns will be automatically indexed (Aztec software), and exported to HKL Channel 5 software (Oxford, Inc.) from which Euler angles and Miller indices will be obtained. Preliminary results showed that all three-pronged spicules had the odd actin elongated in the direction [211]. Spicules with two tips showed other directions of elongation. A small variation was observed in each type of spicule that may be related to the position of the spicule in the sponge tube. This variation will be studied by comparing the orientation of the spicule with its position in the sponge tube.

REFERENCES

- [1] M. Manuel et al., Class Calcarea Bowerbank, 1864.
- [2] A.L. Rossi et al., Journal of Structural Biology, 2 (2016) 164.



Green synthesis of gold nanoparticles with Epigallocatechin Gallate

Gisele Pereira Diniz Schuenck¹, Carina Knidel² and Marco Cesar Cunegundes Guimarães^{1*}

1. Laboratório de Ultraestrutura Celular Carlos Alberto Redins - LUCCAR, Universidade Federal do Espírito Santo-UFES - Av. Marechal Campos, 1468, Vitória, E.S., Brazil.

2. Laboratório de Biologia Molecular e Virulência Bacteriana, Universidade Federal do Espírito Santo-UFES - Av. Marechal Campos, 1468, Vitória, E.S., Brazil.

*Email: marco.guimaraes@ufes.br

Tea polyphenols have strong in vitro antioxidant activity. The compound epigallocatechin gallate (EGCG) is the major catechin found in green tea [*Camellia sinensis* L. Ktze. (Theaceae)]. This polyphenol have been shown to have various health benefits, as anti-metastasis, neuroprotective effects, anti-cancer, anti-inflammatory, antimicrobial and antioxidant effects [1]. Functionalized gold nanoparticles (AuNP's) with molecules, as EGCG, may be an effective strategy for optimizing drug delivery, diagnostics and therapeutic nanomedicine products [2]. In this study, we synthesized gold nanoparticles (AuNPs) using EGCG as a reducing agent. The process synthesis was optimized by four factors (time, concentration of EGCG, temperature and agitation). UV-vis spectroscopy (Fig. 1) and transmission electron microscopy (TEM) were performed to characterize the formation of AuNP's. TEM (Fig. 2) was used to view size and shape of AuNP's. The UV-Vis spectra gave surface plasmon resonance peak between 426-470 nm. TEM showed AuNP's with different sizes and no agglomeration. We have used EGCG to successfully reduce gold to corresponding gold nanoparticles in a single step; a process that fulfills all criteria of green nanotechnology as no chemical other than gold acids are used. This nanomaterial having potential applications in medicine and nanotechnology.

Keywords: Green synthesis, gold nanoparticles and epigallocatechin gallate.

[1] B. PETER et al., Biophysical characteristics of proteins and living cells exposed to the green tea polyphenol epigallocatechin-3-gallate (EGCg): review of recent advances from molecular mechanisms to nanomedicine and clinical trials, *Eur Biophys J*, v. 46, p. 1–24, 2017.

[2] S. NUNE et al., Green nanotechnology from tea: phytochemicals in tea as building blocks for production of biocompatible gold nanoparticles, *Journal of Materials Chemistry*, v. 19, p. 2912-2920, 2009.

Acknowledgements

This work was supported by FAPES and FINEP.

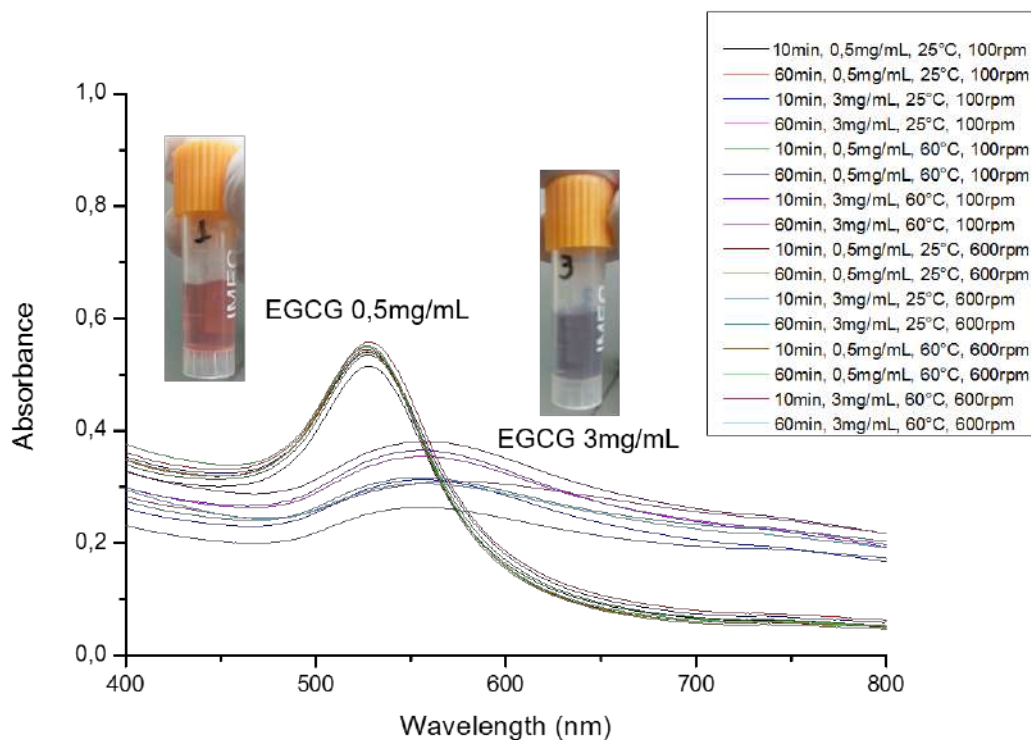


Figure 1. UV-Vis absorption spectroscopy measurements of the colloidal gold nanoparticles synthesized with EGCG in different experimental conditions.

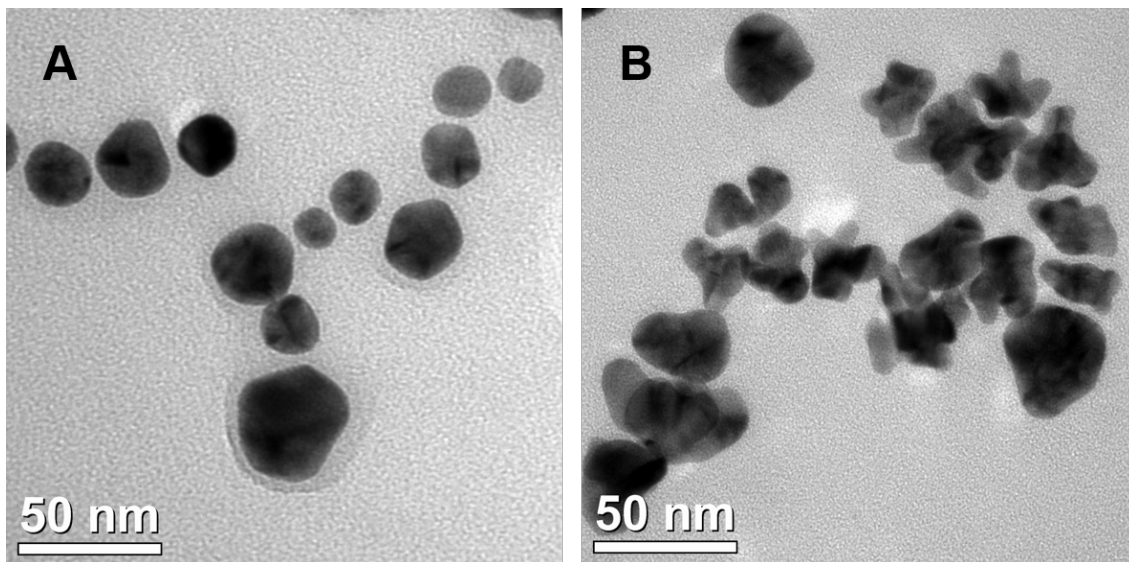


Figure 2. TEM images of gold nanoparticles produced in different conditions; (A) 60min, 0,5mg/mL EGCG, 25°C, 100rpm; (B) 60min, 3mg/mL, 60°C, 600rpm.



Synthesis and Characterization of Alginate/Chitosan Nanoparticles Containing Lapazine with Potential Antituberculosis Activity

Mariana M. Longuinho^{1*}, Suzana G. Leitão¹, Raphael S. F. Silva², Pedro E. A. Silva³, André L. Rossi⁴ and Priscilla V. Finotelli¹.

¹. Federal University of Rio de Janeiro, Pharmacy Faculty, Natural Products and Food Department, Rio de Janeiro, Brazil.

². Núcleo de Ciências Químicas, Instituto de Educação, Ciência e Tecnologia do Rio de Janeiro, Rio de Janeiro, Brazil.

³. Universidade Federal do Rio Grande, FURG, Laboratório de Micobactérias, Rio Grande, RS, Brazil

⁴. Condensed Material, Applied Physics and Nanoscience Coordination, Brazilian Center for Physics Research, Rio de Janeiro, Brazil.

*Email: mariana.longuinho@gmail.com

Lapazine is a benzo[a]phenazine synthesized from lapachol (a naphthoquinone extracted from various species of Ipê) with activity against *M. tuberculosis* susceptible and resistant to antibiotic strains [5]. However, lapazine low solubility restricts *in vivo* toxicity tests, as described below. Nanoparticle systems can be used to encapsulate lipophilic drugs such as lapazine, improving their solubility. Being promising to therapeutics where the infectious agent encounters inside the cell [6, 7]. The aim of this work was to propose a polymeric nanoparticle system to improve lapazine's solubility. In order to improve lapazine solubility, a polymeric nanoparticle is proposed using alginate and chitosan by emulsification, interfacial complexation and solvent evaporation method. Nanoparticles (NP) presented loading capacity equal to 8.87 µg/mg, medium size of 1099 ±450.68 nm, polydispersity index of 0.366 ±0.048 and zeta potential equal to -26.84 ±4.51 mV. Through transmission electron microscopy (TEM), analyses of Lapazine-loaded Alginate/Chitosan NP by electron microscopy (Figure 1) showed high variability of nanoparticles size confirming the polydispersity of the system observed previously on DLS results. Small crystals (white arrows) are observed isolated from the nanoparticles. These crystals were related to the lapazine or the sucrose added before the freeze-drying process. When analyzed by electron diffraction (Figure 2), diffracted planes from organic crystals were comparable with 2 most intense lapazine peaks found by x-ray diffraction (DRX) equal to 22.36° and 28.54° (Data not shown). DRX also proved that lapazine do not suffer structural modifications when encapsulated. *In vitro* kinetic studies showed that the NP release profile have two phases: first in accordance with Korsmeyer-Peppas model, and the second phase following zero order model. NP *in vitro* anti-mycobacterial activity was equal to 100 µg/mL. These results prove lapazine safety on tests that were able to verify it, and that NP synthesized for lapazine encapsulation attended physical-chemical characteristics for a drug release system and was able to improve lapazine solubility through the management of its release.

REFERENCES

[1] Silveira, N. *et al.* Mater. Sci. Eng. C 58 (2016) 458.

[2] Pinto Reis, C. *et al.* Nanomedicine Nanotechnology, Biol. Med. 2 (2006) 8.

[3] Kisich, K. O. *et al.* Int. J. Pharm. 345 (2007) 154.

[4] This research was supported by CNPq (Brazil).

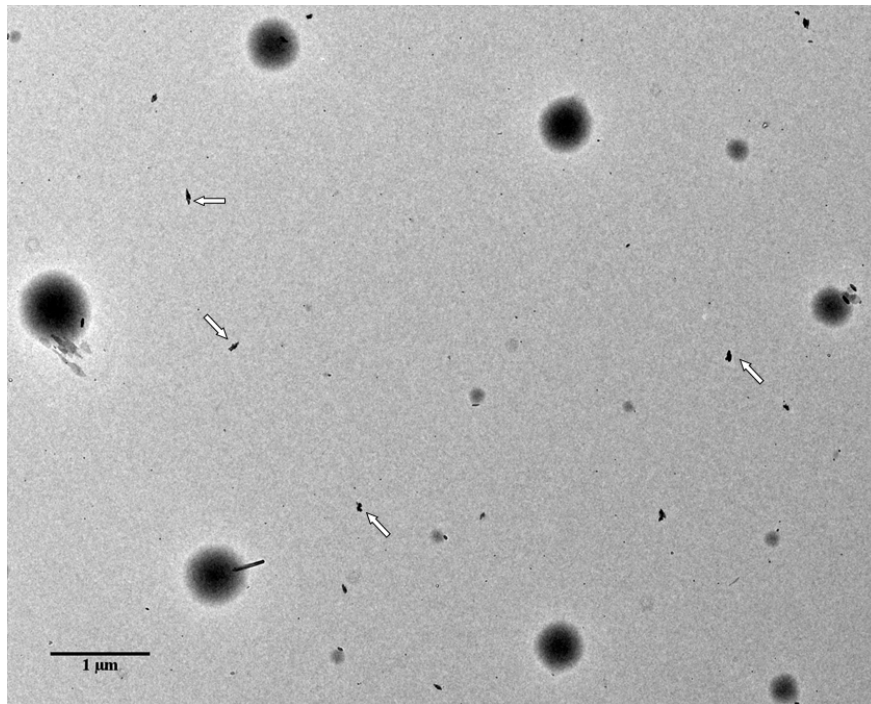
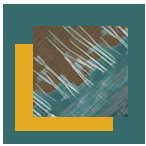


Figure 1. TEM images of Alg/Chi-Lap NP. Crystals are indicated with white arrows.

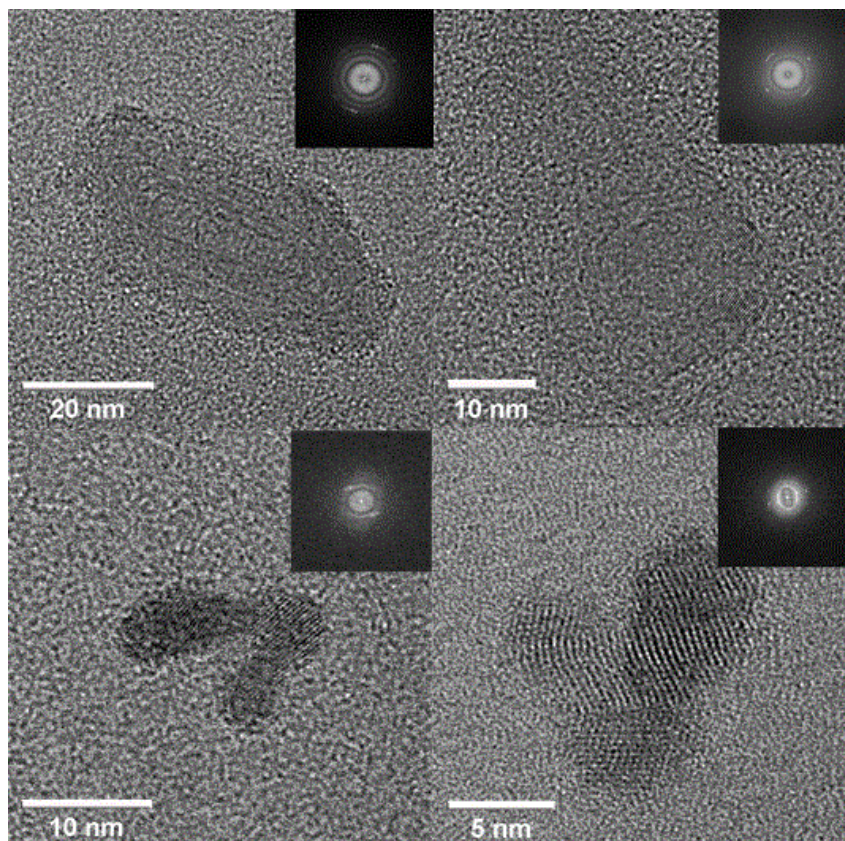


Figure 2. High-resolution TEM images of crystals associated to NPs. Inset: corresponding fast Fourier Transform (FFT).



Biosynthesis, Characterization and Evaluation of Antibacterial Effects of Silver-based Nanoparticles

Mateus Eugenio¹, Veronica Ferreira¹, Nathalia Müller¹, Susana Frases², Leandro³ Lemgruber, Marcos Farina⁴, Wanderley de Souza² and Celso Sant'Anna^{1*}

1. Laboratory of Microscopy Applied to Life Science - Lamav, Inmetro, Duque de Caxias, RJ, Brazil;
2. Laboratory of Cellular Ultrastructure Hertha Meyer, UFRJ, Rio de Janeiro, Brazil.
3. Wellcome Trust Centre for Molecular Parasitology, University of Glasgow, Glasgow, Scotland;
4. Laboratory of Biomineralization, UFRJ, Rio de Janeiro, Brazil.

*Email: cbfilho@inmetro.gov.br

Biological synthesis of silver-based nanoparticles, such as silver/silver chloride (Ag/AgCl-NPs) and silver chloride (AgCl-NPs), is considered an economic and green method for replacing the expensive and toxic physical and chemical approaches that currently dominate the field of nanotechnology [1]. The main objective of the bioproduction of silver-based nanoparticles is their use for treatment of several diseases [2]. This current work aimed to produce Ag/AgCl-NPs from culture of yeast *Candida lusitanae*. The produced nanoparticles were characterized by different microscopy techniques, such as conventional transmission electron microscopy (CTEM), high resolution transmission electron microscopy (HRTEM), scanning electron microscopy with energy-dispersive X-ray spectroscopy (SEM/EDS) and focused ion beam scanning electron microscopy (FIB/SEM). In addition, the antibacterial effects of microalgae-derived AgCl-NPs were evaluated through antiproliferative, viability and morphological assays, by optical density, high-content analysis (HCA) and CTEM, respectively. UV-visible spectroscopy and SEM/EDS supported the Ag/AgCl-NPs biosynthesis from *C. lusitanae*. CTEM analysis evidenced that these nanoparticles mainly presented a circular shape and their diameters varied mostly in the range from 2 to 10 nm. When analyzed by HRTEM (111) (octahedral) and (200) (cubic) symmetry facets appeared systematically in one side of the nanoparticles. Analysis of ultra-thin sections by CTEM indicated that the domain of the synthesis of Ag/AgCl-NPs was mainly between the yeast cell wall and the plasma membrane. By using 3D reconstruction obtained from FIB/SEM the spatial distribution of the domains of nanoparticle synthesis was mapped and nanoaggregates of Ag/AgCl-NPs up 35 nm in diameter were observed. Microalgae-derived AgCl-NPs (from 10 $\mu\text{g mL}^{-1}$) decreased by 98% the growth of Gram-positive *Staphylococcus aureus* and Gram-negative *Klebsiella pneumoniae* bacteria, and had a dose-dependent effect on cell viability. Ultrastructural analysis of treated bacteria revealed the abnormal arrangement of the chromosomal DNA. Our findings strongly indicated that both Ag/AgCl-NPs and AgCl-NPs have characteristics compatible with a strong potential for use in biomedical applications.

REFERENCES

[1] K. Paulkumar et al., Int. J. Green Chem. Bioprocess 3 (2013) 12-16.

[2] A. Haider et al., Adv. Mater. Sci. Eng. (2015) 1-16.

This research was supported by FAPERJ, CNPq and CAPES (Brazil).

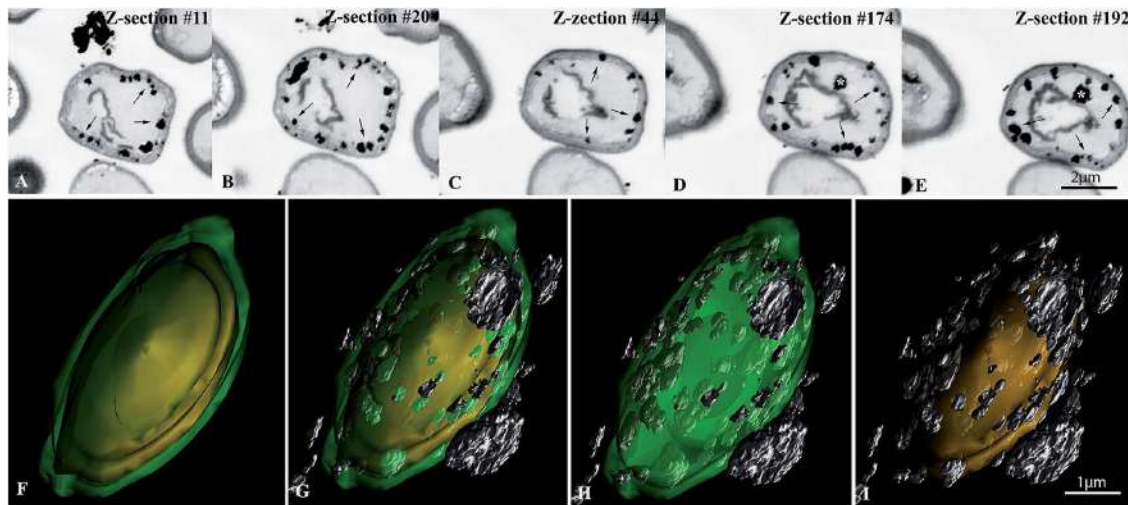
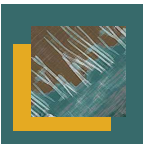


Figure 1: FIB/SEM analysis of *C. lusitanae* producing Ag/AgCl-NPs. (A–E) Z-slices from one representative yeast cell containing Ag/AgCl-NPs nanoaggregates (arrows) associated with the cell surface and outside the cells. Note that the nanoaggregates were mostly associated with the inner part of the cell wall (arrowheads). In few cases, nanoaggregates were found in the cell cytoplasm (D and E, asterisks). (F–I) Different views of a 3D model showing the spatial distribution of Ag/AgCl-NPs nanoaggregates inside and outside a yeast cell. Green, outermost cell wall layer; yellow, innermost cell wall layer; silver, Ag/AgCl-NPs nanoaggregates.

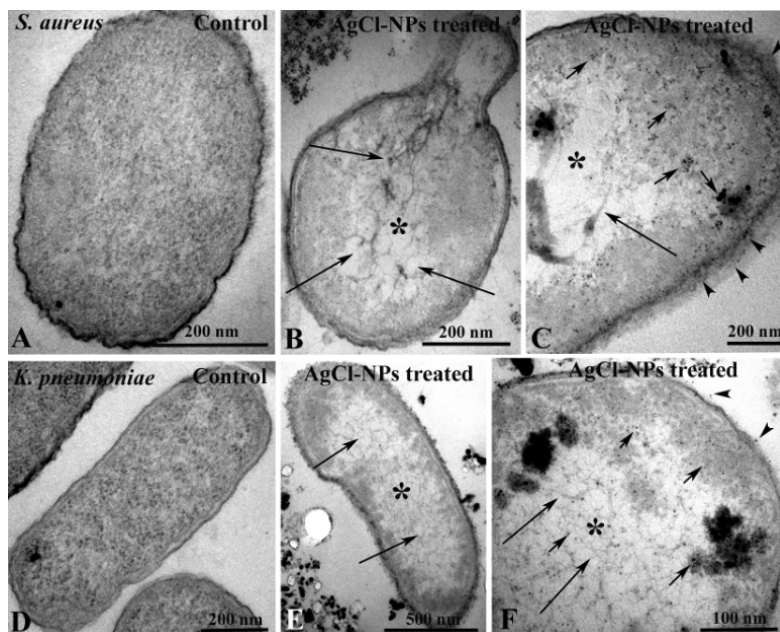


Figure 2: Ultrastructural analysis of *S. aureus* and *K. pneumoniae* treated with AgCl-NPs. Untreated *S. aureus* (Fig. 2A) and *K. pneumoniae* (Fig. 2D) cells showing the typical cell morphology of these pathogens, with electron-dense cytoplasmic material homogeneously distributed. *S. aureus* (Fig. 2B, C) and *K. pneumoniae* (Fig. 2E, F) treated with 157 and 247 $\mu\text{g mL}^{-1}$, respectively, showing the loss of chromosomal DNA (asterisks), generating an cytoplasmic electronlucent area. Big arrows in Fig. 2B, C (*S. aureus*) and Fig. 2E, F (*K. pneumoniae*) indicate filamentous structures likely corresponding to stretched DNA fibers and small arrows indicate the interaction of AgCl-NPs with bacterial surface. Fig. 2C and Fig. 2F show the accumulation of AgCl-NPs inside the treated *S. aureus* and *K. pneumoniae*, respectively.



NaX zeolite synthesis employing microwave heating source and its surface functionalization via esterification reaction.

Ana Paula Ribeiro Povinelli^{1*,a}, Gabriel Zazeri^{1,a}, Michelle Thomazine do Sacramento Mendes²,
Juliana Bergamasco Laurenti¹, José Geraldo Nery¹.

Department of Physics, Institute of Biosciences, Letters and Exact Sciences, UNESP-São Paulo State University, Campus of São José do Rio Preto, São Paulo, Brazil.

Structural Characterization Laboratory, department of materials, Federal University of São Carlos, UFSCAR, São Paulo state, Brazil.

Both authors have contributed equally for this work

*Email: anapovinelli@sjrp.unesp.br

Zeolites are aluminosilicate polycrystalline materials with properties such as nanosized pores, negative charges, channels and large surface area.¹ Due to these physicochemical properties, zeolitic materials have a wide range of applications such as ion exchangers, molecular sieves, heterogeneous catalysts and hemostatic coagulation agent.² Nevertheless, one of the drawback concerning the preparation of NaX zeolites is that the synthesis takes long time, which is about 2 days using conventional heat source³, therefore the synthesis time optimization of this zeolite without loss of crystallinity and phase purity is a real challenge. Another aspect is that when the zeolite is synthesized in a nanometric dimension, these materials tend to agglomerate when dispersed in a solvent following DLVO theory. In this context, this research aims at employing the microwave heating source in order to decrease the time of synthesis of this zeolite and modify zeolite's surface by changing silanols groups for hydrocarbon groups via esterification reaction. For this study, NaX zeolite was synthesized with the following gel composition: $1\text{Al}_2\text{O}_3:3.8\text{SiO}_2:4\text{Na}_2\text{O}:50\text{H}_2\text{O}$. The method used for the synthesis was sol-gel technique and the heating source was microwave heating, after the synthesis the material was modified via esterification reaction at 180°C using two different kinds of alcohols (1-propanol and 1-butanol). The synthesized material was characterized by X-rays diffraction (XRD) obtained from RigakuMiniFlex II (Tokyo, Japan) on a rotating anode source with a flat-plate Bragg-Brentano geometry, operating with $\text{CuK}\alpha$ radiation (wavelength = 1.5418 Å) at e 40 kV - 15 mA and scanning electron microscopy (SEM) obtained from FEI Magellan 400 L with Schottky thermal field emitter operated at a high accelerating voltage between 2 to 30 kV with gold coating and the differences between the original material and the modified material was analyzed from SEM images. According to XRD data (inset of figure 1(a)), NaX could be made without impurities under microwave heating with only 2 hours. Related to SEM figures with magnitude of 8000X, the figure 2(a) refers to NaX synthesized employing microwave heating without surface modification and it is showed that zeolites are agglomerated being impossible to measure the zeolite size. Figures 2(b) and 2(c) refer to NaX functionalized with 1-propanol and 1-butanol respectively, comparing these both images with figure 2(a) it is clear that the functionalization got the zeolites more dispersed. Figure 2(d) shows NaX without surface modification in a increase of 60000X and it is seen NaX agglomerated without possibility of size measurement whereas figures 2(e) and 2(f) that contains the same material after surface modification with in a increase of 60000X show clearly the size of NaX as being 200nm. In conclusion, this present work showed that the use of microwave decreased the synthesis time without loss the NaX phase and the functionalization of NaX zeolite was efficient to get the zeolite more dispersed avoiding agglomerates and allowing size measurements.

REFERENCES

[1] A. Corma. Chem. Rev. 95 (1995) 559–614



[2] T. A. Ostomel, Q. H. Shi, G. D. Stucky. *Journal of the American Chemical Society*, 128, (2006), 8384-8385.

[3] S. Mintova, V. Valtchev. *Studies in Surface Science and Catalysis*, 125, (1999), 141-148.

[4] D. Myers. *Surfaces, interfaces, and colloids*. Wiley-VCH. 1999

[5] This research was supported by CNPq and Fapesp (Brazil).

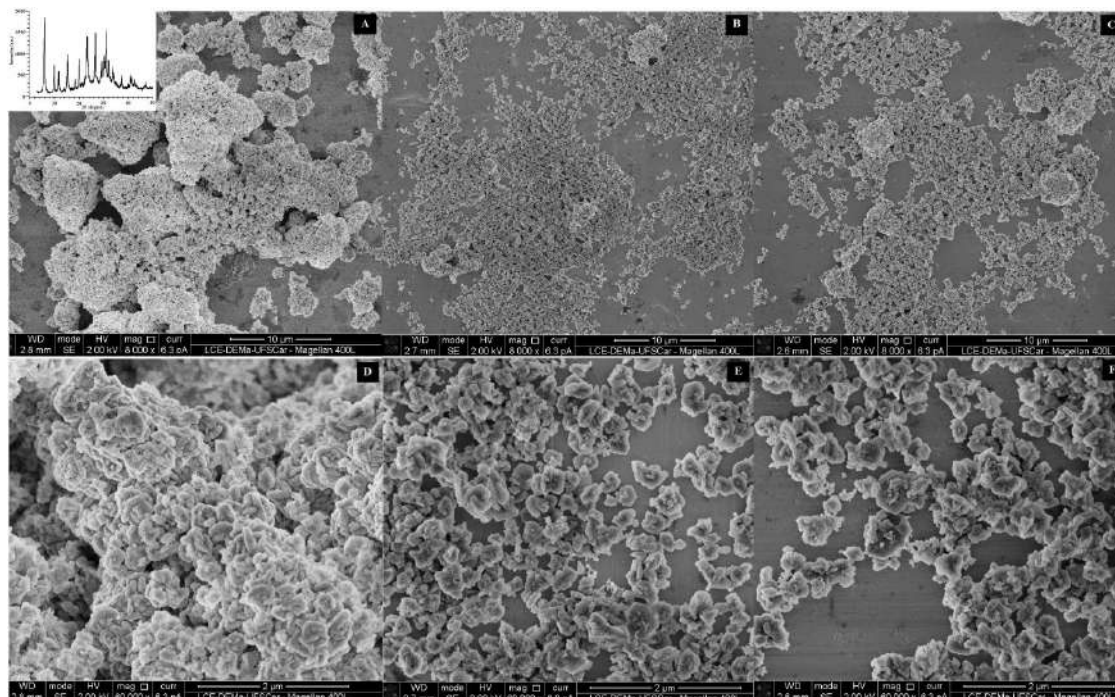


Figure 1: NaX synthesized under microwave heating (a) with magnitude of 8000X and XRD as inset (b) functionalized with 1-propanol and magnitude 8000X (c) functionalized with 1-butanol and magnitude 8000X (d) with 60000X (e) functionalized with 1-propanol and magnitude 60000X (f) functionalized with 1-butanol and magnitude 60000X.



Image-based high content analysis to access the antiproliferative effect of silver chloride and silver/silver chloride nanoparticles against glioblastoma multiforme

Nathalia Müller¹, Mateus Eugenio^{1,4}, Loraine Campanati³, Luís Maurício T. R. Lima², Celso Sant'Anna^{1,4*}

1. Laboratory of Microscopy Applied to Life Science - Lamav, Directory of Metrology Applied to Life Science, National Institute of Metrology, Quality and Technology, Duque de Caxias, RJ, Brazil.

2. Laboratory of Pharmaceutical Biotechnology, School of Pharmacy, Federal University of Rio de Janeiro – UFRJ, Rio de Janeiro, RJ, Brazil.

3. Laboratory of Cellular Morphogenesis, Federal University of Rio de Janeiro, Rio de Janeiro, RJ, Brazil.

4. National Institute of Science and Technology for Structural Biology and Bioimaging, Rio de Janeiro, RJ, Brazil.

*Email: cbfilho@inmetro.gov.brSB

High content analysis (HCA) is an automated microscopy technique that has notable advances over traditional toxicity testing methods by applying accurate multi-parameter measurements of phenotypes in many individual cells and whole organisms [1]. Glioblastoma is the most aggressive malignant primary brain tumor in humans. Patients with GBM have a poor prognosis, with a median survival of approximately 15 months. The treatment involves surgery, radiation therapy and chemotherapy with Temozolomide (TMZ), an oral first-line drug [2]. In this sense, silver-based nanoparticles have potential for cancer therapy. Their effectiveness against a broad spectrum of pathogenic bacteria, including antibiotic-resistant strains, as well as fungi, protozoa and virus is well known. In this work, HCA was performed to evaluate the antiproliferative effect of biologically synthesized silver chloride (AgCl-NPs) and silver/silver chloride (Ag/AgCl-NPs) nanoparticles against glioblastoma multiforme (GBM). AgCl-NPs and Ag/AgCl-NPs were obtained from bacteria and yeast cultures, respectively. Tumor and healthy astrocyte cells were treated with different concentrations of TMZ, AgCl-NPs or Ag/AgCl-NPs, as well as the combination of nanoparticles and TMZ. The antiproliferative assay on GBM02 cells showed that lower concentrations (0.1 – 1.0 $\mu\text{g mL}^{-1}$) of both nanoparticles were less effective than TMZ (9.7 – 29.1 $\mu\text{g mL}^{-1}$). At higher concentrations, GBM cell growth decreased by 95% and 82.5% after exposure to AgCl-NPs and Ag/AgCl-NPs, respectively. On the other hand, the treatment with TMZ reduced by 60% the GBM proliferation. The combined treatment (AgCl-NPs + TMZ and Ag/AgCl-NPs + TMZ) resulted in a GBM02 growth inhibition of 54 – 87%. Moreover, the antiproliferative assay on astrocytes showed that nanoparticles were less aggressive than TMZ. These findings pointed out to antitumoral activity of AgCl-NPs and Ag/AgCl-NPs with minimal effect on astrocyte cells. In addition, the data here presented evidenced that automated image-based analysis at cellular level was a reliable approach to explore the antiproliferative efficacy of nanoparticles against tumor cells.

REFERENCE

[1] C. M. Garvey *et al.* *Sci. Rep.*, vol. 6, no. February, p. 29752, 2016.

[2] M. Pineros, *et al.* *Cancer Epidemiol.*, vol. 44, pp. S141–S149, 2016.

This work was supported by FAPERJ



Table 1 – Average percent of proliferation inhibition after different treatments

Treatment ($\mu\text{g mL}^{-1}$)	GBM02 / Astrocytes (%)		
	24 h	48 h	72 h
AgCl-NPs (0.1)	3.6 (± 6.0) / 3.0 (± 0.9)	5.3 (± 10.5) / 4.1 (± 1.0)	7.7 (± 13.7) / 4.1 (± 0.6)
AgCl-NPs (0.5)	1.9 (± 7.3) / 1.0 (± 9.5)	2.6 (± 3.7) / -0.3 (± 11.0)	7.6 (± 7.1) / -0.1 (± 11.1)
AgCl-NPs (1.0)	49.8 (± 5.7) / -1.1 (± 2.5)	68.1 (± 1.5) / -2.6 (± 6.2)	76.5 (± 0.1) / -1.2 (± 4.1)
AgCl-NPs (2.5)	46.0 (± 1.6) / -9.2 (± 13.2)	80.5 (± 4.1) / -10.8 (± 15.6)	92.2 (± 2.9) / -13.0 (± 17.1)
AgCl-NPs (5.0)	52.9 (± 3.9) / 5.8 (± 1.2)	86.3 (± 1.4) / 2.4 (± 2.8)	95.8 (± 0.3) / -0.1 (± 5.1)
Ag/AgCl-NPs (0.1)	5.4 (± 3.8) / 1.6 (± 3.8)	11.6 (± 6.7) / <u>0.3 (± 8.0)</u>	18.1 (± 8.2) / <u>0.1 (± 4.1)</u>
Ag/AgCl-NPs (0.5)	5.2 (± 3.8) / <u>0.9 (± 3.9)</u>	11.2 (± 6.3) / <u>2.3 (± 7.3)</u>	13.6 (± 9.3) / <u>3.1 (± 9.5)</u>
Ag/AgCl-NPs (1.0)	10.4 (± 2.7) / 1.9 (± 2.1)	18.4 (± 6.0) / <u>0.2 (± 5.5)</u>	22.9 (± 6.7) / <u>2.0 (± 4.8)</u>
Ag/AgCl-NPs (2.5)	35.5 (± 1.3) / 5.8 (± 3.7)	65.3 (± 2.1) / 16.9 (± 5.1)	75.5 (± 1.3) / 8.6 (± 4.8)
Ag/AgCl-NPs (5.0)	35.3 (± 2.8) / 8.6 (± 5.5)	65.5 (± 2.4) / 27.5 (± 0.7)	82.5 (± 1.5) / 27.0 (± 7.1)

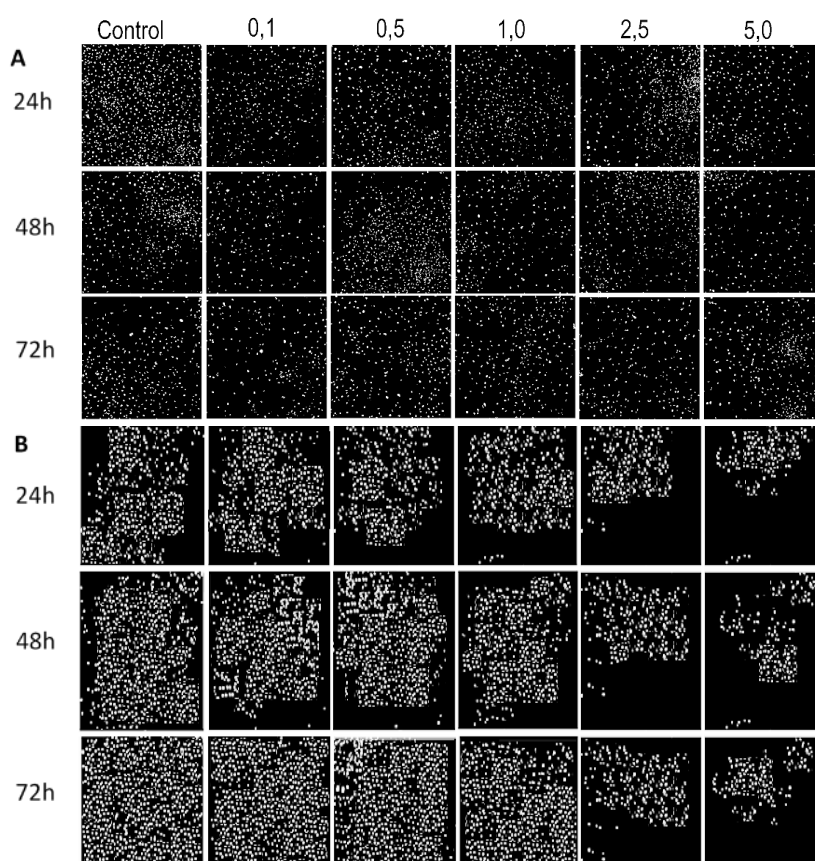


Figure 1. Representative images of antiproliferative test on GBM02 cells and treated with AgCl NPs (A) and Ag/AgCl-NPs (B). The images represent the control ($0 \mu\text{g mL}^{-1}$) and different concentrations of AgCl NPs and Ag/AgCl-NPs ($0.1, 0.5, 1.0, 2.5$ and $5.0 \mu\text{g mL}^{-1}$) for 72 h. All images are representative of one of the six fields that images were obtained to perform the graphics. Scale bar: $50 \mu\text{m}$.



Titanium rutile nanoparticles: a glance of nanobiointerface applied to sunscreens

P. L. Sanches¹, S. Gemini-Piperni², W. Souza³, André Linhares Rossi², L.A. Rocha⁴, R. Borojevic⁵, M. Granjeiro³, M. Benchimol¹, A. R. Ribeiro¹

1. Postgraduate Program in Translational Biomedicine, University of Grande Rio, Duque de Caxias, Brazil (Email: sara.gemini@hotmail.com)
2. Applied Physics Department, Brazilian Center for Physics Research- CBPF Rio de Janeiro, Brazil
3. Directory of Life Sciences Applied Metrology, National Institute of Metrology Quality and Technology, Rio de Janeiro, Brazil
4. Physics Department, University Estadual Paulista, Bauru, Brazil
5. Center of Regenerative Medicine, Faculty of Medicine - FASE, Petrópolis, Brazil

Nanoparticles (NPs), particularly rutile titanium dioxide nanoparticles (TiO₂ NPs) are regularly used as inorganic physical sun-blockers due to their photo protective capacity [1]. However, the interactions between skin cells and NPs are poorly investigated [2]. The aim of this study is to investigate the interactions between NPs and biological milieu and how those interactions can predict NPs internalization in skin cells, particularly fibroblasts and keratinocytes. Firstly, a dispersion protocol for rutile TiO₂ NPs was established: physical and chemical characterization of titanium nanoparticles was performed using dynamic light scattering (DLS) to evaluate agglomerates size, and X-ray diffraction to confirm that titanium dioxide nanoparticles crystallographic phases was rutile. To reduce the natural agglomeration of rutile nanoparticles, a dispersion protocol was performed before the transmission electron microscopy (TEM) analysis. Results showed that rutile NPs were successfully dispersed in both cell culture media, using BSA as stabilizing agent. After 48 hours, the skin cells internalization of the TiO₂ rutile nanoparticles was observed by TEM. Despite to the high internalization of TiO₂ nanoparticles, no toxicity was detected in cytometer analysis of fibroblast cells. In contrast, keratinocytes showed an increase of death after exposition to high dose of NPs. The nano-bio interactions in two different culture media (Dulbecco Modified Eagle Medium (DMEM) High Glucose and Keratinocyte Growth Medium (KGM)) suitable for *in vitro* toxicological studies for cosmetic applications, was explored by TEM and Element Dispersive Spectroscopy (EDS) analyses as well by proteomics. Results showed the presence of a specific bio-complex adsorbed to the NPs. This bio-complex is rich in ions, such as calcium and phosphorus, and proteins, such as serum albumin, thrombospondin and fibronectin, which are involved in regulating cell-to-cell and cell-to-matrix interactions and in internalization process. This EDS analysis associated with mass spectrometry showed that the bio-complex composition is dependent upon the composition of biological milieu as well as the physicochemical characteristics of the nanoparticles surface. Those results hypothesize that the bio-complex can mask nanoparticles, modulating its internalization in human skin cells.

REFERENCES

- [1] Smijs, T. & Pavel., *Microsc.*, NSA 95 (2011)
- [2] Newman, M. D. et al, *Journal of the American Academy of Dermatology* 61, (2009) 685–692.
- [3] This research was supported by FAPERJ, INMETRO, UNIGRANRIO, and CBPF

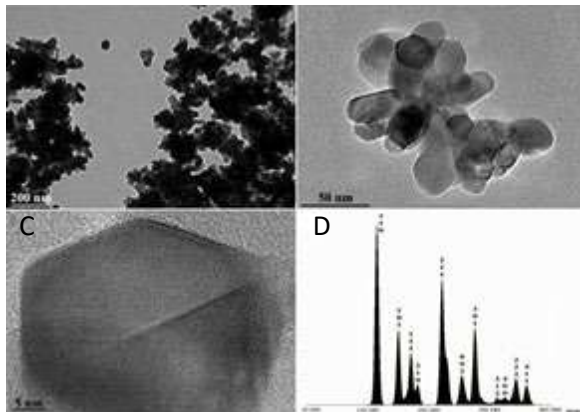
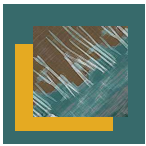


Figure 1:

TEM characterization of rutile nanoparticles: (A) Image of rutile agglomerates, (B) small agglomerates and (C) primary particle size, (D) SAED indicating the rutile phase.

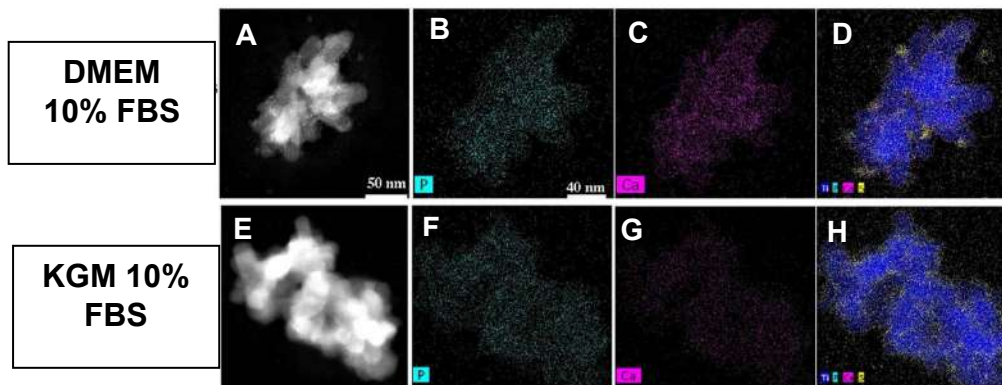


Figure 2: Physicochemical characterization of rutile dispersions in cell culture media: dark-field STEM images showing where the corresponding elemental maps were obtained; (A and E) STEM micrograph of rutile nanoparticles in medium, (B and F) STEM/EDS P-K map; (C and G) STEM/EDS Ca-K map and (D and H) STEM/EDS overlay of Ti, P, Ca, S for rutile nanoparticles in DMEM 10% FBS and KGM 10% FBS. EDS spectrum.

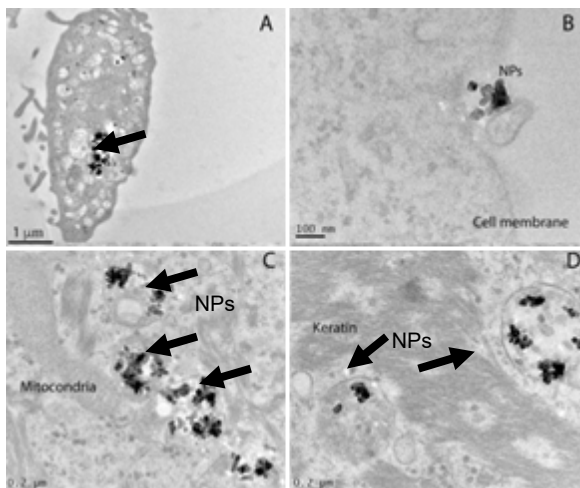


Figure 6: TEM micrographs of primary human keratinocytes cells after rutile exposure: (A) a whole keratinocyte with internalized NPs (black arrow), (B) NPs in process of internalization just on the cell membrane, (C) NPs (black arrows) in vesicles and across cell cytoplasm and (D) high magnification of vesicles with NPs (black arrows) contents.



Coumarin-containing Thermoresponsive Hyaluronic Acid-based Nanogels as Delivery Systems for Anticancer Chemotherapy

Talitha Fernandes Stefanello^{1,4,5*}, Benoit Couturaud², Anna Szarpak-Jankowska¹, David Fournier², Benoit Louage³, Francielle Pelegrin Garcia^{1,4}, Celso Vataru Nakamura⁴, Bruno De Geest³, Patrice Woisel², Boudewijn van der Sanden⁵, Rachel Auzély-Velty^{1*}

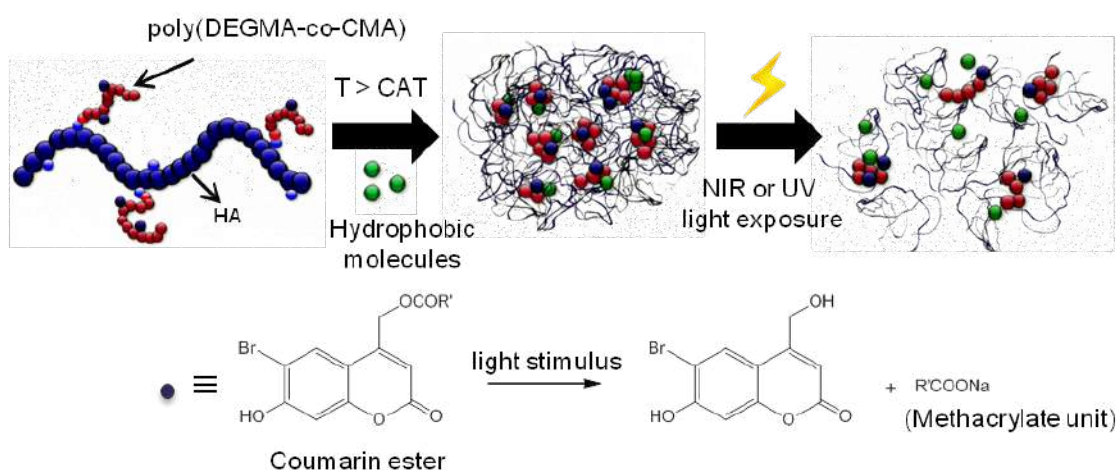
1. Grenoble Alpes University, CERMAV-CNRS, Grenoble, France
2. Unité des Matériaux et Transformations, University Lille 1, Villeneuve d'Ascq, France
3. Department of Pharmaceutics, Ghent University, Ghent, Belgium
4. Laboratory of technological innovation in the development of pharmaceuticals and cosmetics, State University of Maringa, Maringa, Brazil
5. Intravital Microscopy Platform Grenoble, France Life Imaging, Clnatec, Grenoble, France

*Email: talitha_stefanello@hotmail.com

Multi-stimuli responsive nanogels based on biocompatible hydrophilic polymers have emerged as promising drug delivery systems to improve the anticancer therapy with hydrophobic drugs, through increase of circulating-time in the bloodstream, tumor-targeting and reduction of systemic toxicity[1]. This study reported the synthesis, characterization and biological perspectives of light- and thermoresponsive hyaluronic acid (HA)-based nanogels containing coumarin as photocleavable groups[2] (Scheme). Our design strategy relied on the incorporation of coumarin moieties within thermoresponsive ethylene glycol-based copolymers followed by their grafting onto HA. We hypothesized that these photochromic moieties could play a dual role in both increasing the colloidal stability of the nanogels in the bloodstream due to their hydrophobicity and leading to nanogel dissociation upon light exposure at the target site. Self-assembled nanogels were obtained by temperature increase above 27 °C, exhibiting a hydrodynamic radius ~110 nm. Removal of coumarin moieties by UV irradiation induced an increase in the critical aggregation temperature of the HA-derivatives, which would result in nanogels destabilization and disruption at body temperature. Poor-water soluble molecules, i.e. fluorescent di-strylbenzene derivative (DSB) and paclitaxel, were incorporated to hydrophobic nanodomains into nanogels as hydrophobic molecule models. DSB-loaded nanogels were successfully uptaken by cancer cells overexpressing the CD44 receptor of HA (HeLa cells) at a concentration-dependent manner, and a lysosomal location were observed for HA-derivatives, whereas the hydrophobic dye seems to scape from high-content organelles (Figure). Intravenous administration of DSB-loaded nanogels in mice with xenografted Hela tumors demonstrated that our nanogels remain circulating in the bloodstream for at least 4 h, exhibiting a gradual accumulation of DSB fluorescence in the blood vessels, probably due an internalization by phagocytic cells. More pronounced accumulation was observed for tumoral vessels and, 24h post-administration, DSB fluorescence in normal ear tissue and in the tumor periphery adjacent to blood vessels was verified. Our findings indicate that coumarin-containing HA-based nanogels may be a promising strategy for anticancer chemotherapy[3].

REFERENCES

- [1] G. Soni, K.S. Yadav, Saudi Pharm. J., 24 (2016), 133.
- [2] S. Kumar, J.-F. et al., J. Mater. Chem., 22 (2012), 7752.
- [3] This research was supported by Agence Nationale de la Recherche - Centre National de la Recherche Scientifique (ANR-CNRS).



Scheme. Formation of light and thermoresponsive HA-poly(DEGMA-co-CMA) nanogels by temperature increase and dissociation upon light exposure (CAT shift).

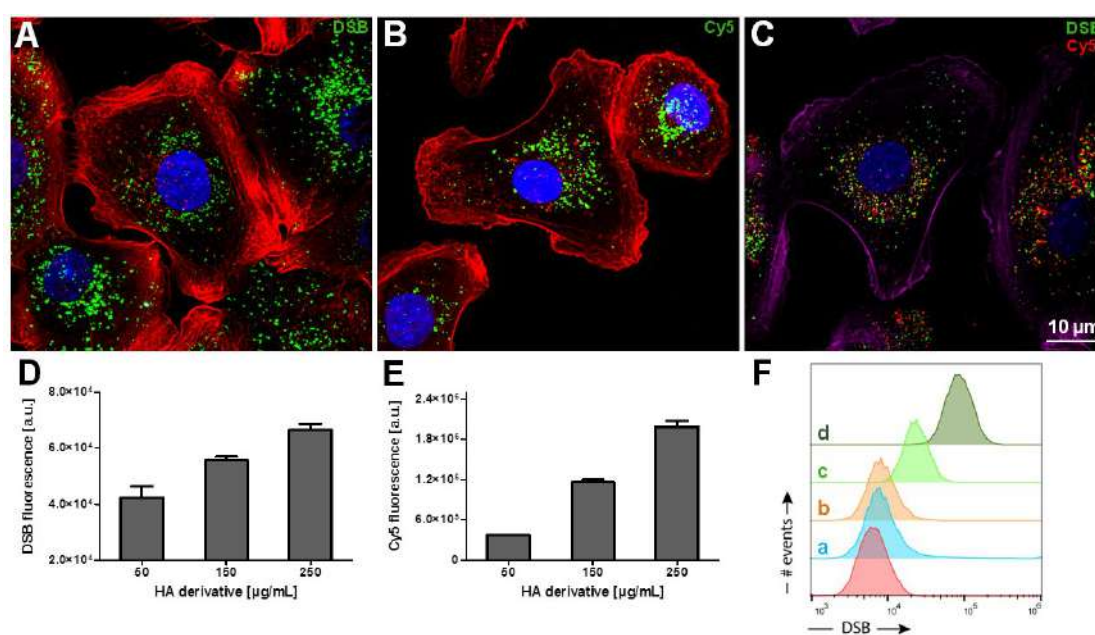


Figure 2. Cellular uptake of HA-m-poly(DEGMA-co-CMA) nanogels by HeLa cells. Confocal microscopy images of HeLa cells incubated for 16h with (A) DSB-loaded nanogels, (B) cyanine5-labelled nanogels and (C) DSB-loaded cyanine5-labelled nanogels. Cell nucleus was stained blue with Hoechst, cell membrane was stained red with Alexa Fluor667 conjugated phalloidin (violet in C), DSB is visualized in the green fluorescence channel and cyanine5 in the red fluorescence channel (green in B). Colocalization of cyanine5 and DSB fluorescences is characterized by yellow color. Flow cytometry analyses of HeLa cells incubated with different concentrations (50, 150 and 250 $\mu\text{g mL}^{-1}$) of (D) DSB-loaded nanogels and (E) cyanine5-labelled nanogels. (F) Flow cytometry histograms from HeLa cells incubated with unfiltered (a) and filtered (b) solutions of native HA and free DSB, HA-m-poly(DEGMA-co-CMA) 3% (250 $\mu\text{g mL}^{-1}$) (c) and 5% nanogels (d).



Temperature-controlled particle size distribution of *Camellia sinensis* silver nanoparticles synthesized

*Wanderson Juvencio Keijok¹, Jairo Pinto de Oliveira¹, and Marco Cesar Cunegundes Guimarães¹

1. Laboratório de Ultraestrutura Celular Carlos Alberto Redins - LUCCAR, Universidade Federal do Espírito Santo-UFES - Av. Marechal Campos, 1468, Maruípe, Vitória, E.S. 29.042-755 – Brasil, Tel.: 55. 27.3335 7365,

*Email: marco.guimaraes@ufes.br

In the present work, we described the synthesis of silver nanoparticles (AgNP's) using an aqueous extract of green tea (*Camellia sinensis* L. Kuntz), a beverage commonly used in Asian countries contains compounds having strong antioxidant capacities. UV-vis spectroscopy (Fig. 1), Fourier transform infrared spectroscopy (FTIR), Energy-dispersive X-ray spectroscopy (EDS) and transmission electron microscopy (TEM) were performed to characterize the formation of AgNP's. TEM (Fig. 2) and EDS were used to view shapes of AgNP's and composition, while FTIR was employed to determine and characterize the wide of functional groups that stabilize AgNP's. Lastly, we proposed this experiment based on antioxidant activity of the extract. The UV-Vis spectra gave surface plasmon resonance peak around 450 nm. FTIR showed in AgNP's the presence of different functional groups. EDS revealed elemental analysis of particles composition. *Camellia sinensis* extract as a potent reducing agent converts silver ions to AgNP's in a rapid, cleaner, non-toxic, environmentally friendly manner [1][2].

Keywords: Green synthesis, silver nanoparticle and nanotechnology.

REFERENCES

[1] KIMLING, J.; MAIERM.; OKENVE, B.; KOTAIDIS, V.; BALLOT, H.; PLECH. A. Turkevich Method for Gold Nanoparticle Synthesis Revisited. *J. Phys. Chem. B*, 2006, 110 (32), pp 15700–15707. Publication Date (Web): July 21, 2006 (Article). DOI: 10.1021/jp061667w.

[2] GADE, A.; GAIKWAD, S.; TIWARI, V.; YADAV, A.; INGLE, A. and RAI, M.

“Biofabrication of silver nanoparticles by *Opuntia fícus-indica*: in vitro antibacterial activity and study of the mechanism involved in the synthesis”. *Current Nanoscience*, vol.6, no.4, pp.370-375. 2010.

Acknowledgements

This work was supported by the Laboratory of Cellular Ultrastructure Carlos Alberto Redins (LUCCAR), CAPES, FINEP and LABIOM.

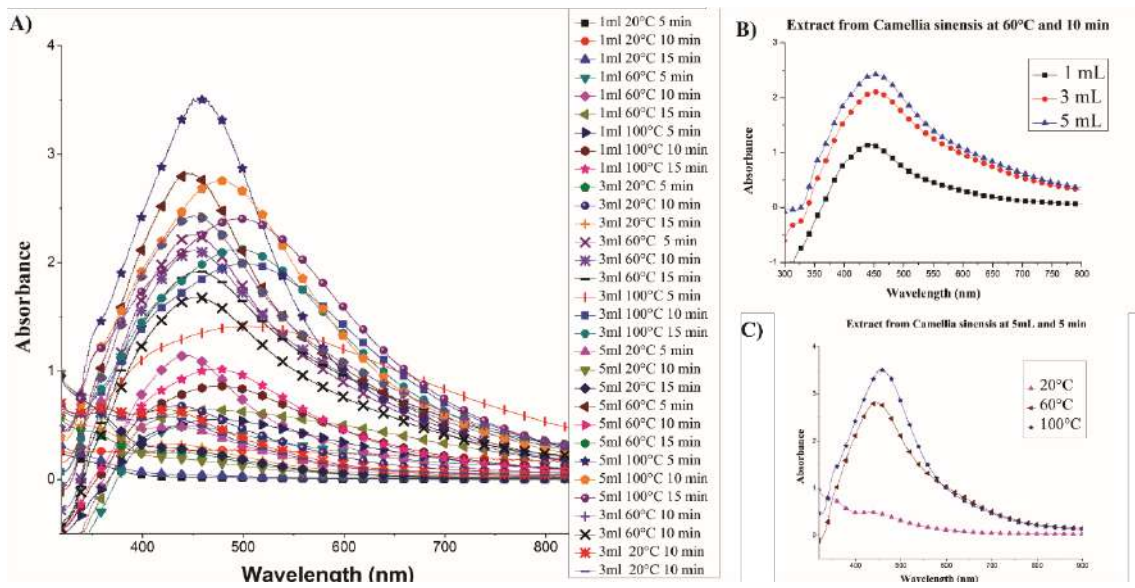
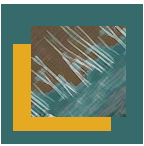


Figure 1. UV-Vis electronic spectra showing the different levels of absorbance of the conditions evaluated with the plant extract of *Camellia sinensis*. Full Spectrum of Factorial Planning (A) and Spectra of Significant Variables: Concentration (B) and Temperature (C).

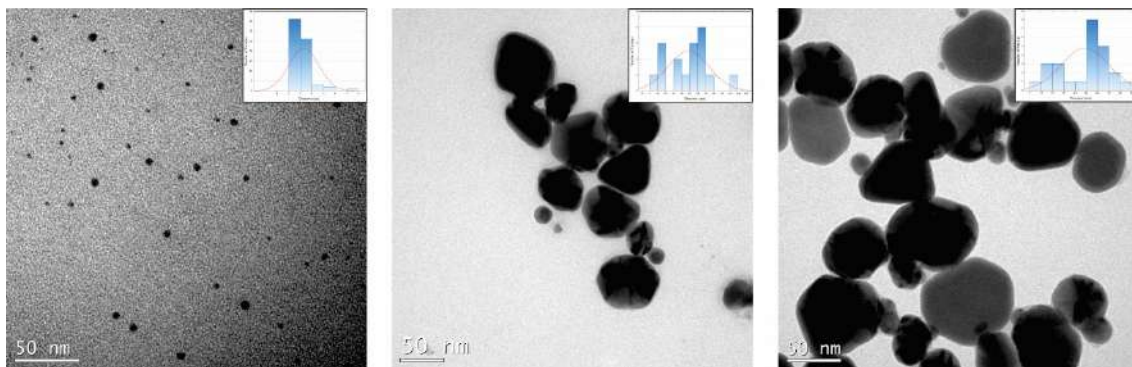


Figure 2. Histogram of distribution of the .AgNP's size obtained from the TEM images. Synthesis of 5 ml of the extract of *Camellia sinensis* at 20 ° C (B) 60 ° C (C) and 100 ° C (D).



Nanoparticles Characterization de Magh-Rh₂(H₂cit)₄

Weskly Feitosa Lago^{1*}, Marcelo Henrique Sousa², Sônia Nair Bão³

1. Mestranda em Nanociência e Nanobiotecnologia, UnB-Brasília. Email: weskly20@hotmail.com.
 2. Faculdade de Ceilândia, UnB-Brasília.
 3. Depto. Biologia Celular, Instituto Ciências Biológicas, UnB.
- *Email: snbao@unb.br.

The magnetic nanoparticles (NPs) allow the drug incorporation that can be directed to their place of action through a magnetic field. When coated with rhodium (II) citrate compound [Rh₂(H₂cit)₄], they reduce the side effects of the drug; besides, they are cytotoxic to tumor cells [1]. To understand the physicochemical properties or synthetic identity of NP (size, shape, load, pH, among others), has a crucial importance, mainly, when it comes to study in a biological environment. This work proposes the characterization of NPs of Magh-Rh₂(H₂cit)₄ will be used, subsequently, to study about protein corona. The proposed synthesis route was previously described [2]. To prepare the fluid, the amount of the rhodium (II) citrate solution was added to 0.788 mL of precursor acid fluid (γ-Fe₂O₃). The sample volume was measured to 10 mL and pH adjusted to 7 with diluted NaOH solution. There was peptized magnetic nanoparticles and stable solution formation. The sample was measured by laser induced breakdown spectroscopy (LIBS) and the final maghemite concentration was 38.07 mmol/L and rhodium (II) citrate was 0.37 mmol/L. To characterize the distribution of diameter and surface charge of NPs, the Zetasizer Nano ZS (Malvern) equipment was used. The morphological characterization and measurement were obtained from the MET (Electronic Microscopy of Transmission), MEV (Scanning Electronic Microscope) and by the technique of DRX (Diffraction of X-Rays). The NPs show midsize hydrodynamic diameter 147,2±2,962, Zeta Potential of surface, ZP -40 mV, with monodisperse characteristic with PDI (Polydispersity Index) 0,173±0,014. Figure 1 (A) shows a sample micrograph Magh-Rh₂(H₂cit)₄, obtained in microscope of transmission JEOL sample JEM 2010. The NPs perceived are approximately spherical and have polydispersity in size. Those characteristics were described in other works [1,2]. The distribution deduction in size for the samples were made, calculating the perimeter of 250 particles. The figure 1 (B) presents the histogram of size corresponding to the particles displayed in micrograph. The mode value was 9 nm and average 9.79 nm±1.707. Figure 2 (A) shows the X-ray diffraction spectrum. In the case of the measured samples, the structure spinel cubic type is confirmed [3] (Figure 2 B). The midsize diameter found in dRX was 9.75 nm which corroborates with the result found in the MET measurement. Figure 3 (A) shows the morphology of agglomerates Magh-Rh₂(H₂cit)₄ NPs analyzed in SEM. When performing Energy Dispersive Spectroscopy (EDS) (Figure 03 - B and C), the chemical elemental composition of the sample under analysis was obtained. Carbon, Oxygen and Iron elements were detected at the two points chosen in the image. Through the characterization carried out, it is concluded that Magh-Rh₂(H₂cit)₄ sample has stable characteristics and can be used for further biological studies, such as the study of protein corona and cell viability.

Acknowledgment: CAPES, CNPq, FAPDF and FINEP.

REFERENCES

- [1] Chaves N.L et al. *Journal of Nanomedicine & Nanotechnology* 6.5 (2015): 1.
- [2] Nunes E.S et al. *Journal of nanoparticle research* 15.6 (2013): 1683.
- [3] Oliveira L.C.A, Fabris J.D & Pereira M.C. *Quim Nova* 36 (2013): 123-130.

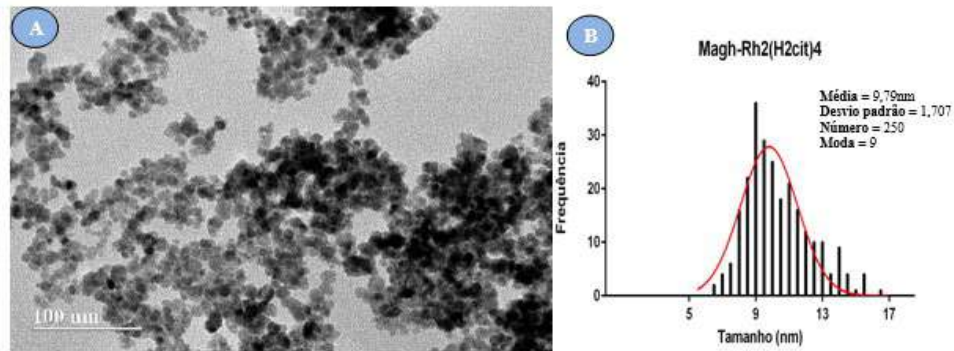
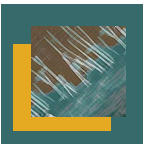


Figure 01 - Morphological characterization and measurement of maghemite nanoparticles by transmission electron microscopy. (A) Micrograph of magnetite nanoparticles coated with rhodium (II) citrate (Magh-Rh₂(H₂cit)₄). (B) Histogram of diameters distribution of Magh-Rh₂(H₂cit)₄. Medium size: 9.79 nm±1.707; Number: 250; mode: 9 nm (*GraphPad Prism 6.0*).

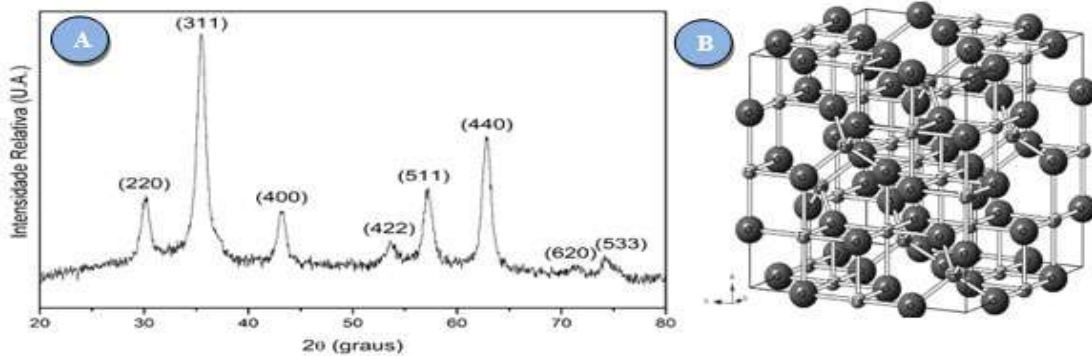


Figure 2 - X-rays Diffractogram of Magh-Rh₂ (H₂cit)₄ compound (A). Crystal structure of Maghemite (B) [3].

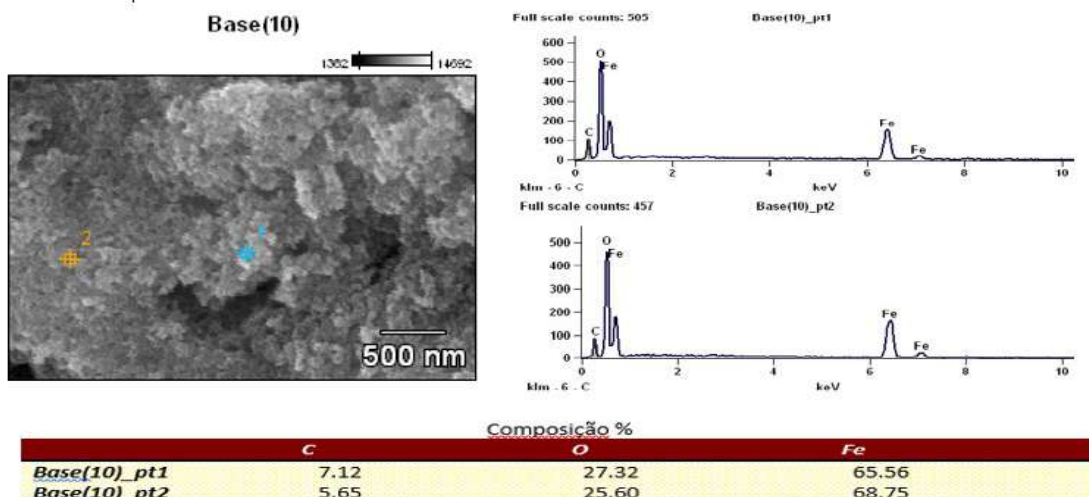


Figure 03 - Morphological characterization and composition of maghemite nanoparticles by Scanning Electron Microscopy. (A) Electronic micrograph of magnetite nanoparticles coated with rhodium (II) citrate (Magh-Rh₂(H₂cit)₄). (B) Graphic of sample composition by EDS/EDX. (C) Values as a percentage of composition elements detected in the two points marked on the micrograph (pt1 and pt2).

E.C. GONÇALVES
EDITOR CIENTÍFICO